LOW-DIMENSIONAL SYSTEMS AND SURFACE PHYSICS

Contribution to the theory of ''incompressible'' regions in an inhomogeneous magnetized 2*D* electronic system

V. B. Shikin

Institute of Solid-State Physics, Russian Academy of Sciences, 142432 Chernogolovka, Moscow District, Russia

Yu. V. Shikina

Institute of Microelectronics Technology and Ultrapure Materials, Russian Academy of Sciences, 142432 Chernogolovka, Moscow District, Russia

(Submitted November 17, 1998)
Fiz. Tverd. Tela (St. Petersburg) **41**, 1103–1109 (June 1999)

A modification of the theory of ''incompressible'' regions in an ideal spinless inhomogeneous magnetized $2D$ electronic system near points on the electron density profile $n(x)$ with an integer filling factor is proposed. Such regions leads to the appearance of a finite capacitance between the parts of the $2D$ system that are separated by an incompressible channel, so that capacitive methods can be used to investigate such a system. The Corbino configuration is especially convenient for these purposes. The parameters of the ''incompressible'' channel in a Corbino disk with a spatially inhomogeneous $2D$ electronic system in the presence of an individual point, near the channel, on the electron density profile with an integer magnetic filling factor are determined. The magnetocapacitance between the edges of the Corbino disk separated by an incompressible interlayer is found for cases of practical interest. It is shown that this magnetocapacitance contains direct information about the width of the integer strip. © *1999 American Institute of Physics.* [S1063-7834(99)03706-5]

References 1 and 2 give a description of the ''incompressible'' regions near points x_i on the electron density profile $n(x)$ where the filling factor is an integer $v=1,2,3,\ldots$ for a two-dimensional ($2D$) electronic system in a magnetic field normal to the plane of the system

$$\nu_i=\pi l_H^2 n(x_i), \quad l_H^2=c\hbar/eH, \tag{1}$$

l_H is the magnetic length, and H is the intensity of the magnetic field.

At low temperatures $T\ll\hbar\omega_c$ (ω_c is the cyclotron frequency) the diagonal conductivity of the integer strip is exponentially small, and the strip becomes essentially an insulator. Under these conditions, to investigate the properties of integer channels arising, as a rule, in inhomogeneous two-dimensional charged systems it is natural to consider the capacitive characteristics of the electronic system in a magnetic field.

The objective of the present work is to clarify the role of the incompressible regions in the problem of the magnetocapacitance of $2D$ electronic systems in contact with additional electrodes. We assume the nonuniformity of the $2D$ electronic system giving rise to incompressible (integer) regions in a quantizing field to be due mainly to phenomena arising when the $2D$ system comes into contact with metal electrodes. Thus, for a one-dimensional unscreened configuration metal–$2D$-system–metal the contact electron-density perturbation has the form[3,4]

$$\delta n_0(x)=\frac{\kappa w\phi_{ab}}{\pi^2 e(w^2-x^2)}. \tag{2}$$

Here ϕ_{ab} is the contact potential difference, κ is the permittivity, and $2w$ is the characteristic size of the $2D$ system in the x direction. The approximation (2) is applicable far from the points $x=\pm w$ of the boundary of the $2D$ region for $a_b^*\ll w$, where a_b^* is the effective Bohr radius.

It is obvious that the perturbation (2) is not compatible with the optimal conditions for observing the quantum Hall effect (QHE) and therefore for observing a finite capacitance between the edges of a Corbino disk (it is well known that a necessary condition for the QHE and the associated features of the magnetocapacitance is spatial inhomogeneity of the electron density of the $2D$ system). The distinguishing freatures of the QHE and, specifically, the appearance of a finite edge–edge capacitance for a Corbino disk appear only to the extent that flat diamagnetic sections arise on a smooth dependence $n(x)$.

The contribution of incompressible regions to the magnetocapacitance of a $2D$ system is analyzed assuming that the metal edges are flat and lie in the same plane as the $2D$ system. For simplicity, we shall assume the Corbino disk to be quasi-one-dimensional, which is valid if

$$R_2-R_1\ll\frac{1}{2}(R_2+R_1), \tag{3}$$

where R_2 and R_1 are the outer and inner radii of the two-dimensional Corbino region. It is obvious that the main property of Corbino samples—the closed nature of the current lines in the Hall direction—remains also in the quasi-one-dimensional approximation (all quantities are independent of the y coordinate, where the y axis lies in the direction of the Hall current).

The problem of the magnetocapacitance of an unscreened Corbino disk with a nonuniform electron density is of special interest. As noted above, the concept of capacitance between the edges of the Corbino disk is meaningless in the absence of magnetic flattening of the electron density. The formation of an integer channel in an inhomogeneous Corbino disk and the observable consequences of the appearance of such a channel are discussed in Sec. 1.

The effect of the controlling electrode on the magnetocapacitance of a $2D$ system is investigated in Sec. 2.

The problem of metastable integer channels in a Corbino disk with a current is studied in Sec. 3.

We believe that the magnetocapacitance is an effective tool for studying the properties of incompressible regions in spatially inhomogeneous $2D$ electronic systems.

1. MAGNETOCAPACITANCE OF AN UNSCREENED CORBINO DISK

The starting assumptions of our analysis are as follows. Assuming that an insulating strip of magnetic origin with dimensions $a<w$ can form at the center of the disk, it is easy to correlate the presence of such a strip with the appearance of finite capacitance C between the edges of the $2D$ system. The problem reduces to determining the function $C(a)$ and the relation between a and the characteristics of the $2D$ system in a magnetic field.

1) For $a \ll w$ the effect of the ends $\pm w$ on the capacitance of the $2D$ system can be neglected. Then

$$C = 2\pi R \ln\frac{R}{a}, \quad R = (R_2 + R_1)/2, \tag{4}$$

if the relation (3) holds. Therefore determining the edge–edge magnetocapacitance of a Corbino disk under QHE conditions reduces to calculating the width $2a$ of the integer channel.

2) The calculation of a is largely based on the ideas of Ref. 2.[a)] The starting point is the requirement that the electrochemical potential μ be constant along the magnetized $2D$ system. Assuming the system to be ideal and spinless (just as in Ref. 2) and confining ourselves to filling factors $\nu<2$, we have

$$\mu(x) = e\varphi - T\ln S(\nu) = 0, \quad -w \leqslant x \leqslant +w, \tag{5}$$

$$S(H,\nu) = \frac{1}{2}\left(\frac{1}{\nu}-1\right) + \sqrt{\frac{1}{4}\left(\frac{1}{\nu}-1\right)^2 + \epsilon\left(\frac{2}{\nu}-1\right)}, \tag{6}$$

$$\nu(x) = \pi l_H^2 n(x), \quad n(x) = n_s + \delta n(x),$$

$$\epsilon = \exp\left(-\frac{\hbar\omega_c}{T}\right) \ll 1, \tag{7}$$

$$\varphi'(x) = \frac{2e}{\kappa}\int_{-w}^{+w}\frac{\delta n(s)}{x-s}\,ds, \tag{8}$$

and $\delta n(x)$ is the deviation of the electron density from the equilibrium value n_s in a $2D$ system with no contacts.

In the absence of a magnetic field the continuity of the electrochemical potential along the Corbino disk leads to the appearance of a disturbance $\delta n_0(x)$ (2). In the range $-w \leqslant x \leqslant +w$ the electric potential is approximately constant (with the exception of the neighborhood of the points $\pm w$), and the conductivity is metallic.

In a strong magnetic field the situation changes in regions where the electron density satisfies the condition (1). At sufficiently low temperatures

$$T \ll \hbar\omega_c \tag{9}$$

the term $T\ln S$ in Eq. (5) changes sharply as a function of ν near $\nu=1$. In the limit $T\to 0$ this change reduces to a discontinuity

$$-T\ln S = \begin{cases} 0, & \nu \to 1-0, \\ \hbar\omega_c, & \nu \to 1+0, \end{cases} \tag{10}$$

with a jump that is independent of temperature T (the width of the transitional region $\sim T/\hbar\omega_c$).

Under the condition (9) the property (10) strongly influences the electron density distribution in the range $-w \leqslant x \leqslant +w$, distorting the distribution (2). Equilibrium in a $2D$ system is now determined by the competition between the electrostatic energy $e\varphi(x)$ and the magnetic contribution $T\ln S(\nu)$ in the electrochemical potential, the required scale $T\ln S$ being determined by small changes in density $\delta n(x) \ll n_s$. As a result, the magnetic part of $\mu(x)$ perturbs the electron density distribution (1) near points x_i. In what follows we shall investigate the character of this disturbance. It can be assumed that the situation near the points (1) resembles a contact situation with the potential difference $e\phi_{ab} = \hbar\omega_c$. For this reason a restructuring of the electron density, similar in some degree to the distribution (2) at the ends $x = \pm w$, should be expected near the points (1).

In reality the magnetically induced electron-density deformation does not undergo jumps at the points x_i. This is easily shown by writing the relation (5) near one of the points (1)

$$-\left.\frac{d\nu(x)}{dx}\right|_{x-x_i} = \frac{2e\epsilon^{1/2}}{T}\frac{d\varphi}{dx}. \tag{11}$$

It is obvious that here $\mu(x)$ flattens out to within exponential accuracy (the derivative (11) approaches zero as $\epsilon\to 0$).

In connection with the remark made above, without pretending to solve Eqs. (5)–(8) exactly for $\delta n(x)$, we shall use as the starting point the solution of the electrostatic problem from Ref. 2, where allowance is made for flattening of the electron density near the points (1). We are talking about the harmonic problem for an electric potential with boundary conditions

$$\varphi(x) = 0, \quad a \leqslant |x| \leqslant w; \quad n(x) = \text{const}, \quad |x| \leqslant a. \tag{12}$$

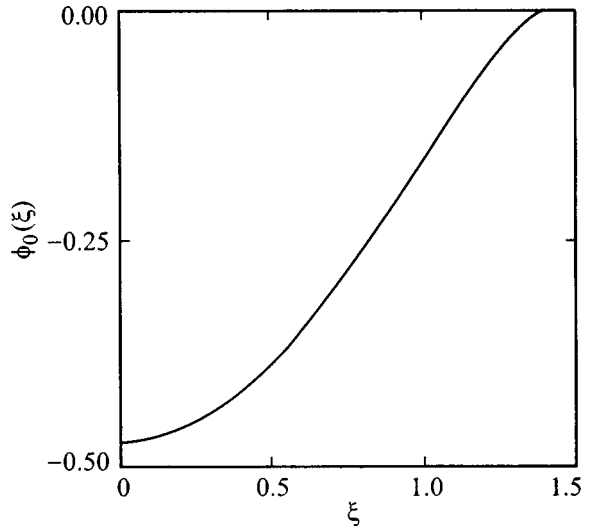

FIG. 1. Distribution of the potential $\phi_0(\xi)$ (13a) in a Corbino disk.

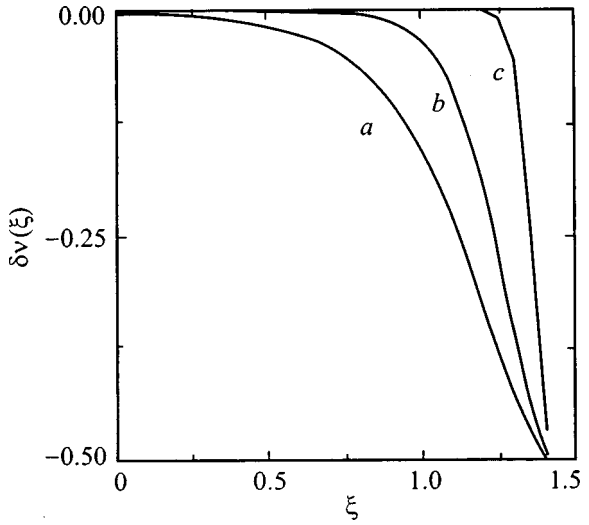

FIG. 2. Distribution $\delta\nu(\xi)$ (14) with $\phi_0(\xi)$ from Eq. (13a) for various values of the parameter t: *a*—0.1, *b*—0.05, *c*—0.01.

In the limit $a \ll w$ the effect of the ends $\pm w$ on the behavior of a can be neglected, and the problem simplifies:

$$\varphi(x)=0, \quad a \leqslant |x| \leqslant \infty, \tag{12a}$$

$$\delta n(x)=\text{const}-\delta n_0(x)=(1-\nu_0)n_l+\frac{n_0''}{2}x^2,$$

$$\pi l_H^2=n_l^{-1}, \quad |x| \leqslant a. \tag{12b}$$

Here $\nu_0=\nu(0)$ is the filling factor at the center of the $2D$ system, $n_0'' \equiv n''(x)|_{x=0}$.

The solution presented in Ref. 2 for Eqs. (12a and 12b) has the form

$$e\varphi(x)=\frac{2\pi e^2}{\kappa}\left[\left((\nu_0-1)n_l+\frac{n''a^2}{4}\right)(d^2-x^2)^{1/2} - \frac{n''}{6}(a^2-x^2)^{3/2}\right], \quad |x| \leqslant a. \tag{13}$$

In contrast to Eq. (2), where the electric potential undergoes a jump at the contact boundary, for the more accurate approximation (13) the electric potential is continuous at the points $\pm a$.

We shall now show that when Eq. (9) holds the condition (5) can be satisfied as a result of a small (in the sense $\delta\nu \ll 1$) change in the filling factor in the range $|x| \leqslant a$. This possibility is due to the above-mentioned property (10) of the function $T \ln S$. In this case the condition (5) can be regarded as a definition of $\delta\nu \ll 1$ as a function of $e\varphi(x)$ (13). Some numerical results are presented in Figs. 1 and 2. We are talking about a truncated variant of $e\varphi(x)$ in Fig. 1 (without the square-root term; a more detailed discussion is given in the next section) written in the dimensionless form

$$\phi_0(\xi)=\frac{\phi_0}{3}(\gamma^2-\xi^2)^{3/2}, \quad \phi_0=\frac{V_c}{\hbar\omega_c},$$

$$V_c=2\pi e^2(1-\nu_0)n_l x_0 \kappa^{-1},$$

$$\xi=\frac{x}{x_0}, \quad -\gamma \leqslant \xi \leqslant +\gamma, \quad \gamma=\frac{a}{x_0} \tag{13a}$$

(x_0 is determined below by Eq. (15a)) and the deviation $\delta\nu$, related to this potential, of the filling factor from its electrostatic value $\nu=1$ used in the formulation of the problem (12). The expression for $\delta\nu$ is determined from Eq. (5) or its dimensionless analog

$$\phi_0(\xi)-t \ln S[\delta\nu(\xi)]=0,$$

$$t=\frac{T}{\hbar\omega_c} \ll 1, \quad -\gamma \leqslant \xi \leqslant +\gamma. \tag{14}$$

The data in Fig. 2 demonstrate that the requirement (14) is satisfied at the cost of small deviations $\delta\nu \ll 1$ at the center of the plateau. Near the ends $\pm\gamma$ deviations $\delta\nu(\pm\gamma)$ of order 1 arise for any finite t. Therefore the approximation of Ref. 2 becomes inaccurate near the points $\pm\gamma$ and all local properties of the channel must be determined more accurately here, which is naturally done by using $\delta\nu$ from Eq. (14) to construct the next approximations.

3) The potential (13) contains an indefinite quantity a, which is one of the main characteristics of the dielectric strip. In Ref. 2 this indefiniteness is removed by assuming that at the ends $\pm a$ of the interval the longitudinal electric field (i.e., the quantity $d\varphi/dx$) cannot have a singularity (even a square-root singularity),

$$\frac{d\varphi(\pm a)}{dx}=0. \tag{14a}$$

This can be accomplished by setting the combination of terms in front of the square-root term in the definition (13) of $\varphi(x)$ to zero. As a result we obtain

$$a_0^2=2x_0^2, \tag{15}$$

$$x_0^2=\begin{cases}\dfrac{2(\nu_0-1)n_l}{n''}, & n''<0, \quad \nu_0<1,\\ \dfrac{2(1-\nu_0)n_l}{n''} & n''>0, \quad \nu_0>1,\end{cases} \tag{15a}$$

The coordinate x_0 corresponds to the point where the density $n(x)$ (12b) changes sign.

But the requirement (14) does not follow from Eq. (5). The authors of Ref. 2 introduce it in addition to Eq. (5), mentioning mechanical equilibrium. However, vanishing of the mechanical forces at the ends $\pm a$ of the range is not at all necessary. We give as an example the problem of the $n-s$ interface in the theory of superconductivity. The Ginzburg–Landau theory of such an interface[5] assumes continuity for the magnetic field and order parameter in the transitional region, but it does not rule out the existence of mechanical forces (magnetic pressure), which compress the superconducting region of the metal, at the $n-s$ interface.

On this basis it is reasonable to give an alternative definition of a without using Eq. (14). The required condition is the natural requirement that the $2D$ system perturbed by magnetic corrections to the electrochemical potential have global neutrality. Specifically, turning to the expression (12b) we see that the deviation of the electron density from its metallic value near the origin of the coordinates (right up to the points $\pm x_0$) is independent of a. Moreover, the solution (13) automatically satisfies the requirement

$$\int_{-\infty}^{+\infty}\delta n(x)dx=0. \tag{16}$$

Therefore the compensating part of the electron density should depend on a, and its value is determined from Eq. (16). Setting

$$a^2=\gamma^2 x_0^2, \tag{17}$$

we find from Eq. (16) an equation for determining γ:

$$\frac{2}{3}=\int_1^{\gamma}(\xi-1)d\xi+\int_{\gamma}^{\infty}\left(\frac{\xi}{\sqrt{\xi^2-\gamma^2}}-1\right)d\xi + \int_{\gamma}^{\infty}\left(\xi^2-\frac{\xi^3-\gamma^2(\xi/2)}{\sqrt{\xi^2-\gamma^2}}\right)d\xi. \tag{17a}$$

$$\gamma=2.001. \tag{17b}$$

It is obvious that all functional dependences for a_0 (15) and a (17) are identical. Therefore they cannot be distinguished by capacitive measurements. However, the linear electrooptic effect is sensitive to the details of the variants under discussion. The appropriate procedure gives information about the local distribution of the electric potential in the $2D$ system (see, for example, Ref. 6), which is qualitatively different for the cases (15) and (17). In the first case the potential $\phi_0(\xi)$ (13a) is monotonic. The variant (17) corresponds to the potential

$$\phi(\xi)=\phi_0\left[(1-\gamma^2/2)(\gamma^2-\xi^2)^{1/2}+\frac{1}{3}(\gamma^2-\xi^2)^{3/2}\right]. \tag{18}$$

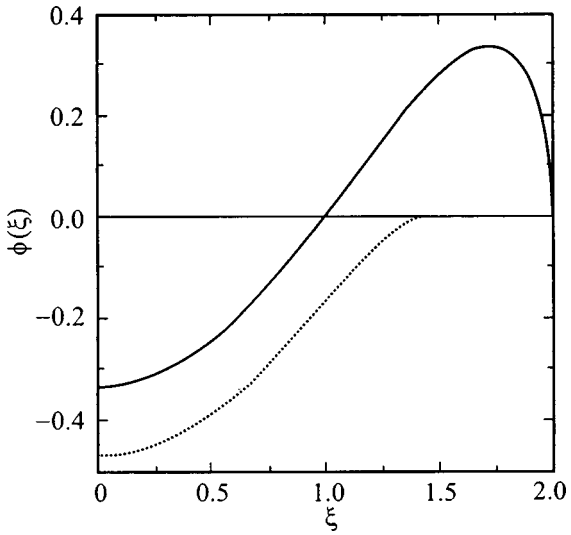

FIG. 3. Comparative behavior of the potentials $\phi_0(\xi)$ (dotted curve) and $e\varphi(x)$, presented in the same dimensionless variables as Eq. (13a) (solid curve).

If $\gamma^2=2$, the expression (18) reduces to Eq. (13a). But in the case $\gamma^2=4$ the potential (18) has different signs near the ends $\pm\gamma$ and at the origin. A similar behavior (which can be seen clearly in Fig. 3) can be observed using the linear electrooptic effect.

Using the explicit form of $\delta n_0(x)$ (2) we find n'' and therefore explicit expressions for a_0 (15) and a (17)

$$a_0^2=2x_0^2; \quad a^2=4x_0^2;$$

$$x_0^2=\frac{2(1-\nu_0)n_l}{n''}, \quad n''>0, \quad \nu_0>1,$$

$$n''=\frac{2\kappa w\varphi_{ab}}{\pi^2 e w^4}. \tag{19}$$

The definitions (19) are correct if

$$e\varphi(0)\leqslant\hbar\omega_c.$$

The maximum value of a_0 in the approximation (15) is

$$\left(\frac{a_0}{w}\right)^3=\frac{3\pi\hbar\omega_c}{2e\phi_{ab}}. \tag{19a}$$

Together with Eq. (4) the relations (19) and (19a) can be directly checked experimentally.

2. TAKING ACCOUNT OF SCREENING

1) To interpret the results of the investigation of the linear electrooptic effect correctly it is important to estimate the effect of the additional screening electrode required in this method. Let this electrode be located at a distance d from the $2D$ system, where

$$2a\ll d\ll 2w. \tag{20}$$

These conditions correspond to the case of weak screening, where the screen is important for determining $\delta n_0(x)$ of the

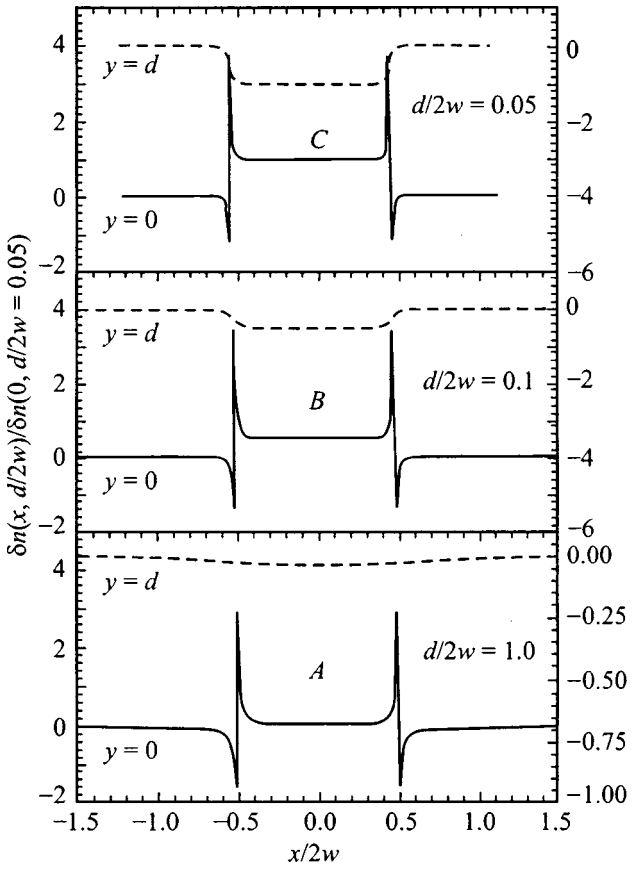

FIG. 4. Demonstration of the role of the screening electrode in the charge distribution in a quasi-one-dimensional Corbino disk and accompanying screen for various values of the ratio d/w: *A*—1.0; *B*—0.1; *C*—0.05.

form (2) but can still be neglected when calculating a. The distribution $\delta n_0(x,d)$ replacing the distribution (2) is then given by

$$\frac{e\,\delta n_0(x,d)d}{\kappa\phi_{ab}}=\frac{1}{4\pi}+\frac{1}{2\pi}\left[\frac{\exp(-\pi x/d)}{\exp(\pi w/d)-\exp(-\pi x/d)}+\frac{\exp(\pi x/d)}{\exp(\pi w/d)-\exp(\pi x/d)}\right]. \tag{21}$$

In the limit $d/w\gg 1$ the expression (21) reduces to Eq. (2)

$$\delta n_0(x)\propto\frac{w}{w^2-x^2}.$$

It is obvious that in this case the condition of global neutrality is insensitive to the presence of the screening electrode.

In the opposite limit $d\ll w$ the contribution of the second term in Eq. (21) far from the points $x=\pm w$ is exponentially small compared to the first term, and an electron density distribution $\delta n_0(x,d)$ typical for a flat two-electrode capacitor arises. The additional charge of the $2D$ system is neutralized by a charge of opposite sign on the screen. The charge distribution is displayed in Fig. 4.

The finiteness of d influences the second derivative of the perturbed electron density. Performing the corresponding calculations using Eq. (21), we find the analog of Eq. (19a)

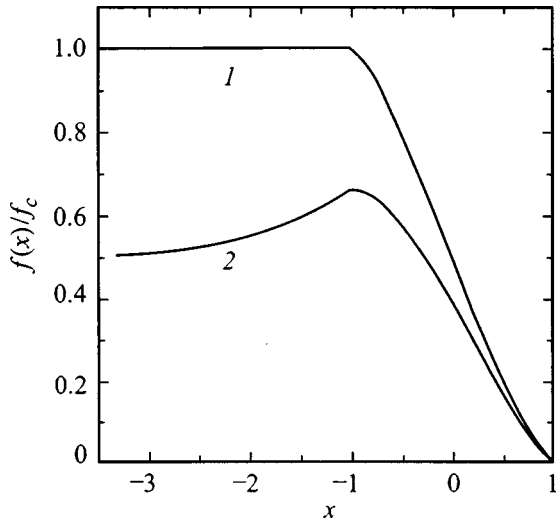

FIG. 5. *1*—Effective distribution of the potential near the contact of a conducting $2D$ Corbino disk with one of the metal electrodes with a laser beam of finite radius scanning the sample; *2*—potential constructed taking account of the finiteness of the laser beam and the insulating behavior of the $2D$ system.

$$\left(\frac{a}{d}\right)^3=\frac{3\hbar\omega_c(\exp(\pi w/d)-1)^3}{\pi^2 e\phi_{ab}\exp(\pi w/d)(\exp(\pi w/d)+1)}. \tag{22}$$

In the limit $w/d\ll 1$ the expression (22) becomes (19a).

2) For $d\ll w$ the question of the effective width $2a$ of the integer region becomes immaterial. It is more interesting to estimate the width $2D$ of the metallic interlayers at the ends of the $2D$ system, which remain so (to the extent that a contact potential difference exists) irrespective of the state of its central part. We give below qualitative considerations making it possible to identify such metallic strips by means of the linear electrooptic effect.

First let the $2D$ system be in a metallic state and let the radius of the scanning laser beam be R. In this case the relief of the electrostatic potential, as follows from the data on the electrooptic effect, should have the form

$$\varphi(x)=\begin{cases} f(x), & w-2R\leqslant|x|\leqslant w,\\ \text{const}, & |x|\leqslant w-2R,\end{cases} \tag{23}$$

where

$$f(x)=\frac{\pi R^2}{2}-x\sqrt{R^2-x^2}-R^2\arcsin\left(\frac{x}{R}\right). \tag{23a}$$

The curve *1* in Fig. 5 shows the transitional region $\varphi(x)$ (23) in dimensionless units, normalized to $\varphi(-\infty)=1$ and $R=1$ at the origin, which correspond to the center of the laser spot on the right-hand boundary of the $2D$ system.

The curves labelled *2* in Figs. 5 and 6 demonstrate the relative behavior of $\varphi(x)$ in two forms of the distribution of sections of the electron density of the $2D$ system with an integer filling factor. In the first figure the entire $2D$ system possesses an integer filling factor and so $\varphi(x)$ decreases in a square-root fashion away from the edges toward the center of the $2D$ system.

Figure 6 presupposes that the insulator part of the $2D$ system is separated from its ends $\pm w$ by metallic strips

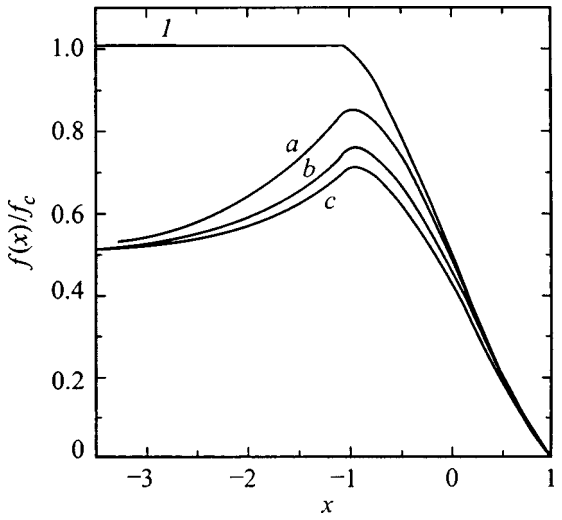

FIG. 6. Comparative distribution of the effective potentials near the boundary: *1*—potential corresponding to a metallic state of the $2D$ system; *a–c*—potentials constructed taking account of the finiteness of the laser beam and the insulating behavior of the $2D$ system in the presence of conducting interlayers of thickness δ separating the $2D$ system and the metallic contact. δ/R: *a*—0.8; *b*—0.4; *c*—0.2.

$\delta=(w-a)/R<1$, so that the square-root decrease in the direction into the system occurs with a delay proportional to $\delta\neq 0$. The difference between Fig. 5 (curve *2*) and Fig. 6 is obvious: In the former the slopes of the curves *1* and *2* are different for the entire transitional region and in the latter the transitional regions 1 and $a-c$ are identical on the finite interval x, after which the deviation of the curves $a-c$ from the metallic reference 1 starts. This circumstance can be clearly observed in experiments with a linear optical effect.[6]

3. METASTABLE STATES

At low temperatures $t\ll 1$ the formation of an incompressible strip should be accompanied by another effect that influences its electrostatics. The point is that varying the magnetic field, ordinarily done to change the filling factor, inevitably leads to azimuthal electric fields and in consequence to charge transport in the radial direction. In the metallic parts of a Corbino disk this process is rapidly stopped by reverse diffusion fluxes. But the charge transferred from one edge of the insulator strip to the other cannot return to the extent that $\sigma_{xx}\ll 1$. The metastable states that arise and have been investigated in detail in a number of special experiments[7–10] possess nontrivial properties, even with respect to the structure of the incompressible strip. Leaving the complete description of this effect for a more detailed paper, we shall confine our attention here to the limit of quite strong transport fields, such that the corresponding potential difference eV_H between the edges of the strip reaches the scale $\hbar\omega_c$.

Quantitative estimates of the transported charge Q are quite difficult to make and depend specifically on the degree to which the disk is insulated from the external devices. If the disk does not react back on vortex-induced charge transport the relations describing such transport follow from the equation of continuity, the local Ohm's law, and Maxwell's equations. As a result we obtain, following Refs. 7–10,

$$e\frac{\partial n_s}{\partial t}=\frac{\sigma_{xy}}{c}\frac{\partial H_z}{\partial t}, \tag{24}$$

or

$$\Delta n_s=\frac{el}{hc}\Delta H_z, \quad l=1,2,3,\ldots. \tag{25}$$

The quantized value of the Hall conductivity $\sigma_{xy}=le^2/h$ is used in Eq. (25).

On the basis of the definitions (24) and (25) charge transport outside the incompressible strip is determined by the entire area of the Corbino disk within the radius R. Therefore for sufficiently large values of R the potential difference eV_H arising can be quite large, in any case comparable to $\hbar\omega_c$. We shall show that for $eV_H\geqslant\hbar\omega_c$ the width of the incompressible strip is formed mainly by this potential difference.

Let us consider once again the two-dimensional part of the disk $R_1\leqslant r\leqslant R_2$ containing the dielectric strip and the adjoining metallic edges. A potential difference V_H exists between the edges and gives rise to a radial current j_i,

$$j_i=e^{-1}\sigma_{ii}\frac{\partial\mu}{\partial x_i}. \tag{26}$$

It is convenient to rewrite Ohm's law (26) in the form

$$\frac{J}{2\pi r}=e^{-1}\sigma_{rr}\frac{d\mu}{dr}, \tag{27}$$

or

$$\mu(r)=\mu_1+\frac{eJ}{\pi\sigma_{rr}}\ln\left(\frac{r}{R_1}\right), \quad R_1\leqslant r\leqslant R_2. \tag{27a}$$

The current J is related to the potential difference V_H on the metal edges by $\mu(R_2)-\mu(r_R)=eV_H$, and since $\mu(R_1)\equiv\mu_1$, we have

$$\frac{J}{2\pi\sigma_{rr}}\ln\left(\frac{R_2}{R_1}\right)=V_H. \tag{28}$$

As a result the expression (27a) can be rewritten in a form independent of σ_{rr}

$$\mu(r)-\mu_1=eV_H\ln\left(\frac{r}{R_1}\right)\left[\ln\left(\frac{R_2}{R_1}\right)\right]^{-1}. \tag{29}$$

The distribution of the electric potential and electron density between the points R_2 and R_1 now follows from the definition of the electrochemical potential

$$\mu(r)=e\varphi(r)-T\ln S(H,T,\nu(r)) \tag{30}$$

together with the expressions (29), (6), and (8).

It is easy to see that the problem (30) is similar to the equilibrium problem (5)–(8), the only difference being that now the electrochemical potential (29) depends on the spatial coordinate.

The assumption that there exists an integral channel within the interval $R_1\leqslant r\leqslant R_2$ means that at a distance $R_1<r^*<R_2$, defined by the condition

$$\mu(r^*)=e\varphi(r^*)-T\ln S(H,T,\nu(r^*)=1), \tag{31}$$

the filling factor $\nu(r)$ becomes an integer.

Near $\nu=1$ the main contribution on the right-hand side of Eq. (30) comes from the term $-T\ln S(H,T,\nu(r))$. Under these conditions

$$\mu(r)-\mu^*\simeq T\ln\left[\frac{S(H,T,\nu=1)}{S(H,T,\nu(r))}\right] \tag{32}$$

right up to the boundary $r=R_2$, if $eV_H<\hbar\omega_c$.

In the region $eV_H>\hbar\omega_c$ the relation (32) determines the size $2a$ of the integral channel,

$$eV_H\ln\left(\frac{r^*+2a}{r^*}\right)\left[\ln\left(\frac{R_2}{R_1}\right)\right]^{-1}=\hbar\omega_c. \tag{33}$$

We note that according to Eq. (33) the effective width $2a$ of the incompressible strip decreases with increasing $eV_H>\hbar\omega_c$. This assertion qualitatively explains the limited growth of the total charge, under QHE conditions, at the edges of a Corbino disk when the magnetic field changed in the experiments of Refs. 7–10.

So, two-dimensional Corbino samples with additional contacts make it possible to study the properties of incompressible regions in magnetized $2D$ systems. The formation (destruction) of such specific channels causes the appearance (disappearance) of a qualitatively new, measurable characteristic of the Corbino configuration—the capacitance between its edges.

The appearance of channels is a quite general phenomenon, occurring in equilibrium problems (magnetocapacitance) and in Hall transport under conditions where local sections of the $2D$ system with an integer filling factor form. The properties of each shelf in the dependence of the $2D$ Hall conductivity on the magnetic field or average electron density is formed with the participation of factors that determine the parameters of the incompressible channels. It is obvious that detailed study of such formations in simple situations like the Corbino disk is of great interest. Coulomb effects (redistribution of the electron density near a channel) accompanying the formation of a channel are not typical just of the boundaries of regions with an integer filling factor. A similar problem arises, for example, in the study of the $n-s$ interfaces in the intermediate state of type-I superconductors. For example, the nonlocal phenomena[11] characteristic of mesoscopic $s-n-s$ channels to a certain extent are due to Coulomb effects at the $n-s$ interfaces.

This work was partially supported as part of the program ''Physics of Solid-State Nanostructures'' (Grant No. 97-1059) and by the Russian Foundation for Basic Research (Grant No. 98-02-16640).

[a)]The prerequisites of the theory of Ref. 2 also contain assertions that are not obvious. Alternative possibilities are discussed below where these prerequisites are use; see the point 3) in this section.

[1] D. B. Chklovskii, B. I. Shklovskii, and L. I. Glazman, Phys. Rev. B **46**, 4026 (1992).
[2] D. B. Chklovskii, K. F. Matveev, and B. I. Shklovskii, Phys. Rev. B **47**, 12 605 (1993).
[3] L. D. Landau and E. M. Lifshitz, *Electrodynamics of Continuous Media* (Pergamon Press, New York) [Russian original, Nauka, Moscow, 1982].
[4] V. B. Shikin and N. I. Shikina, JETP Lett. **62**, 894 (1995).
[5] V. L. Ginzburg and L. D. Landau, Zh. Éksp. Teor. Fiz. **20**, 1064 (1950).
[6] W. Dietsche, K. von Klitzing, and K. Ploog, Surf. Sci. **361/362**, 289 (1996).
[7] V. T. Dolgopolov, N. B. Zhitenev, and A. A. Shashkin, JETP Lett. **52**, 196 (1990).
[8] V. T. Dolgopolov, A. A. Shashkin, and N. B. Zhitenev, Europhys. Lett. **14**, 255 (1991).
[9] V. T. Dolgopolov, A. A. Shashkin, N. V. Zhitenev, S. I. Dorozhkin, and K. von Klitzing, Phys. Rev. B **46**, 12 560 (1992).
[10] V. T. Dolgopolov, A. A. Shashkin, G. V. Kravchenko, S. I. Dorozhkin, and K. von Klitzing, Phys. Rev. B **48**, 8480 (1993).
[11] V. T. Petrashov and V. N. Anotonov, JETP Lett. **54**, 241 (1991).

Translated by M. E. Alferieff

FULLERENES AND ATOMIC CLUSTERS

Two-photon-excited luminescence spectra in diamond nanocrystals

S. N. Mikov* and A. V. Igo

Ul'yanovsk State University, 432700 Ul'yanovsk, Russia

V. S. Gorelik

P. N. Lebedev Physics Institute, Russian Academy of Sciences, 117924 Moscow, Russia

(Submitted January 17, 1996)
Fiz. Tverd. Tela (St. Petersburg) **41**, 1110–1112 (June 1999)

Two-photon-excited luminescence (TEL) spectra have been recorded in the blue (400–500 nm) and near-ultraviolet (300–400 nm) ranges for diamond particles with 4 nm average size, which were obtained by detonation synthesis from explosives. The observed TEL bands are attributed, by comparing the obtained spectra with the impurity luminescence spectra in large diamond crystals, to $N2$ and $N3$ defects associated with the presence of nitrogen impurities in diamond. The TEL spectra presented are found to have certain distinguishing features: short-wavelength shift of the maximum and changes in the shape and width of the spectral bands for ultradispersed diamond compared with the spectrum in bulk crystals. [S1063-7834(99)03806-X]

Together with the absorption spectra, the impurity luminescence spectra of crystals carry important information about the structure of defects and the electron–phonon interaction mechanisms in these crystals. The spectral properties of the absorption and luminescence in natural and artificial diamond crystals have now been quite well studied in essentially all spectral regions. Specifically, the absorption spectra in the infrared range have been studied in Ref. 1; a detailed review of the spectral properties in the visible and near-ultraviolet (UV) ranges is given in Ref. 2; and, the recombination radiation spectra of diamond crystals in the UV region are presented in Ref. 3. A characteristic feature of the optical properties of diamond as compared with most other crystals is the presence of luminescence in the blue and UV ranges of the spectrum. This feature is used, for example, to determine the quality of diamonds.

So-called ''explosion diamonds''—ultradisperse diamond powder obtained by detonation synthesis from explosives[4]—have been generating great interest in recent years. X-ray crystallographic investigations[5,6] and the study of Raman scattering spectra (RS)[6–8] have made it possible to identify reliably a diamond-type crystal lattice in explosion diamonds. A unique property of these materials is that the particle sizes of the diamond powder lie in the range 3–6 nm.

This circumstance is attracting special attention to the investigation of these objects, since quantum-size effects should arise in them. Specifically, it is shown in Ref. 9 that the characteristic features of the RS spectra of explosion diamonds with average size of the order of 4 nm can be explained by size-quantization of the phonon spectrum and the influence of spatial confinement on the photon–phonon interaction.

The study of TEL spectra is also of interest because there are few published data on the TEL spectra of diamonds, and for ultradispersed diamonds there are no such data at all.

In the present paper we report the results of an investigation of impurity TEL excited in ultradispersed powders of explosion diamonds by a visible-range laser source.

1. EXPERIMENTAL PROCEDURE

To record the TEL spectra the samples were prepared by the following procedure. Diamond powder was carefully mixed with pulverized potassium bromide (KBr), after which the mixture was compacted in a special press. Compressing the mixture of powders with a force of about 2 kN produced a 10 mm in diameter and 3 mm thick tablet, which was used for the investigations. The mass content of diamond powder in the tablet was about 2%. This method of preparing the samples has definite advantages over the conventional method of recording the spectra of micropowders. Here the KBr matrix plays the role of an immersion medium, which to a large extent decreases reflection and scattering of light by the boundaries of the particles.

A copper vapor laser with average radiation power 3 W and two lasing lines—green ($\lambda = 510.6$ nm) and yellow ($\lambda = 578.2$ nm)—was used as the excitation source in the experiment. The duration of the laser pulses was 20 ns and the pulse repetition frequency was 8 kHz. The radiation emanating from the sample was focused onto the entrance slit of an MDR-2 monochromator and then detected using a photon-counting scheme. The TEL spectra were investigated in two frequency ranges. To record the spectrum in the 400–500 nm range a BG-12 filter was placed in front of the monochro-

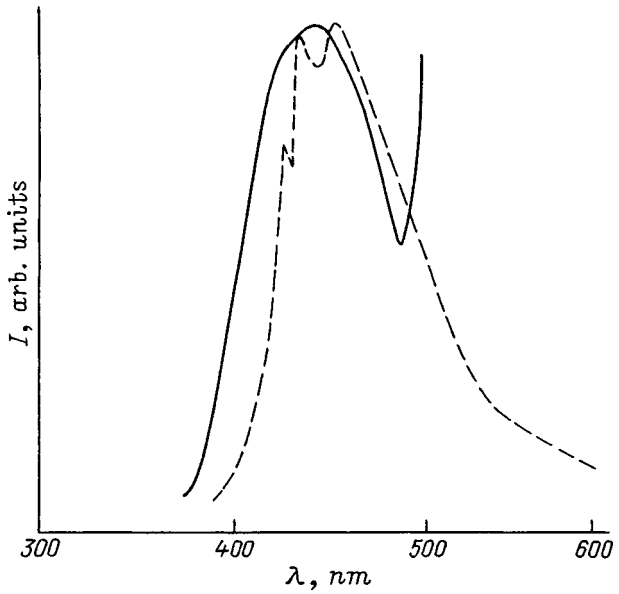

FIG. 1. TEL spectrum of diamond particles with average size 4 nm in the 400–500 nm range with excitation by the yellow laser line 578.2 nm (solid line); the dashed line shows the luminescence spectrum from Ref. 10 for an $N3$ defect of large diamond.

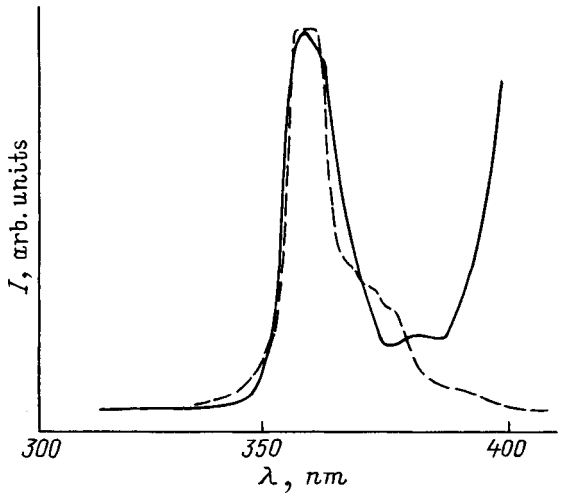

FIG. 2. TEL spectrum of diamond particles with average size 4 nm in the 300–400 nm range with simultaneous excitation by two laser lines with $\lambda = 510.6$ and 578.2 nm (solid line). The dashed line shows the spectrum calculated for an $N2$ defect according to the theory of Ref. 2.

mator slit and the spectrum was excited only by the yellow line (the green line was suppressed by a filter placed in front of the sample). To record the spectrum in the 300–400 nm range a UFS-1 light filter was placed in front of the monochromator slit and the spectrum was excited by both laser lines. Appropriate light filters prevented the exciting laser radiation from entering the detection system. All measurements were performed at room temperature.

2. EXPERIMENTAL RESULTS DISCUSSION

In Fig. 1 the solid line shows the TEL spectrum of the experimental sample in the 400–500 nm range. The spectrum is rescaled taking account of the spectral dependence of the transmission of the BG-12 light filter. The spectrum consists of a smooth wide band (the width at half-maximum is about 85 nm) with a maximum at wavelength $\lambda = 440$ nm. The increase in the radiation intensity near 500 nm is due to incomplete suppression of the green laser line at 510.6 nm. The dashed line shows the known luminescence spectrum of natural diamond.[10] It possesses several local peaks which are absent in our spectrum, superposed on a 90 nm wide band. The strongest peak of the intensity lies at 455 nm. The second difference of our spectra from the known spectrum of Ref. 10, corresponding to a large crystal, is a general blue-shift of the contour of the spectrum.

It is known[2] that luminescence in diamond in this range of the spectrum is due to electronic transitions between a doubly degenerate excited state E_1 and the nondegenerate ground state A_1 of an $N3$ defect, which possesses C_{3v} symmetry. Such defects consist of three nitrogen atoms, replacing carbon at the vertices of the unit cell and bound either to a common carbon atom or to a common vacancy. The excitation of the electronic subsystem of the defect distorts the lattice near the defect, specifically, displaces the atoms out of the initial position of equilibrium. The direction of the shift is determined by the decrease δE of the energy of the system. The decrease δE and the vibrational energy $h\nu$ of the lattice determine the Huang–Rhys factor $S = \delta E/h\nu$, which according to the theory of Ref. 2 relates the spectral shape of the luminescence line with the nature of a specific defect. The position of the line is determined by the energy (wavelength) of the zero-phonon transition, which in turn is related to the nature of the defect.

The close arrangement and the resemblance between the shape of the spectral line obtained in our experiment and the known line corresponding to an $N3$ defect in a large diamond allow us to conclude that the observed line belongs to a defect of this type. The absence of local peaks in the spectral curve presented in the present paper can apparently be explained either by heating of the sample by the laser radiation or by the presence of defects in the crystal structure. Another difference between the spectrum and the known spectrum of a large crystal is the appreciable shift (20 nm) of the short-wavelength edge in the direction of higher frequencies.

Figure 2 (solid line) shows the TEL spectrum of the sample in the 300–400 nm range, rescaled taking account of the spectral dependence of the transmission of the UFS-1 light filter. The spectrum contains a sharp maximum at $\lambda = 356$ nm and a weak maximum at $\lambda = 380$ nm. The width of the line at half-maximum with $\lambda = 356$ nm is 16 nm. This spectral line can be attributed to an $N2$ defect, which is formed by substitution of nitrogen atoms for the two neighboring carbon atoms located on the body diagonal. According to Ref. 11, such a defect possesses D_{3d} symmetry and two dipole transitions with zero-phonon transition wavelengths of 317 and 330 nm.

It should be noted that the position of the TEL line and its relatively small width, which we determined in the experiment, do not agree with the data from Ref. 11, where the position of the energy levels of the defect and the strength of the electron–phonon interaction were calculated. If phonons

with the highest density of states in diamond ($h\nu = 0.155$ and 0.112 eV) are used to estimate the phonon energy, then the experimental luminescence spectrum presented here in the 300–400 nm range can be described, using the theory of Ref. 2, by a contour with $S = 0.5$ and the wavelength 344 nm of the zero-phonon transition (dashed curve in Fig. 2). This corresponds to a weak Jahn–Teller relaxation ($S \leqslant 1$). In Ref. 11, where the luminescence spectra of large diamonds with one-photon excitation are presented, the Huang–Rhys factors for the two indicated lines are estimated to be quite large ($S \sim 10$).

In summary, in the present work the first investigation of the two-phonon-excited luminescence spectrum for ultradispersed powders of explosion diamonds in the near-ultraviolet and blue ranges of the spectrum was performed using the two-photon excitation method. It was shown that diamond particles with an average size of 4 nm manifest luminescence properties which are typical of large diamond crystals, but there are definite differences in the position and shape of the corresponding spectral lines between the ultradisperse diamond powders and large single crystals.

This work was supported by the Russian Foundation for Basic Research (grants Nos. 97-02-16710 and 98-02-03327).

*E-mail: mikov@fesc.mv.ru; mikov@sv.uven.ru

[1] C. A. Klein, T. M. Hardnett, and C. J. Robinson, Phys. Rev. B **45**, 12 854 (1992).
[2] G. Davies, Rep. Prog. Phys. **44**, 787 (1981).
[3] *Handbook of the Optical Properties of Semiconductors*, edited by M. P. Lisitsa (Naukova Dumka, Kiev, 1987).
[4] A. I. Lyamkin, E. A. Petrov, A. P. Ershov, G. V. Sakovich, A. M. Staver, and V. M. Titov, Dokl. Akad. Nauk SSSR **302**, 611 (1988) [Sov. Phys. Dokl. **33**, 705 (1988)].
[5] M. B. Gusev, V. G. Babaev, V. V. Khvostov, and Z. Kh. Valiullova, Izv. Ross. Akad. Nauk, Ser. Fiz. **58**(1), 191 (1994).
[6] M. Yoshikawa, Y. Mori, H. Obata, N. Maegawa, G. Katagiri, H. Ishida, and A. Ishitani, Appl. Phys. Lett. **67**, 694 (1995).
[7] E. D. Obraztsova, K. G. Korotushenko, S. M. Pimenov, V. G. Ralchenko, A. A. Smolin, V. I. Konov, and E. N. Loubin, Nanostruct. Mater. **6**, 827 (1995).
[8] S. N. Mikov, A. V. Igo, and V. S. Gorelik, Fiz. Tverd. Tela (St. Petersburg) **37**, 3033 (1995) [Phys. Solid State **37**, 1671 (1995)].
[9] V. S. Gorelik, A. V. Igo, and S. N. Mikov, Zh. Éksp. Teor. Fiz. **110**, 2141 (1996) [JETP **82**, 1154 (1996)].
[10] G. Davies, Proc. R. Soc. London, Ser. A **336**, 507 (1974).
[11] G. Davies and M. H. Nazare, Proc. R. Soc. London, Ser. A **365**, 75 (1979).

Translated by M. E. Alferieff

IR photoconductivity of C_{60} fullerene single crystals

E. V. Korovkin* and R. K. Nikolaev

Institute of Solid-State Physics, Russian Academy of Sciences, 142432 Chernogolovka, Moscow District, Russia

(Submitted August 6, 1998)
Fiz. Tverd. Tela (St. Petersburg) **41**, 1113–1114 (June 1999)

The photoconductivity in the range 0.3–0.9 eV was investigated in a high-quality C_{60} fullerene single crystal. It was concluded that the crystal investigated is an extrinsic semiconductor.
 [S1063-7834(99)03906-4]

The photoconductivity of fullerenes has usually been investigated in the intrinsic absorption range 1.5–2.5 eV to establish the basic parameters of the band structure in thin films[1] and in single crystals[2] at comparatively high temperatures ($T>120$ K). In the present work the photoconductivity in the IR range (0.3–0.9 eV) in nominally pure high-quality single crystals to observe and study the energy levels produced by intrinsic defects of the crystal or typical impurities, existing even in a nominally pure crystal. The method developed to investigate the photoconductivity of insulators and used previously to study the photoconductivity of colored alkali-halide crystals[3,4] was used.

A C_{60} single crystal was grown from the vapor phase in a sealed, evacuated, quartz ampul. The raw materials contained at least 99.95% C_{60}. An approximately $2\times2\times6$ mm^3 sample with an irregular shape was placed between the plates of a capacitor in a closed circuit consisting of a dc voltage source, the capacitor itself, and an electrometer. The source voltage was 50–500 V, and the current amplitude detected with the electrometer was 10–0.1 pA. An IKS-21 spectrophotometer was used as a source of monochromatic light.

The spectral dependence of the IR photoconductivity and the temperature dependence of these spectra in the range 10–160 K are presented in Fig. 1. The spectrum itself and the photoconductivity depend strongly on temperature. Since the photoconductivity at 160 K is approximately 200 times greater than at 10 K, the spectra are presented on an arbitrary scale and are shifted along the vertical axis (indicated on the left side of the figure for each spectrum). It is evident from the spectra presented that the spectrum consists of individual peaks whose amplitude increases with temperature, and the maximum of the general spectrum shifts with increasing temperature to higher energy so that for $T>110$ K it falls outside the experimental range. This means that either the amplitude of the shorter-wavelength peaks grows more rapidly or, if they have the same temperature dependence, on the higher-energy side outside the experimental range a photoconductivity peak exists whose amplitude and (or) width possibly increases with temperature, causing the long-wavelength shoulder of this peak to shift into the experimental range in addition to the peaks existing here and giving the observed effect.

An attempt was made to distinguish from the general spectrum the individual peaks near 650 and 900 meV to determine the activation energy responsible for their temperature growth. It is evident from the spectra presented that besides the peaks near 650 and 900 meV there is also a peak near 500 meV. Since the material employed in the IKS-21 lithium fluoride prism contains in the range 450–550 meV a series of narrow absorption lines due to the presence of hydroxyl groups in the material, the treatment of the light-beam intensity in this range is unreliable. For this reason, the data only from the range 550–1000 meV are used for further analysis and an optimal fit assuming the existence of three peaks—near 650 meV, near 900 meV, and outside the experimental range near 1200 meV—is made. The amplitude and half-width of the peaks and the exact position in the first step were treated as adjustable parameters. At the second step of the fit the position and half-width of the 650 and 900 meV peaks were approximated by a linear temperature de-

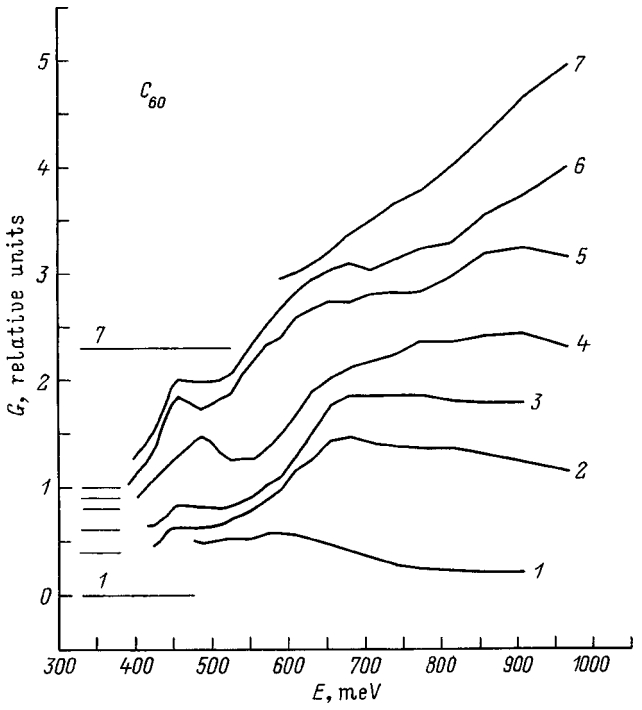

FIG. 1. IR-photoconductivity spectrum of a C_{60} single crystal for different temperatures: *1*—10 K, *2*—30 K, *3*—60 K, *4*—80 K, *5*—100 K, *6*—120 K, *7*—150 K.

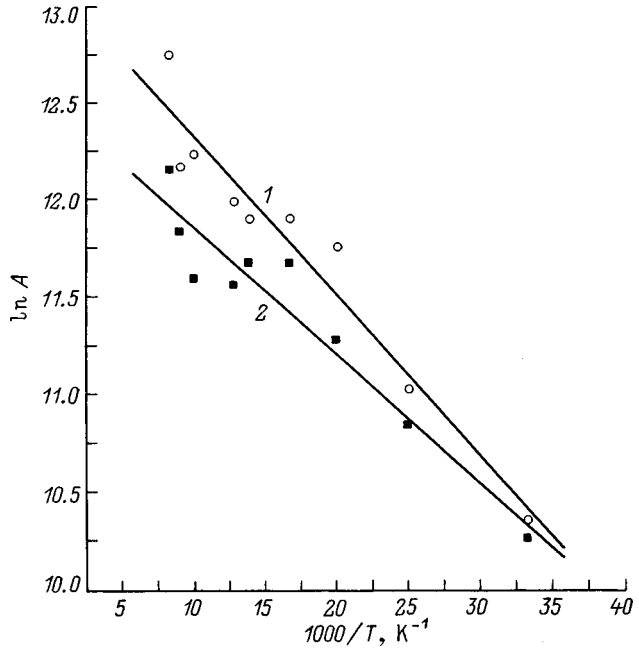

FIG. 2. Temperature dependence of the amplitude of the IR-photoconductivity peaks (*1*—885 meV and *2*—665 meV).

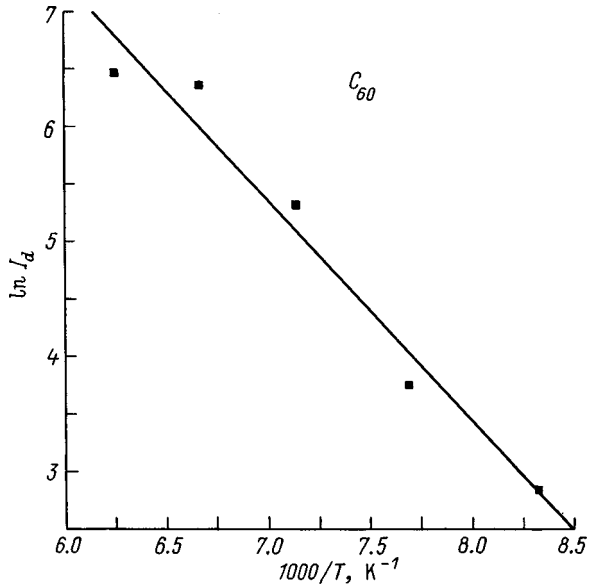

FIG. 3. Temperature dependence of the dark current.

pendence obtained on the basis of the data from the first step. The position of the first peak was found to be essentially temperature-independent and was 665 meV (865–905 meV for the second peak). The temperature dependence obtained for the amplitudes of both peaks is presented in Fig. 2. The activation energies were 5.6 meV for the first peak and 7 meV for the second peak. The reliability of the estimates is not high; the only sure thing is that both quantities lie in the range 5–10 meV.

Next it was found that a dark current is first observed at $T=120$ K. This current increased rapidly with a further increase in temperature (Fig. 3). The activation energy of this process is 165 meV.

It follows from the data obtained that the experimental fullerene crystal is an extrinsic semiconductor. If it is assumed (only for definiteness) that its conductivity is electronic, then the activation energy 165 meV can be associated with the depth of the Fermi level from the conduction-band bottom. The position of individual peaks in the photoconductivity spectrum should be associated with the depth of the donor levels corresponding to these peaks (large lattice relaxation should probably not be expected in this crystal). The activation energy 5–10 meV can be associated with the conditions of conduction electron transport, for example, the depth of the levels of attachment centers or irregular modulation of the conduction band bottom because of small but numerous intrinsic defects, for example, due to disorientation of individual C_{60} molecules. In this case this activation energy should be expected to be the same for any peaks.

However, if it is assumed that donor centers responsible for the observed photoconductivity peaks have, besides a ground state, a shallow excited state below the conduction band bottom, then the photoionization process will proceed in two stages—a light-induced transition into the excited state and further ionization due to temperature. In this case the activation energy 5–10 meV can be associated with the depth of the excited states, and then generally speaking this energy will be different for different peaks. Of course, a mixed case where some donor centers will have such excited states and others will not is also possible.

*E-Mail: korovkin@issp.ac.ru

[1] C. H. Lee, G. Yu, D. Moses, V. J. Srdanov, X. Wei, Z. V. Vardeny, Phys. Rev. B **48**, 8506 (1993).
[2] S. Matsuura, T. Ishiguro, K. Kikuchi, and Y. Achiba, Phys. Rev. B **51**, 10 216 (1995).
[3] E. V. Korovkin and T. A. Lebedkina, Fiz. Tverd. Tela (Leningrad) **29**(9), 2807 (1987) [Sov. Phys. Solid State **29**, 1612 (1987)].
[4] E. V. Korovkin and T. A. Lebedkina, Fiz. Tverd. Tela (St. Petersburg) **37**(11), 3536 (1995) [Phys. Solid State **37**, 1945 (1995)].

Translated by M. E. Alferieff

Small-inelastic-strain rate spectrum of C_{60} single crystals near the phase transition at 250–260 K

V. V. Shpeĭzman,*) N. N. Peschanskaya, V. M. Egorov, V. I. Nikolaev, and B. I. Smirnov

A. F. Ioffe Physicotechnical Institute, Russian Academy of Sciences, 194021 St. Petersburg, Russia

R. K. Nikolaev

Institute of Solid-State Physics, Russian Academy of Sciences, 142432 Chernogolovka, Moscow District, Russia

(Submitted October 23, 1998)
Fiz. Tverd. Tela (St. Petersburg) **41**, 1115–1118 (June 1999)

The temperature spectrum of small-inelastic-strain rates in a vapor-phase-grown C_{60} single crystal has been measured within the 200–290 K interval with a high-precision strain-rate meter based on a laser interferometer. The spectrum exhibits a strong peak in the region of the phase transition at 250–260 K and a slight strain acceleration at ~ 240 K, which correlates well with the calorimetric curve. The first maximum is associated with strain that developes more easily in an fcc than in a primitive cubic lattice, and the second, to the effect on the strain rate of annealing of the defects created with fast crystal heating. © *1999 American Institute of Physics.* [S1063-7834(99)04006-X]

It was shown[1,2] that compression of C_{60} single crystals at temperatures above and below the phase transition from the primitive cubic (pc) to fcc lattice affects differently the energy characteristics of the transition determined by differential scanning calorimetry (DSC). The strain-induced distortions of the peak shape at $T=77$ K were substantially smaller than the distortions produced by compression at room temperature, where the peak became almost fully washed out even after application of comparatively low pressures. A conjecture was put forward[2] that this was due to the fact that local strains preceding fracture were more likely to develop in the highly symmetric fcc than in the pc lattice or the glassy state in which C_{60} fullerites reside below 85 K (Ref. 3). One of the consequences of the strain responsible for the strong peak distortion could be formation of dimers and more complex polymerized structures.[4,5] Small inelastic strains can be detected by laser-based interferometry, which proved to be very useful in studies of small strains occurring at phase and relaxation transitions in metals (the ductile-brittle transition in zinc and steels[6,7]) polymers (α- and β-transitions[8]), and high-T_c superconductors (the superconducting transition[9]). The temperature spectra of inelastic strain rates of various materials obtained in Refs. 6–9 and in a number of other studies proved to be a high-resolution tool for detection of transitions of various nature and analysis of the effects of various factors on microplasticity. In the present work, the rate spectrum of small inelastic strains was used to investigate structural transitions in the C_{60} fullerite crystal and the role they play in microplasticity. The work was aimed also at revealing small strains, which until recently were studied only by microhardness measurements.

1. EXPERIMENTAL TECHNIQUES

C_{60} single crystals were grown from the vapor phase, the starting material being small C_{60} crystals purified preliminarily by multiple vacuum sublimation.[2,10] The C_{60} single crystals obtained by this technique were well faceted, weighed up to 30 mg, and varied in size up to a few mm.

The interferometric method of strain recording in time in the form of successive beats,[11] which was used in this work, permits one to determine strain rates $\dot{\varepsilon}$ from small changes in sample length to within 5%. One beat in an interferogram corresponds to a strain increment $|\Delta l_0|=0.3\,\mu$m. The technique employed to obtain rate spectra of small inelastic strains and their interpretation was described in considerable detail elsewhere.[6–9] To obtain a spectrum, the C_{60} single crystal was placed in the test chamber[11,12] and cooled rapidly to a temperature ~ 150 K, after which it was warmed up slowly and loaded several times by a compressive force of 20 N at progressively increasing temperatures from 200 to 300 K. Heating from 150 to 200 K favored the onset of a stable thermal regime, which improved the accuracy of subsequent measurements. The average heating rate was 1 K/min, and the isothermal loading pulse was 2 min long. The error with which the temperature was determined and maintained constant during the loading was ± 0.5 K, and the strain rate was measured 1 min after the beginning of loading at each temperature.

The data subjected to the analysis included also those obtained by DSC. The calorimetric measurements were performed on a Perkin–Elmer DSC-2 calorimeter by the techniques described in Refs. 1 and 2. To make both methods close in temperature conditions, the C_{60} sample was cooled rapidly with liquid nitrogen[2] before being placed in the calorimeter chamber. The measurements were carried out within the 220–300 K interval at a constant heating rate of 5 K/min. The DSC curves recorded thermal effects occurring in a sample during the pc–fcc transition, as well as other thermal

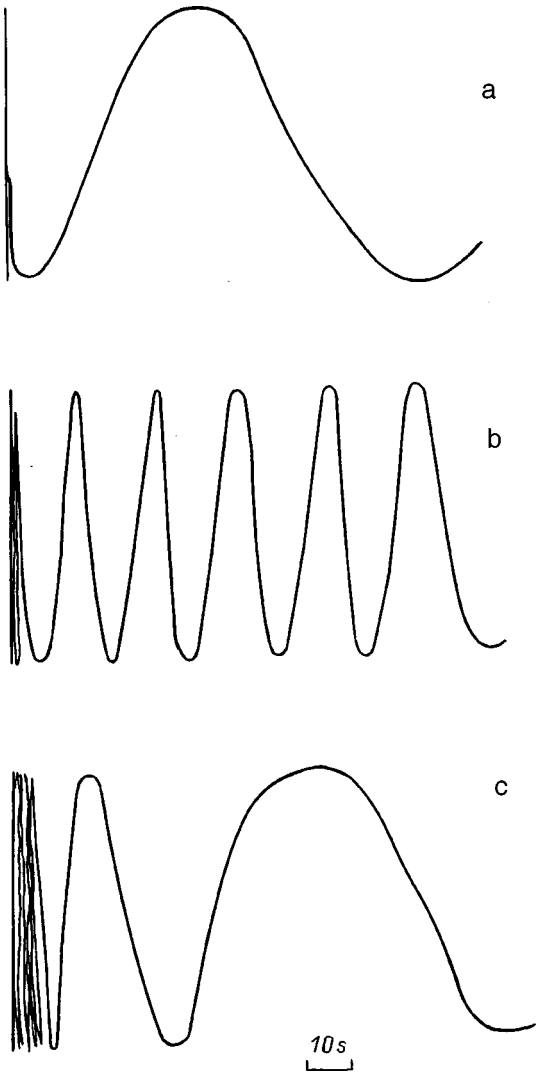

FIG. 1. Strain interferograms of a C_{60} single crystal obtained at T (K): (a) 218, (b) 260, and (c) 280. One beat corresponds to a strain change by $|\Delta l_0| = 0.3\ \mu$m.

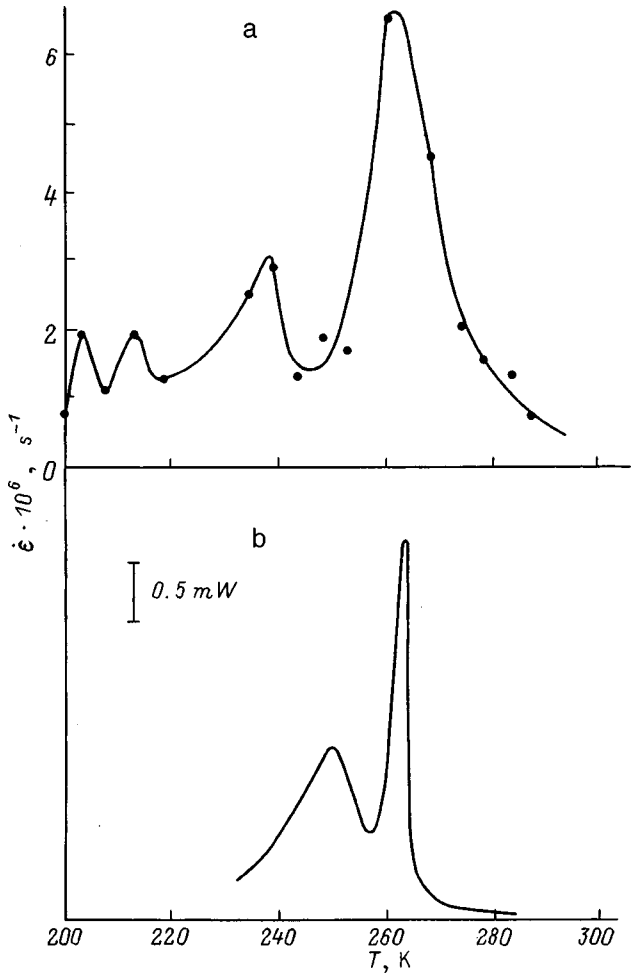

FIG. 2. (a) Rate spectrum of small inelastic strains and (b) DSC curve obtained at a heating rate of 5 K/min on a quenched C_{60} single crystal.

phenomena which could be observed in the temperature range under study.

2. EXPERIMENTAL RESULTS AND DISCUSSION

Figure 1 presents interferograms of a C_{60} sample loaded at 218 and 280 K (far from the phase transition), as well as at 260 K (in the transition region). It is seen that small inelastic strains can occur throughout the temperature range studied. At the same time the interferograms obtained at different temperatures exhibit the following features: at 218 K, the strain rate is small, and the strain is damped rapidly, at 260 K one observes a comparatively long (1.5–3 μm), nearly steady-state stage, and at 280 K, one can see noticeable microplasticity at the time of loading, followed by a fast decrease in the strain rate. This behavior is characteristic of various solids near relaxation transitions[6–8] or a superconducting transition in high-T_c superconductors.[9] The sample strain limit in the region of microplasticity is small and undergoes a jump in the transition zone; the low rate is due either to the original strain in the pc lattice being small (Fig. 1a) or to its becoming exhausted in the fcc lattice before the measurements (Fig. 1c). The transition region itself is characterized by a nearly uniform strain rate in the first stage (Fig. 1b), followed by damping in the final stage. The procedure chosen to measure the rate a preset time after the beginning of loading (in our case, in one min) reveals a maximum in the temperature dependence of the rate of small inelastic strains $\dot{\varepsilon}(T)$.

The $\dot{\varepsilon}(T)$ relation, or the rate spectrum of small inelastic strains, obtained on a C_{60} single crystal within the 200–300 K region is presented in Fig. 2. Also shown for comparison is a calorimetric curve obtained on the same sample. Both curves are seen to have the same shape. The main peak in $\dot{\varepsilon}(T)$ corresponding to the phase transition is obviously related to local strains in the fcc lattice developing easier than those in the pc lattice. This suggestion is buttressed by the monotonic growth of the strain with increasing temperature in the initial, nonstationary part of the interferograms which characterizes the so-called short-time creep, i.e., the strain at the instant of load application (compare the left-hand parts of panels *a*, *b*, and *c* in Fig. 1). An alternative to this explanation of the increase in the strain rate at the phase transition could be stimulation of strain by a simultaneous structural rearrangement, which may increase the defect mobility.

It should be also pointed out that the strain-associated maximum is considerably broader than the calorimetric one. This effect cannot be initiated by heating rate effects, because, if we disregard the isothermal stage in the strain experiments, the heating rates in both cases are close in magnitude. It may be conjectured that the strain spectrum is affected by loading-induced defects forming in the fcc lattice, as well as in the pc lattice in the region adjoining the phase transition. The strain-induced maxima are, as a rule, fairly broad, and some peaks measured with small temperature steps often exhibit a complex structure, which implies a complex nature of the transition under loading, provided the loading is small.[6–9] While the reasons for the appearance of broad maxima in the rate spectrum of small inelastic strains remain unclear, nevertheless the results obtained in this work suggest that the approach involving construction of strain rate spectra may be used besides other techniques, such as microhardness studies or ultrasonic methods, to detect and analyze phase transitions in fullerites and other solids. For instance, the review in Ref. 13 compares the temperature dependences of microhardness obtained by various authors. The microhardness $H_v(T)$ of C_{60} single crystals exhibits breaks at $T\approx 155$ and 240–260 K.[14] The break in $H_v(T)$ observed to occur in C_{60} single crystals near the phase transition temperature was found also in Ref. 15, while according to Ref. 16 the $H_v(T)$ relation for C_{60} polycrystals is monotonic within the 80–570 K range. An internal friction peak and a minimum in the temperature dependence of sonic velocity were detected at $T=250$ K.[17] The observation of a peak in the temperature dependence of the rate of small inelastic strains provides support for the suggestions[1,2,13–16] that the phase transition affects the deformation properties of fullerites.

Besides the main peak in $\dot{\varepsilon}(T)$ at $T\approx 260$ K, one can see a small maximum at $T\approx 240$ K, similar to that observed[2] in a DSC curve and called a ''quenching'' peak, because it appears only in rapidly cooled samples. The quenching effect was associated[2] with the existence of nonequilibrium orientational order in quenched fullerite crystals. The orientational order is determined by the population ratio of the pentagon (n_p) to hexagon (n_h) configuration, n_p/n_h, whose equilibrium value depends on temperature. For instance, at room temperature, where C_{60} molecules rotate nearly freely, one may accept $n_p/n_h\approx 1$. Within the temperature interval $85<T<260$ K, this ratio is $n_p/n_h\approx 4$, and for $T<85$ K, i.e. in the orientational-glass state, $n_p/n_h\approx 5$.[3] Fast cooling (quenching) fixes at a low temperature the nonequilibrium state corresponding to a higher one, where the n_p/n_h ratio is shifted in favor of the higher-energy hexagon (h) configuration. Thus the quenching defects present in the pc lattice of the fullerite are annealed before the pc-fcc transition is reached, a phenomenon becoming manifest in DSC curves, as well as in strain curves, which respond to the mobility of defects in the course of their annealing. The shift of the strain-induced maximum by about 10 K towards lower temperatures compared to the calorimetric one (Fig. 2) is possibly associated with the effect of loading on the quenching defects, as well as with the lower heating rate. It is known that, unlike phase transitions, relaxation transformations are characterized by a more pronounced decrease of the transition temperature with decreasing heating rate.[18]

The weakly pronounced deviation of the strain spectrum from a monotonic course in the 200–220 K interval is similar to the multiple transitions observed[12] to occur in complex systems. It may be conjectured that this spectral shape indicates nonuniformity of the defect structure in single crystals, an aspect discussed, for example, in Ref. 8.

Thus the temperature spectrum of the rates of small inelastic strains offers a possibility of detecting phase and other transitions in C_{60} single crystals, as well as in other solids, from their effect on microplasticity. This spectrum differs somewhat from a DSC curve of a single crystal in that the maximum in the phase-transition region is broader, and the second peak, assigned to quenching defects, is shifted toward lower temperatures. It is conjectured that these changes are caused by the effect of mechanical loading on structural transformations of different nature (phase transition and a transition related to defect state).

Support by the Russian Scientific-Technical Program ''Fullerenes and Atomic Clusters'' (Grant 98052) is gratefully acknowledged.

*)E-mail: shpeizm.v@pop.ioffe.rssi.ru

[1] V. M. Egorov, B. I. Smirnov, V. V. Shpeĭzman, and R. K. Nikolaev, Fiz. Tverd. Tela (St. Petersburg) **38**, 2214 (1996) [Phys. Solid State **38**, 1219 (1996)].
[2] V. M. Egorov, V. I. Nikolaev, R. K. Nikolaev, B. I. Smirnov, and V. V. Shpeĭzman, Fiz. Tverd. Tela (St. Petersburg) **41**, 550 (1999) [Phys. Solid State **41**, 494 (1999)].
[3] M. I. F. David, R. M. Ibberson, T. J. S. Dennis, J. P. Hare, and K. Prassides, Europhys. Lett. **18**, 219 (1992).
[4] A. M. Rao, P. C. Eklund, U. D. Venkateswaran, J. Tucker, M. A. Duncan, G. M. Bendele, P. W. Stephens, J.-L. Hodeau, L. Marques, M. Núñez-Regueiro, I. O. Bashkin, E. G. Ponyatovsky, and A. P. Morovsky, Appl. Phys. A: Mater. Sci. Process. **64**, 231 (1997).
[5] A. L. Kolesnikova and A. E. Romanov, Fiz. Tverd. Tela (St. Petersburg) **40**, 1178 (1998) [Phys. Solid State **40**, 1075 (1998)].
[6] V. V. Shpeĭzman, N. N. Peschanskaya, A. K. Andreev, G. E. Kodzhaspirov, Yu. P. Solntsev, and P. N. Yakushev, Prob. Prochn. **7**, 115 (1987).
[7] V. V. Shpeĭzman, N. N. Peschanskaya, and P. N. Yakushev, in *Nondestructive Characterization of Materials VIII* (Plenum, New York, 1998), p. 157.
[8] N. N. Peschanskaya, P. N. Yakushev, A. B. Sinani, and V. A. Bershtein, Thermochim. Acta **238**, 429 (1994).
[9] N. N. Peschanskaya, B. I. Smirnov, V. V. Shpeĭzman, and P. N. Yakushev, Fiz. Tverd. Tela (Leningrad) **31**, 271 (1989) [Sov. Phys. Solid State **31**, 703 (1989)].
[10] M. Tachibana, M. Michiyama, H. Sakuma, K. Kikuchi, Y. Achiba, and K. Kojima, J. Cryst. Growth **166**, 883 (1996).
[11] N. N. Peschanskaya, P. N. Yakushev, and V. A. Stepanov, Fiz. Tverd. Tela (Leningrad) **26**, 1202 (1984) [Sov. Phys. Solid State **26**, 729 (1984)].
[12] N. N. Peschanskaya, P. N. Yakushev, and V. Yu. Suvorova, Fiz. Tverd. Tela (St. Petersburg) **37**, 2602 (1995) [Phys. Solid State **37**, 1429 (1995)].
[13] V. D. Natsik, S. V. Lubenets, and L. S. Fomenko, Fiz. Nizk. Temp. **22**, 337 (1996) [Low Temp. Phys. **22**, 264 (1996)].
[14] L. S. Fomenko, V. D. Natsik, S. V. Lubenets, V. G. Lirtsman, N. A. Aksenova, A. P. Isakina, A. I. Prokhvatilov, M. Strzhemechnyĭ, and R. Ruoff, Fiz. Nizk. Temp. **21**, 465 (1995) [Low Temp. Phys. **21**, 364 (1995)].
[15] M. Tachibana, M. Michiyama, K. Kikuchi, Y. Achiba, and K. Kojima, Phys. Rev. B **49**, 14945 (1994).

[16] Yu. A. Ossipyan, V. S. Bobrov, Yu. S. Grushko, R. A. Dilanyan, O. V. Zharikov, M. A. Lebyodkin, and V. S. Sheckhtman, Appl. Phys. A: Solids Surf. **56**, 413 (1993).
[17] N. P. Kobelev, A. P. Moravskiĭ, Ya. M. Soĭfer, I. O. Bashkin, and O. G. Rybchenko, Fiz. Tverd. Tela (St. Petersburg) **36**, 2732 (1994) [Phys. Solid State **36**, 1491 (1994)].
[18] V. A. Bershteĭn and V. M. Egorov, *Differential Scanning Calorimetry in the Physical Chemistry of Polymers* (Ellis Horwood, 1994) [Russian original, Khimiya, Leningrad, 1990].

Translated by G. Skrebtsov

Properties of the microhardness of single-crystal C_{60} fullerite in sclerometric tests

A. G. Melent'ev, N. V. Klassen, N. P. Kobelev, R. K. Nikolaev, and Yu. A. Osip'yan

Institute of Solid-State Physics, Russian Academy of Sciences, 142432 Chernogolovka, Moscow District, Russia

(Submitted June 9, 1998; resubmitted November 11, 1998)
Fiz. Tverd. Tela (St. Petersburg) **41**, 1119–1123 (June 1999)

The mechanical properties of single-crystal fcc C_{60} fullerite are investigated by sclerometry and precision contact profilometry. Quantitative estimates are obtained for the microhardness anisotropy on the (100) and (111) planes. Polarity of the mechanical properties is observed in the (111) plane. The mechanisms considered for the orientational deformation of C_{60} single crystals by a moving indentor confirm existing data showing that plastic deformation in solid C_{60} occurs along the [011] (111) systems. © *1999 American Institute of Physics.* [S1063-7834(99)04106-4]

Until recently the mechanical properties of fullerites were investigated mainly by indentation.[1–3] Methods such as volume deformation by compression, bending, and so on were difficult to use because of a lack of sufficiently large single-crystal samples. The recent synthesis of C_{60} single crystals with volumes up to several tens of cubic millimeters[4] opens up prospects for investigating the mechanical properties of fullerites by other methods also, specifically, sclerometry, which makes it possible to obtain more complete information about the character of the deformation of the material (especially about its orientational dependence) than does indentation. Moreover, since a scratch is an elementary event of many mechanotechnological processes, sclerometric investigations are of not only scientific but also practical interest.

The present work is devoted to the investigation of the mechanical properties of single-crystal fcc C_{60} fullerite by sclerometry and precision contact profilometry.

1. SAMPLES AND PROCEDURE

All measurements were performed on single-crystal fcc samples of solid C_{60}. The method of sublimation and desublimation (growth from the gas phase) was used to grow the C_{60} single crystals. Chromatographically purified 99.95% pure fullerite powder in amounts of 100–150 mg was placed in a quartz ampul 8–10 mm in diameter and 250 mm long, which was evacuated to 1×10^{-6} mm Hg and heated to 300 °C. Organic solvents and volatile impurities were removed from the powder over 8–10 h in a dynamic vacuum. Then the powder was subject to triple vacuum sublimation. Small C_{60} crystals purified in this manner were once again placed in a quartz ampul 8–10 mm in diameter and 150 mm long, which was evacuated to 1×10^{-6} mm Hg, sealed, and placed in a horizontal two-zone furnace. The single crystals were grown under the following conditions: sublimation temperature 600 °C, crystallization temperature 540 °C, and growth time 8–10 h.

Well-faceted C_{60} fullerite single crystals up to 10 mg were obtained and then slowly cooled together with the furnace to room temperature. The exterior faceting of the crystals was characterized by square, rectangular, triangular, and hexagonal faces. Laue diffraction patterns and x-ray topograms confirmed that the C_{60} fullerite samples obtained were single-crystalline.

The sclerometric tests were conducted on the growth faces of samples with two crystallographic orientations: (100) and (111). Scratches (primarily in the form of rectangular loops) were made on the (100) faces in the [100] and [110] directions and on the (111) faces in the [112] and [110] directions, using a PMT-3 apparatus, by a Vickers diamond

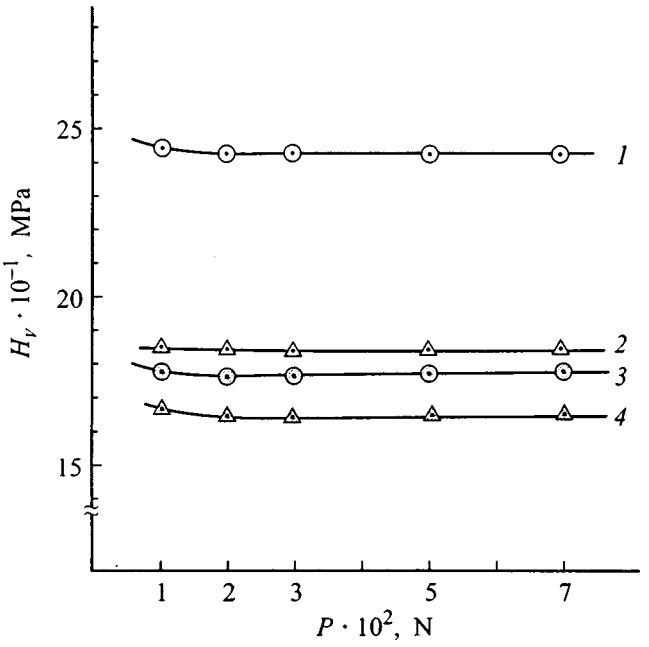

FIG. 1. Sclerometric microhardness H_ν of fcc C_{60} fullerite versus the load P on an indentor for different planes and crystallographic directions: *1*—$\langle 1\bar{1}2\rangle(111)$, *2*—$\langle 110\rangle(100)$, *3*—$\langle 11\bar{2}\rangle(111)$, and *4*—$\langle 010\rangle(100)$.

prism with apex angle 136° and fixed loads from 1 to 7 g. The width of a scratch was determined either visually in a Neofot-2 optical microscope or (to tenths of a micron) with a Talystep profilometer.[5] The microhardness of the crystals was estimated using the well-known relation

$$H_v = kP/b^2,$$

where H_v is the microhardness in kg/mm^2, $k = 3.71$ is a dimensionless coefficient, b is the scratch width in mm, and P is the load on the indentor in kg. All experiments were performed on fresh samples (within a few hours after extraction from the ampul) at room temperature.

2. MEASUREMENT RESULTS AND DISCUSSION

Investigations showed that the microhardness H_v for sufficiently large values of P (Fig. 1) is virtually independent of the load and even at $P = 3$ g we have $H_v(P) = \text{const}$. The typical form of scratches made in different crystallographic directions under $P = 3$ g on the (100) and (111) faces of a C_{60} single crystal is shown in Fig. 2. As one can see from the figure, the scratches are mainly of a viscoplastic character, and they are accompanied by small cleavages, a few cracks, and fault lines.

Scratches made in the [010] and [001] directions on the (100) plane are identical and symmetric. The fault lines along the edges of the scratches make an angle of 45° with the scratch axis and are directed opposite to the motion of the indentor. Cracks on these scratches are relatively rare and make an angle of 45° with the scratch axis.

Scratches made in the [011] directions are also symmetric and identical to one another. The width of these scratches is somewhat smaller, i.e., a small so-called anisotropy of microhardness of the first kind (Figs. 2 and 3) is observed on the (100) plane. A few cracks, emanating from a scratch at an angle of 45°, which change direction away from the scratch by 90° with respect to the scratch axis, are observed for scratches made in these directions. Fault lines are not always observed on these scratches. However, when they were observed (Fig. 2), these lines made an angle of 90° with the scratch.

The scratch width on the (111) plane and consequently the microhardness of the crystal depend on not only the orientation of the scratch but also the sign of the direction of motion of the indentor (Fig. 4), i.e., the so-called mechanical polarity effect is observed on this surface.[6] Here the exterior form of scratches also depends on the direction of motion of the indentor (Fig. 2). For example, scratches made in the direction $[11\bar{2}]$ are of a viscosplastic character, they have virtually no cracks, and they are accompanied by frequent fault lines, making an angle of 30° with the scratch axis and opposite to the direction of motion of the indentor. The scratches made in the opposite direction $[\bar{1}\bar{1}2]$ are brittle-plastic; they are often accompanied by cleavages and by infrequent and short fault lines perpendicular to the scratch axis. For scratches made on this plane in the [110] directions the mechanical polarity effect is manifested in the asymmetry of the scratches: on one side of a scratch numerous fault lines make an angle of 60° with the scratch axis, while on the other side of the scratch the fault lines are very infrequent and are parallel to the scratch axis.

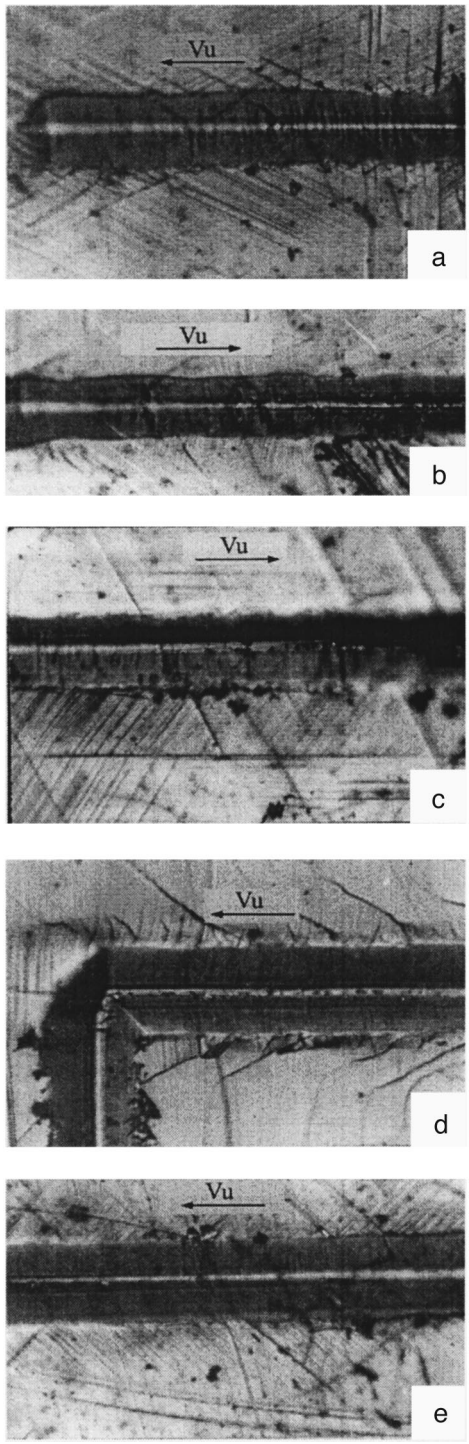

FIG. 2. Typical form of scratches made on (111) and (100) planes by a moving indentor with $P = 3$ g: a, b, c—(111) plane, directions: $\langle 11\bar{2}\rangle$—(a), $\langle \bar{1}\bar{1}2\rangle$—(b); $\langle 110\rangle$—(c); d, e—(100) plane, directions: $\langle 110\rangle$—(d); $\langle 010\rangle$—(e). The arrows indicate the direction of motion of the indentor.

The experimentally observed character of the formation of scratches and the arrangement of the fault lines and cracks along them agree on the whole with existing published data on planes of plastic glide and cleavage planes of the fcc phase of solid C_{60}. Thus, according to Refs. 3 and 7 the

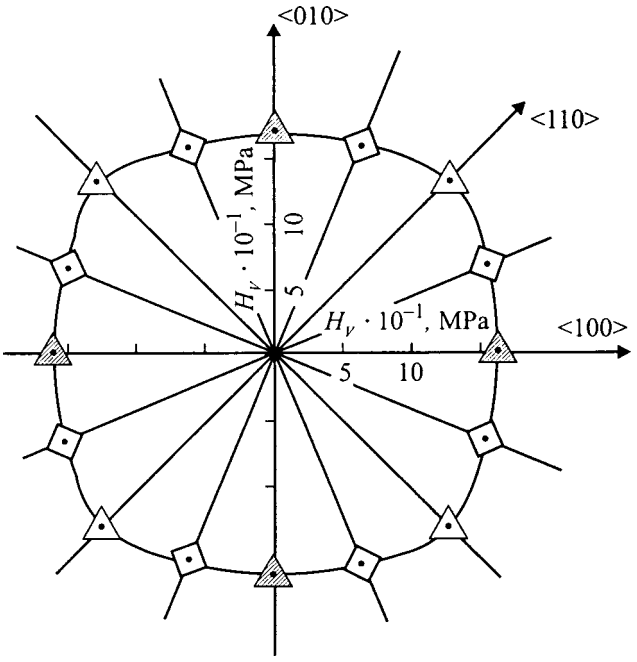

FIG. 3. Microhardness H_v anisotropy of the first kind on a (100) plane of fcc C_{60} fullerite with $P=3$ g.

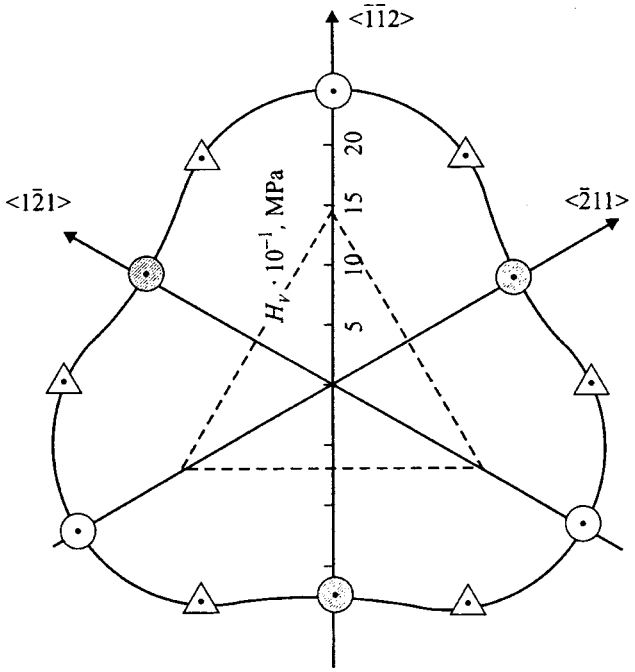

FIG. 4. Mechanical polarity effect for microhardness on the (111) plane of fcc C_{60} fullerite, $P=3$ g.

glide systems in C_{60} are the systems [110] {111} and the cleavage planes are {111} planes. Figures 5 and 6 show projections onto the (100) and (111) planes of the planes and directions of dislocation glide along which material can be pressed into the interior volume and ejected onto the surface of the crystal during the motion of the indentor in different crystallographic directions. Comparing the experimentally observed fault lines (Fig. 2) with Figs. 5 and 6 suggest the following schemes for the operation of the dislocation glide systems.

On the (100) plane (Fig. 5), as the indentor moves in the [010] direction (and also directions similar to it) material is pressed into the crystal along the $(11\bar{1})$ plane to the left of a scratch and along the (111) plane to the right of the scratch, while material is ejected along the $(\bar{1}11)$ and $(1\bar{1}1)$ planes, respectively. In the process, converging fault lines along the $[01\bar{1}]$ and [011] directions should form on the surface of the sample, and this is observed experimentally.

For scratching in the [011] direction material can be pressed in along the (111) plane (in front of a scratch) and along the $(11\bar{1})$ and $(1\bar{1}1)$ planes, respectively, to the left and right of a scratch, while material is ejected along the $(\bar{1}11)$ plane (in front of the indentor) and along the $(1\bar{1}1)$ and $(11\bar{1})$ planes to the right and left of a scratch. In the process the microhardness of the crystal can be expected to increase somewhat, at least because of the fact that, as profilometric investigations have shown, for scratching in this

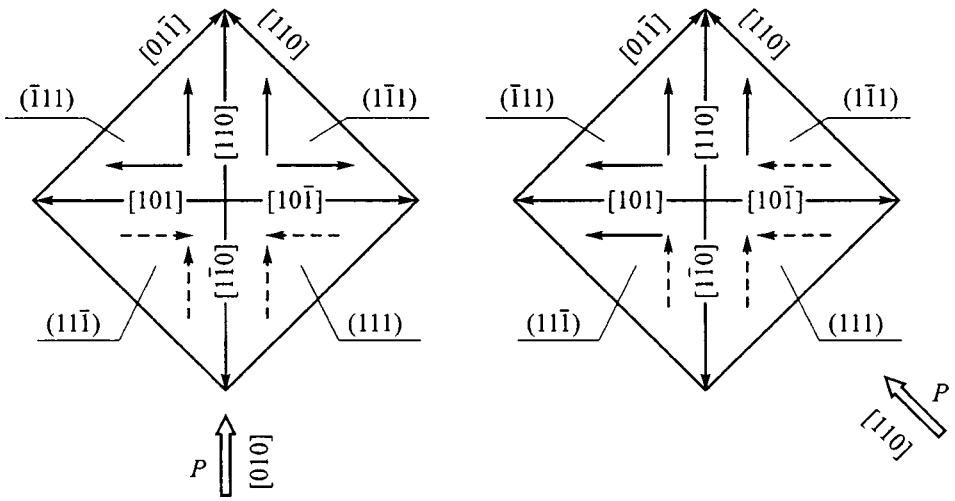

FIG. 5. Diagram of the operation of glide systems during the motion of an indentor on the (100) plane of fcc C_{60} fullerite. Solid arrows—direction of ejection of material on the surface of the crystal; dashed arrows—direction of development of deformation into the crystal.

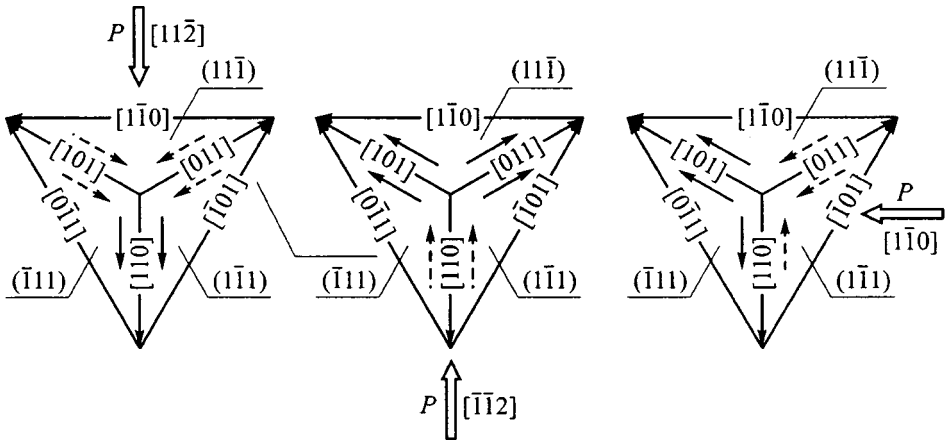

FIG. 6. Diagram of the operation of glide systems during the motion of an indentor on the (111) plane of fcc C_{60} fullerite. Solid arrows—direction of ejection of material on the surface of the crystal; dashed arrows—direction of development of deformation into the crystal.

direction a so-called deformation zone, which prevents advancement of the indentor and results in narrowing of the scratch, forms in front of the moving indentor. It should also be noted that in this case the crystal can deform along several glide systems simultaneously, and this means that here the probability that the glide systems intersect with one another is high, which therefore can result in a high concentration of internal stresses—which is probably the reason why a large number of cracks are present for scratching in the [011] and similar directions.

For scratching of the (111) plane, as one can see from the diagram in Fig. 6, the character of scratch formation in the directions $[11\bar{2}]$ and $[\bar{1}\bar{1}2]$ is different. This is responsible for the polarity of the mechanical properties. Thus, for scratching along $[11\bar{2}]$ material in front of a scratch is pressed into the crystal—by glide along the $(11\bar{1})$ plane; in addition, here the systems $[101](\bar{1}11)$ to left and $[110](1\bar{1}1)$ can operate to the right, respectively, of a scratch; ejection of material on the surface of the sample occurs along the systems $[110](\bar{1}11)$ and $[110](1\bar{1}1)$ to the left and right, respectively, of a scratch. In the process a converging system of fault lines making an angle of 30° with the scratch should form on the surface (Fig. 2a). For indentor motion along $[\bar{1}\bar{1}2]$ material is pressed in along two glide systems $[110](\bar{1}11)$ and $[110](1\bar{1}1)$), so that the scratch depth should be smaller here. Moreover, material is ejected on the surface of the crystal along the $(11\bar{1})$ plane directly in front of the indentor, which should also give rise to an additional resistance to the processes forming the scratch. The increase in microhardness (polarity of mechanical properties) expected in this case is observed experimentally (Fig. 4).

For scratching along the $[1\bar{1}0]$ direction, as follows from Fig. 6, the operation of the glide systems to the left and right of a scratch is different. To the left of a scratch material is pressed in along the systems $[011](11\bar{1})$ and $[011](1\bar{1}1)$ and to the right of the scratch along the system $[\bar{1}10](1\bar{1}1)$. In this case ejection of material on the surface to the left of the scratch occurs along $(\bar{1}11)$ plane, which should lead to the formation of converging fault lines making an angle of 60° with the scratch axis. To the right of a scratch material can be ejected on the surface of the crystal along the system $[101](11\bar{1})$ and fault lines can form parallel to a scratch. All this is observed experimentally (Fig. 2c).

In summary, in this work the sclerometric microhardness of C_{60} fullerite in the (100) and (111) planes was investigated. It was established that scratches on the investigated planes of fcc C_{60} fullerite are mainly of a viscoplastic character. It was shown that the (100) plane is characterized by microhardness anisotropy of the first kind, and polarity of mechanical properties was observed on the (111) plane. The results of the investigations of microhardness and scratch formation processes in different crystallographic directions agree with the existing ideas about dislocation-glide systems in solid fcc C_{60} fullerite.

We thank S. S. Khasanov for performing the x-ray crystallographic certification of the samples.

This work was performed as part of the Russian Science and Technology Program ''Current Directions in Condensed-Media Physics: Fullerenes and Atomic Clusters.''

[1] J. Li, S. Komija, T. Tamura, and C. Nagasaki, Physica **195**, 205 (1992).
[2] Yu. A. Osipyan, V. S. Bobrov, Yu. Grushko, K. A. Dilanyan, O. V. Zharikov, M. A. Lebyodkin, and V. Sh. Sheckhtman, Appl. Phys. A: Solids Surf. **56**, 413 (1993).
[3] V. I. Orlov, V. I. Nikitenko, R. K. Nikolaev, I. N. Kremenskaya, and Yu. A. Osip'yan, JETP Lett. **59**, 704 (1994).
[4] N. P. Kobelev, R. K. Nikolaev, Ya. M. Soifer, and S. S. Khasanov, Chem. Phys. Lett. **276**, 263 (1997).
[5] A. G. Melent'ev, Kristallografiya **40**, 736 (1995) [Crystallogr. Rep. **40**, 704 (1994)].
[6] Yu. S. Boyarskaya, D. Z. Grabko, and M. S. Kats, *The Physics of Microindentation Processes* (Shtiintsa, Kishinev, 1986), p. 183.
[7] S. V. Lubenets, V. D. Natsik, L. S. Fomenko, A. P. Isakina, A. I. Prokhvatilov, M. A. Strzhemechnyĭ, and N. A. Aksenova, Fiz. Nizk. Temp. **23**, 338 (1997) [Low Temp. Phys. **23**, 251 (1997)].

Translated by M. E. Alferieff

Electronic structure of C_{60} fullerite

V. V. Sobolev* and E. L. Busygina

Udmurtia State University, 426034 Izhevsk, Russia
(Submitted May 6, 1998; resubmitted October 29, 1998)
Fiz. Tverd. Tela (St. Petersburg) **41**, 1124–1125 (June 1999)

The complete systems of fundamental optical functions of single crystals and polycrystalline films of fullerite (C_{60}) are calculated on the basis of known reflection spectra and the imaginary and real parts of the permittivity. The integrated permittivity spectra are decomposed into elementary components. The three basic parameters of each component (the energy of the maximum, the half-width, and the oscillator strength) are determined. The nature of these components of the permittivity is discussed on the basis of existing theoretical calculations of fullerite bands. © *1999 American Institute of Physics.* [S1063-7834(99)04206-9]

1. Two modifications of carbon are well known: diamond and graphite. Their properties have been studied in many works.[1] A flood of publications devoted to a third and unusual modification—fullerite—has been observed in the last few years.[2,3] The most common modification among them is fullerite C_{60}: the unit cell of the cubic face-centered lattice contains four formula units. A number of properties of great scientific and practical interest have already been established for it, including the existence of a high superconductivity temperature in intercalated fullerite ($T_c \approx 30\,\mathrm{K}$). For this reason, investigations of the electronic structure of C_{60} over a wide energy range of intrinsic absorption are of fundamental importance.

It is generally accepted that the most complete information on this problem is contained in an assortment of optical functions.[4] Among them the real part ε_1 and imaginary parts ε_2 of the permittivity as well as the reflection coefficient R are distinguished. This is due primarily to the fact that their spectra can be measured experimentally over a wider energy range than for many other functions (the absorption coefficient, the refractive index, and others). The energies of the maxima of the R and ε_2 spectra are ordinarily taken as the energy of intrinsic interband or excitonic transitions. Their specific nature is determined after comparing experiment and theory.[4,5]

However, all measured spectra give the integrated curve as a sum of all transitions. Of fundamental importance is the fact that because of strong overlapping many of them may not be observed structurally.[1,4,6] For this reason a fundamental problem of any spectroscopy is to decompose the measured spectral curve into elementary components and to determine their basic parameters: the peak energies E_i and half-widths H_i and the transition probabilities f_i. We have employed a unique method for solving this problem using Argand diagrams with no adjustable parameters. However, the ε_2 and ε_1 spectra must be taken into account simultaneously.

2. We have calculated complete systems of fundamental optical functions, decomposed the integrated ε_2 and ε_1 spectra into components, and determined the parameters of the components (E_i, H_i, f_i) of C_{60} single crystals and polycrystalline films. The calculations were performed using the well-known methods[1,4,6] based on the experimental R spectra over the range 1–35 eV,[7] the ε_2 and ε_1 spectra over the range 1.5–5 eV (Ref. 8) for single crystals, and the ε_2 and ε_1 spectra over the ranges 1.5–5 eV,[9] 1.5–9.5 eV,[10] and 1.5–7 eV (Ref. 11) for films. Only the results of the decompositions of the integrated ε_2 and ε_1 spectra into components are presented here.

Twenty-two components of the ε_2 spectrum in the range 2–10 eV, instead of the four peaks of the integrated curve, were established. Figure 1 shows the oscillator strengths f_i of these components (vertical bars); the numbers label the components in order. Even though the integrated curves from five different treatments were used, the positions of the peaks of the components were determined to a high degree of accuracy (± 0.01 and $\pm(0.01-0.04)$ eV for the most intense and all other bands).

Two attempts have been made to reproduce (but not decompose!) the integrated ε_2 curves of C_{60} films using 16 and 10 Lorentzian oscillators with 38 (Ref. 10) and 40 (Ref. 12) adjustable parameters. The fact that such a gigantic number of adjustable parameters was used underscores once again that such methods of reproducing the integrated curve with an arbitrary set of components are doubtful.

Analysis of the characteristic features of the decomposition of the ε_2 and ε_1 spectra of fullerite by a parameter-free method of Argand diagrams and reproduction of the ε_2 spectra using an enormous number of adjustable parameters convincingly supports the first method. Of course, this parameter-free method of decomposing the ε_2 and ε_1 spectra into elementary components is still not entirely adequate and is the zeroth approximation of a more perfect solution of this problem. It should be stressed that in the standard approximation where the total permittivity is represented as a sum of contributions of individual Lorentzian oscillators the Argand diagram method makes it possible to decompose uniquely the integrated ε_2 and ε_1 spectra into a minimum number of bands. Transitions with close energies but not necessarily close properties are summed in each band. For this reason

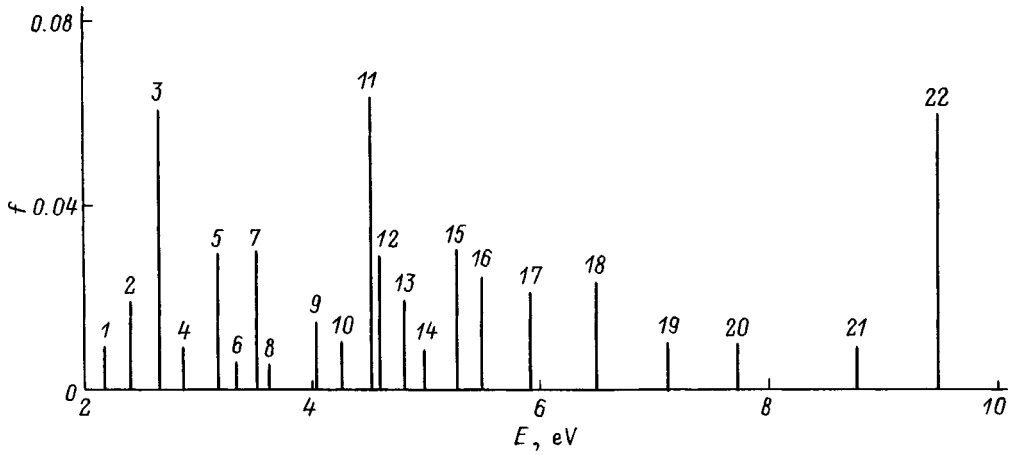

FIG. 1. Oscillator strengths f_i of 22 components of ε_2 for C_{60} fullerite versus the energy of the components.

the spectra can be additionally decomposed into several components each on the basis of theoretical models of the possible fine structure of the bands.

3. The electronic structure and optical spectra of a C_{60} molecular crystal have been calculated in many treatments.[3] The absorption spectra vary comparatively little in the free molecule—C_{60} in solution—crystal series. For this reason it is assumed in advance that at least the intense bands are due to small-radius Frenkel excitons, which are usually characteristic for molecular crystals. The electronic structure of C_{60} fullerite has been calculated in a simplified manner in the approximation employing the molecular terms h_u, h_g, g_u, g_g, and t_u and bands; the three upper valence bands V_1, V_2, and V_3 and the three lower conduction bands C_1, C_2, and C_3 are chosen from all bands.[3] These calculations provide a basis for suggesting a general model of the nature of the 22 components of ε_2 which we have established for C_{60} fullerite. In the band model they are due to the transitions $h_u \rightarrow t_{1g}$ ($V_1 \rightarrow C_2$) for Nos. 1–3, h_g, $g_g \rightarrow t_{1u}$ ($V_2 \rightarrow C_1$) for Nos. 4–8, $h_u \rightarrow h_g$ ($V_1 \rightarrow C_3$) for Nos. 9–12, h_g, $g_g \rightarrow t_{2u}$ ($V_2 \rightarrow C_2$) for Nos. 13–15, g_u, $t_{2u} \rightarrow h_g$ ($V_3 \rightarrow C_3$) for Nos. 16–19, and $V_1 \rightarrow C_4$, C_5 and $V_2 \rightarrow C_3$, C_4 for Nos. 20–22. In the simplest approximation all occupied (unoccupied) terms are five-fold (three-fold) degenerate. In real crystals various perturbations lift this degeneracy. The terms split, and each band always has a complicated fine structure. This gives a general, satisfactory explanation of the quite complicated structure of the spectrum that we have established for the components of transitions in fullerite. A similar, general scheme of the nature of the components of the spectrum ε_2 can also be proposed in the small-radius exciton model. The fullerite C_{60} is a molecular crystal with very flat bands. Therefore it is likely that the ε_2 components which we have established are due to small-radius excitons. One can hope that the use of the new information that we have established about the most complete component composition of transitions and their parameters (E_i, H_i, f_i) over a wide energy range of fundamental absorption (1.5–35 eV) will aid in developing much more accurate and complete models of the electronic structure of fullerite and related materials.

We thank W. E. Pickett, Y. Iwasa, M. K. Kelly, G. Guizetti, and H. Kataura for providing reprints.

This work was supported by the Center for Fundamental Studies (St. Petersburg University).

*E-Mail: sobolev@uni.udm.ru

[1] V. V. Sobolev, *Instrinsic Energy Levels of Group A^4 Solids* [in Russian] (Shtiintsa, Kishinev, 1978).
[2] A. V. Eletskiĭ and B. M. Smirnov, Usp. Fiz. Nauk **165**(9), 977 (1995).
[3] W. E. Pickett, Solid State Phys. **48**, 225 (1994).
[4] V. V. Sobolev and V. V. Nemoshkalenko, *Methods of Computational Solid-State Physics. The Electronic Structure of Semiconductors* [in Russian] (Naukova Dumka, Kiev, 1988).
[5] V. V. Sobolev and V. I. Donetskikh, Zh. Éksp. Teor. Fiz. **59**, 3 (1970) [Scand. J. Metall. **32**, 1 (1971)].
[6] V. V. Sobolev and V. Val Sobolev, Fiz. Tverd. Tela (St. Petersburg) **36**, 2560 (1994) [Phys. Solid State **36**, 1393 (1994)].
[7] Y. Iwasa, T. Yasuda, Y. Naito, and T. Koda, *Activity Report of Synchrotron Radiation Laboratory* (The Institute for Solid State Physics, Tokyo, 1992).
[8] P. Milani, M. Manfredini, G. Guizzetti, F. Marabelli, and M. Patrini, Solid State Commun. **90**, 639 (1994).
[9] M. Patrini, F. Marabelli, G. Guizzetti, P. Milani, and M. Manfredini, in *Proceedings of Symposium on Recent Advances in the Chemistry and Physics of Fullerenes*, Proc. **92–24**, 632 (1994).
[10] M. K. Kelly, P. Etchegoin, D. Fuchs, W. Kratschmer, and K. Fostiropoulos, Phys. Rev. B **46**, 4963 (1992).
[11] H. Kataura, J. Endo, J. Achiba, K. Kikuchi, T. Hanyu, and Sh. Yamaguchi, Jpn. J. Appl. Phys., Part 2 **34**, L1467 (1995).
[12] J. Hora, P. Panek, K. Navratil, B. Handlirova, J. Humlicek, H. Sitter, and D. Stifter, Phys. Rev. B **54**, 5106 (1996).

Translated by M. E. Alferieff

METALS. SUPERCONDUCTORS

Properties of positron annihilation in metals

V. I. Grafutin,*) E. P. Prokop'ev, G. G. Myasishcheva, and Yu. V. Funtikov

Institute of Theoretical and Experimental Physics, 117259 Moscow, Russia
(Submitted June 11, 1998)
Fiz. Tverd. Tela (St. Petersburg) **41**, 929–934 (June 1999)

Positron annihilation in bulk metals has been studied by examining the angular distribution of the annihilation photons in polycrystalline samples of magnesium, aluminum, copper, zinc, indium, tin, lead, and bismuth. It has been shown that conduction electrons as well as core electrons take part in this process. The conduction electron densities and Fermi energies have been determined. It is found that the electron density in the vicinity of a positron is significantly higher than the density of the free electron gas. We believe that this is due to the formation of Wheeler complexes and we estimate its charge. We have analyzed various means of measuring the conduction electron density and conclude that the positron method gives the most reliable information. © *1999 American Institute of Physics.* [S1063-7834(99)00106-9]

Positron annihilation has been actively investigated in metals (see, for example, Refs. 1–4). The reason is that the annihilation method allows one to determine such important properties of metals as the electron momentum distribution, the Fermi energy level ε_F (eV), the number of free electrons Z_c per metal atom, and their number density n_p (cm^{-3}) in the conduction band. These parameters, as is well known,[5–8] determine in large part the mechanical, electrical, and magnetic properties of metals.

In the crystalline lattice of a metal not all the valence electrons are bound to their atoms. Some of them ($Z_c \geqslant 1$ per atom) are mobile in the bulk of the metal and form an electron gas in which the framework of positive ions is, as it were, immersed. The electron gas in turn compensates the electrostatic repulsion forces between ions and binds them to the solid (metallic bonding). The number of mobile electrons Z_c and the electron number density n_p, of course, differ for ideal and real (e.g., polycrystalline samples) metals. Therefore, in the present work we have undertaken an experimental study of positron annihilation [that is to say, of the angular distribution of the annihilation photons (ADAP)] in a number of polycrystalline samples of metals to clarify the mechanism of annihilation and determine the parameters ε_F, Z_c, and n_p, and also their dependence on the nature of the metal in question.

1. TECHNIQUE, THEORY, AND RESULTS OF EXPERIMENT

ADAP measurements were performed on a setup incorporating a parallel-gap geometry for recording the annihilation photons. The setup underwent a redesign which included automation of the experiment and recording of the loading of both detectors simultaneous with recording of coincidences,[9] which makes it possible to introduce corrections to the ADAP curves due to absorption of photons in the subject sample. A quantity of the radioactive isotope Na^{22} with an activity of 100 mCi served as the positron source. The number of coincidences at maximum was ~20 000. The investigated samples with dimensions $\sim 10\times 20\times 10\ \mathrm{mm}^3$ were cut from whole chunks of metal and were not subjected to any special kind of treatment. We chose Mg, Al, Cu, Zn, In, Sn, Pb, and Bi for study. Two metals of this series (Al and Cu) were already investigated earlier,[10] but these were samples with a different prehistory.

It is well known that for an experimental setup with a parallel-gap geometry of recording annihilation photons the electron density n_e in momentum space is related to the ADAP of the investigated metal $f(\theta)$ by the expression[10]

$$f(\theta)\cong A_0 \int_{p_z-\frac{1}{2}\Delta p_z}^{p_z+\frac{1}{2}\Delta p_z} dp_z \int_{-\Delta p_y}^{+\Delta p_y} dp_y \int_{-\infty}^{+\infty} n_e(p_x,p_y,p_z)\,dp_x, \tag{1}$$

where A_0 is a normalization constant; Δp_y and Δp_z are the resolutions of the setup in the momentum projections p_y and p_z, satisfying the conditions

$$\Delta p_y \gg 2p_{\max}; \quad \Delta p_z \ll p_{\max}.$$

Here $p_{\max}$ is the maximum value of the electron momentum in the metal; θ is the deviation of the emission angle of the annihilation photons from 180°,

$$p_z = \theta mc,$$

where m is the effective mass of the electron in the metal and c is the speed of light. Therefore, if we are considering isotropic materials (e.g., polycrystalline samples) the electron momentum density (the z component) can be determined from the ADAP data as

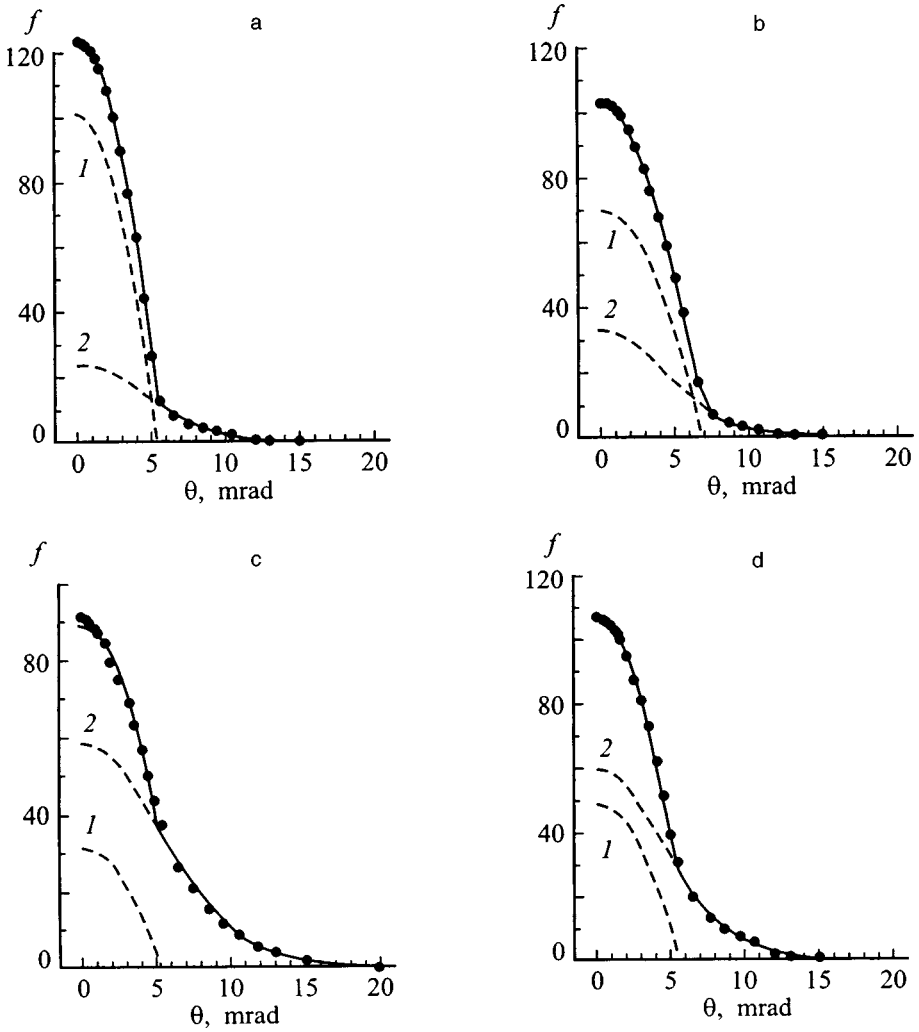

FIG. 1. Angular distributions of annihilation positrons in samples of magnesium (a), aluminum (b), copper (c), and indium (d). The dashed lines show their expansion into a parabolic (*1*) and a Gaussian (*2*) component. The solid line is the sum of these components, the points are experimental values.

$$n_e(p_z) \sim \frac{1}{\theta}\frac{df(\theta)}{d\theta}. \tag{2}$$

In metals[5–8] the valence electrons are usually divided into two groups: the conduction electrons (free electrons) and the electrons found in the ion cores of the atoms (bound electrons). The conduction electrons have the momentum distribution

$$n_e(p) = \left[\exp\left(\frac{p^2/2m - \varepsilon_F}{\kappa_B T}\right) + 1\right]^{-1}, \tag{3}$$

where ε_F is the Fermi energy, κ_B is the Boltzmann constant, and T is the absolute temperature. At low temperatures this distribution is nearly rectangular. Hence it follows that a parabolic component should be observed in the ADAP curves of polycrystalline metals

$$f_p(\theta) = \begin{cases} (3I_p/4\theta_p^3)(\theta_p^2 - \theta^2), & |\theta| \leqslant \theta_p, \\ 0, & |\theta| > \theta_p. \end{cases} \tag{4}$$

Indeed, this component shows up quite clearly for all metals even at room temperature. Figure 1 plots the ADAP spectra of a number of polycrystalline metals obtained in our experiments. The dependence remaining after subtracting out the parabolic part, $f_g(\theta)$, is described quite well by a Gaussian

$$f_g(\theta) = (I_g/\sqrt{2\pi}\theta_g)\exp(-\theta^2/2\theta_g^2). \tag{5}$$

Here I_p and I_g are the intensities of the parabolic and Gaussian components, respectively, numerically equal to the relative area of the given component in the ADAP spectrum, θ_g is the variance of the Gaussian, and θ_p is the intersection angle of the parabola with the abscissa (the θ axis) (see Fig. 1).

Thus, the angular distributions of the annihilation photons of the investigated metal samples are described quite well by the sum of a parabola and a Gaussian:

$$f(\theta) = f_p(\theta) + f_g(\theta). \tag{6}$$

Here, by virtue of the normalization of the ADAP of a defect-free metal

$$\int_{-\pi/2}^{\pi/2} f(\theta)\, d\theta = 1, \tag{7}$$

the relation

$$I_p + I_g = 1 \tag{8}$$

is fulfilled, which relates the relative contributions of the parabolic and Gaussian components.

TABLE I. Calculated and experimental parameters of the investigated metals.

Metal	Z_c	n_A, 10^{22} cm^{-3}	λ_{exp}, ns^{-1} Refs. 1–3	θ_p^{exp}, mrad	θ_g^{exp}, mrad	θ_g^{calc}, mrad	I_p	$n_p(\tau)$, 10^{22} cm^{-3}	$n_p(\theta)$, 10^{22} cm^{-3}	n_p, 10^{22} cm^{-3}	σ	f	ε_F^{exp}, eV	ε_g^{exp}, eV	ε_F^{calc}, eV
Mg	2	4.3	4.44	5.41	4.63	3.5	0.72	43.1	9.4	8.6	2.15	4.6	7.5	8.2	7.1
Al	3	6.0	6.13	6.83	4.46	4.3	0.69	57.2	18.8	18.1	2.85	3.1	11.6	7.6	11.6
					6.4 Ref. 10									15.6	
Cu	1	8.4	8.80	5.5	4.84	2.8	0.38	45.9	10.3	8.45	2.3	4.5	8.0	8.9	7.0
				5.57	6.3 Ref. 10									15.2	
Zn	2	6.5	6.76	5.85	4.85	3.5	0.45	41.1	11.9	13.1	2.05	3.5	8.7	9.0	9.4
In	3	3.8	5.08	5.77	4.43	4.0	0.56	38.5	11.4	11.5	1.93	3.4	8.5	7.5	8.6
Sn	4	3.6	4.98	6.15	5.02	4.7	0.64	43.4	13.8	14.5	2.17	3.2	9.6	9.6	10.0
Pb	4	3.3	5.15	5.62	4.63	3.8	0.41	28.6	10.5	13.2	1.4	2.7	8.0	8.2	9.4
Bi	5	2.8	4.27	6.01	4.72	4.3	0.55	31.5	12.9	14.1	1.5	2.5	9.2	8.4	9.9

Note. The errors in (θ_p, θ_g) and (I_p, I_g) do not exceed 0.5 and 5%, respectively.

Next, using the parameter θ_p (the angle at which the parabola intersects the θ axis, Fig. 1), determined from the experiment, it is possible to estimate the Fermi momentum p_F and the Fermi energy ε_F of the investigated metal

$$p_F = \theta_p mc, \tag{9}$$

$$\varepsilon_F = \theta_p^2 (mc^2/2). \tag{10}$$

In the approximation of a free electron gas[5] the parameter θ_p also determines the number of free electrons Z_c (number of conduction electrons) per metal atom and their number density $n_p(\theta)$

$$Z_c = (8\pi/3)(mc^2/h)^3 (A/\rho N_A)\theta_p^3, \tag{11}$$

$$n_p(\theta) = Z_c n_A = (8\pi/3)(mc^2/h)^3 \theta_p^3, \tag{12}$$

and also the energy of the core electrons (i.e., of those electrons for which the angular distribution of annihilation photons in the ADAP spectra has a Gaussian distribution)

$$\varepsilon_g = (3/2)(mc^2/2)\theta_g^2. \tag{13}$$

Here N_a is Avogadro's number, h is the Planck constant, A is the atomic weight of the metal, and ρ is its density.

It is customary to compare experimentally obtained values of Z_c, ε_F, n_p, with the corresponding parameters of an ideal metal. We assume, following Kittel,[5] that an ideal metal is one in which all the valence electrons go into the conduction band. In this case,[5–8] the number of conduction electrons per metal atom, Z_c, is determined by the number of the group of the Periodic Table that the metal belongs to, and the Fermi energy ε_F and number density of the conduction electrons n_p, within the framework of the model of a free electron gas, are constants for that particular metal

$$\varepsilon_F = (h^2/8m)(3/\pi n_A Z_c)^{2/3}, \tag{14}$$

$$n_p = Z_c \ \ n_A = (N_A \rho/A) Z_c. \tag{15}$$

Here n_A is the atomic number density of the metal.

2. BEHAVIOR OF THE ADAP SPECTRA OF THE INVESTIGATED METALS

Figure 1 plots measured ADAP curves for magnesium, aluminum, copper, and indium together with their breakdown into parabolic and Gaussian components (dashed curves). The solid curves are the sums of these components and provide a good description of experiment. Table I lists the ADAP breakdown parameters of the investigated metals, and also data from Ref. 10 for aluminum and copper. It is noteworthy that there are substantial differences in the values of θ_p, I_p, θ_g, and I_g obtained in the present work and taken from Ref. 10, for copper as well as aluminum. In light of the fact that different samples were used in the two works, such differences can be explained in defect content of the samples.

Table I does not list values of I_g since $I_g = 1 - I_p$. As can be seen from the table, the values of the intensities of the Gaussian component I_g and the parabolic component I_p are comparable, i.e., positrons, with quite high probability, interact with electrons of the conduction band as well as with valence electrons of the ion cores. The high value of the probability I_p is probably due to the fact that a positron in a metal is employed by electrons due to the Coulomb attraction the positron exerts on the conduction electrons, which leads to its screening. According to Ferrante,[11] in metals even the formation of a three-particle Wheeler lepton system[12] with the makeup $e^- e^+ e^-$ (a positronium ion) is not excluded.

In general we assume that in a metal a negatively charged Wheeler complex $Ps^{-\eta}$ is formed, whose effective charge $\eta(-e)$ depends on the nature of the metal. Such a complex can interact quite strongly with the valence electrons of the ion cores through the formation of relaxing metastable quasi-atomic systems $Ps^{-\eta}+$ (valence electrons in the region of the ion core+the ion core) in analogy with the formation of quasi-atomic systems of the sort positron +anion in ionic crystals, which is the reason for the high values of I_g (see Table I). The electron wave functions of the complex $Ps^{-\eta}$ are transformed in the region of the ion cores into electron atomic wave functions of the outer valence electrons, while the positron wave function of a weakly bound positron, apart from the possibility of finding the positron at the nucleus of the metal ion, can be chosen in the form[13]

$$\Psi_+(r) = Ar \exp(\alpha r) \sim Ar, \quad \text{for } \alpha \to 0, \ 0 < r \leqslant r_c. \tag{16}$$

The constant A, according to Ref. 13, is significantly smaller

than unity; r_c is the radius of the ion core of the metal. At the point $r=r_c$ the wave function (16) should satisfy the matching condition $\Psi_+(r)=\Psi_+=\text{const}$, where Ψ_+ is the wave function of a thermalized positron in the bulk of the metal in the limit $k_+\to 0$ (Ref. 14), k_+ being the wave vector of the positron.

In the Slater orbital approximation of the electron wave functions[15] and the positron wave function (16) the half-width Γ_g at half-maximum of the ADAP curves (see Fig. 1) can be calculated by the formula[13]

$$\Gamma_g = C_{n(s,p,d)}\beta_{n(s,p,d)}/2, \tag{17}$$

and the width θ_g, corresponding to the variance of the Gaussian component, is equal to

$$\theta_g = \Gamma_g/\sqrt{2\ln 2} = \Gamma_g 0.85,$$

where $C_{n(s,p,d)}$ is a conversion factor: $C_{2(s,p)}=3.52$, $C_{3(s,p)}=2.86$, $C_{4(s,p)}=2.52$, $C_{5(s,p)}=2.48$, and $C_{6(s,p)}\sim 2$; $\beta_{n(s,p,d)}$ are the Slater parameters of the electron $n(s,p,d)$ orbitals of the atoms. We present an example of values of θ_g calculated for magnesium [^{12}Mg$(1s^2)(2s^2,2p^2)(3s^2)$]. According to Ref. 15, $\beta_{1s}=11.7$, $\beta_{2(s,p)}=7.85$, and $\beta_{3s}=2.85$. Calculating according to formula (14) gives $\theta_g(2(s,p))=11.7$ mrad and $\theta_g(3s)=3.47$ mrad. Comparison of these values of $\theta_g(2(s,p))$ and $\theta_g(3s)$ with the experimental value $\theta_g=4.63$ mrad (see Table I) indicates that positron annihilation in the region of an ion core occurs mainly on the outer valence $3s$ electrons of the atom and not on the inner $2(s,p)$ electrons [since $\theta_g(3s)\sim\theta_g$ while $\theta_g(2(s,p))$ is much greater than the experimental value of θ_g]. Estimates show that this is the case for all the metals we investigated: positrons in the region of the ion core annihilate mainly on the outer valence electrons of the atoms, which is confirmed by theoretical calculations.[14] Table I presents calculated values of $\theta_g(n(s,p))$ and experimental values of θ_g for the investigated series of metals. The agreement of the calculated and experimental values of θ_g, despite the roughness of the model (a free quasi-atom), is entirely satisfactory, which indicates that the chosen mechanism of annihilation in metals is entirely reasonable.

3. DETERMINATION OF THE ELECTRON NUMBER DENSITY (n_p) IN THE CONDUCTION BAND OF THE METAL

As was mentioned, the number density of the conduction electrons n_p (cm^{-3}) is an important characteristic of the metallic state. Various methods are used to determine n_p (Ref. 16): electrical, optical, galvanomagnetic (e.g., the Hall effect), measurements of the electronic part of the specific heat of the metal and the surface impedance at radio frequencies. Note that all of these methods measure the number density of the conduction electrons, which have energy near the Fermi energy,[6,7] and the temperature dependence of n_p allows one to determine successively p_F, ε_F, and the number density of the electrons of the free electron gas ($n_p=N/V$, where N is the total number of electrons and V is the volume). For example, the electrical conductivity of the metal σ is related to n_p by the well-known formula

$$\sigma = n_p e l/p_F = n_p e\tau/m; \quad \tau = 1/\nu_F; \quad m = p_F/\nu_F, \tag{18}$$

where l and τ are the mean free path and collision time of the electron in the metal. Thus, to determine n_p it is necessary, for the given sample, to determine the quantities σ and l or τ, which sometimes causes some difficulties. The positron annihilation method is a direct method for determining the value of n_p in a metal. Starting out from formula (12) and assuming that all the positrons annihilate in free collisions, we can write down an expression for determining the value of $n_p(\theta)$ from the given ADAP spectra (see Table I and Fig. 1)

$$n_p(\theta) = 5.942\times 10^{20}\theta_p^3, \ \text{cm}^{-3}. \tag{19}$$

Information about the electron density in the conduction band can also be obtained from measurements of the positron annihilation rate in metals. Indeed, in this case positronium is not formed and the positron annihilation rate is determined by the number density of the electrons with which they collide

$$\lambda_d = \sigma_d v n_e. \tag{20}$$

Here $\sigma_d=\pi r_0^2/\beta=\pi r_0^2/vc$ is the Dirac cross section of 2γ annihilation, v is the positron velocity, and r_0 is the classical electron radius.

Taking n_e to mean the sum of conduction electron (n_p) and core electron (n_g) number densities, expression (20) can be written in the form

$$\lambda_d = \lambda_p + \lambda_g, \tag{21}$$

where λ_p and λ_g are the annihilation rates of positrons on conduction electrons and on core electrons, respectively. Thus, the probabilities of annihilation via each of the enumerated channels are equal to

$$I_p = \lambda_p/(\lambda_p+\lambda_g), \tag{22}$$

$$I_g = \lambda_g/(\lambda_p+\lambda_g). \tag{23}$$

From expressions (20), (22), and (23) we can find a relation between the measured positron annihilation rate in the metal $\lambda_m=\lambda_d$, the electron number densities (conduction n_p and core n_g) and the corresponding annihilation probability (I_p and I_g) determined from the measurements of the angular distributions

$$n_p(\tau) = \lambda_m I_p \pi r_0^2 c = 1.354\lambda_m I_p\times 10^{23} \ \text{cm}^{-3}, \tag{24}$$

$$n_g(\tau) = \lambda_m I_g \pi r_0^2 c = 1.354\lambda_m I_g\times 10^{23} \ \text{cm}^{-3}. \tag{25}$$

Here $\lambda_m=1/\tau_m$ is the total positron annihilation rate, τ_m are measured lifetimes, and I_p and I_g are the relative areas under the parabola and the Gaussian in the ADAP spectra (see Fig. 1). Note that in formulas (19), (24), and (25) θ_p and θ_g have units of milliradians (mrad), and λ_m has units of inverse nanoseconds (ns^{-1}). Thus, expressions (20) and (24) allow one also, like expression (12), to estimate the number density of the conduction electrons n_p, but now using the results of measurements of the positron annihilation rate.

Table I lists number densities of the conduction electrons determined from the ADAP data $n_p(\theta)$ (12), measurements of the positron annihilation rate $n_p(\tau)$ (24), and values of n_p for ideal metals (15). Comparison of these number densities

shows that the values of $n_p(\theta)$ and n_p are similar but differ significantly from the values of $n_p(\tau)$. In light of this, the table also gives values of the factor

$$f = n_p(\tau)/n_p(\theta) = Z_c(\tau)/Z_c(\theta_p), \quad (26)$$

which characterizes, in our opinion, the increase in the electron density in the region around the positron in comparison with the electron density of the free electron gas.[4] As can be seen from the table, the values of this parameter for the investigated metals lie in the interval from 2.5 to 4.5. Thus, the interaction of positrons with the electron gas leads to a local increase in the electron density and, consequently, to an increase in the positron annihilation rate. At the same time, the increase in the electron density probably does not have a marked effect on the values of the momenta and energies of the electrons (and, consequently, on the values of θ_p) entering into the makeup of the $Ps^{-\eta}$ complex, since the ADAP spectrum describing annihilation from this complex is well approximated by a parabola while the experimentally determined value of the Fermi energy is in completely satisfactory agreement with its theoretical value. Consequently, it may be assumed that the values of the electron density determined by formula (19) using only ADAP data will most reliably reflect the values of the number density n_p of the free electron gas. This is indeed the case (see Table I).

The value of the effective charge η of the Wheeler complex $Ps^{-\eta}$ can be estimated by comparing the number density $n_p(\tau)$ of the electrons in the region around the positron with the number density $n(\mathrm{Ps})$ in a free positronium atom

$$n(\mathrm{Ps}) = 3/4\pi r_{Ps}^3 = 2\times 10^{23}\ \ \mathrm{cm}^{-3}, \quad (27)$$

where $r_{\mathrm{Ps}} = 1.06\times 10^{-8}$ is the radius of a Bohr orbital of positronium.

The ratio of these quantities $\varphi = n_p(\tau)/n(\mathrm{Ps})$ is listed in the table. The value of φ averaged over all the investigated metals turns out to be equal to 2.04. Obviously, this value of the effective charge η is related to the parameter φ by the formal relation

$$\eta = \varphi - 1,$$

i.e., $\eta = 1$, as it should in a Wheeler complex.

Thus, the mechanism of positron annihilation in metals via formation of a Wheeler complex seems to have found experimental confirmation.

In conclusion, we note that the method based on measurements of the angular distribution of annihilation photons allows one to determine parameters of the electron gas $(n_p, \varepsilon_F, Z_c)$, which are in quite good agreement with the corresponding parameters obtained from the theory of the free Fermi gas. At the same time, a combination of methods using the angular distribution and the temporal distribution of annihilation photons allows one to obtain information about the increase in the electron density in the region around the positron.

It should be stressed that using different methods of positron spectroscopy is undoubtedly extremely promising for studying the electronic properties of metals.

*)E-mail: grafutin@vitep5.itep.ru

[1] A. Seeger, F. Banhart, and W. Bauer, *Positron Annihilation*, edited by L. Dorikens-Vanpraet, M. Dorikens, and D. Segers (World Scientific, Singapore, 1989), p. 275.
[2] A. Baranowski and E. Dębowska, Acta Phys. Pol. A **88**, 13 (1985).
[3] M. J. Puska and R. M. Nieminen, Rev. Mod. Phys. **66**, 841 (1994).
[4] W. Brandt and J. Reinheimer, Phys. Rev. B **8**, 3104 (1970).
[5] C. Kittel, *Introduction to Solid State Physics*, 5th ed. (Wiley, New York, 1976).
[6] A. A. Abrikosov, *Introduction to the Theory of Normal Metals* (Academic, New York, 1972) [Russian original, Nauka, Moscow, 1972].
[7] I. M. Lifshits, M. Ya. Azbel', and M. I. Kaganov, *Electron Theory of Metals* (Consultants Bureau, New York, 1973).
[8] J. C. Slater, *Insulators, Semiconductors, and Solids* (McGraw-Hill, New York, 1967).
[9] V. I. Grafutin, V. P. Komlev, Yu. A. Novikov, A. V. Rakov, M. K. Filimonov, Yu. V. Funtikov, and V. P. Shantarovich, Izv. Ross. Akad. Nauk, Ser. Fiz. **58**, 79 (1994).
[10] Yu. A. Novikov, A. V. Rakov, and V. P. Shantarovich, Fiz. Tverd. Tela (St. Petersburg) **36**, 1710 (1994) [Phys. Solid State **36**, 935 (1994)].
[11] G. Ferrante, Phys. Rev. **170**, 76 (1968).
[12] J. Wheeler, Ann. (N.Y.) Acad. Sci. **48**, 219 (1946).
[13] E. P. Prokop'ev, *Introduction to the Theory of Positron Processes in Semiconductors and Ionic Crystals* [in Russian], Dep. at TsNII ''Élektronika,'' R-2837, Moscow (1979).
[14] S. De Benedetti, K. Kouén, V. Konekker, and G. Primakov, in *Positron Annihilation in Solids* [Russian translation] (Innostranaya Literatura, Moscow, 1960).
[15] S. É. Frish, *Optical Spectra of Atoms* [in Russian] (GIFML, Moscow–Leningrad, 1963).
[16] *Encyclopedic Dictionary of Physics* [in Russian] (Sov. Éntsiklopediya, Moscow, 1963), Vol. 3, p. 194.

Translated by Paul F. Schippnick

Image states on beryllium surfaces with low indices

V. M. Silkin

Institute of Durability Physics and Materials Science, Siberian Branch of the Russian Academy of Sciences, 634021 Tomsk, Russia

E. V. Chulkov and P. M. Échenique

Departamento de Fisica de Materiales, Facultad de Quimica, Universidad del Pais Vasko/Euskal Herriko Unibertsitatea, Apdo. 1072, 200080 San Sebastian/Donostia, Spain

(Submitted June 6, 1998)
Fiz. Tverd. Tela (St. Petersburg) **41**, 935–940 (June 1999)

Using the self-consistent pseudopotential method, we have calculated the binding energy of the image states for the (0001) $(10\bar{1}0)$, and $(11\bar{2}0)$ surfaces of beryllium. It is shown for the (0001) face that there exists a pronounced resonance image state with $n=1$ and energy -0.95 eV at the point $\bar{\Gamma}$ of the surface Brillouin zone. In the $(10\bar{1}0)$ surface, which has a wide band gap in the vicinity of the vacuum level, the calculated image state with $n=1$ at the point $\bar{\Gamma}$ has energy -1.2 eV and is a surface state of gap type. For the $(11\bar{2}0)$ face in the vicinity of the point $\bar{\Gamma}$ band gaps are absent. However, the symmetry of the bulk states near the vacuum level enables the existence of a resonance image state with $n=1$ and energy -0.6 eV.
 [S1063-7834(99)00206-3]

It is well known that near metal surfaces, along with true surface electron states, whose charge density is localized for the most part in the vicinity of the surface atomic layer, there also exist states associated with the image potential.[1–4] The larger part of the charge density of such states (image states) is found outside the crystal, and its maximum is localized quite far from the surface (from several angstroms to several hundreds of angstroms[5]). The energies of these states are located within 1 eV below the vacuum level E_v, forming an energy series converging to E_v, similar to the case for a hydrogen atom.[1–4] Experimentally, the binding energies of the image states were determined using inverse photoemission,[6–8] two-photon photoemission,[9,10] time-resolved photoemission,[11] and scanning tunneling spectroscopy.[12] Experimental and theoretical treatments of image states have been carried out mainly for surfaces on which there exists a forbidden energy gap in the vicinity of the vacuum level. In this case the crystal possesses a significant reflectivity, which is a deciding factor for the formation of image states. This idea lies at the basis of theoretical models operating in the language of multiple scattering.[3,13–15]

On the other hand, results of a series of experimental works for Al(111) surfaces, where the forbidden gap is located far from the vacuum level, testify to the existence of a feature in the inverse photoemission spectrum around 0.5 eV below the vacuum level.[12,16,17] It has been suggested that this feature is associated with the existence of a resonance image state with $n=1$. This has stimulated the appearance of a large number of theoretical studies of image states on (111) and (001) aluminum surfaces attempting to clarify the nature of the formation of these states on a surface not having a forbidden gap near the vacuum level. Using various models it has been shown that the energy of an image state with $n=1$ for these surfaces lies in the range between -0.4 eV (Ref. 18) and -1.0 eV (Refs. 19 and 20) relative to the vacuum level. In more recent works the binding energy has been located between -0.8 and -1.0 eV (Refs. 20 and 21), which exceeds the experimentally observed value by almost twofold. Thus, as of the present time there exists a wide discrepancy between the results of different studies for an aluminum surface. Although most of these works confirm the existence of a resonance image state on an aluminum surface whose existence is linked with reflection from the crystalline lattice,[12,21] the question of the magnitude of the binding energy of this state remains open.

In the present study, we turn our attention to image states on a beryllium surface with low indices, specifically for the faces (0001), $(10\bar{1}0)$, and $(11\bar{2}0)$. For these three surfaces various situations are realized from the point of view of the existence and location of a bulk energy gap relative to E_v.[22–25] Therefore the possibility exists of studying the influence of the real crystalline structure on the appearance and position of image states for the same material. For the (0001) face the wide energy gap in the center of the surface Brillouin zone is located in the vicinity of the Fermi level.[23] Although for beryllium the forbidden gap is much wider and is located closer to E_v than for aluminum, the situation for this face is fundamentally similar to the situation that exists for an aluminum surface. For a $(10\bar{1}0)$ face in the vicinity of E_v there exists a wide forbidden gap,[24] and therefore the arising image states should exist as gap states. For a $(11\bar{2}0)$ face the energy gap at the point $\bar{\Gamma}$ is absent.[25] To describe these three different situations it is preferable to carry out self-consistent calculations from first principles which take into consideration the actual three-dimensional

structure of the crystal. Such calculations were performed for the (0001), $(10\bar{1}0)$, and $(11\bar{2}0)$ faces of beryllium to examine occupied surface states.[23–25] The present paper presents results of a calculation using the self-consistent pseudopotential method of image states for these three surfaces.

1. CALCULATIONAL METHOD

The calculations were made using a model of thin films periodically repeating in the direction perpendicular to the surface in question and separated by vacuum gaps. For each surface the z axis was chosen perpendicular to the surface and oriented toward the vacuum part. For the (0001) and $(11\bar{2}1)$ faces the calculations were performed without an account of any relaxation or reconstruction. For the (0001) surface, where relaxation of the surface layer by several percent actually does take place,[26,27] this relaxation does not affect the results obtained for image states, which are mainly localized far into the vacuum. An experiment performed for a Be $(11\bar{2}0)$ surface employing the method of low-energy-electron diffraction showed that this surface undergoes reconstruction from the (1×1) structure to the (1×3) structure (Ref. 28). Therefore, the results obtained for an ideal surface can be considered as preliminary. For a $(10\bar{1}0)$ face there are two possibilities of surface formation. Earlier it was shown that it is preferable to cleave the crystal between atomic planes with a larger interlayer distance, i.e., when as a result of the cleavage the distance between the surface layer and the second atomic layer is two times smaller than the distance between the second and third layers.[29,30] Therefore, the calculations were performed only for this crystalline structure with relaxation of the two upper atomic layers taken into account. In our calculations the obtained relaxation amounts to a 19% decrease for the first interlayer distance and an 8% increase for the second, which agrees with other experimental and theoretical results.[29,31] A norm-preserving nonlocal pseudopotential for beryllium was generated according to Refs. 32 and 33. In the self-consistent calculation the exchange–correlation potential was calculated in the local-density approximation.[34] As the basis functions in which to expand the wave functions we used plane waves up to a cutoff energy of 15 Ry. Since the local-density approximation (LDA) does not correctly describe the asymptotic behavior of the potential in the vacuum part, to obtain final results we modified the crystal potential in such a way that on the side of the crystal with $z<z_{\mathrm{im}}$ (z_{im} is the position of the image plane) it coincides with the potential obtained in the self-consistent local-density approximation, and for $z>z_{\mathrm{im}}$, into the vacuum, it has the form

$$V(z)=-\frac{1-\exp(-\lambda(z-z_{\mathrm{im}}))}{4(z-z_{\mathrm{im}})}. \tag{1}$$

The unknown parameter λ in expression (1) is determined from the matching condition in the $z=z_{\mathrm{im}}$ plane for the potential (1) with the self-consistent LDA potential. The position of the image plane z_{im} was obtained by calculating the center of gravity of the induced electron density in a weak external electric field. To introduce an external electric field, a small part of the electron density is removed from the film toward the center of the vacuum gap in the form of a thin film of negative charge with surface charge density σ. Thus, overall, the unit cell remains electrically neutral throughout the calculations. A similar model was used, for example, in Ref. 35. Together with the film, this electron density creates an electric field in the vacuum part with field strength

$$\varepsilon=4\pi\sigma. \tag{2}$$

To obtain the induced charge density, we calculated for field strengths $\varepsilon=0.0025$, 0.0050, 0.0075, and 0.0100 a.u. (1 a.u.$=5.14\times10^{7}\,\mathrm{eV\cdot cm^{-1}}$). In this case the position of the image plane is given by

$$z_{\mathrm{im}}=\lim_{\varepsilon\to0} z_{\mathrm{im}}(\varepsilon). \tag{3}$$

The values of z_{im} obtained for the (0001), $(10\bar{1}0)$, and $(11\bar{2}0)$ faces are respectively 2.75, 2.63, and 2.74 a.u. relative to the atomic surface layer.

2. RESULTS OF CALCULATIONS AND DISCUSSION

2.1. *The (0001) surface.* The projection band structure at the point $\bar{\Gamma}$ of the surface Brillouin zone for the (0001) face is obtained by projecting the energy spectrum along the $\Gamma-A$ direction of the bulk Brillouin zone. The bulk spectrum for beryllium in this direction is shown in Fig. 1. The forbidden gap at the point $\bar{\Gamma}$, formed by the states Γ_{3+} and Γ_{4-}, is located in the interval from -9.8 to -4.1 eV. The self-consistent calculation for this face was performed using a 10-layer film. Then 10 additional atomic bulk layers were inserted in the center of the film and final results were obtained for a 20-layer film. Because of the finite thickness of the film used in the calculation we obtain as a result a series of discrete energy levels. To obtain the surface density of states (SDS), the calculated energy spectrum was smeared out taking into account the Gaussian distribution and fraction of the charge density of each state outside the geometrical boundary of the crystal. In the resulting surface density of states there exists a maximum for the state with $n=1$ and energy -0.95 eV. Jurczyszyn and Steslicka[21] have proposed a method for calculating the surface density of states, where to construct the potential inside the crystal they used the local part of the potential obtained by a self-consistent pseudopotential calculation, averaged over a plane parallel to the surface. In this case the resulting potential depends only on the z coordinate, and it is possible to perform calculations taking into account several hundreds of atomic layers. To check the adequacy of this approach we performed a calculation using the averaged local part of the potential, as depicted in Fig. 2, for the same 20-layer beryllium film that we used in the three-dimensional calculation. One-electron energies of the obtained states in the vicinity of the local image state with $n=1$ coincide with those found in the full three-dimensional calculation to within 0.1 eV. The position of the maximum corresponding to the SDS potential coincides with that obtained for the three-dimensional potential to within 0.05 eV. Thus, for this face the reflectivities of the two po-

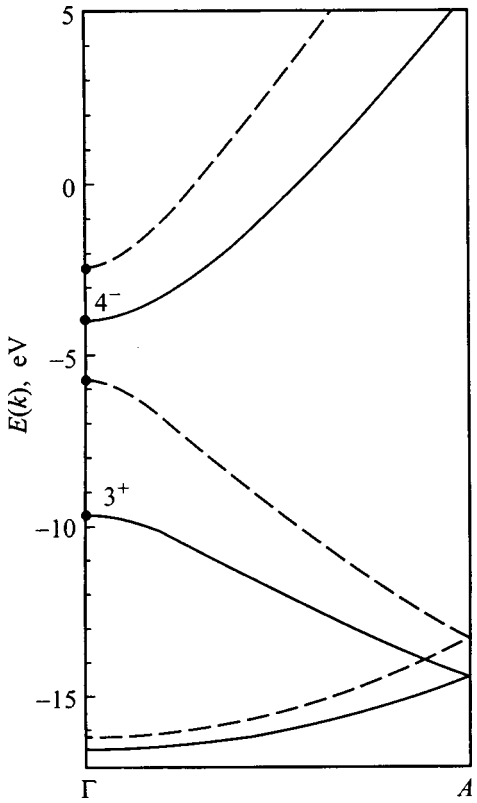

FIG. 1. Experimental spectrum in the $\Gamma - A$ direction of the bulk Brillouin zone, corresponding to projection onto the point $\bar{\Gamma}$ for the (0001) surface. The spectrum calculated by the self-consistent pseudopotential method is shown by the solid lines. The bulk spectrum obtained using the one-dimensional potential is shown by the dashed lines. The states determining the edges of the band gap are marked by points. All energies are reduced to the vacuum level for the (0001) surface. The calculated value of the work function for this face is 5.35 eV.

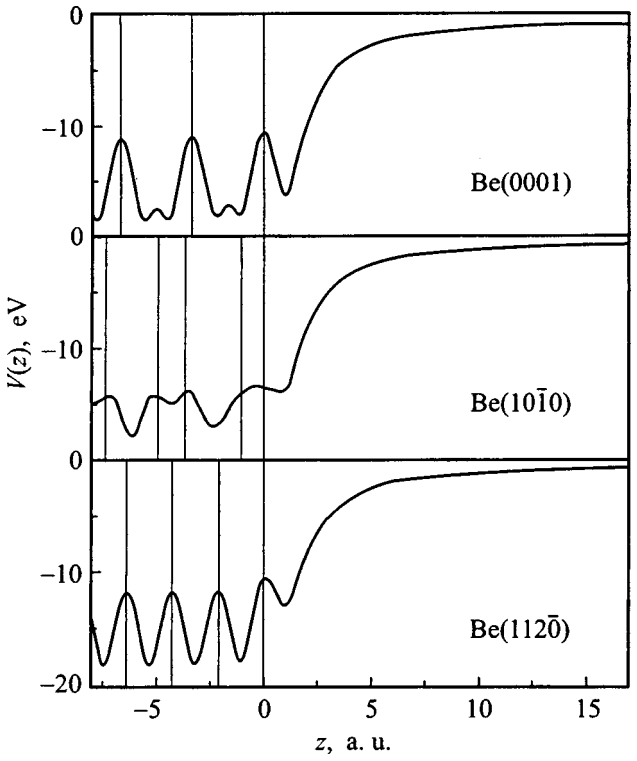

FIG. 2. Local parts of the self-consistent pseudopotential, averaged in a plane parallel to the surface, for three beryllium surfaces. The origin of the z coordinate was chosen to coincide with the surface atomic layer.

tentials are probably very close, although the electronic structure for the averaged potential inside the crystal differs quantitatively from the structure that exists for the three-dimensional potential. As can be seen from Fig. 1, the spectrum for the one-dimensional potential has a narrower gap and is situated noticeably higher in energy. Earlier, in Ref. 36 it was shown that, for example, for a Li(110) surface, where the image state with $n=1$ is located in the gap, replacing the full three-dimensional potential by the averaged potential leads to a change of up to 0.2 eV in the binding energy of this state. This was explained by a different magnitude and position of the energy gap for the two potentials. It is probably the case for image states realized in the form of resonances and situated quite far from the energy gap that a change in the parameters of the gap does not have such a marked effect on the energy positions of these resonances. On the other hand, it is possible that some compensation occurs for the Be(0001) surface due to the fact that the gap is narrower for the one-dimensional potential than for the three-dimensional potential. Therefore it influences the image states more weakly. At the same time, it is located closer to the vacuum level, which enhances the reflectivity. Calculations of this kind, carried out by us for an Al(001) surface, lead to an analogous result.

To examine the dependence of the results on the film thickness, we carried out a calculation using the one-dimensional potential for a film consisting of 401 atomic layers. The calculated surface density of states is depicted in Fig. 3. It can be seen from the figure that the position of the peak for $n=1$ coincides with that obtained for a thinner film. Whereas the state with $n=1$ shows up sooner, in the form of a shoulder, for an aluminum surface, for Be(0001) it is clearly expressed and should be noticeable when making photoemission measurements.

2.2. *The (1010) surface.* The projection of the bulk band structure for this face at the point $\bar{\Gamma}$ is obtained by projecting

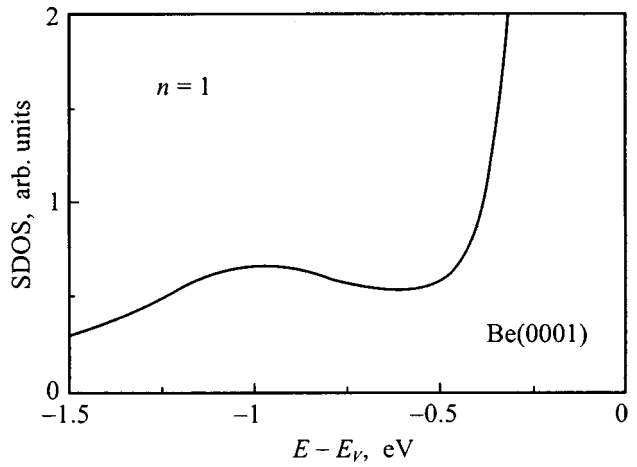

FIG. 3. Surface density of states at the point $\bar{\Gamma}$ for the Be(0001) surface. The peak in the energy region around -0.95 eV corresponds to the image state $n=1$.

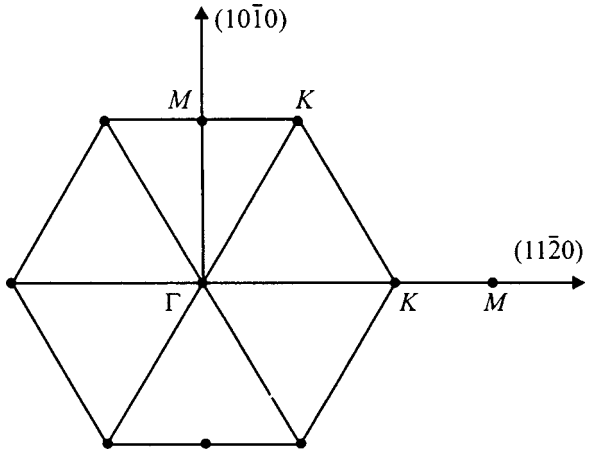

FIG. 4. $\Gamma-K-M$ plane of the bulk Brillouin zone.

the bulk Brillouin band in the $\Gamma-M$ direction (the $\Gamma-K-M$ plane for this band is depicted in Fig. 4). The energy spectrum in the $\Gamma-M$ direction is depicted in Fig. 5. It can be seen that for this face in the energy interval under consideration there exist two forbidden gaps. The lower gap, formed by the states M_{1+} and M_{2-}, is located in the interval from -9.7 to -7.7 eV. For energies from -9.7 to -9.05 eV it is absolute, and from -9.05 to -7.7 eV it is relative (due to states near the point Γ_{3+}). On the whole, this gap is forbidden for bulk states possessing symmetry of s and p_z type. The upper gap also has two parts. The lower part, the so-called symmetric gap, lies between -3.15 (the point **a**) and -1.0 eV (the point M_{4-}), and the absolute gap is located between -1.0 and 1.45 eV (the point **b**). Like the lower gap, on the whole this gap is forbidden for bulk states of s and p_z type.

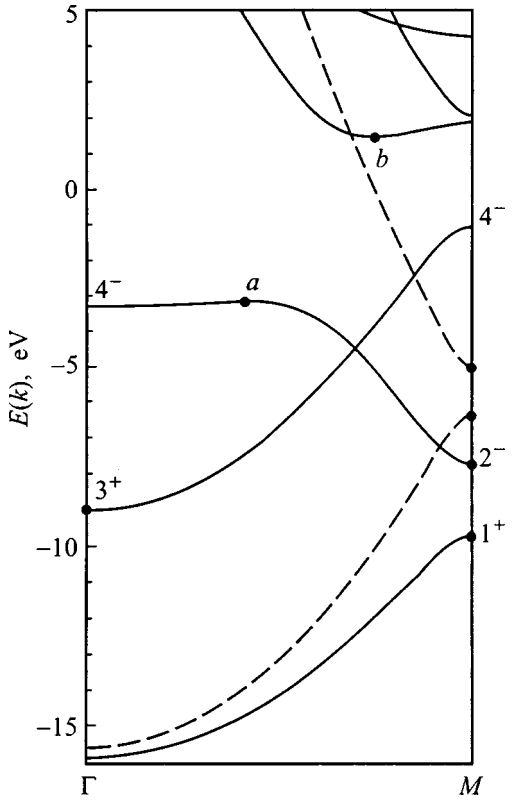

FIG. 5. Energy spectrum in the $\Gamma-M$ direction of the bulk Brillouin zone, corresponding to the projection onto the point $\bar{\Gamma}$ for the (10$\bar{1}$0) surface. Notation is the same as in Fig. 1. All energies are reduced to the vacuum level for the (10$\bar{1}$0) surface. The calculated value of the work function for this face is 4.7 eV.

A self-consistent calculation was carried out for this face using a 12-layer film. Then, as was done for the (0001) face, 12 atomic layers were added inside the film and final results were obtained for the resulting 24-layer film. The calculation shows that an image state with $n=1$ is found near the middle of the upper forbidden gap. Its energy is $E_1=1.2$ eV. Although this state is located in the region of existence of bulk states, it shows up as a nonresonance image state, since its wave function in the vicinity of the surface atomic layers possesses symmetry of s and p_z type and is therefore orthogonal to the bulk states located in this energy range. The second image state, with energy $E_2=-0.31$ eV, is located inside the absolute energy gap. Figure 2 depicts the local part of the potential for this face, averaged over the xy plane. The band structure corresponding to the bulk part of this potential is depicted by the dashed lines in Fig. 5. It can be seen that it differs qualitatively from the spectrum for the three-dimensional potential. For a one-dimensional potential there is only one forbidden gap, which can be identified with the lower forbidden gap for a real potential, since this gap can be described for both potentials by matrix elements corresponding to the same inverse lattice vector. The upper gap for the three-dimensional potential bears no relation to any matrix element and cannot be obtained within the framework of the one-dimensional model. Its existence is connected wholly with the three-dimensional structure of the crystal. As a result, for the averaged potential the obtained energy spectrum in the region of the vacuum level differs substantially from that obtained for the three-dimensional potential. In this case image states appear in the existence region of the bulk states and are manifested in the form of resonances. The corresponding surface density of states does not contain a pronounced maximum corresponding to a state with $n=1$, and there only exists a shoulder in the energy region of -0.8 eV. Thus, for this face it is impossible to obtain a physically valid result for image states using the averaged potential. Their appearance on this face in the form of true image states is connected with the existence of a forbidden gap, which is a direct consequence of the three-dimensional atomic structure of the crystal.

2.3. *The (11$\bar{2}$0) surface.* The projection of the bulk band structure for the (11$\bar{2}$0) face at the Γ point of the surface Brillouin state is obtained by projecting the spectrum in the $\Gamma-K-M$ direction of the bulk Brillouin zone. As follows from Fig. 6, which depicts the corresponding electron structure, for this face at the $\bar{\Gamma}$ point there is no forbidden gap in the energy range under consideration. An analysis of the orbital composition shows that the corresponding forbidden gap for the three-dimensional potential could be obtained by projecting the spectrum from the points M_{3-} and M_{4+}. However, several energy bands exist in the energy range $E_{M_{4+}}-E_{M_{3-}}$. These bands possess mainly symmetry of p_x

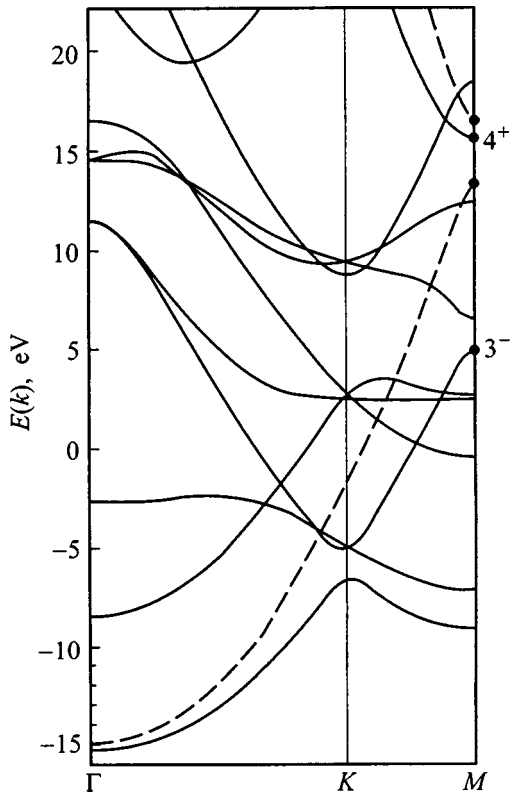

FIG. 6. Energy spectrum in the $\Gamma-K-M$ direction of the bulk Brillouin zone, corresponding to the projection onto the point $\bar{\Gamma}$ for the $(11\bar{2}0)$ surface. Notation is the same as in Fig. 1. All energies are reduced to the vacuum level for the $(11\bar{2}0)$ surface. The calculated value of the work function for this face is 4.05 eV.

and p_y type with a small admixture of states of s type. Therefore, despite the absence of an explicit forbidden gap for this face, the majority of the bulk energy bands in the $\Gamma-K-M$ direction have no effect on the existence or energy positions of the image states.

A self-consistent calculation for this face was performed for a 9-layer film. Final results were obtained for a 17-layer film. As a result of smearing out the corresponding energy spectrum with allowance for the fraction of charge in the vacuum region in the resulting surface density of states, there is a noticeable peak with energy -0.6 eV corresponding to the state with $n=1$. As for the two other surfaces, we also performed a calculation using the corresponding one-dimensional potential depicted in Fig. 2. In Fig. 6 the dashed lines depict the energy spectrum corresponding to the crystalline part of this potential. It can be seen from this figure that the forbidden gap is located very high above the vacuum level between 13.5 and 16.6 eV, i.e., it is much narrower and located higher than the gap for the three-dimensional potential. This higher position of the energy gap for the averaged potential leads to the result that there is no pronounced peak in the corresponding surface density of states in the energy interval below -0.5 eV. There is only a shoulder with energy -0.5 eV associated with the image state with $n=1$.

Thus, the reported self-consistent pseudopotential calculations for the (0001), $(10\bar{1}0)$, and $(11\bar{2}0)$ beryllium surfaces show that for them there exist various conditions for the existence of image states, and that these conditions are linked with the size and position of the energy gaps at the $\bar{\Gamma}$ point of the surface Brillouin zone. For the (0001) face, for which there is a wide forbidden gap in the vicinity of the Fermi level, a well-defined image state with $n=1$ of resonance type with energy -0.95 eV should exist. On the $(10\bar{1}0)$ surface having a wide forbidden gap in the vicinity of the vacuum level, the calculated image state with $n=1$ has binding energy -1.2 eV and is an image state of gap type. The energy spectrum for the $(11\bar{2}0)$ face does not have an absolute energy gap. But because of the symmetry of most of the bulk energy bands there exist conditions for the appearance of image states. As a result it is possible for a resonance image state with $n=1$ and energy -0.6 eV to exist. A comparison of the results obtained for the (0001) face using the three-dimensional crystal potential and with the averaged one-dimensional potential shows that on the whole they coincide. For the $(10\bar{1}0)$ surface the one-dimensional potential does not allow one to describe image states either quantitatively or qualitatively. On the $(11\bar{2}0)$ surface the results for both potentials testify to the existence of a resonance image state with $n=1$, but there is a difference in its energy position on the order of 0.1 eV. Thus, use of the averaged one-dimensional potential is not always justified although for tightly packed faces it can probably adequately describe the reflectivity of the crystalline lattice.

The authors wish to thank the Department of Education of the government of the Basque Region, which partially funded this work.

[1] M. Cole and M. H. Cohen, Phys. Rev. Lett. **23**, 1238 (1969).
[2] V. B. Shikin, Zh. Éksp. Teor. Fiz. **31**, 936 (1970) [Sov. Phys. JETP **58**, 1748 (1970)].
[3] P. M. Echenique and J. B. Pendry, J. Phys. C **11**, 2065 (1978).
[4] P. M. Echenique and J. B. Pendry, Prog. Surf. Sci. **32**, 11 (1990).
[5] U. Höfer, I. L. Shumay, Ch. Reuss, U. Thomann, W. Wallauer, and Th. Fauster, Science **277**, 1480 (1997).
[6] F. J. Himpsel, Comments Condens. Matter Phys. **12**, 199 (1986).
[7] N. V. Smith, Rep. Prog. Phys. **51**, 1227 (1988).
[8] F. J. Himpsel and J. E. Ortega, Phys. Rev. B **46**, 9719 (1992).
[9] T. Fauster and W. Steinmann, in *Electromagnetic Waves: Recent Developments in Research*, edited by P. Halevi (Elsevier, Amsterdam, 1995), Vol. 2, p. 350.
[10] K. Giesen, F. Hage, F. J. Himpsel, H. J. Riess, and W. Steinmann, Phys. Rev. B **35**, 971 (1987).
[11] M. Wolf, E. Knoesel, and T. Hertel, Phys. Rev. B **54**, R5295 (1996).
[12] S. Yang, R. A. Bartynski, G. P. Kochanski, S. Papadia, T. Fondén, and M. Persson, Phys. Rev. Lett. **70**, 849 (1993).
[13] E. G. McRae, Rev. Mod. Phys. **51**, 541 (1979).
[14] M. Ortuno and P. M. Echenique, Phys. Rev. B **34**, 5199 (1986).
[15] P. M. Echenique and M. E. Uranga, Surf. Sci. **247**, 125 (1991).
[16] D. Heskett, K.-H. Frank, E. E. Koch, and H.-J. Freund, Phys. Rev. B **36**, 1276 (1987).
[17] D. Heskett, K.-H. Frank, K. Horn, E. E. Koch, H.-J. Freund, A. Baddorf, K.-D. Tsuei, and E. W. Plummer, Phys. Rev. B **37**, 10 387 (1988).
[18] A. G. Eguiluz, M. Heinrichsmeier, A. Fleszar, and W. Hanke, Phys. Rev. Lett. **68**, 1359 (1992).
[19] F. Finocchi, C. M. Bertoni, and S. Ossicini, Vacuum **41**, 535 (1990).
[20] T. Fonden, S. Papadia, and M. Persson, J. Phys.: Condens. Matter **7**, 2697 (1995).
[21] L. Jurczyszyn and M. Steslicka, Surf. Sci. Lett. **376**, L424 (1997).
[22] D. A. Papaconstantopoulos, *The Band Structure of Elemental Solids* (Plenum Press, New York, 1986).

[23] E. V. Chulkov, V. M. Silkin, and E. N. Shirykalov, Surf. Sci. **188**, 287 (1987).
[24] V. M. Silkin and E. V. Chulkov, Fiz. Tverd. Tela (St. Petersburg) **37**, 2795 (1995) [Phys. Solid State **37**, 1540 (1995)].
[25] V. M. Silkin and E. V. Chulkov, Poverkhnost' **11**, 46 (1993).
[26] H. Davis, J. B. Hannon, K. Ray, and E. W. Plummer, Phys. Rev. Lett. **68**, 2632 (1992).
[27] P. Feibelman, Phys. Rev. B **46**, 2532 (1992).
[28] J. B. Hannon, E. W. Plummer, R. M. Wentzcovitch, and P. K. Lam, Phys. Rev. Lett. **46**, 7942 (1992).
[29] Ph. Hofmann, K. Pohl, R. Stumpf, and E. W. Plummer, Phys. Rev. B **53**, 13 715 (1996).
[30] Ph. Hofmann, R. Stumpf, V. M. Silkin, E. V. Chulkov, and E. W. Plummer, Surf. Sci. Lett. **355**, L278 (1996).
[31] O. Hjorstam, J. Trygg, J. M. Wills, B. Johansson, and O. Eriksson, Surf. Sci. **355**, 214 (1996).
[32] V. M. Silkin, E. V. Chulkov, I. Yu. Sklyadneva, and V. E. Panin, Izv. Vyssh. Uchebn. Zaved. Fiz. **9**, 56 (1984).
[33] E. V. Chulkov, V. M. Silkin, and E. N. Shirykalov, Fiz. Met. Metalloved. **64**, 213 (1987).
[34] L. Hedin and B. I. Lundqvist, J. Phys. C **4**, 2062 (1971).
[35] S. C. Lam and R. J. Needs, Surf. Sci. **277**, 173 (1992).
[36] E. V. Chulkov, V. M. Silkin, and P. M. Echenique, Surf. Sci. Lett. **391**, L1217 (1997).

Translated by Paul F. Schippnick

Diffuse scattering of x-rays by a crystal of an aging alloy

V. M. Agishev and O. A. Gafiatullina

Bashkir State Pedagogical Institute, 450000 Ufa, Russia
(Submitted July 9, 1998)
Fiz. Tverd. Tela (St. Petersburg) **41**, 941–943 (June 1999)

We consider a theory of diffuse scattering of x-rays in a generalized model of the structure of an aging alloy. A formula is derived for calculating the intensity distribution of diffuse scattering of x-rays in such a model that allows one to obtain a theoretical intensity distribution of diffuse scattering in various particular models. © *1999 American Institute of Physics.* [S1063-7834(99)00306-8]

There are a number of theoretical studies of diffuse scattering of x-rays by a crystal of an aging alloy which have been proposed to explain various properties of the diffuse scattering intensity distribution. Any theory of diffuse scattering on all possible defects of the crystalline structure is tied up with the choice of a model of the structure, in particular the structure of a crystal of an aging alloy. In the earliest studies, diffuse scattering effects were explained as a shape effect. Here the calculation of the diffuse scattering intensity was carried out within the framework of a two-phase or three-phase model of the structure of a crystal of an aging alloy in the initial stages of its decay. Theories have appeared describing x-ray scattering on various modulated structures formed as a consequence of a spinodal mechanism of alloy decay, or as a consequence of the interaction of long-range elastic strain fields arising around particles of new formations. Diffuse scattering theories based on various specific models of the structure of a crystal of an aging alloy have also been proposed. However, all these theories of diffuse scattering are suitable for describing only some aspects of the picture of the diffuse scattering intensity distribution observed in experiment in some alloys in certain stages of their decay. These theories cannot be used to analyze the diffuse scattering of x-rays by a crystal of an aging alloy after zone formation, especially for its initial stages. Therefore, any calculation of the diffuse scattering intensity for these cases should start out by adopting a generalized model of the structure of the alloy: in the alloy Guinier cluster-complexes are formed, in which the composition of the dopant component, the lattice parameters, elastic and shear displacements of the atoms vary according to a definite law described by some function, and the Guinier cluster complexes themselves are distributed in the matrix crystal with some definite degree of order.

Let us consider a crystal of an aging alloy in which N Guinier cluster-complexes are formed as a result of fluctuational decay.

Following Ref. 1, we first calculate the intensity distribution of diffuse scattering by one Guinier cluster-complex,[2] applying Krivoglaz's method of fluctuation waves.[3] This requires that we specify a law of variation of composition of the Guinier cluster-complex and of its other structural characteristics. Next, using the scattering amplitude of one Guinier cluster-complex, we calculate the intensity of diffuse scattering of x-rays by all N cluster-complexes taking into account the prescribed law governing their distribution (correlation) in the crystal of the aging alloy.[4]

Let N fluctuation centers of enhanced concentration of the dopant component form in a crystal of aging alloy of volume V_0, where these centers are surrounded by regions depleted of the dopant component. These regions are the Guinier cluster-complexes and have arbitrary shape and varying volume. This means that in a Guinier cluster-complex there exists a frozen wave of compositional modulation. Therefore, the scattering power in a Guinier cluster-complex in the crystal direction $\mathbf{r}(n)$ from the center of the cluster-complex can be described by the function[2]

$$f(\mathbf{r}) = \overline{f} + (f_2 - f_1)\psi(\mathbf{r}) = \overline{f} + (f_2 - f_1)\left[\sum D(k)\sin\{\mathbf{kr}\} - c\right], \tag{1}$$

where $\psi(\mathbf{r}) = c(\mathbf{r}) - c$, and $\overline{f} = f_1 + (f_2 - f_1)c$ is the mean scattering power of the atoms of the second component in the cluster-complex, where we have $\psi(\mathbf{r}) = 1 - c$ if an atom of the dopant component is found at the lattice site $\mathbf{r}(n)$ and $\psi(\mathbf{r}) = -c$ if an atom of the main component is found there. In the general case of a non-periodic function $\psi(\mathbf{r})$ the Fourier series transforms into a Fourier integral,[5] and the frozen compositional modulation wave entails the appearance of frozen modulation waves of elastic and shear displacements.[2]

The x-ray diffuse scattering amplitude in the generalized model of the structure of a Guinier cluster-complex of arbitrary shape has the form[4]

$$\begin{aligned} A(h') = {} & (\overline{f} + \overline{f_m})N_A\Phi(\mathbf{G}) + N_A\left\{\pi\mathbf{H}(h')\mathbf{k}_g\boldsymbol{\theta}(q)(\mathbf{a}''_{\mathbf{k}_q} - \mathbf{a}'_{\mathbf{k}_q})\right. \\ & \left.\times(\overline{f} - \overline{f_m}) + \frac{1}{2i}(f_2 - f_1)\right\}D(k)\Phi(\mathbf{G} - \mathbf{K}) \\ & + N_A\left\{\pi\mathbf{H}(h')\mathbf{k}_g\boldsymbol{\theta}(q)(\mathbf{a}''_{\mathbf{k}_g} - \mathbf{a}'_{\mathbf{k}_q})(\overline{f} - \overline{f_m})\right. \\ & \left. - \frac{1}{2i}(f_2 - f_1)\right\}D(k)\Phi(\mathbf{G} + \mathbf{K}) + N_A\pi\mathbf{H}(h')\boldsymbol{\theta}(\rho) \\ & \times(\mathbf{a}''_{\mathbf{k}_\rho} - \mathbf{a}'_{\mathbf{k}_\rho})\mathbf{k}_\rho(\overline{f} - \overline{f_m})D(k)\Phi(\mathbf{G} \pm \mathbf{K}), \end{aligned} \tag{2}$$

where $A(h')$ is the x-ray diffuse scattering amplitude of one

Guinier cluster-complex, calculated with allowance for scattering by a ''hole'' in analogy with the Babinet principle in optics[6] in the presence of static modulation waves of the composition and the lattice parameter and of waves of static shear displacements; $\Phi(\mathbf{G})$ is the Fourier transform of the shape function $s(\boldsymbol{\rho})$ of the Guinier cluster-complex; $D(k)$ is the Fourier transform of the function $\psi(\mathbf{r})=c(\mathbf{r})-c$ (Refs. 2 and 4) over the harmonics of the compositional modulation waves in the Guinier cluster-complex; f_2 and f_1 are the scattering powers of the atoms of the second and main components, respectively; $\mathbf{H}(h')$ is an arbitrary vector in the inverse lattice space; $\mathbf{G}$ is an arbitrary displacement vector from the sites of the inverse lattice of the Guinier cluster-complex; k is the order of the harmonics of the compositional modulation waves; $\mathbf{k}_q$ is the wave vector of the compositional modulation waves; $\mathbf{k}_\rho$ is the wave vector of the modulation waves of the elastic displacements.

Note that the general form of the function $\psi(\mathbf{r})$, allowing for the nature of variation of the composition (or scattering power of the atoms), in a Guinier cluster-complex should follow in a natural way from the solution of the diffusion equation in Cahn's theory of spinodal decay[7] or the equation of mass balance in Prigogine's theory of self-organization.[8] Of course, the latter approach is more general, but at present it has not been worked out.

In the calculation of the amplitude of the wave scattered by all the cluster-complexes it is necessary to allow for the path difference between waves scattered by different cluster-complexes. Thus, the intensity of diffuse scattering by all N cluster-complexes in electron units can be written in the form[4]

$$I(h')=\sum_j\sum_m A_m(h')A_j^*(h')\exp\left\{\frac{2\pi i}{\lambda}\mathbf{s}\cdot(\mathbf{r}_j-\mathbf{r}_m)\right\}$$
$$=|A(h')|^2\left(N\sum\Phi^2(\mathbf{G})+\sum_{j\neq m}\sum_m\Phi^2(\mathbf{G})\right.$$
$$\left.\times\cos\left\{\frac{2\pi i}{\lambda}\mathbf{s}\cdot(\mathbf{r}_j-\mathbf{r}_m)\right\}\right), \tag{3}$$

if we assume that all of the cluster-complexes are identical in shape and size. Next, this expression for the intensity must be averaged over all possible positions of the N cluster-complexes in the matrix solution. For a random distribution of N cluster-complexes the average of the sum of the terms $\cos\{2\pi/\lambda\,\mathbf{s}\cdot(\mathbf{r}_j-\mathbf{r}_m)\}$ is equal to zero. Thus, the intensity of diffuse scattering by N randomly distributed cluster-complexes in the alloy crystal is equal to

$$I(h')=N|A(h')|^2\Phi^2(\mathbf{G}), \tag{4}$$

i.e., to the sum of the intensities of diffuse scattering by each of the N cluster-complexes (with the exception of the intensity at the point $\mathbf{s}=\mathbf{0}$, i.e., in the direction of the primary ray, where $I(h')=N^2|A(h')|^2\Phi^2(\mathbf{G})$. However, if there is a correlation in the mutual arrangement of the N cluster-complexes in the alloy crystal, then the problem of calculating the intensity distribution of diffuse scattering by N cluster-complexes becomes considerably more complicated.

As in the theory of x-ray scattering by gases and liquids,[9] we introduce a correlation function for the cluster-complexes, $W(\mathbf{r}_m)$, as follows. Let the jth cluster-complex occupy in the arbitrary volume dV_j in a crystal of volume V_0. Then the probability that the mth cluster-complex will occupy the volume element dV_m with relative displacement $\mathbf{r}_{jm}=\mathbf{r}_j-\mathbf{r}_m$ is $W(\mathbf{r}_{jm})dV_m/V_0$, where $W(\mathbf{r}_{jm})=|F(\mathbf{R}_{jm})|^2|s(\boldsymbol{\rho})|^2$. Here the function $F(\mathbf{R}_{jm})$ appears in the form of its absolute value squared, since this function itself can be devoid of meaning. If the density distribution is completely random, then the probability is equal to $|s(\boldsymbol{\rho})|^2(dV_m/V_0)$ and $|F(\mathbf{R}_{jm})|^2=1$. If the distribution is not completely random, then $|F(\mathbf{R}_{jm})|^2\neq 1$. In these relations $s(\boldsymbol{\rho})$ is the shape function of the Guinier cluster-complex and is equal to 1 if $|\boldsymbol{\rho}|<|\mathbf{a}_\gamma|/2$, and to 0 if $|\boldsymbol{\rho}|>|\mathbf{a}_\gamma|/2$, where $\boldsymbol{\rho}=\mathbf{r}_{jm}-\mathbf{R}_{jm}$ is the displacement of the arbitrary vector $\mathbf{r}_{jm}$ in the space of the crystalline lattice from the center of the mth cluster-complex, whose position is assigned by the vector $\mathbf{R}_{jm}$, and $\mathbf{a}_\gamma$ are the dimensions of the cluster-complex in the three principal directions.

The correlation function $W(\mathbf{r}_{jm})$ $(j\neq m)$ depends only on the relative displacement $\mathbf{r}_{jm}=\mathbf{r}_j-\mathbf{r}_m$. This relative displacement enters as the argument in the exponential in Eq. (3). Therefore, the center of one of the cluster-complexes in the alloy can be taken as the origin and then $\mathbf{r}_{jm}=\mathbf{r}_{0m}=\mathbf{r}$, and the position of the centers of the other cluster-complexes located a distance r from the origin is defined as the distribution function $F(\mathbf{R}_{0m})=F(\mathbf{R})$. Thus, for the intensity of diffuse scattering by N cluster-complexes we obtain the expression

$$I(h')=|A(h')|^2\left\{N\left(\Phi^2(\mathbf{G})-\int_{V_0}\int_{V_0}|F(\mathbf{R})|^2|s(\boldsymbol{\rho})|^2\right.\right.$$
$$\left.\times\exp\left\{\frac{2\pi i}{\lambda}(\mathbf{s}\cdot\mathbf{r})\right\}\frac{dV_\mathbf{R}}{V_0}\frac{dV_\mathbf{r}}{V_0}\right)$$
$$+N^2\int_{V_0}\int_{V_0}|F(\mathbf{R})|^2|s(\boldsymbol{\rho})|^2\exp\left\{\frac{2\pi i}{\lambda}(\mathbf{s}\cdot\mathbf{r})\right\}$$
$$\left.\times\frac{dV_\mathbf{R}}{V_0}\frac{dV_\mathbf{r}}{V_0}\right\}, \tag{5}$$

where $\mathbf{r}=\boldsymbol{\rho}+\mathbf{R}$ is an arbitrary vector in the alloy lattice space. Calculation of the diffuse scattering intensity reduces to calculation of the integral

$$\int_{V_0}\int_{V_0}|F(\mathbf{R})|^2|s(\mathbf{r}-\mathbf{R})|^2\exp\left\{\frac{2\pi i}{\lambda}(\mathbf{s}\cdot\mathbf{r})\right\}dV_\mathbf{R}dV_\mathbf{r}, \tag{6}$$

which requires that we assign the function $F(\mathbf{R})$ and the shape function $s(\boldsymbol{\rho})$ in explicit form.

The integral (6) is easily calculated using the convolution theorem: the transform of the convolution of two functions is the product of the transforms of the functions. Consequently, the integral (6) is equal to $|F(\mathbf{G})|^2\Phi^2(\mathbf{G})$, where $|F(\mathbf{G})|^2$ is the Fourier transform of the function $|F(\mathbf{R})|^2$. Thus, formula (5) can be represented in the form

$$I(h')=|A(h')|^2\{N(1-|F(\mathbf{G})|^2)\Phi^2(\mathbf{G}) + N^2|F(\mathbf{G})|^2\Phi^2(\mathbf{G})\}. \quad (7)$$

Thus, as follows from formula (7), to calculate the diffuse scattering intensity distribution for N cluster-complexes we need to assign the functions $\psi(\mathbf{r})$ and $s(\boldsymbol{\rho})$, which are needed to calculate $A(h')$ and also $W(\mathbf{r})$, which defines the correlation of the cluster-complexes in the crystal.

Equation (7) does not include scattering by the averaged lattice of the matrix crystal, which gives Bragg reflections at the positions defined by the angles θ_B. Depending on the depth of the fluctuational decay, the content of the dopant component in the matrix crystal can vary from its content in the α solid solution c_0 to its content in the equilibrium matrix solid solution c_1, depending on the conditions in which the alloy is found. Granted, in some cases the matrix crystal can also be absent, for example, in the case of the formation of modulation structures for a spinodal mechanism of alloy decay.

In Ref. 4 this approach to calculating the diffuse scattering intensity was applied to the model of spherical Guinier cluster-complexes following Gerold[10] and Guinier[11] in the case in which the complexes were randomly distributed and for the case of a three-dimensional periodic distribution in the alloy crystal. The formulas obtained are easily processed numerically with a wide spectrum of variation of the structure parameters of the alloy. Thus, using formula (8), it is possible to calculate the diffuse scattering intensity distribution for a crystal of an aging alloy with N cluster-complexes as a function of θ with a wide spectrum of reasonable values of the introduced quantities defining the structure of the alloy, and to construct a graph of the dependence of $I(h')$ on the deflection angle θ near all reflections (hkl) from the averaged lattice of the cluster-complexes. To establish the real structure of the alloy crystal, it is necessary to compare the distribution curves so obtained with the experimental diffuse scattering intensity distribution.

The present approach to calculating the diffuse scattering intensity distribution allows one to consider the theory of diffuse scattering of x-rays in any model of the structure of a crystal of aging alloy. To this end it is necessary to choose a correlation function $W(\mathbf{r})$ with more general form and a function $\psi(\mathbf{r}(n))$ containing some parameters whose variation will make it possible to describe the variation of the composition and of the lattice parameter in a cluster-complex from stepped to periodic (sinusoidal).

On the basis of formula (8) we can draw the following conclusions.

1) In the case of a fluctuational origin of decay of the alloy, satellite reflections are always observed in the diffraction pattern and are located symmetrically relative to the Bragg reflections from the averaged lattice of cluster-complexes.

2) The satellites are smeared out due to the shape effect, as are the Bragg maxima from the averaged lattice of cluster-complexes.

3) The contribution to the smearing of diffraction effects from the complexes will also depend on the structure of the cluster-complexes, and on the nature of their distribution.

4) In general, the satellites are asymmetric relative to the Bragg reflections from the matrix crystal, and the greater the difference in the lattice parameters of the matrix and the Guinier complex, the greater will be this asymmetry.

5) The intensity of the satellites is always asymmetric as a consequence of the dependence of the scattering power of the atoms on the scattering angle.

[1] Yu. A. Bagaryatskiĭ, Dokl. Akad. Nauk SSSR **92**, 1157 (1953).
[2] V. M. Agishev, Izv. Akad. Nauk SSSR **3**, 159 (1975).
[3] M. A. Krivoglaz, *Theory of of X-Ray and Thermal Neutron Scattering by Real Crystals* (Plenum Press, New York, 1969).
[4] V. M. Agishev, Izv. Akad. Nauk. SSSR, Met. **4**, 161 (1981).
[5] E. K. Titchmarsh, *Introduction to the Theory of Fourier Integrals*, 2nd ed. (Clarendon Press, Oxford, 1948).
[6] M. Born and E. Wolf, *Principles of Optics*, 4th ed. (Pergamon Press, Oxford, 1969).
[7] J. W. Cahn, Trans. AIME **242**, 166 (1968).
[8] G. Nicolis and I. Prigogine, *Self-Organization in Non-Equilibrium Systems* (Wiley, New York, 1977).
[9] V. I. Iveronova and V. I. Revkevich, *Theory of X-Ray Diffraction* [in Russian] (Moscow State Univ. Press, Moscow, 1978).
[10] V. Gerold, Phys. Status Solidi **1**, 37 (1961).
[11] A. Guinier, Acta Metall. **3**, 5 (1955).

Translated by Paul F. Schippnick

Conductivity, magnetoresistance, and the Hall effect in granular Fe/SiO_2 films

B. A. Aronzon*) and D. Yu. Kovalev

Russian Scientific Center ''Kurchatov Institute,'' 123182 Moscow, Russia

A. E. Varfolomeev, A. A. Likal'ter, V. V. Ryl'kov, and M. A. Sedova

Scientific-Research Center of Applied Problems of Electrodynamics, 127412 Moscow, Russia
(Submitted September 3, 1998)
Fiz. Tverd. Tela (St. Petersburg) **41**, 944–950 (June 1999)

We have investigated the conductance, magnetoresistance, and Hall effect in granular Fe/SiO_2 films with size of the iron grains around 40 Å, whose volume fraction x lies in the range 0.3–0.7. The conduction activation regime has been established for $x<0.6$. On the insulator side of the transition we observed a giant negative magnetoresistance, falling off sharply as the metal volume fraction decreases. For $x<0.4$ we observed a large positive magnetoresistance of premagnetized samples, showing up in fields ~ 100 Oe and characterized by large response times. The field dependence of the Hall effect in the dielectric samples, as in the metallic samples, correlates with their magnetization. We found that the Hall resistance is proportional to the square root of the longitudinal resistance, which cannot be explained by known models of the anomalous Hall effect. © *1999 American Institute of Physics.* [S1063-7834(99)00406-2]

Granular films are composites consisting of metal grains several tens of angstroms in diameter and an insulator filling the spaces between the grains. The small size of the grains occupying an intermediate position between atoms, molecules, and the solid state is reflected in the properties of these composites and in the nature of the insulator–metal transition. If the volume fraction occupied by the grains is greater than the percolation threshold, then such a composite is a ''dirty'' metal. Below the threshold, the composites possess a hopping conductivity due to electron tunneling through the dielectric interlayers, and behave similar to doped uncompensated semiconductors.[1]

Of especial interest are studies of nanocomposites based on ferromagnetic metals, in which giant magnetoresistance (GMR, Ref. 2) and the giant Hall effect (GHE, Ref. 3) are observed. Although the first studies of these materials were undertaken quite a long time ago,[4] their properties near the metal–insulator transition are still not completely understood. In particular, a number of contradictions arise in the description of the temperature dependence of the conductivity[5] and the question of the mechanisms of the giant magnetoresistance and the giant Hall effect remains open. Interest in these materials has revived in the last few years[2,3,6–11] and is linked to possible applications of GMR and the GHE in micro-electronics, and also in the intractability of the indicated questions.

At present, it has been determined that GMR is observed near the percolation threshold, reaches its maximum in the dielectric region, has a negative sign, and saturates in fields on the order of 10 kOe (Ref. 2). In the present work, studies of GMR have been carried out over a wide range of metal concentrations. In the dielectric region, for metal concentrations $x<0.4$, we observed a large positive magnetoresistance, appearing after preliminary storage of the sample in a magnetic field and saturating at significantly lower fields.

The mechanism of the anomalous Hall effect (AHE) in disordered magnetic media, i.e., under conditions in which spin-orbit interaction has a strong influence on the scattering of spin-polarized electrons, has still not been completely elucidated.[12] In contrast to granular alloys with metallic conductivity, for which there are several models of the anomalous Hall effect,[10,13] no conceptions of the mechanism of the Hall effect in the dielectric region have been put forward.

The present work describes results of studies of the temperature dependence of the conductivity, and also of the magnetoresistance and the Hall effect, in magnetic granular Fe/SiO_2 films over a wide range of compositions, primarily in the dielectric region. Note that studies of iron-containing nanocomposites are quite rare, although such composites have definite advantages associated with the magnetic properties of Fe, over composites based on Ni or Co.

1. SAMPLES AND TECHNOLOGY OF THEIR PREPARATION

Samples, outfitted with a pair of current contacts and two pairs of potential (Hall) probes, were prepared in the form of a double cross.[14] The width of the conducting channel was $W=2$ mm, its length was $L=7$ mm, and the length and width of the projections on the lateral faces of the sample were 1.5 and 0.5 mm, respectively. The samples were prepared in a vacuum setup by simultaneous ion-beam sputtering of Fe and SiO_2. A composite target was used, which made it possible to vary the ratio of metal and insulator. Film deposition was realized on polished substrates at room temperature through precision shaped masks of nickel. The accuracy with which the projections (Hall probes) were combined was on the order of 10 μm. Film thicknesses were measured with the help of a MII-4 micro-interferometer and varied in the range 0.2–0.8 μm. The iron volume fraction in

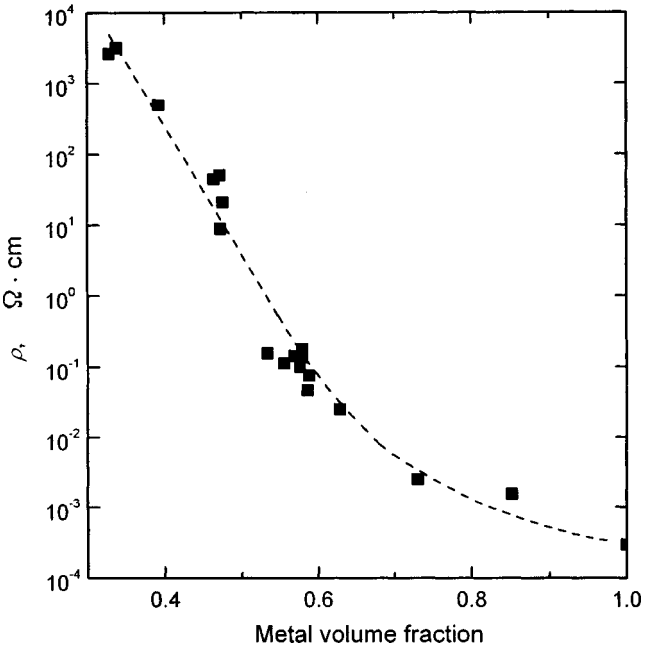

FIG. 1. Dependence of the resistivity of the samples on the iron volume fraction at room temperature.

the samples was determined by x-ray micro-analysis in an SEM515 Philips scanning electron microscope equipped with a LINK AN 10 000 system of energy dispersion analysis. Based on the microanalysis data, we calculated the volume fractions of Fe and SiO_2 under the assumption that not all of the iron is oxidized. Measurements of Mössbauer spectra of the samples confirmed this assumption. Analysis of the spectra showed that the fraction of pure α-Fe exceeds 80%. With the aid of x-ray photoelectron spectroscopy we also determined that oxidized iron is present; however, it is found on the surface of the samples. On the basis of electron-microscope studies we estimated the characteristic diameter of the grains to be ~ 40 Å. The Mössbauer spectra obtained on samples with low iron content were consistent with the grains being in the superparamagnetic state, not the ferromagnetic state. This gives an estimate for their diameter less than 50Å (Ref. 15).

The dependence of the resistivity of the samples ρ on the iron volume fraction at room temperature is plotted in Fig. 1. This dependence is typical for the given systems.[2] In a dielectric sample for relatively low metal volume fractions the resistance grows exponentially with decreasing x. Measurements of the asymmetry resistance of the Hall probes R_a (the ratio of the voltage across the Hall probes in the absence of a magnetic field V_a to the current I_x flowing through the sample) at $T=300$ K showed that the ratio of the total resistance of the samples R_{xx} to R_a reaches 600–800. This is an indication of the geometrical accuracy of collocation of the Hall probes and testifies to the high degree of uniformity of the films relative to large-scale fluctuations of the composition.

The magnetoresistance and the Hall effect were measured in fields up to 10 kOe at temperatures $T=77-300$ K. The magnetoresistance was measured for different orientations of the magnetic field relative to the plane of the sample and the direction of the electric field. Preliminary studies have shown that both the magnetoresistance and the Hall effect depend most strongly on the iron content below the metal–insulator transition ($x<0.6$). At the same time, the accuracy of determination of the composition in our experiments was no better than 10% (Fig. 1), which is insufficient to examine the behavior of galvanomagnetic effects in the dielectric region. In this regard, it would be more natural to characterize the samples according to their closeness to the transition with the help of the activation energy w, which was determined from the temperature dependence of the conductance $G_{xx}=1/R_{xx}$ in the low-temperature limit.

2. TEMPERATURE DEPENDENCE OF THE CONDUCTANCE

The temperature dependence of the conductance $G(T)$ was measured in the interval $T=4.2-300$ K. $G(T)$ curves for several samples with iron content near the percolation threshold ($x<0.6$) are plotted in Fig. 2(a). The vigorous decrease of G with increasing temperature (by a factor of 4×10^4 for the highest-resistance sample) is evidence of the activation character of the conductivity; however, the shape of the dependence $G(T)$ deviates significantly from an Arrhenius law. Values of the activation energy w, found in the low-temperature limit from the slope of the curves $\ln[G(1/T)]$, are given in the caption to Fig. 2. Significant is the smallness of w, less than 3 meV. In granular metals the activation energy is estimated by the formula[5]

$$w\approx E_c/2=e^2/2\varepsilon_d r_g, \tag{1}$$

where E_c is the energy of pair formation from negatively and positively ionized grains (the charging energy of the capacitance of the grain), e is the charge of the electron, ε_d is the dielectric constant of the insulator, and r_g is the radius of the grains. For grains of radius 20Å in SiO_2 ($\varepsilon_d=3.73$, Ref. 16), formula (1) yields $w\approx10^2$ meV, which is two orders of magnitude greater than the value observed in experiment. The small values of w measured in experiment at low temperatures, and the form of the $G(T)$ curves of the type shown in Fig. 2(a), are usually explained in terms of the model of hopping conductivity with variable hopping length. Here $G(T)=G_0\exp(-2s/a_d-E_c/kT)=G_0\exp[-(T_0/T)^\gamma]$, where a_d is the falloff length of the electron wave function in the insulator and s is the distance between grain surfaces; the exponent is $\gamma<1$ (Ref. 5). According to numerous experimental data, for granular systems in the dielectric region near the insulator–metal transition we have $\gamma\approx0.5$. In our case, the curves of $\ln(G)$ plotted as a function of $T^{1/2}$ for $T<100$ K are also nearly linear [Fig. 2(b)], although as the resistance of the samples increases a marked deviation from linearity is observed (this fact is apparently of general significance, Ref. 5).

There are several models which explain the value $\gamma=0.5$; however, they all have certain drawbacks, as noted in Ref. 5. One of the well-known models[17] assumes that $E_c s=\text{const}=C$. By minimizing the argument of the exponential in the expression for $G(T)$ under this constraint we obtain $\gamma=0.5$, $T_0=4C/ka_d$. The shortcoming of this model

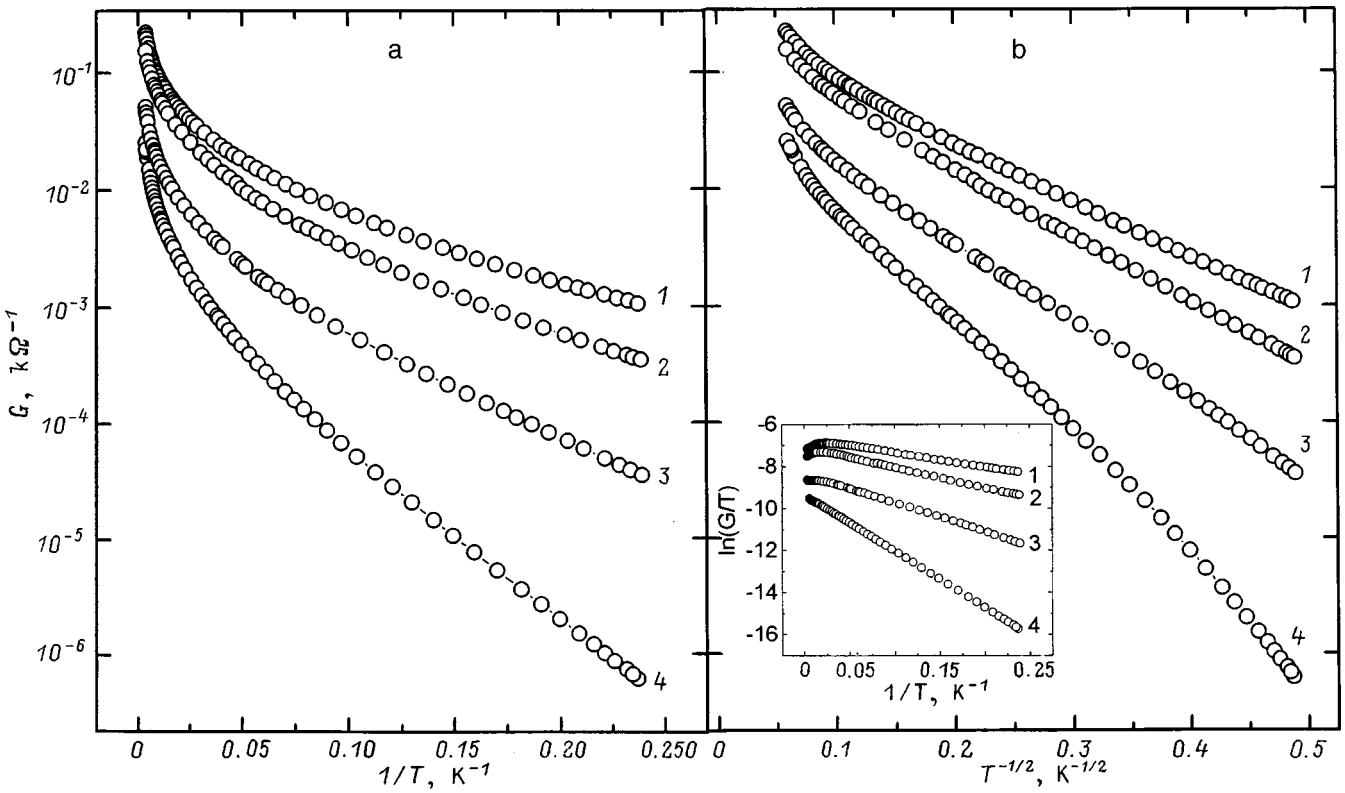

FIG. 2. Temperature dependence of the conductance on the insulator side of a percolation transition in the coordinates $\ln(G)-1/T$ (a) and in the coordinates $\ln(G)-1/T^{1/2}$ (b). Conduction activation energies, found from the slope of the $\ln(G)-1/T$ curves in the low-T limit, meV: *1*—1.0; *2*—1.25; *3*—1.69; *4*—2.83. Inset shows the dependence of $\ln(G/T)$ on $1/T$.

is the absence of weighty arguments in favor of the existence of correlations between the grain diameters $d=2r_g$ and the tunneling gaps s between them, following from the condition $E_c s=\text{const}$ (Ref. 5). This probably explains the contradictions which can arise in the processing of the experimental data. Thus, proceeding from the values of T_0 [for curves *2* and *3* in Fig. 2(b) $T_0\approx 200$ K] and setting $d\sim s$, we estimated the falloff length of the electron wave function in the insulator. We obtained values several orders of magnitude greater than the typical value $a_d\sim 1$ Å (Ref. 5).

Another model[18] is based on a picture of hopping conductivity with a variable hopping length in the presence of a Coulomb gap in the density of states.[19] As is well known, in this case $\gamma=0.5$ (Ref. 19). In this case, however, the parameter T_0 turns out to depend on the dielectric constant of the medium ε_m, which can significantly exceed ε_d in the region of the insulator–metal transition and is not accurately known. For this reason, an analysis of the temperature dependence of the conductivity in terms of the given model is hindered. Estimates of ε_m made in Ref. 5 on the basis of the theory of an effective medium give in principle reasonable values for a_d although the optimal hopping length S_{opt} in this case turns out to be $\sim d$. In particular, for a sample with such parameters ($T_0=200$ K, $x=0.5$) at $T=80$ K we have $S_{\text{opt}}=29$ Å. It is also noted in Ref. 5 that an effort to obtain absolute-value estimates of the conductivity leads, all the same, to noticeably overestimated values of a_d in comparison with the expected values. It is suggested that the reason for this circumstance is not taking account of the possibility of indirect electron tunneling through intermediate states possibly associated with the presence in the nanocomposite of a finely or even atomically dispersed metallic phase. Note that the results of recent studies of Fe/SiO_2 (Ref. 20) and Cu/SiO_2 (Refs. 21 and 22) systems confirm the existence of such a phase. Moreover, in Refs. 21 and 22 it was found that even for optimal annealing temperatures around 20% of the Cu in SiO_2 remains in dispersed form (in grains of diameter <10 Å).

Noteworthy also is the remark made in Ref. 5 touching on the possibility of using Boltzmann statistics to describe the conductivity of nanocomposites at high temperatures, i.e., for $kT>w$. If this condition is fulfilled, one expects a transition from the exponential temperature dependence of the conductivity to a linear dependence ($G\propto T$, Ref. 5). The inset to Fig. 2(b) plots the temperature dependence in the coordinates $\ln(G/T)-1/T$. It can be seen that at temperatures $T>40$ K the curves of $\ln(G/T)$ versus $1/T$ flatten out, and the transition temperature of the transition to a linear dependence ($G\propto T$) is that much higher, the larger are the low-temperature values of the conduction activation energy. It is also interesting that at low temperatures $T<20$ K the curves of $\ln(G/T)$ versus $1/T$ are nearly linear for all of the samples, but the values of the activation energy found from their slopes coincide with the values given in the caption to Fig. 2 to within 10%. This fact indicates that the conductivity in the region of the insulator–metal transition is most likely associated with hops between nearest neighbors. In this case, however, the shape of the $G(T)$ curves is substantially de-

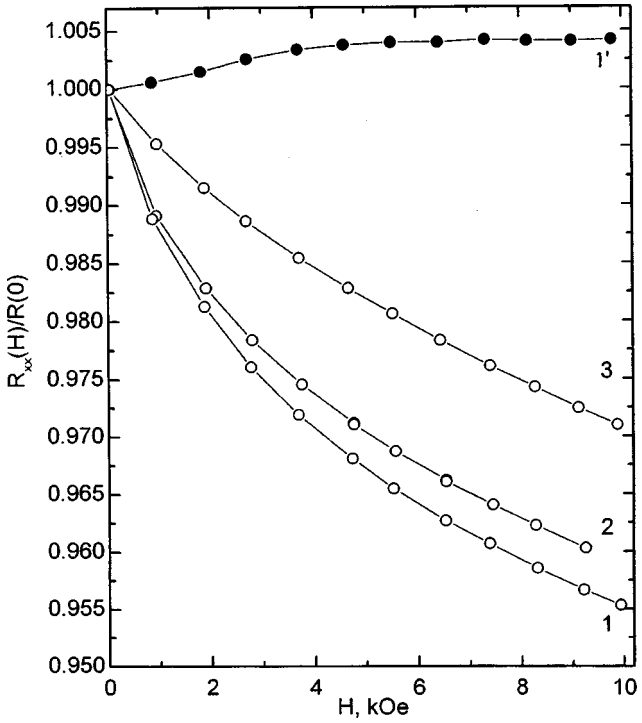

FIG. 3. Dependence of the resistance at $T=77$ on the magnetic field for a sample with metallic conductivity ($x\approx 0.7$, curve *1′*) and for ''insulating'' samples with activation energies, meV: *1*—1.0; *2*—1.25; *3*—2.83.

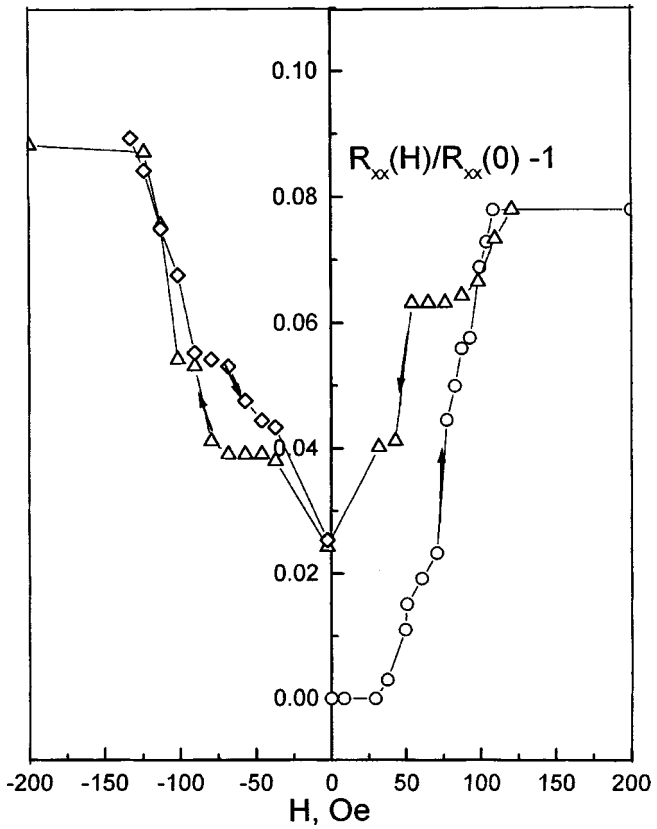

FIG. 4. Magnetoresistance of a high-resistance sample [$R_{xx}(0)=20$ MΩ, $x\approx 0.4$] after being kept in a 10-kOe magnetic field for 10 minutes. Arrows show the direction of variation of the magnetic field. $T=300$.

termined by the temperature dependence of the preexponential factor, which, as far as we know, is not taken into account in existing models of the conductivity of granular systems. Note also that the small values of the activation energy can be connected with the noticeable increase in ε_d due to the existence of a finely dispersed metallic phase.

Next, we present results of a study of the magnetoresistance and the Hall effect in samples with iron content near the critical value x_c, and also data on high-resistance samples with $x<0.4$, in which a positive magnetoresistance is manifested. It is interesting that the idea of the existence of dispersed metal atoms in dielectric gaps makes it possible to explain some aspects of the behavior of the Hall effect on the insulator side of the percolation transition.

3. MAGNETORESISTANCE

The field dependence of the magnetoresistance for samples with different iron content is shown in Fig. 3. The measurements were performed in magnetic fields that were either parallel or perpendicular to the plane of the sample; taking the anisotropic magnetoresistance effect into account,[2] the data coincide. It can be seen from Fig. 3 that for metallic conductivity (curve *1′*, $x\approx 0.7$) there is a small positive magnetoresistance, as was also observed in Ref. 2. At the same time, on the insulator side of the percolation threshold (curves *1–3*, $x<x_c$) a giant negative magnetoresistance (NMR) is observed. The magnitude of the NMR reaches 5%, which is significantly greater than for the system Ni/SiO_2 (Ref. 4), and is close to the value 4.5% obtained in Ref. 2 for the system Co/SiO_2. The data in Fig. 3 show that in the region of the transition the dependence on the composition is extraordinarily strong, and that the magnitude of the effect falls off at activation energies $w>1$ meV.

For iron content $x<0.4$, along with a GMR whose value in this concentration region was less than 1%, we also detected a large positive magnetoresistance (PMR) in premagnetized samples (Fig. 4). This phenomenon, which as far as we know has not been observed before, is characterized by a number of interesting properties. PMR is observed only after preliminary storage of the samples in magnetic fields $\geqslant 10$ kOe. Saturation of PMR is reached in magnetic fields ≈ 100 Oe, i.e., much smaller than the NMR; here the magnitude of the PMR is 10% (Fig. 4). In addition, the PMR is isotropic, i.e., it does not depend on the mutual orientation of the magnetic field and the current, and has a large response time (2 min) to a sudden (discontinuous) change in the magnetic field. It is important to underscore that the appearance of PMR in samples with low iron content does not contradict the presence of NMR in the same samples. In other words, the PMR and NMR effects coexist in some range of compositions. In such samples previously stored in fields >10 kOe, PMR is manifested at first with growth of the magnetic field, reaching 10%, but at a field strength around 100 Oe it is superseded by a weak decrease of the resistance with further increase of the field. In contrast to PMR, for NMR we were not able to observe a delay in the change of variation of the resistance upon introduction of a magnetic field during the characteristic response times of the apparatus of the order of

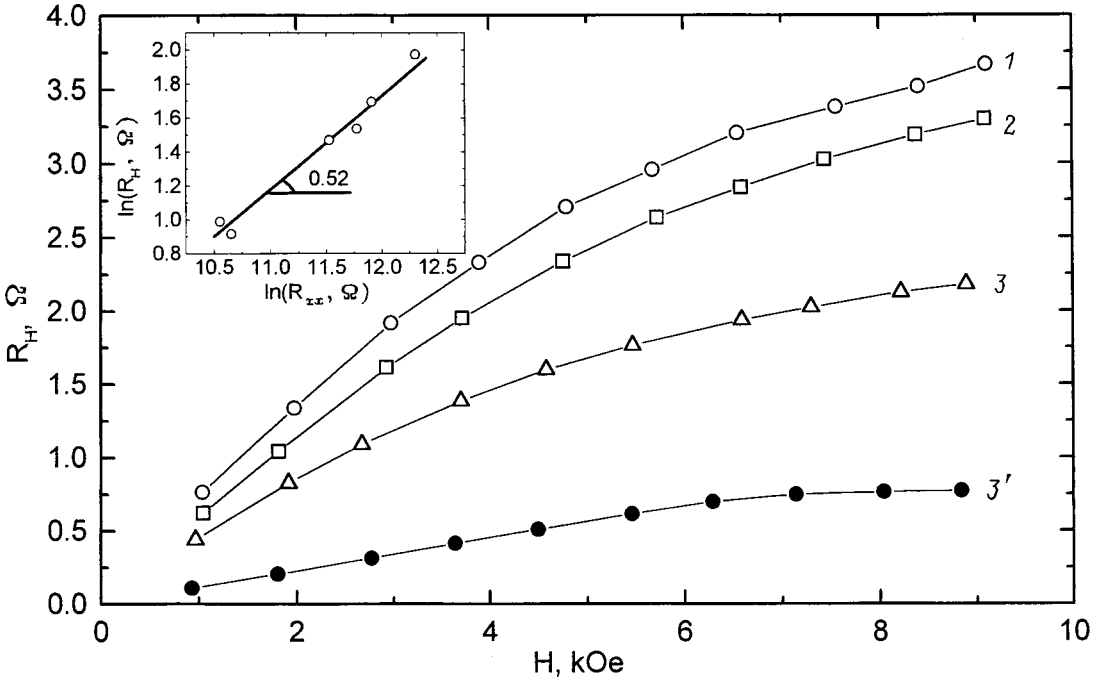

FIG. 5. Dependence of the Hall resistance on the magnetic field for samples with dielectric (curves *1–3*, $w=1.69$ meV) and metallic (curve *3′*, $x\approx 0.7$) conductivity at different temperatures, K: *1*—100; *2*—120; *3,3′*—300. Inset shows the parametric dependence of the Hall resistance on the longitudinal resistance of insulating samples in the temperature interval 77–300 K.

several fractions of a second. The detected PMR effect is difficult to interpret and requires additional study. Indeed, a magnetic field on the order of 100 Oe is not strong enough to significantly reorient the magnetic moments of superparamagnetic particles. It is possible, however, that this effect is due to cluster formations made up of grains whose magnetic moments can reorient in comparatively weak fields. A more detailed study of the dependence of the resistance on the magnetic field has revealed the presence of several reproducible steps in the magnetic field dependence of the resistance (Fig. 4). The discrete steps in the magnetoresistance and its large response time (2 min) point to a possible connection between PMR and a rearrangement of the magnetic structure and a relaxation of the magnetic moments of the clusters.

4. THE HALL EFFECT

The difficulties of measuring the Hall effect in the dielectric region are connected with the unavoidable asymmetry in the location of the Hall probes and with the parasitic influence of the giant magnetoresistance (GMR) arising under these conditions,[8] and also with an abrupt increase in the additive noise belonging to percolation systems.[23] This is probably the main reason for the absence of systematic measurements of the Hall effect in nanocomposites in the region of activation conductivity. In the present work measurements of the Hall effect were performed with the help of an automated setup. In digital form, the voltage between the Hall probes V_y and the current flowing through the sample I_x were recorded for two opposite directions of the magnetic field H. The measurements were taken at constant voltage $V_x=5$ V. To subtract out the ''zero'' of the measuring devices, the signal V_y at each experimental point was measured several times relative to its value for $V_x=0$ and accumulated. In this regime the accuracy of determination of the transverse resistance $R_{xy}=V_y/I_x$ was 10^{-2} %. In order to eliminate the effect of the asymmetry of the probes, the Hall resistance R_h was defined as a difference in values of R_{xy} corresponding to a positive sign (R_{xy}^{+}) and a negative sign (R_{xy}^{-}) of the magnetic field: $R_h=(R_{xy}^{+}-R_{xy}^{-})/2$. For all the samples the sign of the Hall effect was found to be positive, as is the case for single-crystal iron.[16] It is interesting that in the dielectric region the dependence of the asymmetry resistance $R_a=(R_{xy}^{+}-R_{xy}^{-})/2$ on the magnetic field for a small asymmetry of the Hall probes as a rule differs noticeably from the magnetoresistance curve $R_{xx}(H)$. We believe that differences in the behavior of $R_a(H)$ and of the magnetoresistance $R_{xx}(H)$ are connected with fluctuations of the electric inhomogeneity scale resulting from reorientation of the magnetic moments of the particles along the field, leading to a change in the topology of the current flow paths and, consequently, R_a. Fluctuations of this kind have a substantial effect on the measurement accuracy of R_{xy} and are probably characteristic of a wide class of Hall objects with percolation-type conductivity.[24] Note also that fluctuations in R_{xy}, as was shown in Ref. 24, are that much stronger, the larger is the cell size of the percolation cluster.

Figure 5 shows a family of curves of the Hall resistance as a function of H at various temperatures for samples with hopping ($x\approx 0.5$) and metallic ($x\approx 0.7$) conductivity. It can be seen that in both samples the $R_h(H)$ curves exhibit noticeable saturation, which is typical of the proportional magnetization of the anomalous Hall effect (AHE) in disordered ferromagnetic metals.[3,8–10,12] The fact that both the sign of the Hall effect and the general character of its magnetic-field

dependence $R_h(H)$ are preserved in the dielectric region probably implies that spin–orbit interaction, which influences the transport of spin-polarized electrons, is responsible for the Hall effect in both cases. At room temperature near the percolation threshold, composites are still ferromagnetic, but as the metal content is increased they transition to the supermagnetic state.[4] The dependence of the magnetization on the magnetic field transforms in this case into a more ''rounded'' Langevin function.[4] This probably underlies the differences in the shape of the $R_h(H)$ curves for metallic and dielectric samples in Fig. 5.

The inset to Fig. 5 plots the parametric dependence of the Hall resistance on the longitudinal resistance with temperature as the parametric variable. This dependence is approximated by the power law

$$R_h \propto R_{xx}^m \tag{2}$$

with exponent $m=0.52\pm0.05$. The theory of the anomalous Hall effect in ferromagnetic metals also predicts a power-law dependence, but with an exponent m equal to 1 (the skew electron scattering model) or 2 (the lateral jump model)[12,25] (in a recent work[13] on granular alloys it was shown that the skew scattering mechanism is the preferred mechanism).

There is no theory of the Hall effect on the insulator side of the metal–insulator transition in granular ferromagnetic films at the present time. Indeed, as was already noted, theoretical representations of the anomalous Hall effect pertain wholly to disordered systems with metallic conductivity.[10,12,13] Nevertheless, it is interesting to compare formula (2) with the results of a recently developed theory of the Hall effect for hopping conductivity in nonmagnetic semiconductors.[26] Despite the large difference in the objects in question, a general approach[26] to the description of the Hall effect in the hopping conduction regime is nevertheless worthy of note.[26] It is based on the idea[27] of the need in this case to take account of indirect tunneling transitions. We will proceed from the assumption that the probability of a direct electron tunneling event between two magnetic grains does not contain corrections linear in the magnetic field (see, e.g., Ref. 28). The appearance of such corrections, which give rise to the Hall effect, is possible only in the presence of a third intermediate state playing the role of a scattering center during tunneling. We assume that in our case the role of scattering centers is played by magnetic metal atoms located in the dielectric spaces between the grains.[5,20–22] This leads to the asymmetry (skewness) in the electron scattering (in distinction to the case considered in Refs. 26 and 27) and consequently to the anomalous behavior of the Hall effect as a function of the magnetic field.

Let us make use of the relation between the experimentally measured Hall resistance and the experimentally measured longitudinal resistance

$$R_h = R_{xx}\beta W/L, \tag{3}$$

where W and L are respectively the width and length of the sample, and β is the tangent of the Hall angle. According to Ref. 26,

$$\beta = E_h/E_x \propto \xi_c^0 \exp(-\xi_c^0 - w/2kT), \tag{4}$$

where for granular systems $\xi_c^0 = 2s/a_d$, and E_h and E_x are the Hall and longitudinal fields, respectively. Note that relation (4) contains an activation energy that is half the activation energy of conduction. Taking this fact into account, it follows from relations (3) and (4) that $R_h \propto \exp(w/2kT) \propto (R_{xx})^{1/2}$. This result is in rough agreement with the experimental dependence (2), although in our case the temperature dependence of the conductivity, strictly speaking, is not activational for $T>77$ K.

To sum up, in the present work we have investigated the conductivity, and also aspects of galvanomagnetic effects in granular Fe/SiO_2 films below the percolation threshold. On the insulator side of the percolation threshold ($x_c=0.5-0.6$) granular Fe/SiO_2 films exhibit a large ($\approx 5\%$) negative magnetoresistance, falling off sharply at activation energies greater than 1 meV. For $x<0.4$ in samples previously stored in a strong magnetic field we have detected a giant positive magnetoresistance, reaching 10% in fields around 100 Oe and characterized by large response times to the action of a magnetic field. We have carried out a first-of-its-kind study of the giant Hall effect in the dielectric region of metal volume fractions. We have shown that the field dependence of the Hall effect in the region of hopping conductivity saturates with increasing magnetic field and is similar to the magnetization curve described by the Langevin function. This indicates that in dielectric samples, as in metallic samples, the Hall effect is due to the spin–orbit interaction and is proportional to the magnetization. We have found that the dependence of the Hall resistance on the longitudinal resistance in the dielectric region is close to a square-root law, in contrast to the known models of the anomalous Hall effect for ferromagnetic metals. The properties thus discovered in the Hall effect and magnetoresistance are apparently associated with indirect spin-dependent electron tunneling through intermediate states in the insulator and with a substantial role of cluster formations.

The authors express their gratitude to A. N. Lagar'kov, A. K. Sarychev, and S. A. Gurevich for discussion and valuable remarks, and V. M. Cherepanov for assistance with the Mössbauer measurements.

This work was carried out with the support of the Russian Foundation for Basic Research (Grant No. 96-02-18412, Grant No. PICS 98-02-22037) and the Interdisciplinary Scientific–Technical Program ''Physics of Solid-State Nanostructures'' (Grant No. 1-052).

*)E-mail: aronzon@mail.imp.kiae.ru

[1] N. F. Mott and E. A. Davis, *Electron Processes in Non-Crystalline Materials* (Clarendon Press, Oxford, 1979).
[2] A. Milner, A. Gerber, B. Groisman, M. Karpovsky, and A. Gladkikh, Phys. Rev. Lett. **76**, 475 (1996).
[3] A. B. Pakhomov, X. Yan, and B. Zhao, Appl. Phys. Lett. **67**, 3497 (1995).
[4] J. L. Gittleman, Y. Goldstein, and S. Bozovski, Phys. Rev. B **5**, 3609 (1972).
[5] C. J. Adkins, ''Hopping conductivity in granular metals revisited,'' in *Metal–Insulator Transitions Revisited*, edited by P. P. Edwards and C. N. R. Rao (Taylor & Francis, New York, 1995).

[6] A. K. Sarychev and F. Brouers, Phys. Rev. Lett. **73**, 2895 (1994).
[7] X. N. Jing, N. Wang, A. B. Pakhomov, K. K. Fung, and X. Yan, Phys. Rev. B **53**, 14032 (1996).
[8] A. B. Pakhomov, X. Yan, and Y. Xu, J. Appl. Phys. **79**, 6140 (1996).
[9] A. B. Pakhomov and X. Yan, Solid State Commun. **99**, 139 (1996).
[10] F. Brouers, A. Granovsky, A. Sarychev, and A. Kalitsov, Physica A **241**, 284 (1997).
[11] B. A. Aronzon, A. A. Likalter, V. V. Rylkov, A. K. Sarychev, M. A. Sedova, and A. E. Varfolomeev, Phys. Status Solidi **205**, 151 (1998).
[12] A. V. Vedyaev, A. B. Granovskiĭ, and O. A. Kotel'nikova, *Kinetic Phenomena in Disordered Ferromagnetic Alloys* [in Russian] (Moscow State Univ. Press, Moscow, 1992).
[13] A. B. Granovskiĭ, A. V. Kalitsov, and F. Brauers, JETP Lett. **65**, 509 (1997).
[14] E. V. Kuchis, *Galvanomagnetic Effects and Methods of Studying Them* [in Russian] (Radio i Svyaz', Moscow, 1990).
[15] J.-L. Dormann, P. Gibart, and P. Renaudin, J. Phys. (France) **6**, 281 (1976).
[16] *Handbook of Physical Quantities*, edited by I. S. Grigoriev and E. Z. Meilikhov (CRC Press, Boca Raton, 1997).
[17] P. Sheng, B. Abeles, and Y. Arie, Phys. Rev. Lett. **31**, 44 (1973).
[18] C. J. Adkins, J. Phys.: Condens. Matter **1**, 1253 (1989).
[19] B. I. Shklovskii and A. L. Efros, *Electronic Properties of Doped Semiconductors* (Springer-Verlag, New York, 1989).
[20] A. B. Pakhomov, X. Yan, N. Wang, X. N. Jing, B. Zhao, K. K. Fung, J. Xhie, T. F. Hung, and S. K. Wong, Physica A **241**, 344 (1997).
[21] S. A. Gurevich, T. A. Zaraĭskaya, S. G. Konnikov, V. M. Mikushin, S. Yu. Nikonov, A. A. Sitnikov, S. E. Sysoev, V. V. Khorenko, V. V. Shnitov, and Yu. S. Gordeev, Fiz. Tverd. Tela (St. Petersburg) **39**, 1889 (1997) [Phys. Solid State **39**, 1691 (1997)].
[22] V. V. Khorenko, *Study of the Structural and Electrical Properties of Composite Metal–Insulator Films with Nanometer-Scale Metallic Grains* [in Russian], Author's Abstract, Candidate's Dissertation, St. Petersburg State Technical University (1998).
[23] D. J. Bergman, Phys. Rev. B **39**, 4598 (1989).
[24] B. A. Aronzon, V. V. Rylkov, A. S. Vedeneev, and J. Leotin, Physica A **241**, 259 (1997).
[25] R. M. White and T. H. Geballe, *Long-Range Order in Solids* (Academic Press, New York, 1979).
[26] Yu. M. Gal'perin, E. P. German, and V. G. Karpov, Zh. Éksp. Teor. Fiz. **99**, 343 (1991) [Sov. Phys. JETP **72**, 193 (1991)].
[27] T. Holstein, Phys. Rev. **124**, 1329 (1961).
[28] J. Inoue and S. Maekawa, Phys. Rev. B **53**, R11 927 (1996).

Translated by Paul F. Schippnick

The $B-B'-U$ Hubbard model in the approximation of static fluctuations

G. I. Mironov

Mari State Pedagogical Institute, 424002 Yoshkar-Ola, Russia
(Submitted July 20, 1998)
Fiz. Tverd. Tela (St. Petersburg) **41**, 951–956 (June 1999)

Within the approximation of static fluctuations, the effect of allowing for electron transport from a given site to the second-nearest neighboring site on the energy spectrum of the two-sublattice two-dimensional Hubbard model and on the dependence of the magnetization on the system parameters is investigated. © *1999 American Institute of Physics.*
[S1063-7834(99)00506-7]

To explain some of the properties of high-temperature superconductors (HTSC) in the normal as well as the superconducting state, the need arises to take account of hopping integrals between nearest-neighbor oxygen atoms in addition to the copper–oxygen hopping integrals.[1–4] It is clear from qualitative considerations that taking oxygen–oxygen hole transport into account should affect the form of the energy spectrum, which in turn will lead to a change in other characteristics of the system. Therefore it is of compelling interest to calculate the energy spectrum of the system with allowance for the possibility of electron (or hole) transport to the second-nearest neighboring site.

The aim of the present work is to investigate the dependence of the energy spectrum and the magnetization of the system on the magnitude of the integral for electron transport to the second-nearest neighboring site in the case of the two-dimensional bipartite Hubbard model.[5,6]

A technique was developed in Refs. 7 and 8 for solving the Hubbard model in the approximation of static fluctuations. In comparison with Ref. 8, we including a term in the Hubbard Hamiltonian[9] describing hops of electrons of the sublattice C to the nearest sites of this sublattice

$$H=H_0+V, \tag{1}$$

$$H_0=\sum_{\sigma,f\in A}\varepsilon_1 n_{f\sigma}+\sum_{\sigma,l\in C}\varepsilon_2 n_{l\sigma}+\sum_{\sigma,f,l}B_{fl}(a^+_{f\sigma}a_{l\sigma}+a^+_{l\sigma}a_{f\sigma})+\sum_{\sigma,l',l}B_{l'l}a^+_{l'\sigma}a_{l\sigma}, \tag{2}$$

$$V=\frac{U_1}{2}\sum_{\sigma,f\in A}n_{f\sigma}n_{f\bar{\sigma}}+\frac{U_2}{2}\sum_{\sigma,l\in C}n_{l\sigma}n_{l\bar{\sigma}}, \tag{3}$$

where $a^+_{j\sigma}$ and $a_{j\sigma}$ are the electron Fermi creation and annihilation operators at the jth lattice site ($j=f,l$) with spin σ; $n_{f\sigma}=a^+_{f\sigma}a_{f\sigma}$; $\varepsilon_1(\varepsilon_2)$ is the self-energy of the electron at a site of the sublattice $A(C)$; $B_{fl}=B(f-l)$ and $B_{l'l}=B(l'-l)$ are transport integrals describing electron hops at the expense of their kinetic energy and the crystal field to the nearest-neighboring site and to the second-nearest neighboring site along the square diagonal, respectively; and $\bar{\sigma}=-\sigma$. In order to have the behavior of the system described by the Hamiltonian (1) mimic the situation arising in the motion of holes in the CuO_2 planes in HTSC compounds, we assume that only electrons of one sublattice (in analogy with oxygen in CuO_2 planes) can be transported along a square diagonal to sites of this same sublattice (we emphasize that in this paper, for simplicity of discussion, we consider a hypothetical square lattice).

The equations of motion for the electron creation operators in the Heisenberg representation ($j=f,l$)

$$a^+_{j\sigma}(\tau)=\exp(H\tau)a^+_{j\sigma}(0)\exp(-H\tau),\quad(\tau=it)$$

have the form

$$\frac{d}{d\tau}a^+_{j\sigma}(\tau)=\varepsilon_j a^+_{j\sigma}(\tau)+\sum_i B_{ij}a^+_{i\sigma}(\tau)+\sum_{j'}B_{jj'}a^+_{j'\sigma}(\tau)+U_j n_{j\bar{\sigma}}a^+_{j\sigma}(\tau), \tag{4}$$

where

$$\varepsilon_j=\begin{cases}\varepsilon_1, & j=f\\ \varepsilon_2, & j=l\end{cases}\qquad U_j=\begin{cases}U_1, & j=f\\ U_2, & j=l\end{cases}$$

$$B_{jj'}=\begin{cases}0, & j=f,\ j'=f'\\ B_{ll'}, & j=l,\ j'=l'\end{cases}\qquad B_{ij}=B_{fl}=B_{lf}.$$

We represent the operators $n_{j\bar{\sigma}}$ in Eq. (4) as follows:[7,8]

$$n_{j\bar{\sigma}}=\langle n_{j\bar{\sigma}}\rangle+\Delta n_{j\bar{\sigma}}. \tag{5}$$

The thermodynamic means $\langle n_{j\bar{\sigma}}\rangle=\mathrm{Tr}\{n_{j\bar{\sigma}}\exp(-\beta H)\}$ are assumed to be independent of the number of the site j in each of the sublattices, and $\Delta n_{j\bar{\sigma}}=\Delta n_{j\bar{\sigma}}(\tau)$ is the particle number fluctuation operator in the Heisenberg representation.

We express the correlation functions $\langle n_{j\bar{\sigma}}\rangle$ in terms of the mean value of the projection of the spin of the site $S=\langle S^z_f\rangle=-\langle S^z_{f+\Delta}\rangle$, where the vector Δ joins neighboring atoms, and the electron density n (we are interested in the case $n=1$) as follows:[8]

$$\langle n_{f\bar{\sigma}}\rangle=\langle n_{l\sigma}\rangle=1/2+S, \tag{6}$$

$$\langle n_{f\sigma}\rangle=\langle n_{l\bar{\sigma}}\rangle=1/2-S. \tag{7}$$

Taking relations (5)–(7) into account, we rewrite the differential equation (4) in the form

$$\frac{d}{d\tau}a_{j\sigma}^{+}(\tau)=\varepsilon_j' a_{j\sigma}^{+}(\tau)+\sum_i B_{ij}a_{i\sigma}^{+}(\tau)+\sum_{j'} B_{jj'}a_{j'\sigma}^{+}(\tau)$$
$$+U_j\Delta n_{j\bar{\sigma}}a_{j\sigma}^{+}(\tau), \tag{8}$$

where $\varepsilon_1'=\varepsilon_1+U_1/2+SU_1$ and $\varepsilon_2'=\varepsilon_2+U_2/2-SU_2$.

We represent the Heisenberg operators in the form[8,10,11]

$$a_{j\sigma}^{+}(\tau)=\exp(H_0\tau)\tilde{a}_{j\sigma}^{+}(\tau)\exp(-H_0\tau), \tag{9}$$

where H_0 is the Hamiltonian entering into Eq. (1), with the renormalization of the electron self-energies taken into account (the substitutions $\varepsilon_1\to\varepsilon_1'$ and $\varepsilon_2\to\varepsilon_2'$). The operator $\tilde{a}_{j\sigma}^{+}(\tau)$ is defined as follows:

$$\tilde{a}_{j\sigma}^{+}(\tau)=\exp(-H_0\tau)\exp(H\tau)a_{j\sigma}^{+}(0)\exp(H\tau)\exp(H_0\tau).$$

In this case we have two equations for the unknown operators ($j=f,l$)

$$\frac{d}{d\tau}\tilde{a}_{j\sigma}^{+}(\tau)=U_j\Delta\tilde{n}_{j\bar{\sigma}}(\tau)\tilde{a}_{j\sigma}^{+}(\tau), \tag{10}$$

where $\Delta\tilde{n}_{j\bar{\sigma}}(\tau)=\exp(-H_0\tau)\Delta n_{j\bar{\sigma}}(\tau)\exp(H_0\tau)$, $\Delta n_{j\bar{\sigma}}(\tau)$ is the particle number fluctuation operator in the Heisenberg representation. The equation of motion for the operators $\Delta\tilde{n}_{j\bar{\sigma}}(\tau)$ has the form

$$\frac{d}{d\tau}\Delta\tilde{n}_{j\bar{\sigma}}=0.$$

Thus, $\Delta\tilde{n}_{j\bar{\sigma}}(\tau)$ is an integral of motion: $\Delta\tilde{n}_{j\bar{\sigma}}(\tau)=\Delta n_{j\bar{\sigma}}(0)$.

In order to obtain a closed system of differential equations, we multiply Eq. (10) by the fluctuation operator $\Delta n_{j\bar{\sigma}}=\Delta n_{j\bar{\sigma}}(0)$ and restrict ourselves to the approximation (see Appendix A)

$$\Delta n_{j\bar{\sigma}}^2=\langle\Delta n_{j\bar{\sigma}}^2\rangle, \quad (j=f,l).$$

In this case we obtain the following equations of motion:

$$\frac{d}{d\tau}\Delta n_{j\bar{\sigma}}\tilde{a}_{j\sigma}^{+}(\tau)=U_j\langle\Delta n_{j\bar{\sigma}}^2\rangle\tilde{a}_{j\sigma}^{+}(\tau). \tag{11}$$

Taking Eqs. (5)–(7) and the properties $n_{j\bar{\sigma}}^2=n_{j\bar{\sigma}}$ into account, we find that

$$\Phi^2=\langle\Delta n_{f\bar{\sigma}}^2\rangle=\langle\Delta n_{l\bar{\sigma}}^2\rangle=1/4-S^2. \tag{12}$$

The solution of the system of equations (10) and (11) has the form [$\tilde{a}_{j\sigma}^{+}(0)=a_{j\sigma}^{+}(0)$]

$$\tilde{a}_{j\sigma}^{+}(\tau)=a_{j\sigma}^{+}(0)\cosh(U_j\Phi\tau)$$
$$+\Delta n_{j\bar{\sigma}}a_{j\sigma}(0)\sinh(U_j\Phi\tau)/\Phi, \tag{13}$$

$$\Delta n_{j\bar{\sigma}}\tilde{a}_{j\sigma}^{+}(\tau)=\Delta n_{j\bar{\sigma}}a_{j\sigma}^{+}(0)\cosh(U_j\Phi\tau)$$
$$+\Phi a_{j\sigma}^{+}(0)\sinh(U_j\Phi\tau), \tag{14}$$

where $\sinh(x)$ and $\cosh(x)$ are the hyperbolic sine and cosine.

Thus, the general solution (9) has the form

$$a_{j\sigma}^{+}(\tau)=\exp(H_0\tau)a_{j\sigma}^{+}(0)\exp(-H_{0\tau})\cosh(U_j\Phi\tau)$$
$$+\Delta n_{j\bar{\sigma}}\exp(H_0\tau)a_{j\sigma}^{+}(0)$$
$$\times\exp(-H_0\tau)\sinh(U_j\Phi\tau)/\Phi. \tag{15}$$

We now calculate the operator $\overline{a}_{f\sigma}^{+}(\tau)=\exp(H_0\tau)a_{f\sigma}^{+}(0)\times\exp(-H_0\tau)$ entering into the solution (15). The operator $\overline{a}_{f\sigma}^{+}(\tau)$ obeys the differential equation

$$\frac{d}{d\tau}\overline{a}_{f\sigma}^{+}(\tau)=\varepsilon_1'\overline{a}_{f\sigma}^{+}(\tau)+\sum_l B_{fl}\overline{a}_{l\sigma}^{+}(\tau). \tag{16}$$

Analogously, for the operator $\overline{a}_{l\sigma}^{+}(\tau)$ of the other subsystem we obtain the following equation of motion:

$$\frac{d}{d\tau}\overline{a}_{l\sigma}^{+}(\tau)=\varepsilon_2'\overline{a}_{l\sigma}^{+}(\tau)+\sum_f B_{fl}\overline{a}_{f\sigma}^{+}(\tau)+\sum_{l'} B_{ll'}'\overline{a}_{l'\sigma}^{+}(\tau). \tag{17}$$

After taking the Fourier transforms[12]

$$a_{f\sigma}^{+}=\sqrt{2/N}\sum_k a_{k\sigma}^{+}\exp(-ikr_f),$$

$$a_{l\sigma}^{+}=\sqrt{2/N}\sum_k b_{k\sigma}^{+}\exp(-ikr_l),$$

we obtain from Eqs. (16) and (17)

$$\frac{d}{d\tau}\overline{a}_{k\sigma}^{+}(\tau)=\varepsilon_1'\overline{a}_{k\sigma}^{+}(\tau)+B_k\overline{b}_{k\sigma}^{+}(\tau), \tag{18}$$

$$\frac{d}{d\tau}\overline{b}_{k\sigma}^{+}(\tau)=\varepsilon_{2k}'\overline{b}_{k\sigma}^{+}(\tau)+B_k\overline{a}_{k\sigma}^{+}(\tau), \tag{19}$$

where ε_{2k}' and B_k are defined as ($d=2$)

$$\varepsilon_{2k}'=\varepsilon_2'+B_k', \quad B_k'=-4B'\cos(k_xa)\cos(k_ya),$$

$$B_k=-2B[\cos(k_xa)+\cos(k_ya)].$$

Equations (18) and (19) have the solutions [$\overline{a}_{k\sigma}^{+}(0)=a_{k\sigma}^{+}(0)$, $\overline{b}_{k\sigma}^{+}(0)=b_{k\sigma}^{+}$]

$$\overline{a}_{k\sigma}^{+}(\tau)=a_{k\sigma}^{+}(0)[((\varepsilon_1'-\varepsilon_{2k}')/2t_k)\sinh(t_k\tau)$$
$$+\cosh(t_k\tau)]\exp(\tau(\varepsilon_1'+\varepsilon_{2k}')/2)$$
$$+b_{k\sigma}^{+}(0)\sinh(t_k\tau)\exp(\tau(\varepsilon_1'+\varepsilon_{2k}')/2)B_k/t_k, \tag{20}$$

$$\overline{b}_{k\sigma}^{+}(\tau)=b_{k\sigma}^{+}(0)[((\varepsilon_{2k}'-\varepsilon_1')/2t_k)\sinh(t_k\tau)$$
$$+\cosh(t_k\tau)]\exp(\tau(\varepsilon_1'+\varepsilon_{2k}')/2)$$
$$+a_{k\sigma}^{+}(0)\sinh(t_k\tau)\exp(\tau(\varepsilon_1'+\varepsilon_{2k}')/2)B_k/t_k, \tag{21}$$

where $t_k=\sqrt{((\varepsilon_{2k}'-\varepsilon_1')/2)^2+B_k^2}$.

After taking the Fourier transform we find the general solution of (15) taking formulas (20) and (21) into account in the following form:

$$a_{k\sigma}^{+}(\tau)=\{[a_{k\sigma}^{+}(0)[((\varepsilon_1'-\varepsilon_{2k}')/2t_k)\sinh(t_k\tau)$$
$$+\cosh(t_k\tau)]+b_{k\sigma}^{+}(0)\sinh(t_k\tau)B_k/t_k]$$
$$\times\cosh(U_1\Phi\tau)+[\Delta n_{1\bar{\sigma}}a_{k\sigma}^{+}(0)[((\varepsilon_1'$$
$$-\varepsilon_{2k}')/2t_k)\sinh(t_k\tau)+\cosh(t_k\tau)]$$
$$+\Delta n_{1\bar{\sigma}}b_{k\sigma}^{+}(0)\sinh(t_k\tau)B_k/t_k]$$

$$\sinh(U_1\Phi\tau)/\Phi\}\exp(\tau(\varepsilon_1'+\varepsilon_{2k}')/2), \qquad (22)$$

where $\Delta n_{1\bar{\sigma}}$ is the homogeneous number fluctuation operator in the sublattice A (Ref. 8). For electrons of the other sublattice

$$\begin{aligned} b_{k\sigma}^{+}(\tau)=\{&[b_{k\sigma}^{+}(0)[((\varepsilon_{2k}'-\varepsilon_1')/2t_k)\sinh(t_k\tau)\\ &+\cosh(t_k\tau)]+a_{k\sigma}^{+}(0)\sinh(t_k\tau)B_k/t_k]\\ &\times\cosh(U_2\Phi\tau)+[\Delta n_{2\bar{\sigma}}b_{k\sigma}^{+}(0)[((\varepsilon_{2k}'\\ &-\varepsilon_1')/2t_k)\sinh(t_k\tau)+\cosh(t_k\tau)]\\ &+\Delta n_{2\bar{\sigma}}a_{k\sigma}^{+}(0)\sinh(t_k\tau)B_k/t_k]\\ &\times\sinh(U_2\Phi\tau)/\Phi\}\exp(\tau(\varepsilon_1'+\varepsilon_{2k}')/2). \end{aligned} \qquad (23)$$

The homogeneous number fluctuation operator in the sublattice $C\Delta n_{2\bar{\sigma}}$ is defined in analogy with the operator $\Delta n_{1\bar{\sigma}}$ (Ref. 8).

Formulas (22) and (23) contain all the information about the physical properties of the Hubbard model within the framework of the chosen approximation. We are interested, first of all, in the spectrum of elementary excitations in the system. As follows from formulas (22) and (23), the Fourier transforms of the anticommutator Green's functions are equal respectively to

$$\begin{aligned} \langle a_{k\sigma}^{+}|a_{k\sigma}\rangle_E=\frac{i}{2\pi}\frac{1}{4}\Bigg\{&\frac{1+(\varepsilon_1'-\varepsilon_{2k}')/2t_k}{E-U_1\Phi-t_k-(\varepsilon_1'+\varepsilon_{2k}')/2}\\ &+\frac{1+(\varepsilon_1'-\varepsilon_{2k}')/2t_k}{E+U_1\Phi-t_k-(\varepsilon_1'+\varepsilon_{2k}')/2}\\ &+\frac{1-(\varepsilon_1'-\varepsilon_{2k}')/2t_k}{E-U_1\Phi+t_k-(\varepsilon_1'+\varepsilon_{2k}')/2}\\ &+\frac{1-(\varepsilon_1'-\varepsilon_{2k}')/2t_k}{E+U_1\Phi+t_k-(\varepsilon_1'+\varepsilon_{2k}')/2}\Bigg\}, \end{aligned} \qquad (24)$$

$$\begin{aligned} \langle b_{k\sigma}^{+}|b_{k\sigma}\rangle_E=\frac{i}{2\pi}\frac{1}{4}\Bigg\{&\frac{1-(\varepsilon_1'-\varepsilon_{2k}')/2t_k}{E-U_2\Phi-t_k-(\varepsilon_1'+\varepsilon_{2k}')/2}\\ &+\frac{1-(\varepsilon_1'-\varepsilon_{2k}')/2t_k}{E+U_2\Phi-t_k-(\varepsilon_1'+\varepsilon_{2k}')/2}\\ &+\frac{1+(\varepsilon_1'-\varepsilon_{2k}')/2t_k}{E-U_2\Phi+t_k-(\varepsilon_1'+\varepsilon_{2k}')/2}\\ &+\frac{1+(\varepsilon_1'-\varepsilon_{2k}')/2t_k}{E+U_2\Phi+t_k-(\varepsilon_1'+\varepsilon_{2k}')/2}\Bigg\}, \end{aligned} \qquad (25)$$

where

$$\begin{aligned} \varepsilon_1'+\varepsilon_{2k}'&=\varepsilon_1+\varepsilon_2+(U_1+U_2)/2+S(U_1-U_2)\\ &\quad-4B'\cos(k_xa)\cos(k_ya),\\ \varepsilon_1'-\varepsilon_{2k}'&=\varepsilon_1-\varepsilon_2+(U_1-U_2)/2+S(U_1+U_2)\\ &\quad+4B'\cos(k_xa)\cos(k_ya). \end{aligned}$$

The poles of the Green's functions (30) and (31) define the energy spectrum:

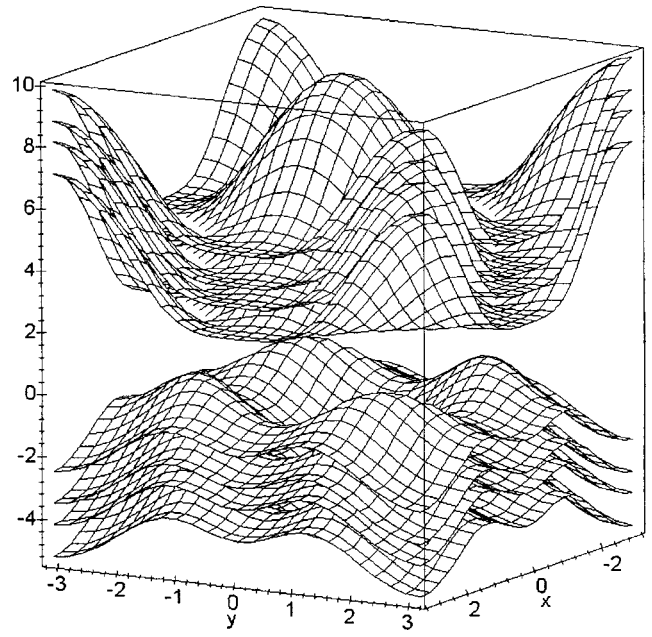

FIG. 1. Energy spectrum of the Hubbard model for the following parameter values: $\varepsilon_1=-4$ eV, $\varepsilon_2=-1$ eV, $U_1=8$ eV, $U_2=2$ eV, $B=1.5$ eV, $B'=-0.3B$ eV, and $S=0$.

$$E_{1-4}=((\varepsilon_1'+\varepsilon_{2k}')/2)\pm U_1\Phi\pm t_k, \qquad (26)$$

$$E_{5-8}=((\varepsilon_1'+\varepsilon_{2k}')/2)\pm U_2\Phi\pm t_k. \qquad (27)$$

Figure 1 plots the energy spectrum of the Hubbard model for the spin $S=0$ (paramagnetism). Figures 2 and 3, for comparison, plot the energy spectra with and without allowance for electron transport from atoms of one kind to atoms of this same kind along a square diagonal. For a given value of B', allowing for hopping of electrons from site to

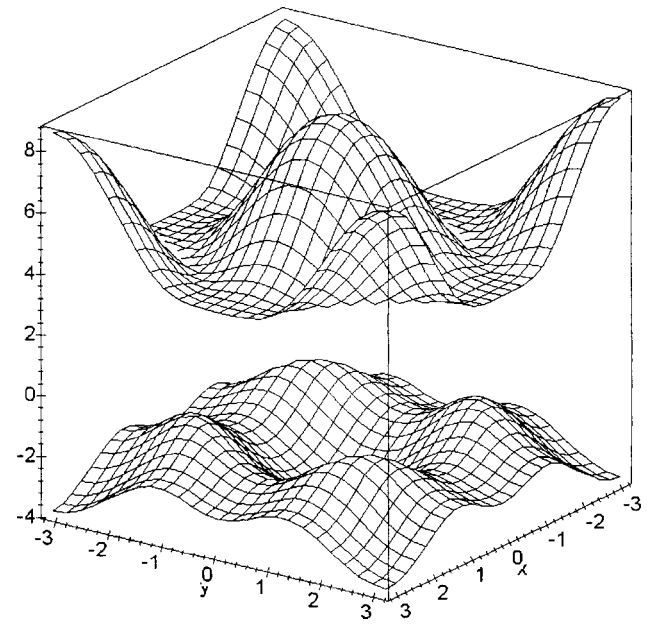

FIG. 2. The same as in Fig. 1, but for $\varepsilon_1=-4$ eV, $\varepsilon_2=-1$ eV, $U_1=8$ eV, $U_2=2$ eV, $B=1.5$ eV, $B'=-0.3B$ eV, and $S=1/2$.

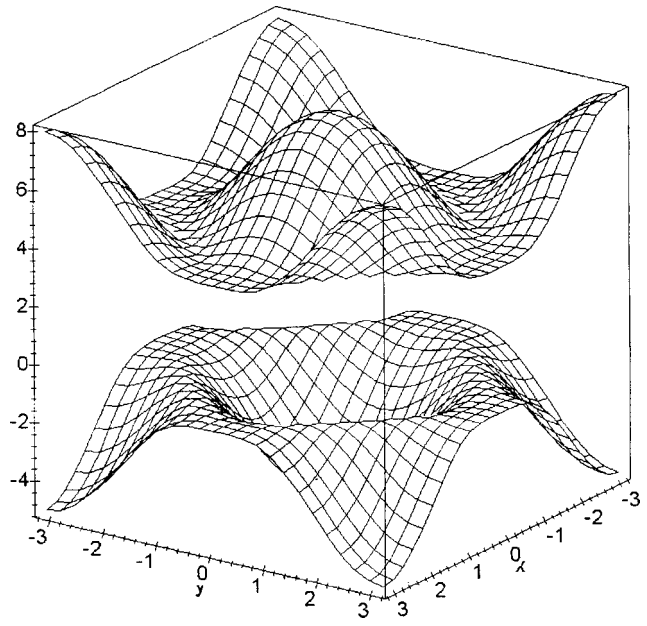

FIG. 3. The same as in Fig. 1, but for $\varepsilon_1=-4$ eV, $\varepsilon_2=-1$ eV, $U_1=8$ eV, $U_2=2$ eV, $B=1.5$ eV, $B'=0$, and $S=1/2$.

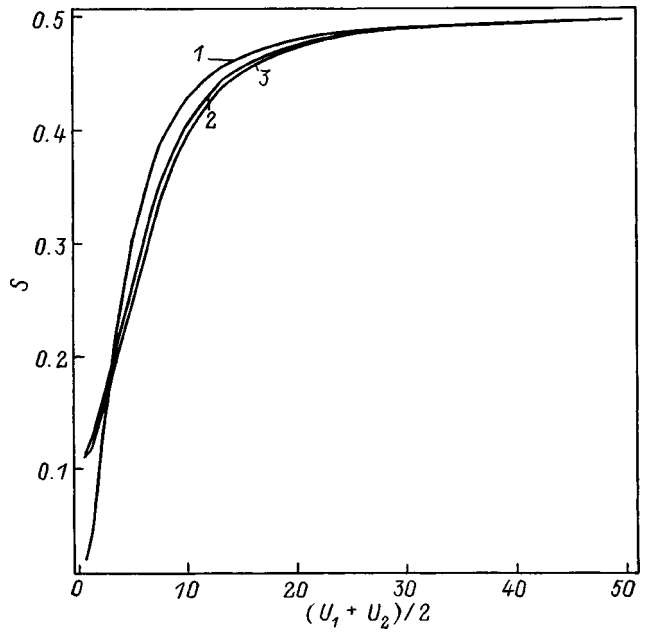

FIG. 4. The spin (magnetization) S as a function of $(U_1+U_2)/2$ for $n=1$, $B=1.5$ eV, and $T=0$ for $B'=0$ (*1*), $B'=-0.3B$ (*2*), and $B'=-0.45B$ (*3*).

site along a square diagonal leads to a narrowing of the lower subband; in this case the shape of the energy surface changes dramatically.

The energy spectra shown in the figures make it possible in a natural way to explain the metal–insulator transition that takes place as the electron density n is varied, whereas the standard Hartree–Fock approximation does not lead to such a result:[13] it is necessary to resort to a different kind of decoupling e.g., the ''flotation analogy.'' [14,2] Note in this regard that the technique for calculating the Green's functions and correlation functions was constructed so as to obtain an exact result in the atomic limit [see Ref. 7 and Appendix B].

With the help of the fluctuation–dissipation theorem[15] we obtain from Eq. (24)

$$\langle a^+_{k\sigma}a_{k\sigma}\rangle=\frac{1}{4}\left(1+\frac{\varepsilon'_1-\varepsilon'_{2k}}{2t_k}\right)\left[f^+\left(U_1\Phi+t_k+\frac{\varepsilon'_1+\varepsilon'_{2k}}{2}\right)+f^+\left(-U_1\Phi+t_k+\frac{\varepsilon'_1+\varepsilon'_{2k}}{2}\right)\right]+\frac{1}{4}\left(1-\frac{\varepsilon'_1-\varepsilon'_{2k}}{2t_k}\right)\left[f^+\left(U_1\Phi-t_k+\frac{\varepsilon'_1+\varepsilon'_{2k}}{2}\right)+f^+\left(-U_1\Phi-t_k+\frac{\varepsilon'_1+\varepsilon'_{2k}}{2}\right)\right]. \tag{28}$$

Analogous equalities can also be obtained for the correlation functions $\langle a^+_{k\sigma}a_{k\bar{\sigma}}\rangle$, $\langle b^+_{k\sigma}b_{k\sigma}\rangle$, and $\langle b^+_{k\sigma}b_{k\bar{\sigma}}\rangle$. Combining the expressions so obtained and summing over all possible values of k within the limits of the first Brillouin zone, we obtain an equation for the chemical potential. Note that the condition $\varepsilon_1+U_1/2=\varepsilon_2+U_2/2=0$ corresponds to the equality $n=1$ at $T=0$.

With the help of Eq. (28) it is possible to obtain a self-consistent equation for the magnetization (spin S). In the case of an exactly half-filled band it has the form

$$\frac{1}{2}-S=\frac{2}{N}\sum_k\frac{1}{4}\left[1+\frac{S(U_1+U_2)-B'_k}{2t_k}\right]\left[f^+\left(U_1\Phi+t_k+\frac{S(U_1-U_2)+B'_k}{2}\right)+f^+\left(-U_1\Phi+t_k+\frac{S(U_1-U_2)+B'_k}{2}\right)\right]+\frac{2}{N}\sum_k\frac{1}{4}\left[1-\frac{S(U_1+U_2)-B'_k}{2t_k}\right]\left[f^+\left(U_1\Phi-t_k+\frac{S(U_1-U_2)+B'_k}{2}\right)+f^+\left(-U_1\Phi-t_k+\frac{S(U_1-U_2)+B'_k}{2}\right)\right], \tag{29}$$

where $t_k=\sqrt{((S(U_1+U_2)-B')^2/4)+B_k^2}$. In the weak-binding region $(U_1+U_2)/16B\ll 1$ $(S\to 0)$ as well as in the tight-binding region $(U_1+U_2)/16B\gg 1$ $(S\to 1/2)$ in the limit $T\to 0$, Eq. (35) yields the following consistency condition for the spin S:

$$S=\frac{1}{2N}\sum_k\frac{S(U_1+U_2)-B'_k}{t_k}. \tag{30}$$

In the region of intermediate values of the Coulomb interaction energies and the hopping integral it is necessary to carry out a direct numerical calculation using formula (29). The dependence of the spin S on the sum of Coulomb interaction energies is plotted in Fig. 4 with and without an account of the transport integral B' at $T=0$. If the system is

found in the strong correlation regime, then taking the transport integral B' into account in the case $B'<0$ $(B>0)$ facilitates electron delocalization and, as a consequence, reduces the value of the magnetization in comparison with the case $B'=0$. If, on the other hand, the system is found in the weak correlation regime, then the electrons are in essence collectivized as a consequence of the smallness of U. Here an account of the transport integral B' in the case $B'<0$ $(B>0)$ leads to a tendency toward ''localization'' of electrons and, for this reason, to an increase in the value of the magnetization in comparison with the case $B'=0$.[a] We note in conclusion that our study of the energy spectrum was carried out as follows: for given values of the parameters U_1, U_2, and T with the help of Eq. (30) we determined the value of the spin S; this value was then substituted into the formulas for the energy spectra (26) and (27). Varying the temperature or other system parameters alters the energy spectrum as a consequence of the resulting variation in the value of the magnetization S.

To summarize, the proposed technique for calculating the anticommutator Green's function and the correlation functions allows one to investigate the spectrum of elementary excitations and the form of the magnetization as functions of the transport integral to second-nearest neighboring lattice sites. Taking the transport integral B' into account causes a substantial change in the form of the energy spectrum and has a marked influence on the dependence of the magnetization S on the Coulomb potential in comparison with the case $B'=0$.

I wish to express my gratitude to R. R. Nigmatullin for discussion of the results of this work and useful advice.

APPENDIX A

Let us estimate the conditions under which the relation

$$\Delta n_{j\bar{\sigma}}^2=\langle \Delta n_{j\bar{\sigma}}^2\rangle, \quad (j=f,l)$$

is valid.

As a result of the relation $\Delta n_{j\bar{\sigma}}=n_{j\bar{\sigma}}-\langle n_{j\bar{\sigma}}\rangle$ we have

$$\|(\Delta n_{j\bar{\sigma}})^2-\langle(\Delta n_{j\bar{\sigma}})^2\rangle\|=\sqrt{\langle n_{j\bar{\sigma}}\rangle(1-\langle n_{j\bar{\sigma}}\rangle)}|1-2\langle n_{j\bar{\sigma}}\rangle|,$$

where $\|\hat{A}\|=\sqrt{\mathrm{Tr}\{\hat{A}^+\hat{A}\exp(-\beta H)\}}$ is the norm of the operator $\hat{A}$, and $|C|$ is the absolute value of the scalar quantity C.

Thus, in the cases $\langle n_{j\bar{\sigma}}\rangle=1/2$, $\langle n_{j\bar{\sigma}}\rangle=0$, and $\langle n_{j\bar{\sigma}}\rangle=1$ the error of calculations performed in the approximation of static fluctuations should tend to zero, and in the regions $\langle n_{j\bar{\sigma}}\rangle\approx 1/2$, $\langle n_{j\bar{\sigma}}\rangle\approx 0$, and $\langle n_{j\bar{\sigma}}\rangle\approx 1$ the error of the calculations should be minimal. The approximation of static fluctuations appears to work best in the case of interest to us—near the antiferromagnetic ordering point.

APPENDIX B

Let us consider the case of the atomic limit by setting $B_{fl}=B_{ll'}=0$ in the Hamiltonian (2). In this case the problem can be solved exactly. For example, for the A sublattice the equations of motion take the form

$$\frac{d}{d\tau}a_{f\sigma}^+(\tau)=\varepsilon_1 a_{f\sigma}^+(\tau)+U_1 n_{f\bar{\sigma}}a_{f\sigma}^+(\tau),$$

$$\frac{d}{d\tau}n_{f\bar{\sigma}}a_{f\sigma}^+(\tau)=(\varepsilon_1+U_1)n_{f\bar{\sigma}}a_{f\sigma}^+(\tau). \tag{B1}$$

The solution of the system of differential equations (B1) for the particle creation operator has the form

$$a_{f\sigma}^+(\tau)=\{a_{f\sigma}^+(0)+n_{f\bar{\sigma}}a_{f\sigma}^+(0)[\exp(U_1\tau)-1]\}\exp(\varepsilon_1\tau). \tag{B2}$$

In this case the Fourier transform of the anticommutation Green's function takes the form

$$\langle a_{f\sigma}^+|a_{f\sigma}\rangle_E=\frac{i}{2\pi}\left\{\frac{1-\langle n_{f\bar{\sigma}}\rangle}{E-\varepsilon_1}+\frac{\langle n_{f\bar{\sigma}}\rangle}{E-\varepsilon_1-U_1}\right\}. \tag{B3}$$

It is possible to obtain an analogous expression for the electrons of the other subsystem.

$$E_1=\varepsilon_1, \quad E_2=\varepsilon_2,$$

$$E_3=\varepsilon_1+U_1, \quad E_4=\varepsilon_2+U_2. \tag{B4}$$

Solving the same problem in the approximation of static fluctuations, we obtain the following expression for the Fourier transform of the anticommutator Green's function:

$$\langle a_{f\sigma}^+|a_{f\sigma}\rangle_E=\frac{i}{2\pi}\left\{\frac{1/2}{E-\varepsilon_1-U_1(1/2+S+\Phi)}+\frac{1/2}{E-\varepsilon_1-U_1(1/2+S-\Phi)}\right\}. \tag{B5}$$

Applying the fluctuation–dissipation theorem,[15] we obtain the following equation for the spin S from Eq. (B5):

$$\frac{1}{2}-S=\frac{1}{2}\{f^+(\varepsilon_1+U_1(1/2+S+\Phi))+f^+(\varepsilon_1+U_1(1/2+S-\Phi))\},$$

from which in the case of exact half-filling of the band for arbitrary values of the temperature it follows that $S=0$.

Substituting the resulting value of the spin S into the Green's function (B4), we obtain the following formula for the Fourier transform of the Green's function:

$$\langle a_{f\sigma}^+|a_{f\sigma}\rangle_E=\frac{i}{2\pi}\left\{\frac{1/2}{E-\varepsilon_1}+\frac{1/2}{E-\varepsilon_1-U_1}\right\},$$

which coincides exactly with expression (B3) if we take into account that in the case of half-filling of the band, as follows from Eq. (B3) $\langle n_{f\sigma}\rangle=\langle n_{f\bar{\sigma}}\rangle=1/2$, where we have evaluated the thermodynamic means with the help of the fluctuation–dissipation theorem.

Thus, in the atomic limit the approximation of static fluctuations leads to an exact result.

[a)]Note that the magnitude of the magnetization depends on the sign of the transport integral B'. If $B'>0$ $(B>0)$, then the possibility of electron transport along a square diagonal leads to still greater localization and, as a consequence, to an increase in S in comparison with the case $B'=0$.

[1] V. I. Belinicher and A. L. Chernyshev, Phys. Rev. B **49**, 14, 9746 (1994).
[2] F. Onufrieva and J. Rossat-Mignod, Phys. Rev. B **52**, 10, 7572 (1995).
[3] R. Hayn, A. F. Barabanov, and J. Schulenburg, Preprint (1996).
[4] M. V. Eremin *et al.*, JETP Lett. **60**, 2, 125 (1994).
[5] E. H. Lieb, Phys. Rev. Lett. **62**, 1201 (1989).
[6] H. Tasaki, Preprint Condens. Matter/9707286 (1997).
[7] V. V. Loskutov, G. I. Mironov, and R. R. Nigmatullin, Fiz. Nizk. Temp. **22**, *3*, 282 (1996) [Low Temp. Phys. **22**, 220 (1996)].
[8] G. I. Mironov, Fiz. Tverd. Tela (St. Petersburg) **39**, *9*, 1594 (1997) [Phys. Solid State **39**, 1420 (1997)].
[9] J. Hubbard, Proc. R. Soc. A **276**, 1365, 238 (1963).
[10] V. J. Emery, Phys. Rev. Lett. **58**, 26, 2794 (1987).
[11] R. R. Nigmatullin and V. A. Toboev, Teor. Mat. Fiz. **68**, 1, 88 (1986).
[12] T. Moriya, *Spin Fluctuations in Itinerant Electron Magnetism* (Springer-Verlag, 1985)].
[13] E. V. Kuz'min, V. A. Petrakovskiĭ, and Z. A. Zavadskiĭ, *Physics of Magnetically Ordered Materials* [in Russian] (Moscow, 1976).
[14] J. Hubbard, Proc. R. Soc. A **281**, 401 (1964).
[15] S. V. Tyablikov, *Methods in the Quantum Theory of Magnetism* (Plenum, New York, 1967) [Russian original, Moscow, 1965].

Translated by Paul F. Schippnick

Simulation of 1/*f* noise spectra in $YBa_2Cu_3O_7$ epitaxial films

A. A. Berzin and A. I. Morozov

Moscow State Institute of Radio Engineering, Electronics, and Automation, 117454 Moscow, Russia

A. V. Bobyl'*) and R. A. Suris

A. F. Ioffe Physicotechnical Institute, Russian Academy of Sciences, 194021 St. Petersburg, Russia

A. I. Dedoborets

State Agricultural University, 320027 Dnepropetrovsk, Ukraine

(Submitted September 15, 1998)
Fiz. Tverd. Tela (St. Petersburg) **41**, 957–964 (June 1999)

A Monte Carlo simulation of the $1/f$ noise spectra in the normal phase of $YBa_2Cu_3O_7$ epitaxial films is reported. It is conjectured that the main contribution to the noise is from oxygen transitions to vacant sites in the CuO plane. It is shown that the annealing regime and the mismatch strains between the film and the substrate are the main factors governing the domain and defect structure of the film and, hence, the $1/f$ noise spectrum. © *1999 American Institute of Physics.* [S1063-7834(99)00606-1]

The intensity and spectrum of the low-frequency noise (with frequency dependence close to $1/f$) in $YBa_2Cu_3O_7$ epitaxial films are important physical parameters determining the possibility of their application in various high-T_c superconductor electronics devices, for instance, in bolometers.[1] It is known that in these films the dimensionless parameter of Hooge,[2] which is customarily used as a noise intensity criterion, exceeds the corresponding values for films of elemental metals by many orders of magnitude.[3,4] The main reasons for this lie in the high concentrations of so-called defect-fluctuators[5] (DFs) acting as noise sources, and the large relative variation of the scattering cross section of free carriers from these defects. In elemental metals, a DF is a pair of closely situated lattice point defects, which changes its scattering cross section as one of the pair defects transfers to a new site.[3,4,6] The concentration of such pairs in a metal is fairly low. In $YBa_2Cu_3O_7$ compounds such DFs are oxygen atoms in the CuO plane. The transition of an oxygen atom from an O1 chain site to the nearest O5 vacant site gives rise to a vacancy–native-interstitial-atom defect pair. This entails a change in the scattering cross section from zero (for no defect pairs present) to a certain value σ_0 (with a defect pair present). Obviously, in this case the relative change in the cross section attains its maximum value, $\Delta\sigma/\sigma_0=1$.[7]

This paper reports a Monte Carlo simulation of the oxygen atom distribution in the CuO plane and a calculation of the corresponding activation-energy spectra for the O1-O5 transitions. A study has been carried out of the effect of various anneal regimes and of uniaxial strain in the CuO plane on these spectra. We have classified the specific features in the structure of spectral distributions of the DFs and of their microscopic nature, i.e., established the types of the corresponding transitions of oxygen atoms and their nearest-neighbor configurations. An analysis has been made of how the noise intensity and its spectrum depend on the structural quality of $YBa_2Cu_3O_7$ epitaxial films.

1. DESCRIPTION OF THE MODEL

The distribution of oxygen atoms over the two sublattices in the CuO plane was calculated by the standard Metropolis Monte Carlo method using the so-called ASYNNNI model[8–11] and taking into account the interaction of nearest-neighbor oxygen atoms (Fig. 1). The potential energies of the attractive interaction V_2 and the repulsive interactions V_1 and V_3 were taken from Ref. 12: $V_2=-0.304$, $V_1=0.364$, and $V_3=0.04$ eV. Periodic boundary conditions were imposed. The film and substrate lattice mismatch causes internal stresses. $YBa_2Cu_3O_7$ epitaxial films were shown[7] to be made up of small-angle blocks with dimensions on the order of the film thickness, 0.1–0.2 μm. Because the simulation was run on a 44×44 oxygen-site square, the size of the simulation region is much smaller than the block dimension and, hence, the strain may be considered uniform. In the absence of shear components, the CuO plane strain u_{ij} is related to the elastic stresses σ_{ik} through

$$\begin{cases} u_{xx}=c_{xxxx}\sigma_{xx}+c_{xxyy}\sigma_{yy}+c_{xxzz}\sigma_{zz}, \\ u_{yy}=c_{yyxx}\sigma_{xx}+c_{yyyy}\sigma_{yy}+c_{yyzz}\sigma_{zz}, \end{cases} \tag{1}$$

where c_{ijkl} are the elastic compliances of the $YBa_2Cu_3O_7$ lattice, and the coordinate axes are parallel to the crystallographic ones.

We shall assume the original phase tetragonal, which is valid in the high-temperature domain, where oxygen atoms are distributed randomly over the sublattices, as well as in the case where the orthorhombic distortions induced by elastic strains exceed by far those present in an unstrained material. Then we have $c_{xxxx}=c_{yyyy}$ and $c_{xxzz}=c_{yyzz}$. For $\sigma_{xx}-\sigma_{yy}\neq0$ a difference appears between the lattice con-

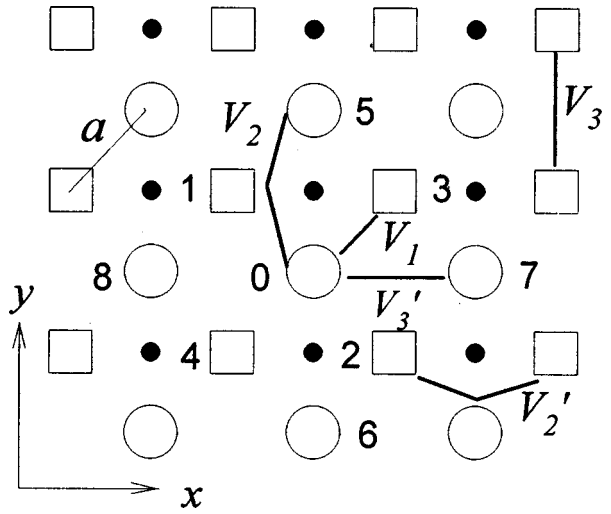

FIG. 1. Attractive interactions V_2 and repulsive interactions V_1 and V_3, among nearest-neighbor oxygen atoms in the CuO plane. Large open circles and squares—oxygen-filled and empty sublattices, filled circles—copper atoms. The lattice cites are numbered in accordance with the corresponding distances in Eqs. (3) and (4)

stants along the x and y axes (Fig. 1), i.e., an orthorhombic distortion, which forces crystalline samples to become single-domain.[13] We introduce a quantity P,

$$P=u_{xx}-u_{yy}=(c_{xxxx}-c_{xxyy})(\sigma_{xx}-\sigma_{yy}). \tag{2}$$

Assuming that the symmetric strain, which satisfies $u_{xx}=u_{yy}$, is already taken into account in the initial values of the interaction potentials, we shall specify in the simulation only the quantity P. Then in the case of a strain along the x axis the distances between oxygen lattice sites can be expressed in terms of P in the following way:

$$r_{01}=\frac{a}{2}\sqrt{(1+P)^2+1}, \quad r_{07}=\sqrt{2}a(1+P), \tag{3}$$

where a is the distance between the nearest-neighbor oxygen-lattice sites, and the indices correspond to site numbering in Fig. 1. The r_{05} distance does not depend on P. Let us estimate the strain-induced change in the interaction potentials coupling the oxygen atoms. To do this, we use the following analytic expressions relating the repulsive potentials V_1 and V_3 to the distance r between oxygen atoms:

$$V_{1,3}\sim r^{-1}\exp(-r/\lambda), \tag{4}$$

where λ is the screening radius, which in what follows will be taken as equal to 1.6 Å.[14] As for the attractive potential V_2, we assume it to be a sum of two terms, a negative attractive one, which only weakly depends on distance and originates from covalent interaction of the copper atom located between the two oxygen orbitals, and a positive repulsive one, which is described by Eq. (4). Equations (3) and (4), combined with the above numerical values of the corresponding parameters, yield the following relations for the relative strain-induced changes of the potentials:

$$\delta\ln V_1=-2.7P, \quad \delta\ln V_2=0, \quad \delta\ln V_2'=-0.45P,$$

and

$$\delta\ln V_3=0, \quad \delta\ln V_3'=-3.4P, \tag{5}$$

which were subsequently used in the computer simulation.

Thus the strain-induced changes $\delta V_2'$ have the same sign as δV_1 and $\delta V_3'$, namely, the energy increases with decreasing distance between atoms. As shown by model anneals, this is a necessary condition to obtain correct orientation of oxygen chains with respect to the strain axis. It is in this case that the orientation was the same as in the single-domain samples prepared experimentally by applying uniaxial pressure to $YBa_2Cu_3O_{7-\delta}$ crystals,[13] namely, the oxygen chains were arranged perpendicular to the compression axis.

The anneal simulation started from a high temperature T_0, at which an oxygen atom distribution was given by a random-number generator, and ended at a low temperature t_0. The running temperature was given by the relation

$$T=T_0\exp(-gn)+t_0, \tag{6}$$

where g is the annealing rate, and n is the number of Monte Carlo steps.

The spectrum of activation energies for the fluctuators was determined by computing the number of barriers with a given E_b met by an oxygen atom on the way to the nearest empty site on the square lattice. The energy E_b was calculated in the harmonic potential approximation for the oxygen site well[15]

$$E_b=V_0+(V_f-V_i)/2+(V_f-V_i)^2/16V_0, \tag{7}$$

where V_i and V_f are the total energies of oxygen atom interaction with the environment at the original site and after the jump, respectively, and V_0 is the barrier height for an isolated atom surrounded by empty sites both before and after the jump. An estimate[11] yields $V_0\sim 0.3$ eV.

2. SIMULATION OF ANNEALING REGIMES

The anneal simulation was carried out for an oxygen index $\delta=0.05$, which maximizes the critical temperature T_c (Ref. 16), on a 44×44-site square. The ranges of variation were $T_0=0.5-0.05$ eV for the starting temperature, $g=10^{-8}-5\times10^{-7}$ for the annealing rate, and $P=0.0-0.05$ for the strain. The maximum value of P corresponded to the characteristic strain of films deposited on the customarily used substrates, $\sim 1-10\%$,[7] and was found to be high enough to reveal the effect of strain on the domain and defect film structure. The situations found in the simulation can be classified with respect to the temperature dependence of the total oxygen-atom interaction energy in the following way.

A. High-T_0 region (>0.22 eV)

Figure 2 [region (1)] shows only two cooling curves for this group, which refer to $T_0=0.45$ eV. The curves calculated for lower values of T_0 start with a steep decline, and at lower temperatures coincide with the curves in Fig. 2. This indicates the quasistatic nature of the cooling processes, which involve equilibrium phase fluctuations and depend only on the running temperature. In this case the temperature dependence of the fluctuation magnitudes can be used to determine the temperature of the structural phase transition.

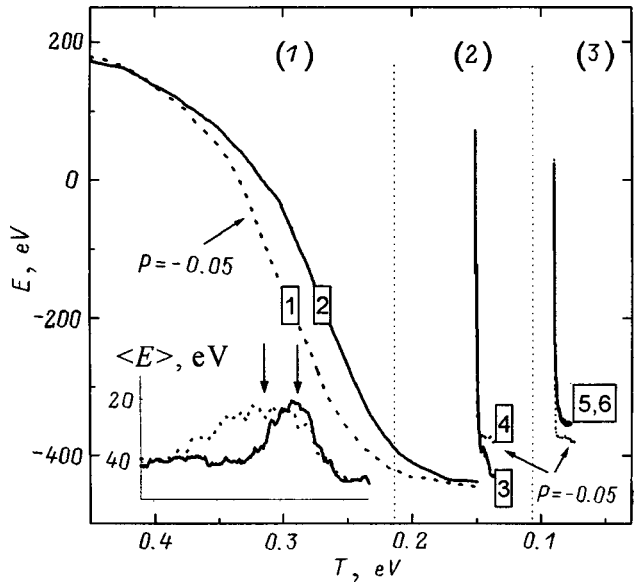

FIG. 2. Temperature dependence of the total oxygen-atom interaction energy in the CuO plane for different anneal temperatures: (*1*) region of equilibrium behavior, (*2*) and (*3*) quasi-isothermal relaxation regime giving rise to formation of metastable point defects ($P\neq 0$) or twins ($P=0$). Solid and dashed curves correspond to strains $P=0.0$ and $P=-0.05$. The annealing rate is $g=5\times 10^{-8}$. The figures in rectangles refer to specific points (see Fig. 3). The inset shows the energy dispersion of the system, and the arrows identify the tetra-ortho transition temperatures.

The fluctuation intensity for a given temperature can be estimated from the rms deviation $\langle E\rangle$ of the total interaction energy E_j derived directly in progressive computer calculations from its average value $E_{\rm av}$ obtained by smoothing. The corresponding temperature dependences are presented in Fig. 2. We readily see that compressive strain shifts the curves and the transition point toward higher temperatures T, which is due to the increasing average energy of nearest-neighbor interaction. Also, the corresponding oxygen-atom distribution exhibits microdomains of one orientation only (Fig. 3a), which implies that the strain-induced transition to single-domain state starts in the earliest stages of cooling. The $P=0.0$ case is characterized by a slower process of spontaneous transition to the single-domain state through intermediate polydomain distributions of fairly large regions (Fig. 3b) and gradual expansion of one of them. This equilibrium cooling ends eventually when the interaction energy and point-defect concentration reach their minimum (Figs. 3c and 4b). It should be pointed out that the results of simulating the final stages in equilibrium cooling depend strongly on the nearest-neighbor interaction parameters and change when one includes the long-range elastic interaction.[9]

B. Intermediate T_0 region ($0.11<T_0<0.22$ eV)

While the temperature dependence of the total energy in this region obtained for $P=0$ does not coincide with the corresponding curve in region (1) of Fig. 2 in the closing stages of relaxation, it nevertheless approaches it asymptotically. This is apparently favored by the presence of microdomains in the intermediate stages of the relaxation and by their subsequent gradual annihilation. The area covered by mobile domain boundaries is free of excess energy. As a result, similar to the case of high T_0, the relaxation proceeds through intermediate polydomain distributions, it is somewhat slower than that observed in region (1) in Fig. 2, and is followed by gradual expansion of one of the domains. This scenario likewise culminates in attainment of the minimum energy and a similar defect distribution, which is shown in Fig. 3c. For $P\neq 0$, the energy has no time to reach the equilibrium level, which is due to formation of metastable point defects, namely, vacancies at oxygen-chain breaking points and excess oxygen atoms between chains distant from these points (Fig. 3d). The density of atoms on the plane depends on the initial random realization of their distribution. The calculated total excess energy of metastable defects is $\sim 30-80$ eV.

C. Low T_0 region (<0.11 eV)

It is this region that corresponds to the growth and anneal temperatures of real $YBa_2Cu_3O_{7-\delta}$ films. For $P\neq 0$, the situation does not differ qualitatively from that in region (2). For $P=0$, however, the process of spontaneous transition to the single-domain state has no time to come to completion, which results in formation of polydomain distributions and of the corresponding metastable defects in the form of domain boundaries. One observes domain boundaries of two types, depending on the magnitude of δ. Figure 3e and 3f presents oxygen atom distributions obtained for two values of δ, 0.05 and -0.05, respectively. In Fig. 3e, the domain boundaries are perpendicular to oxygen chains in domains of one type and parallel to chains in domains of the other type (90°-boundaries). In Fig. 3f, the domain boundaries are oriented at 45° to the chains (45°-boundaries). With the domain boundaries is associated the excess energy, and it is here that the fluctuators having the lowest activation energy are localized (Fig. 3h and 3i). The total excess energy is calculated as $\sim 60-160$ eV.

Thus by properly varying the anneal simulation parameters (starting temperature, cooling and strain rates) one can reproduce the technological conditions of the growth and annealing of $YBa_2Cu_3O_{7-\delta}$ epitaxial films. It turns out that the oxygen distributions forming in low-temperature quasi-isothermal rapid relaxation of the oxygen system in the CuO plane come closest to those observed experimentally. In particular, one typically finds polydomain distributions in the form of bands with alternating orientation (distributions *e, f* in Fig. 3). This appears to have particular significance, because earlier such distributions were obtained only when the long-range components of oxygen–oxygen interaction were taken into account.[9] Investigation of these distributions may shed light on the micromechanisms governing domain-boundary motion.

3. STRUCTURE OF THE FLUCTUATOR SPECTRAL DISTRIBUTION

To understand the structural features in the DF spectral distributions presented in Fig. 4, i.e., to establish their microscopic nature, consider the case of the most random atom distribution (Fig. 3b), which comprises the maximum num-

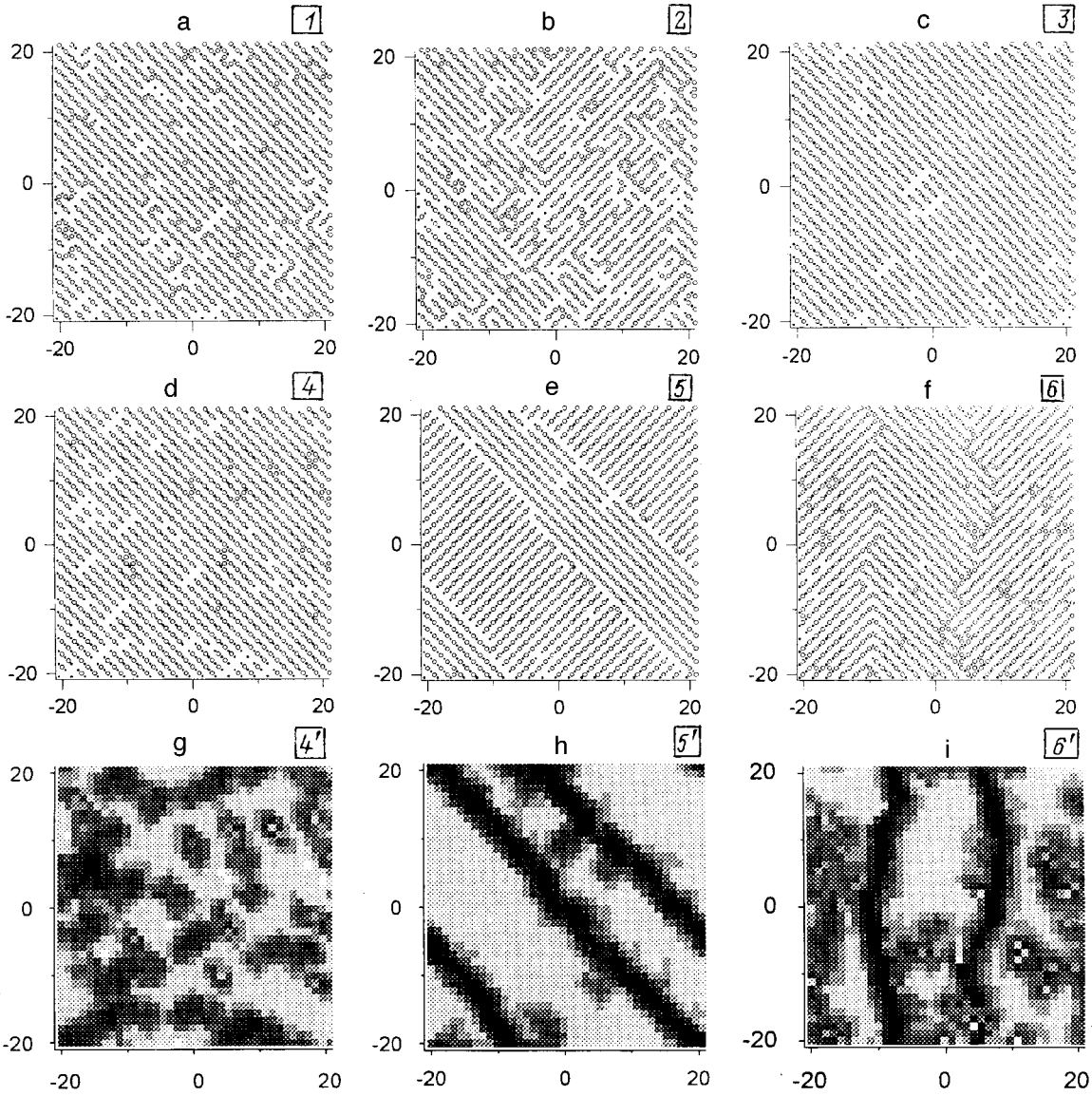

FIG. 3. Spatial distribution of oxygen atoms at points a–f (denoted by figures in rectangles; see also Fig. 2) and of barrier activation energies (g–i) for oxygen transitions to the vacant nearest-neighbor sites at points d–f. For each of the seven gray-scale code levels, the energy increment $\Delta E_b = 0.15$ eV, starting from the lowest (dark) level $E_b = 0.5$ eV.

ber of various versions of possible nearest-neighbor environments around an oxygen atom. A fragment of distribution 2 is displayed in Fig. 5. It is seen that the same atom may enter different groups, depending on the four versions of transition to the adjacent site and on the corresponding values of V_f, which, according to Eq. (7), give different barrier heights E_b. Obviously, the most probable will be the transitions involving the lowest barriers, and therefore out of the four values one should leave only the smallest. This factor, in particular, was taken into account when constructing the spatial barrier-energy distributions in Fig. 3. Of fundamental importance in an analysis of the situations depicted in Fig. 5, as well as of Table I listing the corresponding interaction energies, is the small magnitude of the repulsive interaction V_3, and the insignificant difference between the V_1 and V_2 interactions in absolute magnitude. First, this permits one to neglect V_3 interactions and to simplify the classification by reducing considerably the number of nearest-neighbor versions. Second, Table I reveals the following regularity. Atoms of the regular orthohedral phase (atoms of group 1), which consists of five roughly equal subgroups, have the highest barriers. The appearance of various combinations of irregular atoms, which are shown in Fig. 5 and listed in Table I, is capable of reducing the number of subgroups in a discrete manner, and this accounts for the presence of the structure itself, or, to be more precise, of the first five DF groups. The energy of group 6 is equal to the barrier height for an isolated atom, V_0, and characterizes the type of the transition in which the condition $(V_f - V_i) \approx 0$ is upheld. A feature characteristic of groups 7 and 8 is the inequality $(V_f - V_i) < 0$; Table I lists the corresponding examples of the transitions. A more comprehensive description of the structure of these low-barrier groups would require already taking into account the contribution to the interaction due to the V_3 potentials. There is, however, no particular need in this, because the DF spectrum in the low-energy region is domi-

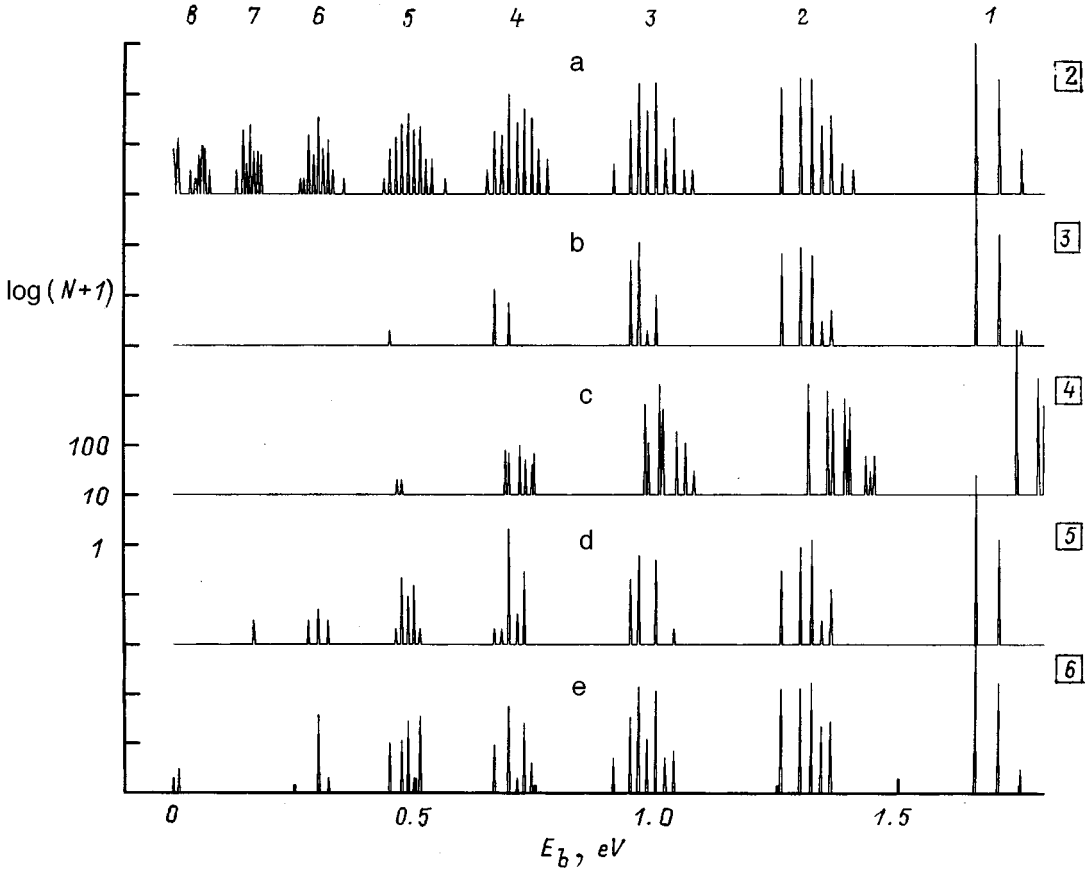

FIG. 4. Spectral distribution of oxygen atoms in barrier energy for atom transition to the nearest vacant site; the distribution numbers in the rectangles correspond to the points in Fig. 2. The fluctuator groups are also numbered (see further).

nated by block boundaries, whose presence is characteristic of $YBa_2Cu_3O_7$ films,[7] and which were disregarded in this work.

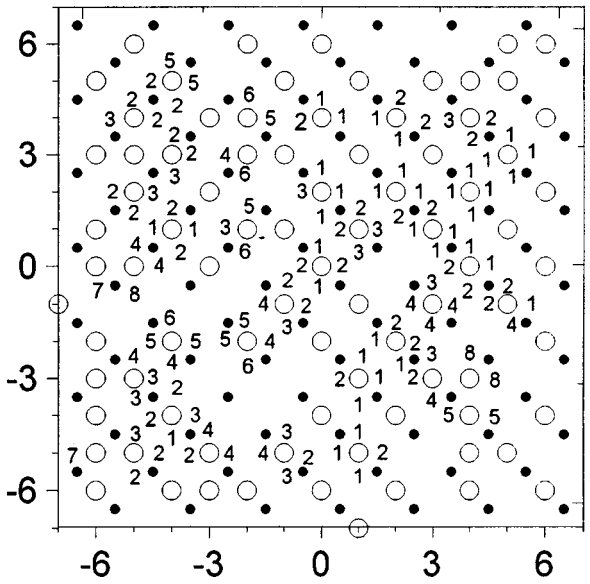

FIG. 5. An enlarged fragment of oxygen-atom distribution 2 presented in Fig. 3b. The figures are placed at the directions of oxygen transitions to the nearest empty site and correspond to the DF group numbers in Fig. 4 and Table I.

4. INTERPRETATION OF NOISE MEASUREMENTS

The DF spectral distributions displayed in Fig. 4 can be used in noise studies by comparing them with the DF energy distribution $F(E)$, which can be calculated directly from the results of the corresponding noise measurements. One should use for this purpose the relationship

$$F(E)=\frac{f}{kT}\frac{S_V(E)}{V^2}=\frac{1}{kTN_e}\alpha(E), \tag{8}$$

where V and $S_V(E)$ are the voltage across a sample and its noise, respectively, N_e is the number of free carriers in the sample, $E=kT\ln(2\pi f\tau_d)$ is the energy of the barrier which can be overcome by an atom with thermal energy in a time $1/f$ at a sample temperature T, with the noise measured at frequency f, and τ_d^{-1} is the Debye frequency ($\approx 10^{-13}\,\mathrm{s}^{-1}$). Figure 6 shows DF spectra, which were calculated using Eq. (8) and the noise measurements[7,11] of $YBa_2Cu_3O_7$ films on various substrates, presented in the form of a dimensionless function $\alpha(E)$. These curves can be analyzed and compared with the results of the simulation in the following way:

(i) $\alpha(E)$ is the largest for films on Si substrates, which, despite the presence of a ZrO_2 buffer layer, have a poor quality from x-ray diffraction measurements, in particular, high internal microstresses $[\langle\varepsilon\rangle=\{\langle(\delta c/c)^2\rangle\}^{1/2}>6\times10^{-3}$, where c is the lattice parameter along the c axis] and a small

TABLE I. Types of oxygen atom transitions (fluctuator model) and interaction energies.

Fluctuator group No.	E_m, eV	V_i	V_f	$\Delta V=V_f-V_i$	Examples of atom transitions (the spatial coordinates $[x,y]$ of the initial and final states correspond to Fig. 5)
1	1.65	$2V_2$	$3V_1$	$3V_1-V_2$	$[-4,1]\rightarrow[-3,1]$
2	1.30	$2V_2$	$2V_1$	$2V_1-2V_2$	$[-4,-4]\rightarrow[-4,3]$
		$2V_2+V_1$	$3V_1$	$2V_1-2V_2$	$[-5,2]\rightarrow[-5,1]$
3	0.95	V_2	$2V_1$	$2V_1-V_2$	$[-1,-1]\rightarrow[-1,-2]$
		$2V_2$	$2V_1+V_2$	$2V_1-V_2$	$[0,2]\rightarrow[-1,2]$
4	0.67	$2V_2+V_1$	$2V_1+V_2$	V_1-V_2	$[3,-3]\rightarrow[3,-4]$
		$2V_2+V_1$	$2V_1$	V_1-V_2	$[-5,0]\rightarrow[-4,0]$
5	0.48	≈ 0	V_1	V_1	$[-4,-2]\rightarrow[-3,-2]$
		$2V_2+2V_1$	$2V_1+V_2$	$-V_2$	$[4,-4]\rightarrow[3,-4]$
6	0.30	≈ 0	≈ 0	≈ 0	$[-2,-2]\rightarrow[-2,-3]$
		$2V_1+V_2$	$2V_1+V_2$	≈ 0	$[-2,4]\rightarrow[-2,5]$
7	0.15	$2V_1$	$2V_1+V_2$	$-V_1$	$[-6,0]\rightarrow[-6,-1]$
		$3V_1+V_2$	$3V_1+2V_2$	V_2	$[-6,-5]\rightarrow[-7,-5]$
8	<0.1	V_1+V_2	V_2	$-V_1$	$[-5,0]\rightarrow[-5,-1]$
		$2V_1$	V_2	V_2-2V_1	$[4,-3]\rightarrow[5,-3]$

Note. The $\approx$ sign means that the entry was calculated in the $V_3=0$ approximation. E_m is the barrier energy averaged over a fluctuator group.

radius of small-angle blocks ($\tilde{r}\approx 0.04\ \mu$m) of which this film is made. As follows from Ref. 7, for such values of $\langle\varepsilon\rangle$ the energy dispersion of DFs of the same species in a sample under study may be as high as 0.3–0.4 eV. As seen from Fig. 4, this is quite enough for the various DF groups to overlap and to form in this way a smooth spectral distribution, which is exactly what is observed experimentally. First, the smooth behavior of the $\alpha(E)$ dependence for these films reflects the considerable interval within which the noise intensity follows a $1/f$ relation ($1/f^n$ with $n=1$) [as can be seen from Eq. (8), if $S_V(E)\propto 1/f$, then $\alpha(E)=$const]; second, the DF distribution over groups for these films is characteristic of the most random pattern presented in Fig. 3b and of the corresponding spectrum in Fig. 4a. Note that the role of the low-energy regions near twin boundaries can be played by the noticeable part of the sample located close to the block boundaries.

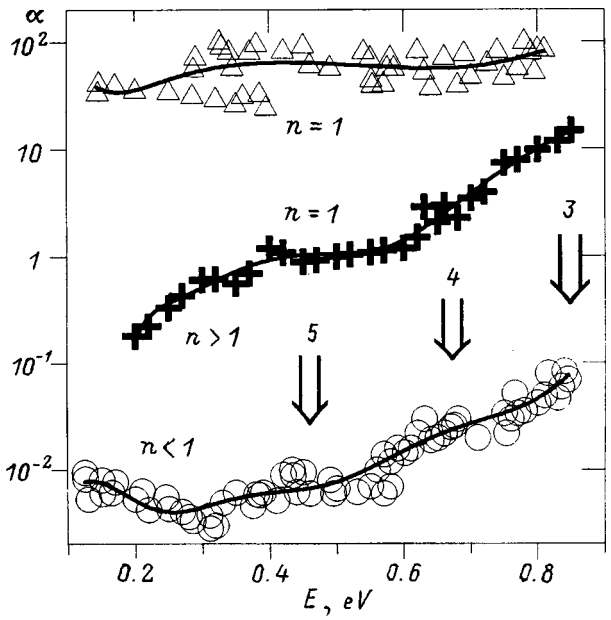

FIG. 6. Spectral distributions of fluctuators in $YBa_2Cu_3O_7$ films grown on ZrO_2/Si (triangles), $NdGaO_3$ (crosses), and $BaSrTiO_3$/MgO (circles) substrates. The solid lines were obtained by a polynomial smoothening of experimental data. The parts of the curves where the noise vs frequency relations are fitted by the corresponding $S_V\propto 1/f^n$ curves are identified. The arrows and figures relate to the position of the corresponding fluctuator groups numbered in Fig. 4.

(ii) Films grown on MgO substrates with a $BaSrTiO_3$ buffer layer exhibit the smallest $\alpha(E)$ and a high structural quality ($\langle\varepsilon\rangle<1\times10^{-3}$, $\tilde{r}\approx 0.2\ \mu$m). For these values of $\langle\varepsilon\rangle$, the dispersion of DF energies is smaller than that in the preceding case, 0.1–0.2 eV, and this is what accounts for the spectral features identified by arrows in Fig. 5. The steeper course of the $\alpha(E)$ relation in the 0.3–0.9-eV interval suggests that at these energies regions near the block boundaries no longer provide an appreciable contribution to the DF spectral distribution (because of a larger $\tilde{r}$). Indeed, the closest to this situation is the single-domain distribution in Fig. 4c, which contains a considerable concentration of metastable point defects. The increment in the number of DFs observed as one crosses over from five to three groups (about a factor of ten) is in a good agreement with the increment in $\alpha(E)$ found between the corresponding experimental features in Fig. 5. Note that analysis of low-energy DF spectra (<0.3 eV) requires invoking a special simulation scenario,[17] which takes into account the possibility of oxygen atom generation at small-angle block boundaries.

The above calculations can be summed up as follows:

(1) An anneal simulation revealed three regimes corresponding to three regions of the initial anneal temperature: (*a*) quasi-equilibrium annealing; (*b*) an intermediate regime, in which the system is transformed to a metastable state in the presence of uniaxial strain; and (*c*) a nonequilibrium regime, in which the system becomes metastable in both the presence and absence of strain. It is regime *c* that relates to the real procedure by which $YBa_2Cu_3O_{7-\delta}$ epitaxial films are prepared.

(2) In the absence of strain, annealing from a low initial

temperature gives rise to polydomain distributions. The orientation of domain boundaries depends on the oxygen concentration, viz., local oxygen deficiency ($\delta>0$) favors formation of 90° twin boundaries, and excess oxygen ($\delta<0$) that of 45° boundaries.

(3) The fluctuators, which have the lowest activation energy, are localized at domain boundaries.

(4) The major noise sources in high-quality $YBa_2Cu_3O_{7-\delta}$ epitaxial films are metastable point defects with a barrier energy of 0.3–0.9 eV and defects near block boundaries with barrier heights <0.3 eV.

Support of the RF program ''Superconductivity'' (Grant 98031) is gratefully acknowledged.

*)E-mail: bobyl@theory.ioffe.rssi.ru

[1] H. Neff, J. Laukemper, I. A. Khrebtov, A. D. Tkachenko, E. Steinbeiss, W. Michalke, M. Burnus, T. Heidenblut, T. Hefle, and B. Schwierzi, Appl. Phys. Lett. **66**, 2421 (1995).
[2] F. N. Hooge, T. G. M. Kleinpenning, and L. K. J. Vandamme, Rep. Prog. Phys. **44**, 479 (1981).
[3] J. Pelz and J. Clarke, Phys. Rev. B **36**, 4479 (1987).
[4] Sh. Kogan, *Electronic Noise and Fluctuations in Solids* (University Press, Cambridge, 1996).
[5] Y. M. Galperin, V. G. Karpov, and V. I. Kozub, Adv. Phys. **38**, 669 (1989).
[6] A. I. Morozov and A. S. Sigov, Fiz. Tverd. Tela (Leningrad) **34**, 457 (1992) [Sov. Phys. Solid State **34**, 245 (1992)].
[7] A. V. Bobyl, M. E. Gaevski, S. F. Karmanenko, R. N. Kutt, R. A. Suris, I. A. Khrebtov, A. D. Tkachenko, and A. I. Morozov, J. Appl. Phys. **82**, 1274 (1997).
[8] D. de Fontaine, L. T. Wille, and S. C. Moss, Phys. Rev. B **36**, 5709 (1987).
[9] A. G. Khachaturyan and J. W. Morris, Jr., Phys. Rev. Lett. **61**, 215 (1988).
[10] M. Goldman, C. P. Burmester, L. T. Wille, and R. Gronsky, Phys. Rev. B **50**, 1337 (1994).
[11] A. V. Bobyl, R. A. Suris, A. I. Dedoborez, A. I. Morozov, I. A. Khrebtov, V. N. Leonov, V. G. Malyrov, and I. I. Shaganov, in *Noise in Physical Systems and* $1/f$ *Fluctuations*, edited by C. Claeys and E. Simoen (World Scientific, Singapore, 1997), p. 397.
[12] D. J. Liu, T. L. Einstein, P. A. Sterne, and L. T. Wille, Phys. Rev. B **52**, 9784 (1995).
[13] V. I. Voronkova and Th. Wolf, Physica C **218**, 175 (1993).
[14] A. A. Aligia, J. Garcés, and J. P. Abriata, Physica C **221**, 109 (1994).
[15] A. M. Bowler and E. S. Hood, J. Chem. Phys. **94**, 5162 (1991).
[16] A. V. Bobyl, M. E. Gaevski, S. G. Konnikov, D. V. Shantsev, V. A. Solov'ev, and R. A. Suris, Scanning Microsc. **10**, 679 (1996).
[17] D. V. Kulikov, R. A. Suris, and Yu. V. Trushin, Fiz. Tverd. Tela (St. Petersburg) **36**, 2975 (1994) [Phys. Solid State **36**, 1583 (1994)].

Translated by G. Skrebtsov

Magneto-optic study of spatial magnetic-field distribution relaxation in an HTSC film strip after transport current turn-on

M. E. Gaevskiĭ, D. V. Shantsev, and A. V. Bobyl'*)

A. F. Ioffe Physicotechnical Institute, Russian Academy of Sciences, 194021 St. Petersburg, Russia

Yu. M. Gal'perin,†) T. H. Johansen, and H. Hauglin

Physical Department, University of Oslo, 0316 Oslo, Norway

(Submitted September 28, 1998)
Fiz. Tverd. Tela (St. Petersburg) **41**, 965–968 (June 1999)

The paper provides the first demonstration of the efficiency of applying the magneto-optic method to studies of the spatial and temporal magnetic-field relaxation in an $YBa_2Cu_3O_7$ film strip after the transport current is switched on. It is shown that the evolution of magnetic flux distribution is adequately described in terms of a modified Bean model with time-dependent critical current. At a time 50 ms after the current is switched on, the critical current of the samples studied decreases by $\approx 15\%$. This proves the significance of thermally activated magnetic flux motion (creep) in the regime investigated. The magnetic vortex pinning energy has been estimated as
$U_0 \approx 20$ kT. [S1063-7834(99)00706-6]

A number of studies have recently been devoted to describing the spatial distribution $B(r)$ of the magnetic field and that of the current, $j(r)$, in superconducting samples of different shapes.[1–6] Investigation of the relaxation of these distributions in time, $B(r,t)$, following a change in the external magnetic field or the current through the sample is also of considerable interest.[7]

This work reports on a combined study of $B(r,t)$ (relaxation evolution in space and time) after switching on of the current made by the magneto-optic (MO) method. This approach has the following merits:

(1) It is known[7] that $B(t)$ relaxation exhibits logarithmic behavior, so that the relevant experiments should be performed over a broad range of times. The disadvantage of using an external magnetic field, which can be changed to an appreciable extent only on the scale of a few seconds, is that in order to obtain reliable results one has to carry out observations over several days. An experiment making use of current pulses and an MO image-recording camera is capable of covering a wider and more interesting time range extending from a few microseconds to a few hours. Note that further development of this method may be useful also in studies of such processes as macroscopic magnetic-flux jumps, annihilation of vortices and antivortices in the Meissner region, etc.[8–10]

(2) Substantial penetration of a magnetic flux into a superconductor takes place only at currents close to the critical threshold. Because the critical current density in high-quality HTSC films $j_c(T \ll T_c) \sim 10^7 - 10^8$ A/cm^2, one has to use narrow strips with a width $\lesssim 100\ \mu$m to pass current pulses of up to 10 A. This imposes constraints on the required spatial resolution of $\lesssim 1-3\ \mu$m, which is well within the capabilities of the MO method.

In this work, the magneto-optical method was employed to study the evolution of the spatial magnetic-field distribution in a $YBa_2Cu_3O_7$ film strip following current turn-on with resolutions of 4 ms and 5 μm. It was stimulated by our previous study[11] of the $B(r)$ distribution in a film strip with a transport current close to the critical value. It had been found that the results obtained cannot be described in terms of the Bean model[12] for a static magnetic-flux distribution at a constant current. The agreement was reached only by including the thermally activated magnetic-flux motion (creep) after the current is switched on, which was done by computer simulation. The objective of the present work was to search for direct evidence for the significance of the creep.

The $YBa_2Cu_3O_7$ films were grown on a $LaAlO_3$ substrate by magnetron sputtering.[13] X-ray diffraction and Raman scattering measurements showed the c axis of the films to be perpendicular to the substrate. The films exhibited a high degree of orientation and a perfect crystal structure. The strips measuring $500 \times 100 \times 0.2\ \mu$m were prepared by photolithography. The transport properties of the samples were investigated with a standard four-probe arrangement. The superconducting transition temperature of the strips was $T_c = 91$ K, the transition width was less than 1 K, and the critical current density was $j_c = 10^6$ A/cm^2 at $T = 77$ K. The strip with the most uniform current-density distribution below the superconducting transition point was selected by means of low-temperature scanning electron microscopy.[14]

The MO method of visualization of magnetic flux distribution is based on the Faraday effect, i.e., rotation of the plane of light polarization by a magneto-optical indicator film placed directly on the superconductor surface. The angle of rotation increases with increasing magnetic-field component perpendicular to the surface of the HTSC sample. A bismuth-doped YIG film with in-plane magnetization served as indicator.[15] The indicator film was coated with a thin

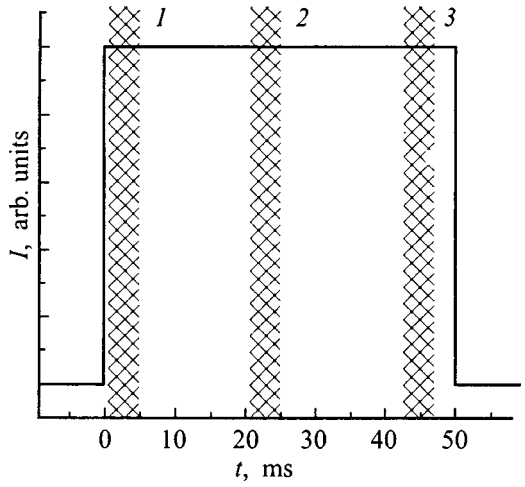

FIG. 1. Schematic representation of current pulse profile. Portions *1–3* correspond to different instants of magneto-optic image recording.

specular aluminum layer providing double rotation of the plane of polarization of incident light. The images were recorded with an 8-bit digital DCS420 Kodak camera. After the recording the temperature was raised to 95 K, and the indicator film was calibrated. This was done by determining the dependence of the brightness of the indicator film image obtained by the camera on the strength of the applied external magnetic field. To exclude the effect of nonuniformities in both the indicator film and the light intensity, the calibration was performed independently at different points with a step of 20 μm.

The current through the sample was supplied in 50 ms-long rectangular pulses, with the leading and trailing edges shorter than 1 ms. The operation of the camera was synchronized with the current supply, which permitted obtaining images a fixed time after application of the current pulse. The images were obtained several times during a current pulse, which is illustrated by Fig. 1. The camera exposure time was 4 ms. To reduce the distance between the MO indicator and the HTSC film, the film with the smoothest surface was chosen. Besides, the distance between the contact pads and the strip was larger than the indicator size. The indicator was 9 μm distant from the strip. The magnetic field generated in the magneto-optic indicator by an $I \approx 1.4$ A current was 1–5 mT, which is close to the sensitivity limit of the method. Therefore all measurements were repeated five times with accumulation to increase the signal/noise ratio.

Figure 2 presents an MO image of the HTSC strip recorded at the end of a current pulse of amplitude $I = 1.4$ A at a temperature of 15 K. The bright areas correspond to a higher absolute magnetic field. The image is fairly uniform along the bridge, which evidences the absence of weak bonds and other macrodefects. The experimental magnetic-field profile averaged over the strip length and corresponding to this MO image is shown in Fig. 3. The magnetic flux is screened by the HTSC sample, which results in field maxima near its edges. The left- and right-hand parts of the profile relate to magnetic fluxes of opposite signs. The magnetic flux does not penetrate into the central part of the sample, and, as a consequence, one observes a field minimum at the

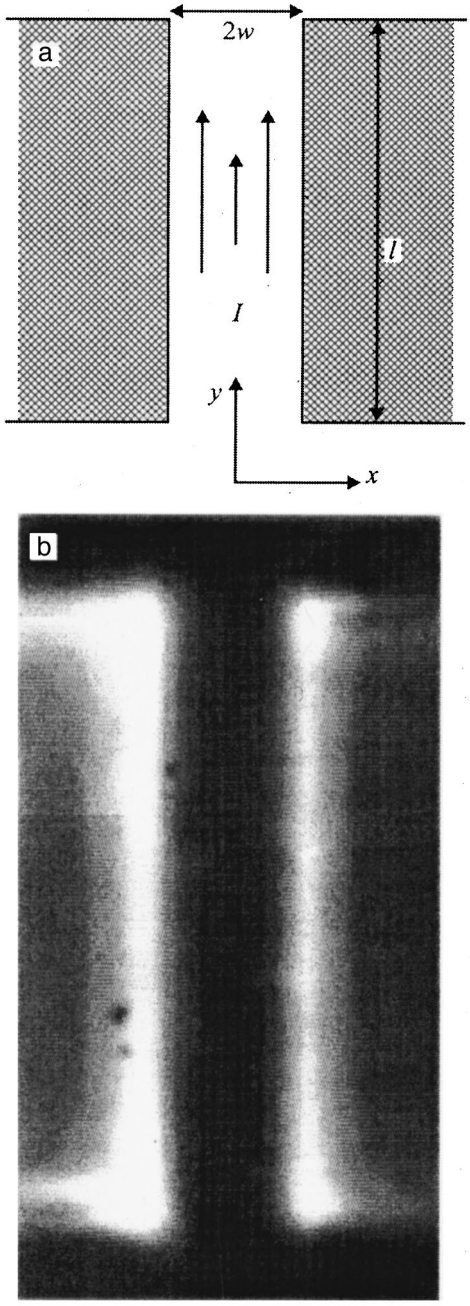

FIG. 2. (a) Schematic representation of current-carrying $YBa_2Cu_3O_7$ strip and (b) its magneto-optic image for a current of 1.4 A obtained at 15 K.

center. The minimum is smoothed out, because the magnetic field is probed not in the superconductor plane but at the 9 μm height of the MO indicator.

We shall use the Bean model for a quantitative analysis of the experimental data. The current distribution in a thin strip calculated within this model can be written[1,2]

$$\frac{J(x)}{J_c} = \begin{cases} \dfrac{2}{\pi}\arctan\left(\sqrt{\dfrac{w^2-a^2}{a^2-x^2}}\right), & |x|>a, \\ 1, & a<|x|<w, \end{cases} \tag{1}$$

where $a = w\sqrt{1-(I/I_c)^2}$, $I_c = 2wdj_c$ is the critical current, d is the thickness, and w is the halfwidth of the strip. The

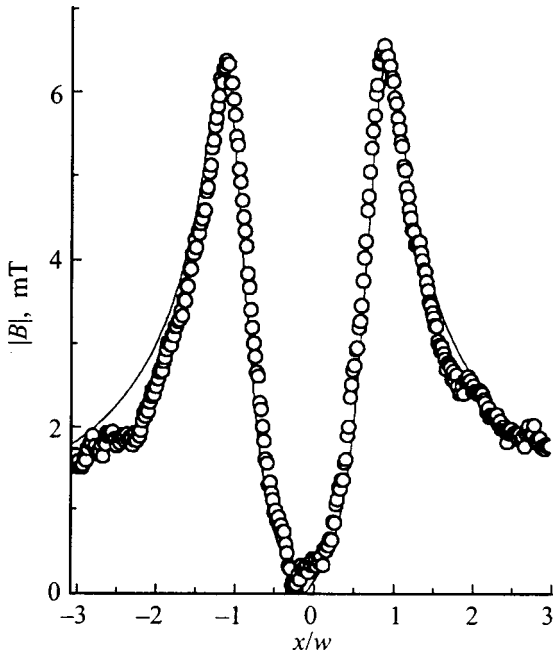

FIG. 3. Profiles of the magnetic-field component perpendicular to sample surface at a height of 9 μm above a strip carrying 1.4-A current. Circles are experimental data, and the solid line is a plot of a calculation made within the Bean model using as parameters $h=9$ μm and $I_c=1.8$ A.

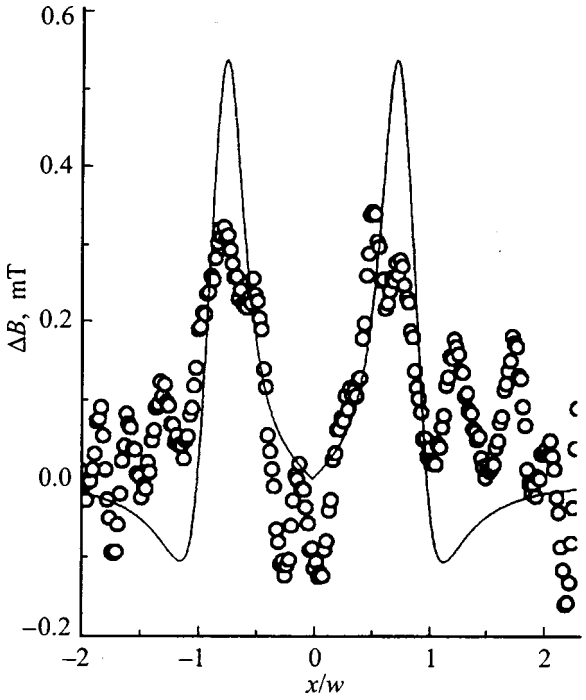

FIG. 4. Profile of magnetic-field variation during a 50-ms long current pulse, $\Delta B(x)=|B_1(x)|-|B_3(x)|$, where $B_1(x)$ and $B_3(x)$ are the profiles obtained in the beginning and at the end of the current pulse, respectively. Circles are experimental data, and the solid line is a plot of a calculation made within the Bean model using $I_c=2.1$ A and 1.8 A as parameters for the beginning and end of the pulse, respectively.

magnetic-field component perpendicular to the film plane at height h can be calculated using the Biot–Savart–Laplace equation

$$B(x)=\frac{\mu_0}{2\pi}\int_{-w}^{w}\frac{x'-x}{h^2+(x'-x)^2}J(x')dx'. \tag{2}$$

The $B(x)$ profile calculated from these equations is shown in Fig. 3 by a solid line. The best-fit parameters used in the calculations are $I_c=1.8$ A and $h=0.18\,w$.

Let us turn now to the relaxation of the $B(x)$ profile during a current pulse. Figure 4 presents the profile of the quantity $\Delta B(x)=|B_1(x)|-|B_3(x)|$, where $B_1(x)$ and $B_3(x)$ are the profiles obtained in the beginning and at the end of a current pulse, respectively (see Fig. 1). We readily see that the change in the field is the largest at the strip edges, while at the center the field practically does not change at all. The reason for the profile relaxation is magnetic flux creep,[7] as a result of which the magnetic field penetrates ever deeper into the sample after the current is switched on. Unfortunately, the equation describing flux creep in a thin current-carrying strip does not allow analytic solution. Previous studies[11,16] show, however, that such relaxation can be described in terms of the Bean model with time-dependent $j_c(t)$. We shall also use this approximation here. The solid line in Fig. 4 is a plot of $\Delta B(x)$ calculated using Eqs. (1) and (2) with the critical currents $I_c=2.1$ and 1.8 A corresponding to the beginning and end of the current pulse. The agreement between the experimental and calculated relations suggests the existence of flux creep during a current pulse. An estimate of the change in the critical current during the pulse yields 15 $\pm 5\%$. Using this result, one can derive the magnetic-vortex pinning energy. Assuming the vortex activation energy to depend logarithmically on current density,[7]

$$U(j)=U_0\ln(j_{c0}/j), \tag{3}$$

one obtains a power-law relation for current density relaxation in time. For the time dependence of the critical current density j_c, which enters Eq. (1), one obtains the following expression:

$$j_c(t)\propto(t/\tau_0)^{-kT/U_0}, \tag{4}$$

where τ_0 is the reciprocal attempt frequency.[17] Substituting $j_c(t_1)/j_c(t_2)=1.15$, where $t_1=4$ ms and $t_2=50$ ms, yields $U_0\approx 20$ kT, which is in accord with available data[18] for $YBa_2Cu_3O_7$.

Thus we have demonstrated for the first time the effectiveness of the magneto-optic method in studies of magnetic-field relaxation in a $YBa_2Cu_3O_7$ strip in space and time following turn-on of transport current. The observed evolution of the magnetic-field distribution is a direct evidence of the significant role played by creep when a magnetic flux penetrates into an HTSC strip carrying transport current. The flux creep can be adequately described in terms of the modified Bean model with a time-dependent critical current. Estimates show that the effective critical current, which is a parameter of the model, decreases by $\approx 15\%$ in 50 ms after the current is switched on. This yields $U_0\approx 20$ kT as an estimate for the vortex pinning energy. Studies over a wider range of currents, temperatures, and times, which are

planned for the future, will provide more comprehensive information on magnetic flux creep parameters.

Support of the Norwegian Ministry of Science and of the Russian program on superconductivity (Grants 96071 and 98031) is gratefully acknowledged.

*)E-mail: bobyl@theory.ioffe.rssi.ru
†)Permanent address: A. F. Ioffe Physicotechnical Institute, Russian Academy of Sciences, 194021 St. Petersburg, Russia.

[1] E. H. Brandt and M. Indenbom, Phys. Rev. B **48**, 12893 (1993).
[2] E. Zeldov, J. R. Clem, M. McElfresh, and M. Darwin, Phys. Rev. B **49**, 9802 (1994).
[3] Th. Shuster, H. Kuhn, E. H. Brandt, M. Indenbom, M. Koblischka, and M. Konczykowsky, Phys. Rev. B **50**, 16684 (1994).
[4] R. J. Wijngaarden, H. J. W. Spoelder, R. Surdeanu, and R. Griessen, Phys. Rev. B **54**, 6742 (1996).
[5] T. H. Johansen, M. Baziljevich, H. Bratsberg, Y. Galperin, P. E. Lindelof, Y. Shen, and P. Vase, Phys. Rev. B **54**, 16264 (1996).
[6] A. A. Polyanskii, A. Gurevich, A. E. Pashitski, N. F. Heinig, R. D. Redwing, J. E. Nordman, and D. C. Larbalestier, Phys. Rev. B **53**, 8687 (1997).
[7] Y. Yeshurun, A. P. Malozemov, and A. Shaulov, Rev. Mod. Phys. **68**, 911 (1996).
[8] A. Vl. Gurevich and R. G. Mints, Rev. Mod. Phys. **59**, 941 (1987).
[9] R. G. Mints and E. H. Brandt, Phys. Rev. B **54**, 12421 (1996).
[10] K. H. Müller and C. Andrikidis, Phys. Rev. B **49**, 1294 (1994).
[11] M. E. Gaevski, A. V. Bobyl, D. V. Shantsev, Y. M. Galperin, T. H. Johansen, M. Baziljevich, and H. Bratsberg (to be published in Phys. Rev. B).
[12] C. P. Bean, Phys. Rev. Lett. **8**, 250 (1962).
[13] S. F. Karmanenko, V. Y. Davydov, M. V. Belousov, R. A. Chakalov, G. O. Dzjuba, R. N. Il'in, A. B. Kozyrev, Y. V. Likholetov, K. F. Njakshev, I. T. Serenkov, and O. G. Vendic, Supercond. Sci. Technol. **6**, 23 (1993).
[14] V. A. Solov'ev, M. É. Gaevskiĭ, D. V. Shantsev, and S. G. Konnikov, Izv. Ross. Akad. Nauk, Ser. Fiz. **60**, No. 2, 32 (1996).
[15] L. A. Dorosinskii, M. V. Indenbom, V. I. Nikitenko, Yu. A. Ossip'yan, A. A. Polyanskii, and V. K. Vlasko-Vlasov, Physica C **203**, 149 (1992).
[16] M. McElfresh, E. Zeldov, J. R. Clem, M. Darwin, J. Deak, and L. Hou, Phys. Rev. B **51**, 9111 (1995).
[17] M. V. Feigel'man, V. B. Geshkenbein, and V. M. Vinokur, Phys. Rev. B **43**, 6263 (1991).
[18] C. W. Hagen and R. Griessen, Phys. Rev. Lett. **62**, 2857 (1989).

Translated by G. Skrebtsov

Influence of transport current and thermal fluctuations on the resistive properties of HTSC+CuO composites

M. I. Petrov, D. A. Balaev, K. A. Shaĭkhutdinov, and K. S. Aleksandrov

L. V. Kirenskiĭ Institute of Physics, Siberian Branch of the Russian Academy of Sciences, 660036 Krasnoyarsk, Russia

(Submitted September 22, 1998)
Fiz. Tverd. Tela (St. Petersburg) **41**, 969–974 (June 1999)

Measurements of the temperature dependence of the electrical resistance $R(T)$ below the superconducting transition temperature have been performed at different values of the transport current in HTSC+CuO composites modeling a network of weak $S-I-S$ Josephson junctions (S—superconductor, I—insulator). It has been shown experimentally that the temperature dependence $R(T)$ at different values of the transport current is adequately described by means of the mechanism of thermally activated phase slippage developed by Ambegaokar and Halperin for tunnel structures. Within the framework of this model we have numerically calculated the temperature dependence of the critical current $J_c(T)$ as defined by various criteria. Qualitative agreement obtains between the measured and calculated temperature dependences $J_c(T)$. © *1999 American Institute of Physics.* [S1063-7834(99)00806-0]

Reference 1 presented results of a study of the effect of thermal fluctuations on the resistive properties of HTSC+CuO composites modeling a network of $S-I-S$ contacts. It showed that the temperature dependence of the resistance $R(T)$ below the superconducting transition temperature in the limit of an extremely small measurement current density is well described by the well-known mechanism of thermally activated phase slippage (TAPS).[2,3] Good agreement has also been obtained for solitary HTSC transitions.[4–6] Reference 3 predicted theoretically that an increase in the transport current would cause additional broadening of the resistive transition. The present paper presents the results of an experimental test of this prediction on the same objects on which good agreement between experiment and theory had been obtained for a small measurement current.[1]

1. EXPERIMENT

Composite samples with different volume fraction of the HTSC $Y_{1/4}Lu_{3/4}Ba_2Cu_3O_7$ were synthesized by rapid sintering (2 min at 910 °C followed by 3 h at 350 °C); for the details see Refs. 1 and 7. We denote the samples as $S+15I$ and $S+30I$, where the number before the letter I indicates the percent volume fraction of CuO in the sample.

Although CuO is a semiconductor, at temperatures below 100 K its resistivity[8] ρ is 10–12 orders of magnitude greater than the value of ρ of the HTSC, and for this reason in the present context CuO can be treated as an insulator.

Resistance measurements, and measurements of the current–voltage characteristic (CVC) were performed using a standard four-probe technique. The experimental values of the critical current J_c were determined using the generally accepted 1 μV/cm criterion.[9]

2. RESULTS AND DISCUSSION

The Debye plots of the composite samples reflected the well-known fact of the absence of any chemical interaction between CuO and $Y_{1/4}Lu_{3/4}Ba_2Cu_3O_7$ (Ref. 10) under ordinary conditions for ceramic technology.

Measurements of the temperature dependence of the magnetization of the composite samples in a 100-Oe field showed that the samples all had the same superconducting transition temperature, equal to 93.5 K, which corresponds with the T_c of the original HTSC material.

Figure 1 plots the CVC's of the composite samples. The CVC of sample $S+15I$ is characterized by an insignificant excess current, while the CVC of sample $S+30I$ possesses a significant excess voltage ($\approx$2 V/cm), which is characteristic of quasi-tunneling structures.[11] As the volume fraction of CuO in the composite is increased, the differential resistance increases, which indicates an increase in the effective thickness of the insulating interlayers in the composites.

According to the classical work by Ambegaokar and Halperin,[3] the current–voltage characteristic of an $S-I-S$ junction under the action of thermal fluctuations is given by the following expression (the basic notation here is taken from Ref. 3):

$$v=\frac{V}{I_1R_N}=\frac{4\pi}{\gamma}\left\{(e^{\pi\gamma x}-1)^{-1}\left[\int_0^{2\pi}d\psi f(\psi)\right]\times\left[\int_0^{2\pi}d\psi'\frac{1}{f(\psi')}\right]+\int_0^{2\pi}d\psi\int_0^{\psi}d\psi'\frac{f(\psi)}{f(\psi')}\right\}^{-1}, \quad (1)$$

where

$$f(\psi)=\exp(0.5\gamma(x\psi+\cos(\psi))),$$

$$\gamma=\frac{\hbar I_1(T)}{ekT}, \quad x=\frac{I}{I_1(T)},$$

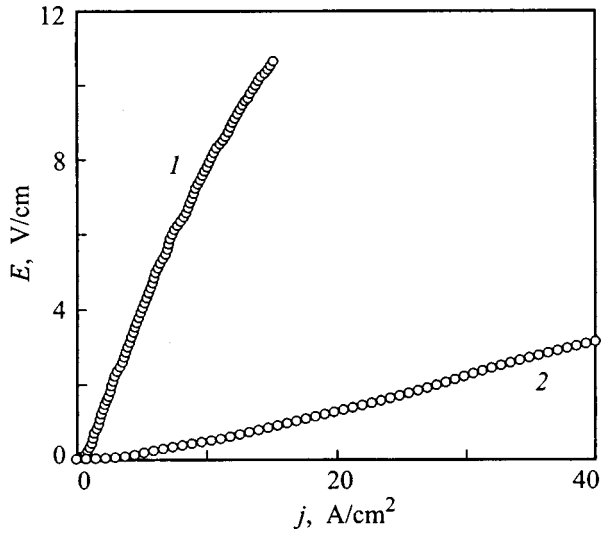

FIG. 1. Current–voltage characteristics of the composite samples $S+30I$ (*1*) and $S+15I$ (*2*) at 4.2 K.

$I_1(T)$ is the maximum Josephson current at the temperature T in the absence of thermal fluctuations,[3] and R_N is the resistance of the junction at $T \geqslant T_c$. We introduce the notation

$$C=\hbar/ekR_N.$$

As was shown in Ref. 3, in the limit of a very small transport current Eq. (1) reduces to

$$\lim_{x\to 0}\frac{v}{x}=[I_0(0.5\gamma)]^{-2}, \tag{2}$$

where I_0 is the modified Bessel function.

The successful application of the Ambegaokar–Halperin theory describing the dependence of $R(T)$ below T_c in the limit of a small transport current to the processing of experimental results[1,12] using formula (2) gives reason to assume that this theory can be also used to describe the results of experiment with finite currents in HTSC–insulator composites.

In order to compare the results of experiment with the conclusions of the theory[3] we measured the dependence $R(T)$ of composite samples for different values of the transport current j in the temperature interval 4.2–100 K. The results are shown in Figs. 2 and 3 (circles). Let us consider the form of the experimental dependence of $R(T)$. The temperature of the onset of the transition to the superconducting state does not depend on the magnitude of the transport current and is 93.5 K. At this temperature an abrupt decrease in the resistance is observed, associated with the transition of the HTSC grains to the superconducting state. This decrease is followed by a smooth ''tail'' associated with the transition of the network of $S-I-S$ junctions. As can be seen from the figure, as the measurement current is increased the temperature at which $R=0$ occurs drops considerably.

The solid lines in Figs. 2 and 3 are the results of a theoretical calculation of the temperature dependences $R(T,j)$ using formula (1) predicted by Ambegaokar and Halperin.[3] For the temperature dependence of the maximum Josephson current $I_1(T)$ we used the theoretical temperature dependence of the critical current predicted by Ambegaokar and Baratoff ($A-B$, Ref. 13) and the theoretical dependence predicted by Furusaki and Tsukuda ($F-T$, Ref. 14) for a classical s-type pair. The difference in the $A-B$ and $F-T$ dependences is that the $F-T$ dependence, following Furusaki and Tsukuda, is calculated for a finite thickness of the insulating barrier in the $S-I-S$ Josephson junction. In the limit of large thicknesses of the I layer in the $F-T$ model goes over to the $A-B$ dependence. The fitted curves in Figs. 2(b) and 3(b) were calculated using the dependence for $J_c(T)$ denoted by Furusaki and Tsukada in Ref. 14 as No. 1. This dependence for $J_c(T)$ is reproduced in Fig. 4 (labelled as $F-T$). The fitted curves in Figs. 2(a) and 3(a) were calculated using the $A-B$ dependence for $J_c(T)$ (Ref. 13). The corresponding values of the fitting parameters are given in the captions to Figs. 2 and 3. Formally, the quantity $J_c(0)$ is a fitting parameter; however, the fitted value of $J_c(0)$ obtained for $S+30I$ is equal to 0.96 A/cm^2, which is close to the experimental value $J_c(0)=0.88\pm 0.05$ A/cm^2 obtained by extrapolation to $T=0$ K from helium temperatures. (The difference in $J_c(0)$ using the $A-B$ and $F-T$ dependences is negligible). For sample $S+15I$ this agreement is somewhat poorer (the fitted value $J_c(0)=1.6$ A/cm^2, the experimental value $J_c(0)=2.00\pm 0.05$ A/cm^2).

It can be seen from Figs. 2 and 3 that good agreement obtains between the experimental curves $R(T,j)$ and the curves calculated for the sample $S+30I$ over the entire range of currents and temperatures. For the sample $S+15I$ the agreement between the calculated and experimental dependences is somewhat poorer, this discrepancy being especially noticeable at large values of the transport current.

It is possible to explain this discrepancy as follows. It can be seen from Fig. 1 that the CVC of the sample $S+30I$ has a quasi-tunneling character (excess voltage) while the CVC of the sample $S+15I$ does not possess an excess voltage, i.e., the influence of the natural boundaries, which have a metallic character,[15] on the transport properties of these composites is still large. The Ambegaokar–Halperin theory was developed for tunnel structures, which also explains the good fit for the sample $S+30I$ and the less-than-good agreement for $S+15I$.

The decrease in the fitting parameter C with increase of the CuO content (see the captions to Figs. 2 and 3) reflects an increase in the differential resistance of the samples, since it satisfies $C\sim 1/R_N$ (Ref. 3), which is clear from the experiment, see Fig. 1.

Let us now consider the problem of the disagreement between the experimental temperature dependence of the critical current and the $A-B$ and $F-T$ theoretical dependences of $J_c(T)$. In Fig. 4 the circles represent the experimental $J_c(T)$ dependence of the composite samples $S+30I$ [Fig. 4(a)] and $S+15I$ [Fig. 4(b)]. These figures also reproduce the $A-B$ and $F-T$ $J_c(T)$ dependence from Refs. 13 and 14, respectively. Although the $A-B$ and $F-T$ dependences were employed successfully as unperturbed values in the processing of the experimental $R(T,j)$ dependences, as we emphasized earlier,[1,12] there is a fundamental difference (even in the sign of the curvature) between the experimentally observed and theoretical $J_c(T)$ dependences

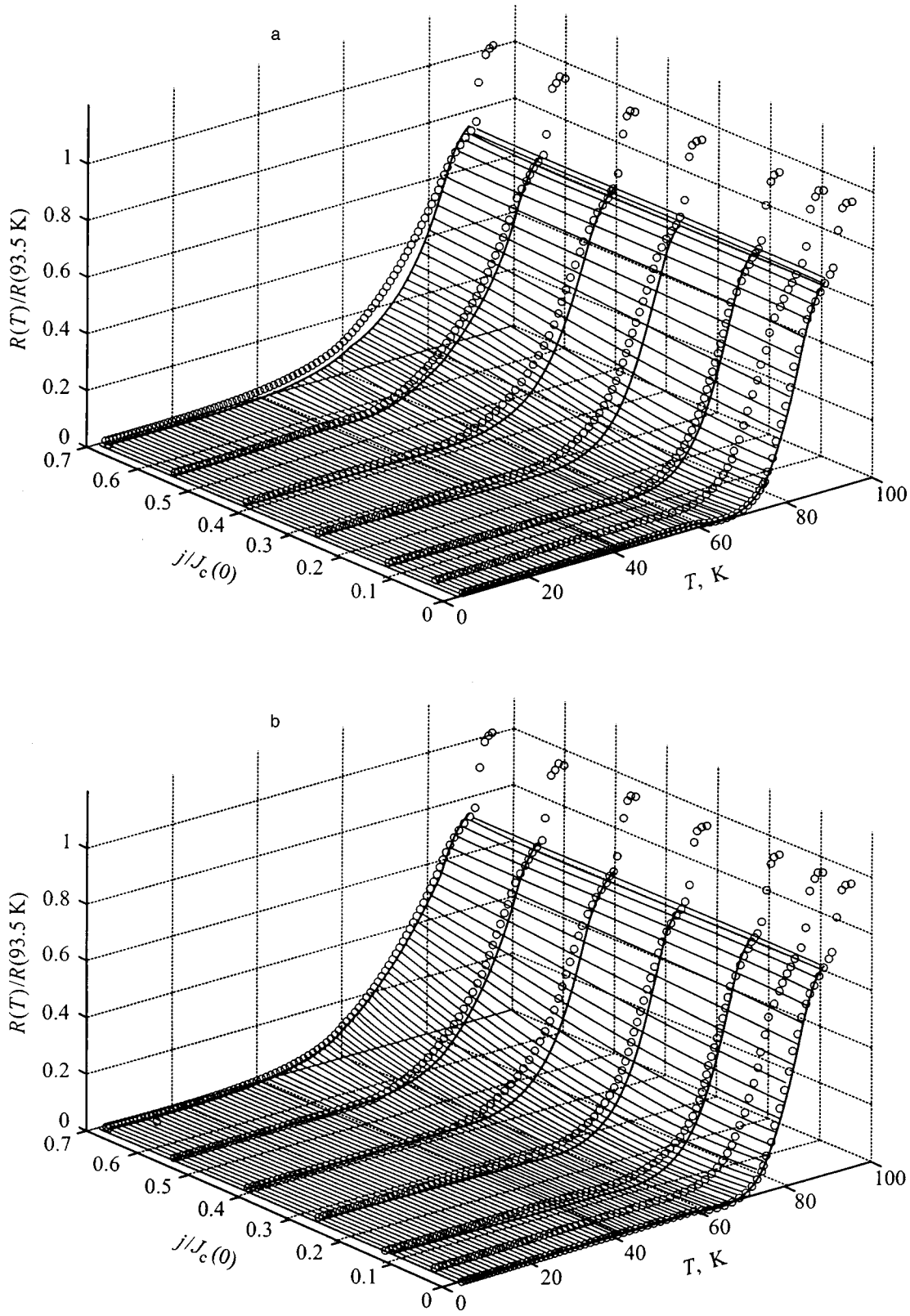

FIG. 2. Experimental dependence $R(T,j)$ for the composite $S+30I$ (circles). The solid lines plot $R(T,j)$ calculated from Eq. (1) using the $A-B$ temperature dependence of the critical current (Ref. 13), $C=800$, $T_c=89$ K (a), and using the $F-T$ temperature dependence (Ref. 14), $C=1000$, and $T_c=89$ K (b).

of $A-B$ and $F-T$. Obviously, the temperature region where the TAPS mechanism is realized is characterized by zero critical current; therefore the temperature dependence $J_c(T)$ should be modified to allow for thermal fluctuations. In the present work this was done in the simplest way, namely that the CVC was calculated according to Eq. (1) for different temperatures for each sample and $J_c(T)$ was calculated according to different criteria.

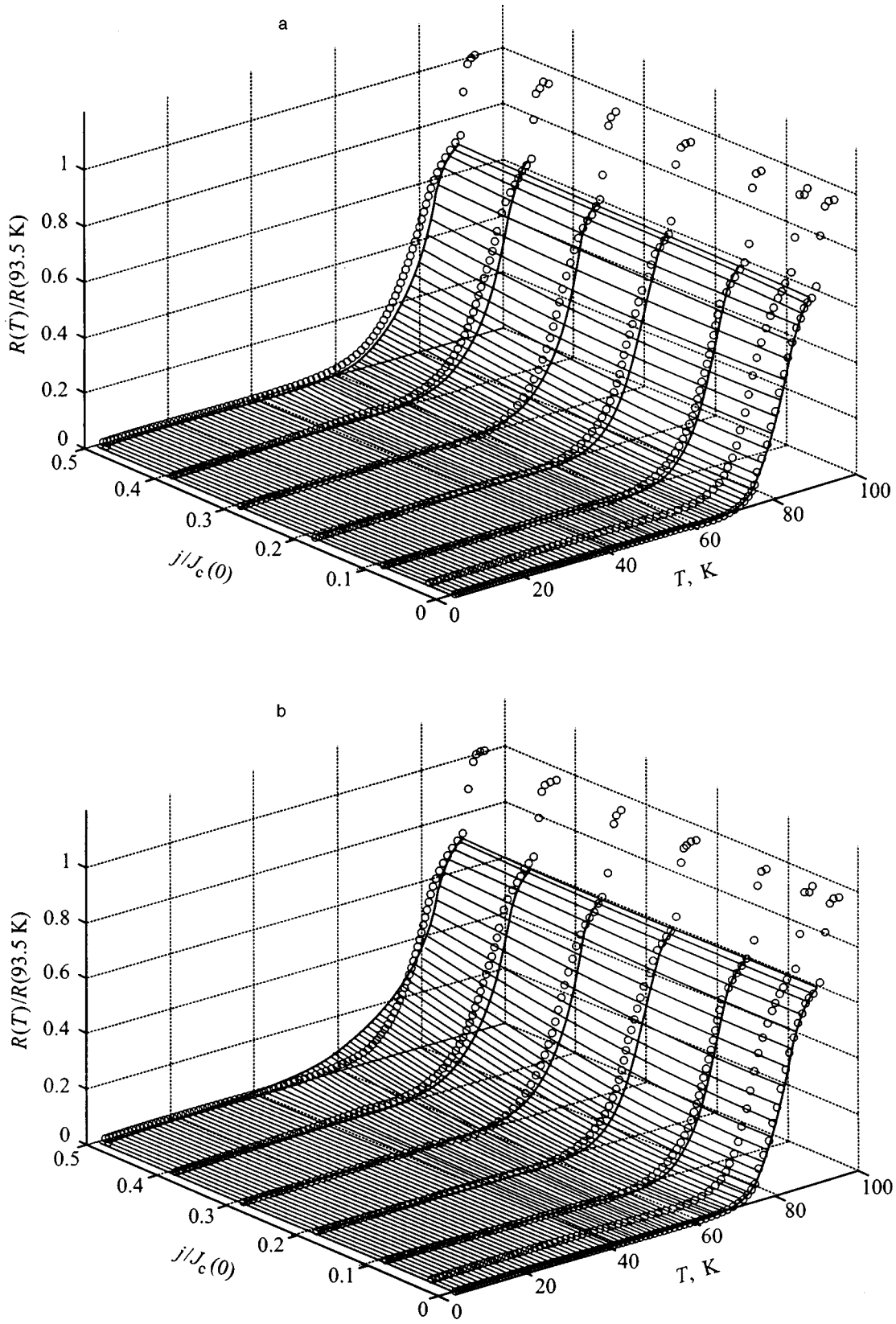

FIG. 3. Experimental dependence $R(T,j)$ for the composite $S+15I$ (circles). The solid lines plot $R(T,j)$ calculated from Eq. (1) using the $A-B$ temperature dependence of the critical current (Ref. 13), $C=900$, $T_c=89$ K (a), and using the $F-T$ temperature dependence (Ref. 14), $C=1300$, and $T_c=89$ K (b).

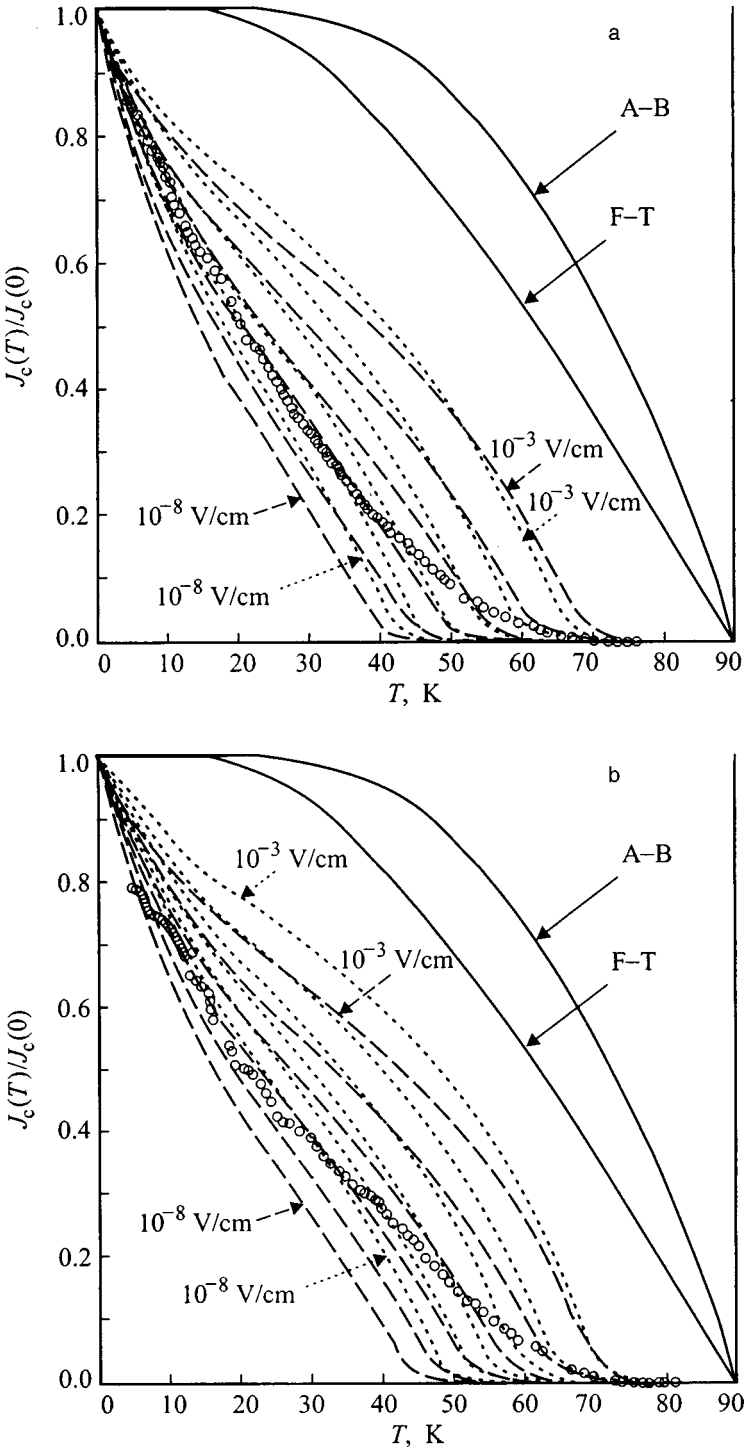

FIG. 4. Experimental dependence $J_c(T)$ for the composite samples $S+30I$ (a) and $S+15I$ (b) (circles), and the $A-B$ and $F-T$ theoretical dependences $J_c(T)$, reproduced from Refs. 13 and 14 ($T_c=89$), respectively. Also shown are curves of the temperature dependence of the critical current calculated from Eq. (1) according to different criteria (from top to bottom: 1×10^{-3} V/cm, …, 1×10^{-8} V/cm) using the $A-B$ dependence $J_c(T)$ (solid lines) and the $F-T$ dependence $J_c(T)$ (dotted lines).

Results of our calculation of the critical current using (1) with different criteria for the voltage falloff in the current–voltage curves (from 1×10^{-8} V/cm to 1×10^{-3} V/cm) are plotted in Figs. 4(a) and (b). The dashed curves were calculated using the $A-B$ theoretical dependence for $C=800$ [Fig. 4(a)] and for $C=900$ [Fig. 4(b)]; the dotted curves were calculated using the $F-T$ theoretical dependence for $C=1000$ [Fig. 4(a)] and $C=1300$ [Fig. 4(b)]. As can be seen, the calculated dependence of $J_c(T)$ has the same sign of curvature as the experimental. This can be considered as significant progress in the description of the transport properties of HTSC Josephson structures. At high temperatures, sufficiently far ($\sim15-20$ K) from the T_c ''banks,'' the experimental values of J_c become vanishingly small and follow a quadratic law. This has been widely discussed in the literature for several years; see, for example, Refs. 16 and 17. It has been shown theoretically that suppression of the pair potential at the $S-I$ interface gives rise to a quadratic dependence of $J_c(T)$ (Ref. 16). In addition to this, works have appeared recently which have theoretically examined the temperature dependence of the critical current of $S-I-S$ junctions for nonstandard pairing mechanisms. For example, in Refs. 18 and 19 it was shown theoretically that in a pairing

model different from the BCS model, the temperature dependence of the critical current $J_c(T)$ of an $S-I-S$ junction can fall off exponentially near T_c. Since the question of the pairing mechanism of the current carriers in a HTSC remains open, we have restricted our treatment to the classical values of the $J_c(T)$ dependence for $S-I-S$ junctions. In the present work we have shown by direct numerical calculation that just taking thermal fluctuations into account within the framework of the BCS theory changes the curvature of $J_c(T)$ from positive to negative.

In conclusion, we would like to express their gratitude to A. D. Vasil'ev for x-ray structural analysis of the samples. We are grateful to A. Yu. Zinov'ev for assistance with the numerical calculations and discussion of the results of this work.

This work was carried out with the partial financial support of a Grant for Young Scientists of the Siberian Branch of the Russian Academy of Sciences.

[1] M. I. Petrov, D. A. Balaev, K. A. Shaĭkhutdinov, and B. P. Khrustalev, Fiz. Tverd. Tela (St. Petersburg), **39**, 1956 (1997) [Phys. Solid State **39**, 1749 (1997)].
[2] Yu. M. Ivanchenko and L. A. Zil'berman, JETP Lett. **8**, 113 (1968).
[3] V. Ambegaokar and B. I. Halperin, Phys. Rev. Lett. **22**, 1364 (1969).
[4] R. Gross, P. Chaudhari, D. Dimos, A. Gupta, and G. Koren, Phys. Rev. Lett. **64**, 228 (1990).
[5] J. Gao, Yu. M. Boguslavskij, B. B. J. Klopman, D. Terpstra, R. Wijbrans, G. J. Gerritsma, and H. Rogalla, J. Appl. Phys. **72**, 575 (1992).
[6] D. Yin, J. Chen, S. G. Wang, Y. D. Dai, S. Z. Wang, G. C. Xiong, K. X. Chen, S. Luo, and Y. S. He, Physica C **282–287**, 2407 (1997).
[7] M. I. Petrov, D. A. Balaev, S. V. Ospishchev, K. A. Shaihutdinov, B. P. Khrustalev, and K. S. Aleksandrov, Phys. Lett. A **237**, 85 (1997).
[8] B. A. Gizhevskiĭ, A. A. Samokhvalov, N. M. Chebotarev, S. V. Naumov, and G. K. Pokazan'eva, Sverkhprovodimost: Fiz., Khim., Tekh. **4**, 827 (1991).
[9] A. Barone and G. Paterno, *Physics and Applications of the Josephson Effect* (Wiley, New York, 1982).
[10] Chan-Joong Kim, Ki-Baik Kim, Il-Hyun Kuk, and Gue-Won Hong, Physica C **255**, 95 (1995).
[11] G. E. Blonder, M. Tinkham, and T. M. Klapwijik, Phys. Rev. B **25**, 4515 (1982).
[12] M. I. Petrov, D. A. Balaev, K. A. Shaihutdinov, B. P. Khrustalev, and K. S. Aleksandrov, Physica C **282–287**, 2453 (1997).
[13] V. Ambegaokar and A. Baratoff, Phys. Rev. Lett. **10**, 486 (1963).
[14] A. Furusaki and M. Tsukada, Phys. Rev. B **43**, 10164 (1991).
[15] M. I. Petrov, D. A. Balaev, B. P. Khrustalev, and K. S. Aleksandrov, Physica C **235–240**, 3043 (1994).
[16] G. Deutscher and K. A. Müller, Phys. Rev. Lett. **59**, 1745 (1987).
[17] R. S. Gonnelli, D. Puttero, and G. A. Ummarino, Appl. Phys. Lett. **68**, 2433 (1996).
[18] S. N. Molotkov, JETP Lett. **61**, 400 (1995).
[19] Y. Tanaka and S. Kashiwaya, Phys. Rev. B **56**, 892 (1997).

Translated by Paul F. Schippnick

Temperature dependence of the upper critical field in the model of a superconductor with singular points near the Fermi surface

N. V. Shchedrina and M. I. Shchedrin

Volga State Academy of Water Transport, 603600 Nizhniĭ Novgorod, Russia
(Submitted July 17, 1998; accepted for publication October 20, 1998)
Fiz. Tverd. Tela (St. Petersburg) **41**, 975–978 (June 1999)

We consider a generalization of BCS theory to the case where the energy spectrum of parent charge carriers near the Fermi energy has a nonlinear character. This nonlinearity can cause an abrupt decrease in the coherence length, growth of the density of states and transition temperature, and non-analyticity of the vertex part as a function of the momentum. As the density of states increases the model exhibits a tendency toward negative curvature of the critical field at the transition point (although a sign change of the curvature is possible near it). Positive curvature can show up upon depletion of the density of states, which in fact corresponds to a departure of the crystal parameters from the conditions maximizing the transition temperature. © *1999 American Institute of Physics.* [S1063-7834(99)00906-5]

For type-II superconductors the upper critical field H_{c2} is a most important characteristic. On the one hand it is quite sensitive to the initial prerequisites of the model under consideration, and on the other, well-developed methods exist for measuring it, and the number of experimental papers on this question is large.[1–5] One of the problems which has recently received much attention is the question of the behavior of $H_{c2}(T)$ near the transition point T_c. The classical result following from the BCS theory and also from the phenomenological Landau–Ginzburg theory gives the linear dependence $H_{c2}\sim T_c-T$ (Ref. 6). This dependence remains valid in more complex models including, for example, a consideration of p pairing and a number of additional interactions leading to growth of the number of coexisting phases.[7] The available experimental data are quite varied: in Refs. 2 and 4 a linear law is closely borne out, with Ref. 2 pertaining to high-temperature superconductors and Ref. 4, to low-temperature superconductors; Ref. 8 provides data on films; in Refs. 1 and 3 a deviation from the linear law with the appearance of positive curvature was observed, and in Ref. 5 almost with zero slope at T_c although there is a segment of linear dependence near it. Writing in the spirit of scaling concepts $H_{c2}\sim(1-T/T_c)^{2\nu}$, we find data for $\nu=0.65$–0.8 in Ref. 9, while we have in the bipolar model of high-temperature superconductivity $\nu=3/4$ (Ref. 9) and for fluctuational corrections $\nu=2/3$. In discussions of this question reference is frequently made to the experimental difficulties of determining the transition point in the presence of a magnetic field $T_c(H)$ (Ref. 10), and also to inhomogeneities and defects.[2,3,5] Also, if vortex motion is present, then $\rho\neq 0$ holds for $T<T_c$, and the condition $\rho(T)=0$ defines rather the temperature at which the pinning mechanism operates. In this regard, of compelling interest is the question of the role of the magnetic field in the suppression of superconductivity (without invoking secondary reasons).

1. Here we consider this question within the framework of a generalized BCS model in which the energy spectrum of parent particles $\xi(p)$ near the Fermi wave vector k_F can have a nonlinear character.[11] The classical BCS theory has $\xi(p)=v_F p$ and $p=k-k_F$, where v_F is the Fermi velocity, which is independent of p. This ensures a constant density of states $N(\xi)$. The simplest nonlinear approximation of $\xi(p)$ is given by a power law $\xi(p>0)=\alpha p^m$, where m is not an integer, and the coefficient α must be determined from the normalization condition on $N(\xi)$. Note that the behavior of ξ for $p<0$ can be important for extinction of the Coulomb state. In this sense odd continuation is optimal: $\xi(p<0)=-\alpha|p|^m$. In the BCS theory $m=1$ and $\alpha=v_F$; the straight line *1* in Fig. 1 forms a boundary between two nonlinear energy spectra $\xi(p)$: a spectrum with $m>1$, which has a zero derivative at $p=0$ and an enhanced density of states, and a spectrum with $m<1$, which has an infinite derivative and a depleted density of states. For the approximate form given above, $2v_F(p)=\alpha m|p|^{m-1}$. In such a generalized model the analytic form of the main parameter of the theory ξ_0, the correlation length at $T=0$, varies, and as a consequence also the expansion parameter of the contribution of the Cooper diagram $\Pi(q)$ (Ref. 12). Indeed, $\xi_0=\hbar/\delta p$, and in the BCS theory, as a consequence of the finiteness of v_F, $\delta p\approx\delta\xi/v_F\approx\Delta_0/v_F\approx T_c/v_F$, i.e., $\xi_0=\hbar v_F/T_c$ (Δ_0 is the width of the energy gap at $T=0$). In the model with power-law nonlinearities the variation $\delta\xi$ is characterized by the magnitude itself of the variation, i.e., $\delta\xi=\alpha|\delta p|^m$, and $\delta p\approx(\delta\xi/\alpha)^{1/m}$, hence $\xi_0\approx(\alpha/\Delta_0)^{1/m}\approx(\alpha/T_c)^{1/m}$ (Δ_0 and T_c are proportional in this case).

For estimates it is convenient to have expressions for ξ_0 in terms of the conduction-band parameters. In the BCS theory, bearing in mind that the Fermi level μ is found somewhere near the middle of the band, which has width W, we can write $\hbar v_F\approx aW\approx W/k_F$, where a is on the order of the lattice constant. Then $\xi_0=(W/T_c)k_F^{-1}$. In the nonlinear model $N(\xi)$ has a singular character for $m>1$

$$N(\xi)=(1-s)N_c(W/2)^s|\xi|^{-s},\quad s=(m-1)/m. \tag{1}$$

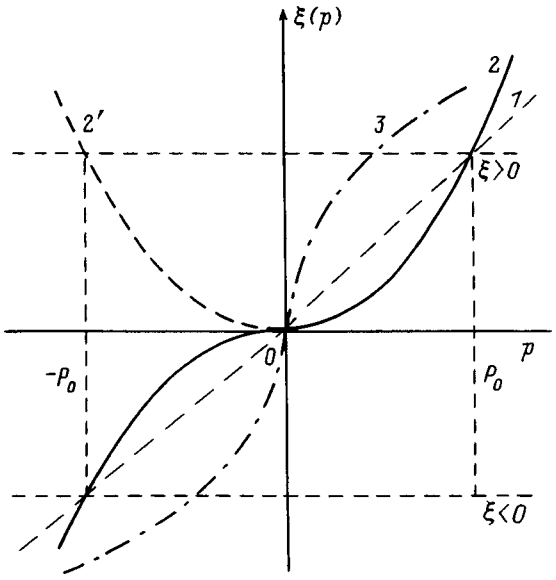

FIG. 1. Energy spectrum of parent particles near k_F ($p=k-k_F$): *1*—BCS; *2*—with enhanced density of states; *2′*—even continuation of *2* into the region $p<0$; *3*—with depleted density of states.

Here W has the meaning of the range of energies affected by the topological singularity in the energy spectrum responsible for the nonlinearity of $\xi(p)$ (an upper limit for it is the width of the conduction band), $N_c=1/Wv$ is the mean density of states, and v is the volume of the unit cell of the crystal. Expression (1) makes it possible to estimate the parameter α: $\alpha^{1/m}=k_F^2/2\pi^2N_c(W/2)^s$, i.e., in order of magnitude the quantities $\alpha^{1/m}\approx aW^{1/m}$, hence $\xi_0\approx(W/T_c)^{1/m}k_F^{-1}$. The presence of the power-law exponent $1/m$ on the large parameter W/T_c is very important since with growth of m ξ_0 falls rapidly. This is in qualitative agreement with the tendency observed in the new superconductors for which $\xi_0\approx(1-10)a$, in contrast with low-temperature superconductors, for which $\xi_0\approx(10^3-10^4)a$. The decrease in ξ_0 is linked with the nonlinearity in $\xi(p)$ and growth of the density of states. Thus, for $W/T_c=10^3$ the BCS theory has $\xi_0=10^3a$, but here for $m=2$ we have $\xi_0=10^{3/2}a\approx30a$, and for $m=3$ we have $\xi_0=10a$. The expansion parameter for $\Pi(q)$ is now $\lambda=\xi_0q/2=(W/T_c)^{1/m}(q/2k_F)$, and since in a magnetic field H the spatial inhomogeneity is defined by the characteristic quantity $q_H^2=2eH/\hbar c$, in the zeroth approximation we have the estimate $H_{c2}(T)\sim k_F^2(T_c/W)^{2/m}(T_c-T)$.

Note that studies of the Fermi surface of new superconductors point to the possible existence of various topological configurations of this surface near which the density of states $N(\xi)$ and also $v_F(\mathbf{k})$ can vary quite abruptly.[13] Important here are not only the quantities N and v_F themselves, but also their rate of change in the energy interval ω_0, where the coupling constant $g\neq0$. In particular, a decrease in $v_F(\mathbf{k})$ causes a growth of N, an increase of T_c, and a number of other features.[11] Although we limit the discussion here to the isotropic model, this is not a loss since it preserves the main physical content, specifically the quite rapid variation of the velocity $v(k)=d\xi_k/dk$ of the parent charge carriers in the vicinity of μ. This means that we assume the existence of a region of inflection of the energy surface of the parent particles ε_k near μ, where $d\xi_k/dk$ and, possibly, some higher derivatives vanish (for m fractional, singularities appear in the higher derivatives). In the isotropic case here, the Fermi surface is spherical (or cylindrical in the two-dimensional case), so that what is important here is not properly the shape of the Fermi surface but how rapidly the equipotential surfaces shift with variation of k.

2. The nonlinearity of ξ_p affects dynamic and static processes differently.[14] In the static limit

$$\Pi(q,T)=(-k_F^2/8\pi^2)\int dp\int dx[\tanh(\xi_+/2T)+\tanh(\xi_-/2T)](\xi_++\xi_-)^{-1}, \qquad (2)$$

where $\xi_+=\xi(p+qx/2)$ and $\xi_-=\xi(p-qx/2)$, the integral over p extends over the range $(-p_0,p_0)$, where p_0 is defined by the region ω_-, and the integral over x extends over the range $(-1,+1)$. In a magnetic field H, in the vicinity of the transition temperature T_c, where the energy gap Δ is small, the connection between T_c and H is determined by the equation $\Delta(\mathbf{r})=g\int\Pi_H(\mathbf{r}',\mathbf{r})\Delta(\mathbf{r}')d\mathbf{r}'$, and $\Pi_H(\mathbf{r},\mathbf{r}')\approx\Pi(\mathbf{r}-\mathbf{r}')\exp[i(2e/c)\mathbf{A}(\mathbf{r}')(\mathbf{r}-\mathbf{r}')]$, where $\mathbf{A}$ is the vector potential. Here $\Pi_H(\mathbf{q},\mathbf{r})=\Pi[\mathbf{q}-(2e/c)\mathbf{A}(\mathbf{r})]$, so that the operator Π_H has the same eigenfunctions and eigenvalues as $\mathbf{q}-(2e/c)\mathbf{A}(\mathbf{r})$. Since the eigenvalues of the square of this operator are known, $q_n^2=(n+1/2)(4eH/\hbar c)+q_z^2$, in the isotropic case the operator $\Pi(q)$ has eigenvalues $\Pi(q_n)$. Therefore the behavior of $H_{c2}(T)$ is found by solving the equation $\Pi_1(q_H,T)=\Pi_0(T_c)-\Pi_0(T)$, so that we are mainly interested in the asymptotic limit $\Pi_1(q)=\Pi(q)-\Pi_0$ for $q\to0$, where $\Pi_0(T)=\Pi(T,q=0)$, and the temperature dependence $\Pi_0(T)$.

Let us discuss the behavior of $\Pi(q)$ for different m. First of all, the BCS case, $m=1$, is exceptional since $N=\text{const}$ and the integral in Eq. (2) does not contain any singularities. As a consequence of this, it is possible to expand in q under the integral. This simple behavior is also manifested in the spatial Fourier component of the Green's function $G(\omega,R)=\int(dp/2\pi)\exp(ipR)(i\omega-\xi_p)^{-1}$, whose behavior is determined only by one simple pole $p_c=iw/v_F$, which in $\Pi(q)=(-Tk_F^2/\pi)\Sigma\int dx\int dRG(\omega,R)\times G(-\omega,R)\exp(iqxR)$ gives a power series in q^2. For $m\neq1$, as a consequence of the dependence of N on ξ, the analytic properties of G are complicated considerably (even for integer values of m there can be branch points, and real parts appear in the poles, so that $G(R)$ is no longer a simple decaying function). For this reason, the asymptotic behavior of expression (2) must be determined after taking the integrals. Note that not all parts of the asymptotic expansion are equally sensitive to the value of m. The most sensitive is Π_0, which determines T_c,

$$\Pi_0(T)=(k_F^2/2\pi^2m\alpha^{1/m})\int d\xi\tanh(\xi/2T)\xi^{-(s+1)}=(k_F^2T/\pi^2m\alpha^{1/m})\sin(\pi/2m)\sum\omega^{(1/m-2)}, \qquad (3)$$

where the upper limit of the integral over ξ is ω_0, and the sum is taken over positive frequencies. For $m \leqslant 1$ the main contribution to expression (3) comes from the vicinity of ω_0 (for $m=1$ this is the logarithmic behavior in the BCS theory). For $m>1$ the integral and the sum converge rapidly; therefore the upper limit can be extended to infinity. This means that the main contribution comes from small $\xi \ll 2T$. In this case

$$\Pi_0(T) = -k_F^2 \pi^{1/m-3}(1-2^{1/m-2})\zeta(2 - 1/m)/m \sin(\pi/2m)\alpha^{1/m}T^{(1-1/m)}, \quad (4)$$

where ζ is the zeta function. For $m \geqslant 1$ T_c falls to zero as $g \to 0$, while for $m<1$ we have the case of weak superconductivity, where the condition for the appearance of T_c is quite strict: $gN_c(\omega_0/W)^{1/m-1}>1$, i.e., a threshold arises, and $\Pi_0(T) \approx -(1/\alpha)^{1/m}(1-m)^{-1}\omega_0^{1/m-1}[1-(2T/\omega_0)^{1/m-1} \times C(m)]$ where $C(m)=2^{2-1/m}(1-2^{2-1/m})\Gamma(1/m)\zeta(1-1/m)$. In general, for $m>1$ expression (2) does not expand in a series in q^2 and contains terms proportional to q^{2m+1}. To estimate the part of expression (2) that depends on q, $\Pi_1(q,T)$, we utilize the circumstance noted above that the main contribution to the integral comes from small ξ. This makes it possible to expand $\tanh(p \pm qx/2)$ into series under the condition $\alpha q^m \ll 2T$

$$\Pi_1(T) = (1/3)(k_F^2/2\pi^2)(1/2T)(2T/\alpha)^{1/m}C_1[A(q)+B(q)], \quad (5)$$

where C_1 is a numerical factor which depends on the parameter m and $A(q)$ is an analytic function of q^2. It is expressed in terms of the dimensionless variable λ as

$$A(\lambda) = -2(m+1)+[(1+\lambda)^{2(m+1)}-(1-\lambda)^{2(m+1)}]/\lambda - (1-\lambda^2)^{(2m+1)/2}-(2m+1)F(-m,1/2,3/2,\lambda^2), \quad (6)$$

where $F(\alpha,\beta,\gamma;x)$ is the hypergeometric function. For small λ, it becomes $A(\lambda) \approx C_2\lambda^2 - C_3\lambda^4$, where C_2 and C_3 are numerical coefficients which depend on m, $C_2>0$, but $C_3>0$ for $m<3/2$ and $C_3<0$ for $m \geqslant 3/2$. The second term in expression (6) is equal to $B(\lambda)=C_4\lambda^{2m+1}$, $C_4>0$.

3. Thus, the expansion of $\Pi(q)$ in noninteger values of $m>1$ contains both an analytic part in q^2 and a non-analytic part in q (for integer values of m Π is analytic), but the lowest degree of q is 2. Therefore, the coefficient of q^2 can be obtained by direct differentiation inside the integral in Eq. (2)

$$\Pi^{(2)}(q) = \frac{k_F^2\alpha^{1/m}[1-2^{-(2+1/m)}]\zeta(2+1/m)}{12\pi^{(3+1/m)}\sin(\pi/2m)T^{(1+1/m)}}q^2. \quad (7)$$

Note that separate parts of the asymptotic expansion can be valid over a wider range than the total expression. Thus, expression (7) goes over to the BCS expression for $m=1$ and remains finite down to values of $m>1/2$. The coefficients of the higher powers of q can diverge for non-integer m, which confirms the non-analyticity of the total expression, but the larger the value of m, the higher the fractional power of q.

To first order, we have from expressions (4) and (7) to within numerical factors $H_{c2}(T) \sim T^{1+1/m}(T^{1/m-1} - T_c^{1/m-1})$, $m>1$. At the transition point T_c itself the second derivative of H_{c2} is negative, but for $T<T_c$ it can change sign. Thus, for $m=1.1$ this happens at $T \approx 0.2T_c$. In principle positive curvature could be provided by the following term of the asymptotic expansion with exponent $r>2$, but under the condition that the coefficient be negative; however, for $1<m<3/2$ we have $3<2m+1<4$, and where $C_3>0$ the power of q in $B(\lambda)$ is less than four and $C_4>0$; therefore the tendency toward negative curvature of H_{c2} at T_c is greater for $m>1$. For $1/2<m<1$ we have $H_{c2}(T) \sim T^{1+1/m}(T_c^{1/m-1}-T^{1/m-1})$. Here the second derivative at T_c is also negative; however, the temperature at which it changes sign is closer to T_c. For $m=0.7$ it is $T=0.4T_c$, and for $m \approx 1/2$ it is $T \approx 0.5T_c$. Finally, for $m<1/2$ nonanalyticity arises in expression (7), which indicates that powers of q with exponent $r<2$ are possible. In this situation H_{c2} can have positive curvature even for zero derivative. Note that this situation corresponds to depletion of the density of states near the Fermi surface and should be accompanied by an abrupt decrease of T_c. In fact, depletion of the density of states occurs when the structure of the crystal and filling of the conduction band deviate from optimal conditions ensuring a maximum transition temperature;[11] most often it is under these conditions that positive curvature with almost zero derivative is observed.

[1] J. S. Moodera, R. Meservey, J. E. Tkaczyk, C. X. Hao, G. A. Gibson, and P. M. Tedrow, Phys. Rev. B **37**, 619 (1988).

[2] N. E. Alekseevskiĭ, A. V. Mitin, *et al.*, Zh. Eksp. Teor. Fiz. **97**, 263 (1990) [Sov. Phys. JETP **70**, 148 (1990)].

[3] N. V. Anshukova, V. B. Ginodman, *et al.*, Zh. Eksp. Teor. Fiz. **97**, 1635 (1990) [Sov. Phys. JETP **70**, 923 (1990)].

[4] N. E. Olekseevskiĭ and V. N. Narozhnyĭ, JETP Lett. **39**, 553 (1994).

[5] R. N. Lyubovskaya, R. B. Lyubovskiĭ, *et al.*, JETP Lett. **51**, 361 (1990).

[6] A. A. Abrikosov, *Fundamentals of the Theory of Metals* (North-Holland, Amsterdam, 1988).

[7] I. A. Luk'yanchuk and V. P. Mineev, Zh. Eksp. Teor. Fiz. **93**, 2045 (1987) [Sov. Phys. JETP **66**, 1168 (1987)].

[8] B. I. Belevtsev, Usp. Fiz. Nauk **160**, 65 (1990) [Sov. Phys. Usp. **33**, 36 (1990)].

[9] A. S. Aleksandrov and D. A. Samarchenko, Zh. Eksp. Teor. Fiz. **99**, 574 (1991) [Sov. Phys. JETP **72**, 321 (1991)].

[10] M. B. Salamon, S. E. Inderheers, J. P. Rice, B. G. Pazol, D. M. Ginsberg, and Nigel Goldenfeld, Phys. Rev. B **38**, 885 (1988).

[11] N. V. Shchedrina and M. I. Shchedrin, Fiz. Tverd. Tela (St. Petersburg) **36**, 2201 (1994); **36**, 3079 (1994); **37**, 2238 (1995); **39**, 1940 (1997) [Phys. Solid State **36**, 1200 (1994); **36**, 1637 (1994); **37**, 1223 (1995); **39**, 1734 (1997)].

[12] A. A. Abrikosov, L. P. Gor'kov, and I. E. Dzyaloshinskiĭ, *Methods of Quantum Field Theory in Statistical Physics* (Prentice-Hall, Englewood Cliffs, N.J., 1963).

[13] V. N. Antonov, Vl. N. Antonov, V. T. Bar'yakhtar, *et al.*, Zh. Eksp. Teor. Fiz. **96**, 732 (1989) [Sov. Phys. JETP **69**, 415 (1989)].

[14] N. V. Shchedrina and M. I. Shchedrin, Fiz. Tverd. Tela (St. Petersburg) **40**, 603 (1998) [Phys. Solid State **40**, 552 (1998)].

Translated by Paul F. Schippnick

Charge states of atoms in $HgBa_2CuO_4$ and $HgBa_2CaCu_2O_6$ lattices

V. F. Masterov,*) F. S. Nasredinov, N. P. Seregin, and P. P. Seregin

St. Petersburg State Technical University, 195251 St. Petersburg, Russia
(Submitted October 20, 1998)
Fiz. Tverd. Tela (St. Petersburg) **41**, 979–981 (June 1999)

Mössbauer emission spectroscopy on the $^{67}Cu(^{67}Zn)$ isotope has been used to determine the parameters of the electric-field gradient tensor at the copper sites of the $HgBa_2Ca_{n-1}Cu_nO_{2n+2}$ lattices ($n=1,2$), as well as to calculate these parameters in the point-charge approximation. An analysis of the results, combined with available NQR literature data for the ^{63}Cu isotope, has shown that the best fit of calculated to experimental data can be reached by assuming that the holes due to the presence of defects in the material localize primarily in the sublattice of the oxygen lying in the copper plane. © *1999 American Institute of Physics.*
[S1063-7834(99)01006-0]

$HgBa_2Ca_{n-1}Cu_nO_{2n+2}$ ($n=1,2$) compounds and HgBaCaCuO are typical representatives of high-T_c superconductors, and determination of the charge state of the oxygen atoms in HgBaCaCuO lattices, which play a decisive role in the onset of superconducting state in these ceramics, is a problem of considerable current interest. This work reports on the use of Mössbauer emission spectroscopy (MES) on the $^{67}Cu(^{67}Zn)$ isotope to determine the charge state of atoms in HgBaCaCuO lattices.

The $HgBa_2Ca_{n-1}{}^{67}Cu_nO_{2n+2}$ Mössbauer sources were prepared by diffusion doping $HgBa_2CaCu_2O_6$ (1212) ($T_c=91$ K) and $HgBa_2CuO_4$ (1201) ($T_c=74$ K) compounds with the ^{67}Cu isotope at 450 °C for two h in an oxygen atmosphere. The $^{67}Cu(^{67}Zn)$ Mössbauer spectra were measured at 4.2 K with a ^{67}ZnS absorber. Figure 1 presents typical spectra, and Fig. 2a, the results of their treatment. It was assumed that the ^{67}Cu parent isotope introduced by diffusion doping occupies copper sites in the lattices, with the daughter isotope ^{67}Zn remaining there. Because copper atoms in the (1201) and (1212) lattices sit at the only [1,2] site, it was expected that $^{67}Cu(^{67}Zn)$ Mössbauer spectra of these samples (compounds) would correspond to the only state of the $^{67}Zn^{2+}$ Mössbauer probe at the copper sites. As seen from Fig. 1, the $^{67}Cu(^{67}Zn)$ spectra of both compounds (their ceramics) are indeed quadrupole triplets corresponding to the only state of the $^{67}Zn^{2+}$ probe.

In a general case, the measured quadrupole coupling constant $C=eQU_{zz}/h$ is a sum of two terms:

$$eQU_{zz}=eQ(1-\gamma)V_{zz}+eQ(1-R_0)W_{zz}, \tag{1}$$

where Q is the quadrupole moment of the probe nucleus, U_{zz}, V_{zz}, and W_{zz} are the principal components of the total, crystal-field, and valence-electron electric-field gradient (EFG) tensors, γ and R_0 are the Sternheimer coefficients of the probe nucleus, and h is the Planck constant.

In the case of the $^{67}Zn^{2+}$ probe, the valence-electron contribution to the total EFG tensor may be neglected, which gives

$$C(\mathrm{Zn})\approx eQ(1-\gamma)V_{zz}/h. \tag{2}$$

The crystal-field EFG tensor can be calculated in terms of the point-charge model, and therefore by comparing the experimental, $C(\mathrm{Zn})$, and calculated, $eQ(1-\gamma)V_{zz}$, values one can determine the effective charges of atomic centers at lattice sites.

We calculated crystal-field EFG tensors for the copper sites on the HgBaCaCuO lattices. The lattices were considered as superpositions of several sublattices, namely, $[Hg][Ba_2][Cu][O(1)_2][O(2)_2]$ and $[Hg][Ba_2][Ca][Cu_2][O(1)_4][O(2)_2]$, and the EFG was calculated as a sum of the contributions due to these sublattices. Note that the O(1) atoms share the same plane with copper atoms. The structural data needed for the calculations were taken from Refs. 1 and 2. The lattice sum tensors for the copper sites due to all sublattices are diagonal with respect to the crystallographic axes and axially symmetric.

Taking $\gamma=-12.2$ (Ref. 3) and $Q=0.174$ b (Ref. 4) for the $^{67}Zn^{2+}$ centers, one obtains within model A corresponding to standard valence states of the atoms involved (Hg^{2+}, Ba^{2+}, Ca^{2+}, Cu^{2+}, O^{2-}) $eQ(1-\gamma)V_{zz}\approx 67$ MHz for the copper sites of the $HgBa_2CuO_4$ lattice, and $eQ(1-\gamma)V_{zz}\approx 73$ MHz for the copper sites in the $HgBa_2CaCu_2O_6$ lattice. These values differ substantially from the experimental values of $C(\mathrm{Zn})$. The nature of this difference can be established by a combined analysis of $^{67}Cu(^{67}Zn)$ MES data and nuclear quadrupole resonance (NQR) measurements on the ^{63}Cu isotope for copper sites in the cuprate lattices. Figure 2a presents a $C(\mathrm{Cu})$ vs $C(\mathrm{Zn})$ diagram.[5] For divalent copper compounds, the experimental data can be fitted with a straight line

$$C(\mathrm{Cu})=197-11.3\,C(\mathrm{Zn}), \tag{3}$$

where $C(\mathrm{Cu})$ and $C(\mathrm{Zn})$ are in MHz.

It was shown that the main reason for the deviation of experimental data from the straight line (3) is that the copper valence differs from 2+.

Additional information can be derived from a $C(\mathrm{Cu})$ vs V_{zz} diagram proposed in Ref. 5 (Fig. 2b). Plotted on the horizontal axis of this diagram are the principal components of the crystal-field EFG tensor, V_{zz}, calculated for the cop-

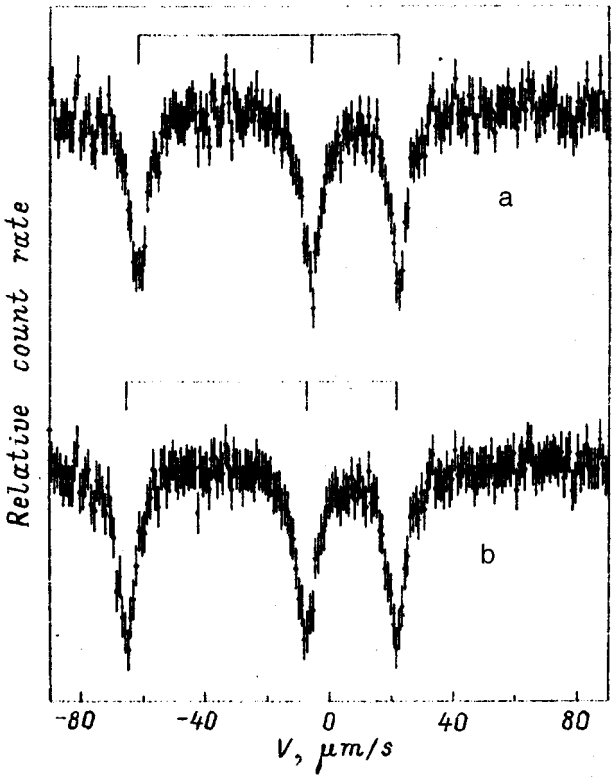

FIG. 1. ^{67}Cu(^{67}Zn) Mössbauer spectra of (a) (1201) and (b) (1212) compounds. The position of the components of the quadrupole triplets corresponding to $^{67}Zn^{2+}$ centers occupying copper sites is identified.

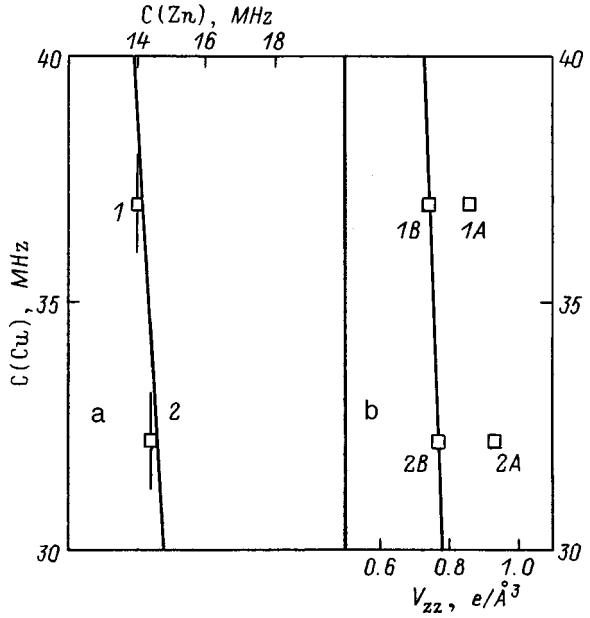

FIG. 2. (a) C(Cu) vs C(Zn) plot for divalent copper compounds (solid line); (b) C(Cu) vs V_{zz} plot for divalent copper compounds. The points refer to data corresponding to (*1*) Cu in compound (1201), and (*2*) Cu in (1212). The indices A and B refer to the models used to calculate V_{zz}.

per sites for which the values of C(Cu) were derived by the ^{63}Cu NQR method. The C(Cu) vs V_{zz} plot can be fitted by an equation

$$C(\mathrm{Cu}) = 179 - 191.4\, V_{zz}, \tag{4}$$

where C(Cu) is given in MHz, and V_{zz} in units of $e/\text{Å}^3$.

There is only one thing that can cause the C(Cu) vs V_{zz} relation deviate from the straight line (4), namely, an error in the calculation of the EFG tensor because of an inappropriate selection of the atomic charges.

Figure 2a presents ^{63}Cu NQR data for the (1201) and (1212) compounds (Refs. 6 and 7, respectively), together with our ^{67}Cu(^{67}Zn) MES results in a C(Cu) vs C(Zn) plot. It is seen that all points fit satisfactorily to relation (3), which implies that copper in the HgBaCaCuO compounds is divalent. There is, however, no agreement with the linear relation (4) in the C(Cu) vs C(Zn) plot (Fig. 2b) if V_{zz} is calculated assuming the atoms to have standard charges (model A). Obviously, the deviation of data from the linear relation (4) should be accounted for by an inappropriate choice of the model of charge distribution over lattice sites used in the V_{zz} calculation. The agreement is reached for models of type B, which postulate localization of holes at the O(1) sites in the (1201) and (1212) compounds. In the compounds under study, such holes can appear as a result of stabilization of a part of mercury atoms in univalent state. Our EFG tensor calculations within the B-type models assumed the fractions of univalent mercury atoms in the (1201) and (1212) compounds to be, respectively, 30 and 90%. Note, however, that photoelectron spectroscopy data (see, e.g., Ref. 8) do not support the presence of univalent mercury, and one cannot exclude that in order to explain the existence of holes in the oxygen sublattices one should take into account defects in the material.

Thus we have determined the EFG tensor parameters for the copper sites in the $HgBa_2Ca_{n-1}Cu_nO_{2n+2}$ lattices ($n=1,2$) by ^{67}Cu(^{67}Zn) MES and calculated these parameters in the point charge approximation. An analysis has been performed of the quadrupole coupling constant for the centers $^{67}Zn^{2+}$ [^{67}Cu(^{67}Zn) MES data] and $^{63}Cu^{2+}$ [published ^{63}Cu NQR and NMR data), as well as of the principal component of the crystal-field EFG tensor for copper sites of various cuprates. The experimental and calculated EFG tensor parameters for the HgBaCaCuO compound can be reconciled if one assumes that the holes created due to the presence of defects in the material are localized primarily on the sublattice of the oxygen sharing the same plane with the copper atoms.

Support of the Russian Fund for Basic Research (Grant 97-02-16216) is gratefully acknowledged.

*)Deceased.

[1] J. L. Wagner, P. G. Radaelli, D. G. Hinks, J. D. Jorgensen, J. F. Mitchell, B. Dabrowski, G. S. Knapp, and M. A. Beno, Physica C **210**, 447 (1993).
[2] L. W. Finger, R. M. Hazen, R. T. Downs, R. L. Meng, and C. W. Chu, Physica C **226**, 216 (1994).
[3] R. Sternheimer, Phys. Rev. **146**, 140 (1966).
[4] A. Forster, W. Potzel, and G. M. Kalvius, Z. Phys. B **37**, 209 (1980).
[5] V. F. Masterov, F. S. Nasredinov, N. P. Seregin, and P. P. Seregin, Fiz. Tverd. Tela (St. Petersburg) **37**, 3400 (1995) [Phys. Solid State **37**, 1868 (1995)].

[6] T. Machi, R. Usami, H. Yamauchi, N. Koshizuka, and H. Yasuoka, Physica C **235-240**, 1675 (1994).
[7] M. Horvatić, C. Berthier, P. Carretta, J. Gillet, P. Ségransan, Y. Berthier, and J. J. Capponi, Physica C **235-240**, 1669 (1994).
[8] R. P. Vasquez, M. Rupp, A. Gupta, and C. C. Tsuei, Phys. Rev. B **51**, 15657 (1995).

Translated by G. Skrebtsov

SEMICONDUCTORS. DIELECTRICS

Infrared lattice-reflection spectroscopy of $Zn_{1-x}Cd_xSe$ epitaxial layers grown on a GaAs substrate by molecular-beam epitaxy

L. K. Vodop'yanov,*) S. P. Kozyrev, and Yu. G. Sadof'ev

P. N. Lebedev Physical Institute, Russian Academy of Sciences, 117924 Moscow, Russia
(Submitted June 2, 1998)
Fiz. Tverd. Tela (St. Petersburg) **41**, 982–985 (June 1999)

Results are presented of the first measurements of infrared reflection spectra of $Zn_{1-x}Cd_xSe$ films ($x=0-0.55$; 1) grown on a GaAs substrate by molecular-beam epitaxy. It is shown by a mathematical analysis of the experimental spectra that the investigated $Zn_{1-x}Cd_xSe$ alloy system manifests a unimodal rearrangement of its vibrational spectrum as the composition is varied. © *1999 American Institute of Physics.* [S1063-7834(99)01106-5]

The recently renewed interest in semiconductor alloys (solid solutions) has been linked with their wide use in the fabrication of quantum-dimensional structures, including quantum wells, threads, and dots. In the fabrication of such structures the problem arises of the validity of assigning the properties of the bulk material to thin layers. Commonly, it is assumed without any special reason that these properties are identical. However, for example, in Ref. 1, it has been shown that the concentration rearrangement of the phonon spectrum of ZnCdTe films differs from that obtaining for bulk crystals of the same alloys.

For current applications connected with the fabrication of integrated opto-electronic devices, it is necessary to grow films of II–VI compounds on a material that is suitable for this purpose, e.g., GaAs. However, in this case, elastic stresses arise due to lattice mismatch, altering the properties of the films.

It is of interest to examine the crystalline lattice dynamics of films of the alloy system $Zn_{1-x}Cd_xSe$. Using thin layers of this alloy, structures with quantum wells[2] and quantum dots[3] were fabricated and studied. However, the properties of this alloy (in contrast to other intensely studied alloys of II–VI compounds) have been investigated only very spottily. There is the work of Brafman,[4] who investigated the Raman spectra of $Zn_{1-x}Cd_xSe$ bulk crystals and suggested that the rearrangement of the vibrational spectrum with composition of this alloy system has a unimodal character. These alloys are also interesting because as the composition varies from ZnSe to CdSe a phase transition of the crystal structure from cubic to hexagonal takes place.

There are no studies in the literature, as far as we know, of lattice vibrations using infrared (IR) spectroscopy in bulk crystals of ZnCdSe, let alone epitaxial layers. In the present paper we present the first results of lattice-reflection measurements for epitaxial layers of $Zn_{1-x}Cd_xSe$ ($0\leqslant x\leqslant 0.55$, $x=1$) grown by molecular-beam epitaxy on a GaAs substrate. A mathematical analysis of experimental lattice-reflection spectra of film-on-substrate structures was performed, and the dispersion parameters of the lattice oscillators were determined. Brafman's conjectures[4] about the unimodal character of the lattice-reflection spectra of this alloy system have been confirmed.

1. FILM GROWTH AND MEASUREMENTS

Hetero-epitaxial layers of $Zn_{1-x}Cd_xSe$ ($0\leqslant x\leqslant 0.55$, $x=1$) on GaAs were grown by molecular-beam epitaxy on the ''Katun'' setup, which was equipped with an ion manometer for monitoring the intensity of the molecular beams, and an Auger electron spectrometer. It was also outfitted with molecular sources with enlarged crucibles to enhance the homogeneity of the growth layers. The limiting gas pressure in the setup was 1×10^{-8} Pa. A built-in high-energy electron diffractometer was utilized to monitor the quality of cleaning of the substrate surface before epitaxy and also the quality of the growth nuclei and epitaxial layer growth.

Epitaxy was performed on chromium-compensated (100) GaAs substrates with 3° misorientation from the {110} direction by evaporation of especially pure ($6N$) charges of Zn, Cd, and Se from individual molecular sources. The layer of natural oxides was removed from the substrate surface by heating in vacuum at 580 °C in the absence of selenium and zinc vapors. After the substrate was cooled to the epitaxial growth temperature (280–320 °C) the substrate was held in zinc vapors with an equivalent pressure of 3×10^{-5} Pa for 100 s to prevent formation of chemical compounds of selenium with gallium, an excess of the latter being present on the surface of the GaAs substrate as a consequence of incongruent evaporation during heating in vacuum.

The samples were grown with the ratio of equivalent pressures of the selenium beam to the total pressure of the Zn and Cd beams close to 2, which ensured the coexistence on the surface of a superstructure consisting of a mixture of 1×2 and $c(2\times2)$ reconstructions and corresponding to conditions of stoichiometric growth. The epitaxy temperature was lowered as the Cd content in the films was increased.

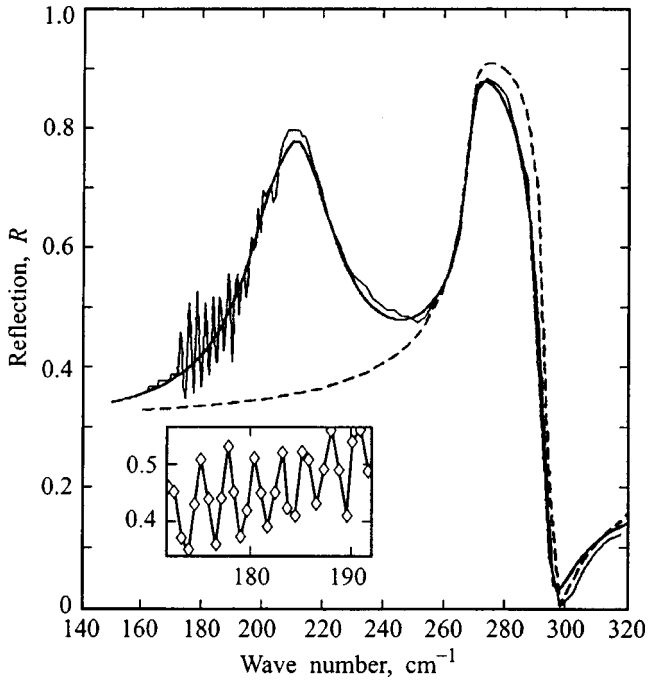

FIG. 1. Infrared lattice-reflection spectrum of an epitaxial ZnSe film on a GaAs substrate. The experimental spectrum is shown by the thin solid line, and the calculated spectrum, by the thick solid line. The dashed line plots the reflection spectrum of the GaAs substrate.

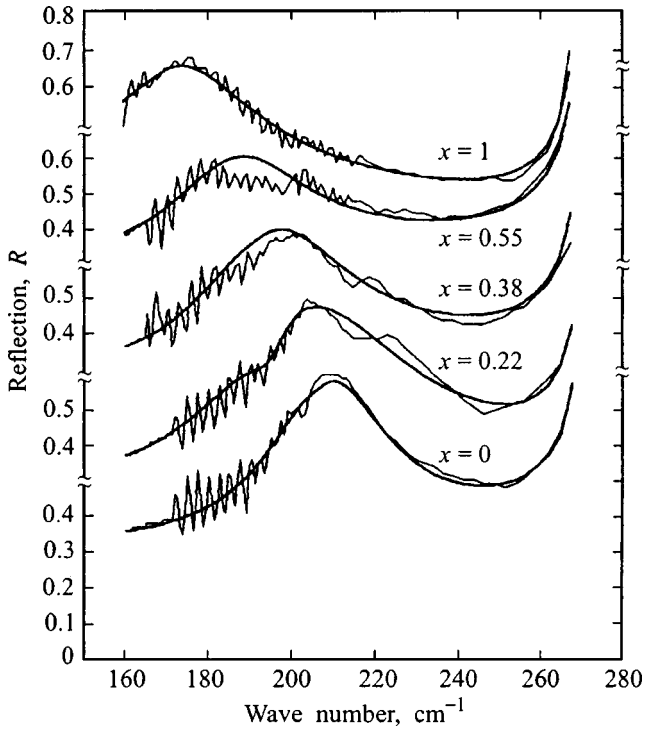

FIG. 2. Lattice-reflection spectra of $Zn_{1-x}Cd_xSe$ films on GaAs. The experimental spectra are shown by a thin solid line, and the calculated spectra, by a thick solid line.

The rate of growth was held equal to 1 μm per hour. The composition of the epitaxial layers was monitored by tracking the ratio of the intensities of the LMM lines of the Zn and Se Auger transitions, and also by monitoring the position of the edge emission lines in the cathodoluminescence spectra.

The long-wavelength IR reflection spectra were recorded on a laboratory-model IR diffraction spectrometer using as the IR detector an OAP-5 opto-acoustical receiver with spectral resolution better than 1 cm^{-1}.

2. RESULTS AND DISCUSSION

IR lattice-reflection spectra at 300 K for a ZnSe film and for $Zn_{1-x}Cd_xSe$ films of some other compositions on a GaAs substrate are displayed in Figs. 1 and 2. The experimental lattice-reflection spectra are shown by a thin line, and the calculated spectra, by a thick line. The dashed line in Fig. 1 shows the lattice-reflection spectrum of GaAs. It is clear from the figure that the reflection spectrum of the thin film relative to the reflection spectrum of the substrate is reminiscent of the absorption curve of the film. To illustrate the dependence of the reflection spectra of the films on their composition, Fig. 2 plots the reflection spectra bounded by the spectral region 160–270 cm^{-1}, which effectively excludes the substrate. On all the reflection curves rapid oscillations are observed associated with interference in the GaAs substrate, which has a thickness of 400–500 μm. The inset to Fig. 1 shows these oscillations together with the experimental points on an expanded wave-number scale. The step of the oscillations is roughly 2.5 cm^{-1} (or 0.8 μm). The experimental points shown in the inset also demonstrate the high spectral resolution of the device (better than 1 cm^{-1}) on which the reflection spectra were recorded. Figure 2 displays reflection spectra of $Zn_{1-x}Cd_xSe$ films for the compositions $x=0$, 0.22, 0.38, 0.55, and 1, offset from one another along the ordinate axis for clarity. The peak of the reflection band for the ZnSe film ($x=0$) is localized at the frequency 206 cm^{-1}, and for the CdSe film ($x=1$), at 169 cm^{-1}. As the Cd concentration in the films increases the lattice-reflection peak changes its shape and position, with only small changes in its intensity. We did not observe any splitting of the lattice-reflection peak into two peaks localized near the frequencies characteristic of ZnSe and CdSe films for any of the compositions up to $x=0.55$. Such behavior of a lattice peak for $Zn_{1-x}Cd_xSe$ films as a function of composition x is characteristic of the unimodal type of rearrangement of the phonon spectrum of a crystalline alloy. But to reach a more definite conclusion, it is necessary to carry out a rigorous mathematical analysis of the experimental reflection spectra.

In our case, we consider a model structure formed by a thin film on top of a bulk (semi-infinite) substrate under the assumption that the film is homogeneous in thickness. In such a model structure for a film of thickness L with dielectric function $\varepsilon_f(\omega)$ and a substrate with dielectric function $\varepsilon_s(\omega)$ for normal incidence of the light, the amplitude reflection coefficient has the form[5]

$$r_{1fs}(\omega)=\frac{r_{1f}(\omega)+r_{fs}(\omega)\exp(i2\beta)}{1+r_{1f}(\omega)r_{fs}(\omega)\exp(i2\beta)}, \tag{1}$$

where

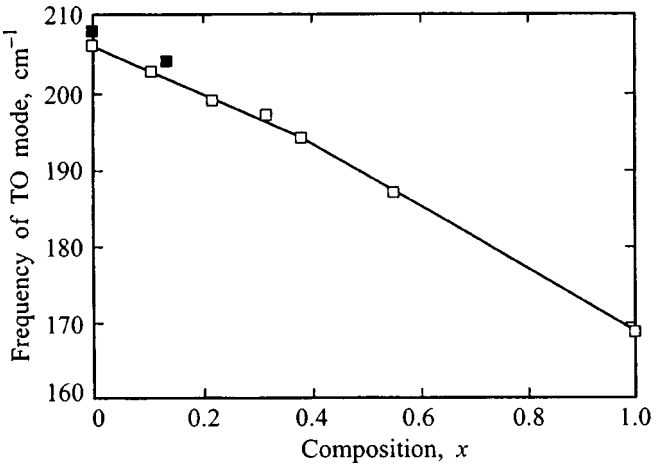

FIG. 3. Dependence of the transverse optical phonon frequencies of $Zn_{1-x}Cd_xSe$ films on alloy composition x.

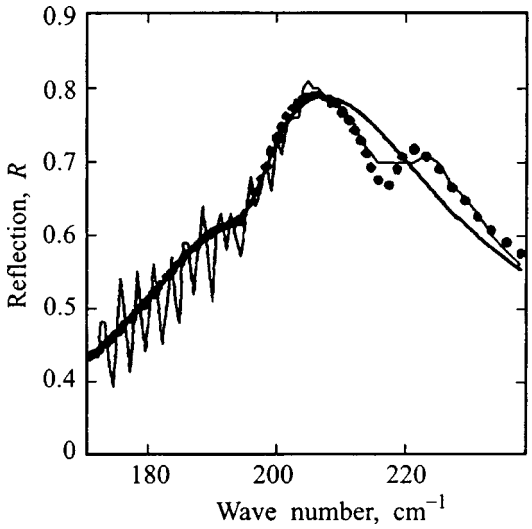

FIG. 4. Lattice-reflection spectrum of a $Zn_{1-x}Cd_xSe$ film ($x=0.22$) and its interpretation by a one-oscillator (solid line) and a two-oscillator model (points) of the vibrational spectrum of the alloy.

$$r_{1f}(\omega)=\frac{1-\sqrt{\varepsilon_f(\omega)}}{1+\sqrt{\varepsilon_f(\omega)}},\quad r_{fs}(\omega)=\frac{\sqrt{\varepsilon_f(\omega)}-\sqrt{\varepsilon_s(\omega)}}{\sqrt{\varepsilon_f(\omega)}+\sqrt{\varepsilon_s(\omega)}}$$

and $$\beta=\frac{2\pi L\sqrt{\varepsilon_f(\omega)}}{\lambda},$$

and λ is the wavelength. The reflection coefficient $R(\omega)=[r_{1fs}(\omega)]^2$. A more detailed discussion of features of the reflection spectrum of thin films on a substrate in the lattice-reflection region and their interpretation was published in Ref. 6.

The dielectric function of the film $\varepsilon_f(\omega)$ is considered in its classical additive form

$$\varepsilon_f(\omega)=\varepsilon_\infty+\sum_j \frac{S_j\omega_{tj}^2}{\omega_{tj}^2-\omega^2-i\omega\gamma_j}. \qquad (2)$$

In the calculation of the reflection coefficient $R(\omega)$ in formula (2) we varied the frequency of the jth TO mode ω_{tj}, its oscillator strength S_j, and the decay parameter γ_j. Figures 1 and 2 show good agreement between the calculated and experimental reflection spectra.

The frequencies of the TO modes for $Zn_{1-x}Cd_xSe$ films of different compositions are plotted in Fig. 3. An almost linear variation of the frequency ω_t as a function of the composition x is observed, which is characteristic of a unimodal system of alloys. In the interpretation of the lattice-reflection spectra it was noted that the frequencies of the TO mode are different for ZnSe films of different thickness: for a film with $L=1.1\,\mu$m the frequency $\omega_t=208\,\text{cm}^{-1}$ (in Fig. 3 it is represented by a filled square) whereas for a film with $L=2\,\mu$m it is equal to $206\,\text{cm}^{-1}$ (empty square). We measured the reflection spectrum of a bulk ZnSe crystal under identical conditions; for it $\omega_t=206\,\text{cm}^{-1}$. Consequently, for a thinner film the frequency of the TO mode exceeds its bulk value by $2\,\text{cm}^{-1}$, and this is not a measurement error, since the measurements were performed under identical conditions and the spectral resolution was not worse than $1\,\text{cm}^{-1}$. For $x=0.14$ and film thickness $L=0.8\,\mu$m, ω_t (represented in Fig. 3 by a filled square) also exceeds the interpolated value by roughly $2\,\text{cm}^{-1}$. Observation of an analogous effect for InGaSb films on a GaAs substrate was reported earlier in Ref. 7. This effect is apparently explained by the influence of elastic stresses arising from the lattice mismatch of the substrate and film although for the pair GaAs and ZnSe the degree of mismatch is very small. In this regard, it would be desirable to compare with bulk $Zn_{1-x}Cd_xSe$ of different composition. As was remarked above, we do not know of any infrared lattice-reflection studies on bulk crystals of $Zn_{1-x}Cd_xSe$.

The interpretation of the reflection curves shown in Fig. 2 is a first approximation, allowing one to judge as to the unimodal or bimodal character of rearrangement with composition of the vibrational spectrum of the alloy system $Zn_{1-x}Cd_xSe$. However, for films with Cd content between 0.22 and 0.38 the structure of the lattice vibrations of $Zn_{1-x}Cd_xSe$ are better modeled by two oscillators. An example of such an interpretation for $x=0.22$ is shown in Fig. 4. The solid thick line shows the calculated spectrum with one lattice oscillator ($\omega_t=199\,\text{cm}^{-1}$, $S=3.5$, $\gamma_t=10\,\text{cm}^{-1}$), and the points plot the calculated spectrum with two oscillators ($\omega_t=199$ and $218\,\text{cm}^{-1}$, $S=3.4$ and 0.15, $\gamma_t=9$ and $6\,\text{cm}^{-1}$). An additional weak oscillator with $\omega_t=218\,\text{cm}^{-1}$ is localized on the short-wavelength side of the main band and therefore cannot be associated with a manifestation of bimodality of the system, since it is far removed in frequency from the CdSe-like mode (for CdSe $\omega_t=169\,\text{cm}^{-1}$). We observed fine structure in the lattice-reflection spectra earlier in the bimodal alloy system $Cd_{1-x}Hg_xTe$ (Ref. 8), where it is associated with a manifestation of correlations in the spatial distribution of impurity atoms in the alloy. The question of the existence of such a structure in the unimodal system $Zn_{1-x}Cd_xSe$ requires additional study, and in particular, studies are needed in bulk crystals.

The unimodal character of the vibrational spectra of the alloy system $Zn_{1-x}Cd_xSe$ observed in the present measurements is extremely unusual for semiconductor alloys of

II–VI compounds. The current criterion for estimating the character of the rearrangement of the vibrational spectrum, based on the arguments expressed in Ref. 9 and formulated in Ref. 10, predicts a bimodal type of rearrangement for the alloy system $Zn_{1-x}Cd_xSe$. The essence of the criterion for realization of bimodal rearrangement in an $(AB)C$ alloy is that the vibrational perturbation energy for substitution of a B atom by an A atom exceeded the vibrational interaction energy in lattice of the binary compound BC. For the binary compound CdSe the criterion reduces to

$$\frac{|\Delta m|}{M}-\frac{3\Omega}{2\omega_t^2+\omega_l^2}>1,$$

where Δm is the mass defect for substitution of Cd by Zn in CdSe, Ω is the frequency of the local mode of Zn in CdSe, M is the reduced mass, ω_t and ω_l are the frequency of the transverse mode and the frequency of the longitudinal mode for CdSe. Substitution of the corresponding parameters shows that the criterion of bimodality is fulfilled, but it follows from experiment that the alloy system $Zn_{1-x}Cd_xSe$ is unimodal.

This work was carried out with the financial support of the Russian Fund for Basic Research (Project No. 97-02-16791).

*)E-mail: vodopian@sci.lebedev.ru

[1] D. Olegro, P. Raccah, and J. Faurie, Phys. Rev. B **33**, 3819 (1986).
[2] P. Gingo, M. De Vittorio, R. Rinald, and R. Cingolani, Phys. Rev. B **54**, 16934 (1996).
[3] M. Strassberg, V. Kutzer, U. Pohl, A. Hoffman, I. Broser, N. N. Ledentzov, D. Bimberg, A. Rosenauer, U. Fischer, D. Gerthsen, I. L. Krestikov, M. V. Maximov, P. S. Kop'ev, and Zh. I. Alferov, Appl. Phys. Lett. **72**, 942 (1998).
[4] O. Brafman, Solid State Commun. **11**, 447 (1972).
[5] H. W. Verleur, J. Opt. Soc. Am. **58**, 1356 (1968).
[6] S. P. Kozyrev, Fiz. Tverd. Tela (St. Petersburg) **36**, 3008 (1994) [Phys. Solid State **36**, 1601 (1994)].
[7] M. Macler, Z. Feng, and S. Perkowitz, Phys. Rev. B **46**, 6902 (1992).
[8] S. P. Kozyrev, V. N. Pyrkov, and L. K. Vodop'yanov, Fiz. Tverd. Tela (Leningrad) **34**, 2372 (1992) [Sov. Phys. Solid State **34**, 1271 (1992)].
[9] Y. Onodera and Y. Toyozawa, J. Phys. Soc. Jpn. **24**, 341 (1968).
[10] J. Dow, W. Packard, H. Blackstead, and D. Jenkins, *Dynamical Properties of Solids: Phonon Physics*, Vol. 7, edited by G. Hortoy (1995), p. 349.

Translated by Paul F. Schippnick

Study of the electro-absorption spectrum of a nickel acceptor exciton in a ZnO:Ni crystal based on a calculation of vibrations associated with a Ni^{+1} impurity

A. N. Kislov,*) V. G. Mazurenko, V. I. Sokolov, and A. N. Varaksin

Urals State Technical University, 620002 Ekaterinburg, Russia
(Submitted September 2, 1998)
Fiz. Tverd. Tela (St. Petersburg) **41**, 986–990 (June 1999)

Localized vibrations in ZnO crystals due to the substitution impurity Ni^{+1} are modeled. The calculations were performed in the shell model using a recursive method for vibrations with A_1 and E type symmetry. Numerical calculations allowed us to analyze the vibronic structure in the electro-absorption spectra for nickel acceptor excitons in ZnO:Ni. © *1999 American Institute of Physics.* [S1063-7834(99)01206-X]

The systematic study over the last several years of electronic–vibrational states of impurity $3d$ elements in II–VI semiconductor compounds has been motivated by the wide practical applications such systems lend themselves to. Of especial interest here are hydrogenlike states, which are called donor excitons (DE) or acceptor excitons (AE) of the $3d$ impurity.[1] Hydrogenlike states form when the number of electrons in the $3d$ shell changes by one. Experimental studies of such excited states of the $3d$ impurity employ different methods to observe the absorption or luminescence spectra. The presence of intracenter states along with the hydrogenlike excitations often leads to nonradiative transitions from the hydrogenlike states to intracenter states. This limits radiative decay of the acceptor excitons or donor excitons of the $3d$ impurity and consequently the use of luminescence methods. A promising and more efficient method is the modulation electro-absorption method,[1] which records changes in the absorption coefficient in an electric field. In the electro-absorption spectra a DE or AE non-phonon line is always accompanied by a complicated vibrational background which is due to creation or annihilation of phonons in the crystal.

In studies of hydrogenlike excitation of the $3d$ impurity situations can arise in which it is quite hard on the basis of the experimental information to specify the type of this excitation, for example, for a crystal of ZnO:Ni. Donor and acceptor excitons of the $3d$ impurity interact differently with the lattice vibrations; therefore a determination of the type of the hydrogenlike excitation can be based on an analysis of the shape of the vibronic echoes of the non-phonon line of the electro-absorption spectrum. An interpretation of the vibrational background presupposes a theoretical study of the background spectrum of the defective crystal.

Mel'nichuk *et al.*[2] analyzed the vibronic structure of the electro-absorption spectrum of ZnO:Ni. However, the vibronic echo was interpreted by comparing it with the calculated vibrational spectrum of an ideal crystal. On the basis of their calculations, the authors concluded that they had observed the nickel donor-exciton spectrum. This analysis is probably not entirely correct since it does not take account of the appearance of defect-induced vibrations.

In the present work we model the vibrational spectrum of the ionic–covalent crystal ZnO with a nickel impurity $Ni^{+1}[3d^9]$ charged relative to the crystalline lattice, using a recursive method in the shell model. On the basis of our calculations we arrived at an interpretation of the vibronic wing of the non-phonon line of the electro-absorption spectrum in ZnO:Ni,[3] which suggests that this spectrum characterizes the $[d^9h]$ nickel acceptor exciton arising in the transition $[d^8]\rightarrow[d^9h]$.

1. TECHNIQUE AND RESULTS OF CALCULATIONS

The self-consistent approach currently in favor for studying the vibrational background of the non-phonon line of the electro-absorption spectrum of the nickel acceptor exciton in ZnO:Ni theoretically entails, first of all, a calculation of the dynamics of the crystal matrix with the defect, allowing for the distortion of the crystalline lattice due to the presence of the defect and, second, a consideration of the change in the electron–phonon interaction associated with the transition $[d^8]\rightarrow[d^9h]$. In a numerical simulation of the lattice dynamics of a defective crystal and in a calculation of the lattice distortion caused by the defect, an important question is how to correctly describe the interaction between the defect and the remaining atoms of the crystal and also between the atoms of the crystal matrix. The traditional approach to practical calculations of various physical characteristics of the oxides of many elements employs the approximation of pairwise central interactions.[4–7] The pairwise interaction potential between the atoms is the sum of a short-range term and a long-range Coulomb term. The first term is approximated by the well-known Born–Mayer potential and by a potential describing the van der Waals interaction. The Coulomb part is written in the form of an interaction of point charges. In the approach under consideration the electron (inertialess) polarization of the atoms is described in the shell model. Note that along with pairwise interaction potentials obtained from a quantum-mechanical calculation,[4] empirical potentials obtained by fitting various physical quantities of the crystal to their experimental values are also widely used.[5–7]

In light of the complexity of the structure of the nickel acceptor exciton, a theoretical study of its interaction with the lattice vibrations is fraught with difficulty. To analyze the vibrational background of the electro-absorption spectrum of the nickel acceptor exciton in zinc oxide, we numerically modeled the phonon spectrum for a somewhat simplified system; specifically, instead of the nickel acceptor exciton, we considered a Ni^{+1} impurity. Therefore, our analysis of the vibrational background of the non-phonon line of the electro-absorption spectrum of the nickel acceptor exciton is based on results of a simulation of the lattice dynamics of $ZnO:Ni^{+1}$.

For nickel-ion (Ni^{+1}) doped zinc oxide with würzite structure, we used the shell-model parameters: the charge of the ion shell and the ''nucleus–shell'' coupling constant, and also the parameters of the short-range part of the pair potential, which for the interaction of the Ni^{+1} ion with the remaining ions were assumed to be the same as in a crystal of NiO (Ref. 7), and for the interaction of the Zn^{+2} ion were assumed to be the same as in a crystal of ZnO (Ref. 8). In all of the calculations we took account of the short-range interion potential out to second-nearest neighbors inclusive.

The static distortion of the crystalline lattice in ZnO by the substitution impurity Ni^{+1} was calculated in the approximation of the molecular statics method[9] without taking into account compensation of excess charge. The calculations showed that the nearest neighbors of the Ni^{+1} impurity are quite removed from it. The nature of the lattice distortion near the Ni^{+1} ion accords with the fact that the Ni^{+1} impurity has a negative excess charge relative to the lattice. The equilibrium position of the nearest O^{-2} ion located on the hexagonal *C* axis is shifted by 0.275 Å, and the remaining three nearest O^{-2} ions are shifted by 0.25 Å. The displacements of the equilibrium positions of the ions of the next coordination sphere (CS) are an order of magnitude smaller than for the four given O^{-2} ions; therefore they were neglected in the lattice dynamics calculations. For the equilibrium configuration of the $ZnO:Ni^{+1}$ lattice so obtained, we calculated the energy of formation of the substitution impurity Ni^{+1}, which was found to be equal to 18.4 eV.

The point defect appearing in the crystal alters the frequencies of the normal vibrations and consequently the total density of phonon states of the ideal crystal infinitesimally, with the exception of the case when a local or gap vibration arises. However, the form of the crystal vibrations near the defect due to alteration of the force constants and mass can vary substantially. In the presence of a defect that is charged relative to the crystalline lattice the lattice perturbation due to the Coulomb interaction is not localized in a small neighborhood of the defect. Note that such modifications of the crystal vibrations also occur in response to changes in the electronic state of the defect.

In the various physical processes in which the defect participates the motion of the ions nearest it usually plays a huge role. For example, for electronic–vibrational transitions at the impurity center, motion of the ions around the impurity is the main determinant of the nature of the vibrational structure accompanying the non-phonon line. This is because the electrons localized near the impurity most strongly interact with vibrations of the ions of the first coordination spheres.

To examine the local lattice dynamics it is convenient to use a function called the local density of phonon states (LDPS). This function describes the dependence of the square of the amplitude of the displacement of a certain atom on the frequency of the normal vibrations of the crystal.[10] Note that summing the local densities of phonon states over nonequivalent atomic displacements for an ideal crystal allows one to reconstruct the total density of phonon states for it. An important property of the LDPS is that it can be used to detect vibrations associated with the appearance of a different kind of defect. The maxima in the LDPS of a crystal with a defect that do not coincide with the maxima of the LDPS of an ideal crystal determine the frequency of the localized vibration induced by the defect.

In an analysis of the vibronic wing of the electronic–vibrational spectrum of a defective crystal, it is important to take into account the properties of the symmetry point group of the defect, which permit a considerable simplification of such an analysis. This is because the electrons belonging to the defect interact only with vibrations of a definite symmetry Γ. Therefore, it is reasonable to work with symmetrized displacements of the atoms, whose frequency dependence is characterized by a symmetrized LDPS (SLDPS). The SLDPS is expressed in terms of the imaginary part of the diagonal element of the Fourier transform of the one-particle Green's function for the displacements. The latter in turn is determined by the dynamical matrix of the crystal for the direct space.[11] Using a recursive method, we transform the dynamical matrix into tridiagonal form. In this case the diagonal element of the Green's function takes the form of an easily calculated continued fraction.

Simulation of the local lattice dynamics of ionic crystals, especially in the presence of a charged impurity, requires an accurate calculation of the dynamical matrix with the long-range Coulomb interaction explicitly taken into account, which entails the construction of a cluster of large dimensions. Our study showed that depending on the type of crystal, the required level of accuracy of the calculations is achieved if we consider a cluster with a radius of approximately 15 to 25 Å. In this case the cluster usually contains 1000–1500 atoms. In the present calculations for $ZnO:Ni^{+1}$ the dynamical matrix was constructed in the shell model for 1000 atoms. And in our calculation of the diagonal elements of the dynamical matrix we considered a cluster containing 4200 atoms.

The calculated total density of phonon states of an ideal ZnO crystal may serve as a check on the accuracy of using these dynamical models and this approach to the lattice dynamics problem in our calculations (Fig. 1). Comparison of the results of our calculation and a calculation based on the valence force model by integrating over the Brillouin zone[2] shows clearly that their correlation is satisfactory. The difference in the position of the photon forbidden region and of some maxima is due to limitations associated with the shell model used in the calculations. Note that according to electron[12] and neutron[13] spectroscopic data the gap between the acoustic and optical regions occupies the interval from 8.0 to 11.5 THz, and the entire frequency spectrum ends at

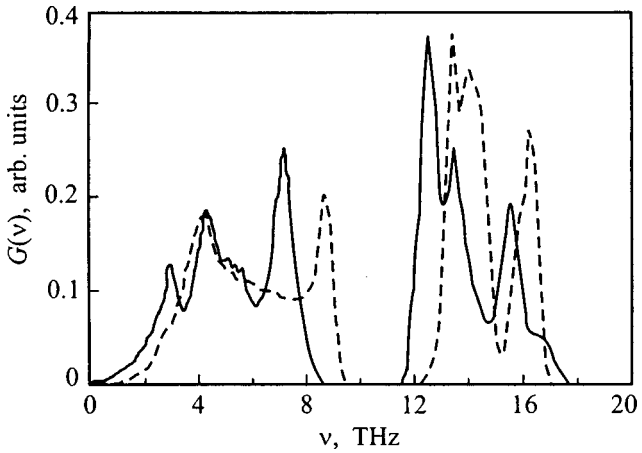

FIG. 1. Total density of phonon states in a ZnO crystal. Solid line—result of calculation in Ref. 2, dashed line—our calculation.

17.7 THz. Our calculated values for the width of the gap are equal to 9.0–12.3 THz, and for the upper limit of the frequency spectrum, 16.9 THz.

In the present work, as our initial vectors for the recursive method we chose the symmetrized displacements that are the normal coordinates of the region around the Zn^{+2} ion or the Ni^{+1} impurity replacing it, bounded by the first coordination sphere. The center of this region in ZnO occupies a position characterized by the symmetry point group C_{3v}. According to a group-theoretic analysis, for the given region there are nine normal coordinates: $4A_1$, A_2, and $5E$. It was for these coordinates that we calculated the symmetrized local density of phonon states.

Figure 2 plots the symmetrized local density of phonon states projected onto displacements, of A_1 and of E symmetry, of the ions of the first coordination sphere for ZnO:Ni^{+1}. A distinguishing feature of this figure is the presence of four intense peaks defining two resonance vibrations of symmetry A_1, the gap vibration of symmetry A_1, and the local vibration of symmetry E. The resonant vibration located in the acoustic band at the frequency $\nu_{Ni}(A_1)=2.4\,\mathrm{THz}$ is associated with motion of the Ni^{+1} impurity, and in the resonant vibration, with the frequency $\nu_O(A_1)=12.3\,\mathrm{THz}$ O^{-2} ions take part. The gap vibration with frequency $\nu_O(A_1)=10.2\,\mathrm{THz}$ is induced by the Ni^{+1} impurity and by the three O^{-2} ions. The local vibration with frequency $\nu_O(E)=17.2\,\mathrm{THz}$, located near the upper limit of the optical band, whose calculated frequency is 16.9 THz, is associated with motion of the O^{-2} ions.

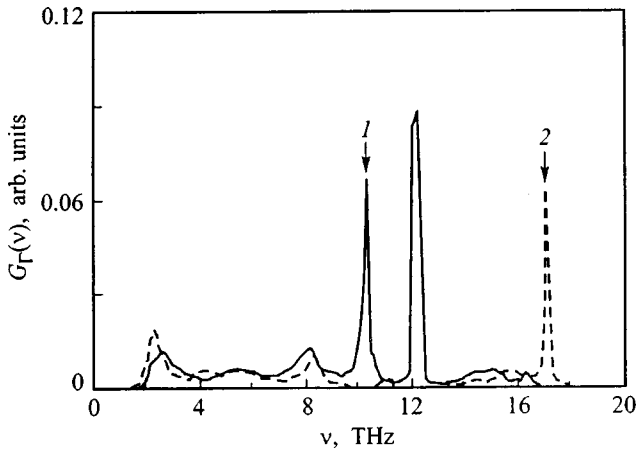

FIG. 2. Symmetrized local densities of phonon states, calculated for a ZnO:Ni^{+1} crystal, projected onto displacements of the ions of the first coordination sphere with symmetry A_1 (solid curve) and with symmetry E (dashed curve).

2. DISCUSSION OF RESULTS

The nickel acceptor exciton is an excited hydrogenlike state of the Ni impurity and is denoted as $[d^9h]$ (Ref. 1). This formation arises in an electromagnetic field of frequency ω_a, during the transition of a hole from a $3d$ shell of the Ni^{+2} impurity to the weakly localized hydrogenlike orbit on which the hole is held by the Coulomb field by the reformed Ni^{+1} impurity. Schematically, the process of formation of a nickel acceptor exciton is written as follows: $Ni^{+2}+\hbar\omega_a\rightarrow[Ni^{+1}h]$ or $d^8+\hbar\omega_a\rightarrow[d^9h]$. It follows from Refs. 1 and 14 that the nickel acceptor exciton state is constructed from states of a Ni^{+1} ion and a hole from some valence subband, where this hole is found in a hydrogenlike orbit with principal quantum number n.

The complete representation of a nickel acceptor exciton in zinc oxide for the ground state is given by the direct product $\Gamma_{AE}=\Gamma(d^9)\times\Gamma(s)\times\Gamma(v)$ of irreducible representations (IR) $\Gamma(d^8)$, $\Gamma(s)$, and $\Gamma(v)$ describing the ground state of the d^9 configuration, the wave function of a hole in a hydrogenlike state of s type with quantum number $n=1$, and the top of the valence band, respectively. Thus, the ground state of the nickel acceptor exciton Γ_{AE} in the hexagonal crystal ZnO with the spin–orbital interaction taken into account is a superposition of states transforming according to the irreducible representations Γ_1, Γ_2, and Γ_3.

Since a nickel ion on which a process occurs involving the formation of an acceptor exciton in ZnO is found in the trigonal field of symmetry C_{3v}, the electric dipole moment operator for an electromagnetic field with π polarization transforms according to the irreducible representation Γ_1, and with σ polarization, according to the irreducible representation Γ_3. According to the selection rules, the transition from the initial state d^8 of symmetry Γ_1 (with spin taken into account) to the final state $[d^9h]$ is allowed in the electric-dipole approximation for both polarizations. Here the vibrations interacting with the given transition, regardless of the polarization type of the electromagnetic field, possess symmetry A_1 or E. Consequently, the phonon wings of the electro-absorption spectrum for nickel acceptor excitons on which all A_1 and E vibrations are manifested should have the same type of features for different polarizations. This fact is well illustrated in Fig. 3.

The shape of the vibronic satellite of the non-phonon line of the electro-absorption line of the nickel acceptor exciton is determined in general by the vibrational states of the crystal with defect found in the initial d^8 state and the final $[d^9h]$ state. In a number of cases in the analysis of the vibrational background, a simple formula is used which does not take account of changes in the elastic constants.[15,16] In

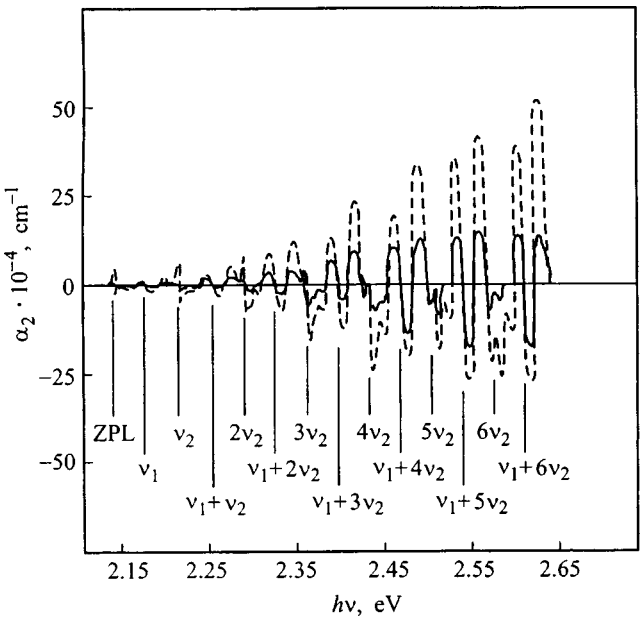

FIG. 3. Electro-absorption spectrum in ZnO:Ni (Ref. 3). The dashed line is for σ polarization, and the solid line is for π polarization.

this formula the vibrational background is expressed in terms of the linear part of the expansion in normal coordinates of the electron–phonon coupling of the transition, on the one hand, and the density of phonon states of the crystal with defect in the initial state, on the other. For a nickel acceptor exciton this formula is probably not applicable. This is because, first, the transition $d^8 \rightarrow [d^9 h]$ occurs for a system with an intermediate electron–phonon interaction; therefore the calculation cannot be restricted to the linear part of the electron–phonon coupling of the transition. Second, in the transition under consideration a strong perturbation of the vibrations of the crystal is observed, as a consequence of which information is also required about the vibrational state of the crystal with defect found in the final $[d^9 h]$ state.

However, if we analyze the contribution to the vibronic wing formed by single-phonon processes via a numerical calculation, it is sufficient to consider the linear part of the electron–phonon coupling of the transition. To obtain numerical values of the frequency dependence of the electron–phonon interaction even in the linear approximation in the normal coordinates is a complicated task. In our analysis of the vibrational background of the electro-absorption spectrum of the nickel acceptor exciton we assumed that the frequency dependence of the electron–phonon coupling of the transition is determined primarily by vibrations of the ions nearest the defect. Proceeding along this line, we interpreted the vibrational background without calculating the electron–phonon and exciton–phonon interactions, basing the interpretation only on the symmetrized local density of phonon states calculated for ZnO with a Ni^{+2} impurity (Ref. 8) and with a Ni^{+1} impurity.

Note that certain points in the electro-absorption spectrum correspond to maxima of the absorption spectrum. In our case, for a nickel acceptor exciton in ZnO:Ni these points in the electro-absorption spectrum are zero-crossing points or points associated with the largest slope in the regions of fall-off of the absorption coefficient. These points are marked by vertical lines in Fig. 3.

The electro-absorption spectrum depicted in Fig. 3 was measured at liquid-helium temperature $T = 4.2$ K; therefore its vibronic part is shifted into the Stokes region of the spectrum and is associated with phonon creation. The vibrational background of this spectrum has a complicated structure due to the superposition of multiphonon transitions. Noting that the electron–phonon interaction for the transition in question $d^8 \rightarrow [d^9 h]$ is not small, guided by Ref. 17 we conclude that the intensity of a given multiphonon transition grows with increasing order of the phonon process and reaches its maximum at an order that is determined by the Franck–Condon principle. This is in good agreement with the fact that in the experimental spectrum (Fig. 3) the intensity of the vibrational background grows with increasing frequency. Among the features in the region of the single-phonon contribution to the vibrational background it is possible to make out two intense structures. Judging from Fig. 3, one is found at a frequency $\nu_1 = 9.0$ THz from the non-phonon line and falls in the region between the acoustic and optical bands of the single-phonon states of the ZnO crystal, and the second, with frequency $\nu_2 = 17.8$ THz, lies above the upper boundary of the allowed frequencies of the single-phonon states. These structures correlate very well with the two intense peaks labeled 1 and 2 in the calculated SLDPS spectra of type A_1 and E for ZnO:Ni^{+1} (Fig. 2).

Note that features belonging to single-phonon transitions are reproduced in the region of multiphonon transitions in various combinations. Such combinations of the most intense features are shown in Fig. 3. It can be seen that the intense features correspond to the series for the local vibration $k\nu_2$, where k is the order of the phonon process, and to Raman echoes of the form $\nu_1 + k\nu_2$. The latter apparently arise because the vibrational background receives another contribution from a mechanism due to the anharmonic interaction of the local vibration with the remaining vibrations of ZnO:Ni. As a result of this interaction, the local vibration and its multiphonon echo are accompanied by some vibronic structure.[17] Since the local vibration has E symmetry, it can interact with vibrations of symmetry A_1 and E. Therefore, the structure of the vibronic part associated with the local vibration is determined by the vibrations of the same symmetry as in the absence of the local vibration. In this case, the interaction of the local vibration and the gap vibration govern the appearance of the strongest features in the vibrational part of the electro-absorption spectrum of the nickel acceptor exciton in ZnO:Ni.

To summarize, the above analysis of the multiphonon vibronic wing of the non-phonon line of the electro-absorption spectrum of ZnO:Ni based on a model calculation of localized lattice states near a Ni^{+1} charged impurity center has advanced our understanding of the vibrational structure of the electro-absorption spectrum and suggests that the spectrum corresponds to the nickel acceptor exciton. This newly won understanding cannot yet be called complete. More detailed experimental results are still needed, including the transformation of the electro-absorption spectra

with increasing temperature, and also the Raman spectra.

This work was supported by the Russian Foundation for Basic Research (Projects No. 96-02-16278-a and No. 96-02-19785).

*)E-mail: ank@dpt.ustu.ru

[1] V. I. Sokolov, Fiz. Tekh. Poluprovodn. **28**, 545 (1994) [Semiconductors **28**, 329 (1994)].
[2] S. V. Mel'nichuk, V. I. Sokolov, T. G. Surkova, and V. M. Chernov, Fiz. Tverd. Tela (Leningrad) **33**, 3247 (1991) [Sov. Phys. Solid State **33**, 1833 (1991)].
[3] V. I. Sokolov, A. N. Mamedov, A. N. Reznitskiĭ, G. A. Emel'chenko, and L. G. Kolinova, Fiz. Tverd. Tela (Leningrad) **27**, 3319 (1985) [Sov. Phys. Solid State **27**, 1998 (1985)].
[4] J. Kendrick and W. C. Mackrodt, Solid State Ionics **8**, 247 (1983).
[5] M. J. L. Sangster and A. M. Stoneham, Philos. Mag. B **43**, 597 (1981).
[6] G. V. Lewis and C. R. A. Catlow, J. Phys. C **18**, 1149 (1985).
[7] A. M. Stoneham and M. J. L. Sangster, Philos. Mag. B **52**, 717 (1985).
[8] A. N. Kislov and V. G. Mazurenko, Fiz. Tverd. Tela (St. Petersburg) **40**, 2180 (1998) [Phys. Solid State **40**, 1977 (1998)].
[9] Yu. N. Kolmogorov and A. N. Varaksin, Dep. at VINITI, No. 2395 (1989), 137 pp.
[10] P. E. Meek, Philos. Mag. **33**, 897 (1976).
[11] J. Hafner, Helv. Phys. Acta **56**, 257 (1983).
[12] A. W. Hewat, Solid State Commun. **8**, 187 (1970).
[13] K. Thoma, B. Dorner, G. Duesing, and W. Wegener, Solid State Commun. **15**, 1111 (1974).
[14] S. A. Kazanskiĭ, A. L. Natadze, A. I. Ryskin, and G. I. Khil'ko, Izv. Akad. Nauk SSSR, Ser. Fiz. **37**, 670 (1973).
[15] A. Maradudin, Solid State Phys. **18**, 273 (1966); **19**, 1 (1966).
[16] I. V. Ignat'ev and V. V. Ovsyankin, in *Spectroscopy of Crystals* [in Russian] (Nauka, Leningrad, 1983).
[17] K. K. Rebane, *Impurity Spectra of Solids: Elementary Theory of Vibrational Structure* (Plenum Press, New York, 1970).

Translated by Paul F. Schippnick

Shubnikov–de Haas effect in tricrystals of the system of alloys $Bi_{1-x}Sb_x$ ($x=0.1$; 0.13) with *n*-type conductivity

F. M. Munteanu, Yu. A. Dubkovetskiĭ, and G. A. Kiosse

Institute of Applied Physics, Moldavian Academy of Sciences, MD-2028 Kishinev, Moldova

A. Gilewski

International Laboratory of Strong Magnetic Fields and Low Temperatures, 53-529 Wrocław, Poland
(Submitted October 22, 1998)
Fiz. Tverd. Tela (St. Petersburg) **41**, 991–993 (June 1999)

The Shubnikov–de Haas effect has been investigated in tricrystals of the alloy system $Bi_{1-x}Sb_x$ ($x=0.1$; 0.13) with *n*-type conductivity in stationary (up to 14 T) and pulsed (up to 40 T) magnetic fields. Reconstruction of the internal boundary of the tricrystals was observed, along with a number of new component oscillations of $\rho(B)$ indicating a rotation of the constant-energy surfaces of the L electrons on the intercrystallite boundary at an angle of $\sim 74°$ in the binary–trigonal plane. © *1999 American Institute of Physics.* [S1063-7834(99)01306-4]

Recently, component Shubnikov–de Haas (ShdH) oscillations have been detected in bicrystals of the alloy system $Bi_{1-x}Sb_x$ with *n*-type conductivity, testifying to rotation of the effective-mass ellipsoids of the L electrons at the interfaces of the crystallites (relative to their position in the single-crystal blocks by roughly 74° (Refs. 1 and 2). The intercrystallite boundary of these bicrystals was very nearly a coherent twin; however, a different contribution of the dislocations to the oscillation plot was observed[3] for small-angle and large-angle boundaries. Of significant interest are objects with more complicated mechanical stresses, such as tricrystals (tricrystal transitions were used in Ref. 4 to investigate the symmetry of the paired state in HTSC's), where three individual crystals meet, having different rotation angles, and where large accumulations of defects and dislocations are observed which are intertwined in a complicated way.

In the present study we investigated two tricrystals of semiconductor alloys belonging to the system $Bi_{1-x}Sb_x$ ($x=0.1$; $x=0.13$) with *n*-type conductivity (the samples were intentionally doped with Te donor impurities). Note that the Fermi surface of these alloys consists of three heteroaxial quasi-ellipsoids centered at the L points of the Brillouin zone and tilted in the binary plane by $\sim 5°$ (Ref. 5).

The samples were prepared in the shape of a parallelepiped. The internal boundaries (*IB*) of the tricrystals, which had width $140 \leqslant L \leqslant 300$ nm, were nearly of the inclination type. The planes of the internal boundaries (*PIB*) were almost parallel to the trigonal axis C_3 of the crystallites. The tilt angle Θ_i of the crystallites for the sample T_1 ($x=0.13$) were $\Theta_1(AC)\sim 12°$, $\Theta_2(CB)\sim 6°$, and $\Theta_3(AB)\sim 4°$, and for the sample T_2 ($x=0.1$) they were $\Theta_1(AC)\sim 10°$, $\Theta_2(CB)\sim 4°$, and $\Theta_3(AB)\sim 2°$. Contacts to the internal boundaries were welded on by electrospark welding (a schematic illustration of the tricrystal with contacts is shown in the inset to Fig. 1). The composition of the samples was monitored by x-ray measurements. The total electron density N was determined from the Hall coefficient in a strong magnetic field (the classical limit) $R_\infty = -(eN)^{-1}$. In our samples, N was on the order of $1.2\times 10^{18}\,\mathrm{cm}^{-3}$ (T_1) and $1.36\times 10^{18}\,\mathrm{cm}^{-3}$ (T_2). The measurements in steady-state (up to 14 T) and pulsed (up to 40 T) magnetic fields were performed at the International Laboratory of Strong Magnetic Fields and Low Temperatures in Wrocław, Poland. The ShdH effect was investigated on setups which made it possible to record the magnetoresistance curves in the forward and reverse fields, compensate for the monotonic component, determine the harmonic frequencies by Fourier analysis, etc. Below we describe the main results of our measurements of the ShdH effect on the T_1 and T_2 samples.

It is well known that for the $B \| C_2$ orientation of the magnetic field in single crystals of the alloy $Bi_{1-x}Sb_x$ with *n*-type conductivity two harmonics of the $\rho(B)$ oscillations are observed: a low-frequency harmonic, associated with the two (smallest) cross sections of the two equivalent quasi-ellipsoids of the L electrons, and a high-frequency harmonic, characterizing the (maximum) cross section of the third quasi-ellipsoid. The oscillations are widely separated in magnetic field because of the anisotropy of the Fermi surface of the L electrons. As can be seen from Figs. 1 and 2b, in tricrystals with orientations of the magnetic field $B \perp PIB$ (close to the C_2 axis of the crystallites) three harmonics of oscillations of the magnetoresistance are clearly revealed, and their frequencies do not depend on the internal boundaries of the specific tricrystal in question. For example, for the tricrystal T_1 the frequencies of these oscillations are equal respectively to $\Delta_1(1/H)^{-1} \approx 2.7T$, $\Delta_2(1/H)^{-1} \approx 52.6T$, and $\Delta_3(1/H)^{-1} \approx 29.7T$. The additional frequency $\Delta_3(1/H)^{-1}$ in the oscillation curves $\rho(B)$, which is not observed in the single crystals, arises beyond the quantum limit for a low-frequency harmonic. We found that the phase of these oscillations, like the sequencing of the oscillation peaks for the spins aligned with the field and against it in the low-frequency harmonic depends on the state of the internal boundaries. This is especially noticeable in the oscillation

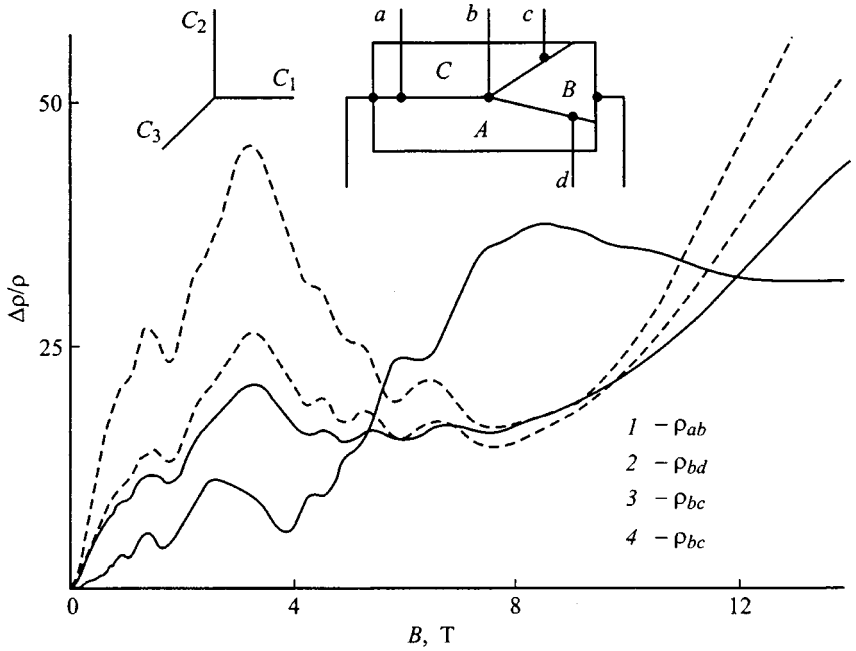

FIG. 1. The ShdH effect in the tricrystal T_1 (stationary magnetic fields) at 4.2 K for $B \perp PIB$. For curves *2* and *4* the magnification scale is $2\times$, and for curve *3* it is $3\times$. Curve *3* was taken before heat treatment, and curve *4* after. Inset: diagram of sample with contacts (*A*,*B*,*C*—single-crystal blocks.

plot $\rho(B)$ on the internal boundary between the single-crystal blocks *B* and *C* [*IB*(*BC*)], where the additional component oscillates in antiphase and the sequencing of the oscillation maxima with opposite spin is violated. After heat treatment the *IB*(*BC*) returns to its equilibrium state, the phase of the oscillations changing by π, and the normal sequencing of Landau sublevels is regained (Fig. 1). Reconstruction of the *IB*(*BC*) most likely occurred with a shift of the crystallographic planes by a quarter period in the directions opposite the two spin directions.[6] This is indicated by direct calculations of the spin splitting factor $\gamma = \Delta_{sp}/\Delta_{orb}$ and the Dingle temperature T_D of the *L* electrons for $B \| C_2$, specifically: before heat treatment for *IB*(*BC*) we had $\gamma \approx 0.32$ and $T_D \approx 1.4$ K; after heat treatment their values were $\gamma \approx 0.7$ and $T_D \approx 0.5$ K.

For the magnetic field oriented parallel to the *PIB* (close to the C_3 axis of the crystallites) in tricrystals of the alloy system $Bi_{1-x}Sb_x$ with *n*-type conductivity, like in the bicrystals,[1,2] two frequencies of oscillations are observed, whereas in single crystals for this field orientation only one frequency is seen, associated with large cross sections of the Fermi surface of the *L* electrons. Their ratio $k = \Delta_1(1/H)^{-1}/\Delta_2(1/H)^{-1}$ $[k_1 \sim 4(T_1);\ k_2 \sim 6(T_2)]$ depends on the concentration of the components in the alloys and the degree of filling of the constant-energy surfaces. For the low-frequency harmonic specific to the bicrystals and tricrystals, the oscillation maxima in the quantum region of the fields are split by the spin, and the phase of the oscillations in the limit $1/B \to 0$ extrapolates to an integer value. The high-frequency harmonic shows up (Fig. 2) mainly in strong magnetic fields ($B > 7$ T), and spin splitting is absent in the last maxima of the oscillations.

A distinguishing characteristic of the oscillation dependences of the magnetoresistance in tricrystals for the magnetic field oriented in the *PIB*(*AC*) (close to the direction of the C_1 axis—the bisectrix—of the crystallites) is the fact that besides the two types of oscillations with frequency ratio 2:1 that are observed in single crystals and bicrystals, for $B > 10$ T a component appears that is associated with large cross sections of the Fermi surface of the *L* electrons.

The results obtained in tricrystals for $B \| PIB$ indeed confirm the conclusions of Refs. 1 and 2 about the formation on the internal boundaries of a discrete spectrum of electron states[7] and a new type of symmetry associated with rotation of the principal axes of the Fermi surface. In this regard, the new low-frequency harmonic characterizes cross sections of the *b* and *c* quasi-ellipsoids, which are identical in magnitude (see the inset to Fig. 2) and whose principal axes are tilted at the internal boundaries by $\sim 74°$ relative to their orientations in the single-crystal block. The high-frequency harmonic is related to the area of the extremal cross section

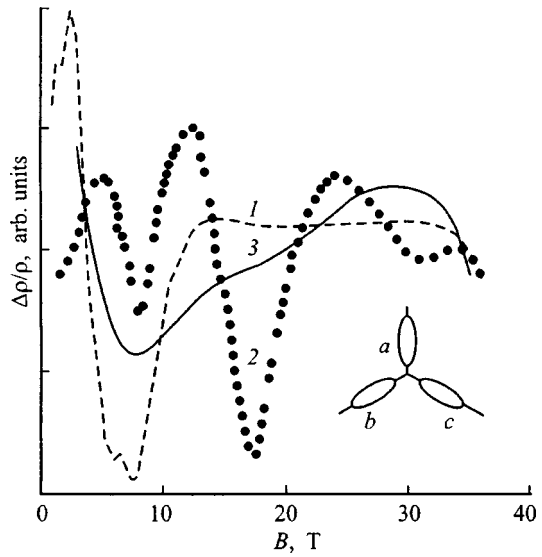

FIG. 2. The ShdH effect in the tricrystal T_1 (pulsed magnetic fields) at 4.2 K. The monotonic part of $\rho(B)$ has been subtracted out. *1*—$B \perp PIB \perp J$, *2*—$B \| PIB \perp J$, *3*—$B \| PIB \| J$. Inset: electronic part of the Fermi surface of Bi–Sb alloys.

of the third quasi-ellipsoid (a), which hardly varies in magnitude upon rotation of the principal axes of this quasi-ellipsoid and always coincides with the area of the large cross sections of the three equivalent quasi-ellipsoids of the single-crystal block for $B \| C_3$. The measured angular dependences of the periods of the oscillations of the tricrystals in the binary–trigonal plane of the single-crystal block show that the low-frequency harmonic for $B \| PIB$ makes a smooth transition (thereby describing a branch of the ellipsoid) to the additional frequency at $B \perp PIB$ in line with the concept of rotation of the Fermi surface at the internal boundary.

The appearance of a frequency associated with large cross sections of the Fermi surface of the L electrons in tricrystals for field orientations in the $PIB(AC)$ (for single crystals and bicrystals this harmonic is absent) is evidence of a contribution from the Fermi surface of the tilted [relative to the $IB(AC)$] intercrystallite boundaries to the oscillation plot $\rho(B)$. Only in the case when the Fermi surface is rotated on these internal boundaries can cross sections close to the maximum value be oriented perpendicular to the direction of the magnetic field.

The authors express their deep gratitude to J. Klamut and T. Palewski for their assistance with this work at the International Laboratory.

[1] F. Munteanu, M. Onu, Yu. Dubkovetskii, and V. Kistol, Czech. J. Phys. **46**, Suppl. S4, 2039 (1996).
[2] F. M. Munteanu and Yu. A. Dubkovetskii, Phys. Status Solidi B **203**, 473 (1997).
[3] F. M. Munteanu, M. Gliński, G. A. Kiosse, and V. G. Kistol, Fiz. Tverd. Tela (Leningrad) **33**, 1881 (1991) [Sov. Phys. Solid State **33**, 1058 (1991)].
[4] Z. G. Zou, Q. Y. Ying, J. H. Miller, Jr., J. H. Xu, and N. Q. Fan, J. Supercond. **8**, 679 (1995).
[5] G. A. Mironova, M. V. Sudakova, and Ya. G. Ponomarev, Zh. Éksp. Teor. Fiz. **78**, 1830 (1980) [Sov. Phys. JETP **51**, 918 (1980).
[6] D. Shoenberg, *Magnetic Oscillations in Metals* (Cambridge University Press, Cambridge, 1984).
[7] S. N. Burmistrov and L. B. Dubovskiĭ, Zh. Éksp. Teor. Fiz. **94**, 173 (1988) [Sov. Phys. JETP **67**, 1831 (1988)].

Translated by Paul F. Schippnick

Applicability of the empirical Varshni relation for the temperature dependence of the width of the band gap

I. A. Vaĭnshteĭn, A. F. Zatsepin,*) and V. S. Kortov

Urals State Technical University, 620002 Ekaterinburg, Russia
(Submitted June 9, 1998; accepted for publication October 27, 1998)
Fiz. Tverd. Tela (St. Petersburg) **41**, 994–998 (June 1999)

We have carried out a comparison of relations used to describe the temperature dependence of the width of the band gap in crystals. It is shown that for $kT \gg \hbar\omega$ the well-known Varshni relation can be obtained from the non-empirical Fan expression in explicit form taking account of the phonon statistics. We have calculated the temperature coefficient β of the width of the band gap for a number of materials in the range where the high-temperature condition is not met. We have found that the Varshni relation overestimates β, whereas calculations based on the Fan expression agree with experiment. © *1999 American Institute of Physics.* [S1063-7834(99)01406-9]

An important characteristic of the energy structure of solids is the temperature coefficient β of the width of the band gap E_g, which for most materials has a negative value.[1] The quantity $\beta = dE_g/dT$ is usually determined from the slope of the linear part of the temperature dependence $E_g(T)$, which, however, in the low-temperature region is strongly nonlinear.[2] Various empirical and semi-empirical methods are presently in widespread use which satisfactorily reproduce the shape of the observed dependence qualitatively.[3–6] As a rule, such calculations do not contain quantitative information about physical quantities, e.g., phonon energies, although there is no doubt that the electronic–vibrational interaction has a significant effect on $E_g(T)$. The main goal of the present work is to compare the applicability of the empirical Varshni relation[5] and the analytical Fan expression,[7] which explicitly satisfies the phonon statistics of the crystal, for approximating experimental data on the temperature dependence of the band gap $E_g(T)$, and also to demonstrate the existence of an interrelationship between these two expressions.

The linear-quadratic relation proposed by Varshni[5] and which has found widespread use for describing the temperature dependence of the band gap $E_g(T)$ has the form

$$E_g(T) = E_g(0) - \frac{\alpha_1 T^2}{\alpha_2 + T}, \tag{1}$$

where $E_g(0)$ is the width of the band gap at zero temperature, and α_1 and α_2 are empirical parameters which have no concrete physical significance. The constant α_2 having the dimensions $[\alpha_2] = [T]$ is taken to be close in value to the Debye temperature.[5,6] In the high temperature limit, when $T \gg \alpha_2$ it follows from Eq. (1) that $\alpha_1 \approx \beta$. In a number of cases the coefficients α_1 and α_2 turn out to be negative,[3,5] which in general complicates a physical interpretation of the recorded dependences. Nevertheless, despite the limited amount of information that can be extracted with it, expression (1) describes the experimentally observed shape of the temperature characteristic of $E_g(T)$ in a completely satisfactory way, as has been checked for a large variety of objects.[3,5,6,8]

At the same time, in the one-phonon approximation and second-order perturbation theory the temperature dependence of the width of the band gap can be represented as[7,9,10]

$$E_g(t) = E_g(0) - A(\langle n \rangle + \text{const}), \tag{2}$$

where A is the Fan parameter, which depends on the microscopic properties of the material;[11] $\langle n \rangle = [\exp(\hbar\omega/kT) - 1]^{-1}$ is the Bose–Einstein factor for phonons with energy $\hbar\omega$; and the constant controls the magnitude of E_g at zero temperature. In the theory of the broadening of electronic levels this constant is equal to zero;[9] in a treatment of energy level shifts, it is equal to unity;[7] and in a treatment of the exciton–phonon interaction an expression of the form (2) was obtained with this constant equal to 1/2 (Ref. 10).[1)] Assuming that the temperature on the right-hand side of Eq. (2) appears only in the phonon statistics, the adjustable parameters $E_g(0)$ and A can be treated as temperature-independent. Then in the calculation of the phonon energy the value of the indicated constant has no effect on the final result, and so we set it equal to zero in what follows.

Note that expression (2) does not take explicit account of the contribution of thermal expansion of the lattice. As was shown in Refs. 5 and 12, this contribution to the total temperature variation of the width of the band gap is on the order of 20% and to first order can be neglected. In addition, it may be assumed that at large temperatures the contribution of thermal expansion to the shift of the energy levels is also proportional to $\langle n \rangle$ (Ref. 12). In this case, the value of the parameter A obtained in the calculations takes account of both the internal (electron–phonon interaction) and the external (thermal expansion) contributions to the dependence $E_g(T)$.

A dependence analogous to expression (2), in which the variation of the width of the band gap is proportional to the

occupation number of the phonon states, can be written in the form[13]

$$E_g(T)=E_g(0)-D(\langle u^2\rangle_T-\langle u^2\rangle_0), \tag{3}$$

where D is a constant of the second-order deformation potential, $\langle u^2\rangle_T$ is the mean square displacement of the lattice atoms from their equilibrium positions at the temperature T, and $\langle u^2\rangle_0$ is the mean square displacement for zero vibrations. Expressing $\langle u^2\rangle_T$ in terms of the one-phonon model using Bose–Einstein statistics, for an oscillator with mass M we can identify a relation between the Fan parameter A and the constant D

$$A=\frac{\hbar}{\omega M}D. \tag{4}$$

It is clear from Eq. (2) that the parameter A has the dimensions of energy and coincides in magnitude with the change in the width of the band gap at the temperature at which the mean number of phonons responsible for the shift of the energy level of the band edges is equal to unity. A microscopic expression for the Fan parameter was given in Ref. 11

$$A=\frac{e^2}{\sqrt{2}\hbar}(m_0\hbar\omega)^{1/2}\frac{1}{4\pi\varepsilon}\left(\frac{1}{\varepsilon_\infty}-\frac{1}{\varepsilon_0}\right)\times\left[\left(\frac{m_c}{m_0}\right)^{1/2}+\left(\frac{m_h}{m_0}\right)^{1/2}\right], \tag{5}$$

where e is the charge of the electron, ε is the dielectric constant, ε_0 and ε_∞ are respectively the static and high-frequency dielectric constants, m_0 is the free electron mass, and m_e and m_h are the effective electron and hole masses, respectively. Expression (5), all the quantities in which are tabulated, can be used to evaluate the Fan parameter in the absence of experimental data on $E_g(T)$ itself.

To compare the applicability of relations (1) and (2) for describing the temperature dependence of the band gap $E_g(T)$, Fig. 1 shows examples of the fitting of experimental data for silicon and zinc selenide. As a criterion of the accuracy of reproduction of the shape of the observed dependences, we used the mean square error

$$\sigma^2=\frac{1}{n}\sum_{i=1}^{n}(E_{g_i}^{\exp}-E_{g_i}^{\mathrm{calc}})^2,$$

where the superscripts ''exp'' and ''calc'' indicate, respectively, experimental and calculated values of E_g. It is evident from Table I that the errors are comparable for all materials, not just the ones indicated above, and expressions (1) and (2) describe the experimental data with a high degree of accuracy.

In addition, Table I gives values of the Varshni coefficients (α_1 and α_2) taken from the original work and values of the Fan parameter (A) calculated by us according to expressions (2) and (5), and also values of A obtained in Refs. 14–16 including values obtained for amorphous modifications of some materials. As the phonon energy in the calculations based on formula (5) we took the energies of the longitudinal optical vibrations (Ref. 1 and literature cited therein). It is clear from Table I that for a number of materials the calculated values of the Fan parameters, obtained using formula (5), are similar to the values obtained using expression (2) for fitting the experimental data.

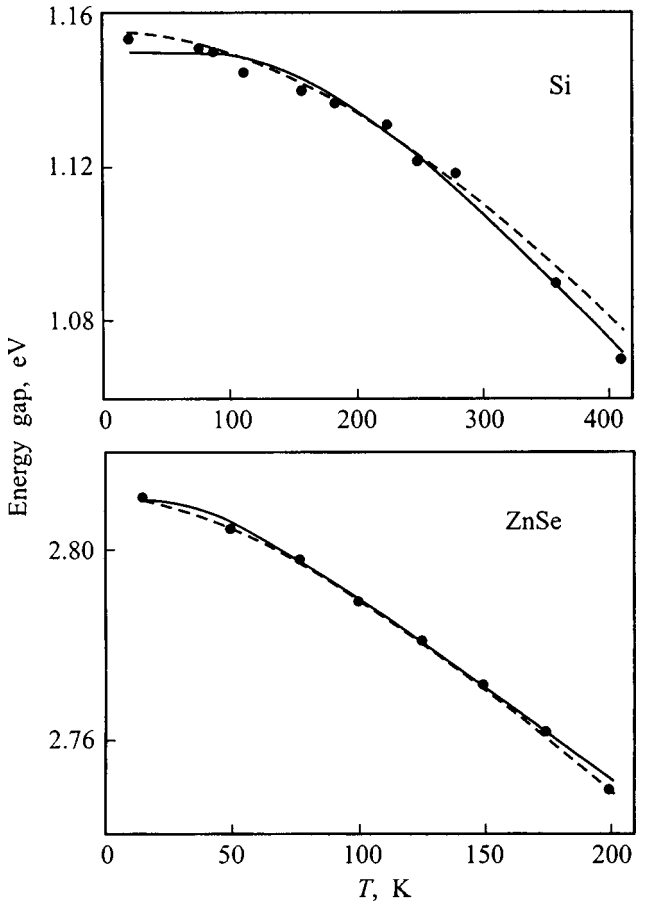

FIG. 1. Temperature dependence of $E_g(T)$ for silicon and zinc selenide. Points—experiment, Si (Ref. 5) and ZnSe (Ref. 8); dashed line—approximation (fit) using the Varshni formula (1); solid line—approximation using the Fan expression (2).

Differentiating expression (2) in the high-temperature limit $kT\gg\hbar\omega$, we obtain the following expression for the temperature coefficient of the width of the band gap:

$$\beta=A\frac{k}{\hbar\omega}. \tag{6}$$

We will now demonstrate an interrelationship between the Varshni (1) and Fan (2) expressions. Expanding expression (2) in a power series in the temperature out to quadratic terms in the limit $kT\gg\hbar\omega$, we obtain an expression that is identical with expression (1), with the following coefficients:

$$\alpha_1=A\frac{k}{\hbar\omega},\quad \alpha_2=\frac{\hbar\omega}{kT};\quad A=2\alpha_1\alpha_2. \tag{7}$$

Consequently, in the limit $T\gg 2\alpha_2$ the Varshni coefficients α_1 and α_2 should contain information about the effective phonon energy.

Table II lists values of $\hbar\omega$ calculated on the basis of relations (7) using expression (2). However, for most materials these quantities do not coincide, since the temperatures of real experiments do not satisfy the high-temperature con-

TABLE I. Parameters of the Varshni (1) and Fan (2) expressions.

Material	Varshni coefficients* (1)		Fan parameter A, eV		σ^2, $(\text{eV})^{2}$**		Source
	α_1, 10^{-4} eV·K^{-1}	α_2, K	(2)**	(5)	(1)	(2)	
Diamond	−1.979	−1437	–	–	–	–	Ref. 5
	–	–	0.740*				Ref. 16
Si	7.021	1108	0.225	0.090	3.0×10^{-6}	5.1×10^{-6}	Ref. 5
	–	–	0.100*		–	–	Ref. 16
Ge	4.561	210	0.082	0.082	1.4×10^{-6}	6.6×10^{-7}	Ref. 5
	–	–	0.095*		–	–	Ref. 16
$6H\cdot$ SiC	−0.3055	−311	0.189	–	1.5×10^{-6}	3.0×10^{-7}	Ref. 6
ZnSe	5.780	175	0.049	0.031	1.2×10^{-6}	1.0×10^{-6}	Ref. 8
As_2S_3	–	–	1.00*	–	–	–	Ref. 14
GaP	6.860	576	0.377	0.037	7.6×10^{-5}	1.1×10^{-4}	Ref. 6
GaAs	8.871	572	0.171	0.020	5.8×10^{-5}	9.6×10^{-6}	Ref. 6
InP	4.906	327	0.050	0.045	6.8×10^{-8}	3.1×10^{-11}	Ref. 6
InAs	3.158	93	0.044	0.020	4.5×10^{-6}	4.1×10^{-7}	Ref. 6
a-Si:H_x	–	–	0.220*	–	–	–	Ref. 16
a-Ge:H_x	–	–	0.096*	–	–	–	Ref. 16
a-As_2S_3	–	–	1.00*	–	–	–	Ref. 15

Note. *Values taken from the literature. **Calculated from data of original works.

dition. The only exception is InAs, for which the values of $\hbar\omega$ are similar [16 meV according to expression (7) and 13 meV according to expression (2)]. Noting that in the given case the value $\alpha_2=93$ K corresponds to the range of temperatures 20–300 K of the experiment, we may assume that the condition $T\gg 2\alpha_2$ (186 K) is well satisfied for InAs.

In other words, in the temperature region where the condition $kT\gg\hbar\omega$ is not fulfilled, and expressions (1) and (2) become mathematically nonequivalent, the interpretation of the Varshni coefficients in terms of relations (7) is incorrect. Moreover, negative values of α_1 and α_2 generally are devoid of physical meaning. In such cases it becomes preferable to use expression (2), which in a description of the dependence $E_g(T)$ for a specific object gives information about the effective phonon energy.

A typical situation in which the temperature of a real experiment does not satisfy the above high-temperature limit is illustrated by the example of germanium and indium phosphide (Fig. 2). It is characteristic that the fitted curves obtained using expressions (1) and (2) describe the experimental points quite well (see the values of σ^2 in Table I), but diverge significantly when extrapolated into the high-temperature region. Such an explicit divergence leads to differences in the estimate of the temperature coefficient of the width of the band gap. The values of β obtained using the Varshni and Fan expressions are compared with the tabulated values[1] in Table II. The Fan estimates are found to be in better agreement with experiment for practically all of the listed materials, while the Varshni formula overestimates the values of β. It can be clearly seen from Fig. 2 that the high-temperature linear segments of the Varshni curves have a greater slope than the linear segments of the Fan curves.

It follows from a comparison of values of physical quantities extracted from the Varshni and Fan parameters with the

TABLE II. Values of physical quantities calculated according to the Varshni (1) and Fan (2) expressions.

Material	$\hbar\omega$, meV			β, 1×10^{-4} eV·K^{-1}			$E_g(0)$, eV			Source
	(7)*	(2)**	exp. (Ref. 1)	(1)	(6)	exp. (Ref. 1)	(1)*	(2)**	exp. (Ref. 1)	
Diamond	(−248)	–	165	(−1.979)	–	1.2	5.41	–	5.41	Ref. 5
	–	117		–			–			Ref.16
Si	191	48	063	7.02	4.05	2.8	1.155	1.150	1.17	Ref. 5
	–	30*		–	2.87		–	1.169*		Ref.16
Ge	36	18	37	4.56	3.84	3.7	0.741	0.739	0.744	Ref. 5
	–	20*		–	4.09		–	–		Ref.16
$6H\cdot$SiC	(−54)	50	89	(−0.31)	3.35	3.8	3.023	3.023	2.86	Ref. 6
ZnSe	30	11	31	5.78	4.04	4.50	2.81	2.81	2.80	Ref. 8
As_2S_3	–	46*	50	–	18.7	7.0	–	2.77*	2.60	Ref.14
GaP	99	55	49	6.86	5.91	5.5	2.330	2.321	2.35	Ref. 6
GaAs	99	28	36	8.87	5.18	5.0	1.521	1.518	1.52	Ref. 6
InP	56	14	43	4.91	3.09	2.9	1.421	1.421	1.42	Ref. 6
InAs	16	13	30	3.16	2.95	2.2	0.425	0.425	0.410	Ref. 6
a-Si:H_x	–	34*	79	–	5.57	–	–	–	–	Ref.16
a-Ge:H_x	–	17*	–	–	4.86	4.5	–	1.045*	–	Ref.16
a-As_2S_3	–	45*	–		16.0	–	–	2.42*	–	Ref.15

Note. Use of the notation * and ** is analogous to Table I. Experimental values of $\hbar\omega$, β, and $E_g(0)$ for all other materials taken from Ref. 1.

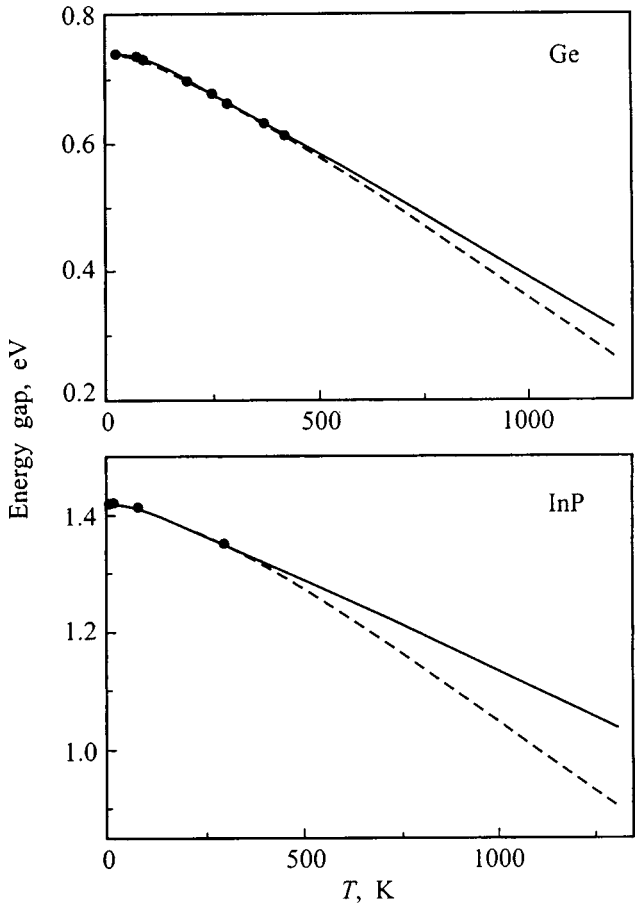

FIG. 2. The dependence $E_g(T)$ for germanium and indium phosphide, extrapolated to the high-temperature region. Points—experiment, Ge (Ref. 5) and InP (Ref. 6); dashed line—calculation using the Varshni relation (1); solid line—calculation using the Fan expression (2).

corresponding experimental data (Table II) that in many cases the Fan expression (2) gives more satisfactory values for the effective phonon energy and the temperature coefficient of the width of the band gap. Moreover, the use of expression (2) is completely free of physically meaningless results. It is also worthy of note (see Tables I and II) that the Fan expression (2) is also completely applicable for analysis of the dependence $E_g(T)$ in amorphous materials, where the edges of the energy bands are smeared out as a consequence of structural disorder and the density of states has extended tails.

In summary, expression (2) for $E_g(T)$, obtained in the one-phonon approximation in the temperature region $kT \gg \hbar\omega$ converges asymptotically to the well-known empirical Varshni relation (1). This being the case, on the basis of the values of the Varshni coefficients it is possible in principle to estimate the effective energy of the phonons responsible for the shift of the edge levels of the energy bands. However, when the condition $kT \gg \hbar\omega$ is not fulfilled, the use of the Fan expression (2) allows one not only to reproduce the shape of the observed dependence with the same degree of accuracy, but also, in contrast to the Varshni relation (1), to obtain reliable quantitative information about the phonon energy and the temperature coefficient of the width of the band gap.

*)E-mail: zats@dpt.ustu.ru

a)In contrast to level broadening, where the actual electronic transitions are taken into account conserving the energy and the wave vector, in the calculation of energy level shifts virtual transitions are considered which necessarily conserve only the wave vector. This is especially important for interactions with the acoustic vibrations, where the matrix element of the transition is proportional to the phonon wave vector.[11]

[1] *Handbook of Physical Quantities*, edited by I. S. Grigor'ev and E. Z. Meĭlikhov [in Russian] (Energoatomizdat, Moscow, 1991).
[2] N. W. Ashcroft and N. D. Mermin, *Solid State Physics* (Holt, Rinehart and Winston, New York, 1976).
[3] J. I. Pankove, *Optical Processes in Semiconductors* (Prentice-Hall, Englewood Cliffs, N.J., 1971).
[4] K. V. Shalimova, *Physics of Semiconductors* [in Russian] (Énergiya, Moscow, 1976).
[5] Y. P. Varshni, Physica (Amsterdam) **34**, 149 (1967).
[6] N. M. Ravindra and V. K. Srivastava, J. Phys. Chem. Solids **40**, 791 (1979).
[7] H. Y. Fan, Phys. Rev. **82**, 900 (1951).
[8] R. C. Tu, Y. K. Su, C. F. Li, Y. S. Huang, S. T. Chou, W. H. Lan, S. L. Tu, and H. Chang, J. Appl. Phys. **83**, 1664 (1998).
[9] A. Radkowsky, Phys. Rev. **73**, 749 (1948).
[10] A. S. Davydov, *Theory of Light Absorption in Molecular Crystals* [in Russian] (Izdat. Akad. Nauk USSR, Kiev, 1951).
[11] H. Y. Fan, *Photon-Electron Interaction: Crystals Without Fields* (Springer-Verlag, Berlin, 1967).
[12] T. Skettrup, Phys. Rev. B **18**, 2622 (1978).
[13] P. B. Allen and M. Cardona, Phys. Rev. B **23**, 1495 (1981); **24**, 7479 (1981).
[14] J. N. Zakis and H. Fritzsche, Phys. Status Solidi B **64**, 123 (1974).
[15] Yu. R. Zakis and A. V. Moskal'onov, Uch. Zap. LGU **231**, 61 (1975) [Lecture Notes, Leningrad State Univ.].
[16] G. D. Cody, ''The optical absorption edge of *a*-Si:H,'' in *Hydrogenated Amorphous Silicon*, Part B, edited by J. Pankove (Academic Press, New York, 1984), p. 11.

Translated by Paul F. Schippnick

Anisotropic magnetic quenching of positronium states in oriented crystals

I. V. Bondarev*

Scientific-Research Institute of Nuclear Problems, Belorussian State University, 220050 Minsk, Belarus
(Submitted July 7, 1998)
Fiz. Tverd. Tela (St. Petersburg) **41**, 999–1002 (June 1999)

We have carried out a theoretical analysis of the anisotropy of magnetic quenching of positronium states in noncubic crystals oriented relative to the direction of the external magnetic field. We show that an initial polarization of the positrons amplifies the anisotropy of magnetic quenching of positronium and lowers the magnitude of the magnetic field in which the anisotropy is maximum. We have obtained numerical estimates of the magnitude of the experimentally observed effect for quasipositronium in a single crystal of crystalline quartz and for a positronium complex in a single crystal of naphthalene. © *1999 American Institute of Physics.* [S1063-7834(99)01506-3]

The formation of positronium (Ps)—a bound system of an electron and a positron—in most crystalline insulators is presently a well-established experimental fact.[1] An atom of positronium in pure or almost pure single crystals of inorganic insulators possesses a number of new properties (for which it has acquired the name quasipositronium[1]), sharply distinguishing it from its comparatively well-studied counterpart Ps in vacuum. For example, the effective mass of quasi-Ps depends on the type of crystal and is 1.5–2 times greater than twice the mass of the free electron.[2–4] The hyperfine splitting of its spin levels preserves their spherical symmetry but is somewhat diminished in comparison with its vacuum value.[1] Therefore, an atom of Ps in inorganic insulators together with quasi-Ps are referred to as ''normal'' Ps, in contrast to the ''anomalous'' Ps atom, discovered in crystalline polymers.[5,6] It is customary to assume[7] that anomalous Ps is a unique sort of positronium complex, where the electron and positron are bound by a hyperfine bond not only to each other, but also with the surrounding nuclei. The hyperfine splitting of the spin levels of anomalous Ps is completely anisotropic and is described by a symmetric tensor of second rank, whose longitudinal and transverse components differ strongly from one another.[5–7]

Anisotropic hyperfine interactions (AHI) of Ps in noncubic crystals were investigated in Refs. 7–9. In Ref. 9 it was shown that anisotropic hyperfine splitting of the spin levels is a property not only of positronium complexes in crystalline polymers, but also of quasipositronium states in noncubic crystals of inorganic insulators, in particular, in crystalline quartz. In such insulators the anisotropy can be caused by the presence in quasi-Ps of an effective quadrupole moment.[10] The effective quadrupole interaction leads, first, to anisotropic splitting of the hyperfine energy levels of quasi-Ps (anisotropic hyperfine coupling of an electron and a positron) and, second, to anisotropy of its magnetic quenching in the crystal. The magnitude of the anisotropy in both cases is proportional to the effective quadrupole constant of quasi-Ps, and its orientational dependence is determined by the relative orientation of the crystal (the optical c axis in quartz) and the external magnetic field.[9] Note that the conclusion that magnetic quenching of positronium states is anisotropic is equally valid for quasipositronium states in inorganic insulators with a noncubic lattice and for positronium complexes in crystalline polymers since it is based only on anisotropic hyperfine coupling of an electron and a positron, which occurs in both cases. The present paper investigates the phenomenon of anisotropy of magnetic quenching of positronium states for the case of nonzero initial polarization of the source positrons. Such a situation is easy to realize experimentally since positrons, being the product of β^+ decay of neutron-deficient nuclei, always have initial polarization along their direction of motion $p \sim v/c$ (Ref. 11), where v is the speed of emission of the positrons from their source, and c is the speed of light in vacuum.

1. MAGNETIC QUENCHING OF POSITRONIUM IN MATTER FOR NONZERO POLARIZATION OF THE SOURCE POSITRONS

As is well known,[12] the presence of an external magnetic field partially lifts the degeneracy of the triplet ground state (the 1^3S_1 level) of a Ps atom: states with projection of the total spin $m = \pm 1$ remain degenerate, while the energy of a state with $m = 0$ grows quadratically with the field. In contrast, the energy of the nondegenerate singlet 1^1S_0 level falls off quadratically with the field. Splitting of the triplet level in a magnetic field is accompanied by magnetic quenching of ortho-Ps. The essence of the phenomenon is that a magnetic field mixes the short-lived singlet state with the long-lived ($m = 0$) triplet state. As a result, the lifetime of the mixed triplet-singlet (ortho-like) Ps state is shortened, i.e., ortho-Ps is ''quenched'' by the magnetic field, and the lifetime of the mixed singlet–triplet (para-like) Ps state is correspondingly extended with growth of the field. Experimentally, magnetic quenching of Ps is manifested in a relative decrease in the probability of 3γ annihilation, amplification of the narrow component in the curves of the angular correlation of the annihilation γ quanta (ACAR—Angular Correlation of Annihilation Radiation), and suppression of the long-lived component of the time spectrum of positron annihilation.[12,13]

The fractions of ortho-like (F_3^0) and para-like (F_1^0) positronium formed by polarized positrons in an external magnetic field **B**, are equal to[14]

$$F_3^0(p,B)=\frac{1}{8(1+y^2)}[(1+y)^2(1-p)+(1-y)^2(1+p)], \quad (1)$$

$$F_1^0(p,B)=\frac{1}{8(1+y^2)}[(1-y)^2(1-p)+(1+y)^2(1+p)]. \quad (2)$$

Here $y=x/(\sqrt{1+x^2}+1)$, $x=4\mu B/\hbar\omega$, μ is the Bohr magneton, $\hbar\omega$ is the hyperfine splitting energy of Ps in matter, and p is the projection of the polarization vector of the positrons onto the direction of the external magnetic field at the moment of formation of Ps. If in what follows P_1^0, P_3^0, and P_3^1 are the probabilities to detect a Ps atom in the singlet state ($m=0$) and the triplet state ($m=\pm 1$), then the system of kinetic equations describing the variation of the populations of these states with time has the form

$$\frac{dP_1^0}{dt}=-\Lambda_s' P_1^0, \quad \frac{dP_3^0}{dt}=-\Lambda_t' P_3^0, \quad \frac{dP_3^1}{dt}=-\Lambda_t P_3^1, \quad (3)$$

where $\Lambda_{s,t}'=\lambda_{s,t}'+\lambda_p$, $\Lambda_t=\lambda_t+\lambda_p$, and λ_p are the rates of pickoff annihilation of Ps in matter, $\lambda_{s,t}'=(\lambda_{s,t}+y^2\lambda_{t,s})/(1+y^2)$ are the magnetic-field mixed annihilation rates of para-like (λ_s') and ortho-like (λ_t') Ps (Ref. 12), $\lambda_{s,t}$ are the annihilation rates of singlet and triplet Ps in matter in the absence of an external magnetic field. The initial conditions for $t=0$: $P_1^0(0)=PF_1^0$, $P_3^0(0)=PF_3^0$, $P_3^1(0)=P/2$. The solution of system (3) has the form

$$P_1^0(t)=PF_1^0 e^{-\Lambda_s' t}, \quad P_3^0(t)=PF_3^0 e^{-\Lambda_t' t}, \quad P_3^1(t)=\frac{P}{2}e^{-\Lambda_t t}. \quad (4)$$

Thus, by defining the probability of 3γ annihilation of Ps ($P_{3\gamma}$), the intensity of the narrow ACAR component (I_N) and the magnetic suppression factor of the long-lived component of the time spectrum (R) by means of the expressions[13]

$$P_{3\gamma}=\lambda_t\int_0^\infty [y^2P_1^0(t)+(1-y^2)P_3^0(t)+P_3^1(t)]dt, \quad (5)$$

$$I_N(p,B)=\lambda_s\int_0^\infty [(1-y^2)P_1^0(t)+y^2P_3^0(t)]dt, \quad (6)$$

$$R(p,B)=\left(\int_{t_1}^\infty f(t)dt\right)_B \Big/ \left(\int_{t_1}^\infty f(t)dt\right)_{B=0}, \quad (7)$$

where $f(t)=-d(P_1^0(t)+P_3^0(t)+P_3^1(t))/dt$, and t_1 is chosen in the experiment to be on the order of the lifetime of the long-lived positronium component ($1/\Lambda_t$), for the relative variation of the probability of 3γ annihilation of Ps ($w_{3\gamma}$), the relative amplification of the intensity of the narrow ACAR component ($\mathscr{E}$), and the magnetic suppression factor of the long-lived component of the time spectrum (R) we obtain

$$w_{3\gamma}(p,B)=\frac{P_{3\gamma}(p,B)}{P_{3\gamma}(0,0)}=\frac{1}{3}\left(2+\frac{1-2py}{1+Q}\right), \quad (8)$$

$$\mathscr{E}(p,B)=\frac{I_N(p,B)-I_N(0,0)}{I_N(0,0)}=\frac{Q+2py}{1+Q}, \quad (9)$$

$$R(p,B)=\frac{1}{3}(2+(1-2py)e^{-Q}), \quad (10)$$

where $Q=y^2\lambda_s/\Lambda_t$ is the magnetic quenching parameter of Ps in matter.[13] In the derivation of expressions (8)–(10) we used the standard approximations which hold as a rule in the experiment: $\lambda_t \ll \lambda_s$, $\lambda_p \ll \lambda_s$, $t_1 \approx 1/\Lambda_t$, and $y^2 \ll 1$. The last of these approximations is valid over a wide range of external magnetic fields since even in a field of 20 kG in vacuum we have $y^2 \approx 0.043$.

2. ANISOTROPIC AMPLIFICATION OF THE NARROW ACAR COMPONENT IN CRYSTALLINE QUARTZ

For quasipositronium in a noncubic crystal the magnetic quenching parameter Q in Eqs. (8)–(10) should be replaced by[9]

$$Q(\vartheta,\varphi)=y^2(\vartheta,\varphi)\frac{\lambda_s}{\Lambda_t}, \quad (11)$$

where $y^2(\vartheta,\varphi)=y^2(1+d\phi(\vartheta,\varphi)/2\omega\sqrt{1+x^2})$, $\phi(\vartheta,\varphi)=3\cos^2\vartheta-1+\eta\sin^2\vartheta\cos 2\varphi$, and $d=Q_{\mathrm{Ps}}\varphi_{zz}$ is the effective quadrupole constant of quasi-Ps in the crystal [Q_{Ps} is the effective quadrupole moment of the Ps atom and φ_{zz} is the zz component of the electric field gradient (EFG) tensor at its center of mass], $\eta=(\varphi_{xx}-\varphi_{yy})/\varphi_{zz}$ is the asymmetry parameter of the EFG tensor, and ϑ and φ are the polar and azimuthal angles characterizing the orientation of the magnetic field vector **B** in the system of three principal axes of the EFG tensor. It is easy to see that the process of magnetic quenching of Ps thus becomes anisotropic, i.e., dependent on the direction of the external magnetic field relative to the system of principal axes of the EFG tensor in the crystal.

Since quasipositronium in crystalline quartz is delocalized,[2,3,15] it is natural to assume that in this case $\eta=0$ holds and the EFG tensor is axially symmetric with the principal axis Z collinear with the optical axis (the c axis) of the single crystal. Thus, the dependence on the azimuthal angle in Eq. (11) disappears, and the anisotropy of magnetic quenching is characterized only by the relative orientation of the single crystal (or more accurately, of its optical axis, i.e., c axis) and the external magnetic field. It is clear from Eqs. (8)–(10) that it is preferable to record the anisotropy in experiments measuring ACAR—the angular correlation of annihilation radiation: in this case the magnitude of the experimentally observed effect, defined in a sufficiently weak field by the difference in the magnetic quenching parameter for different orientations of the field relative to the c axis, is at least three times higher than in experiments measuring the relative probability of 3γ annihilation and the time spectrum

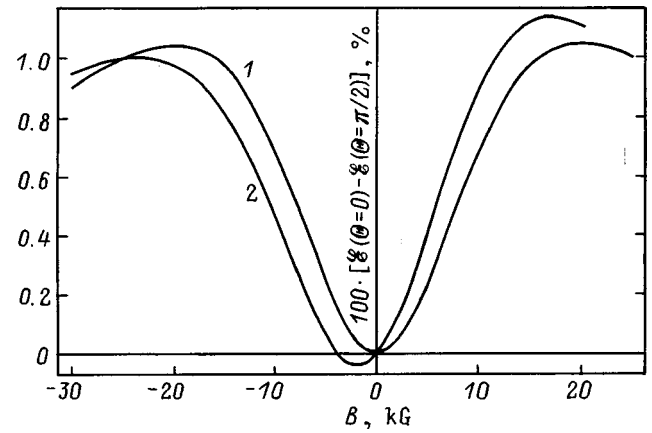

FIG. 1. Anisotropy of magnetic quenching of quasipositronium in crystalline quartz as a function of the external magnetic field for zero (*1*) and nonzero (*2*) positron polarization ($p=0.5$).

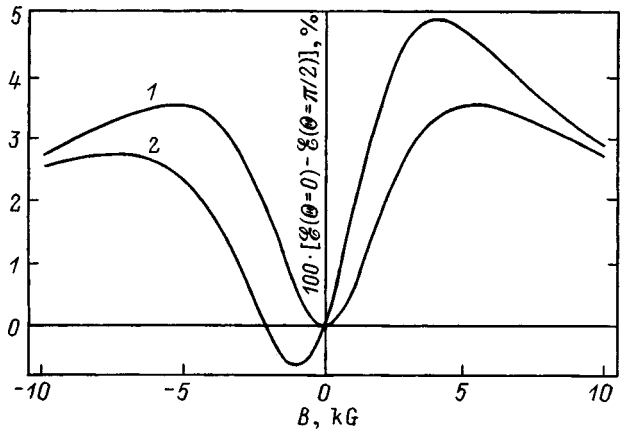

FIG. 2. Anisotropy of magnetic quenching of a positronium complex in a single crystal of naphthalene as a function of the external magnetic field for zero (*1*) and nonzero (*2*) positron polarization ($p=0.5$, $\varphi=0$).

of the positron lifetime. Therefore, the discussion that follows is based on an analysis of ACAR experiments.

It is clear from Eq. (9) taking Eq. (11) into account that anisotropy of magnetic quenching of quasi-Ps in crystalline quartz should be manifested for a nonzero value of the difference $\mathscr{E}(\vartheta=0,p,B)-\mathscr{E}(\vartheta=\pi/2,p,B)$. To estimate this difference, it is necessary to know three parameters characterizing the interaction of quasi-Ps with matter:[9] $\alpha=\lambda_{s,t}/\lambda_{s,t}^0=\omega/\omega_0$ (here $\lambda_{s,t}^0$ and ω_0 are the vacuum values of the rates of decay of para- and ortho-Ps in the absence of an external magnetic field and hyperfine splitting of the ground level of Ps, respectively), λ_p, and d/ω_0. These parameters were determined by fitting the experimental data of Ref. 15 with formulas (9) and (11) for the case $p=0.5$, $\vartheta=0$ experimentally realized in this study. The fitted values are $\alpha=0.84$, $\lambda_p^{-1}=1.16\times10^{-9}$ s, and $d/\omega_0=0.03$. Note that the fitted value of α is in satisfactory agreement with the value $\alpha=0.71$ estimated in Ref. 2 (see, however, Ref. 16); the fitted value of λ_p^{-1} agrees with the value $\lambda_p^{-1}=1.13\times10^{-9}$ s obtained in Ref. 15. The values of the parameters α, λ_p, and d/ω_0 determined in this way were then used to estimate the anisotropy of magnetic quenching of quasi-Ps in crystalline quartz. The obtained values of the differences $\mathscr{E}(\vartheta=0,p,B)-\mathscr{E}(\vartheta=\pi/2,p,B)$ are plotted in Fig. 1 for the cases of unpolarized positrons and polarized positrons with polarization $p=0.5$.

3. ANISOTROPIC AMPLIFICATION OF THE NARROW ACAR COMPONENT IN A SINGLE CRYSTAL OF NAPHTHALENE

For a positronium complex in crystalline polymers the magnetic quenching parameter in expressions (8)–(10) has the form (11), where, however, the quadrupole coupling constants d and η should in their more general form be replaced by the parameters of the CTB matrix A_{ik} (or, more accurately, its anisotropic part D_{il}: $A_{ik}=\omega\delta_{ik}+D_{ik}$, where D_{ik} is a symmetric tensor of second rank with zero trace) as follows:[17]

$$d=\frac{1}{3}(2D_{zz}-D_{xx}-D_{yy}),\qquad \eta=\frac{3(D_{xx}-D_{yy})}{2D_{zz}-D_{xx}-D_{yy}}. \tag{12}$$

Correspondingly, the function $y^2(\vartheta,\varphi)$ in Eq. (11) takes the form

$$y^2(\vartheta,\varphi)=y^2\left(1+\frac{2}{\omega\sqrt{1+x^2}}\left(\frac{D}{3}(3\cos^2\vartheta-1)+E\sin^2\vartheta\cos 2\varphi\right)\right), \tag{13}$$

where $D=-3(D_{xx}+D_{yy})/2$ and $E=(D_{xx}-D_{yy})/2$ are the two independent CTB constants in the system of principal axes of the D_{ik} tensor.[18]

It is easy to see from formulas (9), (11), and (13) that the absolute value of the difference $\mathscr{E}(\vartheta=0,\varphi,p,B)-\mathscr{E}(\vartheta=\pi/2,\varphi,p,B)$ takes its maximum at $\varphi=\pi/2$ if D and E have the same sign and at $\varphi=0$ if D and E have different signs. It is well known, for example, that electron–electron CTB in the triplet form of naphthalene is characterized by the values $D=3007$ MHz and $E=-411$ MHz (Ref. 18). These values can also be used to estimate the anisotropy of magnetic quenching of anomalous ortho-Ps in a single crystal of ordinary naphthalene since the anisotropic CTB constants are mainly determined by the magnitude of the interacting magnetic moments and the distance between them. Thus we find that the anisotropy of magnetic quenching of a positronium complex in a single crystal of naphthalene should be more strongly manifested for a nonzero value of the difference $\mathscr{E}(\vartheta=0,\varphi=0,p,B)-\mathscr{E}(\vartheta=\pi/2,\varphi=0,p,B)$. To estimate this difference using formulas (9), (11), and (13) we used the above electron–electron CTB constants for triplet naphthalene, and also the constants $\alpha=\lambda_{s,t}/\lambda_{s,t}^0=0.25$ and $\alpha'=\omega/\omega_0=0.13$ (Ref. 6) (see, however, Ref. 19), which allow for variation of the decay rates and the hyperfine splitting of anomalous PS in comparison from their vacuum values. The resulting values of the difference $\mathscr{E}(\vartheta=0,\varphi=0,p,B)-\mathscr{E}(\vartheta=\pi/2,\varphi=0,p,B)$ are plotted in Fig. 2 for the cases of unpo-

larized positrons and polarized positrons with polarization $p=0.5$.

As can be seen from Figs. 1 and 2, the anisotropy of magnetic quenching of positronium states in crystals oriented relative to the direction of the external magnetic field is a nonmonotonic function of the magnetic field. For zero polarization this dependence is an even function of the field, tending toward zero at small and large B. For nonzero polarization the anisotropy of magnetic quenching ceases to be an even function of the magnetic field, growing faster with growth of the field when the positrons are polarized in the direction of the field (right half-plane of the figures) and more slowly and with change of sign when the positrons are polarized opposite to the direction of the field (left half-plane of the figures). In this case the anisotropy maximum in the right half-plane (polarization with the field) is increased, and the field strength at which it is reached is decreased. This latter property must be taken into account in the setting up of the experiments: experiments with polarized positrons allow one to efficiently increase the maximum anisotropy while at the same time weakening the field (which is not unimportant from the point of view of setting up the experiment) at which it is reached. Thus, for example, in crystalline quartz (Fig. 1) for $p=0$ the maximum value of the anisotropy is 1.0% in a field of 19.8 kG while for $p=0.5$ it grows to 1.1% in a field of 17.0 kG. In naphthalene (Fig. 2) the anisotropy maximum at $p=0$ is 3.5% in a field of 5.2 kG while for $p=0.5$ it grows to 4.9% in a field of 4.0 kG.

For a positronium complex in naphthalene the anisotropy of magnetic quenching is significantly higher than for quasi-Ps in crystalline quartz. This is easy to explain since delocalized Ps in quartz ''feels'' an average crystal field, which, as a consequence of averaging over the entire crystal, is weaker than the crystal field acting on a well-localized anomalous Ps atom in naphthalene. Correspondingly, the wave function of the positronium state in naphthalene is distorted by the crystal field to a significantly greater extent than in quartz, thereby causing a stronger anisotropy of its magnetic quenching. The small anisotropy of magnetic quenching of quasi-Ps in crystalline quartz estimated in the present work ($\sim 1\%$) does not agree with the results of experiments[11] (as high as 30%). They disagree, in our view, because in Ref. 11 the effect of anisotropy of the electron density of the crystal was not subtracted out from the ''total'' observed anisotropy, which led to overestimates of the anisotropy of magnetic quenching of Ps in quartz.

I am grateful to S. A. Kuten', T. Hyodo, A. P. Mills, and E. Roduner for helpful discussions.

This work was carried out with the financial support of the Ministry of Education and Science of the Republic of Belarus (Grant No. 19971274) and the Foundation for Basic Research of the National Academy of Sciences of the Republic of Belarus (Grant No. F97-055).

*E-mail: bond@inp.minsk.by

[1] A. Dupasquier, in *Positron Solid State Physics*, edited by W. Brandt and A. Dupasquier (Academic Press, New York, 1983), p. 510.
[2] C. H. Hodges, B. T. McKee, W. Triftshauser, and A. T. Stewart, Can. J. Phys. **50**, 103 (1972).
[3] Y. Nagai, M. Kakimoto, H. Ikari, and T. Hyodo, Mater. Sci. Forum **255–257**, 596 (1997).
[4] J. Kasai, T. Hyodo, and K. Fujiwara, J. Phys. Soc. Jpn. **57**, 329 (1988).
[5] A. Bisi, G. Consolati, G. Gambarini, and L. Zappa, Nuovo Cimento D **6**, 183 (1985).
[6] A. Bisi, G. Consolati, and L. Zappa, Hyperfine Interact. **36**, 29 (1987).
[7] M. Schwager and E. Roduner, Chem. Phys. Lett. **182**, 445 (1991).
[8] A. Z. Varisov, Opt. Spektrosk. **53**, 278 (1982) [Opt. Spectrosc. **53**, 162 (1982)].
[9] I. V. Bondarev and S. A. Kuten, Acta Phys. Pol. A **88**, 83 (1995).
[10] V. G. Baryshevskii, Phys. Status Solidi B **124**, 619 (1984).
[11] A. Seeger, Mater. Sci. Forum **255–257**, 1 (1997).
[12] V. I. Gol'danskiĭ, *Physical Chemistry of the Positron and Positronium* [in Russian] (Nauka, Moscow, 1969).
[13] A. Z. Varisov and F. M. Nabiullina, Opt. Spektrosk. **46**, 448 (1979) [Opt. Spectrosc. **46**, 250 (1979)].
[14] A. Bisi, A. Fiorentini, E. Gatti, and L. Zappa, Phys. Rev. **128**, 2195 (1962).
[15] A. Greenberger, A. P. Mills, A. Thompson, and S. Berko, Phys. Lett. A **32**, 72 (1970).
[16] A. Bisi, G. Consolati, F. Quasso, and L. Zappa, Nuovo Cimento D **10**, 1069 (1988).
[17] V. G. Baryshevskii, S. A. Kuten, and V. I. Rapoport, Phys. Lett. A **88**, 289 (1982).
[18] J. E. Wertz and J. R. Bolton, *Electron Spin Resonance* (McGraw-Hill, New York, 1972).
[19] W. Gorniak and T. Goworek, Chem. Phys. Lett. **177**, 1, 23 (1991)

Translated by Paul F. Schippnick

Thin sol–gel bismuth silicate films

E. O. Klebanskiĭ, A. Yu. Kudzin, V. M. Pasal'skiĭ, S. N. Plyaka, L. Ya. Sadovskaya, and G. Kh. Sokolyanskiĭ

Dnepropetrovsk State University 320625 Dnepropetrovsk, Ukraine
(Submitted September 3, 1998)
Fiz. Tverd. Tela (St. Petersburg) **41**, 1003–1005 (June 1999)

The sol–gel method is used to obtain thin films with the composition $Bi_{12}SiO_{20}$. The characteristic features of the technology for obtaining the films are presented. Diffractometry confirmed that the films possess γ-Bi_2O_3-type structure. The transmission spectra of the films were investigated. The spectral dependence of the absorption coefficient of the films matches well with the spectra determined using bulk $Bi_{12}SiO_{20}$ crystals. © *1999 American Institute of Physics.* [S1063-7834(99)01606-8]

Bismuth silicate $Bi_{12}SiO_{20}$ (BSO) is a photorefractive material used for information storage and processing. The nature of its photorefractive sensitivity is not entirely understood and is now being actively studied. The crystalline forms of the compounds, whose preparation characteristics are well known, are used in most development and investigatory work on BSO. Thin-film samples are of interest for detailed study of the optical absorption edge. Progress in obtaining and utilizing thin films of many promising crystals have led to work on the synthesis of films with the composition $Bi_{12}SiO_{20}$ by different methods. Thus, data on the preparation of BSO films by high-frequency sputtering exist.[1] However, the authors were not able to obtain reproducible results, and the physical properties of the films were substantially worse than those of the crystals. Moreover, film production was a complicated technological process, and the yield of acceptable samples was low ($\sim$3% of the initially consumed materials). The preparation of a BSO film by vacuum evaporation followed by heating in air is described in Ref. 2. A perfect structure with a point-like electron diffraction pattern was obtained. The lattice parameters of the film matched well with the parameters of crystals. At present the best-developed method for obtaining insulating oxide films is the sol–gel method.[3] This method has a number of advantages over conventional chemical and physical technologies: expensive, unique equipment is not required, the degree of purification can be high even for the initial raw materials, composition uniformity is good, the processing temperatures are low, wastes are minimal, and so on. The method makes it possible to obtain doped films, which permits varying their physical properties purposefully (electric conductivity, photoconductivity, optical absorption spectra, and others). The main obstacle to using the sol–gel method is the complexity of the chemical process, due to the multicomponent nature of the composition. However, modern advances in organoelemental and colloidal chemistry have made it possible to use this method to obtain thin films of active dielectrics with a complicated composition (for example, ferroelectrics[3]).

In the present paper we present the results on the development of a method of chemical homogenization and synthesis of crystalline films with the silicosillenite structure $Bi_{12}SiO_{20}$ by the sol–gel method and the result of an investigation of their properties.

Methods for obtaining thin films of SiO_2 and Bi_2O_3 from solutions of easily hydrolyzing and thermally dissociating compounds are described in Ref. 4. Usually, solutions of tetraethyl orthocilicate and bismuth nitrate were used as precursors. The stability of these solutions was ensured by adding strong acids (KCl, HNO_3 and others). It should be noted that solutions of bismuth nitrate in organic solvents form sediments and they are unstable, which makes it difficult to prepare solutions with a precise bismuth concentration. It is impossible to obtain stable Bi–Si precursors for synthesis of $Bi_{12}SiO_{20}$ films using the methods described. It can be assumed that the use of 1,3-diketones as stabilizing additives or even solvents will improve the stability of solutions containing tetraethyl orthosilicate and bismuth titrate in the stoichiometric ratio required for synthesis of a $Bi_{12}SiO_{20}$ film.

To obtain films with the composition $Bi_{12}SiO_{20}$ in the present work, bismuth nitrate $Bi(NO_3)_35H_2O$ (ultrapure), tetraethyl orthosilicate $Si(OC_2H_5)_4$ (analytically pure), ethoxy ethanol $HOCH_2CH_2OC_2H_5$ (analytically pure), acetyl acetone $CH_3COCH_2COCH_3$ (analytically pure), and nitric acid (analytically pure) were used as the starting reagents. Liquid reagents were distilled prior to use. Bismuth nitrate was dissolved in ethoxy ethanol at 30 °C, and nitric acid and acetyl acetone were added. The obtained solution was mixed with a solution of tetraethyl orthosilicate in ethyoxy ethanol and allowed to stand for 24 h. The stability of the final solution (precursor) was one month. Solutions with 2–3% bismuth nitrate were used in this work. Semiconductor silicon and fused quartz were used as substrates. The precursor was deposited on a substrate rotating at 3000 rpm, dried in air, and heated at 400 °C. To obtain a prescribed thickness the required number of layers, each layer annealed at 400 °C, was deposited. The film thickness was estimated by weighing and was $\sim 0.23\,\mu$m for six layers. The crystalline structure of silicosillenite was formed by thermal annealing at 650 °C. The holding time was 1 h.

To identify the film composition diffraction, patterns of the film, substrate, and powder from a Czochralski-grown

TABLE I. Diffractometric data for a film and crystalline powder with the composition $Bi_{12}SiO_{20}$.

	Finely divided crystal				Film		
No.	2Θ	d, Å	I_{rel}	hkl	2Θ	d, Å	I_{rel}
1	21.75	4.081	6	211	21.45	4.17	100
2	28.05	3.19	55	310	27.65	3.24	90
3	33.2	2.70	50	321	32.8	2.73	95
4	35.5	2.536	10	400	35.15	2.56	20
5	43.9	2.067	10	422	43.35	2.094	40
6	45.8	1.984	20	510	45.25	2.05	40
				431			
7	52.9	1.746	100	440	52.15	1.759	20
8	56.05	1.645	25	611	55.3	1.664	20
				532			

BSO single crystal were recorded using a DRON-2.0 diffractometer with monochromatized CuK_α radiation. Table 1 gives the interplanar distances and relative intensities of the reflections observed on a film and crystalline BSO power. The table also gives the hkl indices for the reflections from powder which were indexed taking account of the space group (T^3) and lattice parameter ($a=10.1$ Å) of the BSO crystal.[5]

The presence of intense peaks in the diffraction pattern of the film indicates that the film structure is crystalline, and the closeness of the interplanar distances of the film and powder show that the film possesses γ-Bi_2O_3-type structure, as does BSO. We note that the diffraction pattern of the film contains no traces of glass formation, and the influence of the fused quartz substrate shows in the form of a diffused peak at small angles. Comparing the film and powder line intensities shows that the film is textured. As one can see from Table 1, an orientation of the crystals such that the {211} atomic planes are parallel to the substrate plane predominates in the film. This is typical for body-centered crystals, where these planes are twinning planes. The direction of the ⟨111⟩ packing planes lies in this plane, and under deformation the system {211}⟨111⟩ often characterizes the texture of the material.

The room-temperature conductivity of the films obtained is $\sigma\sim 10^{-10}\,\Omega^{-1}\cdot\mathrm{cm}^{-1}$, and its activation energy is approximately 0.44 eV. The charge-carrier mobility was determined from the quadratic sections of the IVC using relations characteristic for space-charge-limited currents. At $T=20\,^\circ$C the charge-carrier mobility is 10^{-4} cm/V·s and increases exponentially with temperature.

The transmission spectrum of a film on a fused quartz substrate were obtained in the wavelength range 0.2–0.7 μm at room temperature with a Specord-M40 spectrophotometer. As one can see from Fig. 1, heating in air substantially increases the transparency of the films obtained. The values of the optical transmission of an annealed film were used to calculate the absorption coefficient α according to the formula[6]

$$\alpha=\frac{1}{d}\ln\left[\frac{2TR^2}{\sqrt{(1-R)^4+4T^2R^2}-(1-R)^2}\right], \tag{1}$$

where d is the film thickness, T is the transmission coefficient, and R is the reflection coefficient of the composition obtained. The latter was found from the relation[6]

$$1-R=(1-R_l)(1-R_q)(1-R_{l-q}). \tag{2}$$

In the course of the calculations the reflection coefficient of a BSO crystal, according to data from Ref. 7, was used for R_l. The reflection coefficient of the quartz substrate was calculated using the Fresnel formula and the values of the refractive index n_q of quartz.[5] The reflection coefficient of the film–quartz interface was calculated as

$$R_{l-q}=\frac{n_l-n_q}{n_l+n_q},$$

where

$$n_l=\frac{1+\sqrt{R_l}}{1-\sqrt{R_l}}.$$

Equation (1) is applicable as long as the thickness of the sample is greater than the wavelength of the optical radiation in the crystal ($\bar{\lambda}=\lambda/n_l$). In our case this condition holds quite well for $\lambda\leqslant 370$ nm, where $n_l\approx 3.3$. At longer wavelengths the refractive index decreases sharply[7] and α becomes virtually independent of λ, fluctuating around the value $\approx 2\times 10^3\,\mathrm{cm}^{-1}$, in agreement with the results obtained on bulk crystals.

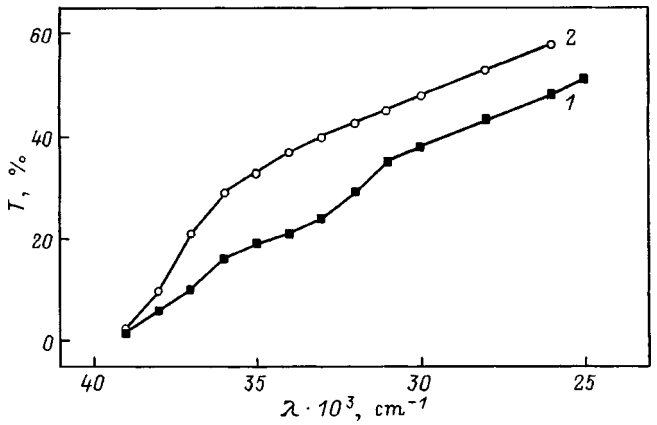

FIG. 1. Optical transmission spectra of a $B_{12}SiO_{20}$ film: *1*—freshly prepared film, *2*—film after annealing at 750 °C.

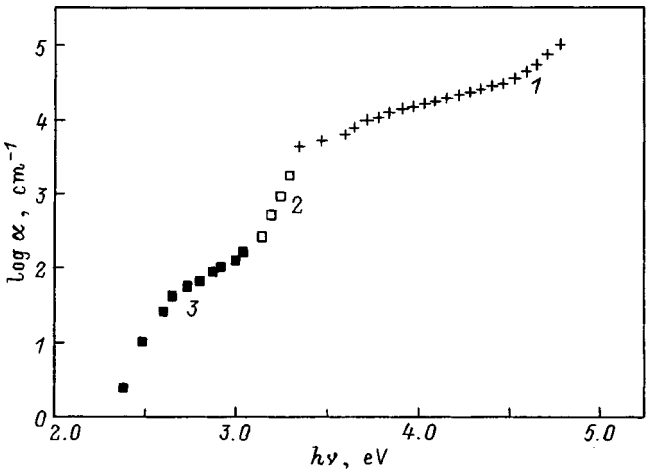

FIG. 2. Spectral dependence of the absorption coefficient of $Bi_{12}SiO_{20}$: *1*—sol–gel film, *2*—according to the data of Ref. 6, *3*—bulk $Bi_{12}SiO_{20}$ crystal.

The spectral dependence obtained in this manner for the absorption coefficient of BSO is displayed in Fig. 2 (curve *1*). Since there are no published data for this energy range, the values of α are presented for lower photon energies according to the data of Ref. 7 (curve *2*) as well as the results of our investigations of absorption in bulk BSO crystals (curve *3*) are also presented here. The latter agree well with the results obtained in Ref. 8. As one can see from Fig. 2, the spectral dependence of the absorption coefficient of the BSO films obtained in the present work by the sol–gel method agrees quite well with the spectra obtained using bulk crystals.

In summary, the results of the crystallographic and optical investigations allow us to conclude that the films obtained by the sol–gel method are crystalline and have the composition $Bi_{12}SiO_{20}$.

[1] V. K. Malinovskiĭ, O. A. Gudaev, V. A. Gusev, and S. I. Demenko, *Photoinduced Phenomena in Sillenites* [in Russian] (Nauka, Novosibirsk, 1990).
[2] Sh. M. Efenliev, V. E. Bagiev, A. Ch. Zeinally, and V. M. Skoricov, Phys. Status Solidi A **50**, Pk141 (1978).
[3] S. Z. Swartz and V. E. Wood, Condens. Matter News **1**, No. 5, 4 (1992).
[4] A. V. Suĭkovskaya, *Chemical Methods of Producing Thin Transparent Films* [in Russian] (Khimiya, Leningrad, 1971).
[5] *Handbook of Acoustic Crystals* [in Russian], edited by M. P. Shaskol'skaya (Nauka, Moscow, 1982).
[6] Yu. I. Ukhanov, *Optical Properties of Semiconductors* [in Russian] (Nauka, Moscow, 1977).
[7] A. A. Reza, D. B. Senulene, V. A. Belyaev, and E. I. Leonov, Pis'ma Zh. Tekh. Fiz. **5**, 465 (1979) [Sov. Tech. Phys. Lett. **5**, 190 (1979)].
[8] S. L. Hou, R. B. Laner, and R. E. Aldrich, J. Appl. Phys. **44**, 2652 (1973).

Translated by M. E. Alferieff

Thermal ionization of impurity centers in Fe-doped $Bi_{12}SiO_{20}$ and $Bi_{12}GeO_{20}$ crystals

T. V. Panchenko

Dnepropetrovsk State University, 320625 Dnepropetrovsk, Ukraine
(Submitted November 12, 1998)
Fiz. Tverd. Tela (St. Petersburg) **41**, 1006–1011 (June 1999)

The spectral and temperature dependence of the optical absorption and thermally stimulated depolarization currents in Fe-doped $Bi_{12}SiO_{20}$ and $Bi_{12}GeO_{20}$ crystals are investigated in the photon energy range 1.36–3.46 eV and temperature 85–750 K. The results show thermally induced electron redistribution between donor and acceptor levels and defect association–dissociation processes and are discussed using the configuration-coordinate model.
 [S1063-7834(99)01706-2]

Impurity iron in photorefractive crystals with sillenite structure $Bi_{12}MO_{20}$ (BMO, where M=Si, Ge, Ti) has been studied in Refs. 1–14. ESR investigations have shown that Fe^{3+} ions are present in nominally pure BMO crystals[1,2] and that they are highly sensitive to temperature and illumination and can play an important role in the photorefractive effect.[1,2,4–6] The Fe^{3+} density decreases under illumination with blue-green light and is restored by light from the range 2.2–1.3 eV (partially) or heating up to ≈ 300 K (completely). Since other ESR spectra do not appear in the process, there exist two possibilities (Fe^{4+} and Fe^{2+}) for the change in the charge state of Fe^{3+}. The first one is examined in Refs. 4 and 5. However, the analysis of the optical absorption spectra of BMO:Fe and $Bi_{25}FeO_{40}$ crystals[3,13] attests to $Fe^{3+}+h\nu \rightarrow Fe^{2+}$ transitions, which were proposed in Ref. 6. The thermally- and photoinduced changes in the EPR signal provided the possibility of using Fe^{3+} ions as a paramagnetic probe for determining the energy position of some levels in the band gap in BMO.[4–6,9,10]

The structural details of the optical absorption spectra of iron-containing BMO crystals can be explained on the basis of optical transition schemes in the ligand crystal-field model or computed by the LCAO–MO method.[3] Investigations of magnetic circular dichroism and optical detection of paramagnetic resonance show that the ligand field model is preferable for Fe ions, which substitute for M in oxygen tetrahedra.[11,14]

However, the identification of the charge state and localization of Fe does not solve the main questions due to the presence of these ions in sillenites. Specifically, the nature of the optical transitions, which form a wide spectrum (visible and near-IR ranges) of photoinduced absorption, is unclear, since the contribution of intracenter transitions of Fe^{3+} and Fe^{2+} ions is negligible. Doping with Fe changes the type (from *n* to *p*) of the dark and photoconductivity of sillenites.[8] This supports the assumption[5] that donors and acceptors participate simultaneously in optical and thermal charge transfer processes on these ions and other centers, but the specific mechanisms have not been considered. Interest in these processes has increased in recent years.[9,10,12] For example, it has been shown that the competition between photoexcited electrons and holes determines the temperature dependence of the diffraction efficiency in BMO:Fe crystals.[12]

In the present work optical and thermal-activation current spectroscopy are used for further investigation of charge transfer on impurity centers in BMO:Fe crystals.

1. EXPERIMENT

$Bi_{12}SiO_{20}$ (BSO) and $Bi_{12}GeO_{20}$ (BGO) crystals doped with ions of the odd isotope ^{57}Fe are investigated. The crystals were Czochralski-grown in the [001] direction and contained (according to emission spectral analysis) $\leqslant 0.01$ (BSO:Fe) and ~ 0.015 (BGO:Fe) mass% Fe.

Samples for optical measurements were prepared in the form of 8×8 mm^2 polished plates with thickness $d=0.1-5$ mm, cut in the (001) plane. They were placed in the crystal holder of a nitrogen cryostat and rapidly ($\sim$20 min) cooled to ~ 85 K before the measurements.

The optical transmission spectra $t(E)$ in the photon energy range $E=1.36-3.4$ eV were measured on a Specord M40 spectrophotometer. The temperature was varied in the range $T=85-700$ K at the rate $b_1=0.02\ \mathrm{K\cdot s^{-1}}$. The spectra $t(E)$ was scanned (60 s for each spectrum) with a 3–5 K step in the range $T_1=85-300$ K and with a 10 K step in the range $T_2=300-700$ K.

The absorption spectra $\alpha(E)$ were calculated from the relation[15]

$$t=\{(1-R)^2\alpha\lambda(4\pi n)^{-2}\}/\{\exp(\alpha d)-R^2\exp(-2\alpha d)\}, \quad (1)$$

where $n(E)$ is the refractive index, λ is the wavelength, and $R(E)$ is the reflection coefficient. The functions $n(E)$ were measured in the range $E_1=1.36-2.8$ eV on prisms using a GS-5 goniometer and ''matched'' with the functions $n(E)$ calculated for the range $E_2=2.8-3.4$ eV from the relation[16]

$$n^2=1+A\lambda_0^2\lambda^2/(\lambda^2-\lambda_0^2)+B\lambda_1^2\lambda^2/(\lambda^2-\lambda_1^2) \quad (2)$$

with the free parameters $A=92.22\ \mu\mathrm{m}^{-2}$, $B=0.534\ \mu\mathrm{m}^{-2}$, $\lambda_0=0.22\ \mu$m, and $\lambda_1=0.37\ \mu$m, which corresponds to the

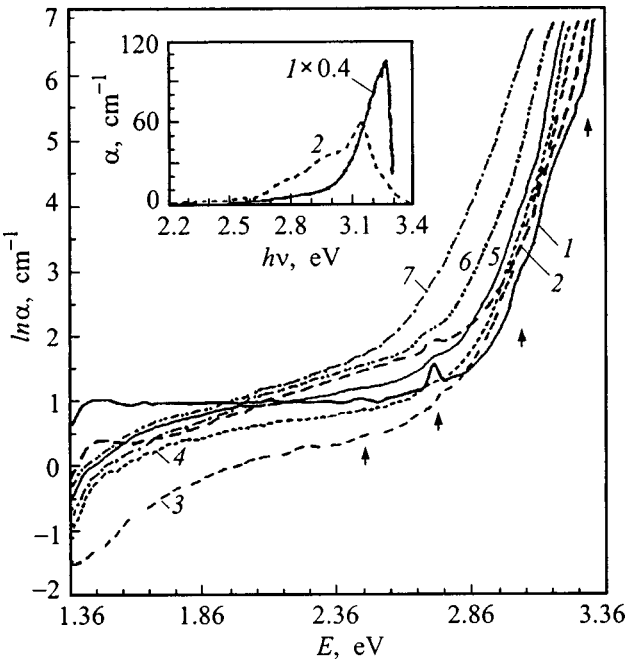

FIG. 1. Spectral dependences of the optical absorption $\ln \alpha(E)$ for BSO:Fe crystals at $T=86$ (*1*), 133 (*2*), 183 (*3*), 210 (*4*), 248 (*5*), 263 (*6*), and 317 K (*7*). Inset: Impurity absorption edge bands in BSO:Fe (*1*) and undoped BSO (*2*) crystals.

fundamental absorption edge of BSO crystals. The computed functions $n(E)$ correlate with the experimental data of Ref. 17.

Samples for measurements of the thermally stimulated currents were prepared in the form of $0.8\times3\times5$ mm^3 polished bars. Platinum electrodes were deposited by cathodic sputtering in vacuum on the 3×5 mm surfaces, cut out in the (001) plane. The samples were placed in a crystal holder with sapphire insulation.

The thermally stimulated depolarization (TSD) currents were measured for thermoelectret states, which were produced beforehand and formed in a field $E_p=10^2-10^4$ V/cm at temperature $T_p=300-450$ K. The polarization time (30 min) was the same in all cases. The microcomputer-controllable apparatus described in Ref. 18 was used for the measurements. The TSD currents were measured in the range $T=300-850$ K with heating at the rate $b_2=0.16\,\mathrm{K\cdot s^{-1}}$.

2. RESULTS

2.1. *Absorption spectra.* The spectra $\alpha(E,T)$ (Fig. 1) obtained for BSO:Fe and BGO:Fe crystals are qualitatively similar. Extinction of the intense absorption shoulder that is characteristic[19,20] of undoped BMO crystals in the range $E=2.2-3$ eV is observed in the entire experimental temperature range. The structural features of the spectra, in the form of weak bands (shown by arrows in Fig. 1), are due to spin-forbidden $d-d$ electronic transitions in Fe^{3+} ions (electron configuration $3d^5$) from the $^6A_1$ ground state into the excited states $^4T_1(t_2^2e_2^2)$, $^4T_2(t_2^2e^2)$, $^4A_1$, $^4E(t_2^3\,{}^2E, e^2\,{}^3H_2)$, $^4T_2(t_2^3e^2)$, $^4E(^4D)$.[13] It should be noted that the transitions have an anomalously large oscillator strength,[13] which could be due to intensity being ''borrowed'' from the ligand–metal type charge-transfer band $O^{2-}\rightarrow Fe^{3+}$.[21]

The curves $\alpha(E,T)$ show nonmonotonic variation of impurity absorption in the range $E=1.36-2.96$ eV with increasing temperature. Urbach's rule $\alpha(E)=\alpha_0\exp[\chi(E-E_0)]$ holds near the fundamental absorption edge in the range of E where the lower limit decreases with increasing temperature (from $E\approx3.16$ eV at $T\leqslant250$ K to $E\approx2.7$ eV at $T=700$ K). The curves $\ln\alpha=f(E)$ have a kink, their linear fragments converge at points with the coordinates $\alpha_{01}=4.23\times10^4\,\mathrm{cm^{-1}}$, $E_{01}=3.36$ eV (BSO:Fe) and $\alpha_{02}=5.1\times10^4\,\mathrm{cm^{-1}}$, $E_{02}=3.38$ eV (BSO:Fe), and they can be represented in the form

$$\ln\alpha(E)=\ln\alpha_{0i}+\sigma(T)(E-E_{0i})/kT, \tag{3}$$

where σ is a parameter characterizing the slope of the absorption edge, k is Boltzmann's constant, and $i=1,2$. The temperature dependence $\sigma(T)=kT\Delta(\ln\alpha)/\Delta E$ can be approximated well by an expression for the absorption edge formed with the participation of the electron–phonon interaction[22]

$$\sigma(T)=\sigma_{0i}(2kT/h\nu_{0i})\tanh(h\nu_{0i}/2kT). \tag{4}$$

The effective phonon energy $h\nu_1=16.6$ meV (BSO:Fe) and $h\nu_1=16.8$ meV (BGO:Ge) is close to the energy of optical phonons with frequency $\omega=134.8\,\mathrm{cm^{-1}}$, which are observed in the Raman-scattering spectra of undoped BMO crystals.[23] The values $\sigma_{01}=1.05$ (BSO:Fe) and $\sigma_{02}=0.95$ (BGO:Fe) are much higher than those found in Refs. 24 and 25 for undoped BSO crystals with nonstoichiometry defects and doped with Al and Ga ions. This indicates that the electron–phonon interaction constant $g=(2/3)\sigma_0^{-1}$ decreases.

The temperature dependence of the isoabsorption energy $E_g^*(T)$, which reflects the variation of the band gap with temperature, can be described by the well-known expression for semiconductors

$$E_g^*(T)=E_{gi}^*(0)-CT^2/(\theta-T), \tag{5}$$

where the empirical constants $E_{g1}^*(0)=3.35$ eV (BSO:Fe), $E_{g2}^*(0)=3.38$ eV (BGO:Fe), $C=3.7\times10^{-5}\,\mathrm{eV\cdot K^{-1}}$, and $\theta=280$ K (with $\alpha=1090\,\mathrm{cm^{-1}}$) likewise differ from those found in Refs. 24 and 25. The anomalies in $\sigma(T)$ and $E_g^*(T)$ observed[24] in BSO crystals in the temperature ranges $\Delta T=190-240$, 270–300, and 400–430 K are weak in BSO:Fe and BGO:Fe crystals (Fig. 2).

The reflection in the curves $\ln\alpha=f(E)$ indicates the presence of a near-edge absorption band. We identify it by extrapolating the upper section of the absorption edge to lower values of α and subtracting the result from the general spectrum. The band is shifted toward the absorption edge compared with the analogous band in undoped BSO crystals (inset in Fig. 1). It is definitely associated with Fe ions and/or charge-compensation defects, since its intensity increases with the concentration of this impurity, and the spectral position ($E_{\max}=3.29$ eV) and doublet structure of the band correspond to $d-d$ electronic transitions in Fe^{3+} ions with coordination number 4.[13] The temperature dependence $\alpha(T)$ on

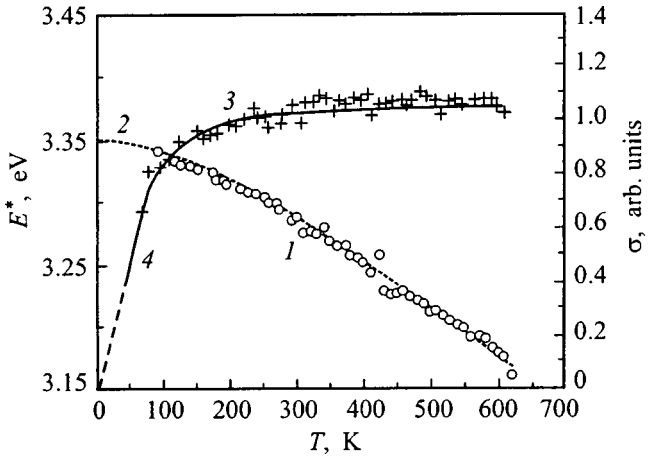

FIG. 2. Experimental (*1, 3*—dots) and fitted (*2, 4*—lines) temperature dependences of the parameter σ and isoabsorption energy E_g^* (for $\alpha = 1090\ \mathrm{cm}^{-1}$) of BSO:Fe crystals.

the long-wavelength slope of this band is characterized by a small peak (at $T = 200-300$ K) superposed on the exponential growth of absorption.

Far from the absorption edge the temperature dependences $\alpha(T)$ can be divided into two groups. One group characterizes absorption in the A range of photon energies ($E_A = 1.36-2$ eV) and the other in the B range of the absorption shoulder of undoped BMO crystals ($E_B = 2.2-3$ eV).

In BSO:Fe crystals a certain correlation of the variation of the absorption is observed for these ranges. In the interval $\Delta T_1 = 86-180$ K the monotonic decrease of absorption in the A range is accompanied by an increase in absorption in the B range and for $\Delta T_2 = 180-280$ K $\alpha(T)$ passes through a minimum in both ranges. Next, for the A range we observe a plateau ($\Delta T_3 = 290-420$ K), a steep drop-off ($\Delta T_4 = 420-490$ K), and indistinct peaks in α ($\Delta T_5 = 500-700$ K). These variations are accompanied by steps superposed on the exponential growth of absorption in the B range. In BGO:Fe crystals these features of $\alpha(T)$ are weak (Fig. 3). Note that the temperature dependence of the photoinduced absorption passing through a minimum in the range 220–280 K has been observed in BGO:Mo and BGO:Ce crystals.[26]

The spectra $\Delta\alpha/\alpha_0 = [\alpha(E,T_i) - \alpha(E,T_0)]/\alpha(E,T_0)$, where $T_0 = 86$ K and $T_i > T_0$ (Fig. 4), characterize the thermally induced changes in $\alpha(E,T)$ for BSO:Fe crystals. It is interesting that the first heating stage (ΔT_1) these spectra in the B range are completely similar to the photoinduced (by light with $E \simeq 2.9$ eV) absorption spectra.[13] In both cases characteristic dips whose spectral position ($E_1 = 2.7-2.8$ eV and $E_2 = 3-3.3$ eV) corresponds to $d-d$ transitions in Fe^{3+} ions are observed, and their appearance itself indicates a decrease of the density of Fe^{3+} ions.

Bleaching over a wide spectral range (up to $E \leqslant 3.1$ eV) corresponds to a decrease in absorption in the interval ΔT_2. The depth of the Fe^{3+}-related dips decreases, attesting to an increase in the density of these ions; in addition an absorption band with $E \approx 2.9$ eV, due to Fe^{2+} ions, appears and disappears (Fig. 5). The subsequent growth of absorption in

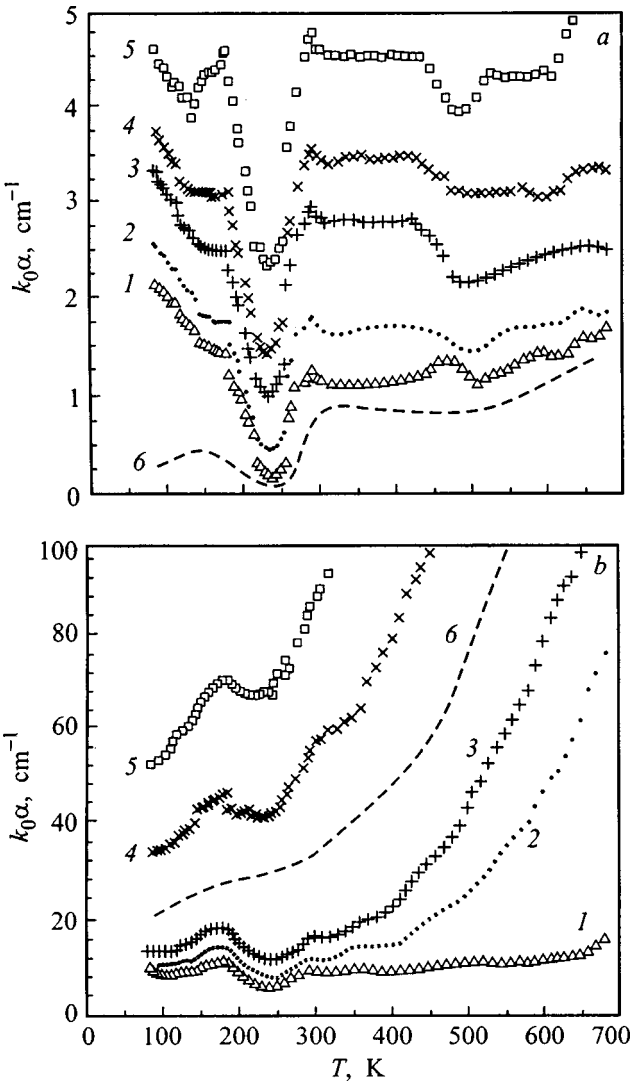

FIG. 3. Temperature dependence of the optical absorption of photons with energy E in BSO:Fe (*1–5*) and BGO:Fe (*6*) crystals for the long-wavelength (a) and short-wavelength (b) ranges of the spectrum. The curves are shifted relative to one another using a factor k_0: a—$E = 1.425$ (*1, 6*, $k_0 = 1$), 1.518 (*2*, $k_0 = 0.9$), 1.735 (*3*, $k_0 = 1.5$), 1.86 (*4*, $k_0 = 1.84$), and 2.08 eV (*5*, $k_0 = 2.35$); b—$E = 2.788$ (*1*, $k_0 = 2.11$), 3.06 (*2*, $k_0 = 1.2$), 3.098 (*3*, $k_0 = 0.58$), 3.221 (*4, 6*, $k_0 = 0.26$), and 3.252 (*5*, $k_0 = 0.23$).

the B range is characterized by a gradual transformation of the spectrum $\Delta\alpha(E,T)/\alpha_0$ so that the additional thermally induced absorption band shifts to the absorption edge, and a long-wavelength shift is observed for the bleaching band in the A range. Finally, the narrow bleaching band $\Delta E = 1.46-2.36$ eV corresponds to the steep drop in absorption over the range ΔT_4 (inset in Fig. 4).

2.2. *TSD currents.* The temperature spectra of the TSD currents $I(T)$ of BSO:Fe and BGO:Fe crystals look like structured bell-shaped curves (Fig. 5). In BSO:Fe crystals at low polarization temperature ($T_p < 400$ K) a characteristic group of narrow peaks, where intensities grow and whose peaks shift in the direction of higher temperatures with increasing intensity of the polarizing field, is traced on the low-temperature slope of these curves. This group of peaks vanishes if $T_p \geqslant 400$ K. The vanishing of the peaks from the TSD current spectrum corresponds to annealing of optically

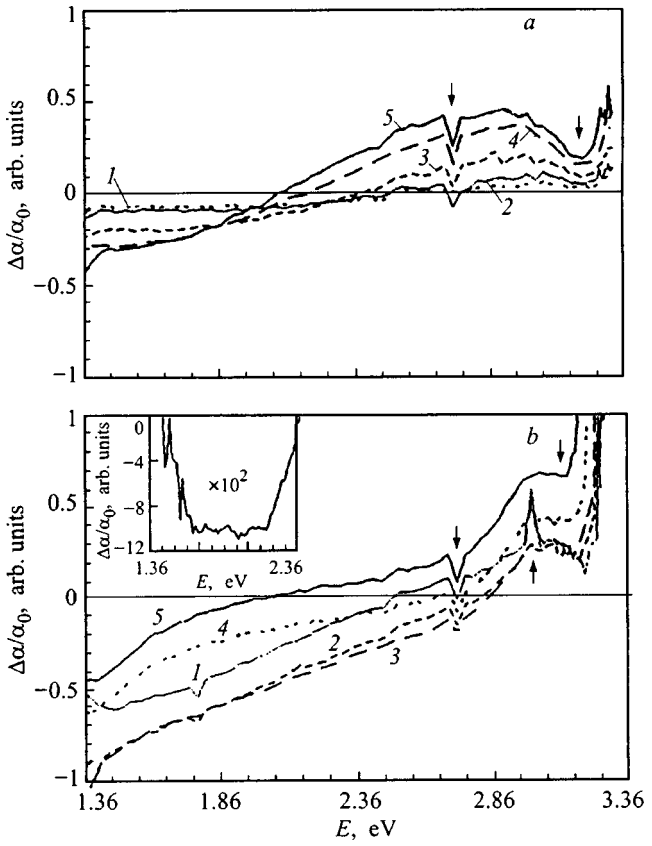

FIG. 4. Thermally induced optical absorption spectra $\Delta\alpha/\alpha_0=[\alpha(E,T_i)-\alpha(E,T_0)]/\alpha(E,T_0)$ of BSO:Fe crystals, where $T_0=86$ K. a—$T_i=105$ (*1*), 115 (*2*), 135 (*3*), 155 (*4*), and 175 K (*5*); b—$T_i=205$ (*1*), 225 (*2*), 245 (*3*), 265 (*4*), and 290 K (*5*). Inset: $\Delta\alpha/\alpha_0(E)$ spectrum for BSO:Fe crystals for $T_i=430$ K and $T_0=300$ K.

active defects in the temperature range ΔT_4 which are responsible for the bleaching band $\Delta E=1.46-2.36$ eV in the absorption spectra. The shift of the peaks was used to estimate the thermal activation energy ${}^{T}E_a$ of electrically active defects from a relation that holds at high temperatures,[27]

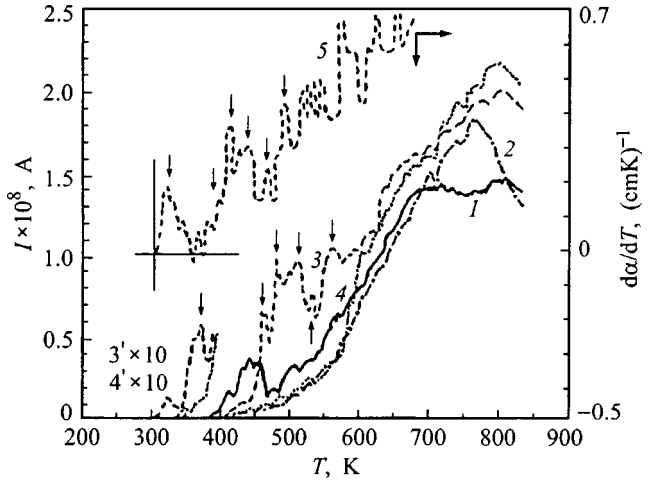

FIG. 5. TSD current spectra $I(T)$ for BSO:Fe crystals for various preliminary polarization conditions: $T_p=340$ (*1, 3, 3′*), 450 K (*2, 4, 4′*), $E_p=4.8\times10^2$ (*1, 2*), 7×10^3 V·cm^{-1} (*3, 3′, 4, 4′*) and the differential spectrum $d\alpha/dT(T)$ of BSO:Fe crystals.

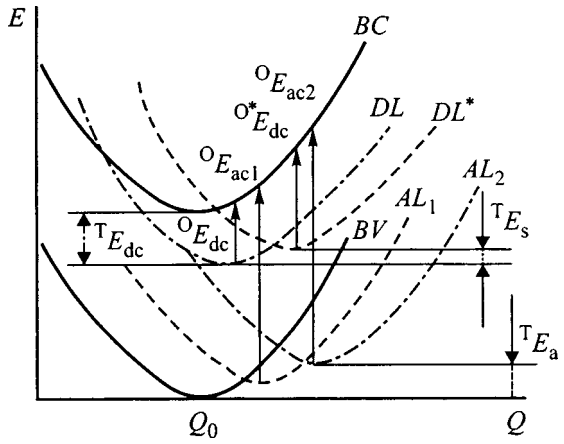

FIG. 6. Total energy E of a BSO:Fe crystal versus the configuration coordinate Q with the main energy characteristics: The curves BC and BV correspond to the total energy of the system in the case where the levels are empty and electrons are in the conduction or valence band; the curves DL and DL^* correspond to the ground and metastable states with electrons in donor levels; and, the curves AL_1 and AL_2 correspond to electrons in acceptor levels.

$$ {}^{T}E_a=\{kT_{m1}T_{m2}/(T_{m2}-T_{m1})\}\{\ln[(I_{m2}/I_{m1})\times(T_{m1}/T_{m2})^2]\}, \quad (6) $$

where T_{m1}, T_{m2}, I_{m1}, and I_{m2} are the temperature positions and intensities of the peaks, respectively. The values obtained, ${}^{T}E_a=0.33$, 0.4, 0.48, 0.52, and 0.56 eV, correlate with the analogous values in Refs. 8 and 9 but found using other experimental methods. As the polarizing field increases, for $T_p\geqslant400$ K, the intensity of the higher-temperature peaks also increases, while their temperature position in the spectrum $I(T)$ remains unchanged (Fig. 5).

3. DISCUSSION

The results can be explained by treating BSO:Fe and BGO:Fe crystals as compensated p-type semiconductors with a high density of acceptor states near the valence-band top and a trail of acceptor levels that extends deep into the band gap. Rapid cooling transfers the crystals into a metastable state, where electrons are frozen in donor levels with ${}^{O}E_{dc}\leqslant2.2$ eV. On heating the frozen electrons are transferred into acceptor levels in the bottom half of the band gap. A characteristic feature of this situation is the large difference between the thermal activation energy (${}^{T}E_{dc}\leqslant30kT_1^*\approx0.5$ eV, where $T_1^*=180$ K is the upper limit of the range ΔT_1) and the optical activation energy (1.36 eV$\leqslant{}^{O}E_{dc}\leqslant2$ eV) for impurity levels responsible for absorption in the A range. This difference can be explained in the configuration-coordinate model by a multiphonon mechanism of electronic transitions from deep levels[28] for metastable and equilibrium states of BSO:Fe crystals (Fig. 6). In a metastable state the optical activation energy for electrons in a donor level (${}^{O*}E_{dc}$) is higher than in the ground state (${}^{O}Fe_{dc}$); this explains the long-wavelength shift of the bleaching band in the A range. The transition to the ground state is a thermally activated process with a low activation energy ${}^{T}E_s=0.015$ eV (determined according to the slope of

the function $\alpha(E)$ in Arrhenius coordinates in the range ΔT_1). As temperature increases, electrons are transferred from the donor levels (ground state) into acceptor levels, whose optical ionization energy ($^{O}E_{ac}$) increases as the levels are filled ($^{O}E_{ac1} > {}^{O}E_{ac2}$). This explains the short-wavelength shift of the thermally induced absorption band in the B range.

The passage of the temperature dependence of absorption through a minimum in the A and B ranges of the spectrum could be due to association–dissociation of impurity centers. All the prerequisites for such processes are present in BMO crystals: the characteristic features of the crystal-chemical structure permit coexistence of several types of elementary point defects between which interactions can arise, creating complex defects. Specifically, thermal-depolarization analysis of the polarization mechanisms in undoped BSO crystals attests to a large contribution due to dipole polarization.[29] Let us examine the formation of dimer complexes from impurity-vacancy quasidipoles[27]

$$dN_{\rm dip}/dt = -\gamma N_{\rm dip}^2 \exp(-E_{\rm ass}/kT) + C(T)N_{\rm com}, \qquad (7)$$

where $N_{\rm dip}$ and $N_{\rm com}$ are, respectively, the densities of dipoles and complexes, γ is a frequency factor, $E_{\rm ass}$ is the thermal association energy of the complexes, and $C(T)$ is the dissociation probability. The solution of this equation gives a function $N_{\rm dip}(T)$ that passes through a minimum and possesses exponential low- and high-temperature initial sections on the shoulders, similar to the function $\alpha(T)$ observed in the experiment. Assuming that the absorption is determined by the density of impurity states due to quasidipoles and their associations, i.e.,

$$\alpha(T) = \sigma(E)N_{\rm dip}(T), \qquad (8)$$

where $\sigma(E)$ is the photon absorption cross section, we obtain $E_{\rm ass}=0.04$–0.06 eV and $E_{\rm dis}=0.07$–0.1 eV, respectively, for the low- and high-temperature shoulders. The spread in the values of $E_{\rm dis}$ and $E_{\rm ass}$ gives $\alpha(T)$ for photon energy $E=1.4$–2 eV.

The correlation of the steep drop in absorption for the A range of the spectrum with the steep increase of absorption for the B range in the temperature range ΔT_4 can be explained assuming that the absorption in the A range is determined by the density N_d of neutral donors, while in the B range it is determined by the density N_a^i of ionized acceptors

$$\alpha_A(T) = \sigma_A(E)N_d(T) + \alpha_{01}$$

and

$$\alpha_B(T) = \sigma_B(E)N_a^i(T) + \alpha_{02}, \qquad (9)$$

where $\sigma_A(E)$ and $\sigma_B(E)$ are the photon absorption cross sections and α_{01} and α_{02} are constants.

The expression[30]

$$N_d(T) = N_d^0\{1 - \beta \exp[\tau_0^* kT^2/(^{T}E_{dc} + 1.85kT)] \times \exp(-{}^{T}E_{dc}/kT)\}, \qquad (10)$$

was found for the temperature dependence of N_d, where N_d^0 is the initial density of neutral donors (at $T=350$ K), β is the degree of compensation of donor levels by acceptors, $\tau_0^* = {\rm const}$, $^{T}E_{dc}$ is the effective energy of thermal activation of donor levels, and $N_d^i(T) = N_d^0 - N_d(T)$ is the relation between the densities of neutral and ionized donors. We obtain an absorption dropoff in agreement with experiment, for example, for photon energy $E=1.735$ eV (curve *3* in Fig. 3a) with $N_d^0 = 1.5\times10^{18}\ {\rm cm}^{-3}$, $\tau_0^* = 2\times10^5\ {\rm K}^{-1}$, $\beta=0.7$, $^{T}E_{dc}=0.65$ eV, $\sigma_A = 1.5\times10^{-18}\ {\rm cm}^2$, and $\alpha_{01}=0.5\ {\rm cm}^{-1}$.

Next we assume that the degree of ionization of the acceptors increases as a result of electrons being transferred from donor to acceptor levels through the conduction band (provided that retrapping in donor centers is negligible). We describe the kinetics of these processes by the equations

$$dN_d/dt = -N_d\omega_d \exp(-{}^{T}E_{dc}/kT),$$
$$dn/dt = N_d\omega_d \exp(-{}^{T}E_{dc}/kT) - n/\tau,$$
$$N_a^i = N_d^0 - N_d - n, \qquad (11)$$

where n is the electron density in the conduction band, τ is the recombination time, and ω_d is a frequency factor, whose temperature dependence we neglect. Under quasistationary conditions, i.e., for $n \ll N_d$, $dn/dt \ll dN_d/dt$, the second equation in this system simplifies: $n = \tau\omega_d \exp(-{}^{T}E_{dc}/kT)$. The boundary condition $N_d = N_d^0$ as $T\to 0$ puts the solution (11) into the form

$$N_a^i = N_d^0\{1 - [1 + \tau\omega_d \exp(-{}^{T}E_{dc}/kT)] \times \exp[(-\omega_d kT^2/b\ {}^{T}E_{dc})\exp(-{}^{T}E_{dc}/kT)]\}. \qquad (12)$$

This expression makes it possible to obtain steep growth of $\alpha(T)$ in the B range in correlation with the dropoff in the A range, for example, for photon energy $E=3.06$ eV (curve *2* in Fig. 3b) with $\tau = 1$ s, $\omega_d = 4\times10^4\ {\rm s}^{-1}$, $\sigma_B = 2\times10^{17}\ {\rm cm}^2$, and $\alpha_{02}=10\ {\rm cm}^{-1}$.

We note that the temperature dependence of the photon absorption cross section in Eqs. (8) and (9) can be neglected, since it is weaker than the exponential dependence,[31] and the values σ_A, $\sigma_B \sim 10^{-17}$–$10^{-18}\ {\rm cm}^2$ are characteristic for deep levels interacting with phonons.[28]

A nearly exponential overall growth of absorption with temperature in the B range is observed due to interband transitions with the participation of phonons and the tail of the energy states next to the valence-band top.

If the temperature dependence of optical absorption is determined by the change in the density of ionized acceptors (or neutral donors), then the temperature dependence of the rate of this change is the analog of the spectrum of the TSD current $I(T)$. The form of $d\alpha/dT(T)$ obtained for the B range of the spectrum confirms this supposition well, reproducing the group of peaks, which are annealed in the range ΔT_4 (marked by arrows in Fig. 5), that is characteristic for TSD currents. The low-temperature ($T<300$ K) peaks of the spectra $d\alpha/dT(T)$ correspond (with respect to position on the temperature axis) to the thermally stimulated luminescence peaks in BSO:Fe and BSO:Ge crystals.[6]

I thank Yu. G. Osetskiĭ for assisting in the experiments.

[1] W. Wardzynski, H. Szymczak, and M. Baran, Physica B **111**, 47 (1981).
[2] H. J. von Bardeleben, J. Phys. D **16**, 29 (1983).

[3] D. B. Senulene, G. A. Babonas, E. I. Leonov, I. Muminov, and V. M. Orlov, Fiz. Tverd. Tela (Leningrad) **26**, 1281 (1984) [Sov. Phys. Solid State **26**, 780 (1984)].
[4] L. B. Kuleva, E. I. Leonov, and V. M. Orlov, Fiz. Tverd. Tela (Leningrad) **29**, 2156 (1987) [Sov. Phys. Solid State **29**, 1240 (1987)].
[5] L. B. Kuleva, E. I. Leonov, and V. M. Orlov, Fiz. Tverd. Tela (Leningrad) **30**(3), 921 (1988) [Sov. Phys. Solid State **30**, 536 (1988)].
[6] M. G. Jani and L. E. Halliburton, J. Appl. Phys. **64**, 2022 (1988).
[7] N. Benjelloun, M. Tapiero, J. P. Zielinger, J. C. Launay, and F. Marsaud, J. Appl. Phys. **64**, 4013 (1988).
[8] V. I. Kalinin, Zh. S. Kuchuk, N. G. Girashchenko, and A. A. Maĭer, Izv. Akad. Nauk SSSR, Neorg. Mater. **24**, 637 (1988).
[9] I. Foldvari, L. E. Halliburton, and G. J. Edrards, Solid State Commun. **77**, 181 (1991).
[10] J. J. Martin, I. Foldvari, and C. A. Hunt, J. Appl. Phys. **70**, 7554 (1991).
[11] B. Briat, J. C. Fabre, and V. Topa, in *Proceeding of the XIIth International Conference ''Defects in Insulating Materials,''* edited by by O. Ranert and J. M. Spaeth (World Scientific, London, 1993), Vol. 2, p. 1160.
[12] I. Foldvari, R. I. Reeves, I. I. Martin, and R. C. Powell, in *Topical Meeting on ''Photorefractive Materials, Effects and Devices PRM'93,''* Kiev, Ukraine, 1993, p. 275.
[13] T. V. Panchenko, Yu. G. Osetsky, and N. A. Truseyeva, Ferroelectrics **174**, 61 (1995).
[14] B. Briat, A. Hamri, F. Ramaz, and H. Bou Rjeily, SPIE Proceeding **3178**, 160 (1997) [*XII-th Conference on Solid State Crystals, Materials Sciences and Applications*, October 7–11, Zakopane, Poland] (1996).
[15] Yu. I. Ukhanov, *Optical Properties of Semiconductors* (Moscow, 1977).
[16] F. Stern, Phys. Rev. **133**, 1653 (1979).
[17] A. T. Futro, J. Phys. Chem. Solids **40**, 201 (1979).
[18] T. V. Panchenko, Yu. N. Potapovich, and G. V. Snezhnoĭ, Izmer. Tekh. **7**, 54 (1992).
[19] R. Oberschmid, Phys. Status Solidi A **89**, 263 (1985).
[20] T. V. Panchenko, V. Kh. Kostyuk, and S. Yu. Kopylova, Fiz. Tverd. Tela (St. Petersburg) **38**(1), 155 (1996) [Phys. Solid State **38**, 184 (1996)].
[21] A. N. Platonov, *The Nature of the Coloration of Minerals* (Naukova Dumka, Kiev, 1976).
[22] Y. Marh, Phys. Rev. **125**, 1510 (1962).
[23] E. I. Leonov, A. E. Semenov, and A. G. Shsherbakov, Fiz. Tverd. Tela (Leningrad) **28**, 1590 (1986) [Sov. Phys. Solid State **28**, 902 (1986)].
[24] T. Toyoda, H. Nakanishi, S. Endo, and T. Irie, J. Phys. C **19**, L259 (1986).
[25] T. V. Panchenko, S. Yu. Kopylova, and Yu. G. Osetskiĭ, Fiz. Tverd. Tela (St. Petersburg) **37**, 2578 (1995) [Phys. Solid State **37**, 1415 (1995)].
[26] M. T. Boroviec, SPIE **3178** Proceeding, 173 (1997) [*XII-th Conference on Solid State Crystals Materials Science and Applications*, October 7–11, Zakopane, Poland (1996)].
[27] Yu. N. Gorokhovatskiĭ, *Principles of Thermal Depolarization Analysis* (Nauka, Moscow, 1981).
[28] B. Ridley, *Quantum Processes in Semiconductors* (Clarendon Press, Oxford, 1982; Russian translation, Mir, Moscow, 1986).
[29] T. V. Panchenko and G. V. Snezhnoĭ, Fiz. Tverd. Tela (St. Petersburg) **35**, 3248 (1993) [Phys. Solid State **35**, 1598 (1993)].
[30] T. V. Panchenko, Fiz. Tverd. Tela (St. Petersburg) **40**, 452 (1998) [Phys. Solid State **40**, 415 (1998)].
[31] A. A. Kopylov and A. N. Pikhtin, Fiz. Tverd. Tela (Leningrad) **16**, 1837 (1974) [Sov. Phys. Solid State **16**, 1200 (1974)].

Translated by M. E. Alferieff

Holographic recording in photorefractive crystals with nonstationary and nonlinear photoconductivity

A. I. Grachev*)

A. F. Ioffe Physicotechnical Institute, Russian Academy of Sciences, 194021 St. Petersburg, Russia
(Submitted July 9, 1998; resubmitted November 24, 1998)
Fiz. Tverd. Tela (St. Petersburg) **41**, 1012–1018 (June 1999)

It is shown that holographic recording in photorefractive crystals made under the conditions of nonstationary and nonlinear photoconductivity is accompanied by nonmonotonic growth of hologram diffraction efficiency because of the specific features in the onset of steady state in an illuminated sample. An analysis of such phenomena observed earlier in sillenite crystals revealed that their interpretation, at least at a qualitative level, does not require invoking the concept of bipolar photoconductivity in these materials. Detailed description of the process of holographic recording occurring in the above conditions requires parallel studies of the photoconductivity kinetics observed in the sample under the same experimental conditions.
 [S1063-7834(99)01806-7]

The mechanism underlying holographic recording of information in photorefractive crystals is based on photoexcitation and subsequent spatial redistribution of free carriers, which, on being trapped at local levels, create a space charge reflecting the light intensity distribution in the image being recorded. The recording proceeds until steady state sets in in the illuminated sample, a process determined by two characteristic times, namely, the time required for the photoconductivity to reach steady state and the time needed by diffusion-drift balance (DDB) (i.e. the state in which the convection current is the same in all cross sections of the sample) to obtain in the sample volume. It is usually assumed (see, e.g., Refs. 1 and 2) that the second time is considerably in excess of the first one, i.e., that recording occurs with constant photoconduction. This conjecture does indeed conform to the conditions of most holographic-recording experiments on photorefractive crystals, which are classed among high-resistivity photoconductors. Note, however, that these materials are characterized by a wide variety of photoconductivity relaxation processes,[3] because essentially different nonequilibrium electron distributions over gap levels can arise. This becomes particularly clear for combined excitation (i.e., simultaneous or successive illumination of a crystal with light differing considerably in spectral composition). Pre-exposure of a sample to light can, in particular, reverse the above-mentioned time ratio, i.e., recording will then be made under nonsteady-state photoconduction. This may affect considerably the hologram recording dynamics and, for instance, make the time dependence of the hologram diffraction efficiency $\eta(t)$ of local maxima (or minima) similar to those observed when recording holograms in crystals of the type of sillenite $Bi_{12}MO_{20}$ (M=Si, Ge, Ti).[4–6]

The observed phenomena were ascribed[4–6] to the effect of the minority carriers (holes) during recording in nominally undoped $Bi_{12}SiO_{20}$ (BSO) and $Bi_{12}TiO_{20}$ (BTO) crystals. Unfortunately, this conjecture was not supported in Refs. 4–6 by reliable experimental data or theoretical estimates. Our analysis[7] of the data on the electronic structure of sillenites and of the studies[8] of surface barrier emf in them suggests that the contribution of holes to the photoconductivity of these materials in the extrinsic absorption region is negligible compared to that of electrons.

This study shows that the behavior revealed[4–6] in holographic recording is readily explainable within the concepts of monopolar photoconductivity in the sillenite crystals used, and the nonmonotonic behavior of $\eta(t)$ is a particular manifestation of the specifics of recording in the conditions of nonstationary and nonlinear photoconductivity, which originate from the nonlinear variation of occupation of local centers in these samples.

1. GENERAL CONSIDERATION

We start with discussing a number of conjectures which, first, define the framework of our consideration and, second, permit one to better understand the specifics of holographic recording in photorefractive crystals in the presence of nonsteady photoconductivity.

(1) One considers the usual case of recording of an interference pattern from two plane waves, with a sinusoidal light-intensity distribution along one of the coordinates (x): $I(x)=I_0[1+m\sin(kx)]$ ($k=2\pi/d$, d is the period of the sinusoidal grating, and m is the modulation depth), and with a constant intensity along the other two. The analysis is done under the usual simplifying approximation $m \ll 1$.

(2) It is also assumed that the condition $(kL_0, kL_d) < 1$ holds, where L_0 and L_d are the drift and diffusion carrier lengths, respectively; this permits one to exclude from consideration the effect of the corresponding carrier flows on the kinetics and spatial distribution of the free-carrier nonequilibrium concentration.

(3) The effect of contacts on the recording process (for instance, in the case of the drift mechanism) is assumed to be unimportant, i.e., one disregards the details of how DDB is established at crystal boundaries.

(4) Recording is carried out in stationary conditions (i.e., without using propagating gratings, alternating fields etc.[2]).

(5) The present consideration does not cover the case of the photogalvanic mechanism of hologram recording.[2]

As already mentioned, when viewed in terms of the electronic processes occurring in a photorefractive crystal, the mechanism of recording reduces to formation of a stationary space-charge distribution $\rho(x)$ corresponding to the intensity distribution $I(x)$. The formation of $\rho(x)$ is described by the well-known system of material equations,[1,2] which in the general case should be complemented by the wave equation. When solving this system, one usually assumes the condition of quasi-stationary recording, which means that recording is performed mainly in a steady distribution of nonequilibrium carrier concentration $n^s_{\rm ph}(x)$ (taking into account the specific features of undoped sillenites, we shall assume in what follows that these carriers are electrons). In other words, it is assumed that $\tau_{\rm rel}$, the time required for $n^s_{\rm ph}$ to set in, is much less than the characteristic hologram recording time τ_w. The latter is essentially the time to attain DDB and is related through $\tau_w=\kappa\tau_M$ to the dielectric relaxation time ($\tau_M=\varepsilon_0\varepsilon/\sigma_0$, where ε_0 and ε are, respectively, the dielectric permittivities of vacuum and the crystal, and σ_0 corresponds to the mean conductivity of an illuminated sample). The coefficient κ depends on the recording mechanism and the relation between k and L_0, and/or L_d, respectively.[1,2] For the condition assumed here (item 3), $\kappa=1$.

Obviously, when recording under conditions of steady-state photoconductivity, the exact form of the kinetics by which it was attained does not practically have any significance. The process by which η attains the steady-state level (η_s) is described by a monotonic relationship.[1,2] The situation may, however, change dramatically if the quasi-steady-state condition is not met, i.e., for $\tau_{\rm rel}\geqslant\tau_M$. The nonequilibrium-electron concentration distribution $n_{\rm ph}(x)$ [and hence, $\rho(x)$] forming in this case in a time $t\sim\tau_M$ is no longer stationary and may vary substantially as the photoconductivity approaches its final state. We shall illustrate this with the diffusion mechanism of interference grating recording under the condition of nonsteady-state sample photoconductivity.

In order to describe the formation of $\rho(x)$, one has to prescribe the shape of the spatial photoinduced-electron distribution $n_{\rm ph}(x)$. When recording takes place under steady-state conditions, the relation between $n^s_{\rm ph}$ and I is usually assumed to be linear (which is indeed valid for most of the known photorefractive crystals), and therefore the shape of $n^s_{\rm ph}(x)$ reproduces exactly the light intensity distribution. The linearity of the $n^s_{\rm ph}(I)$ relation does not, however, exclude the possibility of existence on the photoconductivity rise curve of sections where $n_{\rm ph}$ depends on I in a nonlinear way, i.e. $n_{\rm ph}\propto I^p$, where $p\neq 1$. Obviously enough, the $n_{\rm ph}(x)$ distribution will now differ from $I(x)$. In our case of recording of low-contrast interference gratings this difference will consist primarily in the difference between the photoelectron grating percentage modulation m^* and m, or, to be more precise, $m^*=pm$. Besides, because the presence of nonlinear-in-I sections in the photoconductivity relaxation curve is inevitably connected with variation of p in the course of attainment of the steady-state value, one has to take into account that m^* will now be time dependent. Thus the spatial distribution of conduction electrons (including their dark concentration n_d) for an arbitrary photoconductivity growth curve can be presented in the form

$$n(x,t)=n_d+n_{ph}(x,t)=n_d+n_0(t)[1+m^*(t)\sin(kx)], \tag{1}$$

where n_0 is the nonequilibrium-electron concentration, which corresponds to the average light intensity I_0.

By a time $t_b\sim\tau_M$ after the illumination turn-on DDB will set in in the bulk of the crystal, which in the case under consideration will correspond to the condition of zero convection current throughout the sample. The space charge $\rho(x,t_b)$ will practically correspond to the $n(x,t_b)$ distribution which has set in by this instant of time. Obviously, this will be true the more, the larger is the difference between $\tau_{\rm rel}$ and τ_M. As $n(x,t)$ continues to change, a corresponding variation of $\rho(x,t)$ acting so as to maintain such a nonstationary DDB (the nonsteady convective photocurrent, by the terminology of Ref. 3) will occur. It is appropriate to point out here that because $\tau_M\sim n^{-1}$, its value will also vary with time if the condition $n_d\ll n_{\rm ph}$ prevails in the experiment. In principle, this circumstance should be taken into account in a detailed description of the dynamics of $\rho(x,t)$ formation.

Thus, starting from the time t_b the grating will be recorded while DDB is maintained, and therefore for $t\geqslant t_b$ the distribution of the space-charge grating electric field, $E^b_{sc}(x,t)$, will be described by the same expression as in the case of recording under steady-state photoconductivity[2]

$$E^b_{sc}(x,t)\propto[1/n(x,t)][dn_{\rm ph}(x,t)/dx]. \tag{2}$$

However, taking into account that $n_{\rm ph}$ may depend nonlinearly on I, Eq. (2) can be conveniently recast in the following form

$$E^b_{sc}(x,t)\propto[1/n(x,t)][dn_{\rm ph}(x,t)/dI(x)][dI(x)/dx]. \tag{3}$$

In contrast to stationary recording, Eq. (3) contains now not the steady-state distribution $n^s_{\rm ph}(x)$ but a distribution corresponding to a time $t\geqslant t_b$. Hence if the illumination is continued, the $E^b_{sc}(x)$ distribution may, in a general case, change, and the dynamics of this change will be associated with the given kinetics of photoconductivity growth [i.e., of $n_{\rm ph}(t)$].

We shall be interested in what follows in the evolution of the $E^b_{sc}(x,t)$ grating amplitude $E_D(t)$, which determines the diffraction efficiency $\eta\propto(E_D)^2$ of recorded gratings. Equation (3) yields the following expression for $E_D(t)$:

$$E_D(t)\propto mk[n_d+n_0(t)]^{-1}[dn_0(t)/dI_0]. \tag{4}$$

Equation (4) permits one to construct the necessary and sufficient condition for the appearance of a local maximum (minimum) in $E_D(t)$ and, hence, in $\eta(t)$. For instance, for a particular time $t_m\geqslant t_b$ the following inequality must be met:

$$[n_d+n_0(t_m)]^{-1}[dn_0(t_m)/dI_0] > [n_d+n_0(\infty)]^{-1}[dn_0(\infty)/dI_0]. \tag{5}$$

[The condition for the appearance of a local minimum in $\eta(t)$ is naturally connected with the opposite inequality or, to be precise, two inequalities, the second of which must hold for $t_b \leqslant t < t_m$]. In the limiting cases of $n_d \ll n_0$ and $n_d \gg n_0$, Eq. (5) reduces to the inequalities

$$d \ln[n_0(t_m)]/dI_0 > d \ln[n_0(\infty)]/dI_0 \tag{6}$$

and

$$dn_0(t_m)/dI_0 > dn_0(\infty)/dI_0, \tag{7}$$

respectively. Obviously, inequality (6) or (7) can hold only if nonequilibrium-carrier recombination proceeds nonlinearly, which gives rise to sections with different intensity-current characteristics in the photoconductivity rise curve. As an illustration, consider two simple examples relating to the cases of linear and quadratic nonequilibrium-carrier recombination.

In the first case, the kinetics of recombination are described by the well-known expression[3]

$$n_{\rm ph}(t) = n^s[1 - \exp(-t/\tau)], \tag{8}$$

where τ is the free-electron relaxation lifetime and $n^s = \beta\alpha I\tau$ (β and α are the quantum yield and light absorption coefficient, respectively). Inserting (8) into Eq. (4) we obtain

$$E_D(t) \propto mk\beta\alpha\tau[n_d + n_0^s(t)]^{-1}[1 - \exp(-t/\tau)], \tag{9}$$

where n_0^s corresponds to $I = I_0$. Using Eq. (3), one can readily verify that as photoconductivity approaches steady state, E_D will vary monotonically.

In the case of quadratic recombination, which allows analytic description of the rise curve, $n_{\rm ph}(t)$ has the form[3]

$$n_{\rm ph}(t) = (\beta\alpha I/\gamma)^{1/2} \tanh[t(\beta\alpha\gamma I)^{1/2}], \tag{10}$$

where γ is the recombination coefficient. Substituting Eq. (10) into (4) yields

$$E_D(t) \propto mk[n_d + n_0(t)]^{-1}\{1/2(\beta\alpha/I_0\gamma)^{1/2} \tanh[t(\beta\alpha\gamma I_0)^{1/2}] + 1/2(\beta\alpha t)\cosh^{-2}[t(\beta\alpha\gamma I_0)^{1/2}]\}. \tag{11}$$

Consider the behavior of relation (11) in the cases of $n_d \gg n_0$ and $n_d \ll n_0$. Differentiation of the corresponding expressions with respect to time shows that in the first case the maximum in $E_D(t)$ appears at t_m satisfying the equation

$$\tanh[t_m(\beta\alpha\gamma I_0)^{1/2}] = [t_m(\beta\alpha\gamma I_0)^{1/2}]^{-1}. \tag{12}$$

In the second case, $E_D(t)$ passes through a maximum at $t = 0$, to fall off subsequently smoothly to the value at which $n_{\rm ph}^s$ is reached. It is obvious, however, that because E_D corresponding to the onset of DDB is reached in time $t \sim \tau_M$, it is in this time domain that $E_D(t)$ will reach a maximum in an experiment.

It becomes clear that the maximum in E_D is physically associated in this case with the monotonic decrease of m^* with increasing photoconductivity, from $m^* = m$ for $t \sim \tau_M$ (where $n_{\rm ph} \sim 1$) to $m^* \approx 0.5m$ for the steady-state value $n_{\rm ph}^s \sim I^{1/2}$. Note that while for $n_{\rm ph} \gg n_d$

$$E_D(t) \propto m^*(t), \tag{13}$$

in the opposite case we have

$$E_D(t) \propto n_{\rm ph}(t)m^*(t), \tag{14}$$

and this explains why the extremum is described by Eq. (12). It should be pointed out that which of Eqs. (13) and (14) is found to be correct does not depend on the actual kind of the nonlinearity in $n_{\rm ph}$ relaxation.

Thus the results obtained here support the conclusion that the photoconductivity must be nonstationary and nonlinear at the same time for local extrema to appear in the $\eta(t)$ dependence in the case of holographic recording occurring by the diffusion mechanism. One can readily show that as long as $kL_0 < 1$ holds this conclusion remains valid for the drift mechanism of recording too.

With this we conclude the general consideration and cross over to an analysis of particular examples of nonsteady behavior of $\eta(t)$, which was observed in the experiments[4–6] on holographic recording in sillenite crystals.

2. RECORDING IN IR-IRRADIATED BSO CRYSTALS

Studies[4] of the diffusion mechanism of holographic recording in BSO crystals pre-exposed to IR light revealed that the diffraction efficiency reaches steady state nonmonotonically. This showed in the appearance of a local maximum in η, which exceeded the steady-state level η_s by an order of magnitude. Significantly, the formation of this maximum was accompanied by a change in the kinetics of photoconductivity, namely, the approach by the photocurrent to its steady-state level was considerably slower, and its growth acquired a characteristic S-shaped pattern (see Fig. 2 in Ref. 4). Unfortunately, this observation did not receive due attention,[4] although we believe it to be of fundamental importance.

The light-intensity–current characteristics of steady-state photoconductivity in BSO crystals exhibit a practically linear $n_{ph}^s(I)$ dependence, which sets in a considerably shorter time than τ_M. However, the kinetics of $n_{\rm ph}$ growth cannot always be fitted by Eq. (8). This relates also to the $n_{\rm ph}(t)$ curves presented in Ref. 4, whose S-shaped character indicates clearly nonlinear filling of the trapping levels in the samples that were pre-exposed to IR light. When describing these photocurrent kinetics, we shall proceed from the electronic-level and optical-transition diagram accepted[9,10] for BSO crystals (Fig. 1), by which local T centers at room temperature play the role of multiple trapping levels for electrons. (Actually, sillenites have a group of relatively low-lying levels,[10] all of which we shall refer to as T levels.) The filling of the latter may vary substantially depending on the prior sample history. For instance, when kept a long time in the dark or subjected to IR illumination, T-level electrons undergoing multiple transitions to the conduction band end up by finally becoming trapped at the D or M levels, which leaves the T levels practically empty. If the sample pretreated in this way is illuminated with blue-green light (transitions from the M levels to the conduction band, Fig. 1), the initial stage of $n_{\rm ph}$ growth will be accompanied by the reverse process of electron capture by the T levels. It is when

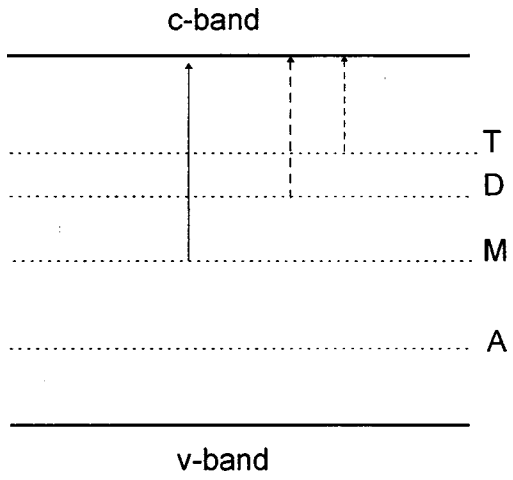

FIG. 1. Diagram of energy levels in the band gap of nominally undoped sillenite crystals. T and D levels—multiple trapping centers and deep traps for electrons, respectively, M—centers responsible for extrinsic absorption in the interval $h\nu \sim (2.3–3.0)$ eV, A—compensating acceptor centers. The solid and dashed arrows identify optical transitions occurring when extrinsic photoconductivity is excited in the blue-green and red (or IR) spectral regions, respectively.

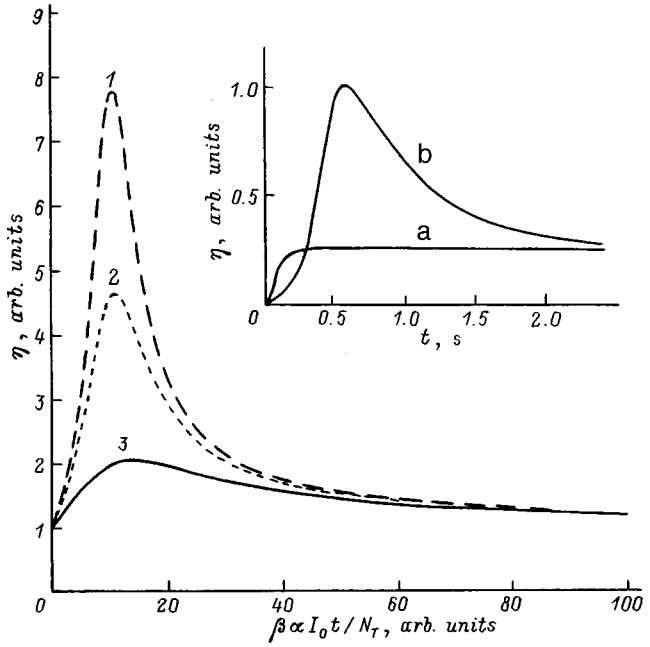

FIG. 2. Time dependences of the diffraction efficiency obtained for the following values of the N_{cT}/N_T parameter: 0.05, 0.1, and 0.4 for curves *1*, *2*, and *3*, respectively. The inset shows similar experimental relations observed in Ref. 4 (a) without and (b) with pre-exposure of a BSO sample to IR illumination.

their filling has changed considerably that the $n_{\rm ph}(t)$ dependence will acquire the S-shaped character. The kinetics of photoconductivity in this case was considered theoretically.[3] We are interested in the initial stage of the $n_{\rm ph}(t)$ relation, because it is there that the local maximum of η in Ref. 4 was observed. The corresponding expression for $n_{\rm ph}(t)$ can be written[3]

$$n_{\rm ph}(t) = -1/2(N_T + N_{cT} - \beta\alpha It) + [1/4(N_T + N_{cT} - \beta\alpha It)^2 + \beta\alpha It N_{cT}]^{1/2}, \quad (15)$$

where N_T is the trapping level density, and N_{cT} is the effective DOS in the conduction band reduced to the T levels.[3]

Substituting now (15) in (4), we can determine the time dependence of η for gratings recorded by the diffusion mechanism. Omitting the fairly lengthy expression, we present here only the time dependences of η obtained from it (or rather, the dependence on a dimensionless variable $\beta\alpha I_0/N_T$) (see Fig. 2) for some values of the N_{cT}/N_T parameter. [Note that because Eq. (4) describes the behavior of E_D only for $t \geqslant \tau_M$, the curves in Fig. 2 do not start from the origin.) It is easy to show that η passes through a maximum at t_m satisfying the condition $N_T + N_{cT} = \beta\alpha I_0 t_m$ [the point of maximum bending in the $n_{\rm ph}(t)$ curve, Ref. 3], and that $\eta_{\max}$ is given by the following expression (for $n_d \ll n_{\rm ph}$, which is in agreement with the actual experimental conditions[4])

$$\eta_{\max}^{1/2} \propto E_D(t_m) \propto m\{1 + [(N_T + N_{cT})/2N_{cT}]^{1/2}\}. \quad (16)$$

As seen from Eq. (16) and Fig. 2, the extent by which $\eta_{\max}$ exceeds η_s depends on such parameters of the material as N_T and N_{cT}, which, in principle, can be derived from a study of photoconductivity kinetics.[3]

A comparison of the curves in Fig. 2 with the data of Ref. 4 (see inset to Fig. 2) shows them to be qualitatively identical, which obviates the need of invoking the model of carrier bipolar diffusion proposed in Ref. 4 to account for the observed dynamics of η growth.

3. IR RECORDING IN BTO CRYSTALS

A study[5] of energy transfer dynamics in two-beam coupling experiments revealed a nonmonotonic behavior of the photorefractive gain factor Γ (Fig. 3), which in the experimental conditions of Ref. 5 was found to be proportional to $\eta^{1/2}$. In contrast to Ref. 4, the writing beam wavelength was here in the IR range ($\lambda = 1.06\,\mu$m), and the nonmonotonic course of Γ was seen most clearly in samples pre-exposed to visible light. The model proposed in Ref. 5 for interpretation of the data obtained was a slightly modified version of the one used in Ref. 4, and it was also based on the concept of holes creating a space-charge grating of opposite phase.

Turning now to an analysis of the data of Ref. 5, we should point out that until now we have been associating the nonlinearity of $n_{\rm ph}(I)$ only with the variation of the lifetime (more precisely, of the relaxation lifetime[3]) of nonequilibrium carriers in the course of attaining $n_{\rm ph}^s$. However in the case of extrinsic excitation the character of $n_{\rm ph}$ relaxation can be affected also by the variation of α, which is caused by substantial variation in the population of the levels involved in photoactive optical transitions. This behavior of $n_{\rm ph}$ is well illustrated by the so-called induced extrinsic photoconductivity,[3] which is observed under simultaneous or successive illumination of a sample in the intrinsic and extrinsic absorption regions. Such a situation was realized in BTO crystals,[5] and, as we are going to show, it may account for the behavior of Γ observed in the quoted experiment.

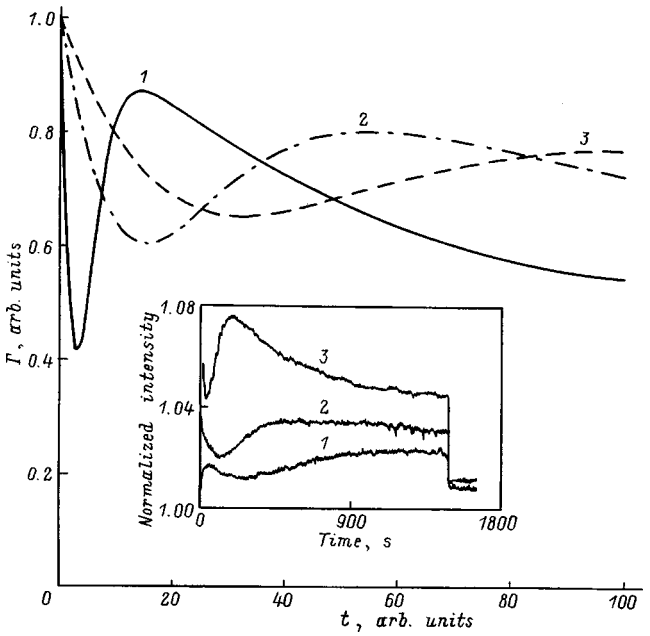

FIG. 3. Time dependence of the gain Γ obtained from Eq. (18) for the following parameters r_1, r_2, q, and ξ: (*1*) 4; 0.5; 0.5; 2.5×10^{-2}, (*2*) 2; 0.5; 0.1; 5×10^{-2}, and (*3*) 2; 1; 5×10^{-2}; 0.1. The inset shows similar experimental relations observed in Ref. 5 in a BTO crystal for various delays between the end of sample pre-exposure and the beginning of recording: 60 h, 18 h, and 20 s for curves *1*, *2*, and *3*, respectively.

The kinetics of $n_{\rm ph}(t)$ in the case of induced extrinsic photoconductivity can be described by the following expression[3]

$$n_{\rm ph}=[qIN_T/(1/\tau-qI)][\exp(-qIt)-\exp(-t/\tau)], \tag{17}$$

where q is the photon capture cross section by electrons at the levels (T levels in our case) which have been populated in the pre-exposure of the sample to intrinsic illumination.

Equation (17) does not, however, adequately describe the real behavior of induced photocurrent, which for large t tends not to zero but rather to a ''quasi-equilibrium'' [3] value. This is because repeated electron capture by trapping levels was disregarded in the derivation of Eq. (17). The real behavior of $n_{\rm ph}(t)$ can be most conveniently fitted by two exponentials with different decay rates, complemented by a time-independent term (the latter is due, first, to a nonzero filling of the T levels for $t\to\infty$, and, second, to optical excitation of other centers, for example, of D levels):

$$n_{\rm ph}=qIN_T\tau\exp(-qIt)+qIn_T^*\tau^*\exp(-\xi qIt)]+\zeta I, \tag{18}$$

where n_T^* and τ^* are the T-level filling and the electron lifetime after the ''quasi-equilibrium'' excited state has been reached, respectively, and parameter $\xi\ll1$. (We have also assumed that the condition $1/\tau\gg qI$ is met, which apparently is applicable to the experiment of Ref. 5).

In the conditions of weak energy transfer,[5] $\Gamma\propto E_D$, and therefore substitution of (18) into (4) yields an expression for the $\Gamma(t)$ relation (for the $n_d\ll n_0$ case)

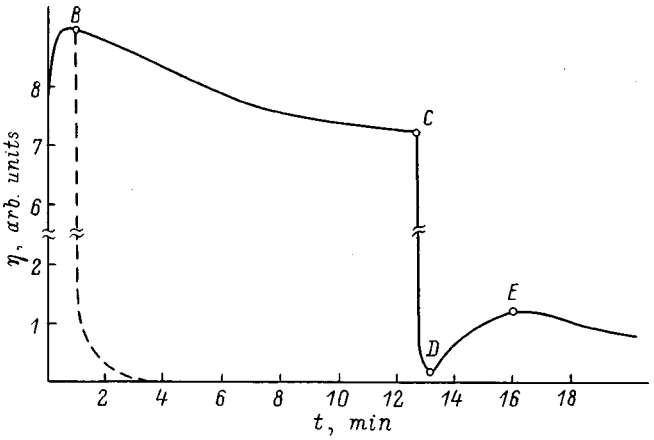

FIG. 4. Time dependence of diffraction efficiency (from Ref. 6).

$$\Gamma(t)\propto I-qI_0t\{r_1+\xi\exp[qI_0t(1-\xi)]\}\{r_1+\exp[qI_0t(1-\xi)]+r_2\exp(qI_0t)\}^{-1}, \tag{19}$$

where $r_1=N_T\tau/n_T^*\tau^*$, and $r_2=\zeta/qn_T^*\tau^*$. Figure 3 displays $\Gamma(t)$ plots obtained using Eq. (19) for different q, r_1, r_2, and ξ (I_0 was assumed to be unity). A comparison with experimental relationships[5] obtained for the dynamics of signal-beam intensity variation (see inset to Fig. 3) shows them to be in a qualitative agreement. We believe that given data on the photoconductivity kinetics observed in the sample in the same experimental conditions, our approach could provide a quantitative description of the results of Ref. 5 as well.

Thus even with the overly simplified character of the model used here, taking into account the clearly nonsteady-state nature of the recording conditions and the nonlinear behavior of photoconductivity in Ref. 5 permits one, while remaining within the frame of the monopolar conduction model for BTO crystals, to explain the cited behavior of $\Gamma(t)$.

4. OSCILLATORY BEHAVIOR OF THE DIFFRACTION EFFICIENCY IN BTO CRYSTALS

We believe that it is a specific combination of nonsteady-state photoconductivity with a variation of local-level filling that is responsible for the oscillatory behavior[6] of η of the gratings recorded in BTO by the diffusion mechanism after interruption of one of the writing beams (Fig. 4). The conditions favoring the onset, and the specific features of the observed effect, such as the high spatial frequency of recorded gratings, the presence of a declining section in the $\eta^{\rm pr}(t)$ relation of the initially recorded gratings, and the 180° spatial shift in phase between the primary and secondary gratings permit us to put forward the following interpretation of its nature.

The behavior of $\eta^{\rm pr}(t)$ indicates that similar to Ref. 5 the photoconductivity of the samples in Ref. 6 illuminated at $\lambda=0.63\,\mu$m was (most likely, partially) of an induced origin involving the T levels. The relatively slow decay rate of $\eta^{\rm pr}$ suggests the quasi-equilibrium state of the T levels, in which the decrease of their population (like the decay of $n_{\rm ph}$) is

described by an exponential with a long time constant [the second term in Eq. (18)). Nonuniformity of illumination in this stage of recording of the primary grating should give rise in this case to a spatially nonuniform distribution in the sample of T levels with different populations, which at time t_c (point C in Fig. 4) can be written

$$n_T^*(x,t_c)=n_T^*(0)\exp[-\xi q t_c I_0(1+\sin(kx))], \qquad (20)$$

where $n_T^*(0)$ is the initial quasi-equilibrium T-level population [Eq. (20) takes into account that the gratings recorded in Ref. 6 had $m=1$). Clearly, a crossover to uniform illumination of the crystal the $n_T^*(x,t_c)$ distribution will produce in the latter a spatially nonuniform electron distribution $n_{\rm ph}^{\rm sec}(x)$. The Fourier component of $n_{\rm ph}^{\rm sec}(x)$ at the fundamental spatial frequency, $n_{\rm ph}^{\rm sec}(x,k)$, will be shifted by 180° with respect to $n_{\rm ph}^{\rm pr}(x,k)$ of the primary grating. The effect under consideration was observed[6] only in the case where uniform illumination was turned on after a fairly long time interval [indeed, the switching at point B (Fig. 4) did not cause oscillations in η], which was considerably in excess of the erasure time of the primary grating (section CD in Fig. 4). Therefore by the end of erasure the nonuniformity in n_T^* could not decrease substantially, which could make possible recording of the secondary (opposite-phase) grating during subsequent illumination (section DE). As time goes on, however, uniform illumination should result in equalization of T-level population, which, in turn, would bring about erasure of the secondary grating, exactly as observed in the experiment (Fig. 4).

Actually, this effect was observed[6] only when recording gratings with a very small period comparable to the diffusion length ($L_d \sim 0.3\,\mu$m). This implies that the nonuniformity in n_T^* created solely by the above mechanism was apparently not large enough for recording holograms with a noticeable $\eta^{\rm sec}$. [Using data in Fig. 4 and Eq. (19), one can estimate the contrast $n_T^*(x,k)$ as $\sim 10^{-1}$, which provides a ratio $\eta^{\rm sec}/\eta^{\rm pr} \sim 10^{-2}$. At the same time the experimental value of this ratio was $\sim 10^{-1}$.] An additional, more precisely, the major contribution to the contrast $n_T^*(x,k)$ in the high spatial frequency domain was provided, in our opinion, by the positive and/or negative $\rho^{\rm pr}(x,k)$ component. The maximum of the first component formed by positively charged donors lies in the region of the maximum in $I(x)$, and that of the second component associated with electron capture into local levels, conversely, at the minimum in $I(x)$. Hence if T levels contribute even partially to $\rho^{\rm pr}(x,k)$, the percentage modulation of the $n_T^*(x,k)$ grating may exceed the value provided by the above mechanism. Also, because $\rho^{\rm pr}(x,k) \propto k^2$, the contribution of the charge to the modulation of $n_T^*(x,k)$ does indeed grow substantially with increasing spatial frequency of the gratings. After this contribution to the nonuniformity of $n_T^*(x)$ has become dominant over the first one (starting with some value of k), one should observe a steep growth $\eta_s^{\rm sec} \propto k^6$ up to the values $kL_d \leqslant 1$, to be replaced thereafter by a $\propto k^2$ behavior. This is apparently what accounts for the observation[6] of the above effect only when recording gratings with high k.

Thus, we see that the characteristics of the effect reported in Ref. 6 can be explained also without invoking the idea of bipolarity of photo- or dark conductivity of BTO, which was put forward in Ref. 6 and developed further in Ref. 11. Turning now to the results of the above analysis, it should be stressed once more that in a general case correct interpretation and detailed description of the process of holographic recording in photorefractive media requires accurate data on sample photoconductivity relaxation observed in the experimental conditions in which the holograms were recorded.

Thus, we have shown that if recording in photorefractive crystals is done in conditions of nonstationary and nonlinear photoconduction, one has to take into account the specifics of how steady state is reached in the illuminated sample. Among these specific aspects is the nonmonotonic way in which the diffraction efficiency of holograms reaches steady-state level, which was observed in some experiments performed on sillenite crystals.[4–6] Our analysis has revealed that the observed[4–6] effects can be explained, at least qualitatively, without invoking the idea of sillenite photoconduction being bipolar. A comprehensive quantitative description of holographic recording in photorefractive crystals, particularly in the conditions discussed above, requires investigation of the photoconductivity kinetics in the samples used.

*)E-mail: grach@shuv.pti.spb.su

[1] N. V. Kukhtarev, Pisma Zh. Tekh. Fiz. **2**, 1114 (1976) [Sov. Tech. Phys. Lett. **2**, 438 (1976)].
[2] M. P. Petrov, S. I. Stepanov, and A. V. Khomenko, *Photorefractive Crystals in Coherent Optical Systems* (Springer, New York, 1991) [Russian original, Nauka, St. Petersburg, 1992].
[3] S. M. Ryvkin, *Photoelectric Effects In Semiconductors* (Consultants Bureau, New York, 1964) [Russian original, Fizmatgiz, Moscow, 1963].
[4] A. A. Kamshilin and M. P. Petrov, Fiz. Tverd. Tela (Leningrad) **23**, 3110 (1981) [Sov. Phys. Solid State **23**, 1811 (1981)].
[5] S. G. Odulov, K. V. Shcherbin, and A. N. Shumeljuk, J. Opt. Soc. Am. B **11**, 1780 (1994).
[6] M. Miteva and L. Nikolova, Opt. Commun. **67**, 192 (1988).
[7] A. I. Grachev, Fiz. Tverd. Tela (St. Petersburg) **40**, 2178 (1998) [Phys. Solid State **40**, 1975 (1998)].
[8] A. I. Grachev, Fiz. Tverd. Tela (Leningrad) **26**, 227 (1984) [Sov. Phys. Solid State **26**, 132 (1984)].
[9] V. N. Astratov, A. V. Il'inskiĭ, and M. B. Mel'nikov, Fiz. Tverd. Tela (Leningrad) **25**, 2163 (1983) [Sov. Phys. Solid State **25**, 1244 (1983)].
[10] V. K. Malinovskiĭ, O. A. Gudaev, and V. A. Gusev, *Photoinduced Phenomena in Sillenites* [in Russian] (Nauka, Novosibirsk, 1990).
[11] S. Zhivkova and M. Miteva, J. Appl. Phys. **68**, 3099 (1990).

Translated by G. Skrebtsov

DEFECTS. DISLOCATIONS. PHYSICS OF STRENGTH

A mechanism for photoinduced electronic reconstruction of the oxygen vacancy in doped quartz glass and its characteristics

K. M. Golant*) and V. V. Tugushev

Fiber-Optics Science Center, Institute of General Physics, Russian Academy of Sciences, 117756 Moscow, Russia

(Submitted July 16, 1998)
Fiz. Tverd. Tela (St. Petersburg) **41**, 1019–1025 (June 1999)

A mechanism is proposed for electronic reconstruction of excited oxygen-deficient (OD) centers in doped quartz glass, associated with partial delocalization of one of the valence electrons. Using Falicov's model Hamiltonian, the binding energy, radius, and criterion for an electron transition from a localized state to a state of intermediate radius are qualitatively determined. Densification of the glass matrix surrounding the OD centers is predicted as a possible consequence of the reconstruction of their valence electrons. An explanation is proposed for the irreversible photoinduced changes in refractive index, photoluminescence spectra, and electron paramagnetic resonance that are experimentally observed in doped quartz glasses after processing with large doses of ultraviolet light. © *1999 American Institute of Physics.* [S1063-7834(99)01906-1]

Doped quartz glasses, which are extensively used in contemporary optoelectronics, have physical properties that are of great interest both to scientists and engineers. Most of these are primarily related to the presence of defects in the glass network. One of the most striking physical phenomena exhibited by these quartz glasses is the photorefractive effect, in which the glass suffers an irreversible and rather large change in refractive index ($\Delta n \approx 10^{-4} - 10^{-3}$) after absorbing a high dose of ultraviolet light.[1] This photorefractive effect underlies the technology of writing filamentary refractive index gratings—important components of optical communications systems and fiber-optic detectors. Although the photorefractive effect has been observed in quartz glasses with various doping additives and has been studied in considerable detail experimentally, it is still unclear at this time what physical mechanism causes it and how to derive an adequate theoretical model to describe it.

Due to their extensive use as constituents in fiber-optic communications systems, glasses and light guides with the composition SiO_2/GeO have been studied in the most detail. It has been established that the magnitude of the photorefractive effect in these glasses depends on the number of germanium oxygen-deficient (Ge-OD) centers in the glass structure. The Ge-OD center is a well-known defect of the ''oxygen vacancy'' type, and has an absorption band in the ultraviolet with a maximum near 242 nm. The photorefractive effect, which appears when the glass is illuminated at a wavelength lying within the absorption band of the Ge-OD center, is accompanied by an irreversible structural change in the glass network associated with the destruction of the Ge-OD center. In addition, processing with high-power ultraviolet light causes densification of the glass (with $\Delta\rho/\rho \approx 10^{-3}$).

Note that in undoped SiO_2, oxygen vacancies lead to the formation of Si-OD centers, with a characteristic absorption band in the neighborhood of 248 nm; however, ultraviolet light does not give rise to a photorefractive effect in this case. It is possible to make germaniumless quartz glass photosensitive by replacing some of the oxygen atoms with nitrogen;[2] in this case a photorefractive effect is observed when the glass is exposed to laser light at a wavelength of 193 nm, but is absent when the glass is excited via the Si-OD center absorption band.

The spectroscopy of OD centers in high-purity quartz glasses has been studied in great detail (see, for example, Ref. 3). Besides the absorption bands already mentioned (248 nm for undoped SiO_2 and 242 nm for SiO_2/GeO_2), there are very interesting luminescence bands with wavelengths of order 400 and 290 nm that are associated with electronic transitions from OD-center excited states to the ground state; the luminescence times for these bands differ by three orders of magnitude. It is characteristic that the photoinduced changes in refractive index observed in SiO_2/GeO_2 are accompanied by photoinduced bleaching away of the luminescence bands of diamagnetic OD centers, with simultaneous formation of other paramagnetic centers which are easily observed by EPR.[4] This conversion of diamagnetic centers to paramagnetic centers is evidence of a photoinduced redistribution of the valence electrons of OD centers. In this case, electronic reconstruction is accompanied by a strong atomic relaxation in the neighborhood of the OD center.[5]

Irreversible reconstruction of the OD center structure during relaxation from the excited state serves as a starting premise for the majority of theoretical models of the photorefractive effect. However, it is usually assumed, as in Ref.

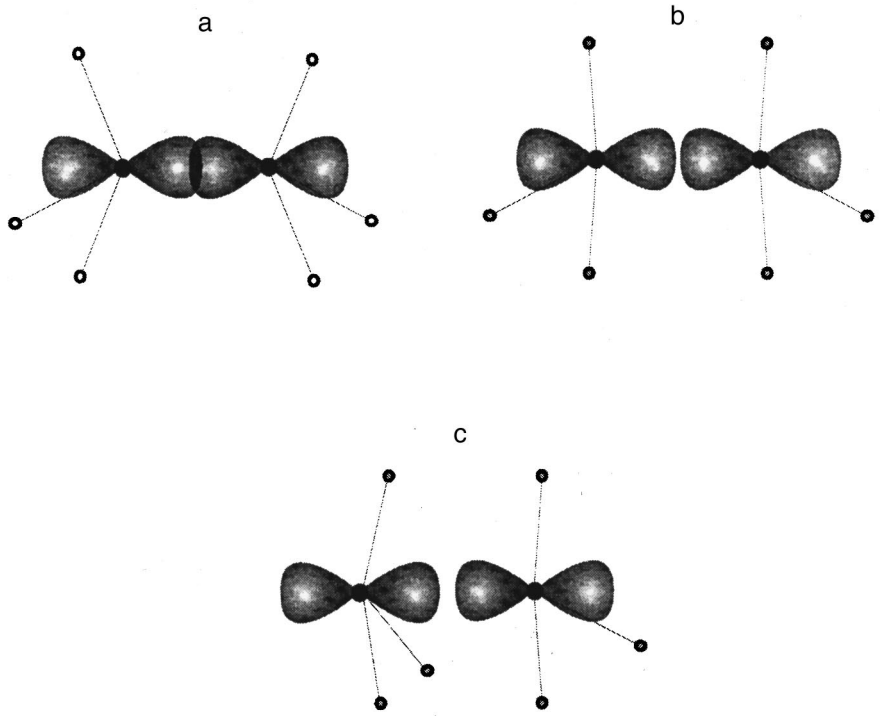

FIG. 1. Sketch of structural reconstruction of an OD center under photoexcitation: a—localized unrelaxed center before excitation; b—localized relaxed photoexcited OD center (''normal'' configuration); c—localized relaxed photoexcited OD center (''anomalous'' configuration).

5, that the atomic reconstruction is limited in scale to the first coordinate sphere of the OD center, and that electronic reconstruction leads to photoionization of a valence electron of the oxygen vacancy with subsequent trapping by another point defect (or the same defect, now relaxed). A weak spot in this ''lattice-site'' approach to the system reconstruction is the fact that in order to obtain the $\Delta n \approx 10^{-4}-10^{-3}$ observed in experiment, postulating reasonable concentrations of $10^{18}\,\mathrm{cm}^{-3}$ for OD centers ''reconstructing'' under the action of light, the reconstruction must increase the polarizability of an individual point center by two to three orders of magnitude. To date, no one has proposed a mechanism for such an increase.

In this paper we discuss an alternative model, in which photoexcitation of OD centers is accompanied by not only structural but also radical electronic reconstruction, with a change in the scale of the wave function of one of the valence electrons. We will assume that this electron makes a transition to a partially delocalized state that is genetically related to the band of delocalized states of the glass matrix. Partial delocalization of a OD center electron in turn initiates a strain-driven reconstruction (densification) of the glass, spread over ten or more SiO_3 tetrahedral-unit volumes around the center. In this case, the electronic contribution (related to partial delocalization) and strain-induced contribution (connected with densification) to the change in index Δn can turn out to be the same order of magnitude, and can easily achieve the values observed in experiment.

1. ENERGY SPECTRUM OF LOCALIZED ELECTRONIC STATES OF PHOTOEXCITED OD CENTERS

In order to investigate the photosensitivity, we will construct an energy scheme for OD centers starting from the model of a neutral oxygen vacancy $V[\mathrm{Si}-\mathrm{Si}]$ (see the survey of the literature in Ref. 5), which is widely used to explain the optical properties of silicon dioxide. At the basis of this model is a representation of the OD center as a peculiar hydrogenic ''molecule'' consisting of two Si atoms that are neighbors of the vacancy and which also form the vertices of SiO_3-tetrahedra. In the ground-state singlet (S_0) state, the Si atoms are strongly shifted towards each other, and the binding of sp-hybrid Si orbitals along the Si=Si axis causes them to form a stable complex which is incorporated into the silicon dioxide matrix (see Fig. 1a). The lowest singly-excited intracenter states S_1 (singlet) and T_1 (triplet) in the $V[\mathrm{Si}-\mathrm{Si}]$ system are characterized by a transition of one of the two sp-electrons from a binding to an antibinding orbital. Experiments on the optical absorption and photoluminescence show that the singlet–singlet dipole-allowed transition energy is $E(S_1)-E(S_0)\approx 4.5-5.0\,\mathrm{eV}$. The singlet–triplet transition is spin-forbidden, but the position of the $E(T_1)$ level relative to the $E(S_1)$ level can be estimated from photoluminescence experiments: $E(S_1)-E(T_1)\approx 1.5-1.8\,\mathrm{eV}$. The exact values of the energies of intercenter single-particle excitations $E(S_1)-E(S_0)$ and $E(T_1)-E(S_0)$ do not in themselves play an important role in the construction of our model. We note only that the doubly excited state S_2 connected with intracenter singlet–singlet transitions lies much higher in energy (more than 10 eV) and will not be discussed here.

We must emphasize[5,6] that transitions to an excited state are accompanied by a considerable relaxation of the Si atoms in the $V[\mathrm{Si}-\mathrm{Si}]$ complex. In particular, the distance between them increases compared to the configuration S_0 (Fig. 1b). Thus, ''equilibrium'' values of $E(S_1)$ and $E(T_1)$ must be understood as total energies (including relaxation) of the corresponding configurations.

In addition to excitations that do not change the charge

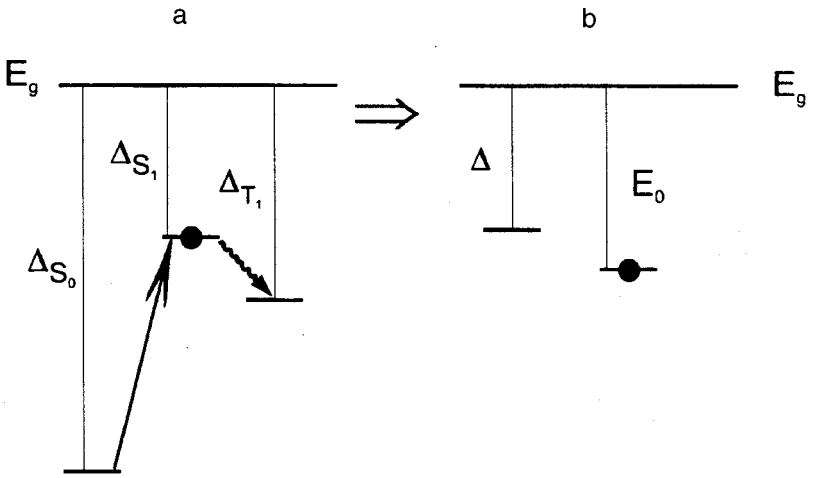

FIG. 2. Change in the single-electron spectrum as an excited oxygen vacancy converts from the normal (a) to the anomalous (b) state.

state of the V[Si–Si] complex, there are also charge-transfer excitations of this complex. Let us discuss in more detail the singly-charged configurations of V[Si–Si]. Denoting the energy of such a configuration by E^+, we introduce the energies $\Delta(A)$ of single-particle excitations with charge transfer to the vacancy, measured relative to the energy E_g of the bottom of the band of delocalized allowed states, that is, $\Delta(A)=E_g-\varepsilon(A)$, where $\varepsilon(A)=E^+-E(A)$. Here $E(A)$ are configuration energies, and $A=S_0$, S_1, T_1 (see Fig. 2a). We can make only a crude estimate of the value of $\Delta(A)$. We will take $\Delta(S_1)\approx 1.5-2.5$ eV, $\Delta(T_1)\approx 3-4$ eV, and $\Delta(S_0)\approx 7-9$ eV; specific values vary strongly when a portion of Si is replaced with Ge in germanium-rich glasses.

The excited configuration of the OD center is structurally nonrigid (see the discussion in Ref. 5), and the departure of one of the electrons from the valence binding sp-orbital may be accompanied by an additional increase (compared to the configuration shown in Fig. 1b) in the distance between Si atoms, followed by total reconstruction of the OD center structure. Following Snyder and Fowler,[7] we will refer to this as a transition from the ''normal'' configuration to an ''anomalous'' configuration (Fig. 1c).

The dynamics and mechanism for irreversible reconstruction of the OD center structure under ultraviolet excitation is a separate problem and is of no immediate interest to us here. It is significant, however, that experimental data suggest that both direct singlet–singlet excitation from S_0 to S_1, and singlet–triplet excitation from S_0 to T_1 change the refractive index.[8] Furthermore, studies of photoluminescence kinetics show that the lifetime for the excited state S_1 is short (a few tens of ns), and that the primary channel for intracenter relaxation of a photoexcitation with substantial quantum yield is a nonradiative transition to the long-lived triplet state T_1 (around 100 μs) with subsequent luminescence.[9] This implies that reconstruction of the OD center structure will take place from the configuration T_1 with high probability. The total energies of the original (unreconstructed T_1) and structurally modified configurations are close in magnitude, to accuracy of a few tenths of an eV, and are separated by an energy barrier of order 0.5 eV.

We point out that in the anomalous configuration the entire nomenclature of single-particle electronic excitations of the OD center changes, because the correlation between sp-electrons of the two constituent Si atoms of the OD center is weakened due to the weak overlap of the corresponding orbitals. As a result, the difference between singlet and triplet excitations practically disappears (see Fig. 2b), and we can speak simply of a single particle excitation energy Δ, omitting the labels S and T. It is natural to assume that the energy Δ does not exceed the minimum $\Delta(A)$ of the most strongly bound complex with the ''normal'' configuration, i.e., $\Delta\leqslant 1-2$ eV, and in any case lies comparatively close to the bottom of the band of allowed states. The latter fact has not been included in calculating the electronic spectra of OD centers up to now, and in the next section we will turn to a discussion of its role.

2. A WEAKLY LOCALIZED STATE IN THE ELECTRONIC SPECTRUM OF EXCITED OD CENTERS, AND CHANGES IN ELECTRON POLARIZABILITY

Based on the assumptions we have made so far, let us construct a model of the electronic spectrum of photoexcitations of a completely relaxed oxygen vacancy for OD centers, taking into account the possibility of charge transfer to the complex V[Si–Si] and a transition of an electron to the outer (delocalized) shells formed by sp-orbitals of silicon dioxide.

Let us turn to a mathematical formulation of our model. We will use the simplest Falicov Hamiltonian,[10] which was proposed for a system with two types of particles (delocalized and localized on a center) and includes the possibility of charge transfer to the center:

$$H_0=-\Delta n_0+\int [\psi^+(\mathbf{r})\varepsilon(\nabla/i)\psi(\mathbf{r})-\psi^+(\mathbf{r})(1-n_0)\times\psi(\mathbf{r})U(\mathbf{r})]d\mathbf{r}, \quad (1)$$

where $\psi(\mathbf{r})$ is the envelope of the wave function of band states, n_0 is the number of filled localized states with energy $-\Delta$ relative to the lower edge of the band of delocalized states, $\varepsilon(\nabla/i)$ is the kinetic energy, and $U(\mathbf{r})$ is the interaction potential of an electron from the band of delocalized states with an OD center in the anomalous configuration. The situation $n_0=1$ corresponds to a localized state of an

sp-electron on the anomalous OD center configuration, while $n_0=0$ represents single excitation (ionization) of this configuration. The state with $n_0=1$ was discussed in the previous section; we now will focus our attention on the state with $n_0=0$.

For simplicity let us assume that the interaction potential $U(\mathbf{r})$ in Eq. (1) is quite large in the neighborhood of the core of the OD center (i.e., over distances of order the distance between Si atoms in the V[Si–Si] complex) and falls off rapidly outside this region. The detailed form of $U(\mathbf{r})$ does not play an important role in discussing the reconstruction of the electron density over scales large compared with the size of the OD center core.

In the model of a spherical rectangular potential well ($U(\mathbf{r})=U_0$ for $r<a_0$, $U(\mathbf{r})=0$ for $r>a_0$, where the effective radius a_0 is the same order as the radius of the OD center core), it is well known that a bound state appears for $U(\mathbf{r})>U_{0\,\min}$, where $U_{0\,\min}=\pi^2/8m^*a_0^2$ and m^* is the effective mass of the particle. For $|U_0/U_{0\,\min}-1|\ll 1$ the binding energy of this state[11] for the Hamiltonian H_0 is

$$|\langle H_0\rangle|=E_0=\frac{\pi^2}{16}U_0(U_0/U_{0\,\min}-1)^2. \tag{2}$$

The wave function $\psi(\mathbf{r})$ at large distances $r\gg a_0$ falls off like

$$\psi(\mathbf{r})\approx\frac{\exp(-r/c_0)}{(r/c_0)}. \tag{3}$$

Here c_0 is the radius of the bound state

$$c_0=(\sqrt{|E_0|})^{-1}\eta\gg a_0, \tag{4}$$

where $\eta=(2m^*)^{-1/2}$. Thus, if $U_0>U_{0\,\min}$ and $E_0>\Delta$, the state with wave function (3) turns out to be energetically favored. This state is very similar to an exciton with intermediate radius and an infinitely heavy hole, and it serves as the key to understanding the reconstruction of the electronic spectrum of the system in model (1). The radius of this new state $c_0\gg a_0$, which immediately leads to a sharp increase in the polarizability of the system. In fact, according to Ref. 11, the polarizability $\alpha_{\rm el}$ of an electron in a spherical well in the presence of a single bound s-state E_0 equals

$$\alpha_{\rm el}=\frac{m^*e^2c_0^4}{4}; \tag{5}$$

for concentrations of reconstructing centers $N_{\rm ODC}$ the change in refractive index $n=\varepsilon^{1/2}$, where ε is the dielectric permittivity of the medium ($\varepsilon=1+4\pi\alpha$, where α is the total polarizability), comes to

$$\Delta n_{\rm el}\approx\frac{2\pi\alpha_{\rm el}}{n}N_{\rm ODC}=\frac{\pi}{2n}\frac{c_0^4}{a_B}N_{\rm ODC}, \tag{6}$$

where a_B is the Bohr radius of an electron with effective mass m^*. At concentrations $N_{\rm ODC}\approx 10^{18}\,{\rm cm}^{-3}$ and values of $n\approx 1.5$, the change in index of refraction due to the electronic reconstruction of the OD centers is estimated to be $\Delta n_{\rm el}\sim(c_0/a_B)^4 10^{-6}$, which for $c_0/a_B\approx 3-5$ can easily reach $\Delta n_{\rm el}\approx 10^{-4}-10^{-3}$. Note that in our model we must have $c_0/a_B\gg 1$ in principle in order for the model to be applicable, because $m^*\sim m$, $a_B\sim a_0\sim 2-4$ Å is the radius of the OD center core, while $E_0\gg U_0$ and $c_0\gg a_0$ according to the conditions of the problem.

3. INTERACTION OF AN EXCITED OD CENTER WITH THE GLASS MATRIX AND CHANGE IN THE REFRACTIVE INDEX CONNECTED WITH DENSIFICATION OF THE MEDIUM

It has been established experimentally that photoexcitation of OD centers under UV illumination leads to densification of the glass. In principle this densification also could be a reason for the change in Δn that is not directly associated with the change in polarizability of the OD center itself. We will relate this densification to strain in the glass matrix around the OD center core when the latter makes a transition to a state with delocalization of one valence electron (i.e., to the state of Hamiltonian (1) with $n_0=0$). The mechanism for this strain arises from the interaction of delocalized electrons with long-wavelength acoustic phonons of the glass matrix, and a microscopic description of it will not be given here. We limit ourselves to a phenomenological model of this interaction in the isotropic approximation for the strain potential (see, e.g., Ref. 12)

$$H_1=\int\left[-\sigma\psi^+(\mathbf{r})\psi(\mathbf{r})\rho(\mathbf{r})+\frac{1}{2}\beta\rho^2(\mathbf{r})+\frac{1}{2}\gamma(\operatorname{grad}\rho(\mathbf{r}))^2\right]d\mathbf{r}, \tag{7}$$

where σ is the electron–lattice interaction potential, $\rho(\mathbf{r})$ is the relative change in the medium density, and β and γ are elastic constants. By varying the Hamiltonian (7) with respect to $\rho(\mathbf{r})$ we obtain the self-consistency equation

$$-\gamma\nabla^2\rho(\mathbf{r})+\beta\rho(\mathbf{r})-\sigma\psi^+(\mathbf{r})\psi(\mathbf{r})=0. \tag{8}$$

To lowest order in perturbation theory with respect to the strain potential σ we can neglect the distortion of electron density $N(\mathbf{r})=\psi^+(\mathbf{r})\psi(\mathbf{r})$ due to the interaction of an electron with the glass matrix, and write the solution to Eq. (8) in explicit form. In the approximation of a rigid medium, assuming that the correlation length for variation in the medium density is $\xi_0=(\gamma/\beta)^{1/2}\ll c_0$, we can neglect the gradient term in Eq. (8) and obtain a simple expression

$$\rho(\mathbf{r})=\frac{\sigma}{\beta}N(\mathbf{r})\sim\frac{\sigma}{\beta}\frac{\exp(-2r/c_0)}{(r/c_0)^2} \tag{9}$$

for $r\gg a_0$. Thus, $\rho(\mathbf{r})$ is nonzero only in the region around the OD center where the charge density changes (of order c_0^3). In the approximation of a soft medium, for $\xi_0\gg c_0$, the change in the density of the glass matrix encompasses a region considerably larger than c_0^3. From Eq. (8) it follows that far from the OD center (for $r\gg c_0$) the function $\rho(r)$ has the form

$$\rho(r)\sim\frac{\sigma}{4\pi\gamma r}\exp\left(-\frac{r}{\xi_0}\right). \tag{10}$$

The change in system energy connected with the matrix strain can be estimated as

$$\Delta E_{\rm def} \sim \frac{\sigma^2}{\beta \lambda^3}, \quad \lambda = \max\{\xi_0, c_0\}, \tag{11}$$

while the relative change in the average density of the glass in the neighborhood of the OD center comes to

$$\overline{\rho} \approx \frac{\Delta E_{\rm def}}{\sigma}. \tag{12}$$

The total relative change in the average density of the glass for a concentration of centers $N_{\rm ODC}$ can be estimated directly from the Hamiltonian H_1 after summing over all the centers:

$$\overline{\rho}_{\rm def} \sim \frac{\sigma}{\beta} N_{\rm ODC} = \overline{\rho}(N_{\rm ODC}\lambda^3). \tag{13}$$

Taking the reasonable values $\overline{\rho} \sim 10^{-2} - 10^{-1}$ and $(N_{\rm ODC}\lambda^3) \sim 10^{-2}$, we obtain $\overline{\rho}_{\rm def} \sim 10^{-4} - 10^{-3}$. The change in refractive index $\Delta n_{\rm def}$ due to densification of the medium can be estimated from the Clausius–Mosotti relation

$$\Delta n_{\rm def} = \frac{(n^2-1)(n^2+2)}{6} \overline{\rho}_{\rm def} \approx 0.6 \overline{\rho}_{\rm def}. \tag{14}$$

Thus, the experimentally observed increase in Δn can include a strain-induced contribution[14] comparable in order of magnitude to the electronic contribution (6). By virtue of their origins, both of these contributions are responsible for a radical electronic and structural transformation of the OD center and the glass matrix atoms surrounding it, caused by the formation of a partially delocalized state (a state of intermediate radius) under ultraviolet photoexcitation.

4. CONDITIONS FOR REALIZATION OF THE MODEL AND ITS INTERRELATION WITH EXPERIMENTAL DATA

The state of the complex described above in which both the intrinsic OD center (i.e., its core) and the glass matrix participate, can be classified as a peculiar type of exciton with intermediate radius, in which the core plays the role of the positively charged center (a hole with infinite mass), while a second electron is partially delocalized and can be ionized fairly easily from its bound state into the conduction band. It is clear that an oxygen vacancy undergoing such a structural change has a completely different photoexcitation spectrum from the original center, and can no longer contribute to the absorption coefficient at a wavelength of 242 nm. This could explain the observed phenomenon of photoannealing of this band, and also the suppression of the intensity of triplet luminescence.[13] We can also explain the complimentary appearance of red luminescence as a byproduct of the creation of structurally altered OD centers,[14] which emit light as they recombine with electrons photoexcited from the state of intermediate radius to the conduction band. It is also clear that the remaining electron bound to the silicon will be a paramagnetic center, and hence should contribute to the EPR signal.

Even if this state with intermediate radius is metastable, its effect on the relaxation dynamics of OD center photoexcitation in glass can still be strong. For example, the level E_0 probably plays the role of the intermediate state introduced empirically into the energy spectrum of the OD center in order to explain the complicated temporal dynamics of its photoluminescence.[15]

A fundamental question is, what is the energy advantage of the new state. It is clear that only if

$$E_0 > \Delta, \tag{15}$$

will the charge transfer state of the center with partial delocalization of one of the electrons be more favorable in energy than a localized state, as shown schematically in Fig. 2b.

Condition (15) is apparently not satisfied in undoped quartz glass. Addition of Ge, on the one hand, reduces Δ while leaving E_0 unchanged, due to lowering of the bottom of the conduction band (recall that Δ and E_0 are measured from E_g, see Fig. 2b). In the solid solution $Ge_xSi_{1-x}O_2$ this effect can come to 1–2 eV when $x \approx 0.1-0.2$. On the other hand, the swelling of the glass matrix when Si is replaced by Ge increases the strain-induced contribution to the energy (11) by decreasing the coefficient β.

This latter effect in itself is not large (of order $10^{-1} - 10^{-2}$ eV), but it can play a role when the difference between E_0 and Δ. is small. Both of these factors work toward satisfying the criterion (15). The swelling of the glass matrix when Si is replaced by Ge can also lead to replacement of the rigid regime for formation of OD center ($\xi_0 < c_0$) by a soft regime ($\xi_0 > c_0$) due to an increase in ξ_0. This in turn will increase the effective fraction of volume in which the densification of the medium takes place.

A special case is quartz glass doped with nitrogen.[16] Technological conditions for its synthesis require that this glass be formed under highly oxygen-deficient conditions. We may therefore expect that the addition of nitrogen leads to formation of V[Si–Si]:N complexes, whose photoexcitation energies are 1.5–2 eV larger than those of V[Si–Si].[16] We may also assume that the nitrogen atom bound in the complex V[Si–Si]:N forms a deep level (occupied) that lies considerably lower than the original level Δ for single-particle excitation of a V[Si–Si] center. The hybridization of these two levels will cause them to repel one another, and as a result the Δ^* state will be higher than Δ (i.e., closer to the bottom of the conduction band), which favors the fulfillment of criterion (15). Thus, in both systems (with Ge and N) doping leads to changes in the electronic spectrum that favor the formation and increase the energy advantage of a state of intermediate radius (in the Ge system, the primary change is probably connected with the parameters of the matrix, while in the N system it is connected with the local parameters of the OD center). We note in passing that in the latter case the V[Si–Si]:N centers are accompanied by the original V[Si–Si] complexes, with excitation energies 4.5–5 eV. As in the case of undoped quartz glass, the absorption of 5 eV ultraviolet light photons by this glass does not make the system photosensitive. This is naturally explained within the framework of our model, since criterion (15) is violated for ''pure'' OD centers in the undoped quartz glass matrix.

Additional experimental confirmation of our model can be obtained by studying how ultraviolet processing of the glass affects the activation energy for electrical conductivity. Since the partially delocalized electron of a reconstructed

oxygen vacancy can act as a donor, with an energy located near the edge of the conduction band, its thermal ionization into the conduction band gives rise to an activated temperature dependence of the electrical conductivity with activation energy E_0.

Thus, according to the scenario we have described, in quartz glass with oxygen vacancies ultraviolet photoexcitation initiates a combined structural and electronic reconstruction of OD centers from their photoexcited states (S_1 or T_1). Relaxation of the atoms that make up the OD center is simultaneously accompanied by a radical change in the electronic spectrum, in particular the appearance of a state of intermediate radius. The redistribution of electron density associated with the creation of this state also causes densification of the glass matrix at considerable distances from the OD center (in the neighborhood of several tens of elementary volumes).

The state of intermediate radius has a large polarizability, two to three orders of magnitude larger than the polarizability of the original (unphotoexcited) OD center state. Together with the densification of the glass matrix around the OD center, this increases the refractive index Δn considerably even at comparatively low concentration levels of OD centers, which allows us to explain the increase $\Delta n \approx 10^{-4} - 10^{-3}$ observed in experiment.

This model also allows us to explain not only the observed change in density of germanosilicate glasses, which results in photoinduced writing of Bragg gratings in light guides,[17] but also the recently observed change in the Raman spectrum when the glass in the core of an optical fiber is exposed to ultraviolet light.[18] However, we need to emphasize the phenomenological nature of our treatment of the interaction between OD center electrons and the glass matrix in this paper. Of course, a more detailed analysis of the experimental data requires a more rigorous microscopic discussion.

If our assumptions are correct, then the state of intermediate radius is energetically favorable in glasses doped with Ge and (or) N, but is unfavorable in undoped glasses. However, even in the latter case a metastable version of this state will have a considerable influence on the dynamics of processes by which photoexcited valence electrons of OD centers relax to their original equilibrium state.

This work was partially supported by a grant from the Russian Foundation for Basic Research (No. 98-02-16361).

*)E-mail: golant@fo.gpi.ac.ru

[1] K. O. Hill, Y. Fujii, D. C. Johnson, and B. S. Kawasaki, Appl. Phys. Lett. **32**, 647 (1978).
[2] E. M. Dianov, K. M. Golant, R. R. Khrapko, A. S. Kurkov, B. Leconte, M. Douay, P. Bernage, and P. Niay, Electron. Lett. **33**, 236 (1997).
[3] M. Gallagher and U. Osterberg, J. Appl. Phys. **74**, 2271 (1993).
[4] K. D. Simmons, S. LaRochelle, V. Mizrahi, and G. I. Stegeman, Opt. Lett. **16**, 141 (1991).
[5] V. B. Sulimov, V. O. Sokolov, E. M. Dianov, and B. Poumellec, Phys. Status Solidi A **158**, 155 (1996).
[6] V. B. Sulimov and V. O. Sokolov, J. Non-Cryst. Solids **191**, 260 (1995).
[7] K. S. Snyder and W. B. Fowler, Phys. Rev. B **48**, 13 238 (1993).
[8] D. S. Starodubov, V. Grubsky, and J. Feinberg, Electron. Lett. **33**, 1331 (1997).
[9] V. N. Bagratashvili, V. K. Popov, S. T. Tsypina, P. V. Chernov, and A. O. Rybaltovskii, Opt. Lett. **20**, 1619 (1995).
[10] L. M. Falicov and F. C. Kimball, Phys. Rev. Lett. **22**, 997 (1969).
[11] L. D. Landau and E. M. Lifshits, *Quantum Mechanics. Non-Relativistic Theory* (3rd ed., Pergamon Press, Oxford, 1977; Russian original, Nauka, Moscow, 1974).
[12] A. S. Davydov, *Quantum Theory of the Solid State* [in Russian] (Nauka, Moscow, 1976).
[13] M. Poirier, S. Thibault, J. Lauzon, and F. Quellette, Opt. Lett. **18**, 870 (1993).
[14] E. M. Dianov, D. S. Starodubov, and A. A. Frolov, Electron. Lett. **32**, 246 (1996).
[15] M. Gallagher and U. Osterberg, Appl. Phys. Lett. **63**, 2987 (1993).
[16] E. M. Dianov, K. M. Golant, R. R. Khrapko, O. I. Medvedkov, A. L. Tomashuk, and S. A. Vasil'ev, Opt. Mater. **5**, 169 (1996).
[17] B. Poumellec, P. Guenot, I. Riant, P. Sansonetti, P. Niay, P. Bernage, and J. F. Bayon, Opt. Mater. **4**, 441 (1995).
[18] E. M. Dianov, V. G. Plotnichenko, V. G. Koltashev, Yu. N. Pyrkov, D. Varelas, H. D. Limberger, and R. P. Salate, *Proc. ECOC'97 Edinburg*, Vol. 2 (1997), p. 61.

Translated by Frank J. Crowne

Anisotropic hyperfine structure in the EPR spectrum of impurity ions in single crystals

O. S. Torosyan and S. M. Yaĭloyan

Institute for Problems in Applied Physics, Armenian Academy of Sciences, 375014 Yerevan, Armenia

F. S. Torosyan and L. M. Mkhoyan

Armenian State Engineering University, 377502 Gyumri, Armenia

(Submitted September 11, 1998)
Fiz. Tverd. Tela (St. Petersburg) **41**, 1026–1027 (June 1999)

Expressions are obtained for the hyperfine splitting in EPR spectra of impurity ions with electron spin 1/2 and arbitrary nuclear spin for arbitrary anisotropy of the g-factor and hyperfine structure constants. These results generalize the previously obtained results of Weil[1] for the case of weakly anisotropic g-factors and hyperfine structure constants. © *1999 American Institute of Physics.* [S1063-7834(99)02006-7]

It is well known that the parameters of EPR spectra with hyperfine structure must be determined either numerically or via perturbation theory. In calculating these parameters, their exact values are determined by computer calculations which involve complete diagonalization of the corresponding spin-Hamiltonian matrix with reference values found from approximate calculations. Therefore, in order to analyze EPR spectra with hyperfine structure it is important to have approximate analytic expressions for the resonance magnetic fields of the hyperfine structure lines and hyperfine splittings, i.e., the spacings (in magnetic field) between the positions of these lines.

In this paper we obtain several useful relations for resonance magnetic fields and hyperfine splittings in EPR spectra described by a spin Hamiltonian of the form

$$H_S=\beta(g_xH_xS_x+g_yH_yS_y+g_zH_zS_z)+A_xS_xI_x+A_yS_yI_y+A_zS_zI_z. \quad (1)$$

Here $S=1/2$, I is arbitrary, and all the remaining notations are conventional. Note that the EPR spectra of many impurity rare-earth ions in crystals are described by the spin Hamiltonian (1) with strongly anisotropic g-factors and hyperfine structure constants. For the case of weakly anisotropic g-factors and hyperfine structure constants, Weil obtained a very simple relation[1] for the magnetic field spacings between hyperfine lines with the same $|m|$ (where m is the nuclear magnetic quantum number). He derived this relation by writing the spin Hamiltonian (1) as the sum of an isotropic and an anisotropic part, and used first-order perturbation theory with the anisotropic part treated as the perturbation. This result, which was very interesting and useful, was introduced in the monograph Ref. 2 where it was analyzed in detail. However, since it is correct only for weak anisotropy of the g-factor and hyperfine structure constants, its applicability is limited.

In this paper we generalize the results of Weil to the case of arbitrary anisotropy of the g-factor and hyperfine structure constants by extending the perturbation-theoretic treatment of the Hamiltonian (1) to third order, using the magnetic hyperfine interaction as a perturbation to the Zeeman energy.

The use of third-order perturbation theory is required because contributions to the spacing between the lines $m\leftrightarrow m$ and $-m\leftrightarrow -m$ are comparable in magnitude for transitions arising from second- and third-order hyperfine corrections, and therefore must be taken into account at the same time. Actually, the shifts in second-order resonance lines are proportional to m^2 and therefore have the same sign for $m\leftrightarrow m$ and $-m\leftrightarrow -m$ transitions; however, they can easily differ in magnitude because the resonance magnetic fields for $m\leftrightarrow m$ and $-m\leftrightarrow -m$ transitions are different in first order. Therefore, the change in spacing between the m and $-m$ lines caused by second-order shifts will differ from these shifts by factors equal to the ratio of the hyperfine interaction energy to the Zeeman energy. Consequently, the change in distance between m and $-m$ lines obtained to second order in perturbation theory is actually a third-order effect. On the other hand, the shifts of $m\leftrightarrow m$ and $-m\leftrightarrow -m$ transition

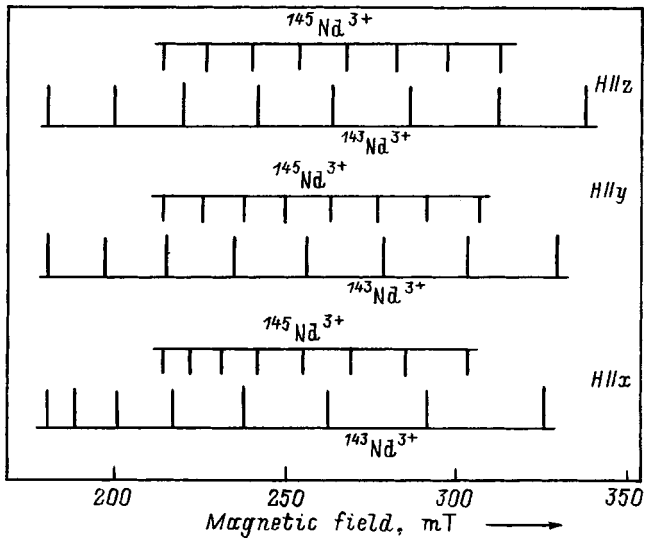

FIG. 1. Theoretically calculated positions of hyperfine structure lines for Nd^{3+} ions in single crystals of $PbCl_2$.

lines calculated to third order contain linear and cubic terms in m and therefore will have opposite signs. Consequently, the change in distance between m and $-m$ lines obtained to third order will be the same order of magnitude as their corresponding shifts, i.e., third-order effects.

If we assume that the magnetic field is directed along the z axis, and calculate the energy levels of Hamiltonian (1) to third order in perturbation theory for resonance magnetic fields, we have for $\Delta m=0$ transitions that

$$H_m=\frac{h\nu}{g_z\beta}-\frac{A_z m}{g_z\beta}\left[1+\frac{A_x^2+A_y^2}{2(2h\nu)^2}\right]-\frac{A_x^2+A_y^2}{4g_z\beta h\nu}[I(I+1)-m^2], \tag{2}$$

where ν is the microwave frequency used to measure the EPR spectrum. From Eq. (2) we can obtain the following simple relation:

$$\frac{H_{-m}-H_m}{2m}=\frac{A_z}{g_z\beta}\left[1+\frac{A_x^2+A_y^2}{2(2h\nu)^2}\right]. \tag{3}$$

From Eq. (2) we also can obtain

$$H_{m-1}-H_m=\frac{A_z}{g_z\beta}\left[1+\frac{A_x^2+A_y^2}{2(2h\nu)^2}\right]-\frac{A_x^2+A_y^2}{2g_z\beta h\nu}(m-1/2). \tag{4}$$

For weak anisotropy of the hyperfine structure constant, Eq. (3) coincides with the result of Weil (Eq. (14) of Ref. 2). Equations (2)–(4) can be used both for $\mathbf{H}\|x$ and $\mathbf{H}\|y$ if the following replacements are made in them: $z\to x\to y\to z$ and $z\to y\to x\to z$ respectively.

Figure 1 shows the positions of the hyperfine lines $\Delta m=0$ for the Nd^{3+} ion ($S=1/2$, $I=7/2$) in single crystals of $PbCl_2$ obtained numerically by exact diagonalization of the spin Hamiltonian (1) and using values of the g-factors and hyperfine structure constants measured in Ref. 3. To illustrate the usefulness of Eqs. (2)–(4) given here, we used them to recalculate these values of magnetic field for the lines shown in Fig. 1. The discrepancy between the results was so insignificant that we could not show it on Fig. 1. Note that for $\mathbf{H}\|x$ and $\mathbf{H}\|y$ the lines shown in Fig. 1 moved in parallel (i.e., maintaining their relative spacings unchanged), so that their origin coincided with that of the $\mathbf{H}\|z$ lines.

[1] J. A. Weil, J. Magn. Reson. **4**, 394 (1971).
[2] M. L. Meĭlman and M. I. Samoĭlevich, *Introduction to EPR Spectroscopy of Activated Single Crystals* [in Russian] (Atomizdat, Moscow, 1977), p. 93.
[3] A. G. Badalyan, P. G. Baranov, V. A. Chramtsov, C. Barta, and J. Rosa, Solid State Commun. **58**, 877 (1986).

Translated by Frank J. Crowne

Diffusion properties of plastically deformed silicon crystals

M. A. Aliev, Kh. O. Alieva, and V. V. Seleznev

Institute of Physics, Daghestan Science Center, Russian Academy of Sciences, 367003 Makhachkala, Russia
(Submitted April 7, 1998; accepted for publication August 31, 1998)
Fiz. Tverd. Tela (St. Petersburg) **41**, 1028–1029 (June 1999)

The effect of dislocations generated by electroplastic strain on the electric-field-driven transport of impurity atoms of indium in single crystals of *P*-silicon is investigated experimentally. It is shown that when electrodiffusion of indium and strain are induced simultaneously, the impurity ions are preferentially dragged towards the anode. © *1999 American Institute of Physics.* [S1063-7834(99)02106-1]

Studies of the role of impurity-dislocation interactions in the electroplastic deformation of silicon crystals have revealed that they influence the plastic properties of this material in several stages.[1] Since electroplastic deformation may also be viewed as an electrodiffusion process, it is entirely appropriate to try to study how impurity-dislocation interactions affect the diffusion properties of single crystals of *P*-silicon as well.

It is well known that structural defects in semiconductor crystals, in particular dislocations, can strongly affect the atomic transport of impurities in these crystals.[2,3] Much contradictory data regarding the nature of impurity migration has been obtained from studies of electrical transport, both through the bulk of the host material and along structural features. In some cases, the transport is observed to speed up, while in other cases it is slowed down.[4,5] The reasons for these disagreements probably lie hidden in the differing defect contents and degrees of structural imperfection of the crystals used in the studies.[6] In contrast, there have been no investigations of the nature of impurity migration in crystals both under strain and in an electric field, i.e., crystals simultaneously subjected to strain and electrodiffusion.

In this work we subjected samples of single-crystal *P*-silicon, initially doped with gallium and with hole concentrations of $10^{16}\,\mathrm{cm}^{-3}$, to electroplastic deformation,[7] thereby initiating electrodiffusion of indium along the [110] crystallographic direction. This same direction also served as the direction of compression of the crystal. Our samples were shaped like parallelepipeds with dimensions $12\times10\times5$ mm and edges that coincided with the crystallographic directions [112], [111], [110] respectively. We strained these samples in the stationary creep regime by applying a constant shear stress of 12 MPa at a temperature of 750 °C for 30 minutes. Samples with broad (110) planes on which a layer of impurities was previously deposited from a constant source were placed together in pairs and compressed between the vice grips of the strain apparatus. A constant current passing through a sample served simultaneously to heat the sample and to create a constant electric field. At the end of the experiment the samples were mechanically separated and strips with dimensions $10\times3\times1$ mm were cut from their anode and cathode regions in order to record their concentration-versus-depth distribution profiles. The impurity distributions with respect to depth were monitored by successively removing layers and measuring the concentration of indium atoms by Auger spectroscopy.

Figure 1 shows plots of the concentration distribution of indium versus penetration depth in the anode and cathode regions of the silicon, obtained by averaging the results of a number of identical experiments. It is clear from these curves that electrodiffusion is accompanied by preferential transport of indium toward the anode. Previously, Sterkhov *et al.*[8] investigated the effect of growth dislocations on electrical transport of indium in *P*-silicon. They observed that for samples kept at a temperature $T=900\,^{\circ}\mathrm{C}$ in an external DC electric field, indium atoms were transported along dislocations to the cathode. These authors postulated a vacancy mechanism as the probable cause of the diffusion process, while associating the direction of preferential transport of indium impurities and the high value of their effective charge along a dislocation with hole drag.

In our experiments we observed transport of indium towards the anode, in contrast to the data of Ref. 8. This happened because of the different conditions under which we created the diffusion, the most important of which was the creation of plastic deformation simultaneously with the electrodiffusion. Under these circumstances, mobile dislocations were being generated as the diffusion was taking place, and were drifting along with the front of diffusing impurities. On the other hand, the different conductivity type of our crystals and temperature conditions under which the experiment was carried out also impose their peculiarities on the results of our trials. In Ref. 9 the authors observed accelerated penetration of helium atoms into crystals of lithium fluoride plastically deformed in liquid helium. The authors of this paper explained the anomalously high diffusion coefficient for helium atoms by postulating that they were penetrating the crystals along growing and moving dislocations, i.e., the diffusion was dynamic and ''pipe-like.'' The interaction of diffusing impurities with mobile dislocations was also discussed by Geruzin and Matsokin in Ref. 10, who argued that the impurity cloud that forms at dislocations significantly affects their motion and the way that the diffusion zone forms. These authors introduced the concept of a ''dislocation-impurity cloud'' system, which migrates in the viscous–diffusion flow regime. It is also well known that

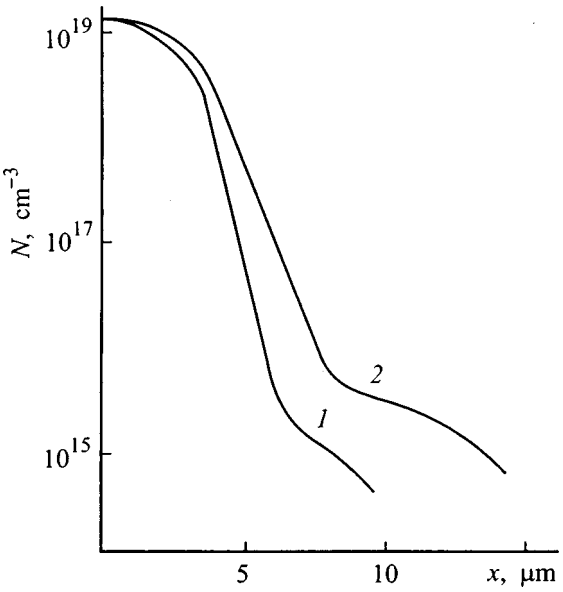

FIG. 1. Distribution of indium concentration N in silicon plotted versus the coordinate x. *1*—Cathode part, *2*—anode part.

doping with impurities changes the electronic states of dislocations, and consequently their electrostatic charge and Peierls potential.[11,12] In objects with a high Peierls potential this factor for interaction of impurities with dislocations can play an important role in modifying the character of diffusion–strain processes.[13]

In light of what was said above, we claim that in our experiment the electrical transport of indium which occurred simultaneously with electroplastic deformation is associated with a vacancy mechanism, since sizable concentrations of vacancies are generated in the neighborhood of nucleating and drifting dislocations. Moreover, the motion of the diffusion front of impurities is facilitated not only by the usual diffusion law arising from concentration gradients, but also by dragging of impurities by a moving dislocation, both along the dislocation and in the direction of its motion.[14]

As we said above, doping changes the charge state of dislocations, which can facilitate their motion in the presence of an applied dc field due to interaction with current carriers via the Fiks mechanism.[15] Thus, in Ref. 16 we observed direct transport of dislocations by an electric field (in the direction of current flow) toward the anode. This fact correlates with the preferential transport of indium toward the anode reported in this paper.

Thus, as we have stated, in our experiment the diffusion front of indium atoms arises from several mechanisms. The first is the ordinary vacancy mechanism for impurity diffusion in the bulk of the crystal caused by a concentration gradient. The second is direct transport of dissolved material by moving dislocations.

The fact that the diffusion is made up of two components is clearly revealed by the presence of a kink in the experimental plots of the impurity concentration profiles shown in Fig. 1. Following Ref. 17, we label these components of the diffusion ''slow'' and ''fast,'' so as to imply the simultaneous presence of two mechanisms for diffusion of a single impurity.

In our experiment, the slow diffusion component arises from the replacement of solvent atoms in the near-surface region via the vacancy mechanism. Thus, the surface of our deformed crystal coated with an electrically active impurity begins to act like a generator of dislocations with a diffusion pump. This means that the actual diffusion of the impurities, which generates dislocations due to the dimensional factor, is slowed down. [The ''fast'' component is identified with diffusion of an impurity along dislocation tubes as it is dragged along by mobile charge carriers of the plastic deformation.]

Our analysis of the possible mechanisms for transport of indium impurities leads us to postulate a special role for mobile dislocations when both diffusion and strain occur simultaneously.

[1] M. A. Aliev, Kh. O. Alieva, and V. V. Seleznev, Fiz. Tverd. Tela (St. Petersburg) **38**, 3372 (1996) [Phys. Solid State **38**, 1839 (1996)].
[2] B. I. Boltaks, *Diffusion and Point Defects in Semiconductors* [in Russian] (Nauka, Leningrad, 1972).
[3] G. S. Kulikov and R. Sh. Malkovich, Fiz. Tekh. Poluprovodn. **29**, 937 (1995) [Semiconductors **29**, 485 (1995)].
[4] *Thin Films: Interdiffusion and Reactions*, edited by J. M. Poate, K. Tu, and J. Meier (Wiley, New York, 1978; Mir, Moscow, 1982).
[5] *Atomic Diffusion in Semiconductors*, edited by D. Shaw (Plenum Press, London, 1973; Mir, Moscow, 1975).
[6] V. I. Sokolov, Fiz. Tekh. Poluprovodn. **29**, 843 (1995) [Semiconductors **29**, 436 (1995)].
[7] M. A. Aliev and V. V. Seleznev, High-Pressure Phys. and Engng. **30**, 46 (1989).
[8] V. A. Sterkhov, V. A. Panteleev, and P. V. Pavlov, Fiz. Tverd. Tela (Leningrad) **9**, 681 (1967) [Sov. Phys. Solid State **9**, 533 (1967)].
[9] O. V. Klyavin, Fiz. Tverd. Tela (St. Petersburg) **35**, 513 (1993) [Phys. Solid State **35**, 261 (1993)].
[10] Ya. E. Geruzin and V. P. Matsokin, Ukr. Fiz. Zh. **26**, 612 (1980).
[11] A. N. Orlov, Fiz. Tverd. Tela (Leningrad) **22**, 3580 (1980) [Sov. Phys. Solid State **22**, 2097 (1980)].
[12] B. V. Petukhov, Fiz. Tverd. Tela (Leningrad) **26**, 3160 (1984) [Sov. Phys. Solid State **26**, 1903 (1984)].
[13] M. I. Molotskiĭ, Fiz. Tverd. Tela (Leningrad) **30**, 1880 (1988) [Sov. Phys. Solid State **30**, 1085 (1988)].
[14] V. Ya. Kravchenko, Fiz. Tverd. Tela (Leningrad) **9**, 1050 (1967) [Sov. Phys. Solid State **9**, 823 (1967)].
[15] V. B. Fiks, Zh. Éksp. Teor. Fiz. **80**, 2313 (1981) [Sov. Phys. JETP **53**, 1209 (1981)].
[16] E. E. Vdovin and A. Yu. Kasumov, Fiz. Tverd. Tela (Leningrad) **30**, 31 (1988) [Sov. Phys. Solid State **30**, 180 (1988)].
[17] V. E. Kosenko, Fiz. Tverd. Tela (Leningrad) **3**, 2102 (1961) [Sov. Phys. Solid State **3**, 1526 (1961)].

Translated by Frank J. Crowne

Manifestation of glass-crack fractal geometry in Raman spectra

A. E. Chmel'

A. F. Ioffe Physicotechnical Institute, Russian Academy of Sciences, 194021 St. Petersburg, Russia

A. D. Semenov, A. N. Smirnov, and V. S. Shashkin

S. I. Vavilov State Optical Institute, 193171 St. Petersburg, Russia

(Submitted September 7, 1998)
Fiz. Tverd. Tela (St. Petersburg) **41**, 1030–1034 (June 1999)

A Raman spectroscopic investigation of the fractal structure on the surface of cracks of different size scales in glassy SiO_2 is reported. A study was made of the crack surface and of the distorted layer formed after grinding and polishing and comminution. The parameters of the fractal structure thus found reflect the properties of the material and the crack nature; namely, fractal dimension is of greater importance for more compact materials, and the geometric size of fractal units (i.e., the size in real space) correlates with crack dimensions. © *1999 American Institute of Physics.* [S1063-7834(99)02206-6]

Investigation of the mechanical behavior of solids on different size scales permits one, by establishing the corresponding correlations, to relate the processes occurring in all stages of fracture, from formation of elementary defects to main-crack propagation. This problem is traditionally approached by finding the response of mechanical parameters to structural changes. Studies of glassy materials made along these lines reveal how the specific features in glass framework structure (concentration of ruptured bonds, size of the correlation sphere, valence-angle distribution, etc.) are related both to the strength of a material[1] and to its mechanical characteristics, such as Young's modulus and hardness.[2–4]

The advent of the theory of fractals provided a radically new tool for establishing the relation between phenomena occurring on the structural and macroscopic levels. The invariance of fractal units with respect to dimensions in real space offers a possibility of extending the results relating to a given scale level to events taking place on a totally different space scale. Thus the problem of the correlation between micro- and macroscopic phenomena in fracture may gain a new appearance if one shows that the process develops in a self-similar manner throughout the range accessible to measurements. This work may be considered as a step in this direction.

It was prompted by data in Ref. 5, where an analysis of microscopic measurements, namely, of the relation between the area and perimeter of the micron-scale islands appearing on a fracture surface led to a conclusion that the surface of a growing crack in glass ceramics has fractal geometry. In view of the above-mentioned scale invariance, the authors suggested that brittle fracture of glassy materials is a fractal process on deeper structural levels as well. This communication reports the first observation of a fractal structure on a glass surface made by measuring the frequency dependence of the Raman scattering (RS) intensity in the region devoid of structural bands (up to $240\,\mathrm{cm}^{-1}$), i.e., actually on the atomic level, because the RS tensor is determined in this case by vibrational displacements of fractons.

1. TECHNIQUES

The fundamentals of the theory of Raman scattering of light from a fractal structure were presented in Ref. 6, where, by analogy with phonons, the concept of fractons as vibrational excitations on fractal units was introduced, and the corresponding density-of-states function $g(\omega)$ and the wave function $\varphi(r)$ were defined:

$$\varphi(r) \propto \exp(-ar^{d_\varphi}), \tag{1}$$

where d_φ is the so-called superlocalization parameter,[7] which characterizes damping with distance r and is related to the parameters of a fractal structure as[8]

$$d_\varphi = (2-\tilde{d})D/\tilde{d}, \tag{2}$$

where $\tilde{d}$ and D are, respectively, the fracton and fractal dimensions. The difference in the physical meaning between these parameters is that D characterizes the geometry of the structure, and $\tilde{d}$ that of the vibrations.

The expression for the frequency dependence of the intensity of light scattering from fractal vibrational modes (corrected for the level population) can be written[9,10]

$$I(\omega)\omega/[n(\omega)+1] \propto \omega^{\nu}, \tag{3}$$

where, assuming the vibrations in a fractal volume to be incoherent,

$$\nu = (\tilde{d}/D)(2d_\varphi + D) - 1, \tag{4}$$

and $n(\omega) = 1/[\exp(h\omega - kT) - 1]$ is the Bose factor. Using Eq. (2), relation (3) can be simplified considerably

$$\nu = 3 - \tilde{d}, \tag{5}$$

and one finds that the scattered intensity at frequency ω depends only on the fractal dimension $\tilde{d}$:

$$I(\omega)\omega/[n(\omega)+1] \propto \omega^{3-\tilde{d}}. \tag{6}$$

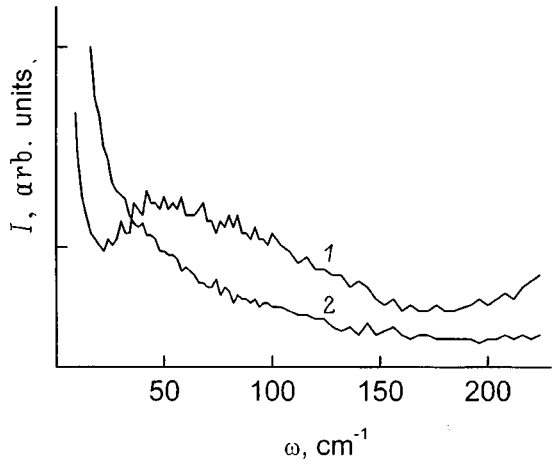

FIG. 1. Low-frequency Raman spectra (*1*) of the volume and (*2*) of the hot-pressed interface zone between fragments of a fractured blank.

Therefore the frequency dependence of fracton-scattered light intensity drawn on a log–log scale, $\log\{I(\omega)\omega/[n(\omega)+1]\}$ vs $\log(\omega)$, is a straight line. Such a spectrum differs radically in pattern from the spectrum of conventional (nonfractal) amorphous material, where in the low-frequency domain ($20-80\,\mathrm{cm}^{-1}$) one always finds the so-called boson peak caused by the correlation function of a disordered structure and the phonon DOS function.

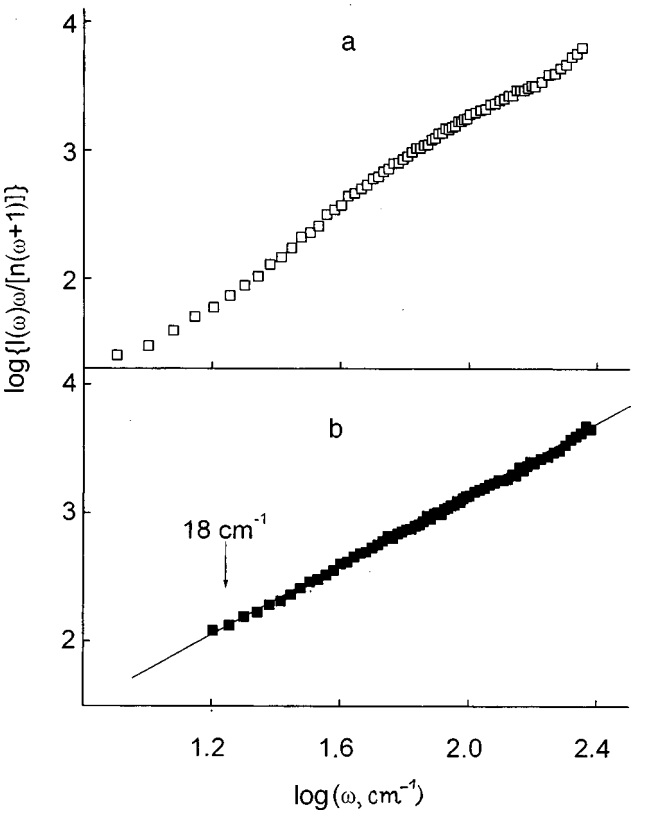

FIG. 2. Spectra of Fig. 1 redrawn in reduced coordinates: (a) spectrum 1, (b) spectrum 2. Here and in Figs. 3b and 5b the arrow identifies the ω_{cutoff} frequency.

2. EXPERIMENT

The measurements were carried out on samples of glassy SiO_2 obtained by gel technology.[11] This material has a capability of reconstituting solid parts under hot pressure from fragments produced in fracture of the original sample. It is the interface between the fragments, which was assumed to retain structural traces of the preceding fracture, that was the subject of the study. The procedure was performed at a pressure of 7 MPa and temperature of 1150 °C over carefully matched surfaces of a crack between a pair of parts obtained by fracturing a blank along a previously cut notch. The comparatively weak pressure and the fact that the hot pressing was performed below the glass formation temperature ($T_g = 1160\,^{\circ}\mathrm{C}$) gave one grounds to hope that the contact zone would retain the memory of the modification of the material caused by crack propagation.

We also prepared samples hot-pressed over polished planes of two fragments. The junction interface could not be discerned by eye in all the solid blocks thus prepared.

The spectra were excited by the Ar^+ laser line at 488 nm and measured with a double-grating monochromator provided with a digital data processing system. The spectra were recorded in 90° geometry as the exciting beam passed through the sample volume, or along the hot-pressed interface. The light beam focused onto the zone under study was about 100 μm in diameter. The region within which the light interacted with the sample (along the beam) was limited by a diaphragm to a length of 1 mm.

3. RESULTS AND DISCUSSION

Figure 1 presents low-frequency spectra of the volume and of the hot-pressed zone of the fractured blank fragments. The spectrum of the volume exhibits a boson peak characteristic of amorphous materials with disordered structure. No bands are seen in the frequency range studied in the light scattered from the hot-pressed zone. The log–log spectrum of the volume also exhibits the boson peak (Fig. 2a), and the spectrum of the healed crack transforms above a certain cutoff frequency $\omega_{\mathrm{cutoff}} = 18\,\mathrm{cm}^{-1}$ to a straight line characteristic of a fractal structure (Fig. 2b). In the case of scattering from phonon vibrational modes one could expect the slope of the straight-line portion to be $\nu = 4$.[8] The experiment yielded 1.36 ± 0.02 for the slope, however, which, in accordance with Eq. (5), gives $\tilde{d} = 1.64 \pm 0.02$ for the fracton dimension.

Let us consider Ref. 12, where low-frequency Raman spectroscopy was used to observe fractal structure in the volume of aerogel, a material consisting of coagulated primary particles with a radius ≈ 2 nm, which retains memory of the original heterogeneous structure. The value of $\tilde{d}$ was found[12] to be 1.50 ± 0.05, with the straight-line relationship found at frequencies from the cutoff $\omega_{\mathrm{cutoff}} = 27\,\mathrm{cm}^{-1}$ up. After the samples were ground to powder the fracton dimension increased to 1.67 and ω_{cutoff} to $47\,\mathrm{cm}^{-1}$. The structure observed in the powder was called[12] fractal dust, because it was believed to have been inherited from fractals of the solid aerogel but distorted by spatial limitations associated with grain size.

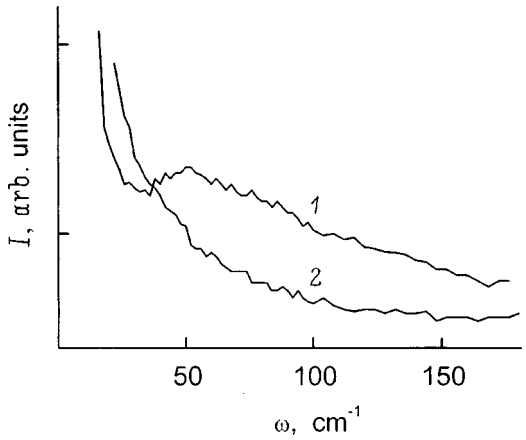

FIG. 3. Low-frequency Raman spectra (*1*) of the volume and (*2*) of the hot-pressed interface zone between polished surfaces.

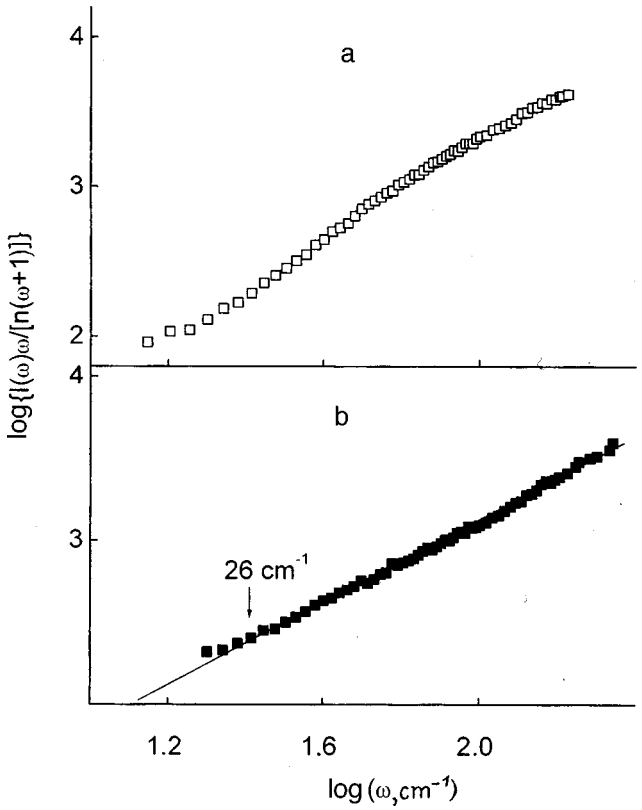

FIG. 4. Spectra of Fig. 3 redrawn in reduced coordinates: (a) spectrum 1, (b) spectrum 2.

When comparing our data with those of Ref. 12, one immediately notices that the value of the parameter $\tilde{d}$ of the powder coincides with that obtained for the fracture zone (1.67 ± 0.05 against 1.64 ± 0.02, respectively), which implies closeness of the fractal geometries in the two cases. In our case, however, the fractal structure could not be of relic nature, because there is no such structure in the volume of the sample (Fig. 2a). Therefore it may be conjectured that the fractal geometry of powder particles described in Ref. 12 is likewise not connected with memory of the original structure and is rather due to submicrocracks created in the course of comminution of glassy SiO_2. In these conditions, the nearly threefold difference between the cutoff frequencies (47 and $18\,cm^{-1}$) reflects a substantial difference between the spatial conditions of microcrack propagation under dispersion to powder and main-crack growth. Roughly, the frequency of the longest-wavelength vibrational mode within a confined region depends on the sonic velocity V and the dimension of this region L as $\omega_{cutoff}=2\pi V/L$. Assuming $V=4\times10^5$ cm/s for amorphous SiO_2 and transforming from wave numbers to cyclic frequency, we obtain for $\omega_{cutoff}=47$ and $18\,cm^{-1}$ $L=27$ and 74 Å, respectively. These values are the upper limits for the geometric dimension of the fractal units, which is limited by the size of the parts of the cracks that remained intact after hot pressing.

To check whether the difference in ω_{cutoff} (and, hence, in the maximum fractal size) is indeed determined by crack type, we measured the spectrum emitted from the hot-pressed interface between two polished surfaces of the fractured block. The cracked layer produced by polishing also includes numerous microfracture surfaces whose scale size (1–2 μm) may be viewed as intermediate between fractal islands[5] on a macroscopic brittle surface and submicron cracks on powder grains.

A spectrum from the hot-pressed interface of polished plates is shown in linear and reduced coordinates in Figs. 3 and 4, respectively. The slope of the linear section in the frequency dependence is 1.31 ± 0.02, which, according to Eq. (5), yields $\tilde{d}=1.69\pm0.02$. Thus we have again obtained for the fracton dimension a value characteristic of SiO_2 of gel origin.[1)]

However the cutoff frequency $\omega_{cutoff}=26\,cm^{-1}$ obtained for a polished surface turned out to be intermediate between its values for a fracture surface ($18\,cm^{-1}$, Fig. 2) and powder grains ($47\,cm^{-1}$, Ref. 12). This is in accord with the conjecture that spatial constraints (crack size in powder grains, polished interface, and brittle surface) affect the size distribution of fractal units.

To verify that fractal geometry does indeed depend on specific features in the structure of a material, we applied the hot-pressing technology used here to conventional fused quartz. Pieces of KU-grade quartz glass were ground in water to grain size ≈2 μm, and the water suspension was electrophoretically precipitated to a dense mass, which was subsequently sintered at 1150 °C. The pressure at sintering was in this case increased to 180 MPa, because interaction among even highly hydrated particles of fused quartz is considerably weaker than that among silica gel grains possessing a high molecular mobility.

The results are displayed in Figs. 5 and 6. While a straight-line section characteristic of fractal structure has indeed appeared in the sintered material (seen in reduced coordinates in Fig. 6b), it is shorter (here $\omega_{cutoff}=50\,cm^{-1}$), and its slope is substantially smoother than that in the hot-pressed interface spectra (Figs. 2b and 3b). The fracton dimension calculated using Eq. (5) is 2.34 ± 0.04.

Note that the procedure used to obtain the last result is not very rigorous. Substituting $\tilde{d}=2.34$ into Eq. (2) yields a

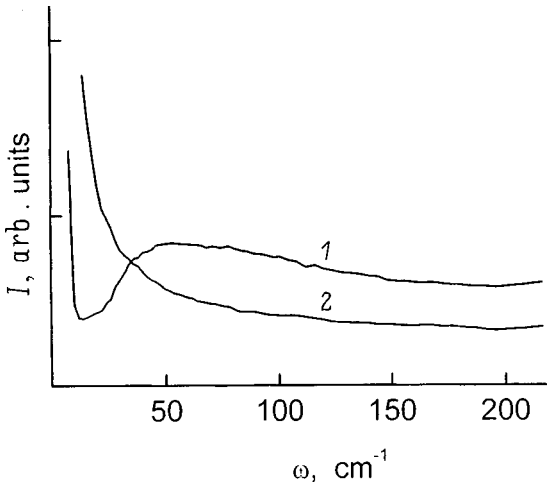

FIG. 5. Spectra of amorphous quartz. (*1*) Starting sample, (*2*) sample sintered from powder at 1150 °C and 180 MPa.

negative value for d_φ, which has no physical meaning here. The inconsistency between these parameters is accounted for by the fact that Eq. (2) was derived for Mie scattering from fractal globules, while the fractals we are dealing with are on the rough surface of particles.

Nevertheless, the increase of $\tilde{d}$ observed as one crosses over from silica gel to fused quartz is in qualitative agreement with the well-known correlation between fractal structure and properties of a substance. It was pointed out[13,14] that as the density of aerogels increases, their fractals become more compact, and this manifests itself in an increase of the $\tilde{d}$ parameter. Similarly, when crossing over to a material with a higher structural connectivity (fused quartz SiO_2), we observed an increase in fracton dimension.

At the same time the onset of the straight-line section ($50\,cm^{-1}$) nearly coincides in this case with the magnitude of ω_{cutoff} quoted[12] for powder ($47\,cm^{-1}$). This indicates that the size of fractal units in real space is dominated by crack extent, and that there is no noticeable dependence on specific features in the structure of an amorphous material.

Thus, low-frequency Raman spectra contain rich information on the fractal structure of fracture regions in glass. The lowest frequency of scattering from fracton vibrations (ω_{cutoff}) is determined by the maximum (Euclidean) size of a self-similar formation and does not depend on individual features in the ''supermolecular'' structure of a given substance. The fracton dimension reflects the degree of compactness in the structure of an amorphous material and is not dependent on the scale size of a self-similar formation. This is indicated by the fact that different types of brittle cracks in samples of identical origin exhibit the same fracton dimension.

The results presented here give one grounds to maintain that fractal surface geometry of brittle fracture, which was previously known from macro- and microscopic observations, manifests itself even on size scales of the order of the correlation sphere of amorphous material, i.e., at the nanostructural level.

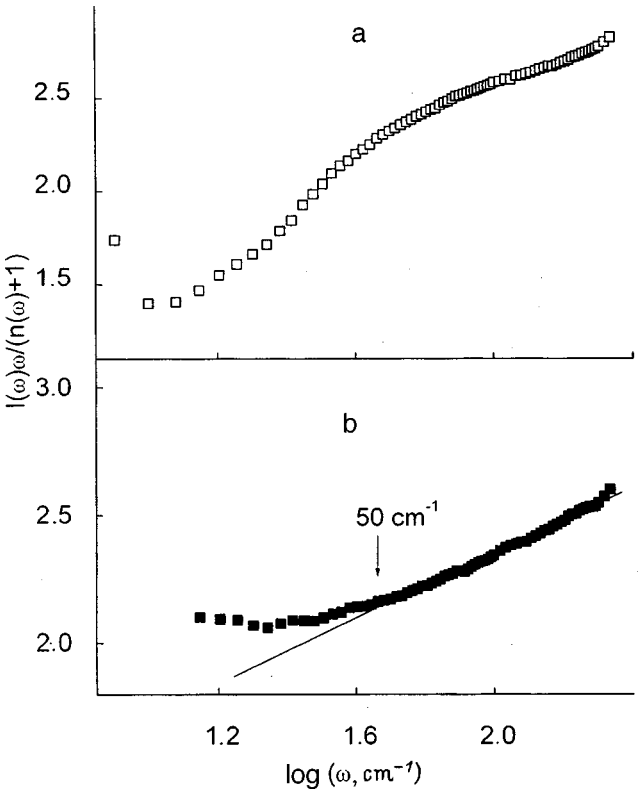

FIG. 6. Spectra of Fig. 5 redrawn in reduced coordinates: (a) spectrum 1, (b) spectrum 2.

[1)]It is appropriate to add here that the coincidence of the fracton dimension for a single macroscopic crack and randomly oriented microcracks indicates a scalar nature of the fracton localization length and, thus, supports the conjecture of incoherent scattering in a fractal volume made when using Eq. (4).

[1] A. Chmel, V. V. Baptizmanski, and A. A. Kharshak, J. Phys. III **2**, 2387 (1992).
[2] A. Chmel, E. K. Mazurina, and V. S. Shashkin, Solid State Commun. **78**, 177 (1991).
[3] A. Chmel, A. Krivda, E. Mazurina, V. Shashkin, and V. Zhizhenkov, J. Am. Ceram. Soc. **76**, 1563 (1993).
[4] A. Chmel, T. Pesina, and V. S. Shashkin, J. Non-Cryst. Solids **210**, 254 (1997).
[5] J. J. Mecholsky, D. E. Passoja, and K. S. Feinberg-Ringel, J. Am. Ceram. Soc. **72**, 60 (1989).
[6] S. Alexander and R. Orbach, J. Phys. (France) Lett. **43**, L625 (1982).
[7] S. Alexander, C. Laermans, R. Orbach, and H. M. Rosenberg, Phys. Rev. B **28**, 4615 (1983).
[8] A. Aharony, S. Alexander, O. Entin-Wohlman, and R. Orbach, Phys. Rev. Lett. **58**, 132 (1987).
[9] A. Boukenter, B. Champagnon, E. Duval, J. Dumas, J. F. Quinson, and J. Serughetti, Phys. Rev. Lett. **57**, 2391 (1986).
[10] A. Boukenter, B. Champagnon, E. Duval, and J. L. Rousset, Philos. Mag. B **59**, 125 (1989).
[11] O. A. Ivanova, G. T. Petrovskiĭ, A. D. Semenov, A. N. Smirnov, V. E. Ter-Nersesyants, V. S. Shashkin, and A. E. Cnmel', Steklo Keram. No. 4, 3 (1998).
[12] H. Abu Hassan, S. R. P. Smith, and J. H. Page, Phys. Solid State **68**, 733 (1988).
[13] R. Vacher, E. Courtens, G. Coddens, J. Pelous, and T. Woignier, Phys. Rev. B **39**, 7384 (1980).
[14] E. Stoll and E. Courtens, Z. Phys. B **81**, 1 (1990).

Translated by G. Skrebtsov

The influence of a magnetic field on the inelastic properties of LiF crystals

N. A. Tyapunina

M. V. Lomonosov State University at Moscow, 119899 Moscow, Russia

V. L. Krasnikov and É. P. Belozerova

Kostroma State Technological University, 156005 Kostroma, Russia

(Submitted August 28, 1998; resubmitted October 21, 1998)
Fiz. Tverd. Tela (St. Petersburg) **41**, 1035–1040 (June 1999)

The effect of weak magnetic fields (0.1–0.8 T) on the internal friction and Young's-modulus defect of LiF crystals is investigated over a range of relative strain amplitudes ε_0 from 10^{-6} to 10^{-4} at frequencies of 40 and 80 kHz. Experiments with these fields show that the internal friction increases and the effective elastic modulus decreases, indicating an increase in the plasticity of the samples. Plots are obtained of the internal friction versus the magnitude of the magnetic field at various values of the strain amplitude ε_0. © *1999 American Institute of Physics.* [S1063-7834(99)02306-0]

The question of how weak magnetic fields affect the mechanical properties of insulators, semiconductors, and metals has attracted much attention from investigators. Many of them have attempted to address this question by investigating the effect of a magnetic field on the behavior of defects in crystals subjected to active loading or creep.[1–3] On the other hand, only a few papers have discussed how a magnetic field affects the inelastic behavior of these materials under an alternating load. Among these we should mention Refs. 4, 5, whose authors investigated the effect of a weak magnetic field on internal friction in metals at hertz and megahertz frequencies respectively.

In this paper we investigate the effect of a weak magnetic field on the inelastic properties of LiF crystals under an alternating load in the kilohertz frequency regime. The inelasticity of the crystals in this frequency range is controlled by dislocation processes. Under the conditions of our experiments these processes were induced vibrations of the dislocations and their multiplication in the field of the ultrasonic wave.

1. EXPERIMENTAL TECHNIQUE AND SAMPLES INVESTIGATED

We used the two-component crystal resonator method[6–8] to investigate the inelastic properties of our LiF samples at frequencies of 40 and 80 kHz. Longitudinal vibrations set up a standing strain wave in a quartz-plus-sample resonator with a relative strain amplitude ε_0 of 10^{-6}–10^{-4}. In these investigations, which were carried out at room temperature, we measured the internal friction (δ) and Young's-modulus defect ($\Delta M/M$) of the crystals. The differences in intrinsic frequencies of the piezoelectric quartz and the compound crystal resonator did not exceed 2%. The internal friction and Young's-modulus defect of the samples were determined to within a maximum error of 8%, the amplitude of relative strain to within 5%. The attenuation of the unloaded quartz was an order of magnitude lower than the system attenuation.

The magnetic field was applied using a permanent magnet or an EM–1 electromagnet powered by a universal UIP–1 power supply. The magnetic induction B was varied in the range from 0.1 to 0.8 T. The orientation of the sample was characterized by the polar angle Θ between the fourth-order axis and the direction of propagation of the ultrasonic wave. In this work we used LiF samples with orientation $\Theta=0$. The magnetic induction B was directed along the crystallographic direction $\langle 100\rangle$ perpendicular to the direction of propagation of the ultrasonic wave.

The initial state of the samples was characterized by a yield stress of 3.5 MPa and dislocation density $6\times10^8\ \mathrm{m}^{-2}$. Fresh dislocations were not introduced into the sample before the start of the ultrasonic-wave tests. The principal divalent impurities in the LiF crystals we investigated, according to spectrographic analysis data, were Ca and Ba.

We followed the change in the state of the sample by monitoring the current–voltage characteristics of the compound crystal resonator. The density of dislocations and their distribution in the sample was monitored by selective etching.

The current–voltage characteristics $I(U)$ or $U_R(U)$ of the two-component crystal resonator are plots of the current strength I in the quartz at series resonance versus the voltage U applied to its package. The value of the current I is proportional to the voltage U_R across an additional resistance R connected in series with the crystal resonator. The amplitude of relative strain in the sample ε_0 is proportional to the voltage U_R. The slope of the I–V characteristics with respect to the current axis can be used to study the dissipative properties of the sample. Using the curve $U_R(U)$, we can determine with high accuracy the amplitude ε_0 at which changes take place in the behavior of dislocations, and the plasticities of different samples can be compared based on the relative positions of their I–V characteristics.[9,10]

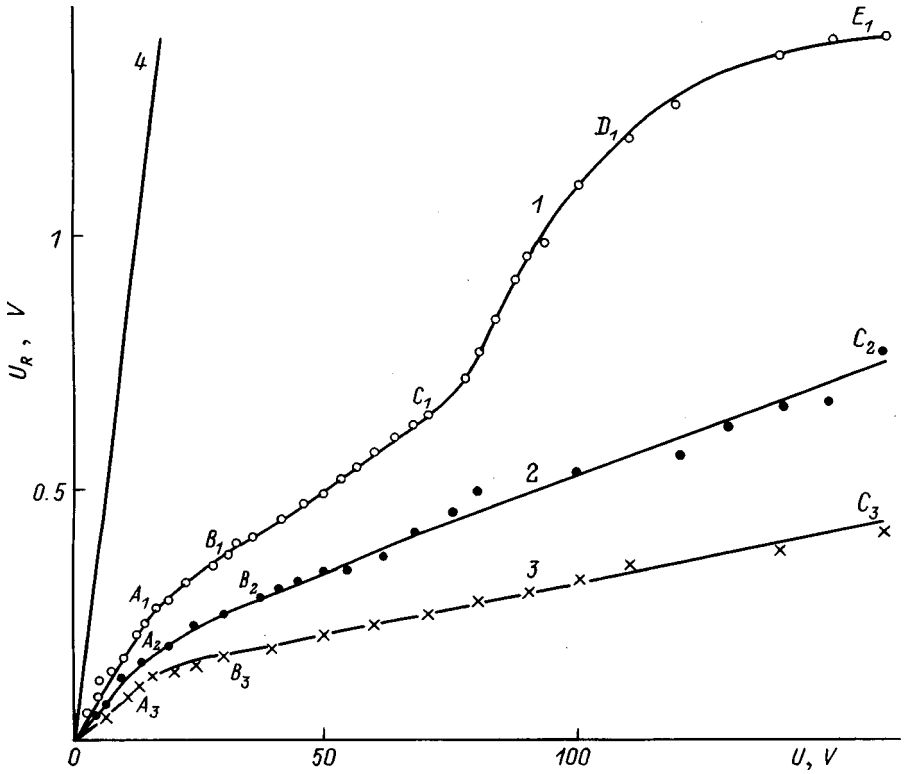

FIG. 1. Comparison of the I–V characteristics $U_R(U)$ of a control LiF sample (curve *1*) with samples measured in magnetic fields $B=0.2$ T (curve *2*) and $B=0.5$ T (curve *3*). $f_p=80$ kHz. The straight line 4 is for unloaded quartz.

Our studies were conducted in two regimes. In the first regime, measurements were made with a magnetic field and an ultrasonic wave present at the same time. The results obtained were compared with data for control samples ($B=0$). In the second regime, U (or U_R) was held fixed and the magnetic field was switched on only for a certain time, and then once more switched off. This regime allows us to investigate the functions $U_R(U)$ or $\delta(\varepsilon_0)$ for the same sample both in the presence of a magnetic field and for $B=0$.

In order to identify a possible influence of the ''switching-on effect'' on the measurement results,[11] we plotted the functions $U_R(U)$ for unloaded quartz under the following conditions: $B=0$; a DC switched-on magnetic field of $B=0.8$ T; and in several cycles of switching a magnetic field $B=0.8$ T on and off. The results obtained all lay on one straight line. Processing this data by the method of linear regression showed that under all the experimental conditions the functions $U_R(U)$ obtained were approximated by the same linear dependence; in all cases the correlation coefficient exceeded 0.99 (curve 4 in Fig. 1).

2. RESULTS OF TRIALS

2.1. Effect of a magnetic field on the I–V characteristics of compound crystal resonators with LiF samples

Figure 1 shows typical examples of I–V characteristics for a crystal resonator with a frequency of 80 kHz at $B=0$ and I–V characteristics obtained in the presence of both a magnetic field and an ultrasonic wave. Curves *1*, *2*, and *3* correspond to values $B=0$, $B=0.2$ T, and $B=0.5$ T respectively. For comparison, the straight line $U_R(U)$ of unloaded quartz is also shown (plot 4). It is characteristic that all three I–V characteristics exhibit low-voltage linear segments (OA_1,OA_2,OA_3) and nonlinear segments (A_1B_1,A_2B_2,A_3B_3) that connect with high-voltage linear segments B_1C_1, B_2C_2, B_3C_3. These I–V characteristic segments exhibit no sign of translational motion or multiplication of dislocations.

Figure 1 shows clearly that the I–V characteristics obtained when a magnetic field and an ultrasonic wave act simultaneously (curves *2* and *3*) lie far below the I–V characteristic for $B=0$ (curve *1*). This shows that the magnetic field is making the samples more plastic. We emphasize that I–V characteristics 1 and 2 correspond to samples with mirror cleaves.

We note yet another peculiarity revealed by comparing I–V characteristic 1 with 2 and 3. The large change in slope of 1 as we pass from segment B_1C_1 to segment C_1D_1 indicates significant hardening of the sample under the action of the ultrasonic wave. Curves *2* and *3*, obtained while the magnetic field was present, did not exhibit any such changes in slope. This shows that when a magnetic field and an ultrasonic wave are present there is no hardening of the samples for voltages less than $U=200$ V.

The change in slope of the first characteristic as we pass into region D_1E_1 is associated with the beginning of multiplication of dislocations in the field of the ultrasonic wave, which is confirmed by data from selected etching.

We used the method described in Ref. 10, based on finding the points of intersection of asymptotes to the segments B_1C_1, B_2C_2, and B_3C_3 with the U_R axis, to determine the

TABLE I. Magnitudes of generalized Peierls–Nabarro barriers τ^{SL}, ratios U/U_R, and vibration amplitudes of dislocation segments $\langle\xi\rangle$ for LiF at a frequency of 40 kHz and for various values of B.

B, T	0	0.2	0.5
τ^{SL}, MPa	0.68	0.38	0.28
U/U_R	66.7	75.0	100.0
$\langle\xi\rangle$, μm, $\varepsilon_0=2.0\times10^{-5}$	0.22	0.31	0.93

stress τ^{st} required to unpin dislocation segments at a given stage of ultrasonic wave action. In the terminology of Ref. 10, τ^{st} is the magnitude of the generalized Peierls–Nabarro barrier. Table I lists estimates of τ^{st} for I–V characteristics corresponding to a frequency of 40 kHz. In Table I we also present estimates of the average displacements of vibrating dislocation segments $\langle\xi\rangle$ for $\varepsilon_0=2\times10^{-5}$, obtained from Young's-modulus defect data using the method of Ref. 12, and the ratio U/U_R measured on the initial segments of the I–V characteristics OA_i. It is clear from Table I that samples investigated in a magnetic field had smaller values of τ^{st} than the control samples, and that these values decrease with increasing induction B. Since according to Ref. 13 τ^{st} is proportional to the yield stress measured under active loading conditions, we can confirm that the latter decreases with increasing B. The ratios U/U_R, and consequently the dissipation of mechanical energy, increase with increasing B. As B increases, the average displacement of a vibrating dislocation segment $\langle\xi\rangle$ increases as well.

We emphasize that the data shown in Fig. 1 are from three different samples, two of which have mirror-like cleaves. The effect of a magnetic field on the inelastic properties of LiF can be demonstrated by results obtained from same-sample trials as well. Thus, in Fig. 2 we show the function $U_R(U)$ for a sample of LiF in a magnetic field $B=0.8$ T (points 2, 4, 6, etc.) and in the absence of a magnetic field (points 1, 3, 5, 7, etc.). It is clear from the plot in Fig. 2 that the magnetic field causes U_R to decrease, and consequently the amplitude of relative strain ε_0 at antinodes of the standing ultrasonic wave decreases as well. The changes in U_R, ΔU_R, and consequently $\Delta\varepsilon_0$, caused by the magnetic field depend on the amplitude ε_0. In Table II we show values of the jumps $\Delta\varepsilon_0=\varepsilon_0^{B=0}-\varepsilon_0^{B}$ for the range of amplitudes ε_0 measured at 80 kHz for $B=0.5$ T. $\Delta\varepsilon_0$ is largest in the amplitude range $\varepsilon_0\sim10^{-5}$, and exhibits a maximum at $\varepsilon_0=2.56\cdot10^{-5}$.

2.2. Effect of a magnetic field on the internal friction and Young's-modulus defect of LiF

The internal friction δ of LiF samples increases in a magnetic field, which can be seen from Fig. 3. In this figure we plot the internal friction versus amplitude for two LiF samples at a frequency of 40 kHz. Curves *1* and *2* refer to the same sample. The points corresponding to curve *1* were obtained in a magnetic field $B=0.2$ T, those for curve *2* are for $B=0$. A comparison of these curves shows clearly that the amplitude dependence of the internal friction in a magnetic field begins at smaller ε_0 than for $B=0$. Curve *3* is from a control sample with a mirror cleave. Comparing curves *1*, *2*

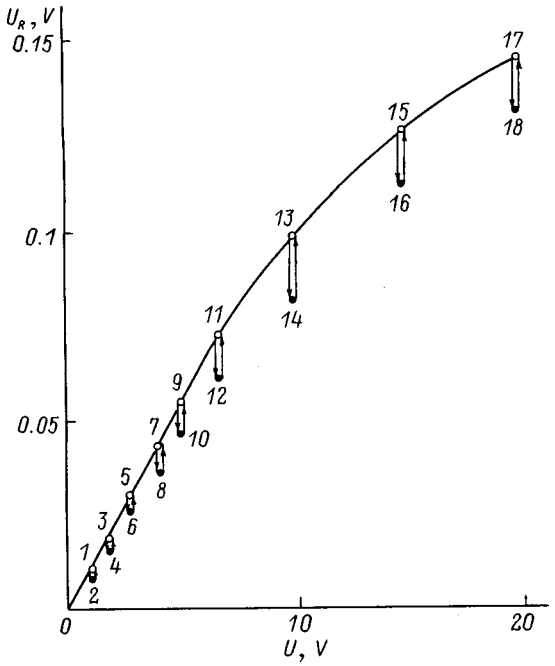

FIG. 2. Jumps $\Delta(U_R)$ in the IV characteristics of a LiF sample caused by a magnetic field $B=0.8$ T. Points 2, 4, 6, 8, etc. correspond to measurements in a magnetic field, points 1, 3, 5, etc. to measurements in the absence of a magnetic field. $f_p=80$ kHz.

with curve *3* in Fig. 3, we see that the amplitude dependence $\delta(\varepsilon_0)$ of a sample subjected to the action of a magnetic field during the experiment begins at smaller ε_0 than the control sample. The corresponding small-amplitude value of internal friction (the so-called amplitude-independent internal friction) turns out to be smaller in the control sample. All three curves $\delta(\varepsilon_0)$ in Fig. 3 are rectified in Granato–Lücke coordinates.[14] This indicates that the amplitude dependences $\delta(\varepsilon_0)$ arise from freeing of dislocations from pinning centers.

The inset to Fig. 3 shows the amplitude dependence of the Young's-modulus defect $\Delta M/M(\varepsilon_0)$ for the sample whose internal friction is shown by Figs. 1 and 2 respectively. It is clear that the amplitude dependence of $\Delta M/M(\varepsilon_0)$ obtained in a magnetic field begins at smaller ε_0 (curve *1a*) than the dependence for $B=0$ (curve *2a*), which agrees with curves *1* and *2* for the internal friction.

In order to obtain curves for the internal friction in a sample versus amplitude at different values of B, we used the following experimental procedure. While keeping a certain value of the amplitude ε_0 fixed, we decreased the magnetic induction from 0.76 T to 0, while measuring the internal friction δ at several values of B chosen in this interval. After

TABLE II. Magnitudes of amplitude jumps in the relative strain $\Delta\varepsilon_0$ for LiF samples in a magnetic field.

ε_0, 10^{-6}	1.2	3.9	6.8	14.6	20.5	25.6	31.7	51.2	73.0	109.0
$\Delta\varepsilon_0$, 10^{-6}	0.2	0.5	0.9	1.7	2.2	6.1	3.7	2.4	1.2	0

Note. ε_0 is the amplitude of the relative strain with the magnetic field switched off, $\Delta\varepsilon_0$ is the corresponding decrease in amplitude caused by the magnetic field. These results were obtained at a frequency $f_p=80$ kHz in a magnetic field $B=0.5$ T.

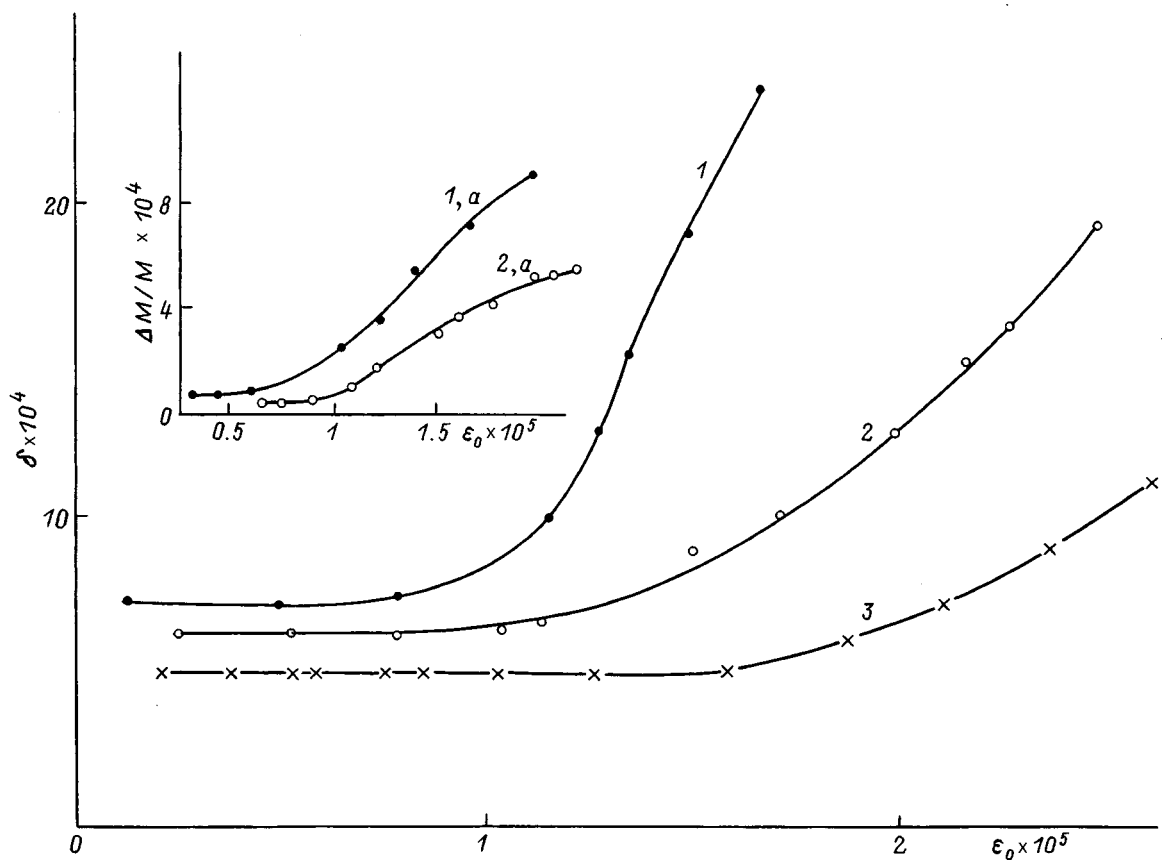

FIG. 3. Internal friction versus amplitude $\delta(\varepsilon_0)$ for a LiF sample plotted in the presence of a magnetic field (curve *1*) and for $B=0$ (curve *2*). Curve *3* corresponds to the control sample. The inset shows the amplitude dependences of the Young's-modulus defect $\Delta M/M(\varepsilon_0)$ for the samples corresponding to curves *1* and *2*. $f_p=40$ kHz, $B=0.2$ T.

this we increased the amplitude to a new value ε_0 and again measured the internal friction at various values of B. In Fig. 4 we show several plots of $\delta(\varepsilon_0)$ for a LiF sample at different values of B in the range from 0.76 T to 0. It is clear that the internal friction of LiF at small amplitudes ε_0 increases with increasing B, and the onset of the amplitude dependence shifts to smaller values ε_0. From Fig. 4 it is also clear that the curves $\delta(\varepsilon_0)$ for $B=0$ and $B=0.14$ T practically coincide. Consequently, there exists a threshold value of B above which the magnetic field ceases to affect the amplitude dependence of the internal friction in LiF. The curves $\delta(\varepsilon_0)$ from Fig. 4 are rectified in Granato-Lücke coordinates. Following Ref. 14, we estimated the ''unpinning strain'' $\Gamma \sim F_m/l_c$, where F_m is the maximum force of interaction of a dislocation with its pinning center and l_c is the average length of a vibrating dislocation segment. The results of these estimates are listed in Table III. Here we also list the amplitude ε_0 corresponding to the onset of amplitude dependence of the internal friction, the corresponding stress amplitude σ_0, $\tau^{\rm st}$, the ratio U/U_R for initial segments OA_i (see Fig. 1), and the average displacement of vibrating dislocation segments for $\varepsilon_0=4.0\cdot10^{-5}$. It follows from Table III that the values of Γ decrease with increasing B. This could be a consequence either of smaller F_m or a larger average length of the oscillating dislocation segments l_c. The ratio U/U_R on segments OA_i, and consequently the amplitude-independent internal friction up to 0.8 T, increases propor-

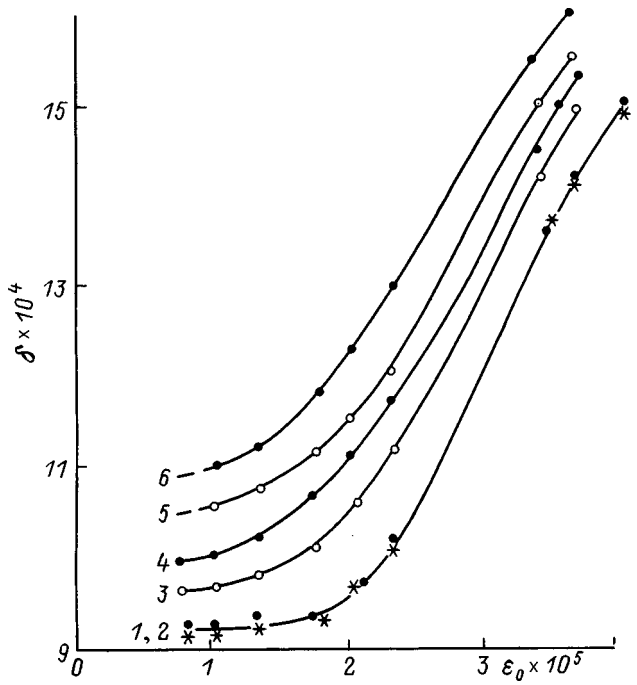

FIG. 4. Amplitude dependences of $\delta(\varepsilon_0)$ for a LiF sample at various values of the magnetic induction B: the points of curve *1* (stars) correspond to $B=0$; curve *2* (filled dots) are $B=0.14$ T; *3*—0.26 T; *4*—0.51 T; *5*—0.64 T; *6*—0.76 T. $f_p=80$ kHz.

TABLE III. Certain quantitative characteristics obtained from experiments using samples of LiF in magnetic fields with various magnetic inductions B.

B, T	0	0.14	0.26	0.51	0.64	0.76
ε_0, 10^{-5}	2.0	2.0	1.5	1.3	1.0	0.87
σ_0, MPa	1.7	1.7	1.3	1.1	0.87	0.76
τ^{SL}, MPa	0.73	0.69	0.64	0.50	0.49	0.42
Γ, 10^{-4}	1.22	1.21	1.17	1.15	1.13	0.94
U/U_R	97.9	98.4	102.3	104.3	111.6	118.8
$\langle\xi\rangle$, μm $\varepsilon_0=4\times10^{-5}$	0.12	0.13	0.22	0.29	0.33	0.4

tional to the magnetic induction B. The average displacements $\langle\xi\rangle$ in the presence of a magnetic field exceed the displacements of dislocation segments when $B=0$, and increase as B increases. Following Ref. 15 we assume that for the same amplitude ε_0 the displacement of a vibrating dislocation segment is proportional to l_c^2. From this we conclude that the value of l_c increases with increasing B, i.e., an ever-increasing number of segments are being released from their pinning centers. These conclusions correspond to a picture in which the magnetic field facilitates the unpinning of dislocations from paramagnetic centers.[16]

Using the experimental procedure described above, it is possible to obtain the dependence of the internal friction on the magnetic induction for different values of $\varepsilon_0=$const. Figure 5 shows characteristic plots of $\delta(B)$ for a LiF sample over a wide range of ε_0. The curves in Fig. 5 correspond to amplitudes ε_0 for which no new dislocations are created as the sample is excited by the ultrasonic wave. For small ε_0, corresponding to amplitude-independent internal friction, δ depends linearly on B (see plot 1 in Fig. 5). This agrees with data indicating that the quantity U/U_R measured on the initial segments of the I–V characteristics OA_i depends linearly on the magnetic induction B. With increasing ε_0 the character of the function $\delta(B)$ becomes more complicated. Thus, for $\varepsilon_0=3.6\times10^{-5}$ (see plot 2 in Fig. 5) there are two ranges of B, $B<0.2$ T and $B>0.55$ T, within which δ is a weak function of B. The amplitude $\varepsilon_0=3.6\times10^{-5}$ lies in the range of amplitudes for which the curves $\delta(\varepsilon_0)$ are rectified in Granato–Lücke coordinates. It is in this range of amplitudes that the magnetic field causes substantial jumps $\Delta\varepsilon_0$ (see Table II). Curves *3* and *4* in Fig. 5 correspond to the range of amplitudes in which the ultrasonic wave causes hardening of the sample (see segment C_1D_1 of I–V characteristic 1 in Fig. 1). A maximum is clearly observable on the curves $\delta(B)$ for this range of ε_0.

Our experimental data, and our analysis of it, prove convincingly that a weak magnetic field can affect the inelastic properties of LiF crystals. Our results agree qualitatively with data indicating an effect of a constant magnetic field on internal friction in other diamagnetic materials,[4,5] and with effects observed in alkali-halide crystals under other loading conditions in the presence of a magnetic field.[1–3]

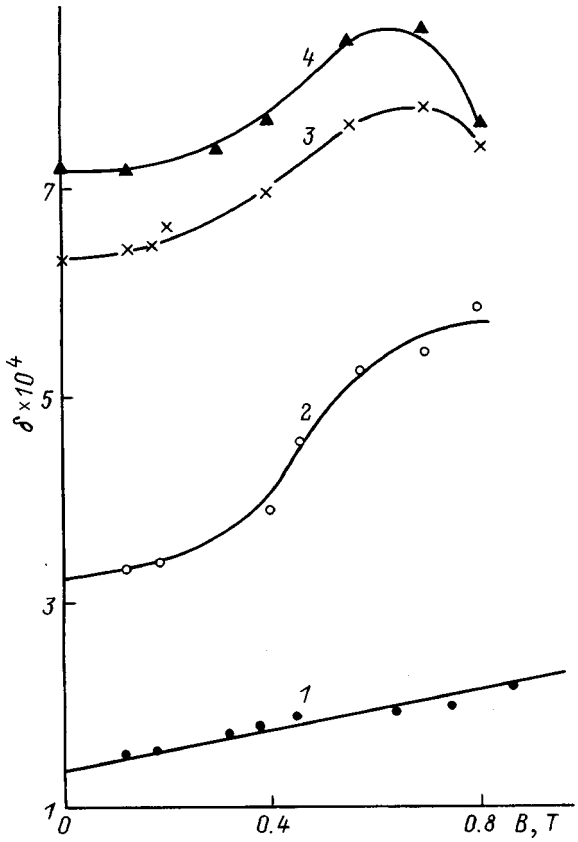

FIG. 5. Plots of $\delta(B)$ for a LiF sample at various amplitudes $\varepsilon_0=$const in the absence of dislocation multiplication in the field of a ultrasonic wave. $f_p=80$ kHz. Curve *1* corresponds to an amplitude $\varepsilon_0=1.7\times10^{-5}$; *2*—$\varepsilon_0=3.6\times10^{-5}$; *3*—$\varepsilon_0=1.8\times10^{-4}$; *4*—$\varepsilon_0=2\times10^{-4}$.

[1] A. A. Urusovskaya, A. E. Smirnov, and N. N. Bekkauer, Izv. Ross. Akad. Nauk, Ser. Fiz. **61**(5), 937 (1997).
[2] Yu. I. Golovin and R. B. Morgunov, Izv. Ross. Akad. Nauk, Ser. Fiz. **60**(9), 173 (1996).
[3] Yu. I. Golovin, R. B. Morgunov, S. E. Zhulikov, and A. M. Karyakin, Izv. Ross. Akad. Nauk, Ser. Fiz. **61**(5), 850 (1997).
[4] O. I. Datsko and V. I. Alekseenko, Fiz. Tverd. Tela (St. Petersburg) **39**, 1234 (1997) [Phys. Solid State **39**, 1094 (1997)].
[5] M. I. Molotskii, R. E. Kris, and V. Fleurov, Phys. Rev. B **51**, 12 531 (1995).
[6] J. Marx, Rev. Sci. Instrum. **22**, 503 (1951).
[7] E. G. Shvidkovskiĭ and A. A. Durgaryan, Scientific Rpts. from Higher Schools in Phys. Math. Sciences **5**, 211 (1958).
[8] S. P. Nikanorov and B. K. Kardashev, *Elasticity and Dislocation-Induced Inelasticity of Crystals* [in Russian] (Nauka, Moscow, 1985).
[9] N. A. Tyapunina, in *Physics of the Strain Hardening of Single Crystals* [in Russian] (Naukova Dumka, Kiev, 1972), p. 228.
[10] E. K. Naimi, *Measurement of Internal Friction, Young's-Modulus Defect, and Startup Stresses for Dislocations by the Method of* I–V *Characteristics of a Dipole Antenna*, Patent Reg. in VINITI No. 2589 (1985).
[11] V. I. Al'shits, E. V. Darinskaya, and E. A. Petrzhik, Fiz. Tverd. Tela (St. Petersburg) **35**, 320 (1993) [Phys. Solid State **35**, 162 (1993)].
[12] G. S. Baker, J. Appl. Phys. **33**, 1730 (1962).
[13] A. A. Predvoditelev, in *Physics of the Strain Hardening of Single Crystals* [in Russian] (Naukova Dumka, Kiev, 1972), p. 74.
[14] A. V. Granato and K. Lücke, in *Ultrasonic Methods of Investigating Dislocations* (IL, Moscow, 1963), p. 27.
[15] D. H. Niblett and J. Wilkes, Usp. Fiz. Nauk **80**, 125 (1963) [Adv. Phys. **9**, 1 (1960)].
[16] V. I. Al'shits, E. V. Darinskaya, O. L. Kazakova, E. Yu. Mikhina, and E. A. Petrzhik, Izv. Ross. Akad. Nauk, Ser. Fiz. **57**(11), 2 (1993).

Translated by Frank J. Crowne

The influence of thermal processing on the relative mobility of edge and screw dislocations in NaCl crystals

R. P. Zhitaru and N. A. Palistrant

Institute of Applied Physics, Moldova Academy of Sciences, 277028 Kishinev, Moldova
(Submitted June 29, 1998; resubmitted October 27, 1998)
Fiz. Tverd. Tela (St. Petersburg) **41**, 1041–1043 (June 1999)

The effect of thermal processing on the mobility of dislocations is investigated in NaCl crystals doped with impurities of various types—high-solubility impurities (Ca^{2+}) and low-solubility impurities (Pb^{2+}). The results obtained after aging and thermal processing indicate that the type of impurity and its state (e.g., level of aggregation) in the crystal have a strong effect on the relative mobility of edge and screw dislocations, and also on the parameters of double transverse slip. © *1999 American Institute of Physics.* [S1063-7834(99)02406-5]

The question of how point defects affect the mechanical properties of crystals and the mobility of dislocations has been discussed in a number of papers.[1–5] However, there have been practically no studies of differences in the behavior of different kinds of dislocations, for example edge and screw dislocations, when point defects are introduced or when their collective state (e.g., level of aggregation) is changed by various external factors, in particular thermal processing. Ionic crystals such as NaCl are convenient objects for these studies. When (001) cleavage planes of these crystals are indented, dislocation rosettes appear around the imprint of the indentor whose rays consist of ensembles of edge and screw dislocation half-loops.[6]

In this paper we study the mobility of edge and screw dislocations in crystals of NaCl containing impurities of various types: high-solubility Ca^{2+} and low-solubility Pb^{2+}.

1. EXPERIMENTAL METHOD

NaCl:Ca and NaCl:Pb crystals were grown by the Czochralsky method, with concentrations of Ca^{2+} in the range 10^{-3} to 1.6×10^{-1} and Pb^{2+} in the range 2×10^{-4} to 1.65×10^{-2} mol. %.

The (001) cleavage planes of these crystals were deformed at room temperature using a PMT-3 microhardness meter with a load of 10 g at the indentor. The dislocation rosettes that appeared around the imprint of the indentor were identified by selective etching. The mobilities of these dislocations were characterized by the ranges l_e and l_s of edge and screw dislocation ensembles in the stress field of the indentor.

The measurement error of these quantities was 10%. The parameter $\xi = l_e/l_s$ was used to compare the mobilities of edge and screw dislocations. The state of the impurities in these crystals was varied by aging (12 years at room temperature) and quenching. Several quenching temperatures T_q were chosen in the range 323–723 K, with the samples kept at each temperature for 6 hours.

2. EXPERIMENTAL RESULTS AND DISCUSSION

Figure 1 shows the effect of aging on the parameter ξ. It is clear that there is one concentration of Ca^{2+} (3.65×10^{-2} mol. %) at which ξ increases considerably (by a factor of 2.6). This comes about because an increase in l_e (~60%) is accompanied by a decrease in l_s (~40%). This unusual change in the mobilities of edge and screw dislocations under the influence of the same defect (i.e., the mobility of some dislocations increases, while that of others decreases) can be explained as follows. Like any other dislocation, these dislocations are braked by ion impurity-cation vacancy dipoles, both singly and in aggregates and precipitates. However, screw dislocations, in contrast to edge dislocations, can undergo double transverse slip. In this case ''fragments'' can form (dipoles made up of edge dislocations, prismatic loops, and point defects) that cause additional braking of the screw dislocations.[8–10] The state of the point defects in the crystal affects the parameters of the double transverse slip.[8,11] As a crystal ages, impurity complexes (precipitates) appear, which stimulate the double transverse slip of screw dislocations and greatly enhance their braking. Hence, the mobility of these dislocations will decrease, despite the ''purification'' of the matrix via aggregation which forms large-scale defects. In such crystals, the motion of edge dislocations becomes easier, and hence l_e increases during aging.

A situation of this kind can only arise in crystals with a certain type of impurity, for a specific value of concentration, and under specific aging conditions. In light of this fact, it is understandable why the concentration dependence $\xi(C)$ exhibits a well-expressed maximum only for NaCl:Ca at one impurity concentration. The low solubility of Pb^{2+} in NaCl:Pb suggests that impurity complexes and precipitates are present in these crystal even before aging; therefore, this process results in a smaller change in the parameter ξ than in NaCl:Ca. However, aging also changes the shape of the function $\xi(C)$ for the lead-containing crystals (curves *3* and *4* in Fig. 1). Note that the post-aging curve *4* has a minimum at $C=8\times10^{-4}$ mol. %. In our paper Ref. 14, we argued that this shape, which is also mirrored in the concentration de-

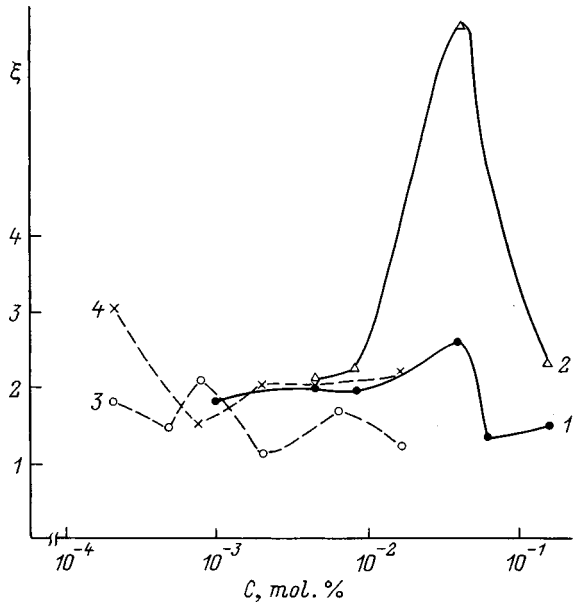

FIG. 1. Effect of aging on the parameter $\xi = l_e/l_s$ for NaCl:Ca (*1*, *2*) and NaCl:Pb (*3*, *4*) crystals. 1 and 3 are before aging, according to the data of Ref. 7; *2* and *4* are after aging.

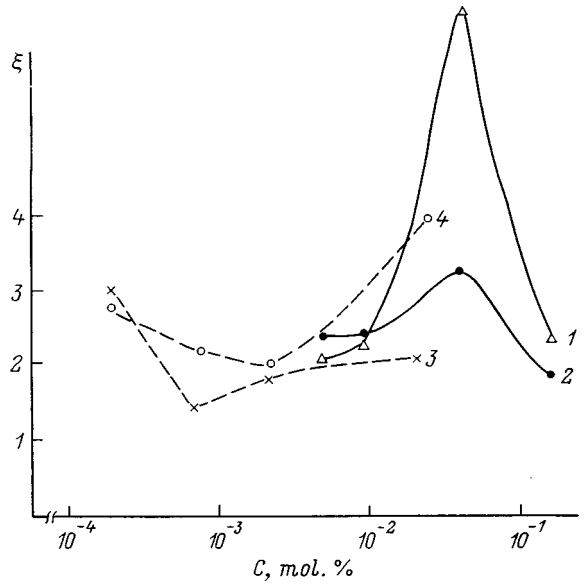

FIG. 2. Effect of quenching ($T_q = 473$ K) on the concentration dependence of the parameter ξ for crystals of NaCl:Ca (*1*, *2*) and NaCl:Pb (*3* and *4*). *1* and *3*—co-aged crystals, *2* and *4*—quenched crystals.

pendence of other plastic deformation parameters of NaCl:Pb crystals[12–14] (yield strength, coefficient of strain hardening) is a consequence of the development of impurity aggregates and precipitates.

Thus, we find for the example of co-aged NaCl:Ca and NaCl:Pb crystals that different impurities can yield strikingly different shapes of the functions $\xi(C)$—in this case, one curve has a maximum while the other has a minimum (see curves *2* and *4* in Fig. 1). The results of aging lead us to conclude that the type of impurity and its state in the crystal can have a strong effect on the relative mobility of edge and screw dislocations, and on the parameters of double transverse slip. Note that in Ref. 15, after investigating the effect of another parameter—temperature—on the ratio of l_s and l_e for NaCl crystals, Klyavin was moved to question the idea that changes in this ratio were associated with changes in the frequency of double transverse slip for screw dislocations.

Trials in which co-aged crystals were quenched show that NaCl:Ca and NaCl:Pb crystals differ markedly in their behavior when subjected to this type of processing as well. As an example of this we show results for $T = 423$ K in Fig. 2. It is clear that after quenching the curve $\xi(C)$ shifts downward for NaCl:Ca, while for NaCl:Pb it shifts upward. These results indicate that the impurity state affects crystals containing Ca^{2+} and Pb^{2+} differently.

Quenching is found to produce especially large changes in the value of ξ for samples with an impurity concentration $C \sim 10^{-2}$ mol. % (i.e., 3.65×10^{-2} for NaCl:Ca, curves *1* and *2* in Fig. 2, and 1.65×10^{-2} for NaCl:Pb, curves *3* and *4* in Fig. 2). In this case ξ changes by roughly a factor of 2, decreasing for NaCl:Ca and increasing for NaCl:Pb. In crystals of NaCl:Ca this corresponds to a decrease in l_e by a factor of 1.1, along with an increase in l_s by a factor of 1.6. In the crystals NaCl:Pb both l_e and l_s decrease, but the change in l_s is less marked (a factor of 2 for l_s, a factor of 1.1 for l_e).

We interpret these results as follows. In crystals of NaCl:Ca, quenching disrupts those impurity complexes that effectively brake screw dislocations by double transverse slip; therefore, l_s increases, despite the contamination of the crystal matrix, which decreases the mobility of edge dislocations l_e. On the other hand, co-aged NaCl:Pb crystals with a significant concentration of low-solubility impurity ($C \geqslant 10^{-2}$ mol. %) probably contain large-scale impurity complexes (~500 Å and larger) and precipitates before quenching, whose effect on double transverse slip of screw dislocations is comparatively slight. After quenching, which leads to some disruption of these defects, the number of defects contaminating the crystal matrix increases, which decreases the mobility of edge and screw dislocations. But, these defects could have an even stronger effect on double transverse slip, in which case screw dislocations will be braked more strongly after quenching than edge dislocations, i.e., l_s will decrease more than l_e.

In Fig. 3 we plot the parameter ξ versus quenching temperature for NaCl:Ca crystals. It is clear that the change in ξ for ''pure'' crystals (which, of course, contain uncontrolled impurities) and for crystals with comparatively small concentrations of impurities (5×10^{-3} mol. %) is smaller than for samples with $C \sim 10^{-2}$ mol. %. In the first case, the change in ξ is within the range 2–3, in the second case in the range 1–4. This indicates once more that the different mobilities of edge and screw dislocations in these crystals depend on the type and concentration of impurities they contain. It is also clear (Fig. 3) that the state of the impurities also significantly affects this difference. For example, for crystals with $C = 3.65\times10^{-2}$ mol. %, ξ decreases by a factor of 4 when we go from $T_q = 323$ K to $T_q = 673$ K (curve *4* in Fig. 3).

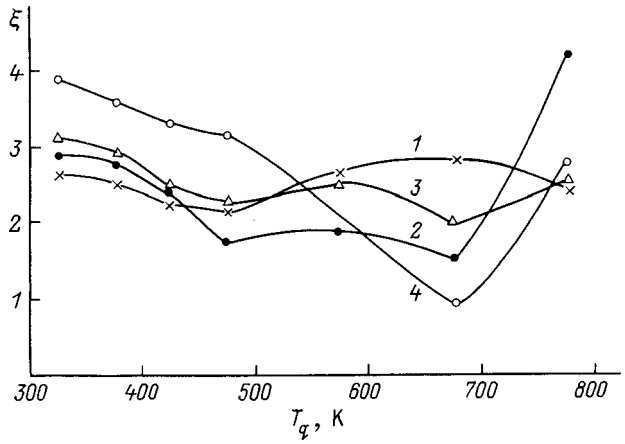

FIG. 3. Dependence of the parameter ξ on quenching temperature for NaCl:Ca crystals. *1*—Undoped crystals, *2–4*—doped crystals. *C*, mol. %: 5×10^{-3} (*2*), 9×10^{-3} (*3*), 3.65×10^{-2} (*4*).

For samples with this impurity concentration we observe a smooth decrease in ξ with increasing T_q as this parameter is varied from 323 to 673 K (curve *4* in Fig. 3). This decrease is connected with the fact that increasing the quenching temperature of the sample usually increases the mobility of edge and screw dislocations, with l_s changing more strongly than l_e due to decreased slowing down connected with double transverse slip. For example, in going from samples quenched at 473 K to samples quenched at 673 K the mobility of edge dislocations increases by a factor of 3.3, that of screw dislocations by a factor of 12. Further increases of T_q lead to an increase in ξ (curve *4* in Fig. 3) because the decrease in l_s is larger than the decrease in l_e (by factors of 8 and 3 respectively), i.e., as T_q changes from 673 to 773 K the braking of screw dislocations via double transverse slip increases.

It follows from Fig. 3 that the shape of the curves $\xi(T_q)$ for samples with impurity concentrations $\geqslant10^{-3}$ mol. % (curves *2* and *3*) is similar to that for crystals with $C=3.65\times10^{-2}$ mol. % (curve *4*).

For NaCl:Pb, as for NaCl:Ca, the shape of the function $\xi(T_q)$ is found to be nonmonotonic. However, aside from this similarity the functions for the two crystal types differ markedly in overall shape. In particular, a rather significant change in ξ for NaCl:Pb is observed (in the range 2–4) even for crystals with impurity concentrations as low as 2×10^{-4} mol. %.

For both types of crystals we can identify the usual regularities: minima for curves $\xi(T_q)$ are connected with decreased additional slowing down of screw dislocations caused by transverse slip, while maxima are connected with its increase. This is also true of the functions $\xi(C)$ (Figs. 1 and 2). Therefore, by studying how the parameter ξ changes under the action of impurity defects we can draw conclusions about the influence of these defects on the additional braking of screw dislocations, and on the intensity of double transverse slip.

Thus, we have shown for the example of doped NaCl crystals that the mobility of edge and screw dislocations vary differently. For samples subjected to aging, the shape of the concentration dependence of the parameter $\xi=l_e/l_s$ depends on the type of impurity introduced. For high-solubility impurities in NaCl (Ca^{2+}) the function $\xi(C)$ has the form of a curve with a maximum, for low-solubility impurities (Pb^{2+}) it has a minimum. The parameter ξ changes significantly during quenching of co-aged crystals. These changes have different characters for NaCl:Ca and NaCl:Pb. Regular changes in the parameter ξ during aging and quenching of these crystals are explained by taking into account additional slowing down of screw dislocations connected with double transverse slip. Based on these changes we may deduce the effect of impurity defects on the intensity of transverse slip.

[1] E. Aerts, S. Amelinckx, and W. Dekeyser, Acta Metall. **7**, 29 (1959).
[2] L. M. Soĭfer, in *Physics of the Condensed State* [in Russian] (Physicotech. Inst. Low Temp. Ukr. SSR Acad. Sci., Khar'kov, 1973).
[3] P. Grau and F. Frohlich, Phys. Status Solidi A **55**, 479 (1979).
[4] E. Orozco, J. Soullard, and F. Agullo-Lopez, Philos. Mag. A **55**, 513 (1987).
[5] Yu. S. Boyarskaya, D. Z. Gradko, and M. S. Kats, *Physics of Microindentation Processes* [in Russian] (Shtinitsa, Kishinev, 1986).
[6] A. A. Predvoditelev, V. N. Rozhanskiĭ, and V. M. Stepanova, Kristallografiya **7**, 418 (1962) [Sov. Phys. Crystallogr. **7**, 330 (1962)].
[7] M. A. Linte, *The Effect of Point Defects on Microhardness and Other Parameters of the Plastic Deformation of Single Crystals of NaCl*. Doctoral Diss. [in Russian] (Inst. of Applied Phys., Acad. Sci. of the Moldavian SSR, Kishinev, 1985).
[8] B. I. Smirnov, *Dislocation Structure and Hardness of Crystals* [in Russian] (Nauka, Leningrad, 1981).
[9] J. J. Gilman, J. Appl. Phys. **33**, 2703 (1962).
[10] W. G. Jonston and J. J. Gilman, J. Appl. Phys. **31**, 632 (1960).
[11] R. P. Zhitaru, V. O. Klyavin, and B. I. Smirnov, in *Physical Processes of Plastic Deformation at Low Temperatures* [in Russian] (Naukova Dumka, Kiev, 1974).
[12] Yu. S. Boyarskaya, R. P. Zhitaru, and M. A. Linte, *The Relation between Various Parameters of Plastic Deformation of Doped NaCl Crystals in the Temperature Range 77–773 K* [in Russian] (Shtinitsa, Kishinev, 1983).
[13] Yu. S. Boyarskaya, R. P. Zhitaru, and M. A. Linte, Cryst. Res. Technol. **19**, 101 (1984).
[14] Yu. S. Boyarskaya, R. P. Zhitaru, and N. A. Palistrant, Pis'ma Zh. Tekh. Fiz. **19**, 60 (1993) [Sov. Tech. Phys. Lett. **19**, 458 (1993)].
[15] O. V. Klyavin, *Physics of the Hardness of Crystals at Helium Temperatures* [in Russian] (Nauka, Moscow, 1987).

Translated by Frank J. Crowne

MAGNETISM AND FERROELECTRICITY

A new type of surface spin wave in magnetoelectric crystals

S. V. Tarasenko

Donetsk Physicotechnical Institute, Ukraine Academy of Sciences, 340114 Donetsk, Ukraine
(Submitted February 9, 1998; resubmitted June 22, 1998)
Fiz. Tverd. Tela (St. Petersburg) **41**, 1044–1049 (June 1999)

It is shown for the case of a two-sublattice model of an antiferromagnet with a linear magnetoelectric effect that a new type of surface spin wave can arise at a boundary between a magnetoelectric and a nonmagnetic metal or between a magnetoelectric and a nonmagnetic insulator. This type of surface magnon arises from hybridization of the exchange and electric-dipole spin-spin interaction mechanisms.
[S1063-7834(99)02506-X]

Many papers, both theoretical and experimental, have discussed the conditions for formation and properties of propagation of surface spin waves in bounded magnetically ordered crystals. A large number of these investigations focus on the short-wavelength asymptotic behavior of the spectrum of transverse-electric (TE) magnetic polaritons, that is, magnetostatic spin waves.[1–4] The widespread use of thin magnetic films and multilayer magnetic structures in various devices for processing and storage of information has recently spurred interest in analyzing the conditions for propagation and generation of surface magnetic polaritons. This type of oscillation, as is well known, consists of an electromagnetic wave localized near the boundary between two media, whose spatial and temporal structure simultaneously satisfy the Maxwell equations, the material relations, and the boundary conditions. In particular, it has been shown that magnetic crystals at a magnetic-vacuum boundary can support two basic types of surface magnetic TE polaritons. Let us derive conditions for their existence for the simplest case, when the dynamic magnetic permeability tensor of the magnet $\hat{\mu}$ is diagonal. Let $\mu_{\parallel}$ and $\mu_{\perp}$ be the principal values of this tensor in the direction of propagation of the electromagnetic TE wave ($\mathbf{k}_{\perp}$) and normal to the surface of the magnet, respectively. If $k_{\perp}$ is the wave number and ω the frequency of an electromagnetic TE wave propagating along the surface of the magnet, then the necessary condition for generation of a surface TE polariton is that one of the conditions

$$\mu_{\parallel}<0, \quad \mu_{\perp}<0; \tag{1}$$

$$\mu_{\perp}<0, \quad \mu_{\parallel}>\frac{k_{\perp}^2 c^2}{\omega^2}. \tag{2}$$

be satisfied. Here c is the velocity of light in a vacuum.

Depending on which of the conditions (1) or (2) is fulfilled, we assert that the magnet-vacuum boundary can support either type-I or type-II surface magnetic TE polaritons, respectively.

An important feature of type-II polaritons is that their spectra have points of termination; hence, this type of localized electromagnetic excitation cannot exist in the quasistatic limit ($\omega/c \to 0$). The spectrum of type-I polaritons, where (1) holds, can be studied without dealing with electromagnetic retardation ($c<\infty$). Using this fact, many authors have been able to study the conditions for formation of type-I surface magnetic TE polaritons by analyzing their short-wavelength asymptotic limit, i.e., magnetostatic spin waves.[5] Of course, by virtue of the principle of duality under field exchange, analogous structure can also appear in the spectra of surface magnetic TM polaritons. However, in order for the system to support this class of magnetic polaritons, the unbounded magnetic material must include among its normal spin-wave oscillations modes of uniform magnetic oscillations that are odd under inversion, and consequently electric-dipole-active. Examples of these crystals are centrosymmetric crystals with magnetic ions in noncentrosymmetric positions (for example, hematite, ferrite-garnets, ferrite-spinels, orthoferrites, etc.). A detailed analysis of the spectra of both bulk and surface excitations in such magnets was given in Refs. 6–8. The types of polariton excitations found there were the result of hybridization of an electromagnetic wave of TM type (an H-wave) with an electric-dipole-active mode of the spectrum of exchange magnetic oscillations of the crystal.

The observation of a high value of the magnetoelectric susceptibility in terbium phosphate[9] provided a strong impetus for further intense study of how magnetoelectric interactions affect the resonance properties of magnetically-ordered crystals. In theoretical papers after Ref. 9 it was shown that the magnetoelectric interaction can strongly affect both the magnetoelastic[10,11] and polariton[12] dynamics of bounded magnets through acoustic magnons. In particular, the results of Ref. 12 indicate that in tetragonal antiferromagnets with structure $4_z^{\pm}2_x^{-}1^{-}$ the magnetoelectric interaction implies the presence of previously unstudied surface magnetic TM polaritons, both type-I and type-II. In this case, in contrast to Ref. 7, these localized electromagnetic excitations in the magnet owe their existence to the fact that the acoustic mode of the magnet's magnon spectrum is odd under inversion

(electric-dipole-active). Properties of the spectrum of this type of surface magnetic polariton are 1) lack of inversion symmetry ($\omega(\mathbf{k}_\perp)\neq\omega(-\mathbf{k}_\perp)$, 2) the possibility of conversion of a type-I surface H-wave into a virtual surface TM wave. However, all the studies to date of how magnetoelectric interactions affect the dynamics of magnetoelastic crystals share a very significant limitation: in their calculations, the authors of these studies neglect spatial dispersion of the magnetic medium induced by the nonuniform exchange interaction. In Ref. 12, after reproducing the results of Ref. 13, Buchel'nikov and Shavrov simply mention that spatial dispersion of the magnetic medium can invalidate the macroscopic approach, in which $ak_\perp\ll 1$ (where a is the lattice constant and $\mathbf{k}_\perp$ is the wave vector of a polariton excitation traveling along the surface of the magnet), to describing polariton dynamics of a magnetic crystal. However, in Ref. 14, de Wames *et al.* show for the case of a semi-infinite easy-axis ferromagnet that the simultaneous inclusion of magnetic-dipole and nonuniform exchange interactions makes it possible to specify conditions for the generation of a new type of propagating surface EH wave. In the limit of no electromagnetic retardation, this type of localized excitation consists of a generalized surface spin wave (the square of the component of the wave vector normal to the surface of the magnet is a complex quantity).

Later, in Ref. 15, Ivanov *et al.* also obtained an analogous result for slow surface TE waves in the quasistatic limit, i.e., as $\omega/c\to 0$, within a model of an easy-axis antiferromagnet. The physical mechanism for creating this type of localized excitation is the coupling in the presence of a quasi-two-dimensional defect (the surface of the magnet) of the electromagnetic TE wave and a normal magnetic-dipole-active spin mode.

Note that all the results described above were obtained for boundaries between a magnet and a nonmagnetic insulator, since it is easy to verify that metallization of the surface of a magnet with a diagonal high-frequency permeability tensor $\hat{\mu}(\mu,\mathbf{k}_\perp)$ leads to delocalization of both types of surface magnetic TE polaritons listed above.

In this paper we will show that nonuniform exchange and magnetoelectric interactions can give rise to a previously unknown propagating surface magnetic polariton of TM type, at either a metal-magnetoelectric boundary or a nonmagnetic insulator-magnetoelectric boundary. The short-wavelength asymptotic limit of this type of magnetic polariton is a new type of surface dipole-exchange spin wave.

1. FUNDAMENTAL RELATIONS

Following Ref. 12, we choose as our example of a magnetoelectric material a two-sublattice model of an antiferromagnet (where $\mathbf{M}_{1,2}$ are magnetizations of the sublattices, $|\mathbf{M}_1|=|\mathbf{M}_2|=M_0$). The energy density as a function of the ferromagnetism vector $\mathbf{m}$ and antiferromagnetism vector $\mathbf{l}$ can be written in the form

$$\Phi=F+F_{\rm me},$$

$$F=M_0^2\left\{\frac{\delta}{2}\mathbf{m}^2+\frac{\alpha}{2}(\nabla\mathbf{l})^2-\frac{\beta}{2}l_z^2-\mathbf{mH}+F_{\rm me}\right\}$$
$$+\frac{\varkappa}{2}P_z^2+\frac{\varkappa_\perp}{2}\mathbf{P}_\perp^2-\mathbf{PE},$$

$$\mathbf{m}=\frac{\mathbf{M}_1+\mathbf{M}_2}{2M_0},\quad \mathbf{l}=\frac{\mathbf{M}_1-\mathbf{M}_2}{2M_0}, \tag{3}$$

where δ, α and β are respectively the constants of uniform and nonuniform intersublattice exchange and anisotropy, $\mathbf{E}$ and $\mathbf{H}$ are respectively the electric and magnetic field, $\mathbf{P}$ is the electric polarization vector, and $\varkappa_\perp$, $\varkappa$ are the inverse dielectric susceptibilities.

The magnetoelectric interaction energy in Eq. (3), as is well known,[10–12] can be written in the form

$$F_{\rm me}=\gamma_{\alpha\beta\gamma}m_\alpha l_\beta P_\gamma, \tag{4}$$

where $\hat{\gamma}$ is the tensor of magnetoelectric constants.

Within the framework of our phenomenological treatment, the dynamic properties of this system are described by a system of coupled vector equations ($\mathbf{H_j}=\delta H/\delta\mathbf{j}$ (where $\mathbf{j}=\mathbf{m},\mathbf{l},\mathbf{P}$):

$$(2/gM_0)\mathbf{m}_t=[\mathbf{mH_m}]+[\mathbf{lH_l}],\quad (2/gM_0)\mathbf{l}_t=[\mathbf{lH_m}]+[\mathbf{mH_l}],$$

$$f\mathbf{P}_{tt}=\mathbf{H_P},$$

$$\mathrm{rot}\,\mathbf{H}=\frac{1}{c}\frac{\partial\mathbf{D}}{\partial t},\quad \mathrm{rot}\,\mathbf{E}=-\frac{1}{c}\frac{\partial\mathbf{B}}{\partial t},$$

$$\mathrm{div}\,\mathbf{D}=0,\quad \mathrm{div}\,\mathbf{B}=0. \tag{5}$$

Here g is the gyromagnetic ratio. If we assume that $|\mathbf{m}|\ll|\mathbf{l}|\cong 1$ (smallness of the relativistic interaction compared to the intersublattice exchange), then if the oscillation frequency of the system satisfies the condition

$$\omega\ll\min\{g\delta M_0,(\varkappa_\perp/f)^{1/2},(\varkappa/f)^{1/2}\}, \tag{6}$$

we can eliminate the vectors $\mathbf{m}$ and $\mathbf{P}$ from the discussion. As a result, the equations that describe the dynamics of a magnetoelectric in approximation (6) can be written in the form

$$\alpha\left[\mathbf{l}\left(\mathbf{l}-\frac{1}{c^2}\mathbf{l}_{tt}-\frac{\partial Wa}{\partial\mathbf{l}}\right)\right]-\frac{8}{\delta\omega_s}(\mathbf{lH})\mathbf{l}_t-\frac{4}{\delta}(\mathbf{lH})[\mathbf{lH}]$$
$$+\frac{2}{\delta\omega_s}\{\hat{\varepsilon}\mathbf{l}\hat{\gamma}\mathbf{P}\hat{\varepsilon}\mathbf{l}\mathbf{l}_t+2(\mathbf{\Gamma P})\mathbf{l}_t+\mathbf{l}\hat{\gamma}\mathbf{P}\mathbf{l}\mathbf{l}_t-\hat{\gamma}\mathbf{P}\mathbf{l}_t\}$$
$$+\frac{2}{\delta}\hat{\varepsilon}\mathbf{l}\{(\mathbf{lH})(\hat{\gamma}\mathbf{Pl})+\mathbf{H}(\mathbf{\Gamma P})-\hat{\gamma}\mathbf{PH}\}=0. \tag{7}$$

Here $\Gamma_\alpha\equiv\gamma_{\alpha\beta\gamma}l_\beta l_\gamma$, $\omega_s=gM_0$, and $\hat{\varepsilon}$ is a unit antisymmetric tensor. The vectors $\mathbf{m}$ and $\mathbf{P}$ entering into the Maxwell equations within the approximation (6) are coupled in the following way to the components of the antiferromagnetism vector $\mathbf{l}$:

$$\mathbf{m}=\left\{\frac{2}{\delta\omega_s}[\mathbf{l}_t\mathbf{l}]+\frac{2}{\delta}(\mathbf{H}-\mathbf{l}(\mathbf{lH}))\right\}+\frac{2}{\delta\omega_s}\{\mathbf{l}(\mathbf{\Gamma P})-\hat{\gamma}\mathbf{P}\},$$

$$\mathbf{P}=(\hat{\varkappa})^{-1}(\mathbf{E}-\hat{\gamma}\mathbf{m}). \tag{8}$$

The tensor $\varkappa$ has the following nonzero components: $\varkappa_{xx}=\varkappa_{yy}=\varkappa_\perp$; $\varkappa_{zz}=\varkappa$.

Thus, in the low-frequency limit (6) the set of dynamic equations that determines the interaction of the electromagnetic and spin subsystems of the magnetoelectric material couples only the components of vectors **l**, **H**, and **E** to each other. This reduction of the system is correct for arbitrary values of the deviation of the antiferromagnetism vector **l** from its equilibrium orientation.

Since in this paper we are interested in the surface dynamics of the magnetoelectric, this system of dynamic equations must be supplemented by the appropriate boundary conditions.

Let us assume that the surface of the magnet is metallized, since, as we have already mentioned above, in this case none of the types of surface magnetic polaritons belonging either to E- or H-waves can exist in a nongyrotropic crystal (assuming external magnetic and electric fields are zero).

If the magnetic material occupies the half-space $\xi<0$ (where ξ is a coordinate along the normal to the boundary between the magnetic and nonmagnetic media n), then for a crystal whose surface is metallized but whose magnetic moments are completely unpinned (a special case of the Rado–Wirtman condition) the following boundary conditions apply:

$$\frac{\partial\tilde{\mathbf{l}}}{\partial\xi}=0, \quad \mathbf{E}_\tau=0, \quad \xi=0. \tag{9}$$

Here $\tilde{\mathbf{l}}$ describes small oscillations of the antiferromagnetism vector **l** around its equilibrium orientation, and $\mathbf{E}_\tau$ is the tangential component of the electric field **E** in the magnet.

Since in this paper we analyze excitations localized near the boundary of the media ($\xi=0$), in addition to Eq. (9) we also must satisfy the conditions

$$|\tilde{\mathbf{l}}|\to 0, \quad |\mathbf{E}_\tau|\to 0, \quad \xi\to-\infty. \tag{10}$$

Calculations show that within this model of an antiferromagnet it is possible to realize one of two equilibrium magnetic configurations: an easy-axis configuration ($\mathbf{l}\|OZ$) and an easy-plane configuration ($\mathbf{l}\perp OZ$).[10,11]

Let us consider the same propagation geometry for the electromagnetic wave and equilibrium magnetic configuration used previously in Ref. 12, whose authors neglected nonuniform exchange interaction: the easy-axis phase ($\mathbf{l}\|OZ$, $|\mathbf{M}|=|\mathbf{P}|=0$) of a tetragonal antiferromagnet $4_z^{\pm}2_x^-I^-$. As the plane of propagation of the electromagnetic wave we pick the plane XZ. We will assume that the normal to the surface of the antiferromagnet coincides with one of the Cartesian coordinate axes (i.e., for $\mathbf{k}\in XZ$ either $\mathbf{n}\|OZ$ or $\mathbf{n}\|OX$ is possible). Calculations show that the Fresnel equation for the spectrum of bulk normal polaritons of the unbounded magnetic medium, taking into account nonuniform exchange interactions, factorizes. As a result, in our geometry we have independent propagation of TE and TM waves (see also Ref. 12).

Since calculations show that for the boundary conditions we have chosen localization of polariton modes of TE type near the metallized magnet surface is impossible whether or not we take into account nonuniform exchange interactions, in what follows we will not consider these modes. As for TM modes, as we said at the beginning of this article, the conditions for their localization near the surface of the magnetoelectric $\xi=0$ with boundary conditions (9) and (10) will be derived for $\omega/c\to\infty$, i.e., the quasistatic limit. In this case, for an unbounded magnetoelectric material (3) the relation between frequency and wave vector for these magnetic TM polaritons (dipole-exchange spin waves) for $\mathbf{k}\in XZ$ is determined by the expression

$$\omega^2=(\omega_0^2+s^2\mathbf{k}^2)\left(1-\frac{\varepsilon k_x^2}{k_z^2+bk_x^2}\right)^{-1},$$

$$b\equiv\left(1+4\pi\varkappa_\perp^{-1}+8\pi\frac{\gamma^2\varkappa_\perp^{-2}}{\delta}\right)(1+4\pi\varkappa^{-1})^{-1},$$

$$\varepsilon\equiv\frac{8\pi\gamma^2\varkappa_\perp^{-2}}{\delta(1+4\pi\varkappa^{-1})}, \quad s^2=\frac{\alpha\delta\omega_s^2}{4}. \tag{11}$$

As an example let us consider two relative orientations of the vector **n** normal to the surface of the magnet: $\mathbf{n}\|OZ$ and $\mathbf{n}\|OX$. From Eq. (11) it follows that in this case the corresponding characteristic equation can be written in the form ($\tilde{\omega}_0^2\equiv\omega_0^2+s^2k_\perp^2$)

$$q^4-P_1q^2+P_2=0, \quad n\|OZ, \tag{12}$$

$$P_1=\frac{\tilde{\omega}_0^2+s^2k_\perp^2b-\omega^2}{s^2}, \quad P_2=\left(\frac{\tilde{\omega}_0^2-\omega^2(b-\varepsilon)}{s^2}\right)k_\perp^2;$$

$$q^4-P_1q^2+P_2=0, \quad n\|OX,$$

$$P_1=\frac{b\tilde{\omega}_0^2+s^2k_\perp^2-\omega^2(b-\varepsilon)}{s^2b},$$

$$P_2=\left(\frac{\tilde{\omega}_0^2-\omega^2}{s^2b}\right)k_\perp^2. \tag{13}$$

Thus, it follows from Eq. (11) that within the electric-dipole approximation ($\omega/c\to0$) the polariton wave propagating along the surface of a magnet that satisfies (3) is an excitation of two-partial type when spatial dispersion is included. This is true both for $\mathbf{n}\|OX$ and $\mathbf{n}\|OZ$. The resulting spatial structure, e.g., of the scalar potential of the electric field ψ (where $E\equiv\operatorname{grad}\psi$) can be expressed in the following form (where $\mathbf{k}_\perp$ is the wave vector of the oscillations under study along the direction of propagation of the spin wave, as determined by the vector $\mathbf{r}_\perp$; note that $\mathbf{r}_\perp\perp\mathbf{n}$):

$$\psi=\sum_{j=1}^{2}A_j\exp(q_j\xi)\exp(i\omega t-i\mathbf{k}_\perp\mathbf{r}_\perp). \tag{14}$$

Here $q^2\equiv-(\mathbf{kn})^2$, $q_{1,2}$ is specified from Eqs. (12) and (13) as a function of the external parameters, i.e., the oscillation frequency ω and wave vector $k_\perp$.

Thus, using Eqs. (12)–(14) we can classify the possible types of propagating dipole-exchange surface spin waves depending on the character of their localization near the surface of the magnetoelectric crystal (3).

2. CLASSIFICATION OF POSSIBLE TYPES OF SURFACE DIPOLE-EXCHANGE SPIN WAVES

Analysis of Eqs. (12)–(14) shows that two-partial surface spin waves ($q_1^2>0$, $q_2^2>0$) will arise in the medium under discussion when

$$\omega_+^2(k_\perp)<\omega^2<\tilde{\omega}_0^2 b_*, \quad k_\perp^2>k_*^2$$

(here $b_*\equiv b/(b-\varepsilon)$), or

$$\omega_-^2(k_\perp)>\omega^2, \quad k_\perp\leqslant\omega_-(0)/s$$

for $\mathbf{n}\|OZ$, and

$$\omega_\pm^2(k_\perp)\equiv\frac{N_1}{2}\pm\left(\left(\frac{N_1}{2}\right)^2-N_2\right)^{1/2}, \quad k_*^2=\frac{\omega_0^2\varepsilon}{s^2 b},$$

$$N_1=2[\tilde{\omega}_0^2+s^2 b k_\perp^2]-4s^2k_\perp^2(b-\varepsilon),$$

$$N_2=[\tilde{\omega}_0^2+s^2 b k_\perp^2]^2-4s^2k_\perp^2\tilde{\omega}_0^2 b, \tag{15}$$

$$\tilde{\omega}_0^2\geqslant\omega^2 \tag{16}$$

for $\mathbf{n}\|OX$.

If the frequency ω and wave number $k_\perp$ of a normal electric-dipole active mode in the spectrum of magnetic oscillations of an unbounded version of the magnet under discussion satisfy the relations

$$\tilde{\omega}_0^2 b_*\leqslant\omega^2, \quad \mathbf{n}\|OZ, \tag{17}$$

$$\tilde{\omega}_0^2<\omega^2, \quad \mathbf{n}\|OX, \tag{18}$$

then near the boundary of this magnet a two-partial pseudosurface ($q_1^2>0$, $q_2^2<0$) dipole-exchange spin wave can form.

In the range of parameters ω and $k_\perp$ specified for $\mathbf{n}\|OZ$ by the relation

$$\omega_-^2(k_\perp)\leqslant\omega^2\leqslant\omega_+^2(k_\perp), \tag{19}$$

the magnetic medium under discussion can support a two-partial generalized ($\mathrm{Re}\,q_{1,2}^2\neq 0$; $\mathrm{Im}\,q_{1,2}^2\neq 0$) surface spin wave.

Finally, for $\mathbf{n}\|OZ$ and

$$\omega_+^2(k_\perp)<\omega^2<\tilde{\omega}_0^2 b_*, \quad k_\perp<k_*, \tag{20}$$

it is possible for a two-partial exchange polariton of TM ($q_{1,2}^2<0$) type to propagate along the chosen surface of the magnet under discussion.

Thus, the results of this analysis imply that for $\mathbf{k}\in XZ$ an electric-dipole-active mode of the spectrum of normal oscillations can be localized near the surface of a magnet of type (3) with $\mathbf{n}\|OZ$ only if the polariton frequency ω and its wave number $k_\perp$ satisfy one of the relations (15) or (19); when $\mathbf{n}\|OX$ they must satisfy relation (16). However, this is only a necessary condition for localization of this type of electromagnetic wave near the surface. The corresponding dispersion relation for the surface-wave spectrum is determined from the condition for existence of a nontrivial solution to the system of boundary conditions (9) and (10), which must br solved with respect to the unknown partial amplitudes $A_{1,2}$ (12).

3. A NEW TYPE OF SURFACE DIPOLE-EXCHANGE SPIN WAVE

If we carry out the calculations proposed above for each of the two orientations of the normal to the surface of the magnet n, we find that for $\mathbf{k}\in XZ$ that conditions (14)–(20) imply a new type of surface magnetic polariton of TM type propagating along the metallized surface of the magnet under study. However, this will be possible only for $\mathbf{n}\|OZ$. The spectrum of the new surface excitation can be found explicitly in the quasistatic limit (where it is a dipole-exchange surface spin wave) for arbitrary values of the wave vector $k_\perp$:

$$\Omega^2=\tilde{\omega}_0^2 b_*-\left\{\frac{sk_\perp}{2}(b-\varepsilon)^{1/2}-\left[\tilde{\omega}_0^2(b_*-1)+\frac{s^2k_\perp^2(b-\varepsilon)}{4}\right]^{1/2}\right\}^2. \tag{21}$$

Comparing this dispersion relation with Eqs. (12)–(19) shows that for $k_\perp<k_{**}$, where k_{**} is defined from the equation

$$\omega_+^2(k_{**})=\omega_0^2+s^2k_{**}^2, \tag{22}$$

the dispersion relation (21) corresponds to a propagating generalized surface magnetic polariton of TM type ($\mathrm{Re}\,q_{1,2}^2\neq 0$, $\mathrm{Im}\,q_{1,2}^2\neq 0$). For $k_\perp=k_{**}$ the dispersion curve determined by Eq. (21) smoothly transforms into the dispersion curve for a TM type of two-partial ($q_1^2>0$, $q_2^2>0$) surface magnetic polariton, which propagates when $k_\perp>k_{**}$.

If we introduce the notation $q_{1,2}=q_r\pm iq_i$ (where $q_i\neq 0$ for $\mathrm{Re}\,q_{1,2}^2\neq 0$, $\mathrm{Im}\,q_{1,2}^2\neq 0$), it follows from Eqs. (12)–(19) that for the surface magnetic TM polariton (21) we have for $\omega=\Omega$ that

$$q_r^2=\frac{1}{2}\left(P_2^{1/2}+\frac{P_1}{2}\right),$$

$$q_i^2=\frac{1}{2}\left(P_2^{1/2}-\frac{P_1}{2}\right). \tag{23}$$

Analysis shows that this type of surface magnetic polariton cannot exist unless we take into account the nonuniform exchange interaction. In the quasistatic ($\omega/c\to 0$) limit the surface magnetic TM polariton whose spectrum is given by (21) constitutes a new type of two-partial generalized surface spin wave for $k_\perp<k_{**}$ or a two-partial surface spin wave for $k_\perp>k_{**}$. In contrast to previously known types of dipole-exchange surface spin wave excitations,[14,15] this type of surface magnon is a result of hybridization in the presence of a quasi-two-dimensional defect (the crystal surface) of the exchange and electric-dipole mechanisms for spin–spin interactions. It is not difficult to verify that dipole-exchange magnons described in Refs. 14 and 15 cannot exist at a boundary between the magnet and a nonmagnetic metal surface.

Metallization of the surface of the magnetoelectric material is not a necessary condition for the existence of the surface magnetic polariton of TM type considered in this paper. If the magnet is bounded by a nonmagnetic dielectric

medium, then the following system of boundary conditions must be satisfied at the surface of the magnetoelectric material when $\mathbf{n}\|OZ$ and the spins are completely free (the label ν refers to the nonmagnetic medium):

$$\frac{\partial\tilde{\mathbf{l}}}{\partial z}=0, \quad \mathbf{Dn}=\mathbf{E}_\nu\mathbf{n}, \quad \mathbf{E}_\tau=(\mathbf{E}_\nu)_\tau, \quad z=0;$$

$$|\mathbf{E}_\nu|\to 0, \quad z\to\infty, \tag{24}$$

where $\mathbf{D}\equiv\mathbf{E}+4\pi\mathbf{P}$ is the electric displacement.

If we have $\mathbf{k}\in XZ$, $\mathbf{n}\|OZ$ as before, taking into account Eqs. (12)–(14) we can write the corresponding dispersion relation that determines the spectrum of surface TM polaritons at the boundary $z=0$ between a magnetoelectric material of type (3) and a nonmagnetic insulating medium (whose dielectric permittivity is unity) in the form

$$rk_\perp(q_1^2+q_2^2+q_1q_2-bk_\perp^2)+q_1q_2(q_1+q_2)=0,$$

$$r\equiv\left(1+\frac{4\pi}{\varkappa}\right)^{-1}. \tag{25}$$

Now it is no longer possible to derive an expression for the spectrum of dipole-exchange surface waves in explicit form for arbitrary values of $k_\perp$. In the short-wavelength limit $k_\perp\gg k_*$, an expression for the dispersion law of this surface magnetic TM polariton can be obtained from Eq. (25) in the form

$$\Omega^2\cong\tilde{\omega}_0^2b_*-\left(\frac{(b_*-1)\tilde{\omega}_0^2r}{sk_\perp(r+b^{1/2})(b-\varepsilon)^{1/2}}\right)^2. \tag{26}$$

Comparing Eq. (26) with Eq. (12) it is not difficult to verify that Eq. (26) specifies the short-wavelength asymptotic behavior of the dispersion law for surface ($q_{1,2}^2>0$) magnetic TM polaritons propagating along the boundary between a magnet and a nonmagnetic insulating medium.

It is worth recalling here the results of Ivanov *et al.* reported in Ref. 15, which showed that a surface dipole-exchange wave can propagate in this same geometry ($\mathbf{k}\in XZ$, $\mathbf{n}\|OZ$, spins at $z=0$ completely free) along the boundary between an antiferromagnetic insulator and the nonmagnetic insulator. This wave is the magnetostatic limit of the magnetic TE polariton.

Thus, this geometry of the problem allows the independent propagation along the boundary between the magnetoelectric and nonmagnetic insulator of two types of surface magnetic polaritons: TM and TE. For a magnetoelectric of type (3), when $\mathbf{k}\in XZ$ the structure of the TM magnetic polariton is specified by nonzero coupled oscillations of $\tilde{l}_x,\tilde{m}_y,E_x,E_z,H_y$, while the structure of the TE magnetic polariton consists of nonzero values of $\tilde{l}_y,\tilde{m}_x,E_y,H_z,H_x$.

4. CRITERION FOR EXISTENCE OF DIPOLE-EXCHANGE SURFACE SPIN WAVES

A question of undoubted interest is: what criterion must the spectrum of a normal electromagnetic H-wave satisfy in a magnet in order to give rise to this new kind of surface magnetic polariton near a surface when boundary conditions (9) and (10) are imposed there? From crystal optics[16] it is known that the form of the wave-vector surface of a normal mode of the spectrum of oscillations of an unbounded crystal is an important factor in determining the distinctive features of the interaction of this mode with the boundaries of the crystal. In the present case, it follows from Eq. (11) that in the quasistatic limit $\omega/c\to 0$ the intersection of such a wave surface in $\mathbf{k}$ space with the plane of propagation of the wave under study (XZ) is determined by an equation of the form ($\tan\vartheta=k_x/k_z$):

$$\omega^2\left(1-\frac{\varepsilon\sin^2\vartheta}{\cos^2\vartheta+b\sin^2\vartheta}\right)-\omega_0^2=s^2k^2. \tag{27}$$

From Eq. (27) it follows that when the condition

$$\omega^2<\frac{\omega_0^2bb_*}{1+b-b_*} \tag{28}$$

is satisfied, a segment forms on the curve (27) with negative curvature and a maximum at $\vartheta=\pi/2$. Comparing this result with the conditions for the existence of the new type of surface magnetic polariton leads us to conclude that the presence of a segment with negative curvature on the curve determined by the intersection of the wave vector surface of the type of normal wave of the unbounded magnet with the wave plane of propagation is a necessary condition for the condensation of this type of normal vibration into the corresponding surface wave. In this case, the direction of the normal to the surface of the magnet $\mathbf{n}$ must be perpendicular to the direction in which the segment with maximum negative curvature forms.

Analysis shows that this criterion is fulfilled not only for magnetic TM polaritons but also for the surface magnetic TE polaritons discussed in Refs. 14 and 15 for a normal magnetized easy-axis ferromagnet or antiferromagnet with the easy-axis perpendicular to the crystal surface.

Thus, in this paper, based on analysis of the short-wavelength asymptotic behavior of the polariton spectrum of a magnetoelectric material, we have shown that 1) a first-principles inclusion of spatial dispersion of the magnetic medium (derived from the nonuniform exchange interaction) leads to localization of a slow electromagnetic H-wave both at the boundary between a magnetoelectric material and a metal and at the boundary between a magnetoelectric material and an insulator, and to the formation of a new type of surface magnetic TM polariton (a surface dipole-exchange spin wave); 2) this type of surface excitation is the result of hybridization in the presence of a quasi-two-dimensional defect (the crystal surface) of the spin and electromagnetic modes of the spectrum of normal oscillations of an unbounded magnetoelectric material; 3) there exists a one-to-one correspondence between the local geometry of the isofrequency surface of the normal polariton mode of an unbounded magnet and the conditions for formation of the new types of surface magnetic polariton, both TM and TE.

In keeping with the results of Refs. 10–12, we can list trirutiles[17] and rare-earth phosphates[9] among the crystals that could support this new type of surface magnetic polariton.

In conclusion, the author is deeply grateful to A. L. Bogdan, I. L. Lyubchanskiĭ, and T. N. Tarasenko for supporting the idea of this work and for fruitful discussions.

[1] M. G. Cottam and D. R. Tilley, *Introduction to Surface and Superlattice Excitations* (Cambridge Univ. Press, Cambridge, 1989).
[2] A. V. Vashkovskiĭ, V. S. Stalmakhov, and Yu. P. Sharaevskiĭ, *Magnetostatic Waves in Microwave Electronics* [in Russian] (Saratov Univ. Publ., Saratov, 1993).
[3] C. E. Patton, Phys. Rep. **103**, 251 (1984).
[4] G. A. Vugal'ter and I. A. Gilinski, Izv. Vyssh. Uchebn. Zaved. Radiofiz. **32**, 1187 (1987).
[5] M. I. Kaganov, N. B. Pustyl'nik, and T. I. Shalaeva, Usp. Fiz. Nauk **167**, 191 (1997) [Phys. Usp. **40**, 181 (1997)].
[6] V. N. Krivoruchko and D. A. Yablonskiĭ, Zh. Éksp. Teor. Fiz. **94**, 268 (1988) [Sov. Phys. JETP **67**, 1886 (1988)].
[7] V. N. Krivoruchko and T. E. Primak, Fiz. Tverd. Tela (Leningrad) **33**, 3205 (1991) [Sov. Phys. Solid State **33**, 1810 (1991)].
[8] S. V. Borisov and I. L. Lyubchanskiĭ, Opt. Spektrosk. **80**, 691 (1996) [Opt. Spectrosc. **80**, 620 (1996)].
[9] S. Bluck and H. G. Kahle, J. Phys. C **21**, 5193 (1988).
[10] E. A. Turov, Zh. Éksp. Teor. Fiz. **104**, 3886 (1993) [JETP **77**, 868 (1993)].
[11] E. A. Turov, V. V. Men'shenin, and V. V. Nikolaev, Zh. Éksp. Teor. Fiz. **104**, 4157 (1993) [JETP **77**, 1014 (1993)].
[12] V. L. Buchel'nikov and V. G. Shavrov, Zh. Éksp. Teor. Fiz. **109**, 706 (1996) [JETP **82**, 380 (1996)].
[13] M. I. Kaganov and G. I. Shalaeva, Zh. Éksp. Teor. Fiz. **96**, 2185 (1989) [Sov. Phys. JETP **69**, 1237 (1989)].
[14] R. E. DeWames and T. J. Wolfram, J. Appl. Phys. **41**, 987 (1970).
[15] B. A. Ivanov, V. F. Lapchenko, and A. L. Sukstanskiĭ, Fiz. Tverd. Tela (Leningrad) **27**, 173 (1985) [Sov. Phys. Solid State **27**, 101 (1985)].
[16] Yu. I. Sirotin and M. P. Shaskol'skaya, *Principles of Crystal Physics* [in Russian] (Nauka, Moscow, 1979).
[17] A. H. Cook, S. J. Swithenby, and M. R. Wells, Int. J. Magn. **4**, 309 (1973).

Translated by Frank J. Crowne

Ferromagnetic resonance in the polycrystalline hexagonal ferrites $Co_{2-x}Zn_xW$

V. A. Zhuravlev*)

Tomsk State University, 634050 Tomsk, Russia
(Submitted August 5, 1998)
Fiz. Tverd. Tela (St. Petersburg) **41**, 1050–1053 (June 1999)

Experimental studies of the ferromagnetic resonance spectra of polycrystalline hexagonal ferrites of the system $Co_{2-x}Zn_xW$ in the frequency range 16–32 GHz are described. It is shown that interpretation of the experimental data requires the assumption of an anisotropic effective magnetomechanical ratio (or g-factor). The results of these experiments are compared with calculations based on the equations of motion, which ensure the conservation of the mechanical moment length. Concentration dependences are determined for the components of the magnetomechanical ratio tensor and the anisotropy field of this system of hexagonal ferrites at room temperature. Possible reasons why anisotropy fields measured in the vicinity of a spin reorientation transition will differ from results given by other methods are discussed.
 [S1063-7834(99)02606-4]

The complex structure of ferromagnetic resonance (FMR) lines—additional maxima in the absorption, steps, etc.—observed in polycrystalline ferrites with large magnetocrystalline anisotropy was first explained by Schlömann within a ''independent grain'' model. In Refs. 1–3 he showed that the features in the FMR curves occur at values of the magnetizing field corresponding to stationary directions in the angular dependence of the resonance field $H_R(\Theta,\Phi)$ for single-crystal grains, i.e., the crystallites that make up the polycrystal. Here Θ,Φ are the polar and azimuthal angles of the magnetizing field vector relative to the crystallographic axes of the crystal. These directions (Θ_i,Φ_i), which correspond to maxima, minima, and saddle points of the surface $H_R(\Theta,\Phi)$, satisfy the condition $H_R(\Theta,\Phi)=0$. In hexagonal crystals, the magnetocrystalline anisotropy energy has the form

$$F_a=k_1\sin^2\theta+k_2\sin^4\theta+k_3\sin^6\theta+k_4\sin^6\theta\cos 6\varphi, \tag{1}$$

where θ,φ are angles of the magnetization vector and k_i are anisotropy constants. The natural stationary directions for a spherical sample in the limit $|k_1|\gg|k_2|,|k_3|$ are along the hexagonal axis $(\Theta_1=\theta_1=0)$ and in the basal plane $(\Theta_{2,3}=\theta_{2,3}=\pi/2,\ \Phi_2=\varphi_2=\pi/6,\ \Phi_3=\varphi_3=0)$. For these directions, the FMR resonance frequencies of a spherical sample can be easily obtained, e.g., by the method of Suhl and Smith,[4] see Eq. (4) below with $\gamma_\parallel=\gamma_\perp=\gamma$. Here $\gamma=ge/2mc$ is the magnetomechanical ratio, g is the effective g-factor, e and m are the charge and mass of an electron respectively, and c is the velocity of light.

The availability of the analytic expression (4) makes it possible to determine the anisotropy field based on features on the experimental FMR curve of the polycrystals. Using this method, the authors of Refs. 2, 5 and 6 found the anisotropy fields for a number of ferrites with hexagonal structure, and ferrites with cubic and tetragonal structures in Refs. 7 and 8. The measurements reported in Refs. 2, 5–7 were made at one frequency; therefore, in calculating the anisotropy fields the authors of Refs. 2, 5, and 6 assumed that the g-factor equaled two, while in Ref. 7 it was left unestimated. However, it is well known (see for example Refs. 8–10) that in hexagonal ferrites the g-factor differs greatly from two, and in uniaxial materials it can also be anisotropic under certain conditions.[11–13]

When $|k_1|\approx|k_2|,|k_3|$ holds, which occurs in the neighborhood of a spin-reorientation phase transition,[14] the angular function $H_R(\Theta,\Phi)$ can develop additional stationary directions[15] at angles Θ other than zero or $\pi/2$. Hence, it is necessary to identify in advance the maxima and steps in the resonance curves observed during the experiments with the stationary directions corresponding to them. Here one must keep in mind that in real materials the damping of uniform precession will smooth out features on the resonance curves and the field values at which they are observed will differ as a rule from the field $H_R(\Theta_i,\Phi_i)$ of the corresponding stationary direction (see Ref. 15, and also Fig. 1 of this paper).

Thus, in order to increase the accuracy of estimates of the anisotropy field based on FMR experiments in polycrystalline hexagonal ferrites, we must first examine the range of frequencies used to determine the value of the g-factor and possible anisotropy of the latter. Secondly, we must compare not simply the values of the fields for the maxima and steps on the experimental curves with Eq. (4), but rather the overall shapes of the calculated and experimental curves. In Ref. 15, the author and his colleagues derived a method of calculating the resonance curve of a polycrystalline hexagonal ferrite in the independent-grain approximation for arbitrary relations between the anisotropy constants, based on solving the equation of motion of the Landau–Lifshits magnetization vector. However, the mathematical relations used there do not apply to a medium with an anisotropic g-factor, since this equation does not conserve the lengths of the mechanical and magnetic moment vectors, nor does it fulfill the law of conservation of energy. A generalization of the calculations of Ref. 15 will be given below.

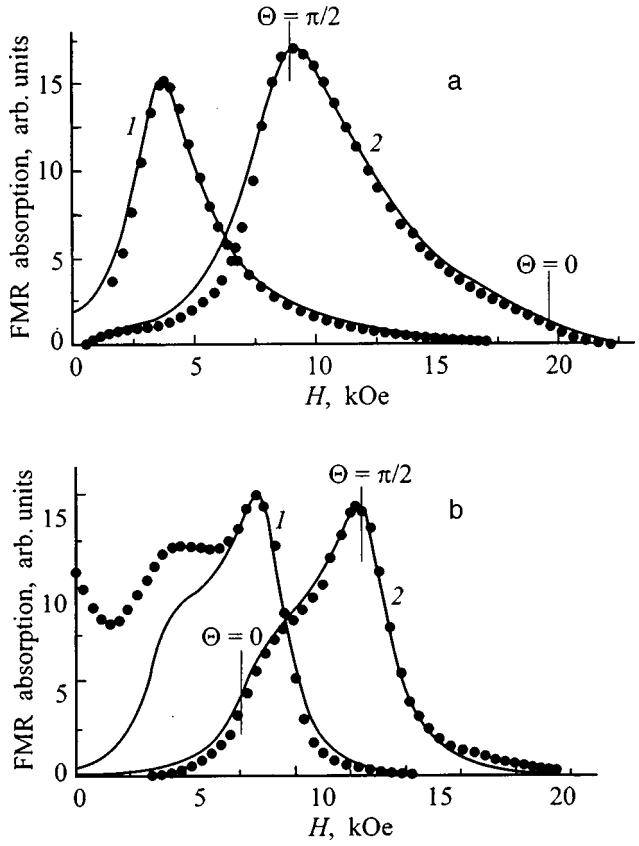

FIG. 1. FMR lines for the hexagonal ferrites $Co_{2-x}Zn_xW$. a—$x=1$, *1*—$f=16.886$ GHz, $\alpha=0.23$; *2*—$f=32.720$ GHz, $\alpha=0.19$; b—$x=1.5$, *1*—$f=21.468$ GHz, $\alpha=0.15$; *2*—$f=32.720$ GHz, $\alpha=0.11$. The vertical segments on the resonance curves indicate the position of stationary directions.

In Ref. 12, Vlasov *et al.* obtained an equation of motion that satisfies the conditions of conservation of the length of the mechanical moment and energy in a medium with an anisotropic g-factor. This equation is useful for analyzing FMR in hexagonal crystals with two collinear sublattices with inclusion of terms with k_1, k_2 (see Ref. 13) in the energy anisotropy. In this latter reference, Gurevich *et al.* also showed that in analyzing low-frequency ''ferromagnetic'' oscillations it is also possible, as in the case of an isotropic g-factor, to treat a ferromagnetic crystal as a ferromagnet with effective parameters. The expression for the free energy density of such a crystal can be written

$$F=F_h+F_a=-IH[\gamma_\perp \sin\Theta \sin\theta\cos(\Phi-\varphi) + \gamma_\parallel \cos\Theta\cos\theta]+F_a, \quad (2)$$

where F_h is the Zeeman energy, H is the value of the magnetizing field, I is the modulus of the mechanical moment vector, and $\gamma_\parallel, \gamma_\perp$ are the components of the effective magnetomechanical ratio tensor in directions parallel and perpendicular to the hexagonal axis respectively. The second term is the anisotropy energy, which is analogous to Eq. (1) but is expanded in powers of the mechanical moment vector. The angular dependence of the resonance field can be found by solving the system of equations

$$F'_\theta(\theta_0,\varphi_0,\Theta,\Phi)=0,$$

$$F'_\varphi(\theta_0,\varphi_0,\Theta,\Phi)=0,$$

$$\omega^2=(I\sin\theta_0)^{-2}[F''_{\theta\theta}F''_{\varphi\varphi}-(F''_{\theta\varphi})^2]. \quad (3)$$

The first two equations in (3) determine the equilibrium orientation of the mechanical moment, i.e., the angles θ_0, φ_0, while the third determines the resonance frequency for uniform precession at preset angles Θ,Φ. The system (3) is solved numerically by the method of successive root refinement, starting with $\Theta=\Theta_3$, $\Phi=\Phi_3$. We varied the angles Θ,Φ within the ranges $\pi/2\geqslant\Theta\geqslant\Delta\Theta$, $0\leqslant\Phi\leqslant\pi/6$ in steps of $\Delta\Theta,\Delta\Phi$. For each direction of the field the solution to Eq. (3) for the previous case is used as the zero-order approximation. The roots of system (3) for an initial direction $H_R(\Theta_3,\Phi_3)=H_3$ and along the hexagonal axis $H_R(\Theta_1,\Phi_1)=H_1$ are found from the resonance frequencies for the stationary directions

$$\omega_1/\gamma_\parallel=H_1+(\gamma_\perp/\gamma_\parallel)H_{a1},$$

$$(\omega_{2,3}/\gamma_\perp)^2=(H_{2,3}\pm H_\Phi)(H_{2,3}-H_\Theta\pm H_\Phi/6). \quad (4)$$

Here $H_{a1}=2k_1/M$, $H_\Theta=2(k_1+2k_2+3k_3)/M$, $H_\Phi=36k_4/M$ is the anisotropy field, ω is the circular frequency, $M=\gamma_\perp I$ is the saturation magnetization, and H_i are the values of the resonance fields. In calculating the resonance curve for the polycrystal, we included the finite width of the crystallite line ($\Delta H=\alpha(\omega/\gamma_\perp)$, where α is the attenuation constant in the equation of motion) using the expression

$$W(h)=\frac{1}{4\pi}\int_0^\pi\int_0^{2\pi}\frac{1}{\pi}\frac{\alpha}{[h-h_R(\Theta,\Phi)]^2+\alpha^2}\times\sin\Theta\,d\Theta\,d\Phi, \quad (5)$$

where $h_R(\Theta,\Phi)=\gamma_\perp H_R(\Theta,\Phi)/\omega$.

The FMR spectra were studied experimentally at room temperature in the frequency range 16–32 GHz using spherical samples with diameters 0.6–0.8 mm, made from polycrystalline hexagonal ferrites of the system $BaCo_{2-x}Zn_xFe_{16}O_{27}$ ($Co_{2-x}Zn_xW$) with $0.5\leqslant x\leqslant 1.6$. Our choice of these materials was dictated by the wealth of available information about hexagonal ferrites of this system: their magnetic structure is known, magnetic phase diagrams have been plotted, and characteristics such as the anisotropy field and saturation magnetization in static and pulsed fields ave been investigated both for single crystals[16] and in polycrystalline samples[17] over a wide temperature range. For materials with low concentrations of zinc ions magnetic ordering of the planar type occurs at room temperature, while at higher concentrations an axis of easy magnetization appears. A spin-reorientation phase transition is observed via an intermediate phase with a cone of easy magnetization at room temperature near the concentration $x\approx 1.3$.[17,18] Thus, for these materials we can compare our FMR measurements of the anisotropy fields with results obtained by other methods, and check the agreement of theory with experiment for several types of magnetic ordering.

Our experimental method was as follows: using feedthrough rectangular multimode resonators with TE_{10n} modes and a standard apparatus KSVn network analyzer, we first plotted ferromagnetic resonance curves at fixed frequencies

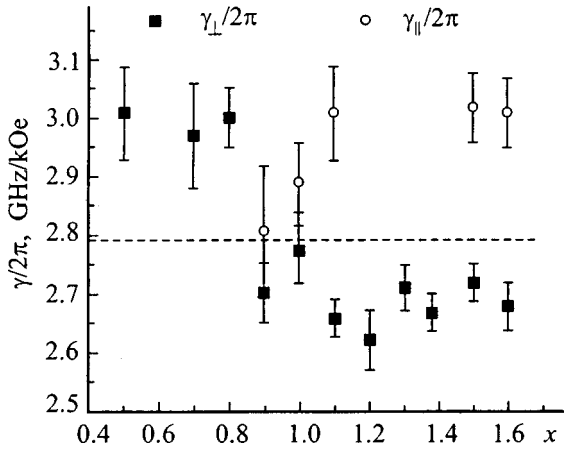

FIG. 2. Concentration dependence of the components of the magnetomechanical ratio tensor of the hexagonal ferrites $Co_{2-x}Zn_xW$.

within the range described above. Then the fields corresponding to steps and maxima on the FMR curves were determined and their frequency dependences were plotted. Least-squares fitting of our data to the function Eq. (4) allowed us to find values of $\gamma_\parallel, \gamma_\perp$, and approximate values of the anisotropy fields. We then chose the magnitude of the anisotropy field and attenuation constant α so as to achieve the best match in the shapes of the calculated and experimental curves at several frequencies, thereby obtaining refined values of the field H_{a1}, H_Θ, H_Φ. In Fig. 1 we show the experimental (points) and calculated (smooth curves) resonance curves for two compositions of the materials investigated, one with a plane (a) and one with an axis (b) of easy magnetization. For all other concentrations of Zn^{2+} ions the agreement between calculations and experiment is found to be good, except for the low-field ($H \to 0$) segments of FMR curves measured in samples with certain compositions. For these samples certain additional losses are observed whenever the measurement frequencies coincide with a band of frequencies for natural ferromagnetic resonance.[18] Figure 1b shows resonance curves that are typical of such samples at a frequency 21.468 GHz. Note that the attenuation parameter α decreases with increasing frequency and concentration x; its value ($\alpha \approx 0.3-0.1$) indicates that the crystallites have a rather large intrinsic linewidth $\Delta H \approx 2-1$ kOe.

Figure 2 shows concentration dependences of the measured magnetomechanical ratios along the hexagonal axis, i.e., $\gamma_\parallel/2\pi$, and in the basal plane, i.e., $\gamma_\perp/2\pi$. The straight line parallel to the abscissa labels the value $\gamma/2\pi = 2.8$ GHz/kOe (for $g=2$). The magnetomechanical ratio is clearly anisotropic at large concentrations of Zn^{2+} ions, such that $\gamma_\parallel - \gamma_\perp > 0$. With increasing x this difference decreases, and near a composition $x=0.9$ we switch to $\gamma_\parallel \approx \gamma_\perp$. For compositions with $x \leqslant 0.8$ the issue of g-factor anisotropy remains unresolved, since no one has yet observed a step on the resonance curves in the direction of difficult magnetization (since the field $H_1 \geqslant 20$ kOe). The magnitude of $\gamma_\parallel$ cannot be determined in the range of concentrations $1.2 \leqslant x \leqslant 1.4$, i.e., in the neighborhood of the spin-reorientation phase transition, since the anisotropy is small there and features on the FMR line are hard to see.

TABLE I. Anisotropy field of hexagonal ferrites from the system $Co_{2-x}Zn_nW$.

Concentration	H_Θ, kOe	H_{a1}, kOe	H_{a2}, kOe
0.5	−13	⋯	⋯
0.7	−11.8	⋯	⋯
0.8	−10.4	⋯	⋯
0.9	−10	−10	⋯
1	−7.7	−7.7	⋯
1.1	−5.8	−4.8	−1
1.2	−5.2	−4.2	−1
1.3	−2.5	−1	−1.5
1.38	−1	0.5	−1.5
1.5	2.1	3.6	−1.5
1.6	4.5	5.5	−1

The anisotropy field in the basal plane can only be given an upper bound, since the experiments do not reveal splitting of the maxima at the resonance fields H_2, H_3. In this case imposing the field H_Φ turns out to have the same effect on the resonance curve as increasing the attenuation parameter α. We find that $H_\Phi < 1.5$ kOe holds for all concentrations of Zn^{2+} ions, which agrees with the results presented in Ref. 18.

Results of measuring the concentration dependence of anisotropy fields are shown in Table I, with an error of ± 0.3 kOe. Away from the vicinity of the spin-reorientation phase transition, the values of the anisotropy fields are in good agreement with data obtained by other methods, both for single crystals[16] and for polycrystalline textured samples.[17] In the neighborhood of the spin-reorientation phase transition ($1.2 \leqslant x \leqslant 1.4$) it is assumed that $\gamma_\parallel/2\pi = 3$ GHz/kOe when estimating the anisotropy field, since this is the value of the magnetomechanical ratio observed both above and below this range of concentrations. The magnitudes and signs of the fields H_Θ, H_{a2} obtained for these compositions differ from those measured for these same materials in Refs. 17 and 18. The field H_Θ changes sign at $x \approx 1.42$; moreover, for compositions $x=1.3$, 1.38 a cone of difficult magnetization is observed, whereas according to Refs. 17 and 18 the following relations should hold at $x=1.3$ and room temperature: $H_\Theta \geqslant 0$, $H_{a1} < 0$, $H_{a2} \geqslant |H_{a1}|$, which are typical for a cone of easy magnetization.

Although the applicability of the independent grain model to materials with anisotropy fields comparable in magnitude to the saturation magnetization, i.e., materials such as the hexagonal ferrites $Co_{2-x}Zn_nW$ with $1.2 \leqslant x \leqslant 1.4$, is open to criticism, the discrepancies between our measured values of the fields H_Θ, H_{a2} and the data of Refs. 17 and 18 have nothing to do with methodological errors. One possible explanation from them involves the presence of g-factor anisotropy. Since the length of the magnetization vector in this case depends on orientation with respect to the crystallographic axes, the expansion of F_a in powers should contain terms of the form[12]

$$F_a = \beta_1 M^2 + \beta_2 M^4 + \beta_3 M_z^2 + \beta_4 M^2 M_z^2 + \beta_5 M_z^4 + \ldots, \tag{6}$$

where the β_i are anisotropy constants. When the g-factor is

isotropic, only terms proportional to β_3 and β_5 appear in this expansion. Using the relation between I and M, we can express the constants entering into Eq. (1) in terms of those that describe anisotropy of the magnetic moment (6), and the k_i will depend on the constants β_i that characterize both the anisotropy of the magnitude and the z component of the magnetization vector. Different methods of defining the anisotropy fields can lead to different combinations of the constants β_i in the k_i, which could also explain the discrepancies between the anisotropy fields we measured and the data of Refs. 16–18, in which g-factor anisotropy was not taken into account.

Moreover, the observed dependence of the type of magnetic ordering (e.g., cones of difficult magnetization versus cones of easy magnetization) on the presence or absence of a magnetic field at concentration $x=1.3$ could indicate the inadequacy of using the expansion (1) to treat anisotropic interactions in the neighborhood of a spin-reorientation phase transition. In Refs. 19 and 20 Acquarone showed that that the presence of nonmagnetic ions in hexagonal ferrites can cause local distortion of the symmetry of exchange couplings and bring about conditions that facilitate anisotropic and antisymmetric exchange interactions. He found that the exchange integrals for these interactions are comparable in order of magnitude to the isotropic exchange integrals.

Thus, our studies of FMR in hexagonal ferrites of the system $Co_{2-x}Zn_xW$ show that the effective g-factors of these materials exhibit considerable anisotropy, at least for compositions $x \geqslant 0.9$. Anisotropy fields deduced from features on the measured resonance curves of polycrystals agree with published data away from the concentration neighborhood in which spin-reorientation phase transitions occur. In this latter concentration neighborhood our measurements disagree in magnitude and sign with anisotropy fields measured by other methods. This could be a sign of the inadequacy of the traditional phenomenological approach and the need to develop a more general treatment of phenomena observed in these materials, based on a multisublattice model whose Hamiltonian includes not only the anisotropy energy but also anisotropic and antisymmetric exchange interaction energies, as proposed in Refs. 19 and 20.

*)E-mail: ptica.rff@elefot.tsu.ru

[1] E. Schlömann, J. Phys. Radium **20**, 327 (1959).
[2] E. Schlömann and R. V. Jones, J. Appl. Phys. **30**, 177 (1959).
[3] E. Schlömann, J. Phys. Chem. Solids **6**, 257 (1958).
[4] A. G. Gurevich, *Magnetic Resonance in Ferrites and Antiferromagnets* [in Russian] (Nauka, Moscow, 1973).
[5] E. P. Naĭden, G. I. Ryabtsev, V. A. Zhuravlev, and V. I. Goleshchikhin, Fiz. Tverd. Tela (Leningrad) **27**, 3155 (1985) [Sov. Phys. Solid State **27**, 1899 (1985)].
[6] V. S. Korogodov, V. A. Zhuravlev, and V. I. Goleshchikhin, Izv. Vyssh. Uchebn. Zaved. Fiz. **5**, 118 (1987).
[7] M. M. Brezgunov and A. E. Petrov, Bull. Acad. Sci. Latvian SSR, Ser. Phys. and Engn. Sci. **3**, 57 (1980).
[8] I. Onyszkievicz and J. Pietrzak, Phys. Status Solidi A **73**, 641 (1982).
[9] L. M. Silber, C. E. Patton, and H. F. Nagvi, J. Appl. Phys. **54**, 4071 (1983).
[10] E. I. Rayess, J. B. Sokoloff, C. Vittoria, and W. Spurgeon, J. Appl. Phys. **67**, 5527 (1990).
[11] E. A. Turov, *Physical Properties of Magnetically Ordered Crystals* (Academic, New York, 1965) [Russian original; Acad. Sci. USSR Publ., Moscow, 1963].
[12] L. B. Vlasov and B. Kh. Ishmukhametov, Fiz. Met. Metalloved. **11**, 3 (1961).
[13] A. G. Gurevich, V. A. Sanina, E. I. Golovenchits, and S. S. Starobinets, J. Appl. Phys. **40**, 1512 (1969).
[14] A. I. Mitsek, N. P. Kolmakova, and D. I. Sirota, Fiz. Met. Metalloved. **41**, 3, 464 (1976).
[15] V. A. Zhuravlev, V. S. Korogodov, and V. I. Goleshchikhin, Izv. Vyssh. Uchebn. Zaved. Fiz. **2**, 58 (1984).
[16] A. Paoluzi, F. Licci, O. Moze, G. Turilli, A. Deriu, G. Albanese, and E. Calabrese, J. Appl. Phys. **63**, 5074 (1988).
[17] E. P. Naiden, V. I. Maltsev, and G. I. Ryabtsev, Phys. Status Solidi A **120**, 209 (1990).
[18] V. A. Zhuravlev, V. I. Suslyaev, E. P. Naĭden, and V. I. Kirichenko, Izv. Vyssh. Uchebn. Zaved. Fiz. **9**, 107 (1990).
[19] M. Acquarone, J. Phys. C **12**, 1373 (1979).
[20] M. Acquarone, Phys. Rev. B **24**, 3847 (1981).

Translated by Frank J. Crowne

Spin fluctuations and properties of the thermoelectric power of nearly ferromagnetic iron monosilicide

A. G. Volkov, A. A. Povzner, V. V. Kryuk, and P. V. Bayankin

Ural State Technical University, 620002 Yekaterinburg, Russia
(Submitted August 20, 1998)
Fiz. Tverd. Tela (St. Petersburg) **41**, 1054–1056 (June 1999)

The thermoelectric power of nearly ferromagnetic iron monosilicide, which passes through an electronic semiconductor–metal transition with increasing temperature, is investigated theoretically. The results of this investigation indicate that a sizable paramagnon-related increase in charge carriers can occur in nearly ferromagnetic semiconductors, and that spin fluctuations can modify the electronic spectrum and thereby renormalize the diffusion component of the thermoelectric power. The transition from semiconductor to metal decreases the paramagnon component sharply and the thermoelectric power changes sign, which agrees with experimental data for iron monosilicide.
[S1063-7834(99)02706-9]

1. Iron monosilicide (FeSi) is typical of a class of nearly ferromagnetic semiconductors that undergo a semiconductor–metal transition with increasing temperature. This transition is accompanied by disappearance of the energy gap in the itinerant d-electron spectrum between the ''valence'' and ''conduction'' bands.[1,2] It also causes a sharp increase in the magnetic susceptibility $\chi(T)$,[3] and, as experiments on inelastic neutron scattering[4] show, a considerable increase in the amplitude of spin fluctuations in the d-electron system. According to spin-fluctuation theory, in nearly ferromagnetic materials the d-electron energies are spin-split in the fluctuating exchange fields ξ, leading to renormalization of their density of states[5,6]

$$g(\varepsilon,\xi)=\sum g(\varepsilon+\sigma'\xi)/2. \tag{1}$$

In almost ferromagnetic semiconductors this process also changes the width of the energy gap between the valence d-band and the conduction d-band:

$$E_g(\xi)=E_g(0)-2\xi, \tag{2}$$

which eventually disappears due to the monotonic increase in $\xi(T)$.

Here $\sigma'=\pm 1$ is the spin quantum number corresponding to axes of quantization connected with the spatial and temporal fluctuations of the ξ fields, $g(\varepsilon)$ is the density of states of noninteracting d-electrons, $\xi=Q\sqrt{\langle m^2\rangle}$, $\langle m^2\rangle^{1/2}$ is the amplitude of spin fluctuations, Q is the parameter for intra-atomic Coulomb interactions, and $E_g(0)$ is the width of the forbidden band in the spectrum of noninteracting d electrons.

The hypothesis that spin-fluctuation-induced renormalization of the d-electron spectrum occurs in FeSi is indirectly confirmed when the results of calculations are compared with experimental data not only for the magnetic susceptibility[5] but also for the heat capacity,[7] the temperature coefficient of thermal broadening,[8,9] and the electrical conductivity.[10] This latter data reveals the dynamic nature of the spin fluctuations, along with the existence of a characteristic time $\tau_{sf}\sim 10^{-12}-10^{-13}s$,[11] and also the fact that the d electrons are the majority carriers of electric current.[10] However, the question of how these dynamic spin fluctuations affect the thermoelectric power of nearly ferromagnetic FeSi, which should be most sensitive not only to spin fluctuation excitations but also to features of the transformation of the electronic spectrum, has remained unaddressed up to now.

2. In this paper we will discuss how spin fluctuations affect the temperature dependence of the thermoelectric power in almost ferromagnetic semiconductors (among them iron monosilicide) using the theory developed in Refs. 5, 6, and 8–10. In calculating the diffusion component of the thermoelectric power of d electrons we will use the well-known relation from Ref. 12, while incorporating the spin-fluctuation-induced renormalization of the electron spectrum and the density of d-states (see Eqs. (1) and (2)):

$$S_d(T)=I_1(\xi)/eTI_0(\xi), \tag{3}$$

where the kinetic integrals are

$$I_n(\xi)=\int_{-\infty}^{\infty}\varphi(\varepsilon,\xi)(\varepsilon-\mu)^n\left(-\frac{\partial f_F(\varepsilon,\mu)}{\partial\varepsilon}\right)d\varepsilon, \tag{4}$$

$$\varphi(\varepsilon,\xi)=k^2(\varepsilon,\xi)\tau\frac{d\varepsilon}{dk}, \tag{5}$$

e is the electron charge, $f(\varepsilon,\mu)$ is the Fermi–Dirac function, the electronic quasimomentum $k(\varepsilon,\xi)$ is defined via the function $g(\varepsilon,\xi)$ in the effective-mass approximation, and the relaxation time

$$\tau=Ck^{2r-1}\frac{d\varepsilon}{dk}$$

for $r=3/2$ corresponds to scattering by phonons.

The function $g(\varepsilon,\xi)$ is modeled with the help of Eq. (1) in conformity with the results of band calculations and the expressions for the spin-fluctuation amplitudes given in Refs. 6, 7, and 9:

$$\xi^2=Q^2m^2=Q\sum_q \int_0^\infty f_B(\omega/T)\,\mathrm{Im}(D^{-1}(\xi)+X(q,\omega))d\omega$$
$$\approx Q^2B^2D(\xi)(D^{-1}(\xi)+a)^{-1}. \quad (6)$$

Here

$$D(\xi)=(1-2Qn_{ef}(\xi)/3\xi-Q\tilde{g}(\mu)/3)^{-1} \quad (7)$$

is the exchange enhancement factor of the magnetic susceptibility,[6,7]

$$\tilde{g}(\mu)=\frac{\Pi_{\sigma'=\pm1}g(\mu+\sigma'\xi)}{g(\mu,\xi)},$$

$$n_{ef}(\xi)=\frac{1}{2}\sum_{\sigma'}\sigma'\int_0^\infty f_F(\varepsilon,\mu)g(\varepsilon+\sigma'\xi)d\varepsilon \quad (8)$$

is the effective number of magnetic carriers,

$$X(q,\omega)=Q(\chi^0(0,0)-\chi^0(\mathbf{q},\omega))=aq^2-iB\omega/(qQ).$$

Here $\mathbf{q}$ is the quasimomentum vector in units of the magnitude of the Brillouin vector, ω is the fluctuation frequency, and $\chi^0(q,\omega)$ is the Pauli susceptibility. The coefficients a and B, which specify the dependence of the susceptibility on frequency and quasimomentum, are determined either from band calculations or from the results of magnetic neutron scattering.[4,11] For FeSi, according to Refs. 1, 7, and 9, we have $a=0$, $B=6$, and $Q=0.8$ eV.

Moreover, according to spin-fluctuation theory, the effect of paramagnon drag, which is analogous to phonon drag, should contribute to the temperature dependence of the thermoelectric power.[12] In order to estimate this contribution, let us calculate the electron pressure caused by interaction of electrons with paramagnons,

$$P_{pm}=\frac{\partial F_{pm}}{\partial V}, \quad (9)$$

where V is the volume, and the paramagnon portion of the free energy is given according to Refs. 6, 7, and 9 by the expression

$$F_{pm}=\sum_{\mathbf{q}}\int_0^\infty f_B(\omega/T)\,\mathrm{Im}\frac{X(q,\omega)}{D^{-1}(\xi)+X(\mathbf{q},\omega)}d\omega. \quad (10)$$

Then, assuming that the force caused by this pressure equals the force arising from the Coulomb interaction of the electrons due to their redistribution over the length of the conductor (under steady-state conditions), we find the following approximate expression for the paramagnon contribution to the thermoelectric power:

$$S_{pm}(T)=\frac{1}{en}\frac{\partial^2F_{pm}}{\partial V\partial T}=\frac{1}{en}\frac{\partial P}{\partial V}\alpha_{pm}, \quad (11)$$

where n is the carrier concentration, which satisfies the relation $n=2n_{ef}$ in the semiconducting phase, α_{pm} is the paramagnon component of the thermal broadening coefficient, P is the pressure, and V is the volume. A similar relation is obtained by using a crude approximation for the contribution to the thermoelectric power from phonon drag as well. Taking into account Eqs. (6)–(8) and (10), we can rewrite Eq. (11) in a form convenient for calculations as follows:

$$S_{pm}(T)=\frac{5Q^2}{3en}\left[\frac{1}{3}Q(4g(\mu,\xi)-n_{ef}/\xi)\right.$$
$$\left.-D^{-1}(\xi)\right]\frac{d\langle m^2\rangle}{dT}. \quad (12)$$

3. In order to compare these expressions for the thermoelectric power with experiment, let us use the results of calculations of the d-electron density of states of FeSi taken from Ref. 1, along with estimates of the spin-fluctuation amplitudes from Refs. 7 and 9. Then, using the function $g(\varepsilon,\xi)$, we calculate the functions $\mu(\xi)$ (from the condition of electrical neutrality) and $k(\varepsilon,\xi)$ (in the effective-mass approximation). Using Eqs. (3)–(5), we then can determine the diffusion component to the thermoelectric power of FeSi. In this case we find that that the diffusion component of the thermoelectric power gives a satisfactory description of the experimental data in the metallic region, but that it becomes much smaller than the observed values of $S(T)$ in the semiconducting phase ($T<T_g\approx100$ K). The latter fact indicates a need to include mechanisms for the drag of electrons by phonons or paramagnons.

At this time it is not possible to estimate the effects of phonon drag in FeSi, due to a lack of information about the phonon spectrum and magnitude of the electron–phonon interaction. On the other hand, the value of the temperature that maximizes the phonon drag in the semiconducting phase, obtained by taking into account the temperature dependence of the concentration n and the phonon and paramagnon contributions to the coefficient α (which, in conformity with the Grüneisen relation, is proportional to the corresponding contributions to the heat capacity), is three times larger than that of the paramagnon contributions.[(1)] In the metal phase, the temperature at which the thermoelectric power connected with phonon drag is a maximum, according to Ref. 12, is estimated to be $0.15\Theta_D$ (for FeSi, $\Theta_D\approx560$ K, see Ref. 13), which does not correspond to temperatures at which FeSi is gapless.[10] At the same time, the temperature at which the contribution to $S(T)$ from paramagnon drag is a maximum (50 K) is close to the experimentally observed value (see Fig. 1). In this case it is worth noting that the abrupt increase in concentration of mobile charge carriers n as the energy gap collapses (see Eq. (1)) can suppress contributions from the drag mechanisms, which according to Ref. 12 and Eq. (12) are inversely proportional to n. Figure 1 shows calculated results for the temperature dependence of the thermoelectric power of FeSi, along with experimental data for a polycrystalline sample (from Ref. 14). Comparison of theory with experimental data shows that below T_g the diffusion component is negligibly small and $S(T)\approx S_{pm}(T)$. In the gapless temperature range the contribution of the negative diffusion component is abruptly enhanced, so that the equation $S(T)=S_d(T)+S_{pm}(T)$ was used in the calculations. In addition, dynamic spin fluctua-

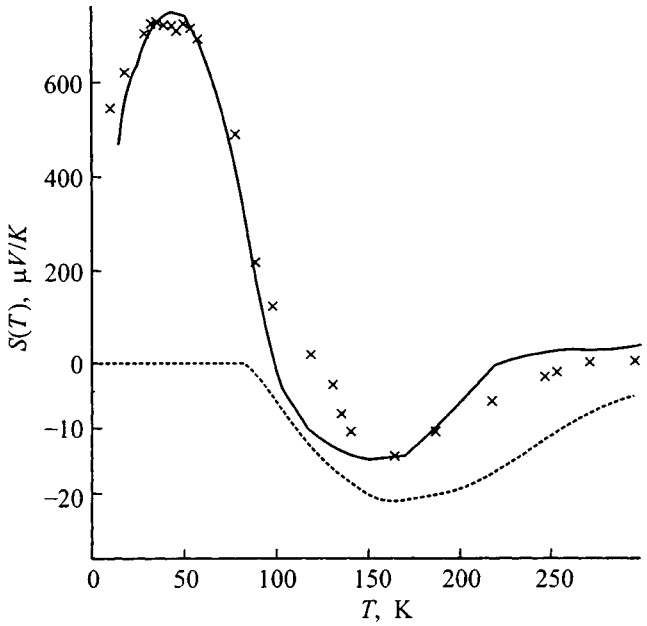

FIG. 1. Temperature dependence of the thermoelectric power of iron monosilicide: points—results of experiments in Ref. 14, solid curve—calculated results for the total thermoelectric power, which for $T<T_g$ coincides approximately with the paramagnetic component. The dots show the temperature dependence of the diffusion component of the thermoelectric power.

tions decisively influence the function $S(T)$ by renormalizing the electronic spectrum. In fact, calculations based on Eqs. (2) and (12) in the static limit ($\omega \ll T$) predict a change in the sign of the function $S(T)$ at $T \approx 300$ K and a maximum value for the thermoelectric power of FeSi equal to 230 μV/K at 253 K, which does not agree with Ref. 14. At the same time calculations based on Eqs. (3), (12), and (13) (within the framework of dynamic spin-fluctuation theory) give a maximum of $S(T)$ near 50 K of roughly 750 μV/K (see Fig. 1). In this case, as we pass through the temperature range where the energy gap disappears and the number of mobile charge carriers increases abruptly, the paramagnon contribution becomes first comparable to and then considerably smaller than $S_d(T)$.

In conclusion, it should be noted that small deviations from the stoichiometric composition of FeSi give rise to a sizable change in the magnitude of the thermoelectric power.[14] In Ref. 15, Jarlborg attempted to analyze these features in terms of spin fluctuations in the static approximation. Although he discussed only $Fe_{1-x}Si_{1+x}$ alloys with $x \ll 1$, he found a considerable disagreement between the results of his calculations and values of the thermoelectric power observed in experiment, especially in the temperature range above 100 K. In this paper we do not discuss these alloys, since we feel that they could actually be two-phase systems, i.e., FeSi–$FeSi_2$ (Ref. 16).

Thus, our analysis of the thermoelectric power of FeSi shows that dynamic spin fluctuations can have a significant effect on the form of the function $S(T)$ in nearly ferromagnetic semiconductors, by subjecting the current carriers to paramagnon drag and splitting the electronic terms. The mechanisms for paramagnon drag and spin fluctuation renormalization of the diffusion component of $S(T)$ are important not only for nearly ferromagnetic systems, but also for transition metals in general and those of their compounds that exhibit itinerant ferromagnetism.

This work was partially supported by a grant from the Competitive Center for Basic Science of the Ministry of General and Professional Education of the Russian Federation (Project 95-0-7.2-165).

[1)]This is because at low temperatures the phonon heat capacity is proportional to T^3, the paramagnon heat capacity to T.

[1] L. I. Vinokurova, A. V. Vlasov, and E. T. Kulatov, Proc. IOFAN **32**, 26 (1992).
[2] Z. Schlesinger, Z. Fisk, and Y. T. Zyang, Phys. Rev. Lett. **71**, 1748 (1993).
[3] V. Jaccarino, G. K. Werthein, and J. H. Wernic, Phys. Rev. **160**, 476 (1963).
[4] K. Tajima, Y. Endox, J. W. Fisher, and G. Shirane, Phys. Rev. **38**, 6954 (1988).
[5] A. A. Povzner, A. G. Volkov, and P. V. Bayankin, Fiz. Tverd. Tela (St. Petersburg) **40**, 1437 (1998) [Phys. Solid State **40**, 1305 (1998)].
[6] A. A. Povzner, Fiz. Tverd. Tela (St. Petersburg) **35**, 3159 (1993) [Phys. Solid State **35**, 1557 (1993)].
[7] P. V. Gel'd, A. A. Povzner, and A. G. Volkov, Dok. Akad. Nauk (SSSR) **283**, 358 (1984) [Sov. Phys. Dokl. **30**, 585 (1984)].
[8] P. V. Gel'd, A. A. Povzner, S. V. Kortov, and R. P. Kretsis, Dok. Akad. Nauk (SSSR) **297**, 1359 (1987) [Sov. Phys. Dokl. **32**, 1006 (1987)].
[9] A. G. Volkov, S. V. Kortov, and A. A. Povzner, Fiz. Nizk. Temp. **22**, 1144 (1996) [Low Temp. Phys. **22**, 875 (1996)].
[10] P. V. Gel'd, A. A. Povzner, Sh. Sh. Abel'skiĭ, and L. F. Romasheva, Dokl. Akad. Nauk (SSSR) **313**, 1107 (1990) [Sov. Phys. Dokl. **35**, 758 (1990)].
[11] T. Moriya, *Spin Fluctuations in Itinerant-Electron Magnetism* (Springer-Verlag, Berlin, New York, 1985; Mir, Moscow, 1988).
[12] F. J. Blatt, *Physics of Electronic Conduction in Solids* (McGraw-Hill, New York, 1968; Mir, Moscow, 1971).
[13] A. S. Ivanov, N. L. Mitrofanov, and A. Yu. Rumyantsev, Problems in Atomic Science and Engineering **2**, 79 (1989).
[14] B. Buschinger, C. Geilbel, F. Steglich, D. Mandrus, D. Young, J. L. Sarrao, and Z. Fisk, Physica B **230-232**, 784 (1997).
[15] T. Jarlborg, Phys. Rev. B **51**, 11 106 (1995).
[16] I. N. Sachkov and A. A. Povzner, Fiz. Tverd. Tela (St. Petersburg) **38**, 2969 (1996) [Phys. Solid State **38**, 1623 (1996)].

Translated by Frank J. Crowne

Electron spectrum and stability of the saturated ferromagnetic state in a Hubbard model with strong correlations

A. V. Zarubin and V. Yu. Irkhin*)

Institute of Metal Physics, Ural Branch of the Russian Academy of Sciences, 620219 Ekaterinburg, Russia
(Submitted August 31, 1998)
Fiz. Tverd. Tela (St. Petersburg) **41**, 1057–1063 (June 1999)

A Hubbard model with infinite Coulomb repulsion is studied in a many-electron operator representation. A picture of the density of states is constructed using expressions for the one-particle Green's functions of first order in $1/z$. Its behavior is studied near the Fermi level, especially Condon effects. The stability of saturated ferromagnetism is examined. The corresponding critical current carrier densities are found for semielliptical and rectangular seed densities of state, and for square and cubic lattices. These results are compared with earlier work. © *1999 American Institute of Physics.* [S1063-7834(99)02806-3]

Despite the large number of publications on the topic, the magnetism of narrow-band electronic systems described by the Hubbard model[1] remains at the center of attention.[2–12] Physically, in this case the picture of magnetism is characterized by the existence of local magnetic moments and differs substantially from the Stoner picture of a weak collectivized magnetism.[13]

According to Nagaoka,[14] in the limit of infinite Hubbard repulsion the ground state for simple lattices is a saturated ferromagnetic state for a low density δ of current carriers (pairs or holes in an almost half-filled band).

Roth[15] used a variational approximation for the electron Green's functions to obtain two critical concentrations. The first (δ_c) corresponds to a transition from a saturated ferromagnetic state into an unsaturated state, and the second (δ_c'), to a transition from a ferromagnetic state into a paramagnetic state. For a simple cubic lattice, they were found to equal $\delta_c = 0.37$ and $\delta_c' = 0.64$.

Next, the region of stability of the ferromagnetic state was studied by various methods in a large number of papers.[16–30] In particular, an improved Gutzwiller method[27] gives $\delta_c = 0.33$ for simple cubic lattices, and an expansion in t/U[23] gives $\delta_c = 0.27$. In the case of a square lattice, a variational method has been used[9] to obtain $\delta_c = 0.251$, while a renormalization group method for the density matrix[10] yielded $\delta_c = 0.22$ and a crude estimate of $\delta_c' \approx 0.40$.

Therefore, in a majority of the calculations the critical concentration δ_c is near 0.30 for a wide variety of lattices. (In Ref. 22, however, a value of 0.045 was obtained for a simple cubic lattice; the similar method of Ioffe and Larkin[25] gives much larger values of δ_c for a square lattice, $\delta_c = 0.25$.)

An interpolation scheme for describing magnetic ordering in narrow bands, which yields saturation ferromagnetism in the case of low current carrier densities and an unsaturated peak for high concentrations, has been proposed[31,32] on the basis of an analysis of the dynamic magnetic susceptibility. However, the critical concentrations themselves were not determined.

The use of high-temperature expansions in the early papers gave vague results regarding the stability of ferromagnetism in the model because of poor accuracy.[19] However, according to the latest results,[6,7] ferromagnetism also develops near $\delta = 0.3$.

Note that a hole concentration $\delta = 1/3$ for a symmetric seed density of states corresponds to a change in sign of the chemical potential (relative to the center of the band) in the ''Hubbard-I'' approximation,[1] and an instability of the paramagnetic state develops at this point.[3]

Experimental data on $Fe_{1-x}Co_xS_2$,[16] a system with strong correlations, give large values of δ_c (saturation ferromagnetism is preserved up to conduction electron concentrations $n = 1 - \delta$ of order 0.2), but degeneracy effects in the conduction band appear to be important in this system.

The approaches that have been considered do not, as a rule, analyze the structure of the one-particle spectrum and density of states in the ferromagnetic phase of the Hubbard model. The simplest approach for the electronic spectrum, ''Hubbard-I,'' proposed in Hubbard's first paper,[1] corresponds to zeroth order in the reciprocal coordination number $1/z$ (average field approximation for electron transport). It is completely unsatisfactory for describing ferromagnetism. (In particular, there are no ferromagnetic solutions at all for simple models of the seed density of states.)

A rigorous calculation of the one-particle Green's functions for a low carrier density (the Nagaoka limit) has been carried out.[33,34] There it was shown that the incoherent (nonquasiparticle) contribution is important for the picture of the density of states, but it is of fundamental importance if the kinematic relations are to be satisfied. (See Section 1.) Expressions for the Green's functions have been obtained which are valid over a wide range of temperatures.[35]

In this paper, the stability of the saturated ferromagnetic state as the current carrier concentration is raised is studied using one-particle Green's functions of first order in $1/z$. This approach makes it possible to construct a rather simple and physically clear picture of the density of states in a saturated Hubbard ferromagnet.

1. CALCULATING THE GREEN'S FUNCTIONS AND THE SELF CONSISTENCY EQUATION

We shall use the Hamiltonian for the Hubbard model in the limit of infinitely strong Coulomb repulsion in the many-electron X-operator representation,[36]

$$\mathcal{H}=\sum_{\mathbf{k},\sigma} t_{\mathbf{k}} X_{-\mathbf{k}}^{0\sigma} X_{\mathbf{k}}^{\sigma 0}, \tag{1}$$

where $t_{\mathbf{k}}$ is the band energy, $X_{\mathbf{k}}^{\alpha\beta}$ is the Fourier transform of the Hubbard operators $X_i^{\alpha\beta}=|i\alpha\rangle\langle i\beta|$ (0 denotes holes and $\sigma=\pm(\uparrow,\downarrow)$ denotes singly occupied states).

It should be noted that in this problem of an infinitely strong Coulomb interaction, a number of difficulties arise in connection with the non-Fermi excitation statistics. These difficulties show both in the diagram technique[2] and in the equations-of-motion method.[37] In particular, it has been found[37] that in an expansion with respect to $1/z$, the analytic properties of the retarded Green's functions were violated for the paramagnetic state.

We shall consider the retarding anticommutator Green's functions

$$G_{\mathbf{k},\sigma}(E)=\langle\langle X_{\mathbf{k}}^{\sigma 0}|X_{-\mathbf{k}}^{0\sigma}\rangle\rangle_E, \quad \mathrm{Im}\,E>0. \tag{2}$$

Splitting the chain of equations of motion in the lowest approximation, which corresponds to the zeroth order in $1/z$ and is known as the ''Hubbard-I'' approximation, gives

$$\langle\langle X_{\mathbf{k}}^{\sigma 0}|X_{-\mathbf{k}}^{0\sigma}\rangle\rangle_E=(n_0+n_\sigma)(E-t_{\mathbf{k},\sigma})^{-1}, \tag{3}$$

$$n_\alpha=\langle X_i^{\alpha\alpha}\rangle, \quad t_{\mathbf{k},\sigma}=t_{\mathbf{k}}(n_0+n_\sigma).$$

As opposed to the approach employing one-electron operators,[1] the many-electron Hubbard operator formalism help clarify why the ''Hubbard-I'' approach is unsuitable for describing ferromagnetism. In fact, the Green's functions (3) strongly violate the kinematic relations at a single site and cannot satisfy the condition

$$\begin{aligned}\delta\equiv n_0=\langle X^{00}\rangle&=\langle X_i^{0\sigma}X_i^{\sigma 0}\rangle\\ &=\sum_{\mathbf{k}}\langle X_{\mathbf{k}}^{0\sigma}X_{-\mathbf{k}}^{\sigma 0}\rangle\\ &=-\frac{1}{\pi}\sum_{\mathbf{k}}\int \mathrm{Im}\,G_{\mathbf{k},\sigma}(E)f(E)dE,\end{aligned} \tag{4}$$

which follows from the spectral representation ($f(E)$ is the Fermi function), for both projections of the spin in the case $\langle S^z\rangle\neq 0$. At the same time, the quasiparticle pole for $\sigma=\downarrow$ corresponding to a narrowed band and lying above the Fermi level of the holes, does not provide an adequate description of the energy spectrum and leads to the appearance of finite $n_\downarrow$, i.e., the saturation ferromagnetism breaks down.

Following Ref. 35, we perform the splitting in the next stage. We write the equation of motion in the form

$$\begin{aligned}&(E-t_{\mathbf{k},\sigma})G_{\mathbf{k},\sigma}(E)\\ &\quad=n_0+n_\sigma+\sum_{\mathbf{q}} t_{\mathbf{k}-\mathbf{q}}\langle\langle X_{\mathbf{q}}^{\sigma-\sigma}X_{\mathbf{k}-\mathbf{q}}^{-\sigma 0}|X_{-\mathbf{k}}^{0\sigma}\rangle\rangle_E,\end{aligned} \tag{5}$$

where we have neglected longitudinal spin fluctuations. The equation of motion for the Green's function $\langle\langle X_{\mathbf{q}}^{\sigma-\sigma}X_{\mathbf{k}-\mathbf{q}}^{-\sigma 0}|X_{-\mathbf{k}}^{0\sigma}\rangle\rangle_E$ has the form

$$\begin{aligned}&E\langle\langle X_{\mathbf{q}}^{\sigma-\sigma}X_{\mathbf{k}-\mathbf{q}}^{-\sigma 0}|X_{-\mathbf{k}}^{0\sigma}\rangle\rangle_E\\ &\quad=\langle X_{\mathbf{q}}^{\sigma-\sigma}X_{-\mathbf{q}}^{-\sigma\sigma}\rangle+\langle X_{\mathbf{q}-\mathbf{k}}^{0-\sigma}+X_{\mathbf{k}-\mathbf{q}}^{-\sigma 0}\rangle\\ &\quad+\sum_{\mathbf{p}} t_{\mathbf{p}}\langle\langle X_{\mathbf{q}}^{\sigma-\sigma}X_{\mathbf{k}-\mathbf{q}-\mathbf{p}}^{-\sigma\sigma}X_{\mathbf{p}}^{\sigma 0}+X_{\mathbf{q}}^{\sigma-\sigma}X_{\mathbf{k}-\mathbf{q}-\mathbf{p}}^{-\sigma-\sigma}X_{\mathbf{p}}^{-\sigma 0}\\ &\quad+X_{\mathbf{q}}^{\sigma-\sigma}X_{\mathbf{k}-\mathbf{q}-\mathbf{p}}^{00}X_{\mathbf{p}}^{-\sigma 0}-X_{\mathbf{q}-\mathbf{p}}^{0-\sigma}X_{\mathbf{p}}^{\sigma 0}X_{\mathbf{k}-\mathbf{q}}^{-\sigma 0}\\ &\quad+X_{-\mathbf{p}}^{0-\sigma}X_{\mathbf{q}+\mathbf{p}}^{\sigma 0}X_{\mathbf{k}-\mathbf{q}}^{-\sigma 0}|X_{-\mathbf{k}}^{0\sigma}\rangle\rangle_E.\end{aligned} \tag{6}$$

Splitting the Green's functions on the right of Eq. (6) and introducing the notation

$$\langle X_{\mathbf{q}}^{\sigma-\sigma}X_{-\mathbf{q}}^{-\sigma\sigma}\rangle=\langle S_{\mathbf{q}}^{\sigma}S_{-\mathbf{q}}^{-\sigma}\rangle=\chi_{\mathbf{q},\sigma}, \quad \langle X_{-\mathbf{k}}^{0\sigma}X_{\mathbf{k}}^{\sigma 0}\rangle=n_{\mathbf{k},\sigma},$$

we find

$$\begin{aligned}G_{\mathbf{k},\sigma}(E)=&\left(n_\sigma+n_0+\sum_{\mathbf{q}} t_{\mathbf{k}-\mathbf{q}}\frac{\chi_{\mathbf{q},\sigma}+n_{\mathbf{k}-\mathbf{q},-\sigma}}{E-t_{\mathbf{k}-\mathbf{q},-\sigma}-\sigma\omega_{\mathbf{q}}}\right)\\ &\times\left(E-t_{\mathbf{k},\sigma}-\sum_{\mathbf{q}} t_{\mathbf{k}-\mathbf{q}}\frac{t_{\mathbf{k}}\chi_{\mathbf{q},\sigma}-t_{\mathbf{k}-\mathbf{q}}-t_{\mathbf{k}}n_{\mathbf{k}-\mathbf{q},-\sigma}}{E-t_{\mathbf{k}-\mathbf{q},-\sigma}-\sigma\omega_{\mathbf{q}}}\right)^{-1}.\end{aligned} \tag{7}$$

In the leading approximation in $1/z$ for the one-particle occupation numbers, it is necessary to use the ''Hubbard-I'' approximation, i.e.,

$$n_{\mathbf{k},\sigma}=(n_0+n_\sigma)f(t_{\mathbf{k},\sigma}),$$

but the chemical potential must already be chosen from the Green's function (7). As opposed to Eq. (3), the Green's functions (7) contain terms with resolvents and have cuts which describe non-quasiparticle (incoherent) contributions to the density of states. It is the latter which ensure qualitative agreement with the sum rule (4) for $\sigma=\downarrow$. At the same time, there are no poles of the Green's function for this projection of the spin for small δ above the Fermi level, i.e., the saturated ferromagnetic state is preserved.

Note that, as opposed to the one-electron approach,[18] the Green's function $G_{\mathbf{k},\uparrow}(E)$ does not reduce to the free electron Green's function, even in the saturated ferromagnetic state, since fluctuations in the hole occupation number contribute to it.

The result (7) can be represented as

$$G_{\mathbf{k},\sigma}(E)=\frac{a_{\mathbf{k},\sigma}(E)}{b_{\mathbf{k},\sigma}(E)-a_{\mathbf{k},\sigma}(E)t_{\mathbf{k}}}, \tag{8}$$

with

$$a_{\mathbf{k},\sigma}(E)=\sum_{\mathbf{q}} t_{\mathbf{k}-\mathbf{q}}\frac{\chi_{\mathbf{q},\sigma}+n_{\mathbf{k}-\mathbf{q},-\sigma}}{E-t_{\mathbf{k}-\mathbf{q},-\sigma}-\sigma\omega_{\mathbf{q}}}, \tag{9}$$

and

$$b_{\mathbf{k},\sigma}(E)=E-\sum_{\mathbf{q}} t_{\mathbf{k}-\mathbf{q}}^2\frac{n_{\mathbf{k}-\mathbf{q},-\sigma}}{E-t_{\mathbf{k}-\mathbf{q},-\sigma}-\sigma\omega_{\mathbf{q}}}. \tag{10}$$

In the case of a saturated ferromagnetic state, the Green's function (7) takes the form

$$G_{\mathbf{k},\uparrow}(E)=\left(E\Big/\left[1+\sum_{\mathbf{q}}\frac{t_{\mathbf{q}}(1-n_0)}{E-t_{\mathbf{q}}n_0}\right]-t_{\mathbf{k}}\right)^{-1}, \tag{11}$$

$$G_{\mathbf{k},\downarrow}(E)=E\sum_{\mathbf{q}}\frac{n_{\mathbf{k}-\mathbf{q}}}{E-t_{\mathbf{k}-\mathbf{q}}+\omega_{\mathbf{q}}}\left(E\left[1-n_0+\sum_{\mathbf{q}}\frac{(E-t_{\mathbf{k}})n_{\mathbf{k}-\mathbf{q}}}{E-t_{\mathbf{k}-\mathbf{q}}+\omega_{\mathbf{q}}}\right]-\sum_{\mathbf{q}}t_{\mathbf{k}-\mathbf{q}}n_{\mathbf{k}-\mathbf{q}}\right)^{-1}, \tag{12}$$

where $n_{\mathbf{k}}=f(t_{\mathbf{k}})$. Neglecting the resolvent in Eq. (11) and the last term in the denominator of Eq. (12), we obtain

$$G_{\mathbf{k},\uparrow}(E)=\frac{1}{E-t_{\mathbf{k}}},\quad G_{\mathbf{k},\downarrow}(E)=\frac{1}{E-t_{\mathbf{k}}-\Sigma_{\mathbf{k},\downarrow}(E)},$$

$$\Sigma_{\mathbf{k},\downarrow}(E)=-(1-n_0)\left(\sum_{\mathbf{q}}\frac{n_{\mathbf{k}-\mathbf{q}}}{E-t_{\mathbf{k}-\mathbf{q}}+\omega_{\mathbf{q}}}\right)^{-1}, \tag{13}$$

which agrees with Refs. 18 and 38 in the limit $U\to\infty$.

It is possible to go to the self-consistent approximation[37] from Eq. (8). To do this, the denominator in Eqs. (9) and (10) must be replaced by the exact Green's functions, i.e.,

$$G_{\mathbf{k},\sigma}(E)=\frac{A_{\mathbf{k},\sigma}(E)}{B_{\mathbf{k},\sigma}(E)-A_{\mathbf{k},\sigma}(E)t_{\mathbf{k}}}, \tag{14}$$

where

$$A_{\mathbf{k},\sigma}(E)=\sum_{\mathbf{q}}t_{\mathbf{k}-\mathbf{q}}\frac{\chi_{\mathbf{q},\sigma}+n_{\mathbf{k}-\mathbf{q},-\sigma}}{B_{\mathbf{k}-\mathbf{q},-\sigma}(E)-A_{\mathbf{k}-\mathbf{q},-\sigma}(E)t_{\mathbf{k}-\mathbf{q}}-\sigma\omega_{\mathbf{q}}}, \tag{15}$$

and

$$B_{\mathbf{k},\sigma}(E)=E-\sum_{\mathbf{q}}t_{\mathbf{k}-\mathbf{q}}^2\times\frac{n_{\mathbf{k}-\mathbf{q},-\sigma}}{B_{\mathbf{k}-\mathbf{q},-\sigma}(E)-A_{\mathbf{k}-\mathbf{q},-\sigma}(E)t_{\mathbf{k}-\mathbf{q}}-\sigma\omega_{\mathbf{q}}}. \tag{16}$$

In the case of the self-consistent approximation, it is also necessary to express the one-particle occupation numbers in terms of the exact Green's function,

$$n_{\mathbf{k},\sigma}=\langle X_{-\mathbf{k}}^{0\sigma}X_{\mathbf{k}}^{\sigma 0}\rangle=-\frac{1}{\pi}\mathrm{Im}\int G_{\mathbf{k},\sigma}(E)f(E)dE.$$

For the density of states, we have an expression in terms of the exact resolvent,

$$N_{\sigma}(E)=-\frac{1}{\pi}\mathrm{Im}\sum_{\mathbf{k},\sigma}G_{\mathbf{k},\sigma}(E)=-\frac{1}{\pi}\mathrm{Im}\,R_{\sigma}(E),$$

with

$$R_{\sigma}(E)=R_0\{B_{\mathbf{k},\sigma}(E)/A_{\mathbf{k},\sigma}(E)\},\quad R_0(E)=\sum_{\mathbf{k}}\frac{1}{E-t_{\mathbf{k}}}.$$

2. NUMERICAL CALCULATIONS AND DISCUSSION

In the case of saturated ferromagnetism, we have

$$\chi_{\mathbf{q},\sigma}\to\chi_{\sigma},\quad \chi_{+}=1-\delta,\quad \chi_{-}=0.$$

For simplified numerical calculations, we use the transformation

$$\sum_{\mathbf{q}}\mathcal{F}(\omega_{\mathbf{q}})=\sum_{\mathbf{q}}\int K_{\mathbf{q}}(\omega)\mathcal{F}(\omega)d\omega,$$

where $K_{\mathbf{q}}(\omega)=\delta(\omega-\omega_{\mathbf{q}})$ is the spin spectral density, which replaces the last expression by the average over the Brillouin zone,

$$K_{\mathbf{q}}(\omega)\to\overline{K}(\omega)=\sum_{\mathbf{q}}K_{\mathbf{q}}(\omega)=\sum_{\mathbf{q}}\delta(\omega-\omega_{\mathbf{q}}).$$

This approximation allows us to correctly describe the energy dependence of the density of states near the Fermi level[18] and can be justified in the limit of high spatial dimensionalities. As a result, the quantities (9) and (10) in the Green's function (8) are independent of the wave vector, with

$$G_{\mathbf{k},\sigma}(E)=\frac{a_{\sigma}(E)}{b_{\sigma}(E)-a_{\sigma}(E)t_{\mathbf{k}}}, \tag{17}$$

where

$$a_{\sigma}(E)=\int\overline{K}(\omega)\sum_{\mathbf{q}}t_{\mathbf{q}}\frac{\chi_{\sigma}+n_{\mathbf{q},-\sigma}}{E-t_{\mathbf{q},-\sigma}-\sigma\omega}d\omega, \tag{18}$$

and

$$b_{\sigma}(E)=E-\int\overline{K}(\omega)\sum_{\mathbf{q}}t_{\mathbf{q}}^2\frac{n_{\mathbf{q},-\sigma}}{E-t_{\mathbf{q},-\sigma}-\sigma\omega}d\omega. \tag{19}$$

In the self-consistent approximation, Eqs. (15) and (16) correspond to an analogous form.

The chemical potential is determined from the normalization condition (4), which must be satisfied for both values of σ, and the magnetization is given by

$$\langle S^z\rangle=\frac{1}{2}\sum_{\mathbf{k},\sigma}\sigma\langle X_{-\mathbf{k}}^{\sigma 0}X_{\mathbf{k}}^{0\sigma}\rangle=-\frac{1}{2\pi}\sum_{\mathbf{k}\sigma}\sigma\int\mathrm{Im}\,G_{\mathbf{k},\sigma}(E)(1-f(E))dE. \tag{20}$$

The approximation of Edwards and Hertz (13) does not violate the analytic properties of the Green's function. At the same time, such a violation is possible for the approximation (7). In the case where the ground state is a saturated ferromagnetic state, the Green's function $G_{\mathbf{k},\downarrow}(E)$ (7) has no singularities in the upper half plane. Thus, the normalization condition (4) is satisfied for $\sigma=\downarrow$, if we choose the chemical potential from the condition on $G_{\mathbf{k},\downarrow}(E)$. The sum rule

$$n_0+n_{\sigma}=-\frac{1}{\pi}\sum_{\mathbf{k}}\int\mathrm{Im}\,G_{\mathbf{k},\sigma}(E)dE, \tag{21}$$

however, fails for both spin projections. This failure is caused by the existence of a parasitic pole of the Green's function (7) in the upper half plane,

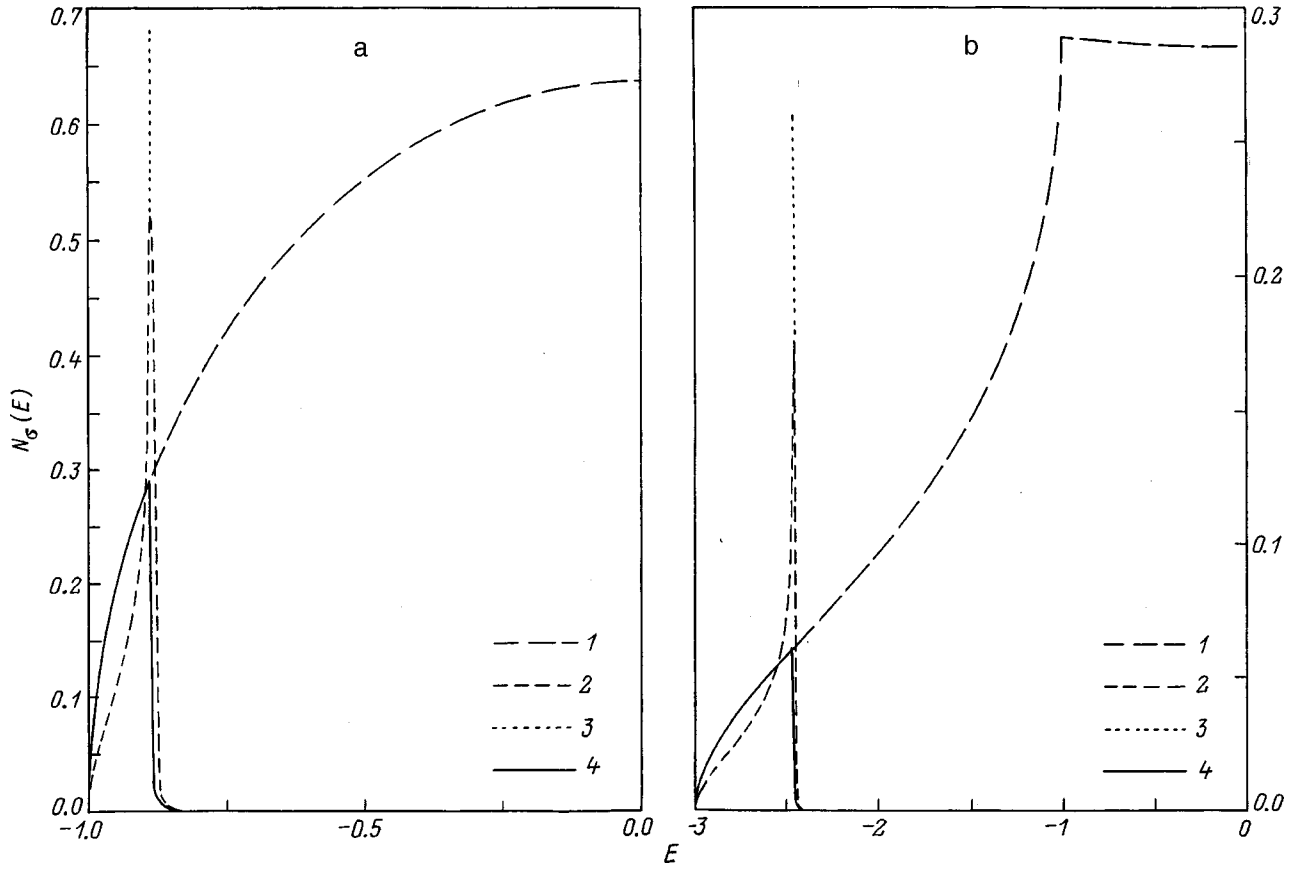

FIG. 1. Density of states in different approximations for a hole concentration $\delta=0.02$: *1* $N_\uparrow(E)$ (the curve is the same in all approximations); *2* and *3* $N_\downarrow(E)$ in the non-self-consistent approximation (7) with and without spin dynamics; *4* $N_\downarrow(E)$ in the self-consistent approximation (14). Curves *2* and *3* essentially overlap right up to the peak tip determined by the dynamics. (a) semielliptical seed density of states, (b) simple cubic lattice; the energy E is in units of the band half width and the transport width, respectively.

$$E=-\left(t_{\mathbf{k},\sigma}\frac{n_\sigma}{n_{-\sigma}+n_0}+\sum_{\mathbf{q}}t^2_{\mathbf{k}-\mathbf{q}}\frac{n_{\mathbf{k}-\mathbf{q},-\sigma}}{E-t_{\mathbf{k}-\mathbf{q},-\sigma}-\sigma\omega_{\mathbf{q}}}\right)\times\left(1-\frac{t_{\mathbf{k}}}{n_{-\sigma}+n_0}\sum_{\mathbf{q}}\frac{\chi_{\mathbf{q},\sigma}+n_{\mathbf{k}-\mathbf{q},-\sigma}}{E-t_{\mathbf{k}-\mathbf{q},-\sigma}-\sigma\omega_{\mathbf{q}}}\right)^{-1}. \quad (22)$$

As can be seen from Eq. (22), this pole exists for any current carrier concentration. It make a small negative contribution to the density of states in the band center. For low hole concentrations δ, however, the failure of normalization is essentially unnoticeable; even for δ close to δ_c it is still small. In the Edwards–Hertz approximation (13), these pathologies are absent. Note that self-consistency can lead to new causes for breakdown of the sum rule (21), but this failure may be even weaker, numerically, than in the non-self-consistent approximation.[37]

An instability of the saturation ferromagnetism develops in this approach because of the appearance of spin-polaron states with spin down, which lie below the Fermi level,[18,38] and the emergence of a corresponding contribution to $n_\downarrow$ for $T=0$.

For simplicity we shall use the Debye approximation for the magnon spectrum. We note, however, that the results do not change significantly with a more realistic choice of spin dynamics. The width of the model band for a semielliptical density of magnon states was chosen to be equal to the width of the magnon density of states for a simple cubic lattice,

$$\overline{K}(\omega)=\begin{cases}D\omega^{3/2}, & \omega<\omega_{\max}\\ 0, & \omega\geqslant\omega_{\max}\end{cases}, \quad (23)$$

where

$$\omega_{\max}=Dq_{\mathrm{D}}^2, \quad q_{\max}=q_{\mathrm{D}}=\left(\frac{6\pi^2}{v_0}\right)^{1/3},$$

q_{D} is the Debye wave vector, v_0 is the unit cell volume, and D is the spin rigidity constant. Using the expression for the magnon frequency to first order in $1/z$,[34]

$$\omega_{\mathbf{q}}=\sum_{\mathbf{k}}(t_{\mathbf{k}-\mathbf{q}}-t_{\mathbf{k}})n_{\mathbf{k}},$$

we obtain $D=|t|\delta$ for a simple cubic lattice, where t is the transport integral.

Calculations of the density of states in the saturated ferromagnetic state using Eqs. (17)–(19) and (23) are shown in Figs. 1 and 2. The density of states $N_\downarrow(E)$ is nonzero below the Fermi level only because of the incoherent contribution. For low hole concentrations, the normalization condition (4) is satisfied with high accuracy for both projections of the spin. When δ is increased, condition (4) begins to depend on

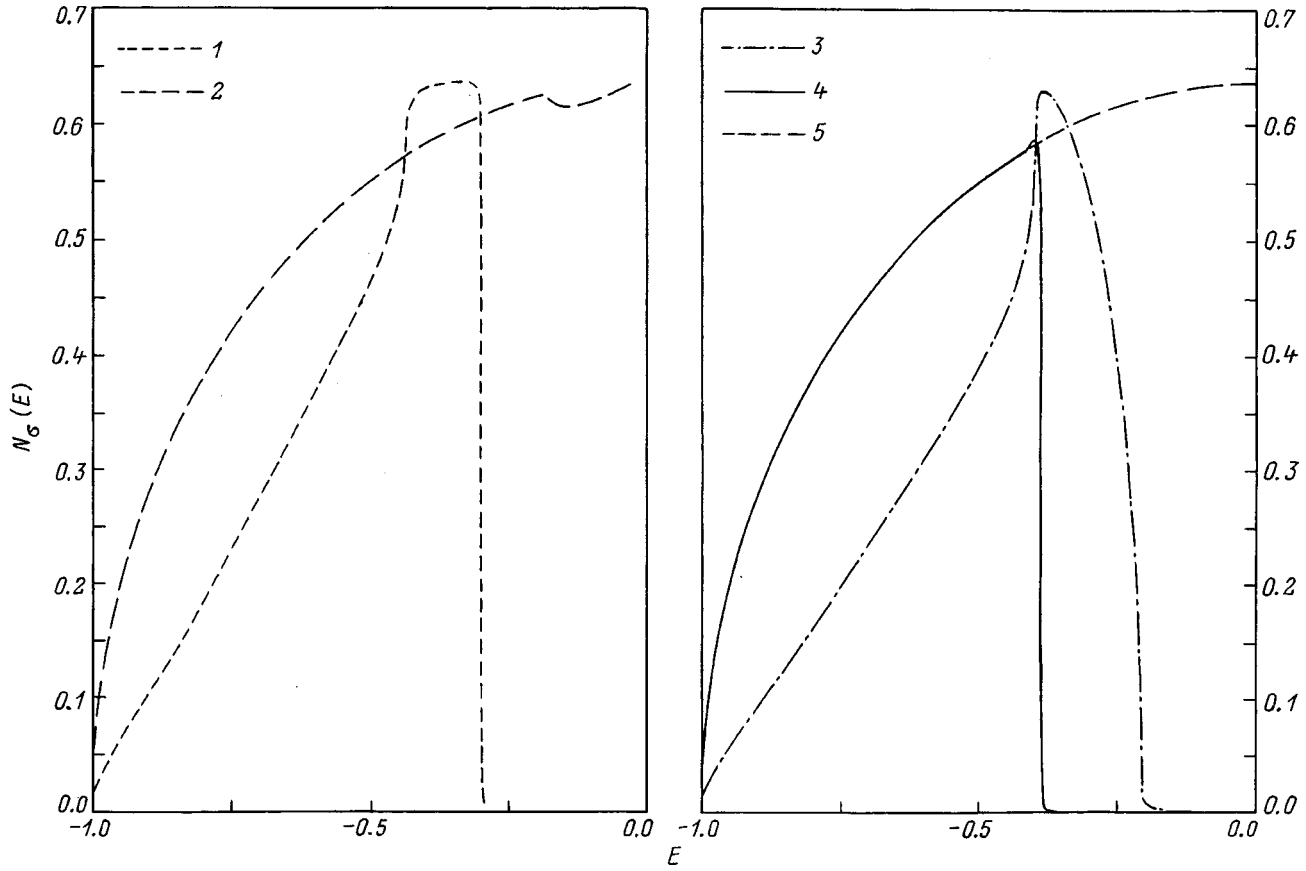

FIG. 2. Density of states in different approximations for a hole concentration $\delta=0.2$, close to critical: *1* and *2* $N_\downarrow(E)$ and $N_\uparrow(E)$ in the non-self-consistent approximation (7) (spin dynamics has no significant effect on the form of these curves); *3* and *4* $N_\downarrow(E)$ in the approximation of Edwards and Hertz (13) including spin dynamics (the peak is sharpened when the dynamics are neglected) and in the self-consistent approximation (14); *5* $N_\uparrow(E)$, which essentially coincides with the seed density of states in the last two approximations. The seed density of states is semielliptical.

the method for choosing the chemical potential, but the failure of normalization is insignificant. (For $\delta=0.20$ the failure of normalization is roughly 2–3%.)

When the spin dynamics are neglected ($\overline{K}(\omega)=\delta(\omega)$), in the non-self-consistent approximation (7) and in the approximation of Eq. (13), the density of states $N_\downarrow(E)$ changes discontinuously to zero on passing through the Fermi level (Fig. 1). For low hole concentrations, below the Fermi level (up to a narrow neighborhood of it), we have $N_\uparrow(E) \approx N_\downarrow(E)$, and when δ is increased, a peak at E_F becomes ever more noticeable in the density of states $N_\downarrow(E)$. Mathematically, it originates in a Condon logarithmic singularity which appears in the integral

$$\sum_{\mathbf{q}} \frac{f(t_{\mathbf{k}+\mathbf{q}})}{E-t_{\mathbf{k}+\mathbf{q}}} \approx -\ln|E-E_F|N(E_F).$$

For very low δ, a significant logarithmic singularity exists only in the imaginary part of the Green's function, which corresponds to a finite jump in the density of states.[33,34] However, when δ increases, it is necessary to take the resolvents into account in both the numerator and denominator of the Green's function, so that the real and imaginary parts ''intermingle'' and a logarithmic singularity appears in the density of states. When the magnon frequencies are included in the denominators of Eqs. (9) and (10), the singularity is spread out over the interval $\omega_{\max}$ and the peak is smoothed out. In terms of the self-consistent approximation (15) and (16), the form of $N_\downarrow(E)$ approaches the seed density of states and the peak is completely spread out, even neglecting the spin dynamics (Fig. 1), so that the latter plays no significant role.

Near the critical concentration, the peak in approximation (7) (but not in the Edwards–Hertz approximation) is again spread out (Fig. 2), a but this spreading out is no longer noticeable for $\delta=0.15$. In Fig. 2 one can also see a significantly different position of the chemical potential (i.e., where $N_\downarrow(E)$ goes to zero) in the different approximations.

The critical concentration for stability of the saturation ferromagnetism for a simple cubic lattice in all the approximations (8), (13), and (14) is determined by the appearance of a pole in the Green's function $G_{\mathbf{k},\downarrow}(E)$ at $\mathbf{k}=(\pi,\pi,\pi)$. In approximations (8) and (14), for $\delta>\delta_c$ the normalization condition (4) fails decisively for both spin projections, while the density of states $N_\downarrow(E)$ ceases to be positive definite below the Fermi energy. (Recall that these pathological features also occur below the critical density, but there they are practically unnoticeable.) Hence, the further evolution of the electronic spectrum and the description of the saturation ferromagnetism cannot be considered in these approximations.

The critical concentrations δ_c for loss of the stability of saturation ferromagnetism for a number of seed densities of state, as calculated in the different approximations consid-

TABLE I. Critical concentrations δ_c for rectangular (ra) and semielliptical (se) seed densities of states, and for square, simple, body-centered, and face-centered cubic lattices in the nearest neighbor approximation.

DOS	I	II	III	IV	V
ra	0.284	0.279	0.272		
se	0.271	0.266	0.265		
square	0.265	0.253	0.253	0.49	0.405
sc	0.243	0.237	0.238	0.32	0.237
bcc	0.231	0.221	0.224	0.32	0.239
fcc	0.253	0.227	0.231	0.62	

Note: (I) Non-self-consistent approximation (7), (II) approximation (13), (III) self-consistent approximation (15) and (16), (IV) Ref. 4, (V) Ref. 29 (RESO calculation; for the fcc lattice no instability was found).

ered here, are listed in Table I. In the case of fcc lattices (where the seed density of states is asymmetric and has a logarithmic divergence on one edge), we have chosen the sign of the transport integral for which the saturated ferromagnetism is stable for low δ.[14] Note that it is necessary to use an equation for the chemical potential (4) that is derived from the complete Green's functions (7). (Using the ''Hubbard-I'' approximation here leads to a drop in δ_c on the order of 0.1.) Here the normalization condition for $\sigma = \downarrow$ is satisfied automatically.

It is clear from the table that the results are fairly stable and do not depend too much on the form of the approximation. In particular, self-consistency changes them little, leading to a slight reduction in δ_c. The dependence on spin dynamics (magnon spectrum), even in the non-self-consistent approximation, is even weaker. (The critical concentration only varies in the third decimal place.) It is interesting to note that results of the Edwards–Hertz approximation are closer to those of the self-consistent approximation (14) than to the non-self-consistent approximation (8). (Unfortunately, in Ref. 18 only a crude estimate of δ_c was made using a quadratic dispersion relation for the electrons.)

The values we have obtained can be compared with those in the limit of an infinite-dimensional space (it should be expected that our method of expanding in powers of $1/z$ is rather close to this approximation), for which $\delta_c = 0.42$ (Ref. 27) and $\delta_c = 0.33$ (Ref. 11) have been obtained. At the same time, our approach makes possible to reproduce the dependence of δ_c on the dimensionality of space and on the form of the seed density of states.

Recently, δ_c has been obtained for a large number of lattices.[4,29] These results are also given in the table for comparison. It can be seen that in a number of cases, our results agree better with a number of other calculations, especially for a square lattice. (See the introduction.) We note, in this connection, that a variational method has been used[5] to obtain a rigorous estimate of $\delta_c < 0.29$ for a square lattice. Therefore, our results can be regarded as fairly reliable, even quantitatively.

We thank A. O. Anokhin for help in the numerical calculations and for useful discussions.

This work was partially supported by the Russian Foundation for Basic Research (Grant No. 96-02-16000).

*)E-mail: Valentin.Irkhin@imp.uran.ru

[1] J. Hubbard, Proc. R. Soc. London, Ser. A **276**, 238 (1963).
[2] Yu. A. Izyumov, Usp. Fiz. Nauk **165**, 403 (1995).
[3] Yu. A. Izyumov, M. I. Katsnel'son, and Yu. N. Skryabin, *Magnetism of Collectivized Electrons* [in Russian] (Fizmatgiz, Moscow, 1994), 368 pp.
[4] B. S. Shastry, H. R. Krishnamurthy, and P. W. Anderson, Phys. Rev. B **41**, 2375 (1990).
[5] W. von der Linden and D. M. Edwards, J. Phys.: Condens. Matter **3**, 4917 (1991).
[6] D. F. B. ten Haaf and J. M. J. van Leeuwen, Phys. Rev. B **46**, 6313 (1992).
[7] D. F. B. ten Haaf, P. W. Brouwer, and J. M. J. van Leeuwen, Phys. Rev. B **51**, 353 (1995).
[8] R. Strack and D. Vollhardt, J. Low Temp. Phys. **99**, 385 (1995).
[9] P. Wurth, G. Uhrig, and E. Müller-Hartmann, Ann. Phys. (Leipzig) **5**, 148 (1996).
[10] S. Liang and H. Pang, Preprint, cond-mat/9404003, Europhys. Lett. **32**, 173 (1995).
[11] T. Obermeier, T. Pruschke, and J. Keller, Phys. Rev. B **56**, R8479 (1997).
[12] D. Vollhardt, N. Blümer, K. Held, M. Kollar, J. Schlipf, and M. Ulmke, Z. Phys. B **103**, 283 (1997).
[13] T. Moriya, *Spin Fluctuations in Magnetic Materials with Collectivized Electrons* (Mir, Moscow, 1988), 287 pp.
[14] Y. Nagaoka, Phys. Rev. **147**, 392 (1966).
[15] L. M. Roth, Phys. Rev. B **184**, 451 (1969); Phys. Rev. B **186**, 428 (1969).
[16] H. S. Jarrett, W. H. Cloud, R. J. Bouchard, S. R. Butler, C. G. Frederick, and J. L. Gillson, Phys. Rev. Lett. **21**, 617 (1968).
[17] J. B. Sokoloff, Phys. Rev. B **2**, 3707 (1970); Phys. Rev. B **3**, 3826 (1971).
[18] J. A. Hertz, and D. M. Edwards, J. Phys. F **3**, 2174 (1973); D. M. Edwards and J. A. Hertz, J. Phys. F **3**, 2191 (1973).
[19] M. Plischke, J. Stat. Phys. **11**, 159 (1974).
[20] Y. Takahashi, J. Phys. Soc. Jpn. **51**, 3475 (1982).
[21] A. V. Bedyaev and M. Yu. Nikolaev, Pis'ma Zh. Éksp. Teor. Fiz. **41**, 18 (1985) [JETP Lett. **41**, 20 (1985)].
[22] M. Yu. Nikolaev N. V. Ryzhanova, A. V. Vedyaev, and S. M. Zubritskii, Phys. Status Solidi B **128**, 513 (1985).
[23] B. H. Zhao, H. Q. Nie, K. Y. Zhang, K. A. Chao, and R. Micnas, Phys. Rev. B **36**, 2321 (1987).
[24] A. V. Bedyaev, S. M. Zubritskiĭ, and N. V. Ryzhanova, Fiz. Met. Metalloved. **65**, 882 (1988).
[25] L. B. Ioffe and A. I. Larkin, Phys. Rev. B **37**, 5730 (1988).
[26] Y. Fang, A. E. Ruckenstein, E. Dagotto, and S. Schmitt-Rink, Phys. Rev. B **40**, 7406 (1989).
[27] P. Fazekas, B. Menge, E. Müller-Hartmann, Z. Phys. B **78**, 69 (1990).
[28] E. G. Goryachev, D. V. Kuznetsov, Pis'ma Zh. Éksp. Teor. Fiz. **56**, 205 (1992) [JETP Lett. **56**, 203 (1992)].
[29] T. Hanisch, G. S. Uhring, and E. Müller-Hartmann, Phys. Rev. B **56**, 13 960 (1997); preprint, cond-mat/9707286.
[30] T. Okabe Phys. Rev. B **57**, 403 (1998).
[31] M. I. Auslender, V. Yu. Irkhin, and M. I. Katsnel'son, Fiz. Met. Metalloved. **65**, 57 (1988).
[32] M. I. Auslender, V. Yu. Irkhin, and M. I. Katsnelson, J. Phys. C **21**, 5521 (1988).
[33] V. Yu. Irkhin and M. I. Katsnel'son, Fiz. Tverd. Tela **25**, 3383 (1983) [Sov. Phys. Solid State **25**, 1947 (1983)].
[34] V. Yu. Irkhin, M. I. Katsnelson, J. Phys. C **18**, 4173 (1985).
[35] V. Yu. Irkhin and M. I. Katsnel'son, Fiz. Met. Metalloved. **66**, 41 (1988).
[36] J. Hubbard, Proc. R. Soc. London, Ser. A **285**, 542 (1965).
[37] A. O. Anokhin and V. Yu. Irkhin, Phys. Status Solidi B **165**, 129 (1991).
[38] V. Yu. Irkhin and M. I. Katsnelson, J. Phys.: Condens. Matter **2**, 7151 (1990).

Translated by D. H. McNeill

Structural and magnetic phase transitions in $La_{0.9}Sr_{0.1}MnO_3$

V. S. Gaviko,*) V. E. Arkhipov, A. V. Korolev, and V. E. Naĭsh

Institute of Metal Physics, Urals Branch of the Russian Academy of Sciences, 620219 Ekaterinburg, Russia

Ya. M. Mukovskiĭ

Moscow Institute of Steels and Alloys, 117936 Moscow, Russia

(Submitted September 3, 1998)
Fiz. Tverd. Tela (St. Petersburg) **41**, 1064–1069 (June 1999)

A study is made of phase transitions in doped $La_{0.9}Sr_{0.1}MnO_3$ compounds using combined x-ray, electrical, and magnetic measurements. Structural phase transitions are observed accompanied by a change in the cell volume at temperatures of 100–110 K and 300–340 K. These structural changes are found to be related to different contributions of the rhombic Jahn–Teller Q_2 mode to the formation of the crystal lattice. The structural transition at 100–110 K is accompanied by distinctive magnetic and electrical properties. The data are analyzed in detail. © *1999 American Institute of Physics.* [S1063-7834(99)02906-8]

Interest in research on the magnetic properties, electronic states, and crystal structures of the perovskite-like $R_{1-x}A_xMnO_{3+\delta}$ manganites, where R=La, Nd or Pr and A=Sr, Ca or Ba has recently grown in connection with the huge magnetic resistance observed in these compounds. There is special interest in studying the ferromagnetic compounds with strontium, which have a Curie temperature near room temperature.[1–9] This makes it easier to use these compounds in practical applications, since the colossal spike in the magnetic resistance is usually observed in the neighborhood of T_c. In addition, for the compounds with strontium, it is much easier to obtain high quality single crystal samples.

Despite a large number of papers on these compounds, the data from structural, magnetic, and electrical studies differ among them. This is especially true for concentrations of the dopant element with $x<0.2$. The structure of the (T,x)-phase diagrams in this concentration range is the most complicated and contradictory.[2–5,8] For example, the diagram of Ref. 3 shows that the compound $La_{0.9}Sr_{0.1}MnO_3$, which we have chosen to study, has only one orthorhombic O′ phase within the temperature range 80–400 K. Another diagram, given in Ref. 2, shows that this compound can have three modifications of the orthorhombic phase, denoted there by O, J, and P. (The symbol O represented a phase whose formation essentially involves no contribution from Jahn–Teller modes, J, a state involving J–T modes, and P, a state with ordering of the Mn^{4+} cations, i.e., a polaron-ordered phase.) However, no quantitative diffraction data which distinguish these phases are presented in Ref. 2. Neutron diffraction data are used in Ref. 8 to show that the J phase is orthorhombic, while the O and P phases (J and P are denoted by O′ and O″, respectively, in Ref. 8) are pseudocubic. It should be noted that the regions where the pseudocubic $Pbnm$ modifications exist differ substantially in Refs. 2, 3, and 8.

The published data on the magnetic state of the lightly strontium-doped manganites are also contradictory. According to Refs. 1 and 8, the compound $La_{0.9}Sr_{0.1}MnO_3$ has two magnetically ordered structures: a ''canted'' antiferromagnetic structure at low temperatures transforms to a ferromagnetic state upon heating. Thus, there are two magnetic phase transitions in this material.[1,8] At the same time, the diagram of Ref. 2 implies that this compound has only one magnetic phase transition, specifically, from a low-temperature ferromagnetic orthorhombic ''polaron-ordered'' P-phase into a paramagnetic (O- or J-) phase.

The task of this paper is to study $La_{0.9}Sr_{0.1}MnO_3$ with the aid of combined x-ray, electric, and magnetic measurements. At present, there are essentially no data in the scientific literature from magnetic studies of the phase transformations in $La_{0.9}Sr_{0.1}MnO_3$ or on the temperature dependence of the crystal lattice parameters.

1. EXPERIMENTAL TECHNIQUE

Samples were obtained by zone melting with radiative heating without a crucible.[5] Blanks for zone melting were prepared by $T=1300\,^\circ$C sintering of a presynthesized compound which had been made beforehand from La_2O_3 and Mn_3O_4 powders and dried $SrCO_3$ powder annealed at $T=1000\,^\circ$C with intermediate grinding. A grown sample consisted of cylinder with a diameter of 4 mm and a length of 20 mm. Along the direction of growth the samples had two types of structural domains at room temperature, with [010] and $[10\bar{1}]$ orientations.

X-ray diffraction studies were done on the powders using DRON automated x-ray diffractometers equipped with a vacuum chamber for studying powders at temperatures from 77 to 370 K using monochromatized Cr K_α-radiation.

The electrical resistance R was measured by the four probe method and the magnetic measurements were made on a Quantum Design MPMS–5–XL magnetometer in fields up to 50 kOe.

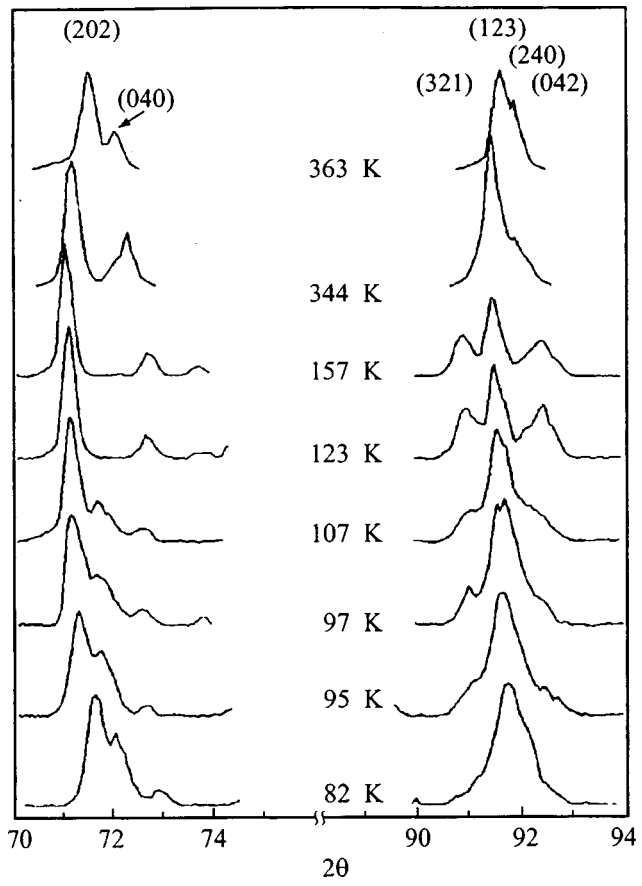

FIG. 1. X-ray diffraction line shapes for different measurement temperatures.

2. RESULTS

X-ray studies of the $La_{0.9}Sr_{0.1}MnO_3$ samples showed that at room temperature they were essentially single-phase with an O′ orthorhombic structure. (Here and in the following we use the notation of Ref. 8.) The spatial group was *Pbnm* with lattice parameters a, b and c equal to 5.580, 7.754, and 5.554, respectively, in good agreement with published data.[3,4,10] As the temperature is reduced, the O′-phase is retained essentially unchanged down to $T=115$ K. Further cooling of the samples causes a shift in several of the diffraction lines and changes in their relative intensities. For example the (004) diffraction line of the O′-phase shifts toward the (202) line ((220) in a cubic description), while its relative intensity decreases. The (123), (042), and (240) lines decrease in intensity and shift toward the (321) line ((222) in a cubic representation), etc. (See Fig. 1.) Note that when the samples are cooled, changes in the first order diffraction patterns show up in the intensities of the diffraction lines (Fig. 1) beginning by $T\sim115$ K, while the shift in these lines is small almost to $T\sim105$ K. Then, near $T=105-100$ K a sudden shift in the diffraction lines is observed accompanied by a change in the cell volume from 239.2 to 238.3 Å^3 (Fig. 2). Below this temperature, additional, weak diffraction lines appear near the intense, wide fundamental lines in the diffraction patterns; it was not possible to label these lines with integers h, k, l. The intensities of these lines decrease with cooling. Figure 2 shows the temperature variations in the orthorhombic lattice parameters a, b, c, and volume V.

Heating the samples above room temperature to 360 K, like cooling them below ~100 K, causes a shift in the diffraction lines, brings the parameters a, b, and c closer together (Fig. 2), and reduces the cell volume, with the distinction that during heating, as opposed to cooling, the unlabelled diffraction lines are not observed. In addition, the cell volume decreases suddenly with cooling at 100 K, while for heating from 310 to 340 K, the change takes place smoothly. The character of the change in the parameters during cooling and heating of the samples is indicative of a transformation of the orthorhombic O′-phase into a pseudocubic phase, in accord with neutron diffraction data[8] on $La_{0.875}Sr_{0.125}MnO_3$.

The electrical resistance R measured at temperatures of 80–300 K has singularities at $T_1\sim100$ K and $T_2\sim150$ K

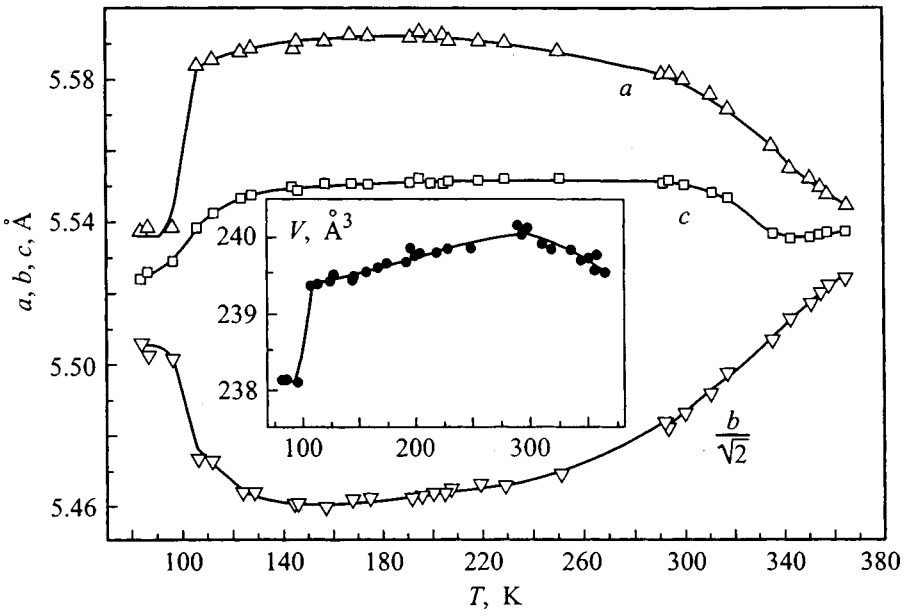

FIG. 2. Temperature variations in the crystal lattice parameters of the compound $La_{0.9}Sr_{0.1}MnO_3$.

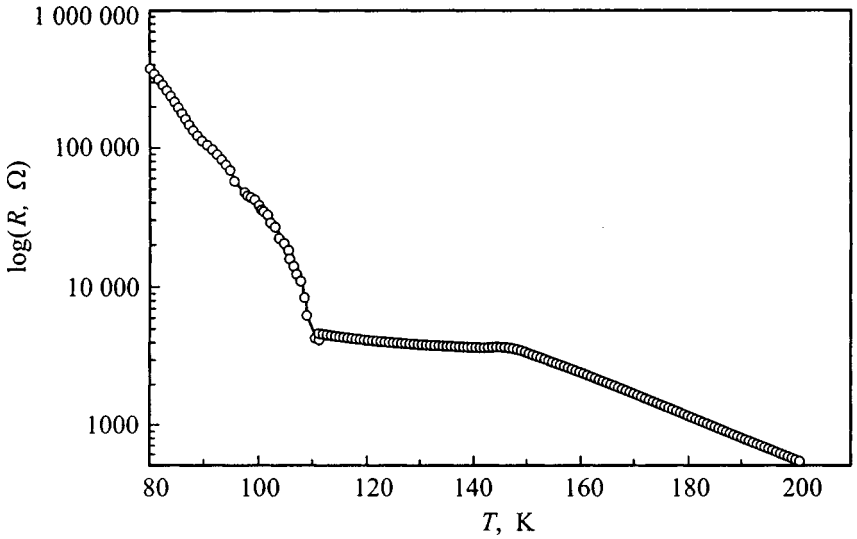

FIG. 3. Temperature variation in the electrical resistivity.

(Fig. 3). At these temperatures the function $R(T)$ changes. The figure shows that over the entire range from 200 to 80 K the electrical resistivity increases with cooling, but this growth is essentially different in the intervals 80–107 K, 107–150 K, and 150–200 K. The most rapid change in the electrical resistance is observed in the range 80–107 K, while the slowest is over 107–150 K.

The temperature variation in the magnetization, $M(T)$, of a pseudo-single crystal measured along the easy direction is shown in Fig. 4 and the magnetization curves $M(H)$, in Fig. 5. The measurements of $M(T)$ were done with cooling of the sample in a magnetic field along the same direction, while $M(H)$ was measured in the following cycle of variations in H: $0\rightarrow+50\,\text{kOe}\rightarrow0\rightarrow-50\,\text{kOe}\rightarrow0\rightarrow+50\,\text{kOe}\rightarrow0$. As can be seen well from these figures, $La_{0.9}Sr_{0.1}MnO_3$ is magnetically ordered at temperatures $T<T_2$. The Curie temperature of this compound, as measured by the Beloff–Harrot method, is 152 K. At $T=T_1$ a change in the magnetic state is observed: the magnitude of the magnetization changes, as does the contribution from the paraprocess to the magnetization. In addition, within the small temperature range $50<T<115\,\text{K}$, a singularity (a clearly distinct inflection) is observed in the magnetization curves at fields $>\sim10\,\text{kOe}$. At high temperatures, this inflection in the $M(H)$ curve shifts toward higher fields. (See curves *2* and *3* of Fig. 5.)

The magnetic measurements showed that in the paramagnetic temperature region $>252\,\text{K}$, there is an anomaly in the reciprocal of the magnetic susceptibility as a function of temperature, $\chi^{-1}=H/M$, measured in a field of 100 kOe (Fig. 6). The temperature of this anomaly coincides with the region of rapid changes in the crystal lattice parameters observed at 300–400 K.

3. DISCUSSION OF RESULTS

In order to establish the nature of the structural phase transitions observed at temperatures of 100–115 K and 300–

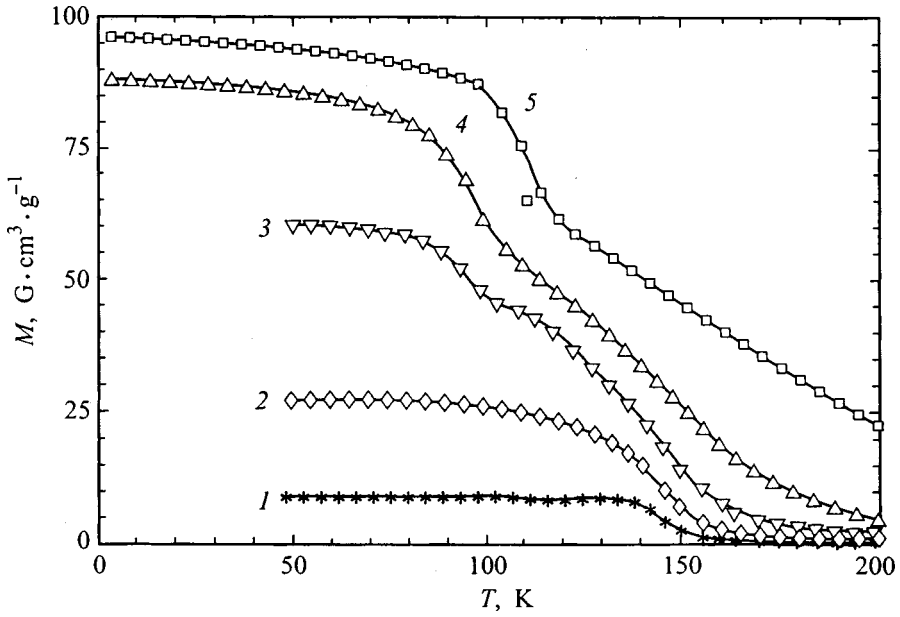

FIG. 4. Temperature variation in the magnetization of pseudo-single crystal $La_{0.9}Sr_{0.1}MnO_3$ for various magnetic field strengths (0.3 (*1*), 1 (*2*), 3 (*3*), 10 (*4*), and 50 kOe (*5*)). The measurements were done by cooling the sample in a magnetic field applied along the direction of easy magnetization.

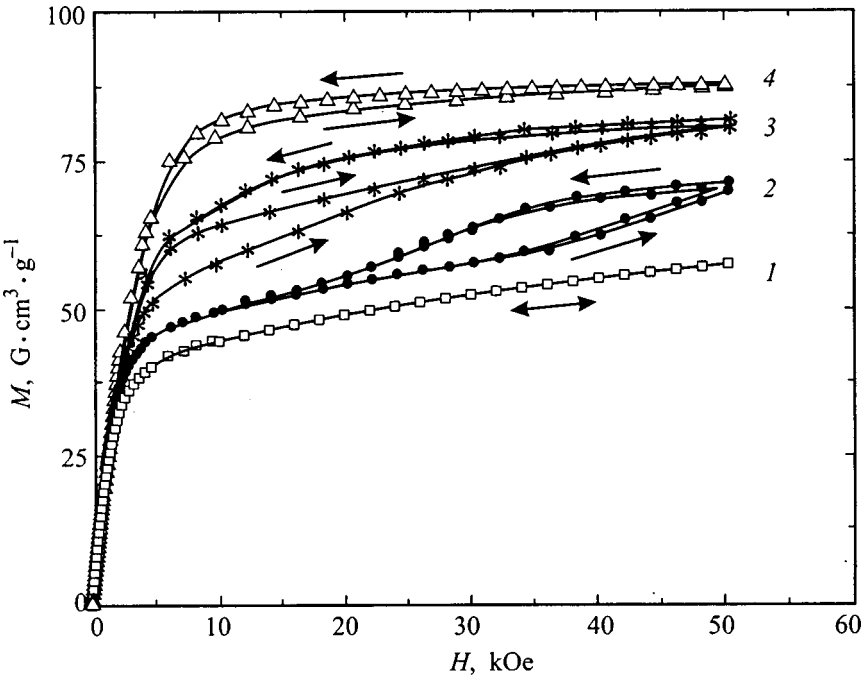

FIG. 5. Isotherms $M(H)$ of pseudo-single crystalline $La_{0.9}Sr_{0.1}MnO_3$ (120 K (*1*), 110 K (*2*), 100 K (*3*), 50 K (*4*)). The measurements were made along the easy direction over the following cycle in the field H (kOe): $0\rightarrow+50\rightarrow0\rightarrow-50\rightarrow0\rightarrow+50\rightarrow0$.

340 K, we have calculated the Mn–O interionic distances (m,s,l) in the MnO_6 octahedron (Fig. 7). For this purpose, the following formulas[9] were used:

$$m^2=\frac{1}{32}(a^2+b^2+c^2), \tag{1}$$

$$s^2=\frac{1}{8}b^2-m^2, \tag{2}$$

and

$$l^2=\frac{a^2s^2}{16s^2-a^2}, \tag{3}$$

where a, b, and c are the lattice parameters. In these calculations rotation of the octahedra is neglected. The results of the calculations are shown in Fig. 8. As can be seen from this figure, the calculated m is constant over the entire temperature range, while l rises suddenly with heating at 100 K and falls slowly above 300 K. The quantity s tends to behave in the opposite manner: a sharp drop at 100 K and a slow rise above 300 K. The observed variation in l is stronger than that in s.

The temperature variation in the Mn–O interionic distance implies that for temperatures below 100 K or above 340 K, there is no contribution of the rhombic J–T Q_2 mode to formation of the crystal lattice in $La_{0.9}Sr_{0.1}MnO_3$. The switching on of the Q_2 mode as the sample is heated at 100 K results in a structural phase transition from a low-temperature pseudo-cubic modification of the orthorhombic O″-phase into a Jahn–Teller orthorhombic O′-phase. As noted above, this transition leads to a sudden change in the unit cell volume typical of first-order transitions. The change in the intensity of the diffraction lines observed at temperatures between 100 and 115 K occurs because the transition does not take place at the same time over the entire volume

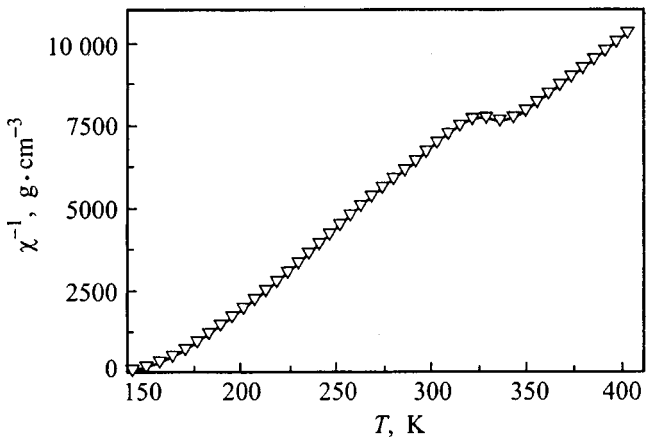

FIG. 6. The reciprocal of the magnetic susceptibility, $\chi^{-1}=H/M$, as a function of temperature for pseudo-single crystalline $La_{0.9}Sr_{0.1}MnO_3$; the experiment was done at $H=100$ kOe.

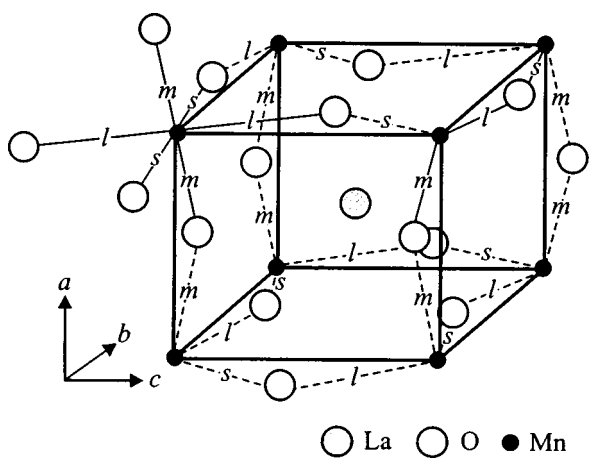

FIG. 7. Structure of the compound $LaMnO_3$.

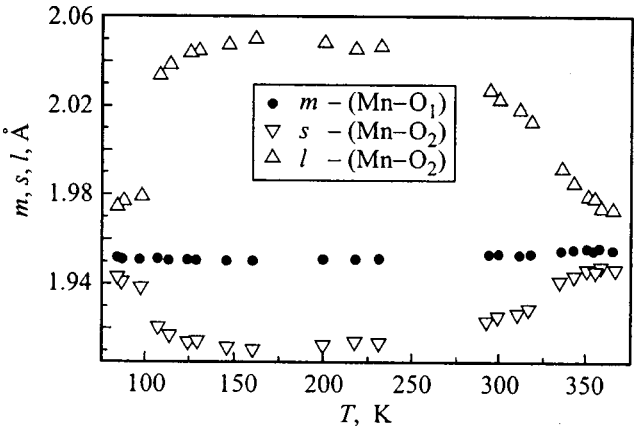

FIG. 8. Temperature variation in the Mn–O interionic distances.

of the sample. This last circumstance is responsible for the existence of a mixture of the two orthorhombic phases O′ and O″ within this temperature range.

When the samples are heated to ~ 340 K, the Q_2 J–T mode is again shut off and there is yet another structural transition from the O′- to the O-phase. As opposed to the low-temperature transition, this transition takes place smoothly as the temperature rises, as indicated by the continuous changes in the distances m, s, and l and in the cell volume V (Figs. 2 and 8).

In the above discussion we have also noted that the low temperature O′–O″ transition is accompanied by a change in the magnitude of the saturation magnetization and a change in the contribution from the paraprocess. The discontinuity in the magnetization observed in the $M(T)$ curves as the sample is cooled in fields $H>1$ kOe at $T\sim 100$ K (Fig. 4), can be ascribed to various causes, such as a possible change in the magnetic moment of the Mn ions or a different exchange energy in the magnetically ordered O′- and O″-phases. If the energy of the magnetic anisotropy in the O′-phase is substantial, then the existence in this phase of structural domains with different orientations can also cause a discontinuity in the magnetization. Detailed additional magnetic studies of the compound $La_{0.9}Sr_{0.1}MnO_3$ are under way in order to establish the reasons for the change in the magnetic state at 100 K, and the results of these studies will be published.

As for the feature observed in the $M(H)$ curve at temperatures $50<T<115$ K (Fig. 5) in fields $H>10$ kOe, it appears to be related to the effect of the magnetic field on the O″–O′ phase transition. In this case the magnetic field evidently raises the temperature of this transition. The mechanism by which the magnetic field influences this temperature is not entirely understood. It may be assumed that the magnetostriction of $La_{0.9}Sr_{0.1}MnO_3$ plays an important role in this mechanism.

Thus, the orthorhombic O′-phase, whose formation involves the rhombic Jahn–Teller Q_2 mode, exists within a limited range of temperatures, 100–340 K, in $La_{0.9}Sr_{0.1}MnO_3$. Below this temperature range the compound undergoes a transformation into pseudo-cubic modifications of the orthorhombic phase O″ and O, in which there is essentially no contribution from Q_2. The effect of the Q_2 mode in this compound causes an increase in the cell volume in the O′-phase by $\sim 0.5\%$. The structural changes at $T\sim 100$ K are accompanied by a discontinuous change in the cell volume and a change in the magnetic state of the samples. According to our magnetic studies, the O″ and O′ phases are magnetically ordered for $T<140$ K, while the O phase is paramagnetic. A magnetic field obviously can cause a change in the temperature of the O″–O′ structural phase transition, shifting it to higher temperatures.

*)E-mail: gaviko@imp.uran.ru

[1] H. Kawano, R. Kajimoto, M. Kubota, Phys. Rev. B **53**, 2202 (1996).
[2] Y. Yamada, O. Hino, S. Nohdo, R. Kanao, T. Inami, S. Katano, Phys. Rev. Lett. **77**, 904 (1996).
[3] H. Kawano, R. Kajimoto, M. Kubota, Phys. Rev. B **53**, R14709 (1996).
[4] J. F. Mitchel, D. N. Argyriou, C. D. Potter, D. G. Hinks, J. D. Jorgense, and S. D. Bader, Phys. Rev. B **54**, 6172 (1996).
[5] A. Urushibara, Y. Moritimo, T. Arima, A. Asamatsu, G. Kido, and Y. Tokura, Phys. Rev. B **51**, 14 103 (1995).
[6] V. E. Arkhipov, V. P. Dyakina, S. G. Karabashev, V. V. Marchenkov, Ya. M. Mayakovskiĭ, V. E. Naĭsh, V. E. Startsev, E. P. Khlybov, and A. Chopnik, Fiz. Met. Metalloved. **84**, 93 (1998).
[7] A. M. Balbashov, S. G. Karabashev, Y. M. Mukovskii, and S. A. Zver'kov, J. Cryst. Growth **167**, 365 (1996).
[8] L. Pinsard, J. Rodriguez-Carvajal, and A. Revcolevschi, J. Alloys Compd. **262-263**, 152 (1997).
[9] A. K. Bogush, V. I. Pavlov, and L. V. Balyko, Cryst. Res. Technol. **18**, 589 (1983).
[10] E. L. Nagaev, Usp. Fiz. Nauk **166**, 833 (1996).

Translated by D. H. McNeill

Dielectric nonlinearity of crystalline $Li_{2-x}Na_xGe_4O_9$ ($x \approx 0.23$)

A. Yu. Kudzin and D. M. Volnyanskiĭ

Dnepropetrovsk State University, 320027 Dnepropetrovsk, Ukraine
(Submitted June 4, 1998; in final form, October 6, 1998)
Fiz. Tverd. Tela (St. Petersburg) **41**, 1070–1072 (June 1999)

The dielectric nonlinearity of ferroelectric $Li_{2-x}Na_xGe_4O_9$ ($x \approx 0.23$) crystals is measured in the neighborhood of the phase transition temperatures. The magnitude of the nonlinear coefficient β is estimated from the shift in T_c and the reduction in ε_{max} under the influence of $E_=$, from the dielectric nonlinearity in the paraphase, and from the temperature dependence of P_s in crystalline $Li_{2-x}Na_xGe_4O_9$ ($x \approx 0.23$). The resulting values of β are 1.87, 1.26, 2.17, and 1.17×10^{-9} $(\text{CGSE cm}^2)^{-2}$, respectively. The mechanism for the phase transition in crystalline $Li_{2-x}Na_xGe_4O_9$ ($x \approx 0.23$) is discussed. [S1063-7834(99)03006-3]

Compounds belonging to the ternary system $Li_{2-x}Na_xGe_4O_9$ ($0 \leqslant x \leqslant 1$) have ferroelectric properties. The composition with $x=1$, i.e., $LiNaGa_4O_9$, has been studied in most detail.[1–4] Solid solutions develop as x is varied. The interesting feature of these compounds is that the phase transition temperature of $Li_2Ge_4O_9$ ($x=0$) is considerably lower than for the solid solution with $x \cong 0.2$.[5,6] The phase transition temperature for $x=0.2$ is ~ 140 K higher than T_c for the composition with $x=0$. Little is known about the dielectric properties of these compounds. The available data for $x=1$ suggest a number of interesting features. In particular, critical retardation has been observed at frequencies below 1 kHz[2] and a Debye frequency dispersion has been observed in the megahertz range during measurements near the phase transition.[4]

Thus, there is some interest in studying the dielectric properties of crystals in this series. In this article we present the results of some measurements of the dielectric nonlinearity of crystals with $x=0.23$. We have chosen this composition because for $x=0.23$ the crystals have a high $T_c = 295$ K, which makes it easier to carry out the experiments. In addition, we were unable to grow crystals with $0 < x < 0.2$ that are suitable for the measurements.

The techniques for growing $Li_{2-x}Na_xGe_4O_9$ crystals by the Czochralski method and preparing the samples for dielectric measurements have been described elsewhere.[3] Samples were prepared in the form of slabs with a principal (100) plane, which were polished before the platinum electrodes were deposited by cathode sputtering. The slab thickness was about 0.5 mm and the electrode area was about 5 mm^2. The dielectric permittivity was measured using an E8-2 capacitive bridge at a frequency of 1 kHz in the temperature region of the phase transition. The constant temperature measurements were made with the temperature stabilized to within 0.05 K. The external bias field was as high as 20 kV/cm.

It is known that polarizing a ferroelectric sample in a constant electric field $E_=$ has a large effect on the anomalous permittivity ε near a phase transition. Figure 1 shows experimental plots of $\varepsilon(T)$ for $Li_{2-x}Na_xGe_4O_9$ ($x \approx 0.23$) crystals at different $E_=$.

As the figure shows, when a field $E_=$ is applied, ε decreases, especially in the region of the phase transition, while the temperature of the phase transition (T_c) is shifted toward higher temperatures. The shift in T_c as a function of $E_=$ follows a curve which tends to saturate in high electric fields (Fig. 2).

Beyond the phase transition, the dielectric permittivity decreases with $E_=$ at a fixed temperature. This is a clear sign of a second-order phase transition. Data from experimental studies of $\varepsilon = f(E)_T$ at different temperatures in crystalline $Li_{2-x}Na_xGe_4O_9$ ($x \approx 0.23$) are shown in Fig. 3. All of the curves were taken with increasing bias fields. These plots are clearly nonlinear, the nonlinearity decreasing as the temperature rises.

The experimental data shown here can be explained in terms of the phenomenological Ginzburg–Devonshire theory[7,8] for second-order phase transitions. In order to determine the coefficient β, which is a quantitative measure of the degree of nonlinearity, we can use several equations which follow from thermodynamic theory. If we stopat terms in P^4 in the expansion of the thermodynamic potential in powers of the polarization, then the shift in temperature corresponding to ε_{max} as a function of the electric field strength obeys the formula

$$\Delta T_c = DE^{2/3}. \tag{1}$$

In this approximation we have $D=(6\beta/\alpha'^3)^{1/3}$, where β is the coefficient of P^4, $\alpha' = 4\pi/C$, and C is the Curie–Weiss constant. Using the data of Fig. 2, we constructed the $\Delta T_c = f(E^{2/3})$ curve, which is linear. Equation (1) then yielded $\beta = 1.87 \times 10^{-9}\,(\text{CGSE cm}^2)^{-2}$.

The drop in the maximum value of ε in the neighborhood of the phase transition can also be used to compare the thermodynamic theory with experiment. In this approximation, the maximum value of ε is related to the electric field strength as

$$1/\varepsilon_{max} = (3/4\pi)\beta^{1/3}E^{2/3}. \tag{2}$$

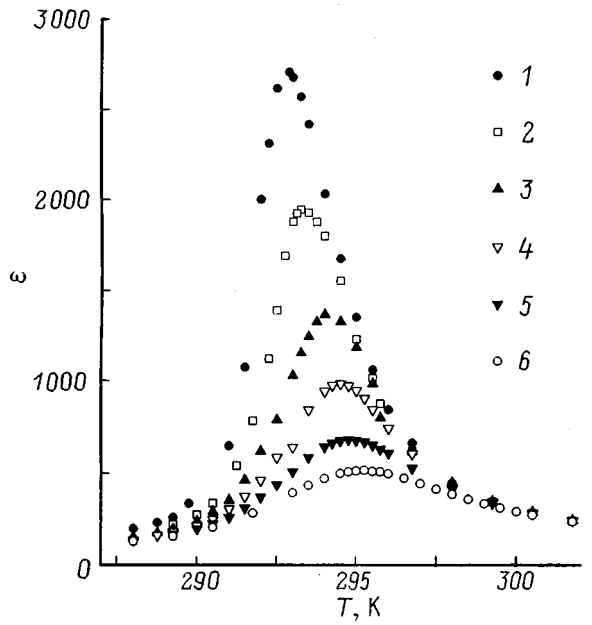

FIG. 1. Permittivity ε of crystalline $Li_{2-x}Na_xGe_4O_9$ ($x\approx0.23$) as a function of temperature for different fields $E_=$: *1*—0; *2*—0.51; *3*—1.12; *4*—1.94; *5*—3.57; *6*—5.61 kV/cm.

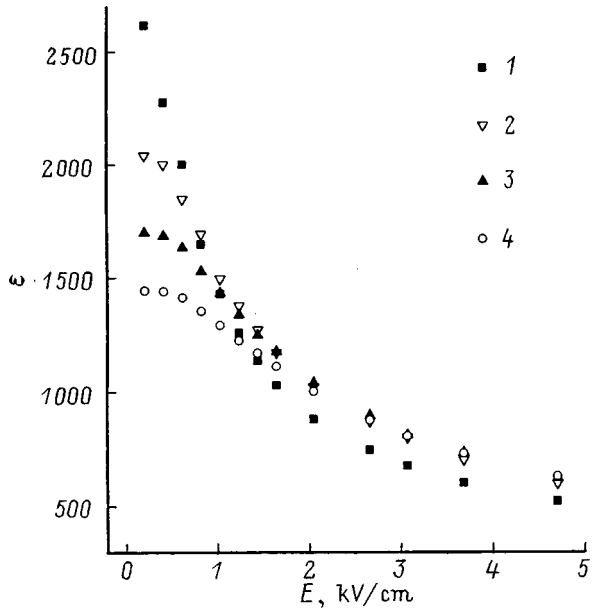

FIG. 3. Permittivity of crystalline $Li_{2-x}Na_xGe_4O_9$ ($x\approx0.23$) as a function of $E_=$ for various temperatures near $T_c=293.3$ K: *1*—$T_c+0.1$ K; *2*—$T_c+0.5$ K; *3*—$T_c+0.9$ K; *4*—$T_c+1.2$ K.

The function $1/\varepsilon_{\max}=f(E^{2/3})$ for crystalline $Li_{2-x}Na_xGe_4O_9$ ($x\approx0.23$), constructed from the data of Fig. 1, is well fit by a straight line. The coefficient β calculated from the slope of the line is 1.26×10^{-9} (CGSE cm^2)$^{-2}$.

The phenomenological theory shows that, in the paraelectric phase for high fields and temperatures near T_c, the function $1/\varepsilon-1/\varepsilon_0=f(E^{2/3})$ is linear with a proportionality coefficient $3/4\pi\times\beta^{1/3}$. Here ε_0 is the permittivity for $E_==0$. The experimental data of Fig. 3 for several temperatures above T_c were used to construct these curves, which fit the straight lines well. The values of β calculated from these data show that near T_c, a larger value of $\beta=2.17\times10^{-9}$ (CGSE cm^2)$^{-2}$ ($T-T_c=0.1$ K) is observed. It decreases linearly with distance from T_c in the paraphase [$\beta=1.09\times10^{-9}$ (CGSE cm^2)$^{-2}$ for $T-T_c=1.2$ K] and reflects a rapid loss of nonlinearity by the crystalline $Li_{2-x}Na_xGe_4O_9$ ($x\approx0.23$). If the $\beta(T)$ curve is extrapolated to intersect the temperature axis, then $\beta\approx0$ occurs at a temperature ~1.6 K above T_c.

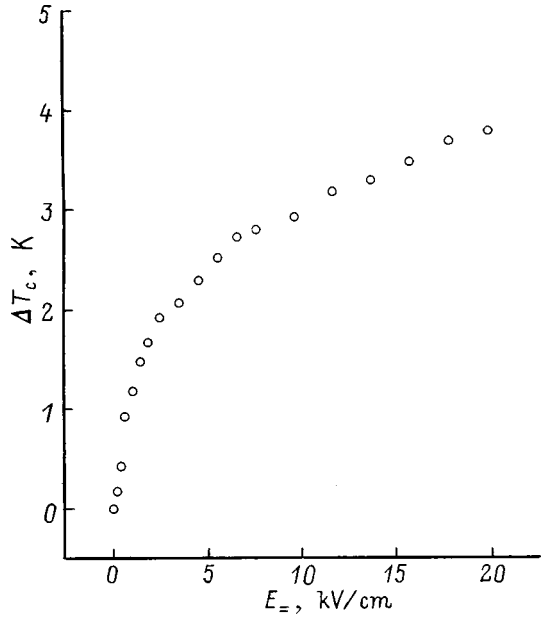

FIG. 2. The shift in the temperature of the phase transition as a function of field strength $E_=$ for crystalline $Li_{2-x}Na_xGe_4O_9$ ($x\approx0.23$).

It is known that for second-order phase transitions, β can also be estimated from the temperature dependence of P_s near T_c, which is given by

$$P_s^2=\frac{\alpha'}{\beta}(T_c-T). \tag{3}$$

It has been found from experimental plots of $P_s(T)$ measured for crystalline $Li_{2-x}Na_xGe_4O_9$ ($x\approx0.23$) over the dielectric hysteresis loops, that in these crystals Eq. (3) is satisfied for $T_c-T\leqslant10$ K. The slope of the straight line gives an estimate for β of 1.17×10^{-9} (CGSE cm^2)$^{-2}$.

We have, therefore, estimated the nonlinearity coefficient β for $Li_{2-x}Na_xGe_4O_9$ ($x\approx0.23$) crystals from the shift in T_c as a function of $E_=$ [1.87×10^{-9} (CGSE cm^2)$^{-2}$], from the dielectric nonlinearity in the paraphase [2.17×10^{-9} (CGSE cm^2)$^{-2}$ for $T-T_c=0.1$ K], and from the temperature variation in P_s [1.17×10^{-9} (CGSE cm^2)$^{-2}$].

β has been determined for various crystals by many authors (e.g., Ref. 8). For free $BaTiO_3$ crystals, β equals -2.5×10^{-13} (CGSE cm^2)$^{-2}$ at the Curie point. The most reliable value of β for crystalline triglycine sulfate is 7.7×10^{-10} (CGSE cm^2)$^{-2}$ near the phase transition temperature. For free crystalline Rochelle salt β is about 6×10^{-8} (CGSE cm^2)$^{-2}$. Therefore, of these three classical ferroelectric materials, the nonlinear properties of crystalline $Li_{2-x}Na_xGe_4O_9$ (for $x\approx0.23$; and, according to preliminary data, for the rest of this system) are closest to those of crys-

tals in the triglycine sulfate group. These crystals also have similar α' and P_s. The quantitative data for α', P_s, and β reflect the mechanism of the phase transition, so we may expect that in crystalline $Li_{2-x}Na_xGe_4O_9$ ($x \approx 0.23$) the phase transition mechanism is similar to that observed in crystals of the triglycine sulfate group, i.e., involves ordering of constant dipole moments.

[1] H. Volenkle, A. Wittman, and A. Nowotny, Monatsch. Chem. **101**, 56 (1970).
[2] M. Wada, M. Shibata, A. Sawada, and Y. Ishibshi, J. Phys. Soc. Jpn. **52**, 2981 (1983).
[3] M. D. Volnyanskiĭ and A. Yu. Kudzin, Fiz. Tverd. Tela **32**, 3160 (1990) [Sov. Phys. Solid State **32**, 1836 (1990)].
[4] M. Wada, Y. Yamashita, A. Sawada, and Y. Ishibashi, J. Phys. Soc. Jpn. **62**, 4503 (1993).
[5] M. D. Volnyanskiĭ and A. Yu. Kudzin, Fiz. Tverd. Tela **33**, 1903 (1991) [Sov. Phys. Solid State **33**, 1073 (1991)].
[6] M. D. Volnyanskiĭ and A. Yu. Kudzin, Fiz. Tverd. Tela **34**, 309 (1992) [Sov. Phys. Solid State **34**, 164 (1992)].
[7] M. Lines and A. Glass, *Principles and Applications of Ferroelectrics and Related Materials* (Clarendon Press, Oxford, 1977) [Russian translation Mir, Moscow, 1981, 736 pp.].
[8] G. A. Smolenskiĭ, V. A. Bokov, V. A. Isupov, N. N. Kraĭnik, R. E. Pasynkov, and M. S. Shur, *Ferroelectric and Antiferromagnetic Materials* [in Russian] (Nauka, Leningrad, 1971), 476 pp.

Translated by D. H. McNeill

Dielectric properties of single-crystal deuterated triglycine sulfate (DTGS) in ultra-weak low- and infra-low-frequency electric fields

A. V. Shil'nikov, V. A. Fedorikhin, A. P. Pozdnyakov, and A. V. Sopit

Volgograd State Architecture-Construction Academy, 400074 Volgograd, Russia

L. A. Shuvalov

Institute of Crystallography, Russian Academy of Sciences, 117333 Moscow, Russia

(Submitted October 8, 1998)
Fiz. Tverd. Tela (St. Petersburg) **41**, 1073–1075 (June 1999)

The complex permittivity ε^* is studied with separate readings for ε' and ε'' at low and infralow frequencies and ultraweak fields. The effective conductivity γ is determined. An Arrhenius dependence is observed for $\ln\varepsilon'(1/T)$, $\ln\varepsilon''(1/T)$, and $\ln\gamma(1/T)$, both in the paraphase and in the polar phase. It is proposed that the conductivity of crystalline DTGS in the paraphase is an ion jump conductivity. © *1999 American Institute of Physics.* [S1063-7834(99)03106-8]

In the last decade there has been renewed interest in experimental and theoretical research on crystals with hydrogen bonds and the contribution of these bonds to various macroscopic (in first order, dielectric) properties of these crystals.[1–5] Despite extremely thorough and wide ranging studies of the role of proton conductivity in various crystals,[1] the character of the conductivity in triglycine sulfate (DTGS) crystals has not been examined yet, as far as we know. The conductivity of these crystals was also not discussed in a comparatively old, specialized monograph.[6]

In this paper we attempt to fill this gap by examining the dielectric properties of crystalline DTGS at low (LF) and infralow (ILF) frequencies ($\nu = 10^{-1} - 10^4$ Hz) with a measurement field amplitude of $E_0 = 0.2$ V/cm at temperatures ranging from 2 to 120 °C, including a phase transition.

The complex permittivity ε^* was measured under quasistatic temperature conditions with a temperature step size of at most 0.2 K in the neighborhood of the phase transition. The value of ε^* was found with separate readings for the real (ε') and imaginary (ε'') components of the complex permittivity with accuracies of 1 and 2%, respectively. The temperature was maintained within 0.05 K, with a measurement sensitivity of 0.001 K. The effective specific conductivity γ was determined from the values of ε'' for the particular frequency of the measurement field.

We have found that (depending on the direction in which the sample temperature is varied) in the paraelectric phase the $\ln\varepsilon''(1/T)$ and $\ln\gamma(1/T)$ curves have an Arrhenius dependence (Fig. 1) over temperatures of $\sim 120 - 85$ °C at frequencies $\nu = 1 - 10$ Hz. The $\ln\varepsilon'(1/T)$ curves has the same

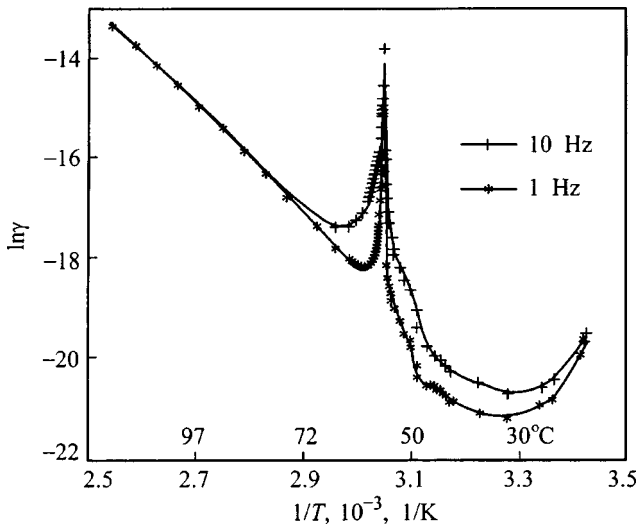

FIG. 1. Temperature variations in the effective conductivity of crystalline DTGS for a measurement field amplitude $E_0 = 0.2$ V/cm at frequencies $\nu = 1$ and 10 Hz.

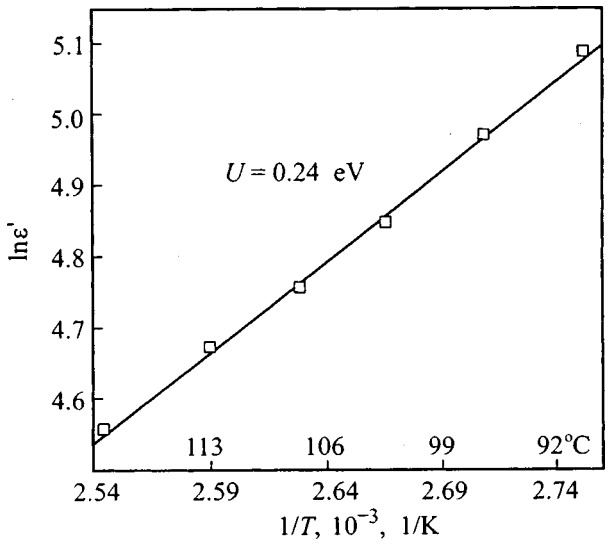

FIG. 2. Temperature dependence of the dielectric permittivity of crystalline DTGS for a measurement field amplitude $E_0 = 0.2$ V/cm at a frequency of $\nu = 1$ kHz.

TABLE I. The effective conductivity γ and activation energy U for crystalline DTGS in the paraphase.

ν, Hz	γ_{max}, 1/(Ωm)	γ_{min}, 1/(Ωm)	U, eV	γ_∞, 1/(Ωm)	$\Delta\gamma/\gamma$,%
10	$1.3\cdot10^{-6}$	$2.8\cdot10^{-8}$	0.93±0.01	$1.09\cdot10^{6}$	2.1
1	$1.6\cdot10^{-6}$	$1.4\cdot10^{-8}$	0.93±0.01	$1.13\cdot10^{6}$	2.3

dependence at a frequency of 1 kHz (Fig. 2). Therefore, the LF polarization and ILF conductivity are thermally activated processes. Here the activation energy for both ε'' and γ, obtained by cooling the sample after annealing at ~120 °C, is $U=(0.93\pm0.01)$ eV (Table I), while for ε' $U=(0.24\pm0.01)$ eV. Note that ε', ε'' and γ also have an Arrhenius dependence in the polar phase, but the temperature interval over which this is true is very narrow ($\Delta T\sim4K$) and lies immediately adjacent to the phase transition. In other words, in effect the polar state suppresses those thermally activated processes which show up clearly in the nonpolar phase. Note, however, that the slope of the line $\ln\gamma(1/T)$ for the polar phase is the same within a narrow range of temperature as for the nonpolar phase, i.e., the activation energy is the same as in the nonpolar phase.

We emphasize that the maximum conductivity at 120 °C at a frequency $\nu=1$ Hz is $\gamma_{max}\approx1.6\times10^{-6}(\Omega^{-1}m^{-1})$, and the minimum, at 62 °C is $\gamma_{min}\approx1.9\times10^{-8}(\Omega^{-1}m^{-1})$. Therefore, within a temperature range of $\Delta T=62$ K, the conductivity changes by two orders of magnitude. At the same time, we note that at the phase transition point, γ (Fig. 1), like ε' and ε'', passes through a maximum of $10^{-5}(\Omega^{-1}m^{-1})-10^{-7}(\Omega^{-1}m^{-1})$ for different measurement frequencies.

Analyzing the behavior of the experimental data, we can assume with great reliability that the conductivity of crystalline DTGS in the paraphase is an ion jump conductivity[1,7] and is probably caused by jumps of deuterons, for which the activation energy is ~0.93 eV. The activation character of the polarization process in DTGS in the unpolarized phase (the Arrhenius dependence of ε' at 1 kHz, Fig. 2), which is characterized by a comparatively low activation energy (0.24 ±0.01) eV, may, we believe, be evidence that above T_c glycine I participates in a thermally activated jump motion between two equivalent potential wells, which determines the characteristic feature of the order–disorder phase transition in crystalline DTGS.[8]

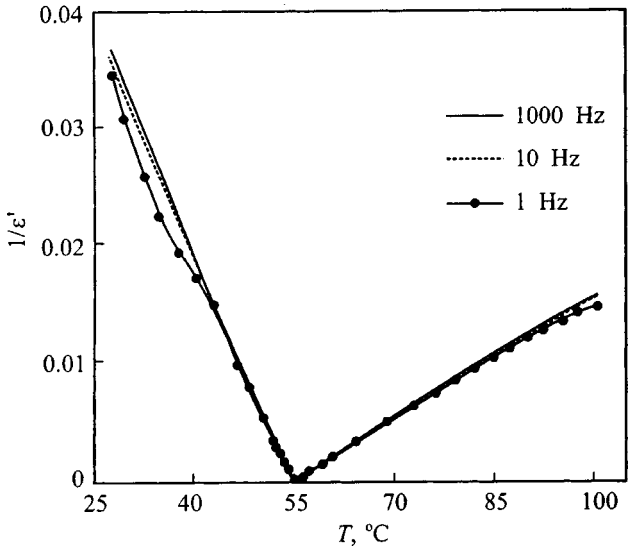

FIG. 3. Temperature dependence of the reciprocal of the permittivity of crystalline DTGS for a measurement field amplitude $E_0=0.2$ V/cm at frequencies $\nu=1$, 10 and Hz.

In conclusion, we note that the function $1/\varepsilon'=f(T)$ obeys the Curie–Weiss law for all the frequencies studied here (Fig. 3), with different deviations from it (spreading in the peak of ε') in the neighborhood of the phase transition, depending on the measurement frequency, the direction in which the phase transition is passed (i.e., a transition from the polar phase to the nonpolar, or *vice versa*), and, in general, the previous history of the crystal. Here the law of two (the ratio of the slopes $\partial(1/\varepsilon)\partial T$ above and below T_c equals two[8]) does not hold (as noted before for Rochelle salt[9]), while the ratio of the corresponding Curie–Weiss constants lies between 1.7 and 3. (See Table II.)

TABLE II. Data on the Curie–Weiss constants $\varepsilon'=C/(T-\Theta)$ of crystalline DTGS.

Crystal	T_k, K	$\omega/2\pi$, Hz	$-C^f$, K	C^p, K	$-C^p/C^f$
Heating DTGS to 125 °C	326.8	1000	3715	10065	2.71
after aging in the polar		10	3756	10060	2.68
phase ($h=5.8\cdot10^{-3}$ m)		1	3791	10055	2.65
Cooling DTGS after	327.8	1000	3604	10622	2.95
annealing in the nonpolar phase		10	3803	11020	2.9
($h=5.8\cdot10^{-3}$ m)		1	4012	11828	2.95
Heating DTGS to 100 °C	327.7	1000	2634	4950	1.88
after aging in the polar		10	2673	4942	1.85
phase ($h=5.8\cdot10^{-3}$ m)		1	2709	4917	1.82
Cooling DTGS without	328	1000	2761	4835	1.75
annealing in the nonpolar		10	2787	4859	1.74
phase ($h=5.8\cdot10^{-3}$ m)		1	2792	4874	1.75

Note. C^f and C^p are the Curie–Weiss constants for the polar (polydomain crystal) and nonpolar phases, respectively; h is the sample thickness.

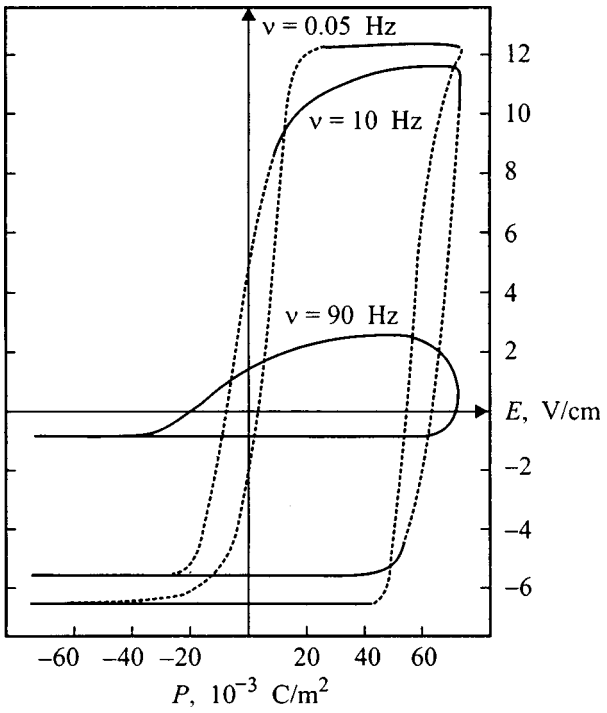

FIG. 4. Polarization loops of crystalline DTGS for a measurement field amplitude $E_0 = 74$ V/cm and temperature $T = 51.7\,^{\circ}$C, at frequencies $\nu = 1$, 10 and 1 Hz.

We emphasize that the high conductivity of crystalline DTGS after annealing in the paraelectric phase may, in particular, initiate unipolarity during the phase transition from the paraphase into the polar phase (Fig. 4).

We thank A. I. Baranov for useful discussions.

This work was supported by the Russian Foundation for Basic Research (Grant No. 98-02-16146) and the Scholarship Center Fund of the Ministry of Education of the Russian Federation for 1998.

E-mail: Shilnikov.001@volggasa.org

[1] A. I. Baranov, Izv. Akad. Nauk SSSR, Ser. Fiz. **51**, 21 (1987).
[2] N. D. Gavrilova, A. M. Lotonov, I. N. Medvedev, and V. K. Novik, *Ferroelectric and Piezoelectric Materials* [in Russian] (Izd-vo. Tverskogo un-ta., Tver, 1991).
[3] N. D. Gavrilova and A. M. Lotonov, Izv. Ross. Akad. Nauk, Ser. Fiz. **57**, 123 (1993).
[4] N. D. Gavrilova, V. K. Novik, and S. V. Pavlov, Izv. Ross. Akad. Nauk, Ser. Fiz. **57**, 128 (1993).
[5] A. V. Shil'nikov, E. G. Nadolinskaya, V. A. Fedorikhin, and S. V. Rodin, Kristallografiya **39**, 84 (1994).
[6] V. M. Gurevich, *Electrical Conductivity of Ferroelectric Materials* [in Russian] (Izd-vo. Komit. Standart. Mer Izmer. Prib. Sov. Min. SSSR, Moscow, 1969), 383 pp.
[7] L. Lydiard, *Ionic Conductivity in Crystals* [Russian translation] (Izd-vo. Inostr. Lit., Moscow, 1962), 220 pp.
[8] M. Lines and A. Glass, *Principle and Applications of Ferroelectrics and Related Materials* (Clarendon Press, Oxford, 1977) [Russian translation Mir, Moscow, 1981, 736 pp.].
[9] A. V. Shil'nikov, N. M. Galiyarova, E. G. Nadolinskaya, and S. V. Gorin, Kristallografiya **31**, 326 (1986).

Translated by D. H. McNeill

Structures responsible for quasisynchronism in second-harmonic generation in $BaTiO_3$:Fe

É. V. Bursian*) and V. G. Zalesskiĭ

Russian State Pedagogical University, 191186 St. Petersburg, Russia
(Submitted October 12, 1998)
Fiz. Tverd. Tela (St. Petersburg) **41**, 1076–1079 (June 1999)

Second harmonic generation (SHG) of light in iron-doped $BaTiO_3$ crystals occurs primarily at an angle of about 7° to incident $\lambda = 1.06\,\mu$m radiation. It is shown that the quasisynchronism is accounted for by a 90° domain structure with a spatial wave vector $\mathbf{q} \| [011]$ and a spatial period of about 3 μm. This result may serve as a basis for interpretation of the anomalous SHG enhancement near the phase transition. © *1999 American Institute of Physics.* [S1063-7834(99)03206-2]

The radiation obtained in barium titanate after frequency doubling (0.532 μm) was observed to exhibit a characteristic distribution in scattering angle. Its intensity reaches a maximum not in the direction of the incident radiation, $\mathbf{k}^{\omega}$, but rather at a small angle to the latter.[1,2]

A substantial enhancement of second-harmonic generation (SHG) efficiency has also been observed when the crystal is heated through the transition to the cubic phase, and a still larger one (by a few times) when moving in the reverse direction, i.e., when cooling through the transition. SHG in barium titanate is caused by spontaneous polarization $\mathbf{P}_s$, and it would thus seem that the second-harmonic intensity $I^{2\omega}$ should decrease with decreasing P_s as one approaches the transition; therefore the observed temperature dependence should be regarded as anomalous.[3]

The refractive indices of $BaTiO_3$ (at room temperature it is a uniaxial crystal with $4mm = C_{4v}$ symmetry) and the wave vector magnitudes at the YAG laser wavelength are listed in Table I.[4]

Thus, the wave synchronism in $BaTiO_3$ does not have any natural direction. Miller[5] therefore proposed as far back as 1964 to use periodic structures of antiparallel domains generated artificially by an electric field.

Later, for ferroelectrics a number of natural (i.e., existing without field application) structures were found which ensure momentum conservation $\mathbf{k}^{2\omega} = 2\mathbf{k}^{\omega} + \mathbf{q}$, where $\mathbf{q}$ is the wave vector of such structures.[6–10] Barium titanate is a ferroelectric with a complex domain pattern. The objective of this work was to identify the structure responsible for the quasisynchronism. We are going to show that SHG of a fairly high intensity in iron-doped $BaTiO_3$ crystals is due to a natural structure with 90° walls.

Crystalline platelets were grown by the Remeika method and contained an Fe impurity (1 wt% in the charge). They were cut along [100]-type crystallographic directions and were 0.2 mm thick. The sample was illuminated with unfocused YAG laser pulses ($\lambda = 1.064\,\mu$m). The pulses were 18 ns long, and the pulse energy was within 40 mJ, with an instability of about 10%. The beam diameter was approximately 3 mm. No electric field was applied to the crystal.

Figure 1 shows the second-harmonic intensity distribution $I^{2\omega}$ as a function of the angles φ and θ, which was derived by computer processing the signal obtained in scanning with a movable detector. In all cases, the directional response function contained two maxima along the direction (identified in Fig. 2 by the $\mathbf{Q}$ vector) at angles of $(7 \pm 1)°$ to that of incident radiation $\mathbf{k}^{\omega}$. As the crystal is rotated about the incident beam, the angular distribution $I^{2\omega}(\varphi, \theta)$ changes so that the $\mathbf{Q}$ line connecting the humps turns together with the crystal through the same angle. The height of the maxima in case *b* is about twice that in case *a*. As the crystal is turned through a small angle about axis 1 (Fig. 2a), one of the maxima decreases, and the other increases.

Scattering of weak cw radiation of frequency 2ω (i.e. without the $\omega \rightarrow 2\omega$ conversion) produces on the screen a band parallel to $\mathbf{Q}$. It does not exhibit any maxima within the 5–10° interval.

The laser light was polarized, with the direction of electric vector oscillations shown in Fig. 2. It was found that the second-harmonic polarization in cases *a* and *b* is parallel to the line $\mathbf{Q}$ connecting the humps, and if the crystal is turned through an angle other than 90°, the 2ω radiation is elliptically polarized.

An essential factor for interpretation of these observations is the symmetry of the optical nonlinearity tensor d_{ijk} in the equation for the second-harmonic field amplitude

$$E_i^{2\omega} \sim d_{ijk} E_j^{\omega} E_k^{\omega}. \tag{1}$$

The tensor d_{ijk} is similar to that of the piezoeffect, and after the alignment only the elements $d_{15} = d_{24}$, $d_{31} = d_{32}$, and d_{33} do not vanish for the $4mm$ symmetry. Direction 3 is chosen parallel to the optical axis. For barium titanate in the tetrag-

TABLE I. Room-temperature refractive indices and wave vectors for $BaTiO_3$.

λ, μm	n_0	n_e	k_0, μm^{-1}	k_e, μm^{-1}
1.064	2.3379	2.2970	13.81 ± 0.01	13.56
0.532	2.4760	2.4128	29.24	28.50

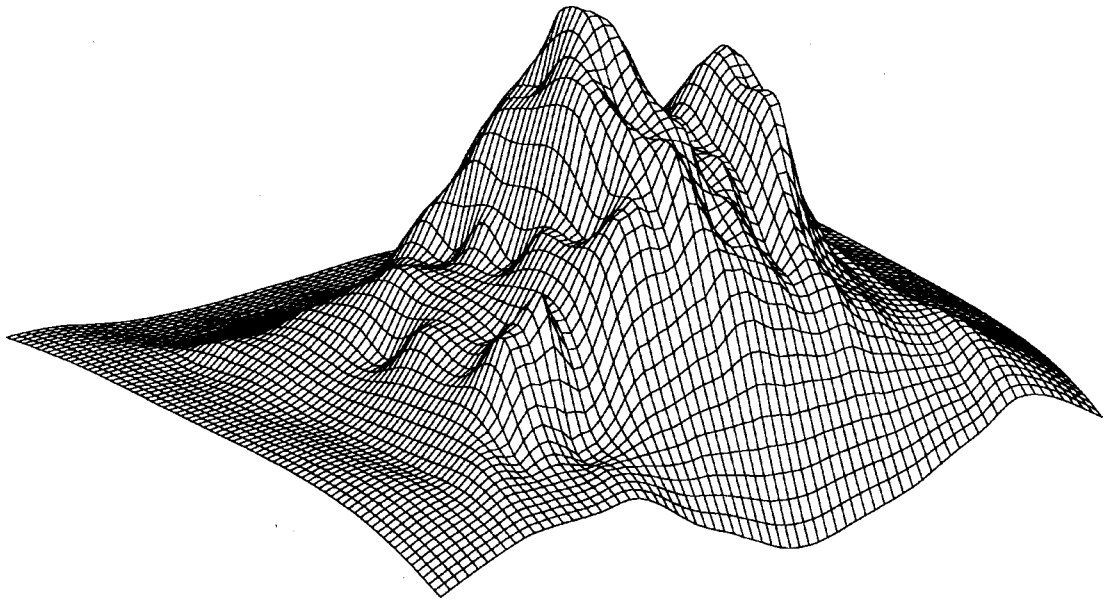

FIG. 1. Second-harmonic intensity distribution in scattering angle. The angular distance between the maxima is about 14–15°.

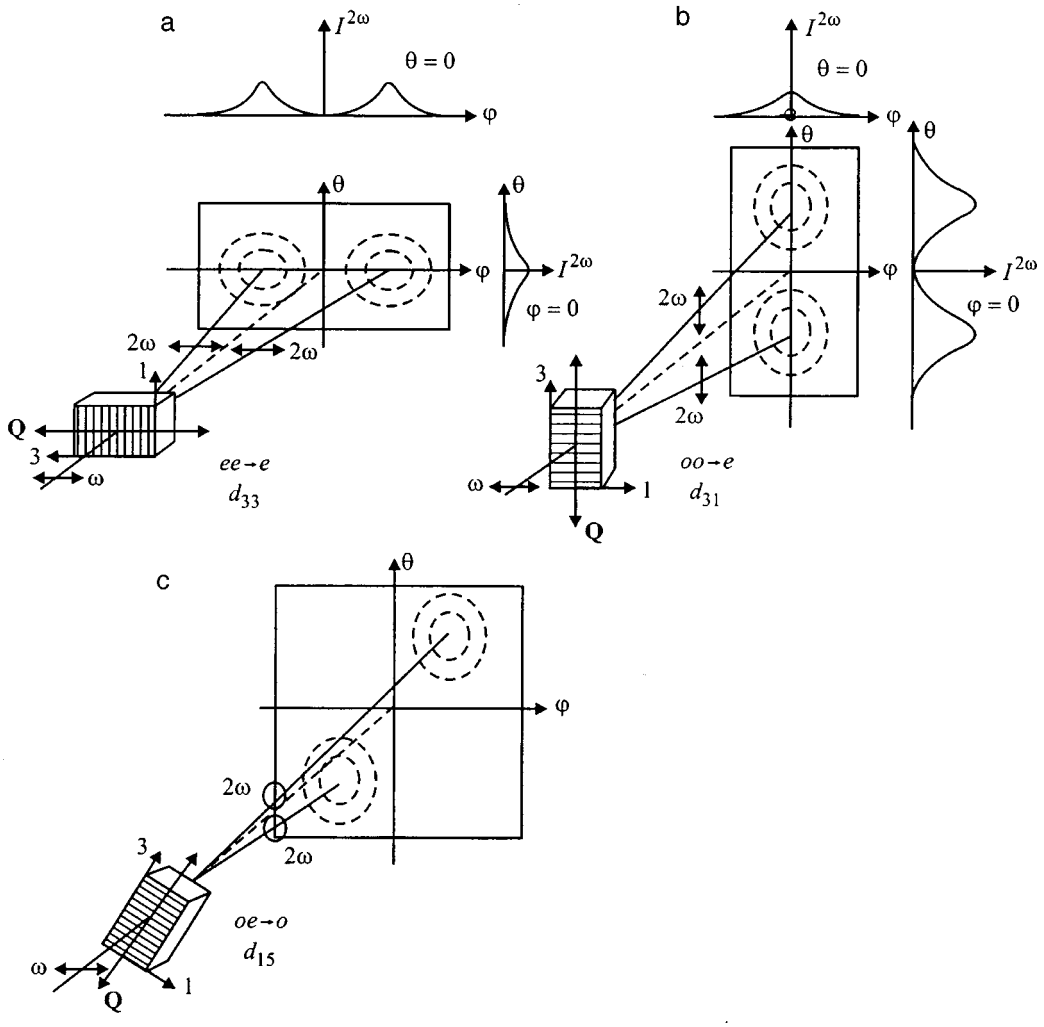

FIG. 2. Geometry of studies of the angular distribution of $I^{2\omega}$ for different crystal orientations with respect to the incident beam.

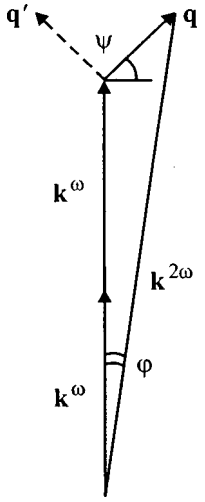

FIG. 3. Momentum conservation in SHG.

onal phase, $d_{31}=-19.33\times10^{-12}$ m/V, $d_{33}=-7.79\times10^{-12}$ m/V, and $d_{15}=17.85\times10^{-12}$ m/V.[4] Figure 2 presents the corresponding geometries for the case of spontaneous polarization $\mathbf{P}_s$ (which at the same time is the optical axis) directed perpendicular to the incident beam $\mathbf{k}^{\omega}$. The $\mathbf{P}_s\|\mathbf{k}^{\omega}$ case is not considered, because $\mathbf{E}^{2\omega}$ does not appear for symmetry considerations.

The direction of the optical axis ($\mathbf{P}_s$) can be determined from the fact that d_{31} is approximately twice d_{33}. Because the generation efficiency in case *b* in Fig. 2 is higher, the spontaneous polarization is always aligned with **Q**.

Thus, the *a* geometry in Fig. 2 corresponds to the case where the extraordinary ray of the second harmonic (e) is created due to that of the first harmonic (ee) and can be identified with coefficient d_{333} (d_{33}). The two other geometries relate to the schemes $(oo)\rightarrow e(d_{31})$ and $(oe)\rightarrow o(d_{15})$. In the latter case there are also $\mathbf{E}^{\omega}$ components along the 1 and 3 axes, i.e., coefficients d_{31} and d_{33}, which gives rise to elliptical polarization of the generated ray.

The predominant scattering to 7° (in a material this angle is $7°/n\approx3°$) implies that the vector **q** is involved in the process (in accordance with Fig. 3). The angle ψ can be found from the relation

$$\psi=\arctan\frac{k^{2\omega}-2k^{\omega}}{2k^{\omega}\varphi}. \tag{2}$$

Using the above figures for geometry *a* in Fig. 2 yields $\psi\approx41°$, and for geometry *b*, $\psi\approx54°$. This discrepancy is possibly associated with experimental errors and inaccuracies in the available values of n^{ω} and $n^{2\omega}$. Thus, the vector of the structure **q** is apparently directed at an angle close to 45° to the crystal surface. This structure is most probably connected with a periodic arrangement (with a high spatial frequency) of 90° walls (Fig. 4). This structure is frequently observed in barium titanate. The sharp wedges in an *a*-domain plate with polarization normal to the surface are usually induced at the surface by the electric field which is always present there. As follows from Fig. 3, the period of this structure is $\Lambda=2\pi/q=2\pi/[(k^{2\omega}-2k^{\omega})\sqrt{2}]\approx2-3\ \mu$m.

Judging from the diffuseness of the peaks in Fig. 1, the scatter in q is large enough, and the spectrum of q is almost continuous, but the SHG mechanism automatically chooses the spatial Fourier component from the domain structure of the type shown in Fig. 4 which is required for quasisynchronism to set in, although it partly involves components close to it as well.

One may ask an obvious question of whether this structure is stationary or forms only in the strong field of a laser pulse. Generally speaking, one observes in ferroelectrics laser-induced structures (see Ref. 11, as well as the recent papers Refs. 12 and 13). To find an answer to this question, special experiments with variation of the $\mathbf{E}^{\omega}$ amplitude were carried out. Decreasing $\mathbf{E}^{\omega}$ down to the threshold of second-harmonic generation, as well as varying the total irradiation dose by properly choosing the number of light pulses incident on the same region of the crystal did not produce any new results, which suggests that this structure is stationary at room temperature. At elevated temperatures this is apparently not so, and this is related somehow to the anomalously large magnitude of $I^{2\omega}$ near the phase transition. This aspect remains, however, unclear.

The authors owe their thanks to V. V. Maslov, V. V. Rychgorskiĭ, and A. A. Leshchev for fruitful discussions.

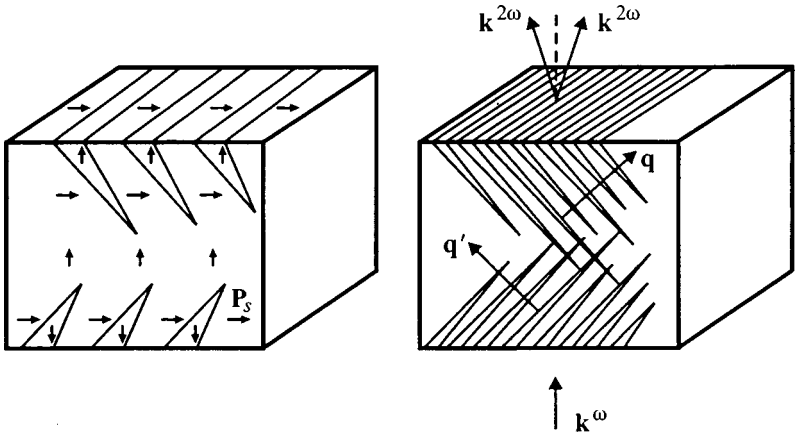

FIG. 4. The most probable domain structure responsible for the quasisynchronism in $BaTiO_3$:Fe crystals.

Support of the Russian Foundation for Basic Research (Grant 98-02-17934) is gratefully acknowledged.

*)Erik.Bursian@altavista.net

[1] É. V. Bursian, V. G. Zalesskiĭ, A. A. Luzhkov, and S. A. Flerova, *Abstracts of the International Conference on the Physics of Solid Dielectrics ''Dielectrics-97''* (St. Petersburg, 1997), Vol. 2, p. 137.
[2] É. V. Bursian, V. G. Zalesskiĭ, A. A. Luzhkov, and V. V. Maslov, JETP Lett. **64**, 270 (1996).
[3] V. G. Zalesskiĭ, V. V. Maslov, and É. V. Bursian, Izv. Ross. Akad. Nauk, Ser. Fiz. **60**(10), 63 (1996).
[4] S. Singh, in *Handbook of Lasers*, edited by R. J. Pressley (The Chemical Rubber Co., Cleveland, 1971), p. 489.
[5] R. C. A. Miller, Phys. Rev. **134**, A1313 (1964).
[6] D. Weinmann and H. Vogt, Phys. Status Solidi A **23**, 463 (1974).
[7] A. M. Arutyunyan, B. Bržesina, S. Kh. Esayan, and V. V. Lemanov, Fiz. Tverd. Tela (Leningrad) **24**, 1434 (1982) [Sov. Phys. Solid State **24**, 814 (1982)].
[8] S. Kh. Esayan, A. V. Kityk, and V. V. Lemanov, Fiz. Tverd. Tela (Leningrad) **29**, 1554 (1987) [Sov. Phys. Solid State **29**, 891 (1987)].
[9] M. M. Fejer, G. A. Magel, D. H. Jundt, and R. L. Byer, IEEE J. Quantum Electron. **28**, 2631 (1992).
[10] V. P. Moiseenko, I. I. Peters, V. I. Pastukhov, and V. N. Sharaĭchuk, Izv. Akad. Nauk SSSR, Ser. Fiz. **55**, 1033 (1991).
[11] S. V. Baryshnikov, É. V. Bursian, Ya. G. Girshberg, V. A. Lyakhovitskaya, and V. V. Maslov, Fiz. Tverd. Tela (St. Petersburg) **26**, 1872 (1984) [Phys. Solid State **26**, 1135 (1984)].
[12] A. K. Popov and V. V. Kimberg, Kvant. Elektron. (Moscow) **25**, 236 (1998).
[13] A. V. Golenishchev-Kutuzov and R. I. Kalimullin, Fiz. Tverd. Tela (St. Petersburg) **40**, 531 (1998) [Phys. Solid State **40**, 489 (1998)].

Translated by G. Skrebtsov

Orientational contribution to the piezoelectric constants of $BaTiO_3$ ceramic in ferroelectric phases with various symmetries

A. G. Luchaninov

Special Design Bureau ''Aurora,'' 400094 Volgograd, Russia

V. I. Aleshin

Scientific-Research Institute for Physics at Rostov-on-Don State University, 344082 Rostov-on-Don, Russia

L. A. Shuvalov

Institute of Crystallography, Russian Academy of Sciences, 117333 Moscow, Russia

(Submitted October 13, 1998)
Fiz. Tverd. Tela (St. Petersburg) **41**, 1080–1083 (June 1999)

A self-consistent method based on the interaction of a piezoelectric sphere with a piezoelectric medium that has anisotropic elastic and dielectric properties is used to calculate the components of the tensor piezoelectric modulus of $BaTiO_3$ ceramic in all three ferroelectric modifications. A comparison of the calculated and measured piezoelectric moduli shows that at least 60–70% of the piezoelectric effect in $BaTiO_3$ ceramic is caused by domain boundary movement throughout the entire ferroelectric region. © *1999 American Institute of Physics.* [S1063-7834(99)03306-7]

It is well known that the physical constants of polycrystalline ferroelectric materials include a so-called orientational contribution owing to reversible motion of domain boundaries. Estimating the magnitude of this contribution is one of the tasks of the physics of piezoceramics.[1] Calculations[2,3] show that the intrinsic piezoeffect associated with lattice deformations is comparatively small in $BaTiO_3$ ceramic, while the large piezoelectric moduli observed experimentally are caused by the domain mechanism. It follows from Ref. 3, for example, that the piezoelectric effect in ceramic samples of $BaTiO_3$ is more than 60–70% determined by vibrations of domain boundaries separating domains with mutually perpendicular spontaneous polarizations. Estimates[4] show that domain processes, together with movements of interphase boundaries, play an equally important role in lead zirconate titanate ceramic. For example, in niobium-modified lead zirconate titanate roughly 70% of the transverse piezoelectric modulus is caused by these processes.

These data[2–4] were obtained at room temperature. In practice, however, it is necessary to know (at least approximately) how important the orientational contribution is at different temperatures. In this paper we use a phenomenological theory to calculate the temperature dependence of the dielectric, elastic, and piezoelectric constants of single-crystal $BaTiO_3$ in its tetragonal, orthorhombic, and rhombohedral phases. Here an expansion of the thermodynamic potential of the form given in Ref. 5 was used. The expansion coefficients were taken from Ref. 6. Analytic expressions for the permittivity and piezoelectric modulus tensors are given in Ref. 7. The elastic compliances s_{ik}^E (for a constant field) are calculated using the following formulas: for the tetragonal phase $4mm$,

$$
\begin{aligned}
s_{11}^E &= s_{11}^P + 4Q_{12}^2 P_s^2 \chi_{33}^T,\\
s_{12}^E &= s_{12}^P + 4Q_{12}Q_{11}P_s^2\chi_{33}^T,\\
s_{13}^E &= s_{12}^P + 4Q_{12}^2 P_s^2 \chi_{33}^T,\\
s_{33}^E &= s_{11}^P + 4Q_{11}^2 P_s^2 \chi_{33}^T,\\
s_{44}^E &= s_{44}^P + Q_{44}^2 P_s^2 \chi_{11}^T,\\
s_{66}^E &= s_{44}^P;
\end{aligned}
\tag{1}
$$

for the orthorhombic phase $mm2$:

$$
\begin{aligned}
s_{11}^E &= s_{11}^P + 4Q_{12}^2 P_s^2 \chi_{33}^T,\\
s_{12}^E &= s_{12}^P + Q_{12}(2Q_{11}+2Q_{12}-Q_{44})P_s^2\chi_{33}^T,\\
s_{13}^E &= s_{12}^P + Q_{12}(2Q_{11}+2Q_{12}+Q_{44})P_s^2\chi_{33}^T,\\
s_{22}^E &= \frac{1}{4}(2s_{11}^P+2s_{12}^P+s_{44}^P)+\frac{1}{4}(2Q_{11}+2Q_{12}\\
&\quad -Q_{44})^2 P_s^2\chi_{33}^T,\\
s_{23}^E &= \frac{1}{4}(2s_{11}^P+2s_{12}^P-s_{44}^P)+\frac{1}{4}[(2Q_{11}+2Q_{12})^2\\
&\quad -Q_{44}^2]P_s^2\chi_{33}^T,\\
s_{33}^E &= \frac{1}{4}(2s_{11}^P+2s_{12}^P+s_{44}^P)+\frac{1}{4}(2Q_{11}+2Q_{12}\\
&\quad +Q_{44})^2 P_s^2\chi_{33}^T,\\
s_{44}^E &= 2s_{11}^P-2s_{12}^P+4(Q_{11}-Q_{12})^2 P_s^2\chi_{22}^T,\\
s_{55}^E &= s_{44}^P + Q_{44}^2 P_s^2 \chi_{11}^T,\\
s_{66}^E &= s_{44}^P;
\end{aligned}
\tag{2}
$$

and for the rhombohedral phase $3m$:

$$s_{11}^E=\frac{1}{4}(2s_{11}^P+2s_{12}^P+s_{44}^P)+\frac{1}{18}(2Q_{12}-2Q_{11}+Q_{44})^2P_s^2\chi_{11}^T+\frac{1}{9}(4Q_{12}+2Q_{11}-Q_{44})^2P_s^2\chi_{33}^T,$$

$$s_{12}^E=\frac{1}{12}(2s_{11}^P+10s_{12}^P-s_{44}^P)-\frac{1}{18}(2Q_{12}-2Q_{11}+Q_{44})^2P_s^2\chi_{11}^T+\frac{1}{9}(4Q_{12}+2Q_{11}-Q_{44})^2P_s^2\chi_{33}^T,$$

$$s_{13}^E=\frac{1}{6}(2s_{11}^P+4s_{12}^P-s_{44}^P)+\frac{2}{9}(4Q_{12}+2Q_{11}-Q_{44})\times(2Q_{12}+Q_{11}+Q_{44})P_s^2\chi_{33}^T,$$

$$s_{14}^E=\frac{\sqrt{2}}{6}(2s_{11}^P-2s_{12}^P-s_{44}^P)+\frac{\sqrt{2}}{18}(2Q_{11}-2Q_{12}-Q_{44})\times(4Q_{11}-4Q_{12}+Q_{44})P_s^2\chi_{11}^T,$$

$$s_{33}^E=\frac{1}{3}(s_{11}^P+2s_{12}^P+s_{44}^P)+\frac{4}{9}(Q_{11}+2Q_{12}+Q_{44})^2P_s^2\chi_{33}^T$$

$$s_{44}^E=\frac{1}{3}(4s_{11}^P-4s_{12}^P+s_{44}^P)+\frac{1}{9}(4Q_{11}-4Q_{12}+Q_{44})^2P_s^2\chi_{11}^T, \quad (3)$$

where Q is the coefficient of electrostriction, χ_{kk}^T is the permittivity of a mechanically free crystal, P_s is the spontaneous polarization, and the s_{ik}^P are the elastic compliances for constant polarization.

The components of the piezoelectric moduli of $BaTiO_3$ ceramic which are determined by the intrinsic piezoeffect in single domain crystallites (these components are sometimes referred to as intrinsic[1]) can be calculated quite accurately using a suitable averaging procedure. Of the known averaging techniques, the most correct are the self-consistent methods proposed in Refs. 8–10, which make it possible to include the piezoelectric interaction between crystallites,[8] possible anisotropies (dielectric and elastic) in the ceramic,[9] and the presence of a piezoelectric effect in the medium.[10] These methods are based on solving the problem of the interaction of a piezoelectric sphere with an isotropic (in its elastic and dielectric properties) nonpiezoelectric medium,[8] with an anisotropic nonpiezoelectric medium,[9] and with an anisotropic piezoelectric medium.[10] The magnitude of the orientational component can be estimated as the difference between the experimental and calculated piezoelectric moduli.

In this paper we use the averaging scheme of Ref. 10, which is the most rigorous and systematic, for calculating the lattice piezoelectric moduli of $BaTiO_3$ piezoceramic in the different ferroelectric phases. In this approximation, the piezoelectric moduli of the polarized ceramic can be found using the corresponding general equations (valid for arbitrary symmetry of the crystallites and for an arbitrary distribution of their orientations)[10] relating the piezoelectric moduli of the ceramic and the piezoelectric moduli of the single crystal. For textures with axial symmetry, such as a polarized ferroelectric ceramic, these equations simplify to the following:

$$\varepsilon_{11}^{*T}=(g_{15}\varepsilon_{11}^{*T}+\beta_{44}d_{15}^*)\lambda_{15}+(1+\alpha_{11}\varepsilon_{11}^{*T}+g_{15}d_{15}^*)\mu_{11},$$

$$\varepsilon_{33}^{*T}=2(g_{31}\varepsilon_{33}^{*T}+\beta_{13}d_{33}^*+\beta_{11}d_{31}^*+\beta_{12}d_{31}^*)\lambda_{31}+(g_{33}\varepsilon_{33}^{*T}+\beta_{33}d_{33}^*+2\beta_{13}d_{31}^*)\lambda_{33}+(1+\alpha_{33}\varepsilon_{33}^{*T}+g_{33}d_{33}^*+2g_{31}d_{31}^*)\mu_{33},$$

$$d_{31}^*=(1+\alpha_{33}\varepsilon_{33}^{*T}+g_{33}d_{33}^*+2g_{31}d_{31}^*)\lambda_{31}+(g_{31}\varepsilon_{33}^{*T}+\beta_{12}d_{31}^*+\beta_{13}d_{33}^*+\beta_{11}d_{31}^*)\chi_{11}+(g_{31}\varepsilon_{33}^{*T}+\beta_{12}d_{31}^*+\beta_{13}d_{33}^*+\beta_{11}d_{31}^*),$$

$$d_{33}^*=(1+\alpha_{33}\varepsilon_{33}^{*T}+g_{33}d_{33}^*+2g_{31}d_{31}^*)\lambda_{33}+(g_{33}\varepsilon_{33}^{*T}+\beta_{33}d_{33}^*+2\beta_{13}d_{31}^*)\chi_{33}+2(g_{31}\varepsilon_{33}^{*T}+\beta_{13}d_{33}^*+\beta_{11}d_{31}^*+\beta_{12}d_{31}^*)\chi_{13},$$

$$d_{15}^*=(1+\alpha_{11}\varepsilon_{11}^{*T}+g_{15}d_{15}^*)\lambda_{15}+(g_{15}\varepsilon_{11}^{*T}+\beta_{44}d_{15}^*)\chi_{44},$$

$$s_{12}^{*E}=(\alpha_{33}d_{31}^*+g_{31}s_{12}^{*E}+g_{31}s_{11}^{*E}+g_{33}s_{13}^{*E})\lambda_{31}+(g_{31}d_{31}^*+\beta_{13}s_{13}^{*E}+\beta_{12}s_{11}^{*E}+\beta_{11}s_{12}^{*E})\chi_{11}+(1+g_{31}d_{31}^*+\beta_{12}s_{12}^{*E}+\beta_{13}s_{13}^{*E}+\beta_{11}s_{11}^{*E})\chi_{12}+(g_{33}d_{31}^*+\beta_{13}s_{11}^{*E}+\beta_{33}s_{13}^{*E}+\beta_{13}s_{12}^{*E})\chi_{13},$$

$$s_{13}^{*E}=(\alpha_{33}d_{33}^*+g_{33}s_{33}^{*E}+2g_{31}s_{13}^{*E})\lambda_{31}+(g_{31}d_{33}^*+\beta_{13}s_{33}^{*E}+\beta_{12}s_{13}^{*E}+\beta_{11}s_{13}^{*E})\chi_{11}+(g_{31}d_{33}^*+\beta_{12}s_{13}^{*E}+\beta_{13}s_{33}^{*E}+\beta_{11}s_{13}^{*E})\chi_{12}+(1+g_{33}d_{33}^*+\beta_{33}s_{33}^{*E}+2\beta_{13}s_{13}^{*E})\chi_{13},$$

$$s_{11}^{*E}=(\alpha_{33}d_{31}^*+g_{31}s_{12}^{*E}+g_{31}s_{11}^{*E}+g_{33}s_{13}^{*E})\lambda_{31}+(1+g_{31}d_{31}^*+\beta_{12}s_{12}^{*E}+\beta_{13}s_{13}^{*E}+\beta_{11}s_{11}^{*E})\chi_{11}+(g_{31}d_{31}^*+\beta_{13}s_{13}^{*E}+\beta_{12}s_{11}^{*E}+\beta_{11}s_{12}^{*E})\chi_{12}+(g_{33}d_{31}^*+\beta_{13}s_{11}^{*E}+\beta_{33}s_{13}^{*E}+\beta_{13}s_{12}^{*E})\chi_{13},$$

$$s_{33}^{*E}=(\alpha_{33}d_{33}^*+g_{33}s_{33}^{*E}+2g_{31}s_{13}^{*E})\lambda_{33}+(1+g_{33}d_{33}^*+\beta_{33}s_{33}^{*E}+2\beta_{13}s_{13}^{*E})\chi_{33}+2(g_{31}d_{33}^*+\beta_{13}s_{33}^{*E}+\beta_{11}s_{13}^{*E}+\beta_{12}s_{13}^{*E})\chi_{13},$$

$$s_{55}^{*E}=(\alpha_{11}d_{15}^*+g_{15}s_{55}^{*E})\lambda_{15}+(1+g_{15}d_{15}^*+\beta_{44}s_{55}^{*E})\chi_{44}. \quad (4)$$

In Eqs. (4), ε_{kk}^{*T} is the permittivity of the ceramic under constant mechanical stress, s_{ik}^{*E} is the elastic compliance of the ceramic in a constant electric field, d_{ik}^* is the piezoelectric modulus of the ceramic. α, β, and g are the matrices of the depolarizing coefficients, and μ, λ, and χ are matrices which account for the orientational distribution of the crystallites. The matrix elements α, β, and g are rather complicated functions of the tensors ε_{kk}^{*T}, s_{ik}^{*E}, and d_{ik}^* which are to be determined. The elements of the matrices μ, λ, and

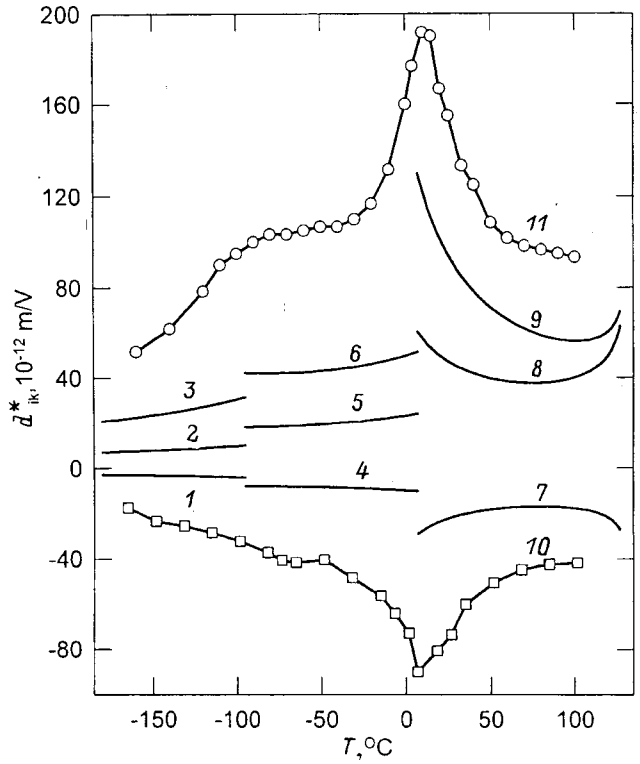

FIG. 1. Piezoelectric moduli of $BaTiO_3$ ceramic as functions of temperature. The calculations are done by a self-consistent method including the anisotropy and piezoeffect of the medium. In the tetragonal phase, 1/6 of the domains participate in 180-degree reorientation, in the orthorhombic phase, 1/12, and in the rhombohedral phase, 1/8. *1, 4, 7, 10*—d^*_{31}; *2, 5, 8, 11*—d^*_{33}; *3, 6, 9*—d^*_{15}. *1–9*—computational results; *10, 11*—experimental data.

χ depend on ε^{*T}_{kk}, s^{*E}_{ik} and d^*_{ik}, as well as on the constants of the single crystal. Algorithms for calculating the elements of these matrices are given in Ref. 11.

In taking the average, the fraction of 90-degree reorientations in $BaTiO_3$ ceramic was neglected for simplicity and in accordance with experiment, which shows that it is relatively small. (This simplification does not affect the essence or generality of the conclusions reached from a discussion of the results.) Thus, the polarization process can be treated in the tetragonal phase, as a change to the opposite orientation by 1/6 of the domains in a given ceramic and in the orthorhombic and rhombohedral phases, respectively, by 1/12 and 1/8 of the domains.

The system of nonlinear equations (4) for the unknowns ε^{*T}_{kk}, s^{*E}_{ik} and d^*_{ik} was solved by successive approximations. The results of the calculations are shown in Fig. 1. Also shown in this figure are some experimental data for the transverse piezoelectric modulus d^*_{31} measured by the resonance–antiresonance method and for the longitudinal piezoelectric modulus d^*_{33} measured by a quasistatic method at a frequency of 78 Hz. The measurements were made on well aged (roughly 5 years), large-grain $BaTiO_3$ ceramic prepared using standard techniques from commercial grade raw materials.

It is clear from the figure that, in all the ferroelectric phases, the calculated piezoelectric moduli lie well below the experimental data. There is no doubt that the origin of the difference between the calculated and experimental values of the piezoelectric moduli of the polarized ceramic in the rhombohedral and orthorhombic phases is the same as that of the corresponding differences in the tetragonal phase at room temperature, which[1–3] are caused by domain processes. It should be noted that the room-temperature piezoelectric moduli calculated here ($d^*_{31}=-22\times10^{-12}$, $d^*_{33}=55\times10^{-12}$, and $d^*_{15}=109\times10^{-12}$ m/V) are in satisfactory agreement with the data of Ref. 3 ($d^*_{31}=-25\times10^{-12}$, $d^*_{33}=47\times10^{-12}$, and $d^*_{15}=94\times10^{-12}$ m/V) and Ref. 3 ($d^*_{31}=-28.3\times10^{-12}$, $d^*_{33}=71\times10^{-12}$, and $d^*_{15}=119\times10^{-12}$ m/V). A comparison with experimental data over the entire range of existence of the tetragonal phase yields roughly the same estimate (60–70%) for the contribution from the orientational component as Ref. 3. As the figure shows, the differences between the calculated and experimental piezoelectric moduli are especially huge in the orthorhombic and rhombohedral phases, so the contribution of the orientational component is considerably larger than in the tetragonal phase. For example, at the midpoint (−50 °C) of the orthorhombic region, the calculation gives $d^*_{31}=-8.3\times10^{-12}$ and $d^*_{33}=19\times10^{-12}$ m/V, while the experiment gives $d^*_{31}=-41\times10^{-12}$ and $d^*_{33}=106\times10^{-12}$ m/V. Correspondingly, for the midpoint (−130 °C) of the rhombohedral region, we have $d^*_{31}=-3.4\times10^{-12}$ and $d^*_{33}=8.4\times10^{-12}$ m/V and $d^*_{31}=-25\times10^{-12}$ and $d^*_{33}=70\times10^{-12}$ m/V. A comparison shows that roughly 80% of the piezoeffect is caused by domain processes in the orthorhombic phase and roughly 85% in the rhombohedral phase. The large contribution from reversible domain boundary motion in these phases is apparently caused by a larger number of possible directions for the spontaneous polarization than in the tetragonal phase and, therefore, by a more complicated domain structure.

This work was supported by the Russian Foundation for Basic Research (grants No. 95-02-06295, 95-02-06366a, and 96-15-96504).

[1] V. A. Isupov, Ferroelectrics **12**, 141 (1976).
[2] A. V. Turik and A. I. Chernobabov, Zh. Tekh. Fiz. **47**, 1944 (1977) [Sov. Phys. Tech. Phys. **22**, 1127 (1977)].
[3] A. G. Luchaninov, L. Z. Potikha, and V. A. Rogozin, Zh. Tekh. Fiz. **50**, 616 (1980) [Sov. Phys. Tech. Phys. **25**, 368 (1980)].
[4] A. G. Luchaninov, A. V. Shil'nikov, L. A. Shuvalov, and I. Ju. Shipkova, Ferroelectrics **98**, 123 (1989).
[5] G. A. Smolenskiĭ, V. A. Bokov, V. A. Isupov, *et al.*, *The Physics of Ferroelectric Phenomena* [in Russian], Nauka, Leningrad (1985).
[6] J. Daniels, Phys. Status Solidi A **21**, 497 (1974).
[7] A. G. Luchaninov, A. V. Shil'nikov, and L. A. Shuvalov, Izv. Ross. Akad. Nauk, Ser. Fiz. **68**, 1563 (1998).
[8] M. Marutake, J. Phys. Soc. Jpn. **11**, 807 (1956).
[9] V. I. Aleshin, Kristallografiya **32**, 422 (1987).
[10] V. I. Aleshin, Kristallografiya **36**, 1352 (1991).
[11] V. I. Aleshin, Deposited in VINITI, reg. No. 3902–V88.

Translated by D. H. McNeill

Evolution of the structure of Rb_2ZnCl_4 over the temperature range 4.2–310 K

B. Sh. Bagautdinov*) and V. Sh. Shekhtman

Institute of Solid State Physics, Russian Academy of Sciences, 142432 Chernogolovka, Moscow Region, Russia

(Submitted July 17, 1998; in final form October 26, 1998)
Fiz. Tverd. Tela (St. Petersburg) **41**, 1084–1090 (June 1999)

X-ray diffraction is used to study the temperature dependence of the lattice parameters and the sequence of structural realignments in crystalline Rb_2ZnCl_4 over temperatures of 4.2–310 K. The appearance of and changes in the system of satellite reflexes indicative of structural ordering are studied. Below 74 K, on going into the monoclinic phase (space group $A11a$), anomalies are observed in the behavior of the lattice parameters, and superstructural reflexes develop with wave vectors $\mathbf{q}=\mathbf{a}^*/3+\mathbf{b}^*/2+\mathbf{c}^*/2$ corresponding to an increase by a large factor in initial parameters *a*, *b*, and *c* of the *Pnma*-phase. © *1999 American Institute of Physics.* [S1063-7834(99)03406-1]

Rubidium tetrachlorzincate Rb_2ZnCl_4 belongs to the β-K_2SO_4 structural type with a general formula A_2BX_4, where A is an alkali metal and BX_4 are tetrahedral groups. Like many crystals of this family, during cooling Rb_2ZnCl_4 undergoes a series of phase transitions, which are listed in Table I. The sequence of phase transitions is normal-incommensurate-commensurate phase, which has been studied in some detail;[1] the data on the low-temperature phase transition at 74 K (monoclinic phase IV) are incomplete and contradictory. Thus, a symmetry analysis[2] based on the hexagonal protophase $P6_3/mmc$ assumes three possible space groups for the low-temperature monoclinic phase: $P11a$, $A11a$, and $P1$. Some Raman spectroscopy data[3,4] imply that the cell size is doubled below 74.6 K compared to the commensurate phase III and the space group becomes $P12_11$ ($Z=24$). According to measurements of the dielectric characteristics, the phase below 74 K is ferroelectric with polarization along the **a** and **b** axes, so in this case a $P11a$ space group has been proposed.[5,6] An NMR study of the Cl atoms in crystalline Rb_2ZnCl_4,[7] as well as molecular dynamics calculations,[8] showed that the symmetry of phase IV is monoclinic $A11a$. The structure of phase IV at 60 K has been determined by neutron diffraction to be of the $Pna2_1$ space group, neglecting the multiplication of the unit cell below 74 K.[9] Later neutron studies below 74 K detected superstructural reflexes at the $(0,\ k+1/2,\ l+1/2)$ sites.[10,11] Recent Raman studies have revealed the formation of new modes at 80 and 50 K, which are the basis for the proposed possible existence of a new incommensurate phase in this temperature range.[12,13] Note that an additional low temperature incommensurate phase in crystals of the A_2BX_4 family has been observed previously only in crystalline K_2ZnCl_4 by neutron diffraction.[10,14,15] Later synchrotron x-ray studies failed to confirm the incommensurate character of this phase.[16]

A reliable explanation for the sequence of phase transitions in crystalline Rb_2ZnCl_4 as a model object is important for understanding the behavior of the A_2BX_4 ferroelectric family. Studies of the low-temperature phase IV, for which x-ray data are current lacking, require special attention. For this purpose, in this paper we have undertaken a systematic x-ray diffraction study of the configuration of the reciprocal lattice and measured the interplanar distances over a wide temperature range, 4.2–310 K.

1. EXPERIMENT

Samples were cut from a crystal of Rb_2ZnCl_4 grown from a water solution by evaporation at 297 K. Optical transparent single-crystal (100), (010), and (001) cuts with dimensions of $2\times1.5\times0.3$ mm^3 were used. For the measurements the samples were placed in a helium cryostat with temperature regulation to within 0.1 K. The measurements were made on a Siemens (Bruker) D500 diffractometer

TABLE I. Sequence of phase transitions in Rb_2ZnCl_4.

Phase transition temp.	$T_1=74$ K	$T_c=192$ K	$T_i=303$ K	
Phase	IV	III	II	I
Space group	$A11a$	$P(Pn21a:-1-1s)$	$P(Pnma:-1ss)$	$Pnma$
Cell parameters	$a'=3a$	$a'=3a$	$a'\sim3a$	$a=9.272$ Å
	$b'=2b$	$b'=b$	$b'=b$	$b=7.285$ Å
	$c'=2c$	$c'=c$	$c'=c$	$c=12.733$ Å
Wave vector	$(1/3)a^*+(b^*+c^*)/2$	$(1/3)a^*$	$(1/3-\delta)a^*$	
Formula number	$Z=48$	$Z=12$		$Z=4$

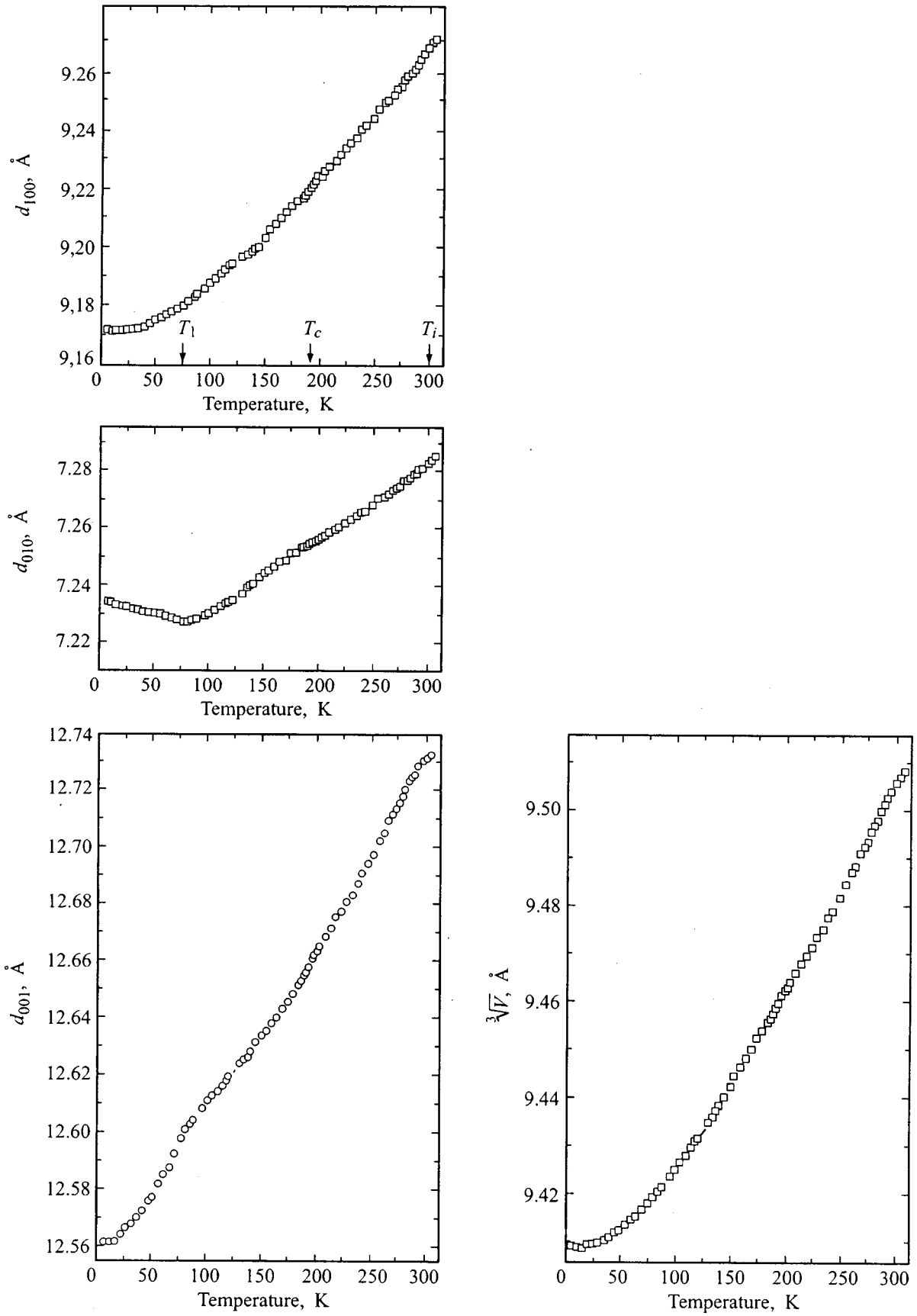

FIG. 1. Temperature variations in the interplanar distances d_{100}, d_{010}, and d_{001} and the volume of crystalline Rb_2ZnCl_4. The measurements were taken as the sample was heated.

TABLE II. Coefficients of thermal expansion within temperature intervals of the four phases of Rb_2ZnCl_4 ($\times 10^{-5}$ K^{-1}).

Space group, temperature interval	α_{100}	α_{010}	α_{001}
Pnma 363−310 K [Ref. 17]	4.38	6.00	4.95
$P(Pnma{:}-1ss)$ 303−195 K	4.68	3.56	5.43
$P(Pn2_1a{:}-1-1s)$ 192−74 K	3.86	3.33	3.92
*A*11*a* 74−4.2 K	1.37	−1.30	11.20

(Cu K_α-radiation) equipped with a two-circle goniometer. The apparatus could record the intensity for $\theta/2\theta$ and θ scan regimes and along an undistorted mesh of the reciprocal lattice (*q*-scanning). Charts of the two dimensional distributions of the intensity in given sectors of the reciprocal lattice were recorded using a computer program based on the previously measured parameters of the crystal lattice. The interplanar distances along the crystallographic axes of the initial high temperature phase were determined from the centers of gravity of the Bragg reflections $(12,0,0)$, (080), and $(0,0,16)$ recorded in a $\theta/2\theta$ configuration. The measurement accuracy was better than 1.4×10^{-4} Å. Before each scan of the diffraction reflex intensity profile, the sample was held for ~10 min at the specified temperature. An analysis of the extinctions of the diffraction peaks and a search for satellite reflexes were conducted by scanning in the $(\mathbf{a}^*\mathbf{b}^*0)$, $(0\,\mathbf{b}^*\mathbf{c}^*)$ and $(\mathbf{a}^*0\,\mathbf{c}^*)$ nodal planes.

2. RESULTS AND DISCUSSION

Temperature variation in the interplanar distances. Data from the measurements of the interplanar distances d_{100}, d_{010}, and d_{001} and of the cell volume from 4.2 to 310 K are shown in Fig. 1. In the initial *Pnma* phase, above T_i the structure of crystalline Rb_2ZnCl_4 (β-K_2SO_4 type) was characterized by the lattice parameters $a=9.272(2)$ Å, $b=7.285(3)$ Å, and $c=12.733(2)$ Å. The relation $c\sim\sqrt{3}b$ provides an indication of the hexagonal paraphase by analogy with related compounds in the β-K_2SO_4 family, although, prior to melting at ~810 K, no transition into a hexagonal phase was observed for Rb_2ZnCl_4. Values of the coefficients of thermal expansion corresponding to the regions where these phases exist are listed in Table II together with published data[17] for the interval 310–363 K. The measurements revealed no noticeable features at the temperature points T_i and T_c (Fig. 1). Clearly distinct anomalies are observed in the neighborhood of the third phase transition at $T_1=74$ K on the **b** and **c** axes. The discontinuities in the coefficient of thermal expansion near 74 K indicate a second-order phase transition. One noteworthy feature is the development of a negative coefficient of thermal expansion along the **b** axis over the entire range of existence of the low-temperature phase. Similar behavior in the coefficient of thermal expansion along the crystallographic **b** axis has been observed in the monoclinic phase for the related crystal K_2ZnCl_4.[18] Note that in the elementary cell of β-K_2SO_4, perpendicular to the smallest parameter *b* there are two mirror *m* planes (at levels of $1/4b$ and $3/4b$), on which all the atoms of the cell A_2BX_4 ($Z=4$) lie, except for eight X atoms belonging to positions of the general configuration. This layered structure is then distorted negligibly in the regions of the incommensurate II and commensurate III phases. According to structural data for the related crystal K_2CoCl_4,[19] in the monoclinic phase the atoms are displaced parallel to the **b** axis. It is possible that a similar displacement in Rb_2ZnCl_4 leads to ''distension'' of the **b** axis during cooling of the crystal. Observations of a soft mode during neutron diffraction studies in the neighborhood of this phase transition[10,11] are further evidence of oriented atomic displacements in crystalline Rb_2ZnCl_4 at 74 K.

Evolution of the incommensurate II–commensurate III phases. The configuration of the reciprocal lattice of Rb_2ZnCl_4 undergoes substantial transformations in all the phase transitions. This shows up especially in the appearance of and changes in the additional (satellite and superstructural) reflexes. Below $T_i=303$ K satellite reflexes show up in a diffraction experiment. Let us consider the development of satellites in the reflection plane $(hk0)$ shown in Fig. 2. The satellites in this plane are associated with ordering of the orientations of the tetrahedrons and displacements of the Rb atoms, which are perpendicular to the **c** axis.[20] The first-order satellite reflexes lie near $\mathbf{G}_{200}/3$ positions and not around $\mathbf{G}_{100}/3$, where $\mathbf{G}_{200}$ denotes the vector of the inverse 200 lattice of the initial normal *Pnma*-phase with respect to the direction of the grazing reflection plane along the **a** axis. In the incommensurate phase, as the temperature is reduced, there is an increase in intensity and a shift in the position of the satellite reflexes, and new higher-order satellites appear. The temperature behavior of the incommensurability parameter δ determined from the position of the first-order satellite $(2/3+\delta,6,0)$ is shown in Fig. 3. In the low-temperature portion of the incommensurate phase, satellites of higher harmonics are observed, ranging from 2nd order at 240 K to 5-th near the phase transition into the commensurate phase. This indicates that, as the amplitudes of the atomic modulations increase, the harmonics at a higher level are damped to form domain-like structures.[21,22] Satellites of order *m* lie at the positions $\mathbf{G}\pm m(2/3+\delta)a^*$, where **G** is the Bragg reflex from which the *m*-th satellite develops. Satellites of order 2, 4, and 5 were observed around the primary satellite reflexes. These positions lie in the region of the expanded Brillouin zone and correspond to distortions in the structure associated with the damping of the optical Σ_2 mode. The asymmetry in the neighborhood of the first-order satellites is related to the effect of the harmonics on the structural distortions. Harmonics 4 and 7, which lie at larger reflection angles relative to the $(2/3+\delta)\mathbf{a}^*$ satellite, are considerably smaller than the harmonics 2 and 5 recorded on the smaller-angle side. Unlike the primary satellites, the Bragg reflexes $(hk0)$ have symmetric surroundings on both sides from 3rd order satellites associated, respectively with the $(2\pm h,k,0)$ reflexes. These satellites extend into the region of the normal Brillouin zone and correspond to the acoustic Σ_3 mode. Distortions in harmonic 3 of the Σ_3 mode with $\mathbf{q}=3\delta\mathbf{a}^*$ deter-

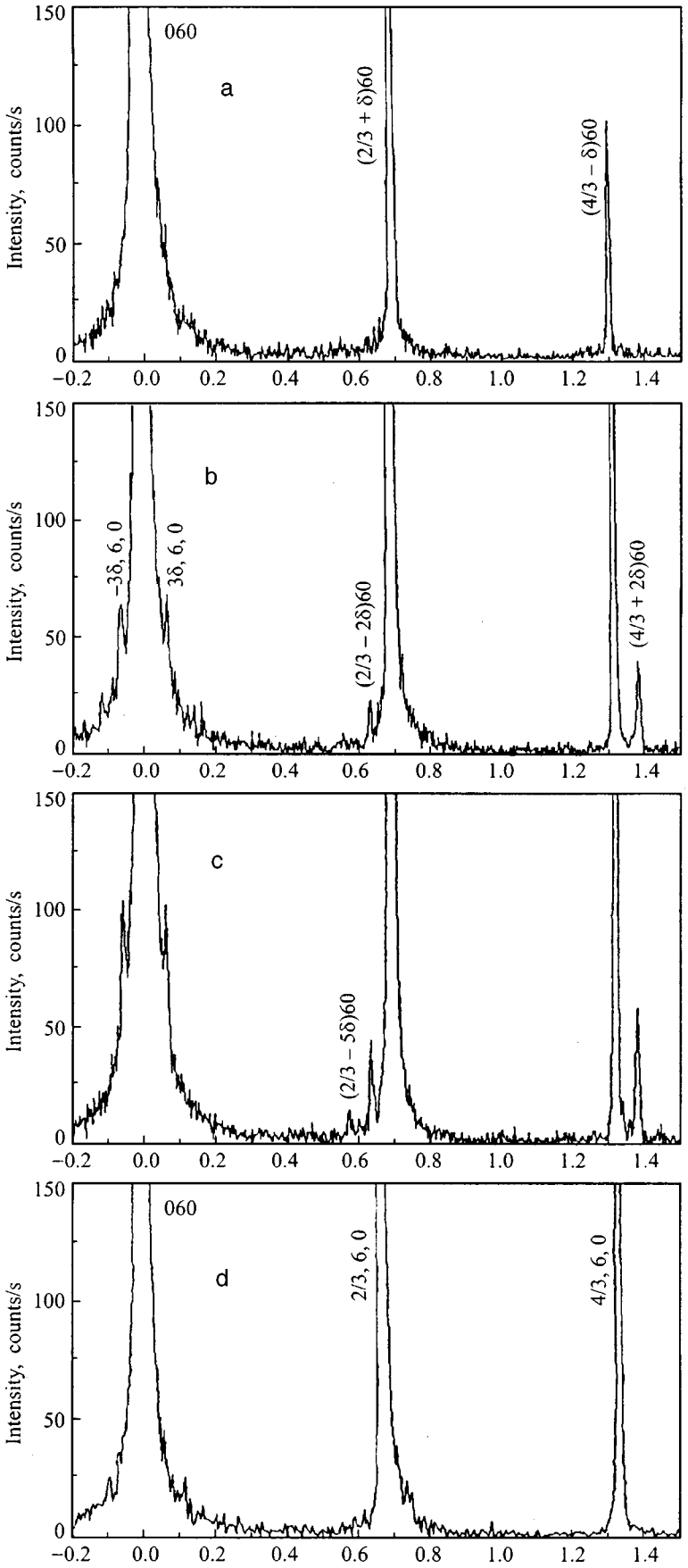

FIG. 2. Position of the Bragg (060) and satellite reflexes along the nodal series ($h60$) at temperatures of 293 (a), 210 (b), 204 (c), and 190 K (d).

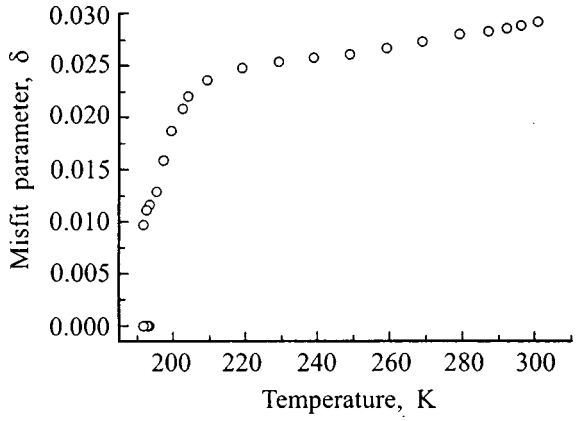

FIG. 3. Temperature dependence of the incommensurability parameter δ.

mine the sinusoidal polarization of the incommensurate phase near the lock-in transition, while in the ferroelectric phase, having transformed into displacements of the B_{2u} mode, they determine the polarization along the b axis.[21] The structure of the incommensurate phase of Rb_2ZnCl_4 has been determined[20] at 210 K in a harmonic approximation, i.e., taking the intensities of only the 1st order satellite reflections into account. Recording the higher harmonics of the satellite reflexes shows that the real structural distortions are described by a superposition of the Σ_2 optical (harmonics 1, 4, and 5) and Σ_3 acoustic (harmonics 3) modes. During cooling the satellites approach rational positions and merge discontinuously into superstructural reflexes corresponding to a wave vector $\mathbf{q}=1/3\mathbf{a}^*$ at 192 K, where $\delta=0$ (Fig. 2). The character of the first order lock-in transition is also indicated by the splitting of the first satellite reflex in the hysteresis region.[23]

Less intense satellites were recorded in the $(h01)$ plane (Fig. 4). In the region of phases II and III, these satellites are not sensitive to displacements of the Rb atoms in the perpendicular direction, so they only contain information about the ordering of the $ZnCl_4$ groups. In this plane the satellites are located at positions close to $\mathbf{G}_{100}/3$ in the direction of the **a** axis. No satellites of higher harmonics were observed in this reflecting plane. In the region of the low-temperature monoclinic phase, satellites in the $(h0l)$ plane become more intense, perhaps because the contribution from displacements of Rb atoms is turned on.

In all the temperature region above 74 K, conditions corresponding to the grazing planes **a** $(hk0:h=2n)$ and **n** $(0kl:k+1=2n)$ were observed for the Bragg reflections. The condition of a grazing plane **a** below 192 K is retained, including a tripling of the translational component along the **a** axis. These conditions are consistent with the space groups of the normal *Pnma* phase, the averaged *Pnma* structure in the incommensurate phase, and the polar $Pn2_1a$ phase (Table I).

Space group of phase IV. The condition for existence of $hk0:h=2n$ phases below 74 K indicates the maintenance of a grazing reflection plane **a**, perpendicular to the **c** axis, in the low-temperature monoclinic phase, as well. This phase is characterized by a transformation of the reciprocal lattice

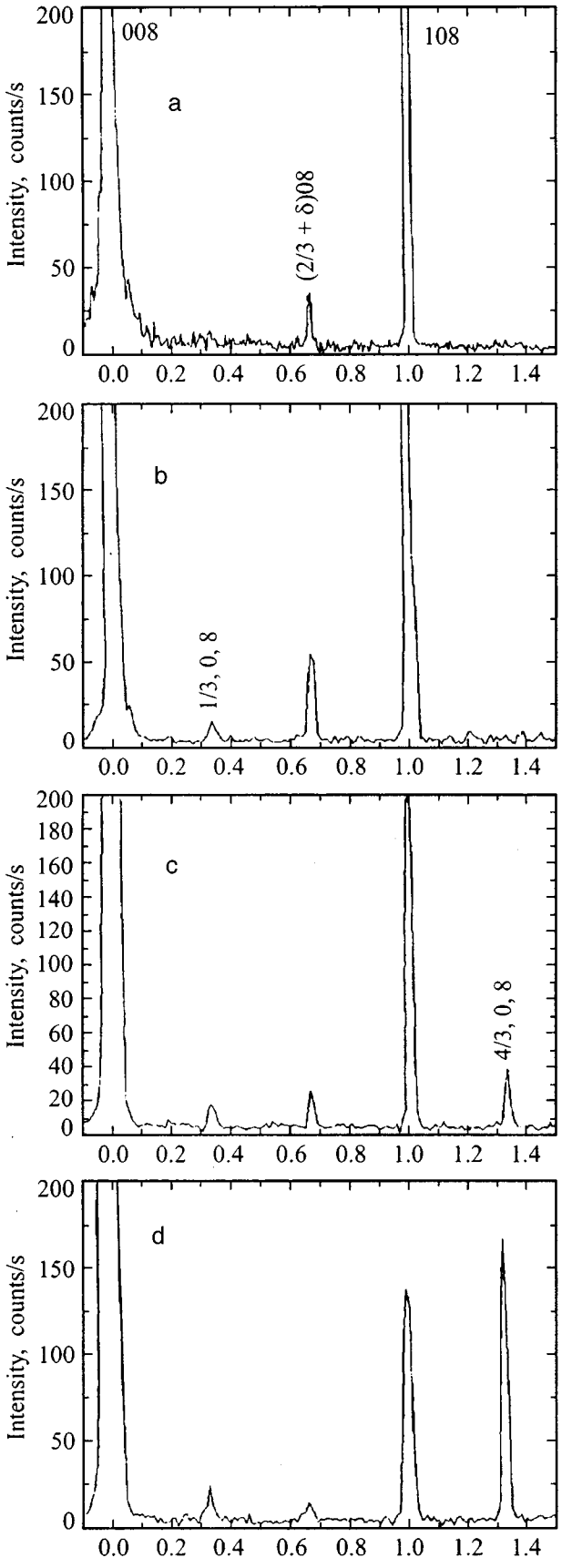

FIG. 4. Position of the Bragg (008) and satellite reflexes along the nodal series $(h08)$ at temperatures of 210 (a), 108 (b), 65 (c), and 9 K (d).

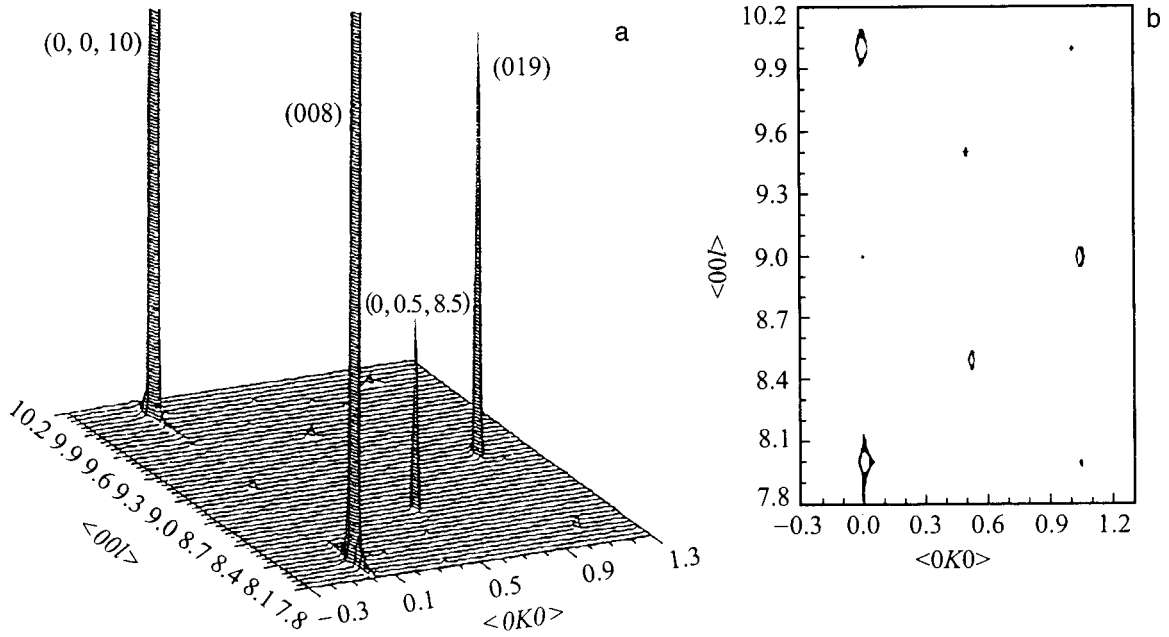

FIG. 5. Map of the distribution of the scattered intensity in part of the $(00l)$ plane at 10 K (a) and a projection of it (b).

into the $(0k1)$ plane. Below 74 K additional reflexes are observed at positions $\mathbf{q}=(\mathbf{b}^*+\mathbf{c}^*)/2$. Figure 5 shows a map of the two-dimensional distribution of the scattered intensity in this plane at $T=10$ K. This map made it possible to determine the position of the maxima of the intensity peaks and to find the conditions for damping in this plane. Superstructural reflexes were recorded at positions where both h and k were half-integral, and when their sum is a half integer, they are damped. In the new, doubled notations ($k'=2k$, $l=2l$), these damping conditions for the diffraction peaks ($0k'l':k'+l'=2n$, $0k'0:k'=2n$, $00l':l'=2n$) in the $(0k1)$ plane are consistent with the centered space group $A11a$. Here the volume of the cell increases by a factor of twelve $(3\times2\times2)$ compared to the initial *Pnma*-phase; hence, the formula number is $Z=48$. We chose the most intense of the accessible structural reflexes, (0,0.5,8.5), to study the temperature behavior of the position and intensity (Fig. 6). The cross sections of the satellite along the **b*** and **c*** axes were scanned at different temperatures. The position of the satellite did not change, and this is evidence of the commensurate character of the modulations. An anomaly in the intensity around 50 K and a residual intensity above 74 K owing to diffuse scattering can be seen in Fig. 6. Here the width of the superstructural peaks became much greater than for the Bragg reflexes. No variations in the damping conditions were observed at temperatures above and below 50 K. Possibly the anomaly in the behavior of the intensity of the superstructural reflex (0,0.5,8.5) in this region is associated with realignments of the ferroelectric domains $(\mathbf{b}^*+\mathbf{c}^*)/2$ into a more uniform distribution along **a***. The realignment of these domains takes place either through local ordering of the $ZnCl_4$ tetrahedrons or through stresses between domains.

The analysis presented here has established that processes associated with ordering of tetrahedral groups take place in crystalline Rb_2ZnCl_4 over the entire temperature range beginning with T_i. These processes have been identified through the appearance and modification of additional x-ray reflexes. The ordering of the tetrahedral groups in crystalline Rb_2ZnCl_4 proceeds through the following steps: in the initial *Pnma* phase the $ZnCl_4$ tetrahedra are characterized by rotations between two equivalent positions which are coupled by a mirror symmetry plane. The incommensurate phase has an infinite number of orientations between

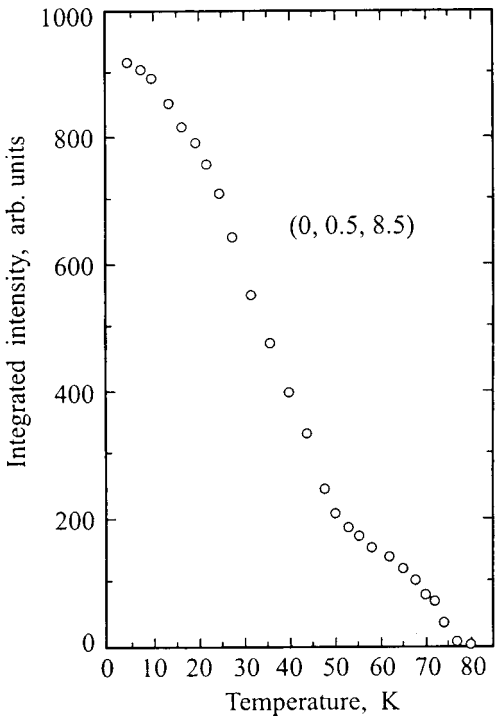

FIG. 6. Temperature dependence of the integrated intensity of the superstructural reflex (0,0.5,8.5).

these positions. In the commensurate phase there are three defined positions and, finally, in the low-temperature monoclinic phase all the tetrahedra typically have a single orientation.

The changes in the interplanar distances are tiny, except in the region of the phase transition into the low-temperature monoclinic phase at 74 K. It has been found that the monoclinic phase has an $A11a$ symmetry and is characterized by superstructral $\mathbf{q}=\mathbf{a}^*/3+\mathbf{b}^*/2+\mathbf{c}^*/2$ reflexes corresponding to trebling of the parameter a and doubling of b and c of the initial $Pnma$ phase. This phase will be of interest for a complete structural analysis in the future. No incommensurate structural realignments between the orthorhombic $Pn2_1a$ and monoclinic $A11a$ phases were observed.

We thank V. V. Gladkiĭ for providing the crystal samples, I. M. Shmytko for the helium cryostat, and N. A. Dorokhova for the q-scanning program.

*)E-mail: bagautdi@issp.ac.ru

[1] H. Z. Cummins, Phys. Rep. **185**, 211 (1990).
[2] V. Dvorak and R. Kind, Phys. Status Solidi B **107**, K109 (1981).
[3] E. Francke, M. L. Postollec, J. P. Mathieu, and H. Poulet, Solid State Commun. **33**, 155 (1980).
[4] M. Wada, A. Sawada, and Y. Ishibashi, J. Phys. Soc. Jpn. **50**, 531 (1981).
[5] P. Gunter, R. Sanctuary, F. Rohner, H. Arend, and W. Seidenbusch, SolidState Commun. **37**, 883 (1981).
[6] H.-G. Unruh and J. Stromich, Solid State Commun. **39**, 737 (1981).
[7] P. Muralt, E. Voit, and R. Kind, Phys. Status Solidi B **119**, K65 (1983).
[8] H. M. Lu and J. R. Hardy, Phys. Rev. B **45**, 7609 (1992).
[9] M. Quilichini and J. Pannetier, Acta Crystallogr., Sect. B: Struct. Sci. **B39**, 657 (1983).
[10] H. Mashiyama, K. Sugimoto, Y. Oohara, and H. Yoshizawa, J. Phys. Soc. Jpn. **61**, 3042 (1992).
[11] M. Quilichini, V. Dvorak, and P. Boutrouille, J. Phys. I **1**, 1321 (1991).
[12] I. Noiret, A. Hedoux, Y. Guinet, and G. Odou, Ferroelectrics **185**, 233 (1996).
[13] I. Noiret, Y. Guinet, and A. Hedoux, Phys. Rev. B **52**, 13206 (1996).
[14] K. Gesi K., J. Phys. Soc. Jpn. **59**, 416 (1990).
[15] K. Gesi K., J. Phys. Soc. Jpn. **61**, 1225 (1992).
[16] K. Hasebe, T. Asahi, H. Kasano, H. Mashiyama, and S. Kishimoto, J. Phys. Soc. Jpn. **63**, 3340 (1994).
[17] K. Itoh, A. Hinasada, H. Matsunaga, and E. Nakamura, J. Phys. Soc. Jpn. **52**, 664 (1983).
[18] I. N. Flerov and L. A. Kot, Fiz. Tverd. Tela **23**, *8*, 2422 (1981) [Sov. Phys. Solid State **23**, 1415 (1981)].
[19] H. Mashiyma, J. Phys. Soc. Jpn. **60**, 180 (1991).
[20] A. Hedoux, D. Grebille, J. Jaud, and G. Godefroy, Acta Crystallogr., Sect. B: Struct. Sci. **B45**, 370 (1989).
[21] S. R. Andrews and H. Mashiyma, J. Phys. C **16**, 4985 (1983).
[22] I. Aramburu, G. Madariaga, D. Grebille, J. M. Perez-Mato, and T. Breczewski, J. Phys. I **7**, 371 (1997).
[23] B. Sh. Bagautdinov, V. V. Gladkiĭ, V. A. Kirikov, and I. M. Shmyt'ko, Fiz. Tverd. Tela **38**, 1368 (1996) [Phys. Solid State **38**, 757 (1996)].

Translated by D. H. McNeill

Dielectric properties of solid solutions $PbMg_{1/3}Nb_{2/3}O_3$–$SrTiO_3$

V. V. Lemanov, A. V. Sotnikov, and E. P. Smirnova

A. F. Ioffe Physicotechnical Institute, Russian Academy of Sciences, 194021 St. Petersburg, Russia

M. Weihnacht and O. Hässler

Institut für Festkörper- und Werkstofforschung Dresden, D-01171 Dresden, Germany
(Submitted February 2, 1999)
Fiz. Tverd. Tela (St. Petersburg) **41**, 1091–1095 (June 1999)

Ceramic samples of the solid solutions $PbMg_{1/3}Nb_{2/3}O_3$–$SrTiO_3$ are synthesized. The dielectric properties are studied and a phase diagram is constructed. The results obtained are discussed in terms of ideas concerning relaxor ferroelectrics for solid solutions on the PMN side and from the standpoint of potential ferroelectrics on the $SrTiO_3$ side. The introduction of $SrTiO_3$ into PMN gradually degrades relaxor properties, and the introduction of PMN into $SrTiO_3$ does not result in initiation of the ferroelectric phase transition, possibly because of the appearance of random fields in the lattice. The possibility of practical applications of the synthesized system is also discussed. © *1999 American Institute of Physics.* [S1063-7834(99)03506-6]

Complicated perovskite-structure compounds with the general formula $A^{2+}(B'_yB''_{1-y})^{4+}O_3$, where y is determined by the valence of the cations B' and B'', form a group of ferroelectrics with a diffuse phase transition or, as they are now called, relaxor ferroelectrics. This class of ferroelectrics was discovered by Smolenskiĭ and his colleagues nearly 40 years ago.[1] The classical relaxor ferroelectric is $PbMg_{1/3}Nb_{2/3}O_3$ (PMN), which can be viewed as a model object for ferroelectrics of this kind. Despite the large number of works devoted to PMN and other relaxors (see, for example, Refs. 2–8), the physical nature of ferroelectric relaxors is still not yet completely understood. For this reason, it is still of interest to obtain new experimental data in this field. Specifically, it is of interest to study the evolution of the properties of a relaxor ferroelectric in solid solutions based on it as a function of the dilution of the solid solution by a different component (neither relaxor nor ferroelectric).

In the literature the data for PMN-based solid solutions are given for two binary systems PMN–$PbTiO_3$ (PMN–PT)[9] and PMN to which up to 50% La is added (PMN–LMN;[10] the latter system can be regarded as the solid solution $PbMg_{1/3}Nb_{2/3}O_3$–$LaMg_{2/3}Nb_{1/3}O_3$). The effect of small concentrations of various impurity ions in A and B positions on the dielectric properties of PMN has also been studied.[11]

For PMN–LMN solid solutions it has been shown that the degree of ordering in the B sublattice increases with the La content and reaches 1 with 50% La.[10,12] This is explained by the excess charge of the La ions. It is known[12,13] that regions of ordered phase with cell doubling are observed in pure PMN, i.e., for the ratio Mg:Nb=1:1 instead of the stoichiometric ratio 1:2. The effective charge per formula unit Pb_2MnNbO_6 is -1, and the charge of a doubled cell becomes -4. The introduction of La^{3+} ions, which replace Pb^{2+}, into the lattice results in an excess positive charge, which compensates the charge arising from cell doubling. This could increase the degree of ordering.

For the solid solution PMN–PT the appearance of a third ion (Ti^{4+}) in the B sublattice should introduce a large disorder in the distribution of B ions, and should therefore strengthen the relaxor properties. However, experiments show[14] that as the $PbTiO_3$ concentration increases, the phase transition becomes less diffuse and acquires features characteristic for a normal ferroelectric. This behavior could be due to the very strong ferroelectric activity of the second component, $PbTiO_3$. The T_c-x phase diagram of PMN–PT apparently contains two branches, corresponding to transitions into a glassy state and into a normal-ferroelectric state. The temperature range where the glassy phase exists decreases with increasing $PbTiO_3$ concentration x and vanishes completely near the morphotropic phase boundary ($x\simeq 0.3$). For example, in the solid solution 0.8 PMN–0.2 PT a transition is observed into a dipole-glass state at 352 K on cooling, and an ordinary ferroelectric phase transition occurs at 324 K.[15]

In the present work we investigate a more complicated PMN-based binary solid solution, specifically, the solid solution PMN–$SrTiO_3$ (PMN–ST), where substitution occurs in the A and B sublattices. The identical structure and close values of the lattice constants (the lattice constant difference is 3.5%) made it possible to obtain a continuous series of solid solutions.

In the PMN–ST system the second component ($SrTiO_3$) is ferroelectrically inactive. On the other hand the substitution of the main ions in the A and B sublattices in this system should increase the degree of disorder and therefore possibly strengthen the relaxor properties.

Another interesting question associated with our system is an impurity-initiated ferroelectric phase transition in the potential ferroelectric $SrTiO_3$. It has been shown[16–18] that in $SrTiO_3$-based solid solutions with $CaTiO_3$, $BaTiO_3$, and

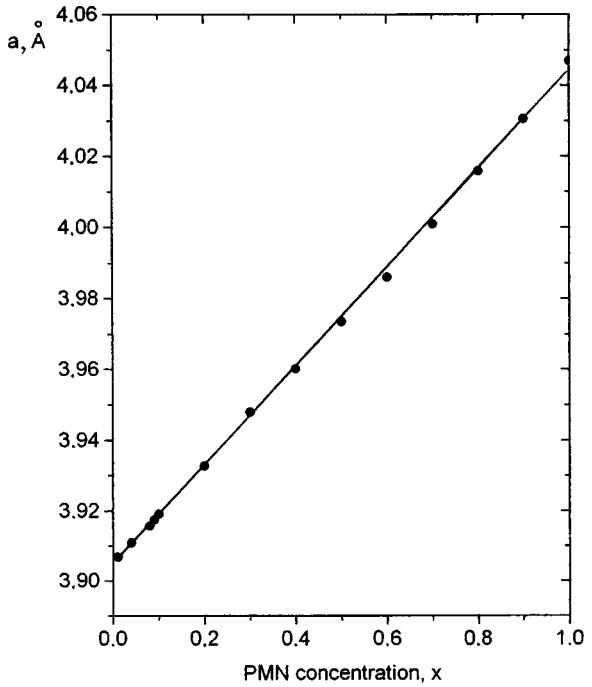

FIG. 1. Lattice constant versus the composition of the solid solution xPMN–$(1-x)$$SrTiO_3$ at room temperature. Straight line—Vegard's law.

$PbTiO_3$ a ferroelectric phase transition is initiated even at low concentrations of the second component at a temperature that depends on the concentration as $T_c = A(x - x_c)^{1/2}$, where x_c is the critical concentration of the second component of the solid solution. It has been found that for Ca, Ba, and Pb the critical concentrations x_c are essentially the same, about 0.002.[18] The system $(1-x)$$SrTiO_3$–$x$PMN considered in the present paper is a case where simultaneous substitution of the main ions at the A and B positions occurs in the $SrTiO_3$ lattice, which in principle could result in even lower critical concentrations.

Finally, the solid solutions $(1-x)$PMN–$x$$SrTiO_3$ on the PMN side could be of practical interest, specifically, for applications in the form of thin films in DRAM (random axis dynamic memory). Ferroelectrics with a high permittivity in the paraelectric phase are used in such devices. Pure PMN has a high permittivity in the working temperature range (more than 10000 at 1 kHz and room temperature), but it depends on the frequency, since the temperature T_m of maximum permittivity depends on the frequency (for example, $T_m = -10\,^\circ$C at 1 kHz and $T_m = +5\,^\circ$C at 1MHz). The temperature T_m should be expected to decrease in PMN-ST solid solutions, since the second component of the solid solutions ($SrTiO_3$) is ferroelectrically inactive. This makes it possible to decrease (or eliminate) the frequency dispersion of the permittivity at high frequencies in the working temperature range while maintaining a high value of the permittivity.

1. EXPERIMENT

Ceramic samples of the solid solutions PMN–ST were prepared by the standard ceramic technology. The most common method for synthesizing PMN via an intermediate compound columbite, $MgNb_2O_6$, was used to obtain samples

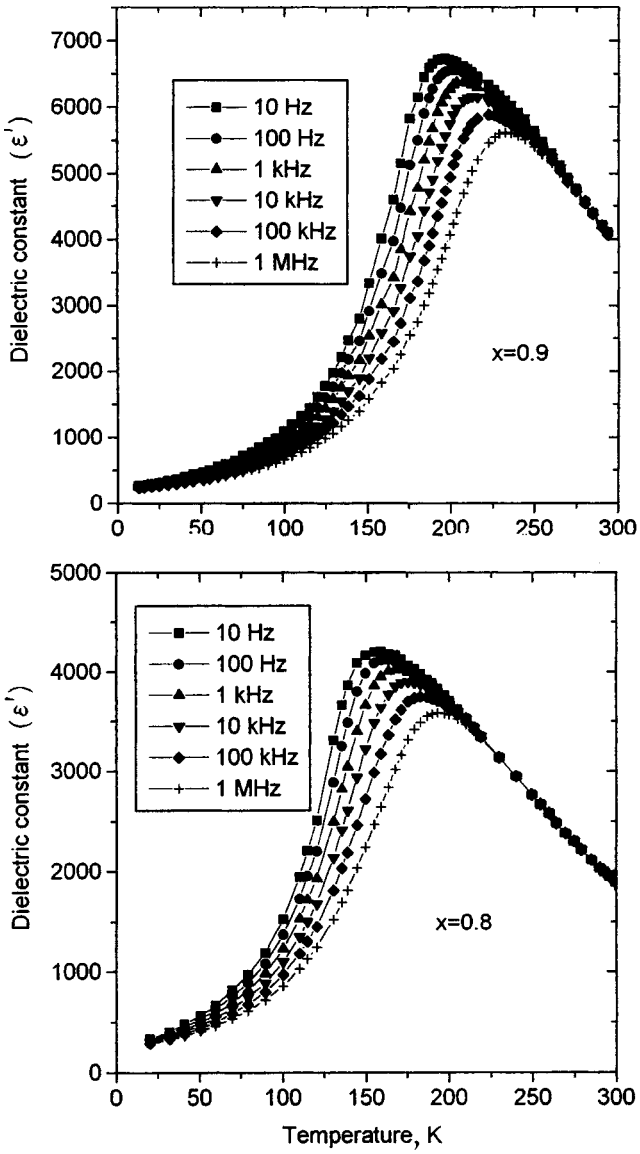

FIG. 2. Temperature dependence of the permittivity ε' of the solid solution xPMN–$(1-x)$$SrTiO_3$ with $x = 0.9$ and $x = 0.8$. The frequencies at which measurements were performed are indicated in the figure.

with the minimum content of the pyrochlore phase.[19] Preliminary annealing of the samples was conducted in platinum crucibles at 1000–1150 °C, depending on the composition, for 2 h. The batch obtained was pressed into 8 mm in diameter and 1.5–2 mm thick disks under 50 MPa pressure. The final annealing of the samples was performed at temperature 1250–1400 °C for 1 h. To prevent loss of lead the annealing process was conducted in a lead oxide atmosphere.

X-Ray structural analysis showed that all samples were single-phase and possessed perovskite structure. The lattice parameter of the solid solutions at room temperature were measured using germanium as the standard.

Figure 1 shows the composition dependence of the lattice parameter in the entire series of solid solutions xPMN–$(1-x)$$SrTiO_3$. As follows from Fig. 1, the experimental system does indeed form a continuous series of solid solutions, and a virtually linear composition dependence (Vegard's law) is observed for the lattice parameter.

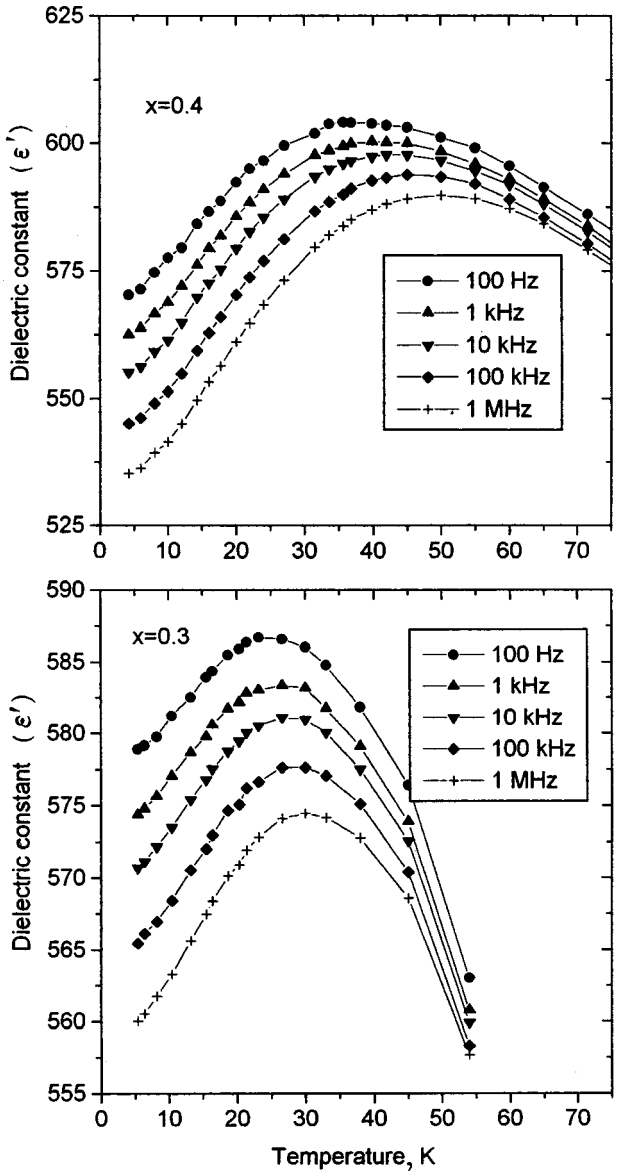

FIG. 3. Same as Fig. 2 with $x=0.4$ and 0.3.

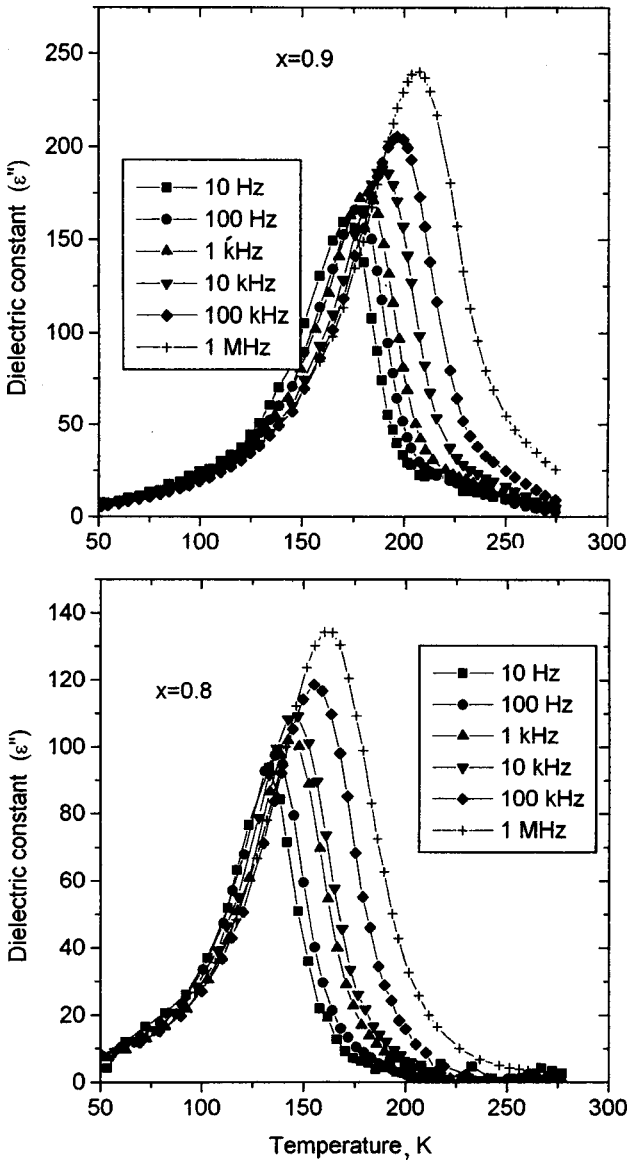

FIG. 4. Temperature dependence of the imaginary part ε'' of the permittivity with $x=0.9$ and 0.8.

The dielectric properties of the synthesized solid solutions were investigated. Samples for the measurements were 7 mm in diameter and about 1 mm thick. Silver paste was used as electrodes; the paste was annealed in the samples at a temperature of about 500 °C. The permittivity measurements were performed on a Solartron Si 1260 impedance analyzer at frequencies ranging from 10 Hz to 1 MHz at temperatures from 4.2 to 300 K. The amplitude of the measuring field was 1 V/cm. The temperature measurements were performed in an Oxford Instruments continuous-flow cryostat with a cooling rate of 1 K/min.

2. EXPERIMENTAL RESULTS AND DISCUSSION

Figures 2–4 show the temperature dependence of the real ε' and imaginary ε'' parts of the permittivity for certain values of x. The measurements showed that peaks, which apparently attest to a transition into a polar state, are observed in the temperature dependence of the permittivity for all compositions with $x \geqslant 0.3$. Just as in pure PMN ($x=1$), the temperature dependence of the permittivity is characterized by a large frequency dispersion, which decreases with the PMN concentration x. This dispersion can be characterized, specifically, by the quantity $\Delta T_m = T_m(1\,\text{MHz}) - T_m(100\,\text{Hz})$. Figure 5 shows ΔT_m versus the concentration x. One can see that ΔT_m decreases with the concentration, attesting to a decrease in the frequency dispersion of the permittivity.

To describe the frequency dispersion it is helpful to use also the Vogel–Fulcher relation

$$\omega = \omega_0 \exp(-U/k(T_m - T_g)),$$

where ω_0 is the frequency of attempts, U is the activation energy, and T_g is the freezing temperature.

Figure 6 shows the experimental curves of the frequency $\omega/2\pi$ versus the temperature T_m for $x=0.9$ and $x=0.8$. These curves were constructed using data on the temperature

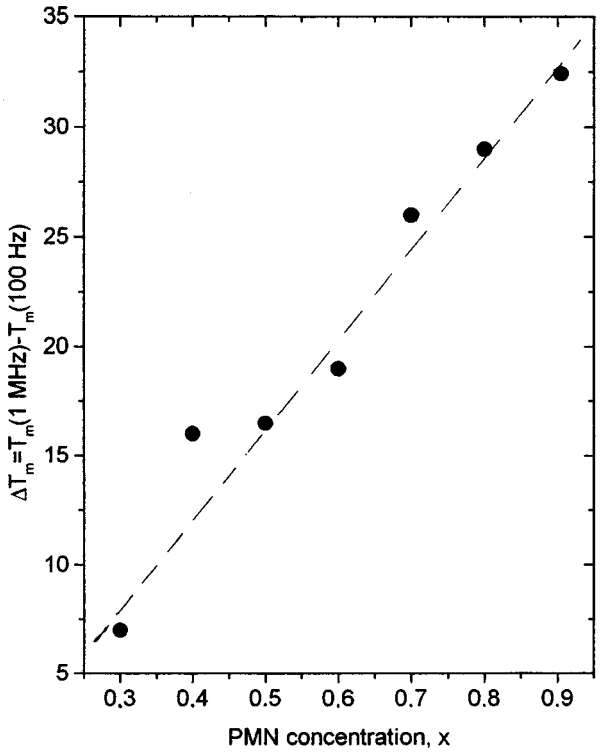

FIG. 5. $\Delta T_m = T_m\,(1\ \mathrm{MHz}) - T_m\,(100\ \mathrm{Hz})$, characterizing the frequency dispersion, versus the concentration x.

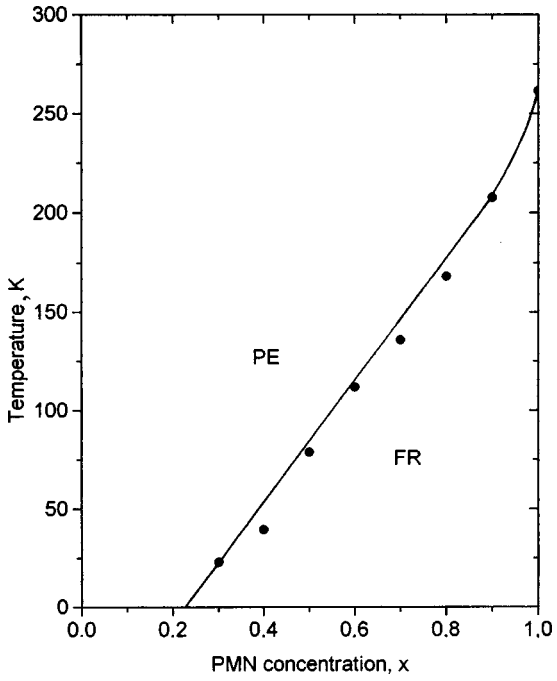

FIG. 7. Phase diagram of the system xPMN$-(1-x)$SrTiO$_3$ (the temperature T_m was determined at 1 kHz). *PE*—paraelectric, *FR*—relaxor ferroelectric.

dependence of the imaginary part of the permittivity at various frequencies. It was found that the Vogel–Fulcher relation holds for all concentrations $x>0.4$, the temperature T_g decreasing monotonically from 200 to approximately 10 K with decreasing PMN concentration x.

Thus as the $SrTiO_3$ concentration in the solid solutions PMN–ST increases, the relaxor properties weaken, and at PMN concentration $x<0.3$ the transition into a polar state vanishes completely.

On the whole the results obtained show that the evolution of the relaxor properties in the system PMN–ST is due not to an increase in the degree of disordering PMN on introduction of $SrTiO_3$, but rather it is due simply to a decrease in the PMN content when it is diluted with a neutral, in the sense of ferroelectric activity, component ($SrTiO_3$).

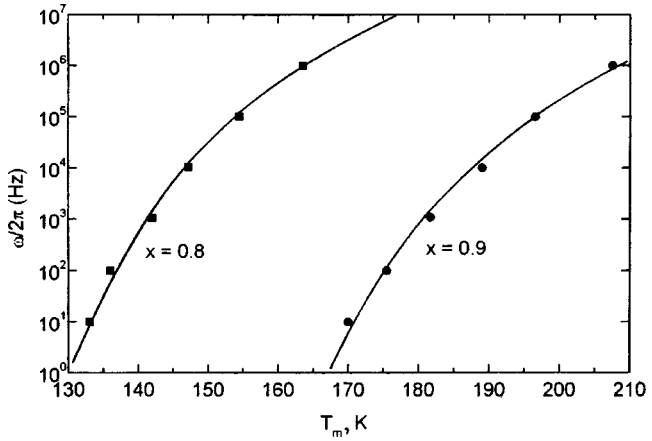

FIG. 6. Frequency $\omega/2\pi$ versus temperature T_m for $x=0.9$ and 0.8. The solid lines correspond to the Vogel–Fulcher relation with $\omega_0 = 1.6\times10^{12}\ \mathrm{s}^{-1}$, $U=0.085$ eV, and $T_g=129$ K ($x=0.9$), $\omega_0=2.2\times10^{12}\ \mathrm{s}^{-1}$, $U=0.072$ eV and $T_g=100$ K ($x=0.8$).

Figure 7 shows the T_m-x phase diagram of the solid solutions investigated. It is evident that the temperature T_m is almost a linear function of x. There is no transition into the polar state in compositions with $x<0.3$. This result is at striking variance with the results for $SrTiO_3$-based solid solutions with $CaTiO_3$, $BaTiO_3$, and $PbTiO_3$, where, as already mentioned, a ferroelectric phase transition occurs at a critical concentration of about 0.002. Moreover, a dependence of the form $T_m = A(x-x_c)^{1/2}$ is also absent in the system investigated.

In summary, substitution of the main ions in $SrTiO_3$ in the A and B positions simultaneously (in addition, the main ion Ti^{4+} in the B positions is replaced by a combination of ions $(Mg_{1/3}Nb_{2/3})^{4+}$) does not result in the initiation of a ferroelectric phase transition at low concentrations, and a transition into a relaxor ferroelectric state is initiated only at concentrations above 0.2.

The result obtained shows that the initiationa of ferroelectric phase transitions in the potential ferroelectric $SrTiO_3$ by impurities depends decisively on the type of ions replacing the main lattice ions and on their position (A or B). In the system investigated a phase transition into the normal ferroelectric state does not occur at all at any concentrations x. This could be because the three ions with different valences at the B positions (Ti^{4+}, Mg^{2+}, Nb^{5+}) give rise to random fields which prevent a ferroelectric phase transition from occurring.

A high permittivity and absence of frequency dispersion of the permittivity in the working temperature range are important for possible practical applications of the system in-

vestigated here in dynamic memory devices. Measurements show that, for example, for $x=0.9$ the permittivity is still quite high (about 4000) and the temperature T_m decreases approximately to 200 K, which essentially eliminates the frequency dispersion of the permittivity at high frequencies in the working temperature range.

We thank N. V. Zaĭtsev for performing the x-ray crystallographic measurements.

At the Physicotechnical Institute this work was supported by the program ''Physics of Solid-State Nanostructures'' (project No. 97-2017). At the Institute of Solid-State Physics and Materials Research it was supported by the Ministry of Science and Culture of Saxony.

[1] G. A. Smolensky, V. A. Bokov, V. A. Isupov, N. N. Krainik, R. E. Pasynkov, and A. I. Sokolov, *Ferroelectrics and Related Materials* (Gordon and Breach, Philadelphia, PA, 1984).
[2] L. E. Cross, Ferroelectrics **76**, 241 (1987).
[3] D. Viehland, S. J. Jang, and L. E. Cross, Philos. Mag. **64**, 335 (1991).
[4] S. N. Dorogovtsev and N. K. Yushin, Ferroelectrics **112**, 27 (1990).
[5] A. Wesstphal, W. Kleemann, M. D. Glinchuk, Phys. Rev. Lett. **68**, 847 (1992).
[6] E. V. Colla, E. Y. Koroleva, N. M. Okuneva, and S. B. Vakhrushev, Phys. Rev. Lett. **74**, 168 (1995).
[7] A. E. Glazounov, A. K. Tagantsev, and A. J. Bell, Phys. Rev. B **53**, 11 281 (1996).
[8] A. Levstik, Z. Kutnjak, C. Filipic, and R. Pirc, Phys. Rev. B **57**, 11 204 (1998).
[9] B. Jaffe, W. R. Cook, and H. Jaffe, *Piezoelectric Ceramics* (Academic Press, New York, 1971).
[10] Li-Jian Lin and Tai-Bor Wu, J. Am. Ceram. Soc. **73**, 1253 (1990).
[11] D. J. Voss, S. L. Swartz, and T. R. Shrout, Ferroelectrics **50**, 203 (1983).
[12] J. Chen, H. M. Chan, and M. P. Harmer, J. Am. Ceram. Soc. **72**, 593 (1989).
[13] H. B. Krause, J. M. Cowley, and J. Whatley, Acta Crystallogr., Sect. A: Cryst. Phys., Diffr., Theor. Gen. Crystallogr. **A35**, 1015 (1979).
[14] S. L. Swartz, T. R. Shrout, W. A. Schulze, and L. E. Cross, J. Am. Ceram. Soc. **67**, 311 (1984).
[15] I. N. Zakharchenko, O. A. Bunina, P. N. Timonin, Yu. A. Trusov, and V. P. Sakhnenko, Kristallografiya **43**, 71 (1998) [Crystallogr. Rep. **43**, 64 (1998)].
[16] J. G. Bednorz and K. A. Müller, Phys. Rev. Lett. **52**, 2289 (1984).
[17] V. V. Lemanov, E. P. Smirnova, P. P. Syrnikov, and E. A. Tarakanov, Phys. Rev. B **54**, 3151 (1996).
[18] V. V. Lemanov, Fiz. Tverd. Tela (St. Petersburg) **39**, 1645 (1997) [Phys. Solid State **39**, 1468 (1997)].
[19] S. L. Swartz and T. R. Shrout, Mater. Res. Bull. **17**, 1245 (1982).

Translated by M. E. Alferieff

LATTICE DYNAMICS. PHASE TRANSITIONS

Modeling of a structural phase transition in $La_{2-x}Sr_xCuO_4$

A. Yu. Zakharov,* A. E. Nikiforov, and S. Yu. Shashkin

Ural State University, 620083 Ekaterinburg, Russia
(Submitted November 19, 1998)
Fiz. Tverd. Tela (St. Petersburg) **41**, 1096–1102 (June 1999)

The structural, vibrational, and elastic properties of La_2CuO_4 are calculated using a model for calculating the energy of the crystal based on interionic potentials with the multiparticle Jahn–Teller contribution included explicitly. The microscopic reasons for the structural instability of the La_2CuO_4 lattice relative to rotations of the oxygen octahedra are investigated. A structural phase transition from the orthorhombic phase (space group D_{2h}^{18}) into the tetragonal phase (space group D_{4h}^{17}) under hydrostatic compression of an $La_{2-x}Sr_xCuO_4$ crystal is modeled. The (P,x) structural phase diagram for $La_{2-x}Sr_xCuO_4$ is constructed. © *1999 American Institute of Physics.* [S1063-7834(99)03606-0]

A large number of investigations of copper–oxygen HTSC compounds have shown that the ground state of these systems is complicated because of the strong interaction of the electronic, spin, and vibration degrees of freedom.[1] The ionic shell model, which takes account of both the short-range repulsion of the ion shells, due to the Pauli principle, and the long-range Coulomb interaction, has been found to be effective for the microscopic description of the vibrational subsystem. Many early treatments[2,3] used a large number of force constants, in consequence of which the force constants obtained there were in many respects physically meaningless. Other treatments employed Born–Mayer ion–ion potentials.[4,5] This made it possible to describe the phonon spectra of La_2CuO_4, Nd_2CuO_4, and $YBa_2Cu_3O_6$ crystals. However, difficulties due to the positive charges of the ion shells and the need to introduce two very different copper–oxygen potentials arose in the interpretation of the model parameters obtained.

On the other hand our experience in working with the Jahn–Teller crystals $KCuF_3$ and K_2CuF_4[6–8] has shown that including the multiparticle Jahn–Teller contribution (with a single linear coupling constant V_e) explicitly in the energy and the dynamic matrix makes it possible to describe the structural and dynamical properties of these crystals without unfounded introduction of a large number of adjustable parameters describing the anisotropy of the Cu–F interaction. Such a model has also been successful in describing La_2CuO_4 in the tetragonal phase.[9] Moreover, the importance of including in the dynamical matrix the pseudospin–phonon interaction (Jahn–Teller by nature) was pointed out in Ref. 10, where it is shown that the dispersion dependence of certain phonon modes of La_2CuO_4 in the tetragonal phase can be explained only if the pseudospin–phonon interaction is taken into account explicitly. Finally, the Jahn–Teller contribution to the energy has been found to be important in describing the changes induced in the crystal and magnetic structure of the K_2CuF_4 crystal by hydrostatic pressure.[11]

In the present paper the model of interionic pair potentials with the Jahn–Teller contribution included explicitly in the energy and dynamical matrix of the crystal is used to describe the effect of hydrostatic pressure on a second-order structural phase transition associated with a change in the space group of the crystal from D_{2h}^{18} (orthorhombic phase) to D_{4h}^{17} (tetragonal phase). The microscopic reason for the instability of the La_2CuO_4 crystal lattice relative to rotations of the oxygen octahedra remains a subject of investigation. Specifically, detailed knowledge of the relationship of the various interionic interactions whose approximate balance leads to lattice instability is of interest. Hydrostatic pressure, changing differently the contributions to the energy of the crystal, disrupts the balance of the contributions and strongly influences the structural phase transition. Such an investigation is of interest primarily because of the fact that hydrostatic compression of $La_{2-x}Sr_xCuO_4$ makes it possible to increase substantially the superconducting transition temperature.

Crystals doped with certain impurities are of interest from the standpoint of using copper–oxygen compounds with layered perovskite structure.[1] In the case of La_2CuO_4 crystals of the form $La_{2-x}Me_xCuO_4$ (Me=Ca, Sr, Ba$\cdots$) are superconducting. From this standpoint it is of interest to follow the relation between the concentration x of impurity Sr^{2+} and the critical pressure P_c at which a structural phase transition occurs.

1. MODEL FOR CALCULATING THE ENERGY OF THE CRYSTAL

The equilibrium lattice constants as well as the equilibrium values of the ion coordinates within the primitive cell of the crystal can be found by minimizing the energy of the crystal. The energy per primitive cell can be represented as a

sum of lattice and Jahn–Teller contributions (the latter is taken into account only for crystals containing Jahn–Teller ions)

$$E = E_{\text{lat}} + E_{\text{JT}}. \tag{1}$$

In the approximation of pair interactions and in the shell model the lattice energy can be written as

$$U_{\text{lat}} = \frac{1}{2}\sum_i \sum_{k(\neq i)} V_{ik} + \frac{1}{2}\sum_i k_i \delta_i^2, \tag{2}$$

where the index i labels all ions in the primitive cell, and k labels all ions in the crystal. The contribution $k_i\delta_i^2$ describes the core–shell interaction energy of the i-th ion if the ion shell is shifted relative to the core by the amount $\boldsymbol{\delta}_i$. The interaction V_{ik} between a pair of ions is

$$V_{ik} = \frac{X_i X_k}{r_{ik}} + \frac{Y_i Y_k}{|\mathbf{r}_{ik} - \boldsymbol{\delta}_i|} + \frac{X_i Y_k}{|\mathbf{r}_{ik} + \boldsymbol{\delta}_k|} + \frac{Y_i Y_k}{|\mathbf{r}_{ik} - \boldsymbol{\delta}_i + \boldsymbol{\delta}_k|} + f_{ik}(r_{ik}) + g_{ik}(|\mathbf{r}_{ik} - \boldsymbol{\delta}_i + \boldsymbol{\delta}_k|), \tag{3}$$

where the term

$$f_{ik}(r) = -A_{ik}\exp(-B_{ik}r)/r \tag{4}$$

describes effects due to interpenetration (or screening) of the electronic densities of the interacting ions, and the term

$$g_{ik}(r) = C_{ik}\exp(-D_{ik}r) - \lambda_{ik}/r^6 \tag{5}$$

describes the close-range repulsion between the ion shells, written in the form of the Born–Mayer potential, and the van der Waals interaction; X_k and Y_k are, respectively, the charges of the core and shell of the ion; and, $r_{ik} = |\mathbf{r}_{ik}|$ is the distance between the ion cores.

The multiparticle Jahn–Teller contribution to the energy for an La_2CuO_4 crystal can be approximated by a sum of expressions for the lower sheets of the adiabatic potentials of the CuO_6 clusters[9]

$$E_{\text{JT}} = -\sum_n |V_e|(Q_\theta^2(n) + Q_\varepsilon^2(n))^{1/2}, \tag{6}$$

where the index n labels all Cu^{2+} ions in the primitive cell, and the symmetrized coordinates Q_θ and Q_ε characterize the e_g distortions of the oxygen octahedra around the copper ions.

The values of the interionic interaction parameters and methods for determining them are presented in Ref. 9. The basic idea of our model of interionic potentials is that the interionic potentials should be transferable between different compounds. For this reason, in Ref. 9 the parameters of the interionic interaction potentials were found either nonempirically or by obtaining the best fit of the structural, vibrational, and elastic properties of NiO, SrO, and La_2NiO_4 (we assume that the difference in the short-range Cu^{2+}–O^{2-} and Ni^{2+}–O^{2-} interaction potentials is negligibly small and the difference in the properties of La_2NiO_4 and La_2CuO_4 is due to the Jahn–Teller contribution to the energy of the latter). The potentials obtained in Ref. 9 for modeling the structure of La_2CuO_4 yield stability of the tetragonal phase (space group D_{4h}^{17}). However, according to the experimental data,[12] at low temperature and in the absence of external pressure the stable phase for the La_2CuO_4 crystal is the phase with the space group D_{2h}^{18}. For this reason the parameter D of the short-range La^{3+}–O^{2-} repulsive potential was redetermined by optimizing the fit between the computed and experimentally determined[12] lattice constants of La_2CuO_4 (assuming the space group D_{2h}^{18}). The value found is $D = 1.664$ a.u.

TABLE I. Lattice constants of La_2CuO_4.

	a, pm	b, pm	c, pm
Calculation	569.37	542.12	1326.51
Experiment[12]	541.60(1)	533.52(1)	1310.58(1)

2. MODELING OF THE STRUCTURE OF AN La_2CuO_4 CRYSTAL

As we have mentioned above, at low temperatures and in the absence of external pressure La_2CuO_4 is in the orthorhombic phase. According to Ref. 13, the elementary translation vectors are

$$\mathbf{a}_1 = (b/2, c/2, 0); \quad \mathbf{a}_2 = (-b/2, c/2, 0); \quad \mathbf{a}_3 = (0, 0, a), \tag{7}$$

where $c > a > b$ are the lattice constants of the crystal. The primitive cell of La_2CuO_4 contains two formula units. The Cu^{2+} ions are in the $2a(0,0,0)$ positions, the La^{3+} ions are in the $4f(0,y,z)$ positions, the O^{2-}_{apex} ions are in the $4f(0,y,z)$ positions, and the O^{2-}_{basal} — ions are in the $4e(1/2,y,1/2)$ positions.

The structure of the La_2CuO_4 crystal was simulated using this model to calculate the energy of the crystal. The computational results for the crystal structure and the experimental data[12] obtained at $T = 60$ K for La_2CuO_4 are presented in Tables I and II. Comparing the computed and experimental values shows that our model reproduces quite well the observed experimental crystal structure of La_2CuO_4 (in making the comparison the fact that only one parameter of our model was found by fitting the experimental data on the lattice constant of La_2CuO_4 should be taken into consideration).

It is of great interest to determine the microscopic reasons for the appearance of a low-symmetry orthorhombic phase in La_2CuO_4. The transition from tetragonal to orthorhombic phase is customarily attributed to freezing of the soft vibrational mode at the X point of the Brilllouin zone. This mode is related to the rigid-body rotation of an oxygen octahedron surrounding the Cu^{2+} ion around the [110] axis (or the [−1, 1, 0] axis for the other ray domain). For this

TABLE II. Coordinates of ions within a primitive cell in La_2CuO_4.

	$La^{3+}(4f)$		$O^{2-}(4f)$		$O^{2-}(4e)$
	y	z	y	z	y
Calculation	−0.0128	0.3627	0.0490	0.1809	0.0122
Experiment[12]	−0.0084(3)	0.3616(1)	0.0403(3)	0.1834(1)	0.0089(2)

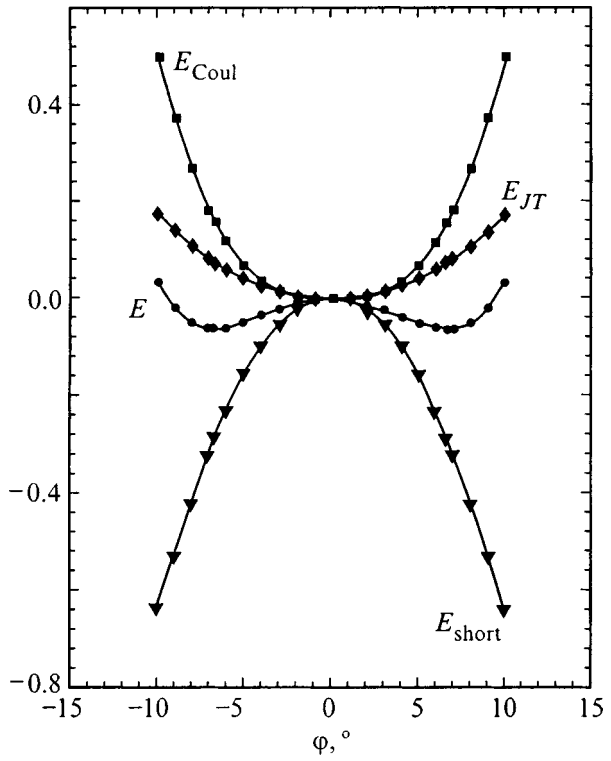

FIG. 1. Total energy E of the crystal, the Coulomb contribution E_{Coul} to the total energy of the crystal, the contribution of the short-range interaction E_{short} to the total energy of the crystal, the Jahn–Teller contribution E_{JT} to the energy of the crystal (all in eV) as a function of the rotation angle φ of the oxygen octahedra (all quantities are given in the form of a difference relative to their values at $\varphi=0$).

reason, we investigated the energy of the crystal as a function of the angle φ of rotation of the oxygen octahedra (in the orthorhombic phase). The results are presented in Fig. 1. As expected, this dependence is symmetric relative to the origin of the coordinate system and possesses two minima for $\varphi \neq 0$ and a maximum at $\varphi=0$. The barrier between the two minima was found to be 62 meV. The figure also shows the φ dependence of various contributions to the energy of the crystal. It can be concluded from Fig. 1 that the instability of the crystal at the point $\varphi=0$ is due to the short-range interaction between the ions in the crystal lattice. On the other hand, stabilization of the crystal structure for $\varphi\neq 0$ is a consequence of the anharmonic dependence of the Coulomb interaction between the ions on the angle φ of rotation of the oxygen octahedra, since the character of the φ dependence for the contribution due to the short-range interaction between the ions and the Jahn–Teller contribution to the total energy of the crystal is harmonic to an adequate degree of accuracy. It is interesting that the Jahn–Teller contribution to the energy of the crystal decreases the orthorhombic lattice distortions.

Besides modeling the structure, calculations were performed of the vibrational and elastic properties of La_2CuO_4 in the orthorhombic phase. Table III gives the computational results for the A_g vibrations at the Γ point of the Brillouin zone. The vibrations with this symmetry are Raman-active; the corresponding experimental data[14] are also presented in Table III. Two of the five A_g vibrations at the Γ point of the Brillouin zone appear in the orthorhombic and tetragonal phases. The remaining three vibrations arise as a result of mixing of vibrations from the Γ and X points of the Brillouin zone in the tetragonal phase. As a result these vibrations should vanish at a structural phase transition to the tetragonal phase. Besides the A_g vibrations, the vibrations with symmetry B_{1g}, B_{2g}, and B_{3g} should also be Raman-active. However, these vibrations could not be identified experimentally. Comparing the computed and experimentally determined frequencies of the A_g vibrations shows that the calculation overestimates the frequencies of all vibrations. This leads to the conclusion that in the modeling the crystal lattice is stiffer than the experimental data.

TABLE III. Frequencies of A_g vibrations at the Γ point of the Brillouin zone in La_2CuO_4, cm^{-1}.

Calculation	165	210	295	353	551
Experiment[14]	126	156	229	273	426

Table IV gives the computational results and experimental data[15] on the elastic constants for La_2CuO_4. Just as in the case of the vibrational properties of the lattice, it is evident that the calculation overestimates the stiffness of the crystal lattice, since all computed elastic constants are greater than the corresponding experimental values. On the other hand, the ratio of the computed elastic constants agrees quite well with the ratio of the experimental elastic constants. Thus, it is interesting that C_{33} is almost two times smaller than C_{11} and C_{22}, indicating substantial anisotropy of the elastic properties of the lattice (we note that the elastic constants are presented in the coordinate system adopted in the present paper).

3. EFFECT OF HYDROSTATIC PRESSURE ON THE STRUCTURAL PROPERTIES OF La_2CuO_4

It is well known that pressure strongly influences the structural properties of $La_{2-x}Sr_xCuO_4$. For a crystal in the orthorhombic phase hydrostatic compression decreases the rotation angle of the oxygen octahedra and the difference between the lattice constants a and b.[12] At a certain critical pressure a second-order structural phase transition occurs, in which the space group of the crystal changes from orthorhombic D_{2h}^{18} to tetragonal D_{4h}^{17} (OT transition).

It has been established experimentally that hydrostatic pressure also makes it possible to increase substantially an important property of the crystal under study: the superconducting transition temperature T_c. In Ref. 16 the effect of pressure on T_c was investigated for $La_{2-x}Sr_xCuO_4$ samples with various Sr contents ($0.15\leqslant x\leqslant 0.22$). In the present work it is shown that hydrostatic compression of a crystal increases T_c, the value of T_c reaching a maximum at the pressure of the OT transition. Thus, at atmospheric pressure $T_c=38$ K, while at 3 GPa $T_c=42$ K. After the crystal makes a transition from the orthorhombic into the tetragonal phase the value of T_c becomes essentially pressure-independent. Judging from these results, it can be concluded that the superconducting transition temperature T_c is related to the

TABLE IV. Elastic constants of La_2CuO_3, GPa.

	C_{11}	C_{22}	C_{12}	C_{13}	C_{23}	C_{33}	C_{44}	C_{55}	C_{66}
Calculation	285	355	106	137	115	165	94	125	79
Experiment[15]	230	276	102	98	92	156	75	102	64

structural properties of $La_{2-x}Sr_xCuO_4$ and that the tetragonal phase of $La_{2-x}Sr_xCuO_4$ is optimal from the standpoint of its superconducting properties.

A detailed experimental investigation of the effect of hydrostatic pressure on the structural properties of both pure and doped $La_{2-x}Sr_xCuO_4$ at low temperatures ($T=60$ K) was performed in Ref. 12. In the present work the lattice constants for $La_{2-x}Sr_xCuO_4$ and the coordinates of the ions in the primitive cell of the crystal were determined up to a pressure 0.6 GPa. However, in the course of the experiment pressures at which a structural OT transition would be observed were not reached.

In the present work the effect of pressure on the structural properties of La_2CuO_4 is investigated using the model described in Sec. 1. However, under hydrostatic compression conditions the equilibrium crystalline structure should be found by minimizing not the energy E (1) of the crystal but rather the thermodynamic potential $H=E+PV$ of the crystal, where P is the pressure and V is the volume of the primitive cell. A theoretical model makes it possible to investigate the change in the structure of the crystal under hydrostatic compression at pressures, which for one reason or another were not obtained experimentally.

In accordance with Landau's theory of phase transitions, a structural phase transition with the space group of the crystal changing from D_{4h}^{17} to D_{2h}^{18} can be described by a two-component order parameter, only one component being nonzero.[17] The order parameter is found to be proportional to the rotation angle of the oxygen octahedra.

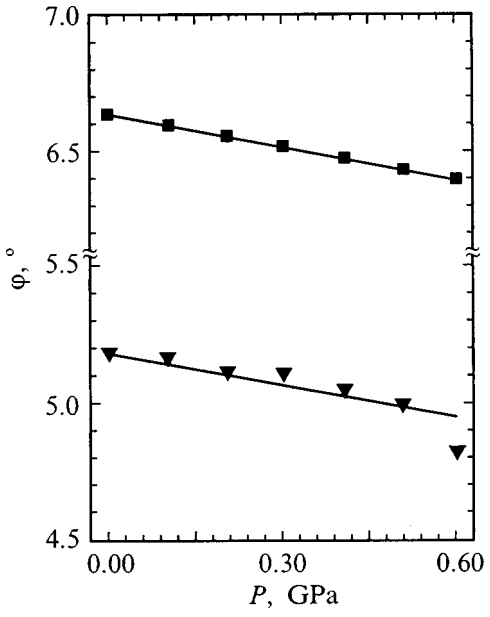

FIG. 2. Rotation angle φ of the oxygen octahedra versus the pressure P. Squares—calculation, triangles—experiment, solid lines—fit using Eq. (8).

Figure 2 shows for comparison the rotation angles φ of the oxygen octahedra calculated in our model and determined experimentally in the pressure range where the experimental investigations were conducted. As already noted above, in Ref. 12 the pressure at which a structural phase transition would be observed was not reached in La_2CuO_4. For this reason, we found the critical pressure, equal to 7.2 GPa, on the basis of Landau's theory of phase transitions. Using Landau's theory it can be concluded that the rotation angle φ of the oxygen octahedra should depend on the applied pressure P as

$$\varphi \sim (P_c - P)^{1/2}, \tag{8}$$

where P_c is the critical pressure. The result of fitting this formula for the computed and experimental values of the rotation angles φ at pressures from 0 to 0.6 GPa are also shown in Fig. 2 (solid lines). The use of this formula for fitting our computed values of φ gives 8.7 GPA for the critical pressure at which a structural OT transition occurs.

However, calculations of the crystal structure of La_2CuO_4 at pressures above 0.6 GPa give a somewhat different pressure dependence of the rotation angles φ of the oxygen octahedra (Fig. 3). The critical pressure at which the angle φ vanishes and the crystal undergoes a structural phase transition into the tetragonal phase is found to be 5.0 GPa. Moreover, although the character of the pressure dependence of φ remains the same, i.e.,

$$\varphi \sim (P_c - P)^{\beta}, \tag{9}$$

the exponent β decreases from 0.5 to 0.28. Therefore using Landau's theory to extrapolate the values of the angle φ calculated using Eq. (8) to pressures far from the critical pressure overestimates the critical pressure P_c. For this reason, from our standpoint the value of P_c presented in Ref. 12 is also higher than the critical pressure that would be obtained if the experiments were performed at higher pressures.

It is of great interest to investigate the pressure dependence of the lattice constants of La_2CuO_4 and to compare the character of this dependence in orthorhombic and tetragonal phases (Fig. 4). The most notable features are the nonlinearity and the nonmonotonicity of the pressure dependence of the lattice constants b and c in the orthorhombic phase. The linear pressure dependence of the lattice constants obtained experimentally[12] can be explained by the fact that the experiments were performed in a narrow pressure range and quite far from the phase transition point. The modeling shows that the nonlinear character of the dependence is due to the substantially anharmonic dependence of the thermodynamic potential of the crystal lattice on the displacements of the apex

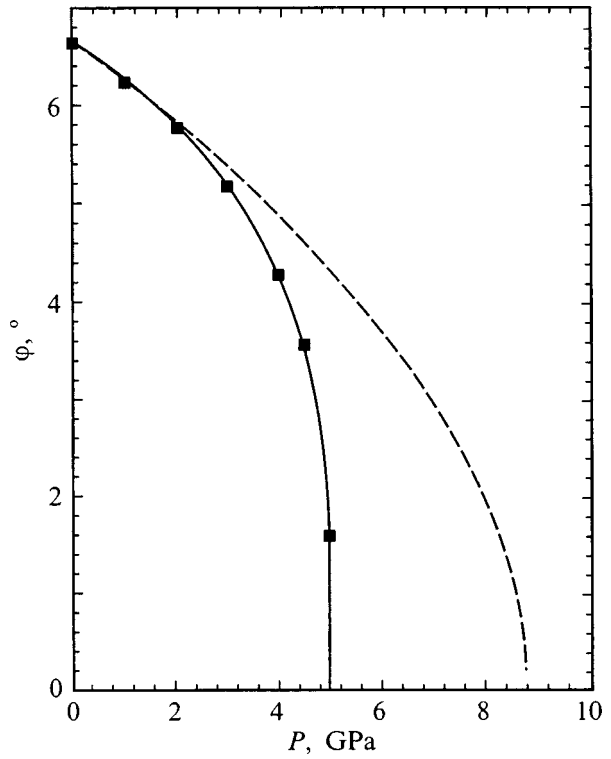

FIG. 3. Computed rotation angle φ of oxygen octahedra versus the pressure P. Squares—calculation, solid line—fit using Eq. (9), dashed line—extrapolation of the computational data in the range $0 \leqslant P \leqslant 0.6$ GPa according to Landau's theory (see text).

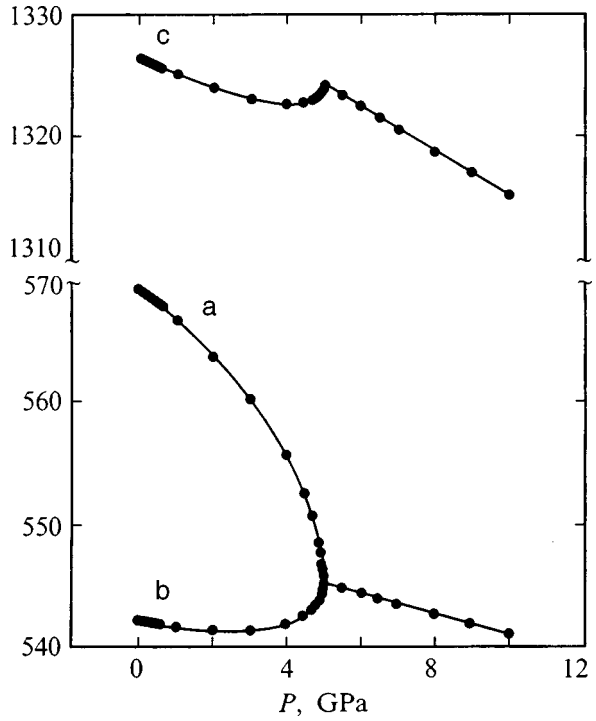

FIG. 4. Lattice constants of La_2CuO_4, in pm, versus the pressure P in the orthorhombic and tetragonal phases.

oxygen ions and lanthanum ions in the direction of the lattice constant a. The nonlinear character of the pressure dependence of the lattice constants implies that other physical properties of La_2CuO_4, in all probability, will show a nonlinear pressure dependence. At the same time it is interesting to note that the primitive cell volume decreases with increasing pressure essentially linearly everywhere except in a narrow range near the phase transition point.

After the crystal passes into the tetragonal phase the dependence of the thermodynamic potential on the lattice constants and the coordinates of the ions within the primitive cell becomes harmonic. For this reason, in the tetragonal phase the pressure dependence of the lattice constants is linear, and the constant c decreases with pressure almost twice as rapidly as the constant a. At the same time the ratio c/a remains essentially constant and equal to 2.43. This type of dependence for the tetragonal phase agrees well with the experimentally observed results.[18] Experimentally, the lattice constants also depend linearly on the pressure, while the ratio c/a is 2.48.

4. EFFECT OF DOPING ON THE STRUCTURAL PROPERTIES OF $La_{2-x}Sr_xCuO_4$

In the case of $La_{2-x}Sr_xCuO_4$ studied in the present work, superconductivity is observed in the range $0.07 \leqslant x \leqslant 0.24$. The maximum superconducting transition temperature, equal to 38 K, is reached at $x \approx 0.15$.[9] Moreover, doping also changes the structural properties of $La_{2-x}Sr_xCuO_4$, leading to a structural phase transition similar to the pressure-induced phase transition. For example, according to the results of Ref. 19 a structural OT transition occurs at $T = 10$ K and $x = 0.21$.

In this section the results of the investigation of the effect of pressure and of the degree of doping on the structural properties of $La_{2-x}Sr_xCuO_4$ are reported. The equilibrium crystal structure of $La_{2-x}Sr_xCuO_4$ was modeled using the following approximations. First, it is assumed that the Sr^{2+} impurity ions are distributed randomly through the lanthanum ion sublattice. As a result it can be assumed that in the primitive cell of $La_{2-x}Sr_xCuO_4$ with a fixed concentration x of impurity ions the positions where lanthanum ions would occur in La_2CuO_4 are occupied by La^{3+} with probability $1-x$ and by Sr^{2+} with probability x. In addition, it is known that when La^{3+} ions are replaced by Sr^{2+} ions holes localized on the oxygen ions in the CuO plane form in the crystal. Therefore it can be assumed that O^{2-} ions occupy with probability $1-x$ the positions of the planar oxygens and the ions O^- occupy these positions with probability x. Such an assumption makes it possible to maintain electrical neutrality of the crystal for any value of x. As a result the charge of the ion occupying the position of lanthanum depends on x as $q = 3-x$, and the charge of the ion occupying the position of planar oxygen depends on x as $q = x-2$. In addition, the short-range interaction interaction potential of the ions occupying the lanthanum positions with oxygen ions should also depend on x. This dependence can be represented as

$$V_{\text{ion-O}} = (1-x)V_{\text{La-O}} + xV_{\text{Sr-O}}, \tag{10}$$

where each potential V describes the short-range ion pair interaction (4) and (5). The average potential can be found

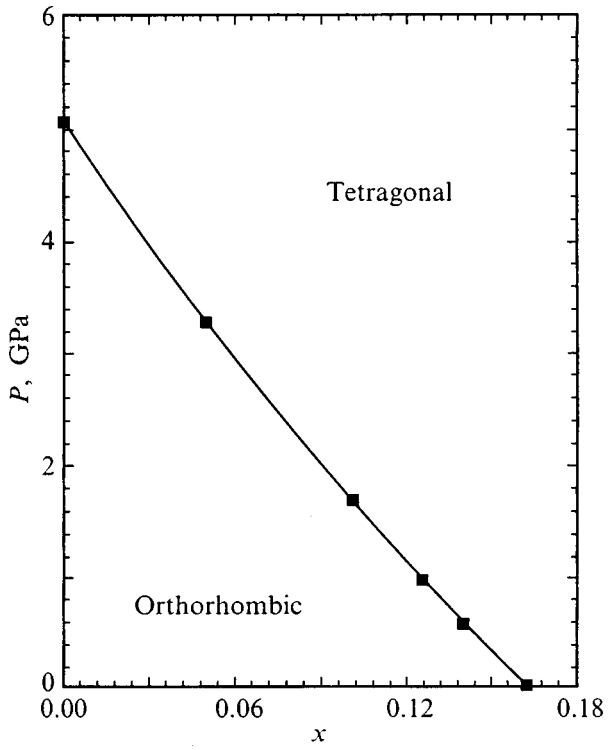

FIG. 5. (P,x) structural phase transition for $La_{2-x}Sr_xCuO_4$.

using Eq. (10) and the parameters found in the present work and in Ref. 9 for the interaction potential between the oxygen ions and the lanthanum and strontium ions.

The results of the modeling of the crystal structure of $La_{2-x}Sr_xCuO_4$ for different values of the concentration x and the pressure P are presented in Fig. 5 in the form of a (P,x) phase diagram relative to the structural properties of the crystal. The form of this diagram is in many respects similar to the (T,x) structural phase diagram determined experimentally in Ref. 12. According to our results, which agree with the experimental data of Ref. 19, just as in the case of hydrostatic compression the introduction of an impurity decreases the rotation angle of the oxygen octahedra and the difference between the lattice constants a and b, and a structural OT transition occurs at some critical impurity concentration. However, it is evident from Fig. 5 that the critical value x_c corresponding to a structural phase transition at atmospheric pressure is 0.16 in our calculation, while the experimentally established value is $x_c=0.21$. In our view this discrepancy is due to the simplicity of our model for taking account of the doping of the crystal. Specifically, it is entirely possible that the Sr^{2+} impurity ions are not arranged chaotically in the crystal but instead form clusters, which undoubtedly should influence the structural characteristics of the crystal as a whole. Moreover, the appearance of holes should result in screening of the Coulomb interaction in the CuO plane.

In closing, it should be noted that the proposed model for calculating the energy of the crystal with the multiparticle Jahn–Teller contribution included explicitly made it possible to describe quite well the structural, vibrational, and elastic properties of La_2CuO_4. Using this model we were able to explain the origin of the structural instability of the crystal lattice of La_2CuO_4, leading to the structural phase transition, and investigate the effect of pressure on the structural characteristics of La_2CuO_4. Moreover, the simple model for describing doping in $La_{2-x}Sr_xCuO_4$ made it possible to investigate theoretically the effect of the degree of doping on the structural properties of $La_{2-x}Sr_xCuO_4$.

This work was supported by the Russian Foundation for Basic Research (grant No. 96-03-32130a).

*E-mail: Anton.Zaharov@usu.ru

[1] N. M. Plakida, *High-Temperature Superconductors. International Educational Program* (Moscow, 1996).
[2] L. Pintschovius, J. M. Bassat, P. Odier, F. Gervais, G. Chevrier, W. Reichardt, and F. Gompf, Phys. Rev. B **40**, 2229 (1989).
[3] S. Koval, R. Migoni, and H. Bonadeo, J. Phys.: Condens. Matter **4**, 4759 (1992).
[4] M. S. Islam, M. Leslie, S. M. Tomlinson, and C. R. A. Catlow, J. Phys. C **21**, L109 (1988).
[5] S. L. Chaplot, W. Reichardt, L. Pintschovius, and N. Pyka, Phys. Rev. B **52**, 7230 (1995).
[6] S. Yu. Shashkin and A. i. Nikiforov, Fiz. Tverd. Tela (Leningrad) **29**, 3133 (1987) [Sov. Phys. Solid State **29**, 1798 (1987)].
[7] A. E. Nikiforov and S. Yu. Shashkin, Fiz. Tverd. Tela (St. Petersburg) **37**, 1325 (1995) [Phys. Solid State **37**, 719 (1995)].
[8] A. E. Nikiforov and S. Yu. Shashkin, Fiz. Tverd. Tela (St. Petersburg) **38**, 3446 (1996) [Phys. Solid State **38**, 1880 (1996)].
[9] A. E. Nikiforov and S. Yu. Shashkin, Fiz. Tverd. Tela (St. Petersburg) **39**, 1094 (1997) [Phys. Solid State **39**, 981 (1997)].
[10] D. V. Fil, O. I. Tokar, A. L. Shelankov, and W. Weber, Phys. Rev. B **45**, 5633 (1992).
[11] V. Ya. Mitrofanov, A. E. Nikiforov, and S. Yu. Shashkin, Solid State Commun. **104**, 499 (1997).
[12] H. Takahashi, H. Shaked, B. A. Hunter, P. G. Radaelli, D. G. Hinks, and J. D. Jorgensen, Phys. Rev. B **50**, 3221 (1994).
[13] O. V. Kovalev, *Representations of the Crystallographic Space Groups: Irreducible Representations, Induced Representations, and Corepresentation* (Gordon & Breach, Langhorne, PA, 1993) [Russian original; Nauka, Moscow, 1986)].
[14] S. Sugai, Phys. Rev. B **39**, 4306 (1989).
[15] E. V. Bezuglyĭ, N. G. Burma, I. G. Kolobov, V. D. Fil', I. M. Vitebskiĭ, A. N. Knigavko, N. M. Lavrinenko, S. N. Barilo, D. I. Zhigunov, and L. E. Soshnikov, Fiz. Nizk. Temp. **21**, 86 (1995) [Low Temp. Phys. **21**, 65 (1995)].
[16] N. Yamada and M. Ido, Physica C **203**, 240 (1992).
[17] N. M. Plakida and V. S. Shakhmatov, Sverkhprovodimost': Fiz., Khim, and Tekh. **6**, 669 (1993).
[18] M. J. Akhtar, C. R. A. Catlow, S. M. Clark, and W. M. Temmerman, J. Phys. C **21**, L917 (1988).
[19] P. G. Radaelli, D. G. Hinks, A. W. Mitchell, B. A. Hunter, J. L. Wagner, B. Dabrowski, K. G. Vandervoort, H. K. Viswanathan, and J. D. Jorgensen, Phys. Rev. B **49**, 4163 (1994).

Translated by M. E. Alferieff